frontiers | Research Topics

Rock physics of unconventional reservoirs, volume II

Edited by
Qiaomu Qi, Lidong Dai, Maxim Lebedev,
Tobias Mueller and Junfang Zhang

Published in
Frontiers in Earth Science

ISSN 1664-8714
ISBN 978-2-8325-5526-2
DOI 10.3389/978-2-8325-5526-2

About Frontiers

Frontiers is more than just an open access publisher of scholarly articles: it is a pioneering approach to the world of academia, radically improving the way scholarly research is managed. The grand vision of Frontiers is a world where all people have an equal opportunity to seek, share and generate knowledge. Frontiers provides immediate and permanent online open access to all its publications, but this alone is not enough to realize our grand goals.

Frontiers journal series

The Frontiers journal series is a multi-tier and interdisciplinary set of open-access, online journals, promising a paradigm shift from the current review, selection and dissemination processes in academic publishing. All Frontiers journals are driven by researchers for researchers; therefore, they constitute a service to the scholarly community. At the same time, the *Frontiers journal series* operates on a revolutionary invention, the tiered publishing system, initially addressing specific communities of scholars, and gradually climbing up to broader public understanding, thus serving the interests of the lay society, too.

Dedication to quality

Each Frontiers article is a landmark of the highest quality, thanks to genuinely collaborative interactions between authors and review editors, who include some of the world's best academicians. Research must be certified by peers before entering a stream of knowledge that may eventually reach the public - and shape society; therefore, Frontiers only applies the most rigorous and unbiased reviews. Frontiers revolutionizes research publishing by freely delivering the most outstanding research, evaluated with no bias from both the academic and social point of view. By applying the most advanced information technologies, Frontiers is catapulting scholarly publishing into a new generation.

What are Frontiers Research Topics?

Frontiers Research Topics are very popular trademarks of the *Frontiers journals series*: they are collections of at least ten articles, all centered on a particular subject. With their unique mix of varied contributions from Original Research to Review Articles, Frontiers Research Topics unify the most influential researchers, the latest key findings and historical advances in a hot research area.

Find out more on how to host your own Frontiers Research Topic or contribute to one as an author by contacting the Frontiers editorial office: frontiersin.org/about/contact

Rock physics of unconventional reservoirs, volume II

Topic editors

Qiaomu Qi — Chengdu University of Technology, China

Lidong Dai — Institute of geochemistry, Chinese Academy of Sciences, China

Maxim Lebedev — Edith Cowan University, Australia

Tobias Mueller — Center for Scientific Research and Higher Education in Ensenada (CICESE), Mexico

Junfang Zhang — Commonwealth Scientific and Industrial Research Organisation (CSIRO), Australia

Citation

Qi, Q., Dai, L., Lebedev, M., Mueller, T., Zhang, J., eds. (2024). *Rock physics of unconventional reservoirs, volume II*. Lausanne: Frontiers Media SA.

doi: 10.3389/978-2-8325-5526-2

Table of contents

frontiers | Frontiers in Earth Science

TYPE Editorial
PUBLISHED 24 September 2024
DOI 10.3389/feart.2024.1477833

OPEN ACCESS

EDITED AND REVIEWED BY
Jeroen van Hunen,
Durham University, United Kingdom

*CORRESPONDENCE
Qiaomu Qi,
qiaomu_qi@163.com
Lidong Dai,
dailidong@vip.gyig.ac.cn
Maxim Lebedev,
m.lebedev@ecu.edu.au
Tobias Müller,
tobias@cicese.mx
Junfang Zhang,
junfang.zhang@csiro.au

RECEIVED 08 August 2024
ACCEPTED 06 September 2024
PUBLISHED 24 September 2024

CITATION
Qi Q, Dai L, Lebedev M, Müller T and Zhang J (2024) Editorial: Rock physics of unconventional reservoirs: Volume II. *Front. Earth Sci.* 12:1477833. doi: 10.3389/feart.2024.1477833

Editorial: Rock physics of unconventional reservoirs: Volume II

Qiaomu Qi[1]*, Lidong Dai[2]*, Maxim Lebedev[3]*, Tobias Müller[4]* and Junfang Zhang[5]*

[1]National Key Laboratory of Oil and Gas Reservoir Geology and Exploitation, Chengdu University of Technology, College of Geophysics, Chengdu University of Technology, Chengdu, China, [2]Key Laboratory for High-Temperature and High-Pressure Study of the Earth's Interior, Institute of Geochemistry, Chinese Academy of Sciences, Guiyang, China, [3]Centre for Sustainable Energy and Resources, School of Engineering, Edith Cowan University, Joondalup, WA, Australia, [4]Department of Seismology, CICESE, Ensenada, Mexico, [5]CSIRO Energy, Kensington, WA, Australia

KEYWORDS

coalbed methane, shale oil, fracture, mineral property, unconventional reservoir

Editorial on the Research Topic
Rock physics of unconventional reservoirs: Volume II

Unconventional oil and gas reservoirs have complex reservoir conditions and different types of resources have their own characteristics. Organic-rich shale and tight sandstone belong to low-permeability reservoirs, with pore structures of strong heterogeneity comprising connected and isolated pores. Coalbed methane reservoirs have the characteristics of low permeability, low reservoir pressure, low gas saturation and strong gas heterogeneity. Due to the diversity of lithology and structural complexity of unconventional reservoirs, the study of their rock properties imposes challenges. Rock physics, a key component of geological and geophysical characterization, establishes the relationship between rock properties and responses of geophysical measurements. Exploring and characterizing different types of unconventional petroleum resources require the development of new rock physics approaches. This theme is intentionally broad in scope, and our special edition provides an overview of 14 articles published in the Research Topic on "Rock Physics of Unconventional Resources: Volume II" which is a sequel to the first volume (Qi et al., 2023). The series addresses a number of key rock physics issues associated with unconventional resources, highlighting laboratory studies, fundamental theories, well-log practices and seismic data processing.

Fracture simulation is important for understanding fluid flow behavior in fractured hydrocarbon reservoirs, especially during the phase of reservoir production. Wang et al. proposed a novel method for Discrete Fracture Network (DFN) modelling constrained by seismic attributes. Compared with the traditional methods, the DFN modelling with the location constraint provides a more realistic fracture model that can accurately reflect the characteristics of fracture distribution. The hydraulic fracturing technique is widely applied to modify the reservoir formation and improving the transport capability in coal seams of low permeability. The evaluation of the hydraulic fracturing process is crucial for hydraulic fracturing operations. Bici et al. addressed the challenges in assessing the location, extension angle, and initial width of fracturing in coal mines. They proposed to evaluate the hydraulic fracturing performance using

reflection borehole radar. They also conducted numerical simulations and investigated the response characteristics of borehole radar signals associated with different types of fracturing-induced cracks. Due to growing global energy demands in recent years, intensified oil and gas exploration activities take place. There is great interest among the industry to explore and develop deep carbonate reservoirs. Due to the strong heterogeneity and diversity of pore spaces in deep carbonate reservoir, the challenges exist in accurately identifying various fracture and cavity types. Lai et al. introduced a Multi-Scale Feature Aggregation Pyramid Network model (MFAPNet) for identifying five different fracture and hole types of carbonate rocks from the Core Rolling Scan images. They summarized the relationship between formation characteristics and the wellbore image data, which provides a basis for the formation evaluation based on image logging data.

Shales are composed of various minerals including quartz, clay and organic matter, etc. The individual properties of these minerals are critical in determining the overall strength and macroscopic deformation of shale. De Lacerda et al. proposed to use energy dispersive spectroscopy and atomic force microscopy to identify different shale components and to evaluate the *in situ* tribo-mechanical properties from the individual phases. The presented methodology provides novel information on friction properties at nanoscale. These measurements provide new insights on the shear deformation behavior of individual components in the shale, which is induced by the presence of mineral-scale asperity contacts. On the other hand, the effects of kerogen maturation on the seismic velocity of shales are difficult to characterize. De Lacerda et al. investigated the effects of kerogen maturation on the shale properties, such as pore volume, microsctructure, organic content, and elastic wave velocities. Their analyses show that the porosity increases through pore creation organic matter consumption. The maturation process results in an increase in the elastic modulus of the organic matter and a decrease in the pore aspect ratio. Shale oil, another important member of unconventional oil and gas resources, mainly exists in the storage spaces such as pores and microfractures. The key parameter for describing the storage space of shale oil is porosity. Su et al. measured the porosity of shale oil samples from the Lianggaoshan Formation of the Sichuan Basin. They applied several methods including saturation liquid method, helium gas charging, and nuclear magnetic resonance (NMR). Based on the results, they developed an calculation method for effective porosity of shale reservoirs of the Lianggaoshan Formation. Another important indicator for movable hydrocarbon in shale oil reservoir is the oil saturation index (OSI). OSI is typically measured by rock pyrolysis experiments. Tian et al. developed a new method to quantitatively calculate the OSI of shale using NMR logging. They conducted 2D NMR measurements on shale oil samples under three states including original, dry and kerosene-saturated. They summarized the NMR T1-T2 characteristics associated with different types of hydrogen-bearing components. Their method shows advantages in avoiding the potential influence from movable oil layers.

Tight sandstone reservoirs normally show complex pore structures and strong heterogeneity. This results in less accurate saturation calculations in tight sandstone formations. The corresponding log interpretations often fail to match with the gas test results. Guo et al. proposed an Archie-type model with variable coefficients to improve the well-logging saturation evaluation in tight sandstone. The results indicate that the cementation and saturation components are largely controlled by clay content and large pore structures, respectively. The new model produces more accurate saturation log in the study area. Coalbed methane (CBM) resources, particularly deep coal seams, have great exploration potential in China. 63% of the total proven CBM resources was found deeper than 1,000 m. There is limited understanding of the primary factors on the occurrence state of deep CBM, which poses significant challenges to the effective exploration of this resources. Shi et al. examined the impact of two external geological control factors (formation temperature and pressure) and three internal geological control factors (pore size, water saturation, and specific surface area) on deep CBM and established a theoretical model for gas content. The results have potential importance in providing key parameters for optimizing deep CBM exploration.

Granite is primarily composed of quartz and feldspar minerals and mainly distributes in crustal strata. Granite exhibits stable structure and high strength under room temperature. With temperature increasing, granite can undergo thermal damages that affect its rock composition, microstructure and pore sizes. This can result in significant change of its mechanical properties. Huang and Li investigated the biotite granite at the Gaoligongshan tunnel site and addressed the relationship between the changes in the mineral composition of granite and mechanical properties at the micro-scale under high-temperature conditions. Tectonogenetic pseudotachylytes are often formed under seismic activities that generate high strain rates within seismic fault zones and/or shear zones. Zhang et al. analyzed the occurrence of ultramafic pseudotachylytes from the Luobusha ophiolite complex in the Yarlung Zangbo suture zone, providing fault-rock evidence of paleo-earthquakes. They presented mineral chemical, microtextural and petrographic data of the ultramafic pseudotachylyte at Luobusha area. Their results provides insights on the interaction mechanism of high-pressure metamorphism and co-seismic deformation. The information of fault gauge properties is important as they greatly affect both the fault slide stability and frictional strength. Ren designed a steady-state velocity step test, and successfully determined the values of friction stability parameter (FSP) for both the gypsum fault gauge and the fault gauge consisting of different components of the kaolinite/calcite mixture. He established a functional relationship between the mass fraction of kaolinite and FSP values of the mixture fault gauge. The study serves as a useful reference for designing future experiments and numerical simulations on fault stability.

Quantitative characterization of reservoir fluid distribution is important for activities such as monitoring of CO_2 geological storage and enhanced oil and gas recovery. Seismic waves can be sensitive to fluid saturation and its distribution and therefore, it is essential to establish the relationship between seismic signatures and reservoir fluid properties. Dispersion and attenuation of partially saturated rocks are primarily due to wave-induced fluid flow mechanism. Sun et al. proposed a new method for numerically predicting seismic dispersion and attenuation due to mesoscopic flow using a 3D fluid distribution obtained by a micro-CT image as input. There is a good match between the experimental data and numerical simulations,

which confirms the validity and accuracy of their method. The quality of seismic data directly affects the results of quantitative seismic interpretation. One of the primary tasks of seismic data processing is to improve the signal-to-noise ratio (SNR). Zhang et al. proposed a joint denoising method using seismic velocity and acceleration signals. The method achieves effective seismic signal and noise suppression by conducting Independent Component Analysis (ICA) based on velocity and acceleration signals of the same trace. The joint denoising method shows advantages in enhancing the dominant frequency and time resolution of seismic data.

In this editorial, we present the main highlights of the 14 articles published in the Research Topic "Rock Physics of Unconventional Reservoirs: Volume II" of the journal Frontiers in Earth Science. While unconventional resources typically are very complex to model, the underlying rock physics plays an important role in integrating geophysical measurements across different scales, i.e., core, well-log, and seismic, to improve the accuracy of formation evaluation and reservoir characterization. We summarize the recent findings on unconventional rock physics and hope they will be useful for petrophysicist, geophysicist, and petroleum engineers to gain deep insights in this field.

Author contributions

QQ: Writing–original draft, Writing–review and editing. LD: Writing–original draft, Writing–review and editing. ML: Methodology, Supervision, Writing–review and editing. TM: Methodology, Supervision, Writing–review and editing. JZ: Methodology, Supervision, Writing–review and editing.

Reference

Qi, Q., Dai, L., Lebedev, M., Müller, T., and Zhang, J. (2023). Editorial: rock physics modeling and well-log practice for unconventional reservoirs. *Front. Earth Sci.* 11:1234699. doi:10.3389/feart.2023.1234699

Funding

The author(s) declare that no financial support was received for the research, authorship, and/or publication of this article.

Acknowledgments

The topic editors would like to thank all contributing authors to this Research Topic and the editorial staff of Frontiers in Earth Science for making this special collection possible.

Conflict of interest

JZ was employed by CSIRO Energy.

The remaining authors declare that the research was conducted in the absence of any commercial or financial relationships that could be construed as a potential conflict of interest.

The author(s) declared that they were an editorial board member of Frontiers, at the time of submission. This had no impact on the peer review process and the final decision.

Publisher's note

frontiers | Frontiers in Earth Science

TYPE Original Research
PUBLISHED 25 May 2023
DOI 10.3389/feart.2023.1131730

OPEN ACCESS

EDITED BY
Junfang Zhang,
Commonwealth Scientific and Industrial Research Organisation (CSIRO), Australia

REVIEWED BY
Jie Zou,
Chengdu University of Technology, China
Quanzhong Guan,
Chengdu University of Technology, China

*CORRESPONDENCE
D. L. P. de Lacerda,
douglas.lacerda@petrobras.com.br

SPECIALTY SECTION
This article was submitted to Solid Earth Geophysics, a section of the journal Frontiers in Earth Science

RECEIVED 26 December 2022
ACCEPTED 23 March 2023
PUBLISHED 25 May 2023

CITATION
de Lacerda DLP, Morschbacher MJ, Justen JCR, Vasquez GF, Spigolon ALD, Menezes TR and Skinner R (2023), On the evolution of artificially matured hydrocarbon source rocks. *Front. Earth Sci.* 11:1131730. doi: 10.3389/feart.2023.1131730

On the evolution of artificially maturated hydrocarbon source rocks

D. L. P. de Lacerda[1]*, M. J. Morschbacher[1], J. C. R. Justen[1], G. F. Vasquez[1], A. L. D. Spigolon[1], T. R. Menezes[2] and R. Skinner[1]

[1]Centro de Pesquisas Leopoldo Américo Miguez de Mello (Cenpes), Rio de Janeiro, Brazil, [2]Petrobras Exploration and Production, Rio de Janeiro, Brazil

The elastic moduli are a function of properties that could vary between samples and change during maturation. Consequently, the effects of organic matter maturation on the elastic wave velocities of organic-rich rocks are challenging to describe. This work analyzes the isolated maturation effects on the organic content, pore volume, microstructure, and propagation velocities of elastic waves. To avoid any initial rock heterogeneity, we prepared a series of homogeneous samples from a unique outcrop block collected on the Eagle Ford formation with mineral composition initially determined using X-ray diffraction. From the initial set, four samples were held in their original condition and four were artificially maturated by hydropyrolysis until transformation rates were up to 95%. Then, the evolution of the sample properties was examined using an association of LECO TOC, Rock-Eval pyrolysis, vitrinite reflectance, mercury intrusion porosimetry (MIP), and ultrasonic pulse propagation. In addition, scanning electron microscopy images registered the microstructure evolution. To evaluate the effects of maturation on pore geometry and the organic matter elastic moduli, we analyze the relationship between the measured quantities using a rock physics inclusion model with the unmeasured properties taken as fitting parameters. The hydropyrolysis maturation increases the vitrinite reflectance from the initial 0.55% to 1.34% on the most matured sample. A total organic carbon reduction from 4.2% to 2.1% and a porosity increase from 9.2% to 21% are associated with observed maturation. The geochemical characterization on cleaned samples reveals an initial increment of soluble organic matter followed by a monotonical reduction related to oil migration out of bulk volume. The measurement of wave propagation velocities as a function of confining pressure displays an increasing pressure sensitivity with a downward trend in both velocity moduli. The petrophysical analysis indicates that the porosity increases through organic matter consumption and pore creation. The rock physics diagnoses indicate a decrease in the pore aspect ratio with an increase in the elastic modulus of the organic matter with maturation.

KEYWORDS

shale, mudrock, Eagle Ford, rock physics, maturation, source rock, organic matter

1 Introduction

In traditional petroleum systems, mudrocks and shales can play the roles of both the cap and source rock (Bjorlykke, 2010). The relevance of understanding the physical properties of these lithologies becomes evident when considering that 30% of failures in exploratory wells are related to charging and 45% are related to sealing problems (Rayeva et al., 2014). More recently, the self-sourced reservoirs on unconventional shales increased the demand to understand the physical properties of those lithologies and the need for mapping them in seismic conditions (Vernik, 2016). In fact, the mapping of geochemical properties in seismic conditions could also contribute to source/cap rock delimitation and the analysis of migration pathways (Hansen et al., 2019). As elastic wave propagation velocities link the geochemical rock properties to the seismic response, characterizing the effects of organic matter content and maturation in the elastic properties are essential for understanding the seismic signal (Avseth et al., 2010).

Natural series of mudrocks were previously characterized in other publications. For example, Vernik and Nur (1992) described black shales from the Bakken Formation as a vertically transverse isotropic medium with wave propagation velocities, its anisotropy, and the effects of confining pressure on those parameters dependent on kerogen content, maturation, and the occurence of bedding-parallel microcracks. Vernik (1994) proposed that the closure of bedding-parallel microcracks, induced by the generation process, causes the high sensitivity of the compressional velocity propagating through shale laminations to confining pressure, especially at low range (Vernik and Landis, 1996; Vernik and Liu, 1997).

Studying the effect of maturation on naturally maturated samples is challenging as they are usually limited to narrow maturation ranges (Allan et al., 2014). Working with a series of artificially maturated samples is one alternative that overcomes the limitation imposed by using the rarely available naturally maturated ones (Lewan and Birdwell, 2013). Allan et al. (2014) measured the compressional wave velocity in samples maturated by dry pyrolysis. Allan et al. (2016) discussed the modification of anisotropic compressional and shear velocities due to fractures induced by hydrocarbon generation in samples of Barnett and Green River shales artificially maturated by dry pyrolysis. Suwannasri et al. (2018) reported increasing porosity and sensitivity of propagation velocities to pressure in a series of Eagle Ford samples maturated by dry pyrolysis. Shitrit et al. (2017) applied a rock physics model (RPM) to analyze the effects of maturation and composition in chalk samples from the Ghareb and the Mishash formations with generation induced by dry pyrolysis.

Despite the successful use of anhydrous pyrolysis in artificial maturation, the hydropyrolysis setup better replicates the generated products and the migration of oil (Lewan, 1994). In one of the few studies with samples prepared using hydropyrolysis, Zargari et al. (2013) reported a reduction in the microscale Young's modulus of samples maturated at 350°C. Environmental relevance was also studied by Moyer and Prasad (2017), who compared both protocols and reported more efficient conversion from kerogen into bitumen with higher variations of elastic properties in samples prepared in hydrous conditions. Still, further investigations are necessary to understand the effects of hydropyrolysis on the elastic properties of organic-rich mudrocks.

The processes triggered by the maturation of organic matter can change the composition, microstructure, porosity, and saturation of the rock. Different approaches describe the individual contribution of those parameters to the macroscopic elastic properties. The presence of kerogen in solid composition was described by a modified Backus average (Vernik and Landis, 1996), inclusions (Wang et al., 2018), and solid substitution (Zhao et al., 2016). The maturation also modifies the kerogen properties, which can be calculated from first principles (Ibrahim et al., 2020), modeled empirically (Sengupta et al., 2022), or defined *a priori* (Zhao et al., 2016). There are studies that model the porosity as inclusions (Zhao et al., 2016) and fractures (Liu et al., 2020), with fluid effects considered after using Gassmann equations (Zhao et al., 2016). The maturation effects on the elastic properties can be obtained as the summation of all previous parameters, in addition to the structural modification from load bearing to filling kerogen considered by some authors (Zhao et al., 2016; Shitrit et al., 2017). Regarding the complexity of the models, Dvorkin et al. (2021) suggested that elaborated models can lead to a high number of unknown inputs and proposed a "simple as possible" theoretical approach to reduce free parameters and the use of unmeasured properties.

In this study, we present experimental results from a series of Eagle Ford samples artificially maturated by isothermal hydropyrolysis with a single heating cycle for each sample. The obtained samples, in addition to a set of four immature ones, had their petrophysical, geochemical, and elastic properties characterized in the laboratory using mercury intrusion porosimetry (MIP), LECO TOC, Rock–Eval pyrolysis, vitrinite reflectance, and ultrasonic pulse propagation. We constructed a petrophysical model from where the density of kerogen and the oil can be estimated. We also elaborated a simple inclusion RPM to diagnose the effects of maturation in pore geometry and the elastic properties of the organic matter.

2 Materials and methods

This section presents the materials and the hydropyrolysis method used to prepare a series of organic-rich samples from immature to depleted. The induced maturation process modifies multiple properties of the rock and kerogen itself, as detected by the characterization methods (MIP, LECO TOC, Rock–Eval pyrolysis, and vitrinite reflectance). The compressional and shear wave velocities, measured by ultrasonic pulse propagation, are functions not only of all these properties but also of the microstructure, which we visualized using scanning electron microscopy (SEM). This section also presents the characterization methods mentioned previously, the parameters calculated from direct measurements, and the RPM used for data analysis.

2.1 Sample preparation

A block of Eagle Ford shale, supplied by Kocurek Industries Inc., was initially segmented in 15 prisms of 4 cm × 5 cm × 4 cm, with a number assigned to each of them as identification. LECO TOC and Rock–Eval pyrolysis on sample 15 allowed the block to be identified

TABLE 1 List of samples and the experimental programs used for artificial maturation.

Sample	Time (h)	Temperature (°C)	Pressure (PSI)	Heating rate (°C/min)
3, 7, 14, and 15	Not maturated			
1	72	320	1,698	8.3
2	72	360	2,843	9.0
9	72	340	2,208	11.7
12	72	300	1,287	8.5

as an organic-rich (TOC = 4%) immature (IH = 629 mg HC/g TOC) mudrock. After the geochemical first result, samples 3, 7, and 14 were preserved for characterization of the immature state, and samples 1, 2, 9, and 12 were chosen to be artificially maturated.

During hydropyrolysis, the sample was positioned with horizontal bedding in the bottom of a pressure vessel. To avoid cracking along the bedding, the sample was held by a clamp made of AISI316 steel, limiting expansion along the vertical direction (Lewan and Birdwell, 2013). The vessel was filled with a calculated amount of distilled and deionized water to keep the sample immersed during the experiment. The closed system was heated for 72 h under temperatures between 300°C and 360°C, as shown in Table 1. A more detailed description of the experimental conditions can be found in Spigolon et al. (2015).

The immature samples and the matured ones were subsampled for mineralogy, geochemistry, and porosity measurements. Then, the remaining material was machined into a 1-inch plug used for petroelastic characterization by ultrasonic pulse propagation. After this, each plug was resampled, and its microstructure was characterized using an SEM.

2.2 Mineralogy

The total mineralogy fractions were examined by X-ray diffraction (XRD) on the original samples. For total mineralogy analysis, each sample was micronized and pressed into one tablet with aleatorily distributed particles. The XRD diffractogram was acquired on a D/MAX-2,200/PC (Rigaku, Tokyo) and analyzed using the Rietveld method to determine the weight fraction of the identified minerals (Young, 1995).

2.3 Organic matter content

A set of geochemical measurements was obtained to describe the evolution of the content, type, and maturation of organic matter. Total organic carbon was measured by the LECO TOC, and its type and oil potential evolution were analyzed using Rock–Eval pyrolysis results. The maturation was described in terms of vitrinite reflectance and transformation rate. In order to make this work self-contained, we describe the techniques and their results in the following paragraphs.

The weight fraction of the organic matter content was determined on a carbon analyzer model SC-144 (LECO, St. Joseph, Michigan) using an infrared detector. Before characterization, the subsample was fragmented, and the mineral carbonates were removed by hydrochloric acid (HCl). Then, the remaining aliquot was combusted at 1,350°C under constant oxygen flux, while the generated CO_2 was measured. By hypothesis, all inorganic carbon was removed by acidification, so all the liberated carbon was from organic matter. We refer to Behar et al. (2001) for more information about sample preparation and the LECO analyzer.

During the Rock–Eval test, the sample is heated from 300°C to 650°C in an inert environment while the hydrocarbon emission is measured. The monitored emission occurs in peaks associated with thermovaporization of free oil, called peak S1, and the organic matter cracking, called peak S2. The surface areas of peaks S1 and S2 are respectively measures of free volatile hydrocarbons content and the petroleum generation potential. The temperature of peak S2 is also recorded as the Tmax parameter. In the second stage, the sample was heated under the oxidizing environment, and the CO_2 yield is recorded in mg CO_2/g rock as peak S3. For a more detailed description, we may refer to Behar et al. (2001).

The LECO TOC and Rock–Eval pyrolysis results were analyzed together to characterize the type and maturation of organic matter. The composition changes since the generation process modifies the proportion of hydrogen, oxygen, and carbon available on the kerogen structure. The hydrogen index (HI = S2/TOC) and oxygen index (OI = S3/TOC), as measurements of hydrogen/carbon and oxygen/carbon proportions, are also altered in a trajectory that is indicative of kerogen type. The Blanc–Valleron plot of S2 as a function of TOC and HI *versus* OI in a van Krevelen-type diagram were used to evaluate and classify the kerogen type and evolution as the function of maturation (Espitalié et al., 1977; Langford and Blanc-Valleron, 1990).

The maturation itself was determined using the transformation rate and vitrinite reflectance. The transformation rate is calculated as

$$TR = \frac{S2o - S2}{S2o} \quad (1)$$

where S2o and S2 are the oil potential for the sample in its original condition and for the actual sample, respectively. The S2 is a measure of how much hydrocarbon the kerogen can generate. This value is reduced with the advancement of maturation until all the oil potential is depleted. TR is a measure of how much of the oil potential was depleted (Spigolon et al., 2015).

Vitrinite is an organic material found on shales and mudrocks. Its reflectivity changes as a function of the heating, allowing the use of reflectance as a method for estimating the maturation of the organic matter. The vitrinite reflectance, Ro, can be used to determine the actual maturation stage. The analytical procedures

of reflectance measurements follow the standardization of the *Measurement of Reflectance on Vitrinite occurring as Dispersed Organic Matter* of the ICCP Accreditation Program–DOMVR (Borrego et al., 2006; ASTM-D7708-14, 2014; Hackley, 2015). The classification followed Horsfield and Rullkötter (1994), with the intervals 0.5% < Ro < 1.3% and 1.3% < Ro < 2.0% measured for samples in oil and wet-gas windows, respectively. In a similar approach, the oil window can be subdivided as early mature (0.6% < Ro < 0.65%), peak (0.65% < Ro < 0.9%), and late mature (0.9% < Ro < 1.35%) (Peters and Cassa, 1994).

2.4 Bitumen saturation

The LECO TOC measures the carbon associated with kerogen and free hydrocarbons. To identify the different contributions, the free hydrocarbons saturating the pores of the rock were removed using accelerated solvent extraction, and LECO TOC was conducted again on the cleaned sample. This procedure completely removes the free oil and part of the polar components, with the remaining TOC being associated with kerogen only.

2.5 Porosity

Mercury intrusion porosimetry (MIP) tests were realized using a Micromeritics' AutoPore IV 9500. Before testing, the sample was heated at 100°C for 24 h to dry pore moisture. A subsample with known mass is placed on a glass sample cell (penetrometer), which is inserted in the equipment. After vacuum, mercury is injected under the increasing applied pressure up to the limit of 60,000 PSI, while the intruded volume is measured. Initially the mercury occupies all the volume in the vase, measuring the sample bulk volume. After a threshold, the mercury intrudes the sample, giving a measure of pore volume. Porosity and density are directly calculated from these measurements (Webb, 1993).

The pore volume accessible to mercury intrusion under a given pressure is limited by the capillary pressure, PC, which is determined by the pore-throat radius, r. According to Laplace equation,

$$r = \frac{2\sigma \cos(\theta)}{PC}. \quad (2)$$

We can convert the applied pressure to pore-throat radius given the surface tension σ = 485 dina/m and the contact angle θ = 130° (ASTM, 2018).

2.6 Microstructure

A set of scanning electron microscopy images was acquired as part of the microstructure characterization procedure (Walls and Sinclair, 2011). As part of this procedure, the subsamples removed from the plug are ion-milled to prepare the surface for acquisition of SEM images. The milled surfaces were imaged with increasing resolutions. In this work, we show a set of images acquired with a pixel resolution of 250 nm. A non-local means filter was applied using the software FIJI to improve the identification of the key features.

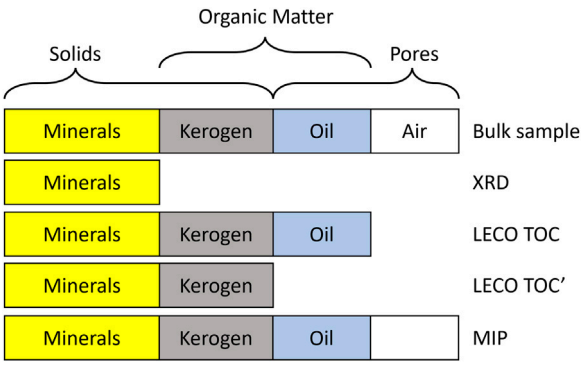

FIGURE 1
The first line shows the representations of material phases that compose the bulk mudrock and its grouping in solids, organic matter, and pores. The following lines show the materials measured by XRD, LECO TOC, and MIP. The LECO TOC' is the measurement after sample cleaning.

2.7 Ultrasonic pulse propagation

The ultrasonic pulse propagation experiment was performed using the Autolab 500 (New England Research) equipped with one pair of transducers positioned to measure propagation velocities through the bedding. Each pair of transducers is composed of one emitter, which can send one compressional and two orthogonal shear waves, and one receiver that can register the arrival of the waves. The registered signal is used to measure the wave travel time. Measuring the distance traveled by the wave, we calculate the compressional and shear wave velocities along this direction. During the experiment, the samples are held under hydrostatic confining pressure, which allows measuring the velocities as a function of confining pressure.

2.8 Petrophysical relations

In general, mudstone rocks present a complex composition, and there are multiple ways to group and classify their components. Zhao et al. (2016), for example, described the matrix as a composition of clay minerals, non-clay minerals, and kerogen, with the pore space filled with water, oil, and gas. Another approach considers the sample as a solid phase of minerals and kerogen with pores partially filled with air and oil/bitumen (Shitrit et al., 2017). We use the measurements to determine the proportions using the second approach.

The characterization methods were applied in different cleaning conditions, consequently changing the fractions measured by each experiment. A summary of the experiments and the measured fractions is shown in Figure 1. In this section, the relationship between the main physical properties is inferred from the experimental results, considering the distribution of fractions.

2.8.1 Mineral fraction

The DRX measurements give the mass fraction for each constituent mineral. Suppose that X_i, $V_i^{'}$, and ρ_i are the mass fraction, the volume, and the density of *i*th mineral phase,

respectively. If $M_m^{'}$ is the total mineral mass, the average density of the mineral phase, ρ_M, is

$$\frac{1}{\rho_M} = \frac{\sum V_i^{'}}{M_m^{'}} = \sum \frac{X_i}{\rho_i}, \tag{3}$$

with the volumetric fraction, χ_i

$$\chi_i = \frac{\rho_i}{\rho_M} X_i, \tag{4}$$

where the summation is over all the identified minerals and the densities. The prime was used to differentiate measurements without OM removal.

2.8.2 Kerogen and oil fraction

LECO TOC measurements were conducted on two conditions: before-cleaning and after-cleaning. The compositional difference between the two conditions is the absence of an oil phase on the cleaned sample, as represented in Figure 1. This section presents an analysis of TOC measured under the two conditions to determine the weight fraction of oil and kerogen on the overall material balance.

The total mass of the materials, M_{mat}, for samples before cleaning is given by summating the minerals, M_m, kerogen, M_k, and oil, M_o, masses.

$$M_{mat} = M_m + M_k + M_o. \tag{5}$$

The TOC is a measure of carbon, M_c, associated with organic mass, although the organic matter has a complex composition with other elements in its structure. The carbon is just a fraction f_k of total organic matter mass, $M_k + M_o$ (Crain and Holgate, 2014). The before-cleaning TOC can be written as follows:

$$TOC = \frac{f_k (M_k + M_o)}{M_m + M_k + M_o}. \tag{6}$$

The contributions of the oil are removed for the after-cleaning measurement.

$$TOC' = \frac{f_k M_k}{M_m + M_k}. \tag{7}$$

The ratio M_o/M_k is obtained from Eqs 6, 7. We isolate the products $M_m TOC$ *and* $M_m TOC'$ on both and divide the resulting equations to obtain

$$\frac{M_o}{M_k} = \frac{TOC}{TOC'} \frac{1 - TOC'}{1 - TOC} - 1. \tag{8}$$

We isolate the factor M_k/M_{mat} on Eq. 6 and use Eq. 8 to recover

$$\frac{M_k}{M_{mat}} = \frac{TOC/f_k}{1 + \frac{M_o}{M_k}} = \left(\frac{TOC'}{TOC} \cdot \frac{1 - TOC}{1 - TOC'}\right) \frac{TOC}{f_k} \equiv \alpha \cdot \frac{TOC}{f_k}, \tag{9}$$

$$\frac{M_o}{M_{mat}} = (1 - \alpha) \frac{TOC}{f_k}. \tag{10}$$

It can be seen from Eq. 8 that the **α** parameter is the fraction of kerogen on the total organic mass. It can be calculated for each sample based on the results of LECO pyrolysis. For our range of measures $(1 - TOC')/(1 - TOC) = 1$.

TABLE 2 Properties of organic and non-organic constituents as given by [1] (Mavko et al., 2009), [2] (Zhao et al., 2016), and [3] found by RPM diagnoses.

	ρ (g/cm^3)	K (GPa)	G (GPa)
Clay[1]	2.46	47	28
Gypsum[1]	2.31	58	30
Quartz[1]	2.65	38	44
Calcite[1]	2.71	77	32
Kerogen[2]	1.10	3.5	1.75
Oil[3]	0.65	2	-

2.8.3 Density relations and volume fractions

The mercury impregnates the porous empty spaces during MIP, giving a measurement of bulk volume, V_b, pore volume, V_p, and impenetrable material volume, V_{mat}. The last one is a combination of mineral, V_m, kerogen, V_k, and oil, V_o, volumes. For this experimental condition, we obtained

$$V_{mat} = V_m + V_k + V_o, \tag{11}$$

$$V_b = V_m + V_k + V_o + V_p, \tag{12}$$

$$M_{mat} = M_m + M_k + M_o, \tag{13}$$

where the material mass, M_{mat}, is expressed again in terms of mineral, M_m, kerogen, M_k, and free fluid, M_o masses, as shown in Eq. 5.

The aforementioned equations result in the traditional one

$$\rho_B = (1 - \phi)\rho_{mat} \tag{14}$$

that describes the relationship between porosity, ϕ, material density, ρ_{mat}, and bulk density, ρ_B. ρ_{mat} can bewritten as

$$\frac{1}{\rho_{mat}} = \frac{V_m}{M_{mat}} + \frac{V_k}{M_{mat}} + \frac{V_o}{M_{mat}}$$

$$\frac{1}{\rho_{mat}} = \frac{1}{\rho_m}\frac{M_m}{M_{mat}} + \frac{1}{\rho_k}\frac{M_k}{M_{mat}} + \frac{1}{\rho_o}\frac{M_o}{M_{mat}}$$

$$\frac{1}{\rho_{mat}} = \frac{1}{\rho_m} + \left(\frac{1}{\rho_k} - \frac{1}{\rho_m}\right)\frac{M_k}{M_{mat}} + \left(\frac{1}{\rho_o} - \frac{1}{\rho_m}\right)\frac{M_o}{M_{mat}},$$

where Eq. 13 was used in the last step and mass fractions were previously determined from TOC measurements. Applying Eqs 9, 10, we get

$$\rho_{mat} = \left(\frac{1}{\rho_m} + \left(\frac{1}{\rho_k} - \frac{1}{\rho_m}\right)\alpha \cdot \frac{TOC}{f_k} + \left(\frac{1}{\rho_o} - \frac{1}{\rho_m}\right)(1 - \alpha)\frac{TOC}{f_k}\right)^{-1}, \tag{15}$$

The volume fractions of the organic materials can be determined converting the mass fractions as

$$\beta_k \equiv \frac{V_k}{V_b} = \frac{\rho_b}{\rho_K}\alpha \cdot \frac{TOC}{f_k}, \tag{16}$$

$$\beta_o \equiv \frac{V_o}{V_b} = \frac{\rho_b}{\rho_o}(1 - \alpha) \cdot \frac{TOC}{f_k}, \tag{17}$$

and the mineral proportion is obtained from the total volume.

TABLE 3 XRD results showing the fraction of mass of the following minerals: clay and mica (C+M), gypsum (GIP), quartz (QTZ), calcite (CAL), dolomite (DOL), and pyrite (Py). We also show the average values and the XRD results reported in Kreisserman and Emmanuel (2018) in the line average and KE2018, respectively.

Sample	C+M	GIP	QTZ	CAL	DOL	PY
3	7	3	29	61	0	0
7	7	3	27	63	0	0
14	7	3	28	62	0	0
15	7	3	25	65	0	0
Average	7	3	27	63	0	0
KE2018	9 ± 2.2	4.7 ± 2.2	21.5 ± 1.3	61 ± 6.6	2.6 ± 1.1	0.8 ± 0.1

2.9 Rock physics modeling

The first step of RPM is to define the properties of the rock elements. The mineral properties were recovered from Mavko et al. (2009), as shown in Table 2. Although the properties of organic materials are more difficult to determine, as they could change as a function of maturity itself (Ibrahim et al., 2020). Therefore, we assume from the start the occurrence of immature kerogen described by Zhao et al. (2016). The remaining parameters f_k and ρ_o were interpreted from MIP intrusion results using Eq. 15. The resulting fluid density is written in the same table with the properties of kerogen.

The next step is the calculation of the effective elastic modulus by successive addition of materials. The mineral elastic modules were calculated using the Voigt–Reuss–Hill (VRH) average with the volume fractions determined from Eq. 5 and XRD results:

$$C = \frac{1}{2}\cdot\left(\sum\frac{\chi_i}{C_i} + \sum\chi_i\cdot C_i\right), \tag{18}$$

where C can be the bulk modulus or the shear modulus.

To allow fine-tuning of the matrix elastic modulus, the mineral–kerogen mixture was calculated using a matrix stiffness index (MSI) as weight in the Voigt–Reuss–Hill (VRH) average (Allo, 2019).

$$C = (1-MSI)\cdot\left(\frac{1-k}{C_m} + \frac{k}{C_k}\right) + MSI\cdot\left((1-k)\cdot C_m + k\cdot C_k\right), \tag{19}$$

where k is the kerogen volume fraction, C is the elastic module, and MSI is an adjustable parameter between 0 and 1. As the model was constructed by successive averages, $k = \beta_k/((1-\beta_o)(1-\varnothing))$. The oil-filled pores were added using the differential effective medium (DEM) model without critical porosity corrections, and the porous aspect ratio (AR) was used as the fitting parameter in a proportion of $\beta_0/(1-\varnothing)$. The empty pores were added using DEM without critical porosity and a fluid with low modulus.

The last step is calculating the propagation velocities of compressional and shear waves. For this task, the mudrocks are usually modeled as vertically transverse isotropic (Vernik and Nur, 1992), although there are works using the isotropic model (Dvorkin et al., 2021). Sone and Zoback (2013) demonstrated that the isotropic Young's modulus calculated in VTI shales are consistent with the anisotropic formal calculation. Inspired by this work, we will assume the isotropic equations as

$$V_P = \left(\frac{K - 4G/3}{\rho_B}\right)^{1/2}, \tag{20}$$

$$V_S = \left(\frac{G}{\rho_B}\right)^{1/2}, \tag{21}$$

where K, G, and ρ_B are the bulk modulus, shear modulus, and density, respectively (Mavko et al., 2009).

3 Results

The XRD results for each sample and the average weight fraction of each mineral are shown in Table 3. Calcite and quartz account for 63% and 27% of the weight, respectively. Together they represent 90%; the other 10% of the mass is composed of clay minerals and gypsum. With less than 50% of clay and more than 30% of carbonates in weight, this sample can be classified as a carbonate mudstone using the Donovan et al. (2017) classification, which is usually associated with oil-prone organic matter.

The geochemical characterization results are shown in Table 4. The same table shows the sample named Original, whose properties are the average of the immature samples properties. We also exhibit the average properties calculated in the low-resolution dataset available in French et al. (2019) as the sample FR2019. To allow the comparison with our immature samples, we filtered the French dataset in the interval of Tmax < 425. The Ro of 0.55% with Tmax < 435 and IH <500 values indicates that the original sample is composed of immature organic matter (Horsfield and Rullkötter, 1994; Peters and Cassa, 1994; Vernik and Landis, 1996). The samples heated at 300°C are at the peak of generation. The samples heated between 320°C and 360°C have 1.07%<Ro<1.34%. Consequently, they are in the late mature oil windows (Peters and Cassa, 1994).

The effects of maturation on the geochemical properties are illustrated in Figure 2. The thermal cracking of kerogen into oil resulted in the reduction of the TOC with the advancement of the transformation rate, as shown in Figure 2A. The proportion of kerogen on the organic matter mass exhibits a fast decrease followed by an almost linear increase that can be interpreted by the migration of the oil out of the sample (Figure 2B). The oil generation also results in S2 reduction, as noticeable in the Blanc–Valleron diagram (Figure 2C). The depletion also reduces HI and OI, which can be seen as the displacement of the points toward the origin on type van Krevelen diagram (Figure 2D). As shown in Figures 2C, D, the original kerogen can be classified as oil-prone I or II–I.

The porosity and density obtained by mercury intrusion results are listed in Table 5. The pore-throat radius distributions are displayed in Figure 3A for the sample in the original condition (gray) and the samples heated at 300°C (red), 320°C (blue), 340°C (green), and 360°C (yellow). The distribution of pore throats for the immature samples are similar between them, whereas, for the maturated samples, the distributions shift towards larger radius values as function of the increasing transformation rate and Ro. The porosity and the variation of OM volume are exhibited in Figure 3B as closed black and open red circles, respectively. The

10.3389/feart.2023.1131730

TABLE 4 LECO TOC and Rock–Eval pyrolysis results with TOC in weight %, S1 in mg HC/g rock, S2 in mg HC/g rock, S3 in mg CO_2/g rock, RI in weight %, HI in mg HC/TOC, IO in mg CO_2/TOC, Tmax in °C, TT in %, and Ro in % and TOC ′ after-cleaning in weight %. The original sample is the average of samples 3, 7, 14, and 15. The FR2019 is the result reported in French et al. (2019).

Sample	TOC	S1	S2	S3	RI	HI	OI	Tmax	TT	Ro	TOC ′
3	4.3	1.5	28.8	0.7	40	667	16	423	0	X	X
7	4.2	1.2	28.1	0.5	34	672	12	424	0	X	X
14	4.2	1.2	28.2	0.6	36	673	14	425	0	X	X
15	4.3	1.5	27.9	0.6	33	649	14	425	0	0.55	4.3
12	4.0	1.4	22.9	0.2	36	572	6	433	20	0.69	2.5
1	3.1	1.3	13.1	0.2	34	422	7	434	54	1.07	2.0
9	2.5	0.7	5.7	0.3	33	228	12	441	80	1.32	2.0
2	2.1	0.6	1.4	0.2	34	69	10	455	95	1.34	2.0
Original	4.2	1.4	28.2	0.6	36	665	14	424	0	0.55	4.3
FR2019	4.3	0.4	26.3	0.6	X	602	15	412	X	X	X

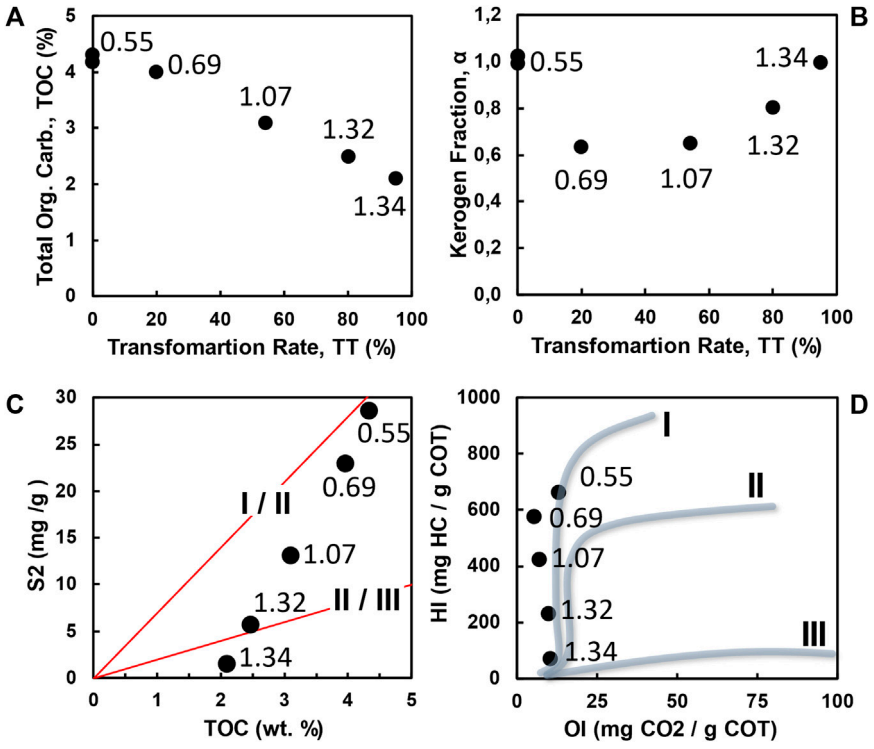

FIGURE 2
(A) TOC and the **(B)** kerogen fraction as a function of TT measured on the samples (black circles). The **(C)** Blanc–Valeron and **(D)** type van Krevelen diagrams are also exhibited. In all plots, the measured points are identified by the Ro value.

porosity is equal to OM volume loss for the samples in the initial condition, by definition. The porosity increases as the TR advances, but the OM volume reduction is smaller than the measured porosity for samples since the beginning of the oil window.

The SEM images are shown in Figure 4. The images are disposed in increasing maturation order with images from samples in the original condition and heated at 300°C, 320°C, 340°C, and 360°C in positions (a), (b), (c), (d), and (e), respectively. For this set of images, it is possible to identify pores by their characteristic darker gray levels in contrast to a brighter background associated with mineral phases. The OM is associated with the intermediate gray level. For all the samples, the OM occurs preferentially in the horizontal direction. Also, the

TABLE 5 Mercury Intrusion Porosimetry results showing porosity and density.

Sample	ϕ (%)	ρ_M (g/cm^3)
3	8.9	2.46
7	9.2	2.45
14	9.6	2.41
15	9.1	2.45
12	9.5	2.35
1	14.3	2.42
9	18.3	2.53
2	21.0	2.57

tendency to increase porosity with maturation is easily identified by a progressive clustering of voids on the presented sequence of images.

Specifically, on the images of samples not pyrolyzed (Figure 4A) and pyrolyzed at 300°C (Figure 4B), it is possible to identify grains of organic matter without internal porosity with well-defined contours and a continuous interface with the surrounding mineral phase (yellow arrows). The continuous grains are also visible on samples prepared at 320°C (Figure 4C) and 360°C (Figure 4D), which also exhibit the creation of porosity mainly at the interfaces between the OM and the mineral (red arrows). In the BSE image of the sample heated at 360°C (Figure 4E), it is possible to identify continuous grains, border shrinkage, and internal pores (blue arrow). The creation of porosity in the contour of the OM grains is consistent with the shrinkage during thermal heating reported previously by other authors.

The ultrasonic pulse propagation measurements are available in supplementary material and shown in Figure 5. The propagation velocities of compressional (Figure 5A) and shear waves (Figure 5B) are present as a function of pressure for the immature samples (gray diamond) and the matured ones at 300°C (black squares), 320°C (red circles), 340°C (upper blue triangle), and 360°C (upper magenta triangle). For all samples, the velocities measured during pressure increase are lower than the velocities measured during unload. Comparing the sample tendencies, the immature gray points are grouped with the higher Vp and Vs modulus for all applied confining pressures, followed by the velocities of the sample heated at 300°C. The velocities of the samples heated at 320°C and 340°C are grouped with Vp between 2.8 and 3.2 km/s and Vs between 1.8 and 2.0 km/s. The smaller velocities are associated to the sample heated at 360°C.

Figure 5 shows velocity moduli are increasing functions of confining pressure with higher rates of increase at lower pressures. The percentual variation of Vp measured at 14 Mpa and 3.5 Mpa is between 1.6% and 2.5%, respectively, for the immature samples. On the same range, there is a variation of 2.8%, 7.2%, 5.8%, and 10.7% for the samples that maturated at 300°C, 320°C, 340°C, 360°C, respectively. Equivalent variation is observed for Vs, where the velocity of immature samples decreases 0.9%, on average. Decreases of 1.2%, 2.8%, 2.8%, and 4.8% are observed for matured samples in the same sequence of samples as mentioned previously.

The RPM model and the velocities measured at 34 MPa are presented in Figure 6 as open circles and closed black circles, respectively. The bulk density predicted by Eq. 14 using the properties listed in Table 2 is exhibited in Figure 6A as red open circles together with the data points in black. As the maturation advances, the porosity also increases, and the velocities have their modules decreased. The measured propagation velocities of compressional (Figure 6B) and shear waves (Figure 6C) are compared to those of the model with porosity inclusions with AR of 0.12 (yellow open circles), 0.14 (red open circle), and 0.16 (green open circles). The samples with porosity below 10% and with 14% are well-described by the pores with an AR of 0.12 and 0.14, respectively, for both waves. The model fails to adjust the velocities for the samples with a porosity beyond 18% because of the change in the kerogen elastic properties as a function of maturation. In fact, the model with mature kerogen (K=7.98 GPa, G=4.18 GPa, and rho=1.34 g/cm^3), and the aspect ratio of 0.097 was added on the Vp and Vs plot as yellow squares. This model calibrates better with the high porosity/high maturation sample.

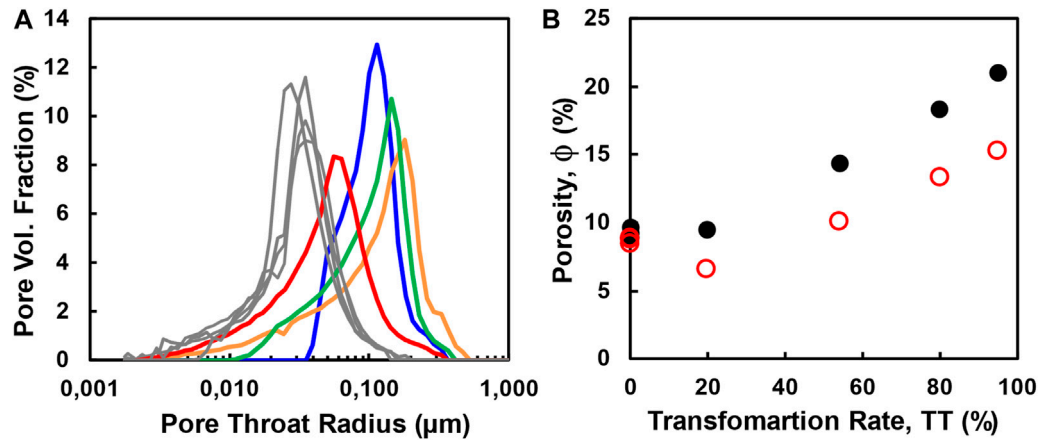

FIGURE 3
(A) Pore-throat distribution as measured for samples in the original state (gray) and after hydropyrolysis at 300°C (red), 320°C (blue), 340°C (green), and 360°C (yellow). **(B)** Porosity as a function of TR as measured by MIP (black closed circles) compared to porosity due to variation in OM volume.

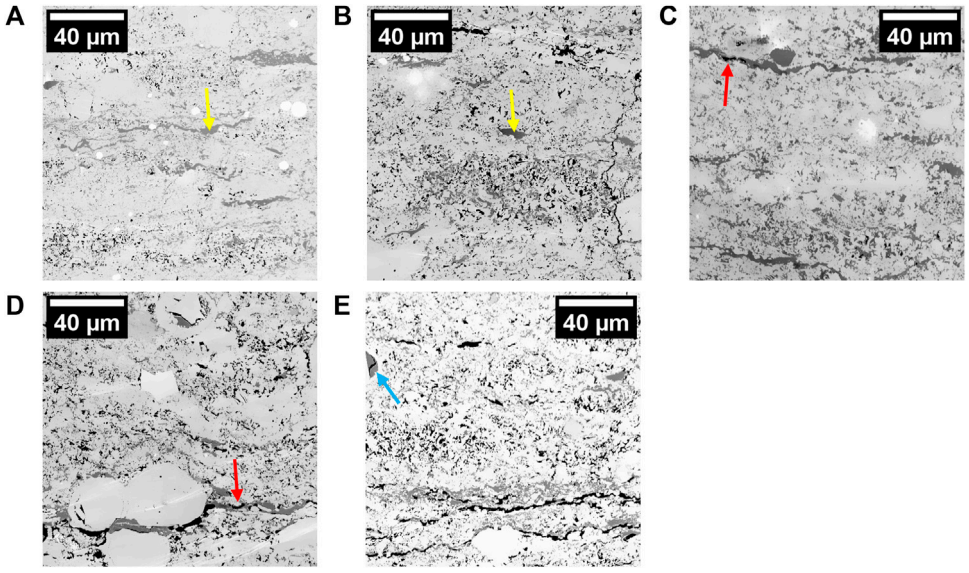

FIGURE 4
SEM images acquired in the samples **(A)** in the original condition and heated at **(B)** 300°C, **(C)** 320°C, **(D)** 340°C, and **(E)** 360°C. The arrows indicate OM grains without porosity (yellow), with porosity in the contour (red), and with porosity across the grain (blue).

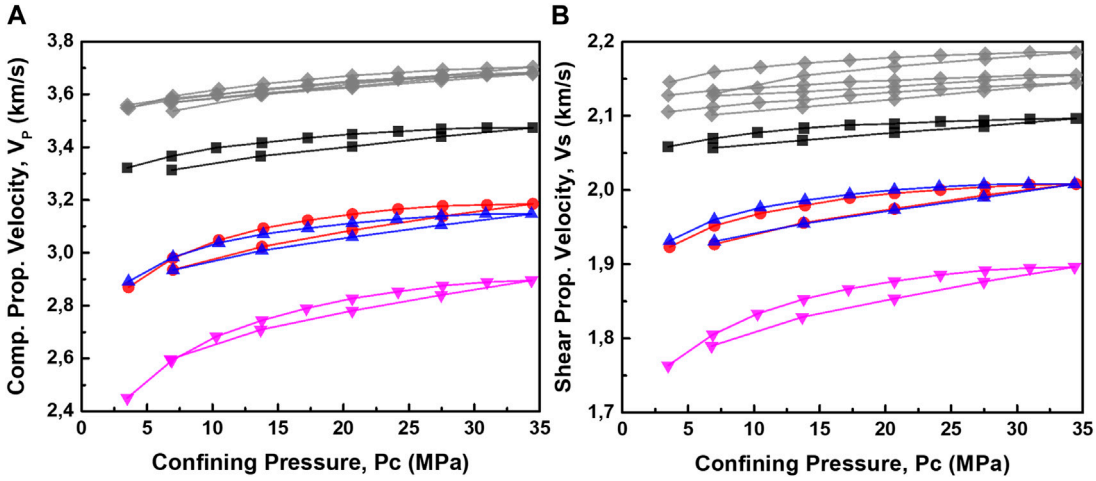

FIGURE 5
Wave propagation velocities of **(A)** compressional and **(B)** shear modes measured in immature samples (gray diamond) and in the matured ones at 300°C (black squares), 320°C (red circles), 340°C (upper blue triangle), and 360°C (upper magenta triangle).

4 Discussion

During the beginning of the maturation process, kerogen content is reduced and the oil content increases. Depending on the mechanical properties of the rock, the introduction of less dense material could induce fracture creation (Vernik, 1994). At some point in the generation (0.75% < Ro < 1.3%), the oil migrates out of the rock (Vernik and Landis, 1996). Altogether, there is a change in porosity, pore geometry, TOC, and kerogen-to-oil proportions as a function of the maturation. In this section, we analyze the effects of maturation on those parameters and the resulting effect on the elastic properties.

4.1 Solid composition

The compositional characterization of our samples is consistent with the mineralogy found by Kreisserman and Emmanuel (2018),

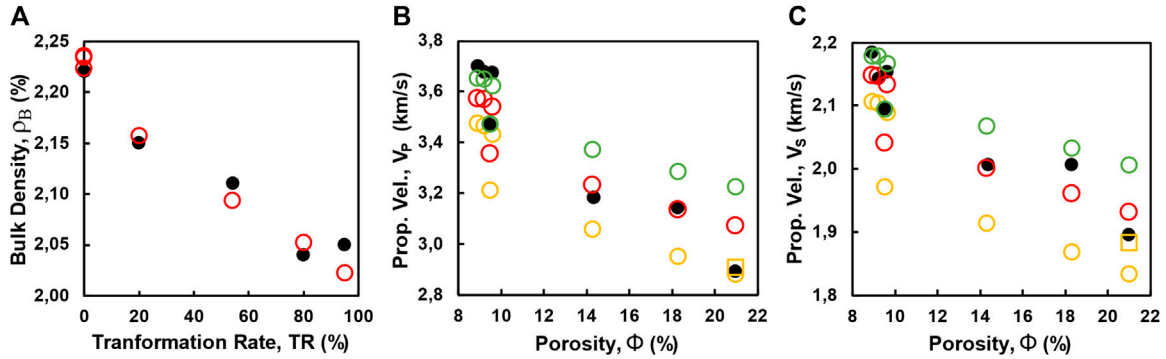

FIGURE 6
Adjusted RPM (open circles) with an aspect ratio equal to 0.12 (yellow), 0.14 (red), and 0.16 (green) compared to **(A)** bulk density and **(B)** Vp and **(C)** Vs measurements (closed circles). The yellow open squares are model data with AR=0.097 and modified elastic modulus.

despite the absence of pyrite and dolomite. Some variation in mineralogy of different Eagle Ford samples is expected. In fact, Jia and Sheng (2017) reported that the content of clay, quartz, carbonates, and pyrites varies in the range of 5%–45%, 15%–26%, 0%–61%, and 3%–5%, respectively. For a comparison of organic fractions, French et al. (2019) characterized a series of immature Eagle Ford samples below the oil window whose average geochemical properties, filtered to Tmax < 425°C, are also exhibited in Table 4 and are consistent with our results. More importantly, the mineralogy and the initial TOC are almost constant in the sampling points and should not introduce any dispersion to the measured velocities.

4.2 Porosity

The geochemical pyrolysis induces hydrocarbon generation at the cost of kerogen consumption, as shown in Figure 2A. The conversion of kerogen into hydrocarbons reduces its volume either by creating internal porosity (Sengupta et al., 2020) or by volume shrinking (Allan et al., 2014; Suwannasri et al., 2018). The qualitative analysis of SEM images (Figure 4) reported in this study indicates that kerogen volume variation occurs mostly through shrinkage of OM volume in the interface kerogen/mineral with associated creation of elongated pores.

The porosity increased as a function of the maturation (Figure 3B). In fact, its increase is expected as a consequence of OM consumption (Suwannasri et al., 2018) and fracturing induced by generation (Vernik, 1994; Allan et al., 2016). The comparison between porosity and OM volume variation indicates that there is porosity creation beyond the change in OM volume. The discrepancy became more accentuated with the maturation, indicating that there is creation of porosity.

4.3 Elastic properties of organic matter

The RPM with constant properties of kerogen calibrates well for the compressional waves but becomes discrepant at Vs measured for the samples with higher porosities. In this range, a model with maturated kerogen calibrates better with the results without changing the aspect ration reduction tendency with maturation. This model indicates that the maturation changes the porosity from less compliant to more compliant pores while increasing the kerogen modulus, as reported in Ibrahim et al. (2020).

4.4 Thermal evolution of wave propagation velocities

There is no significant porosity variation between the immature samples and the sample at the peak of the oil window (Ro < 0.7%). The pores are approximately 9.2% of volume, and the RPM indicates an AR of 0.16 for these samples. Therefore, the change in the elastic properties for these samples is mainly related to the difference in the kerogen/oil ratio that diminishes the effective elastic properties of the organic components with the convertion to oil.

The sample with Ro = 1.07% shows a fraction of kerogen almost equal to that of the sample with Ro = 0.69%. Consequently, there is no significant variation in the organic phase proportions. The sample porosity increased from 9.3% measured in the immature group to 14.3%. There is also a reduction in the aspect ratio from 0.16 to 0.14. The main factors that describe the evolution of the elastic properties in this maturation range are porosity and pore geometry.

There is significant oil migration with a visible increase in the kerogen fraction for the two samples at the end of the oil window (Ro > 1.3%). There is also a porosity increase and reduction in the AR. The RPM indicates a significant increase in the elastic properties of the kerogen. For this range of maturation, the elastic properties result from a competition between oil migration, pore elongation and increases both on porosity and kerogen stiffness.

The pressure sensitivity is consistent with the conceptual model discussed previously. The discrepancy between porosity and organic matter volume indicates that porosity at 300°C increased with small fracture creation. Therefore, the pressure sensitivity for this sample is to immature for immature samples and the same RPM model that

describes immature samples also describes the sample heated at 300°C. With the advance of maturation, the velocity modulus at a given pressure is reduced, and sensitivity becomes more relevant as more compliant pores are added.

A similar dynamic of fluid accumulation and fracture creation was described by Vernik and Landis (1996) in a series of natural samples. Using the vitrinite reflectance to classify the samples according to their stages, we find that the sample heated at 300°C is in stage III, with the samples prepared at higher temperatures identified in stage IVb. Stages III and IVb are the peaks of bitumen accumulation and fracture creation, as observed. Suwannasri et al. (2018) described a dynamic of porosity creation based on the reduction in the kerogen volume for samples maturated in dry pyrolysis. A possible explanation for the difference between the results is the presence of water during the maturation (Lewan, 1994).

5 Conclusion

We have used a combination of direct measurements and RPM diagnoses to elaborate a complete picture of the effects of maturation on the Eagle Ford samples artificially maturated by hydropyrolysis. The Eagle Ford outcrop is a carbonate mudstone with 4.2% of its mass composed of kerogen type I or I/II. The hydropyrolysis induces organic matter maturation, TOC reduction, TR increase, and Ro increase. The organic matter conversion into light hydrocarbons increases porosity, but the more compliant pores are introduced by fracturing, as suggested by the RPM. The oil saturation initially increases with the beginning of maturation and diminishes as the Ro increases.

The effective elastic properties respond to the overall modifications imposed by maturation to porosity, pore geometry, kerogen-to-oil proportion, and elastic properties of kerogen. Kerogen-to-oil ratio controls the velocities for the samples with Ro below 0.7%. As the TR increases, more elongated pores are created, contributing to a reduction in propagation velocities. This change in porosity and pore geometry explains the modification of the elastic properties observed for the sample with Ro = 1.07%. In addition to the porosity increase and pore geometry change, the change in the elastic properties of kerogen is important for explaining propagation velocities measured for the last two samples in the limit of the oil window.

Data availability statement

The original contributions presented in the study are included in the article/Supplementary Material; further inquiries can be directed to the corresponding author.

Author contributions

DL, MM, JJ, and GV were responsible for the experimental planning, ultrasonic pulse propagation experiments, and rock physical analysis. AS conducted hydropyrolosis experiments besides LECO TOC and Rock–Eval pyrolysis analysis. TM measured and analyzed the vitrinite reflectance. RS performed and analyzed the mercury intrusion porosimetry.

Acknowledgments

The authors would like to thank the Petrobras for permission to publish the work and the data.

Conflict of interest

The authors declare that the research was conducted in the absence of any commercial or financial relationships that could be construed as a potential conflict of interest.

Publisher's note

Supplementary material

The Supplementary Material for this article can be found online at: https://www.frontiersin.org/articles/10.3389/feart.2023.1131730/full#supplementary-material

References

Allan, A. M., Clark, A. C., Vanorio, T., Kanitpanyacharoen, W., and Wenk, H-R. (2016). On the evolution of the elastic properties of organic-rich shale upon pyrolysis-induced thermal maturation. *Geophysics* 81 (3), D263–D281. doi:10.1190/geo2015-0514.1

Allan, A. M., Vanorio, T., and Dahl, J. E. P. (2014). Pyrolysis-induced P-wave velocity anisotropy in organic-rich shales. *Geophysics* 79 (2), D41–D53. doi:10.1190/geo2013-0254.1

Allo, F. (2019). Consolidating rock-physics classics: A practical take on granular effective medium models. *Lead. Edge* 38 (5), 334–340. doi:10.1190/tle38050334.1

ASTM (2018). *Test method for determination of pore volume and pore volume distribution of soil and rock by mercury intrusion porosimetry d4404-18*. PA: ASTM International. doi:10.1520/d4404-18

ASTM-D7708-14 (2014). *Standard test method for microscopical determination of the reflectance of vitrinite dispersed in sedimentary rocks*. West Conshohocken: ASTM International.

Avseth, P., Mukerji, T., and Mavko, G. (2010). *Quantitative seismic interpretation*. Cambridge, UK: Cambridge University Press.

Behar, F., Beaumont, V., and de Penteado, H. L. (2001). Rock-eval 6 Technology: Performances and developments. *Oil Gas Sci. Technol.* 56 (2), 111–134. doi:10.2516/ogst:2001013

Bjorlykke, K. (2010). *Petroleum geoscience*. Berlin, Heidelberg: Springe. doi:10.1007/978-3-642-02332-3

Borrego, A. G., Araujo, C. V., Balke, A., Cardott, B., Cook, A. C., David, P., et al. (2006). Influence of particle and surface quality on the vitrinite reflectance of dispersed organic matter: comparative exercise using data from the qualifying system for reflectance analysis working group of ICCP. *Int. J. Coal Geol.* 68 (3-4), 151–170. doi:10.1016/j.coal.2006.02.002

Crain, E. R., and Holgate, D. (2014). *A 12-step program to reduce uncertainty in kerogen-rich reservoirs: Part 1 – getting the right porosity*. Calgary, Alberta, Canada: CSPG Reservoir, 19–23.

Donovan, A., Evenick, J., Banfield, L., McInnis, N., and Hill, W. (2017). "An organofacies-based mudstone classification for unconventional tight rock and source rock plays," in Paper presented at the SPE/AAPG/SEG Unconventional Resources Technology Conference (Austin, TX: SPE/AAPG/SEG), 3683–3697. doi:10.15530/URTEC-2017-2715154

Dvorkin, J., Walls, J., and Davalos, G. (2021). Velocity-porosity-mineralogy model for unconventional shale and its applications to digital rock physics. *Front. Earth Sci.* 8. doi:10.3389/feart.2020.613716

Espitalié, J., Laporte, J. L., Madec, M., Marquis, F., Leplat, P., Paulet, J., et al. (1977). Méthode rapide de caractérisation des roches mètres, de leur potentiel pétrolier et de leur degré d'évolution. *Rev. l'Institut Français Pétrole* 3, 23–42. doi:10.2516/ogst:1977002

French, K. L., Birdwell, J. E., and Whidden, K. J. (2019). Geochemistry of a thermally immature Eagle Ford Group drill core in central Texas. *Org. Geochem.* 131, 19–33. doi:10.1016/j.orggeochem.2019.02.007

Hackley, P. C., Araujo, C. V., Borrego, A. G., Bouzinos, A., Cardott, B. J., Cook, A. C., et al. (2015). Standardization of reflectance measurements in dispersed organic matter: Results of an exercise to improve interlaboratory agreement. *Mar. Pet. Geol.* 59, 22–34. doi:10.1016/j.marpetgeo.2014.07.015

Hansen, J. A., Mondol, N. H., and Fawad, M. (2019). Organic content and maturation effects on elastic properties of source rock shales in the Central North Sea. *Interpretation* 7 (2), T477–T497. doi:10.1190/int-2018-0105.1

Horsfield, B., and Rullkötter, J. (1994). "Diagenesis,Catagenesis, and metagenesis of organic matter," in *The petroleum system—from source to trap: AAPG memoir 60* (Tulsa, Oklahoma, United States: AAPG), 189–200. doi:10.1306/m60585c10

Ibrahim, M. A. A., Mukerji, T., and Scheirer, A. H. (2020). "A thermal-maturation dependent elastic rock physics template for organic-rich mudrocks: Construction and application," in Fifth EAGE workshop on rock physics (Milan, Italy: European Association of Geoscientists & Engineers). doi:10.3997/2214-4609.2020603028

Jia, H., and Sheng, J. (2017). Discussion of the feasibility of air injection for enhanced oil recovery in shale oil reservoirs. *Petroleum* 6 (2), 249–257. doi:10.1016/j.petlm.2016.12.003

Kreisserman, Y., and Emmanuel, S. (2018). Release of particulate iron sulfide during shale-fluid interaction. *Environ. Sci. Technol.* 52 (2), 638–643. doi:10.1021/acs.est.7b05350

Langford, F. F., and Blanc-Valleron, M-M. (1990). Interpreting rock-eval pyrolysis data using graphs of pyrolizable hydrocarbons vs. Total organic carbon (1). *AAPG Bull.* 74 (6). doi:10.1306/0c9b238f-1710-11d7-8645000102c1865d

Lewan, M. D. (1994). "Assessing natural oil expulsion from source rocks by laboratory pyrolysis," in *The petroleum system—from source to trap*. Editors L. B. Magoon and W. G. Dow (Tulsa: The American Association of Petroleum Geologists), 201–210. doi:10.1306/m60585c11

Lewan, M. D., and Birdwell, J. E. (2013). "Application of uniaxial confining-core clamp with hydrous pyrolysis in petrophysical and geochemical studies of source rocks at various thermal maturities," in *Unconventional resources Technology conference* (New York, United States: Society Publishers').

Liu, X., Guo, Z., Zhang, Q., Liu, Y., and Chen, H. (2020). Rock physical characterisation of microstructural fabrics and elastic anisotropy for a shale oil reservoir. *J. Geophys. Eng.* 17 (2), 377–389. doi:10.1093/jge/gxz123

Mavko, G., Mukerji, T., and Dvorkin, J. (2009). *The rock physics handbook: Tools for seismic analysis of porous media*. Cambridge, Uk ; New York: Cambridge University Press.

Moyer, J., and Prasad, M. (2017). Property changes of oil shale during artificial maturation: The Irati Formation from the Paraná Basin, Brazil. *Geophysics* 82 (6), MR175–MR190.

Peters, K. E., and Cassa, M. R. (1994). "Applied source rock geochemistry," in *The petroleum system—from source to trap: AAPG memoir 60* (Tulsa, Oklahoma, United States: AAPG), 93–120.

Rayeva, N., Kosnazarova, N., Arykbayeva, Z., and Shaikhina, D. (2014). "Petroleum systems modeling and exploration risk assessment for the eastern margin of the precaspian basin," in SPE annual caspian technical conference and exhibition (Astana, Kazakhstan: Society of Petroleum Engineers). doi:10.2118/172332-ms

Sengupta, M., Jacobi, D., Eichmann, S., Wallet, B., Altowairqi, Y., and Alsinan, S. (2022). "Seismic assessment of maturity and richness in carbonate source rocks," in Second international meeting for applied geoscience & energy (SEG/AAPG), 2283–2287. doi:10.1190/image2022-3736741.1

Sengupta, M., Jacobi, D., Eichmann, S. L., Altowairqi, Y., and Alsinan, S. (2020). "Modeling and estimation of kerogen evolution in source rocks," in SEG technical program expanded abstracts 2020 (Society of Exploration Geophysicists). doi:10.1190/segam2020-3425803.1

Shitrit, O., Hatzor, Y. H., Feinstein, S., and Vinegar, H. J. (2017). Acoustic and petrophysical evolution of organic-rich chalk following maturation induced by unconfined pyrolysis. *Rock Mech. Rock Eng.* 50 (12), 3273–3291. doi:10.1007/s00603-017-1325-9

Sone, H., and Zoback, M. D. (2013). Mechanical properties of shale-gas reservoir rocks — Part 1: Static and dynamic elastic properties and anisotropy. *Geophysics* 78 (5), D381–D392. doi:10.1190/geo2013-0050.1

Spigolon, A. L. D., Lewan, M. D., de Barros Penteado, H. L., Coutinho, L. F. C., and Mendonça Filho, J. G. (2015). Evaluation of the petroleum composition and quality with increasing thermal maturity as simulated by hydrous pyrolysis: A case study using a Brazilian source rock with Type I kerogen. *Org. Geochem.* 83-84, 27–53. doi:10.1016/j.orggeochem.2015.03.001

Suwannasri, K., Vanorio, T., and Clark, A. (2018). Monitoring the changes in the microstructure and the elastic and transport properties of Eagle Ford marl during maturation. *Geophysics* 83 (5), MR263–MR281. doi:10.1190/geo2017-0797.1

Vernik, L. (1994). Hydrocarbon-generation-induced microcracking of source rocks. *Geophysics* 59 (4), 555–563. doi:10.1190/1.1443616

Vernik, L., and Landis, C. (1996). Elastic anisotropy of source rocks: Implications for hydrocarbon generation and primary migration. *AAPG Bull.* 80 (4). doi:10.1306/64ed8836-1724-11d7-8645000102c1865d

Vernik, L., and Liu, X. (1997). Velocity anisotropy in shales: A petrophysical study. *Geophysics* 62 (2), 521–532. doi:10.1190/1.1444162

Vernik, L., and Nur, A. (1992). Ultrasonic velocity and anisotropy of hydrocarbon source rocks. *Geophysics* 57 (5), 727–735. doi:10.1190/1.1443286

Vernik, L. (2016). *Seismic petrophysics in quantitative interpretation*. Tulsa, Ok: Society Of Exploration Geophysicists.

Walls, J. D., and Sinclair, S. W. (2011). Eagle Ford shale reservoir properties from digital rock physics. *First Break* 29 (6). doi:10.3997/1365-2397.29.6.51280

Wang, B., Chen, Y., Lu, J., and Jin, W. (2018). A rock physics modelling algorithm for simulating the elastic parameters of shale using well logging data. *Sci. Rep.* 8 (1), 12151. doi:10.1038/s41598-018-29755-2

Webb, P. A. (1993). "PoreSizer 9320 and AutoPore II 9220 data collection, reduction and presentation," in *Micromeritics, 1993*.

Young, R. A. (1995). *The Rietveld method*. Oxford, United Kingdom: Oxford University Press on Demand.

Zargari, S., Prasad, M., Mba, K. C., and Mattson, E. D. (2013). Organic maturity, elastic properties, and textural characteristics of self resourcing reservoirs. *Geophysics* 78 (4), D223–D235. doi:10.1190/geo2012-0431.1

Zhao, L., Qin, X., Han, D-H., Geng, J., Yang, Z., and Cao, H. (2016). Rock-physics modeling for the elastic properties of organic shale at different maturity stages. *Geophysics* 81 (5), D527–D541. doi:10.1190/geo2015-0713.1

frontiers | Frontiers in Earth Science

TYPE Original Research
PUBLISHED 30 May 2023
DOI 10.3389/feart.2023.1178861

OPEN ACCESS

EDITED BY
Lidong Dai,
Chinese Academy of Sciences, China

REVIEWED BY
Qing Wang,
Beijing Information Science and Technology University, China
Zhen Yang,
SINOPEC Petroleum Exploration and Production Research Institute, China

*CORRESPONDENCE
Li You,
youli@stu.cdut.edu.cn

RECEIVED 03 March 2023
ACCEPTED 17 April 2023
PUBLISHED 30 May 2023

CITATION
Zhang G, Zhang H, You L, Yang Y, Zhou H, Zhang B, Chen W and Liu L (2023), Joint denoising method of seismic velocity signal and acceleration signals based on independent component analysis. *Front. Earth Sci.* 11:1178861. doi: 10.3389/feart.2023.1178861

Joint denoising method of seismic velocity signal and acceleration signals based on independent component analysis

Guangde Zhang[1], Huaibang Zhang[2], Li You[3]*, Yuyong Yang[3], Huailai Zhou[3], Bohan Zhang[4], Wujin Chen[5] and Liyuan Liu[3]

[1]Sinopec Petroleum Engineering Geophysics Co., Ltd., Beijing, China, [2]The Shengli Branch of the Sinopec Petroleum Engineering Geophysics Co., Ltd., Dongying, Shandong, China, [3]College of Geophysics, Chengdu University of Technology, Chengdu, China, [4]School of Ocean and Earth Sciences, Tongji University, Shanghai, China, [5]R&D Center of Science and Technology, Sinopec Petroleum Engineering Geophysics Co., Ltd., Nanjing, China

The signal-to-noise ratio (SNR) of seismic data is the key to seismic data processing, and it also directly affects interpretation of seismic data results. The conventional denoising method, independent variable analysis, uses adjacent traces for processing. However, this method has problems, such as the destruction of effective signals. The widespread use of velocity and acceleration geophones in seismic exploration makes it possible to obtain different types of signals from the same geological target, which is fundamental to the joint denoising of these two types of signals. In this study, we propose a joint denoising method using seismic velocity and acceleration signals. This method selects the same trace of velocity and acceleration signal for Independent Component Analysis (ICA) to obtain the independent initial effective signal and separation noise. Subsequently, the obtained effective signal and noise are used as the prior information for a Kalman filter, and the final joint denoising results are obtained. This method combines the advantages of low-frequency seismic velocity signals and high-frequency and high-resolution acceleration signals. Simultaneously, this method overcomes the problem of inconsistent stratigraphic reflection caused by the large spacing between adjacent traces, and improves the SNR of the seismic data. In a model data test and in field data from a work area in the Shengli Oilfield, the method increases the dominate frequency of the signal from 20 to 40 Hz. The time resolution was increased from 8.5 to 6.8 ms. The test results showed that the joint denoising method based on seismic velocity and acceleration signals can better improve the dominate frequency and time resolution of actual seismic data.

KEYWORDS

denoising, velocity signal, acceleration signal, independent component analysis, Kalman filter

1 Introduction

With the development of exploration technology, exploration targets have changed from large, thick, and high porosity reservoirs to small, thin, low porosity reservoirs, and from structural reservoirs to stratigraphic, lithological, and other complex reservoirs. Requirements for exploration resolution and accuracy are increasing. Seismic data

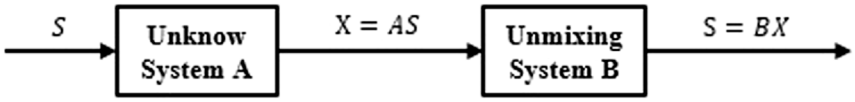

FIGURE 1
Independent component analysis model.

denoising is a key step in seismic data processing and affects subsequent data interpretation (Han and Van, 2013). Conventional suppression methods for random noise in seismic data are mainly divided into space domain and transform domain methods (Necati, 1986; Joachim, 1997). Noise suppression methods in the space domain can be divided into median filtering (Wang et al., 2012), diffusion filtering (Perona and Malik, 1990), etc.,; The methods in transform domain noise suppression can be divided into frequency domain denoising (Necati, 1986), wavelet transform denoising (Morlet et al., 1982), meander transform denoising (Cao et al., 2015), and empirical mode decomposition-based denoising methods (Mirko and Maiza, 2009). Median filter denoising can easily destroy the continuity of events and lose detail (Chen et al., 2019). Diffusion filtering lacks the use of nonlocal information, which may damage some effective signals (Wang et al., 2021). Although frequency-domain denoising is one of the most commonly-used denoising methods, it cannot suppress noise in the frequency range that coincides with the effective signal (Sergio and Tad, 1988). Wavelet transform denoising can only perform signal transformation in a single direction, and cannot adapt to signals with multi-directional changes (Spanias et al., 1991). Curved transform denoising is a derivative of wavelet transform denoising, which overcomes the above disadvantages; however, it has other problems, such as slow computing efficiency (Cao et al., 2012). The denoising method based on empirical mode decomposition has the problems of low accuracy or instability in the decomposition process due to boundary effects, and mode aliasing occurs during the decomposition process (Damaševičius et al., 2017). In addition, these methods only use one type of data for processing, and so cannot take into consideration the advantages of multiple signals from different geophones.

Velocity and acceleration geophones are widely used in seismic exploration to satisfy the requirements of high-precision exploration (Nicolas and Jérôme, 2017). By comparing the frequency characteristics and waveforms of the velocity and acceleration signals, Hons et al. (2007; 2008) proposed that the two signals were similar after mathematical conversion, and that there was only a slight difference in the main wave. However, the acceleration signal has a wider frequency band than the velocity signal, which improves seismic resolution (Denis, 2004; Zhang et al., 2020). In addition, some researchers have shown that the acceleration signal has little waveform distortion, high signal-to-noise ratio (SNR), and fidelity (Lansley et al., 2008; Liu et al., 2012; Bai et al., 2014). By comparing the frequency band information of different signals in the same domain, Ren (2018) proposed that the velocity signal has more information in the low-frequency region than the acceleration signal, and the acceleration signal has more information in the high-frequency region than the velocity signal. Wei (2018) pointed out that in the filed seismic data, the SNR of the velocity signal is higher than the acceleration signal. But the acceleration signal has a higher dominate frequency. Although in theory the velocity and acceleration signals can be consistent after mathematical transformation, different types of geophones have different advantages in actual acquisition. Therefore, the velocity and acceleration signals can be combined for denoising, and the respective advantages of the two signals can be retained.

Using the observed signal to separate the effective signal and noise is a problem of blind source separation. Blind source separation problem is that only the observed mixed signal is used to recover the source signal when both the source signal and transmission channel are unknown During signal transmission (Zhang et al., 2022). Independent component analysis (ICA) is one of the most effective and widely-used methods for solving this problem. Based on the adjacent seismic traces approximation theory, Meng and Su (Meng et al., 2021) used ICA to separate noise and effective signals to improve the resolution of seismic data. At the same time, ICA requires that the number of observed signals be greater than or equal to the number of source signals. For consistency, conventional ICA approximates the reflection coefficients of adjacent seismic traces. However, when the spacing between adjacent traces is too large, or when there are special geological structures between adjacent traces, there are large differences between the formation reflection coefficients of adjacent seismic traces. Nonetheless, when the formation reflection coefficients of the same trace of the velocity and acceleration signals are consistent, and there is no such problem. Owing to the consistency of the reflection coefficient, the effective signals of the velocity and acceleration signals can be consistent after mathematical transformation, but different types of signals have different noise signals due to different acquisitions. Therefore, the velocity and acceleration signals of the same trace can be considered to have certain differences that satisfy the requirements of ICA.

In this paper, we propose a joint denoising method based on seismic velocity and acceleration signals. First, based on the mathematical relationship between the speed and acceleration signals, ICA is used to obtain approximately independent effective and noise signals. Second, the effective and noise signals obtained by ICA are taken as the prior information for the Kalman filter, which provides the Kalman estimation components more comprehensive prior information. Denoising data can then be obtained after joint processing.

This method is based on the theoretical relationship between seismic velocity and acceleration signals, and uses ICA and Kalman filter for denoising. At the same time, this method takes into account the advantages of velocity and acceleration signals, solves the problem of the inconsistency of adjacent traces data, and thus

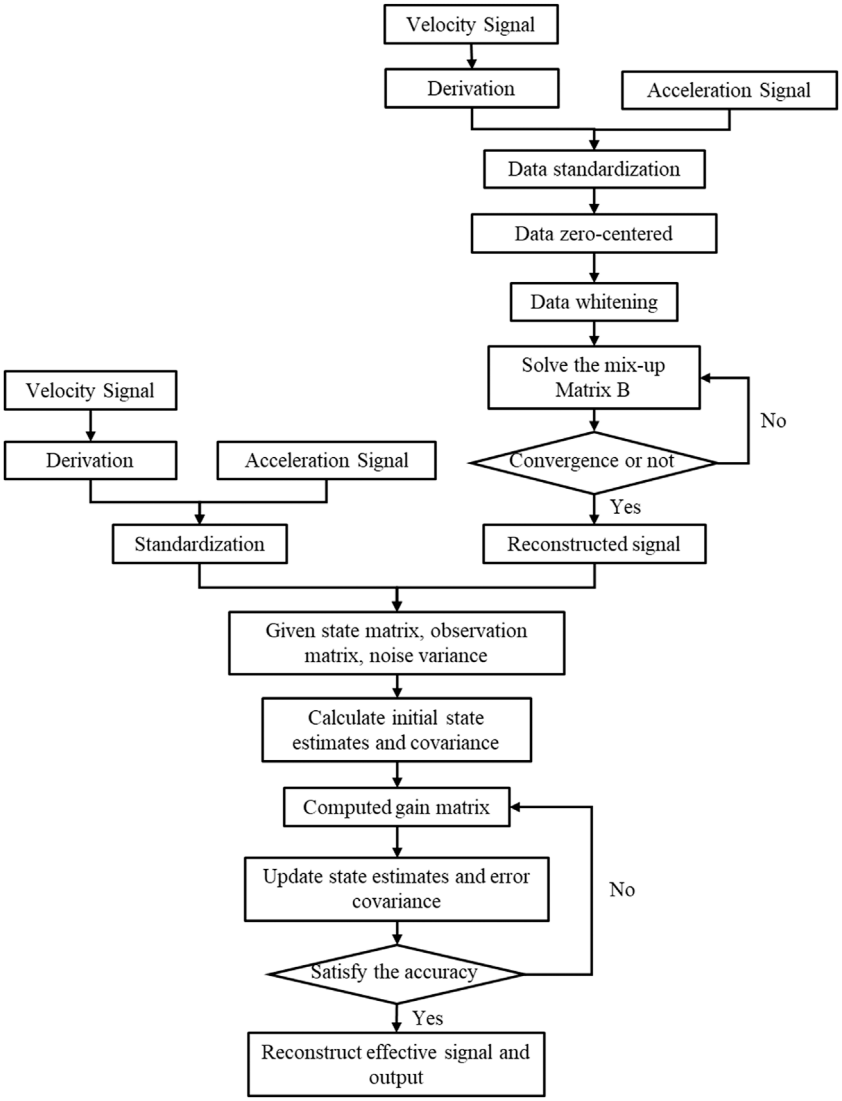

FIGURE 2
Flow chart of seismic velocity and acceleration signal combined denoising.

improves the resolution of seismic signal and is suitable for further application.

2 Materials and methods

2.1 Independent component analysis

As an independent source signal separation method, ICA is one of the most effective and widely-used methods for solving the problem of blind source separation (Saruwatari et al., 2006). The ICA method can realize the separation of effective seismic signal and random noise according to their statistical characteristics (Liu et al., 2007). ICA is a method for determining a set of non-orthogonal coordinate systems in multidimensional data, and obtaining another set of statistically independent data in the original multidimensional data through the projection of coordinates. This method requires that the number of observed signals be greater than the number of source signals, and that the source signals are independent of each other and follow a non-Gaussian distribution (Qin et al., 2018). In seismic data, the required effective signal and noise are independent of each other. In addition, a seismic wavelet can be considered as a non-Gaussian distribution. Therefore, seismic signals meet the preconditions of the ICA method, which can be used to separate seismic signals from noise.

The ICA requirement that the number of observed signals be greater than the number of source signals is generally based on multiple observations of data from the same or similar channels. The actual seismic data have many seismic traces, and each seismic data point can be regarded as an independent one-dimensional signal. If each seismic trace is processed separately, the number of observed data points is less than the number of source signals. The data obtained from separate observations of the velocity and acceleration signals of the same seismic trace satisfy the preconditions of ICA.

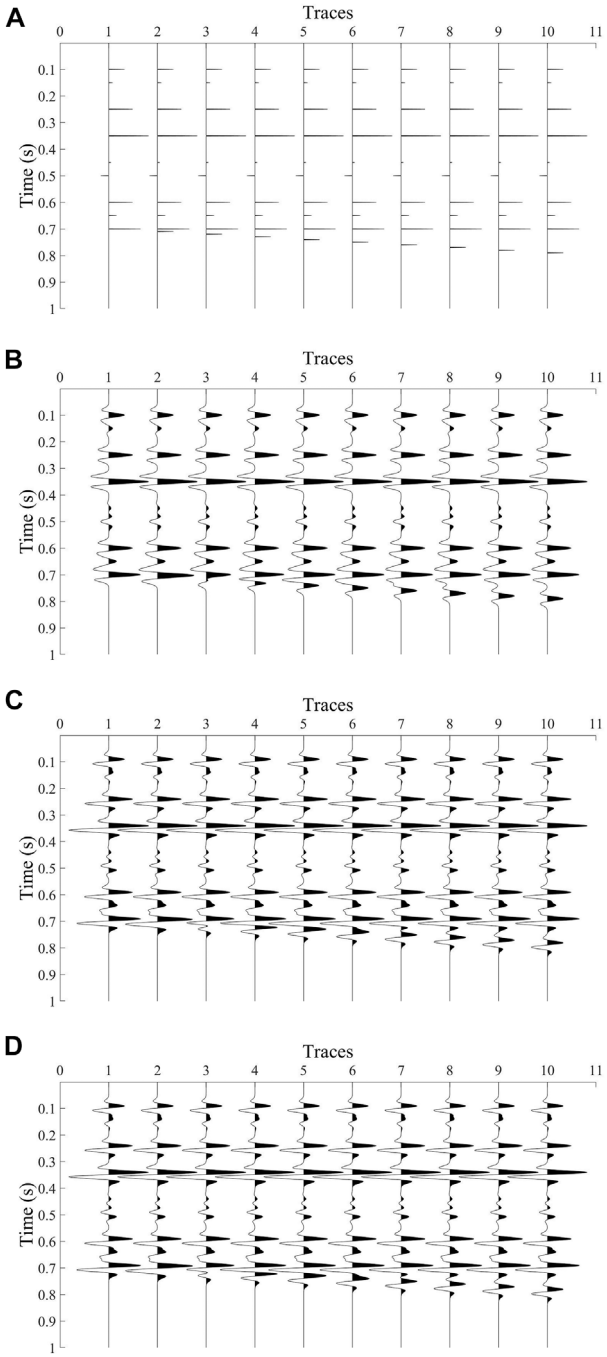

FIGURE 3
Comparison of the processing results of theoretical models **(A)**. Theoretical reflection coefficient; **(B)**. Synthesize velocity signal; **(C)**. Synthetic acceleration signal; **(D)**. Acceleration signal obtained.

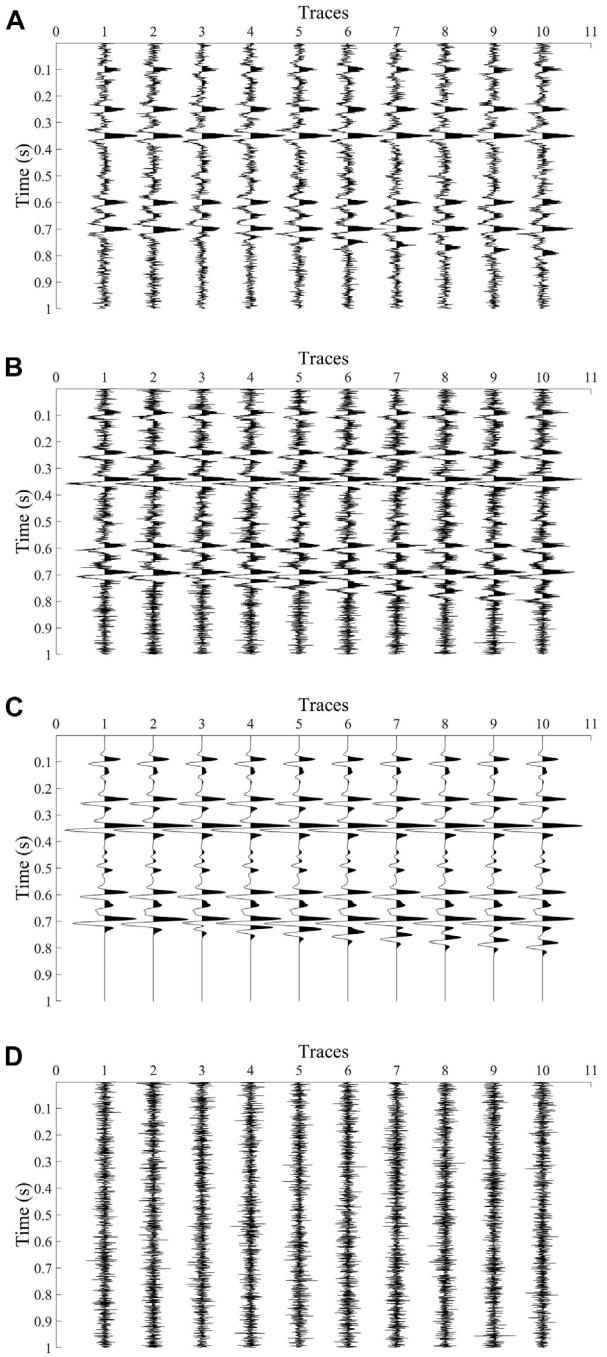

FIGURE 4
Comparison diagram of processing results of noisy data **(A)**. Velocity signal with noise; **(B)**. Acceleration signal containing noise; **(C)**. Acceleration signal obtained; **(D)**. Residual difference between original acceleration signal and processed acceleration signal.

In the mathematical model of ICA it is assumed that there are m source signals $\boldsymbol{S} = (\boldsymbol{s}_1, \boldsymbol{s}_2, \ldots, \boldsymbol{s}_m)^T$, n mixed signals $\boldsymbol{X} = (\boldsymbol{x}_1, \boldsymbol{x}_2, \ldots, \boldsymbol{x}_n)^T$. Mixed signals composed of mixed source signals are obtained after passing through an unknown system $\boldsymbol{A}$, and then m estimated source signals $\boldsymbol{Y} = (\boldsymbol{y}_1, \boldsymbol{y}_2, \ldots, \boldsymbol{y}_m)^T$ are obtained by blind separation system $\boldsymbol{B}$. When the estimated source signal $\boldsymbol{Y}$ is infinitely close to the real source signal $\boldsymbol{S}$, source signal $\boldsymbol{S}$ (which cannot be obtained by direct observation) is obtained. Figure 1 shows the system model of ICA.

The denoising method based on ICA can be described as follows:

Assume there are m source signals $\boldsymbol{S} = (\boldsymbol{s}_1, \boldsymbol{s}_2, \ldots, \boldsymbol{s}_m)^T$, and n observed signals $\boldsymbol{X} = (\boldsymbol{x}_1, \boldsymbol{x}_2, \ldots, \boldsymbol{x}_n)^T$, which can be expressed as

$$\boldsymbol{x}_i = \boldsymbol{a}_{i1}\boldsymbol{s}_1 + \boldsymbol{a}_{i2}\boldsymbol{s}_2 + \ldots + \boldsymbol{a}_{im}\boldsymbol{s}_m \quad (1)$$

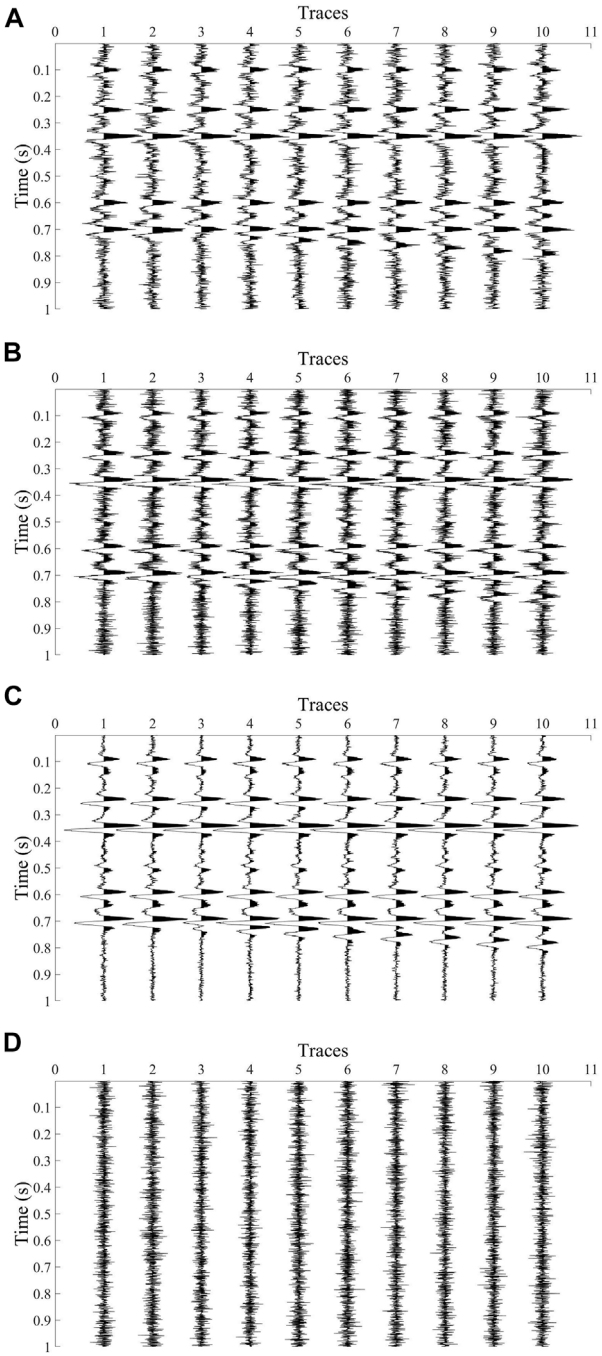

FIGURE 5
Comparison diagram of processing results of additional noisy data **(A)**. Velocity signal with noise; **(B)**. Acceleration signal with additional noise; **(C)**. Acceleration signal obtained; **(D)**. Residual difference between original acceleration signal and processed acceleration signal.

where $i = 1, 2, \ldots, n$.

Rewrite Eq. 1 into vector form,

$$X = AS \tag{2}$$

where A is the mixed matrix of the unknown system, which can be expressed as

$$A = \begin{pmatrix} a_{11} & \cdots & a_{1j} \\ \vdots & \ddots & \vdots \\ a_{i1} & \cdots & a_{ij} \end{pmatrix} \tag{3}$$

where a_{ij} represents the influencing factor of the jth source signal in the ith observed signal, $i=1,2\ldots\ n,\ j=1,2\ldots\ m$.

Equation. 2 represents the standard ICA model. In actual seismic data, the observed signal X is known, whereas the source signal S and mixed matrix A are unknown. Assuming that the mixture matrix A is invertible, Eq. 2 can be written as

$$S = BX \tag{4}$$

where B is the inverse of the mixed matrix A.

The core function of ICA is to obtain the above Eq. 4, obtain matrix B, and then realize the separation of the observed signal X, and finally obtain different source signals S.

Prior to ICA, the data need to be zero-centered and whitened. The purpose of zero-centering is to make the mean value of each data observation zero, and simplify the ICA algorithm. The purpose of whitening is to remove the correlation between observed signals, so that the algorithm convergence speed is faster and the algorithm is more stable during ICA.

Zero-centering can be expressed as:

$$X_{i,j} = X_{i,j} - Xm_j \tag{5}$$

where X is the observed data, $X_{i,j}$ is the i-row data of the jth channel, and Xm_j is the mean value of the observed data of the jth channel.

Whitening can be expressed as:

$$Xw = D^{-1}I^{-1}X \tag{6}$$

where Xw is the data after whitening, D is the eigenvalue of the covariance data of data X after zero-centering, and I is the identity matrix.

When calculating the separation matrix B, negative entropy was adopted in this study as a measure of non-Gaussian signal. The iterative equation of the ICA algorithm can be expressed as (Hajsadeghi et al., 2020):

$$b_{k+1} = E\left\{X_w G'\left(b_k^T X_w\right)\right\} - E\left\{G''\left(b_k^T X_w\right)\right\} b_k \tag{7}$$

where b is the row vector of separation matrix B, X_w is the observed data after whitening, and G can be selected in different expressions according to the type of signal. This method selects (Hajsadeghi et al., 2020):

$$\begin{cases} G'(X_w) = -\dfrac{1}{a} exp\ \left(-aX_w^2/2\right) \\ G''(X_w) = X_w\, exp\ \left(-aX_w^2/2\right) \end{cases} \tag{8}$$

where X_w is the observed data after whitening, the value of a is about 1, G' represents the first derivative of G, G'' represents the second derivative of G.

The final separation matrix B can be obtained after satisfying the iteration termination condition. Using the separation matrix B, the observed signal X can be reconstructed to obtain the source signal S.

2.2 Kalman filter method

Although the ICA method has the advantages of fast convergence speed, ease of use, simple calculation, and small

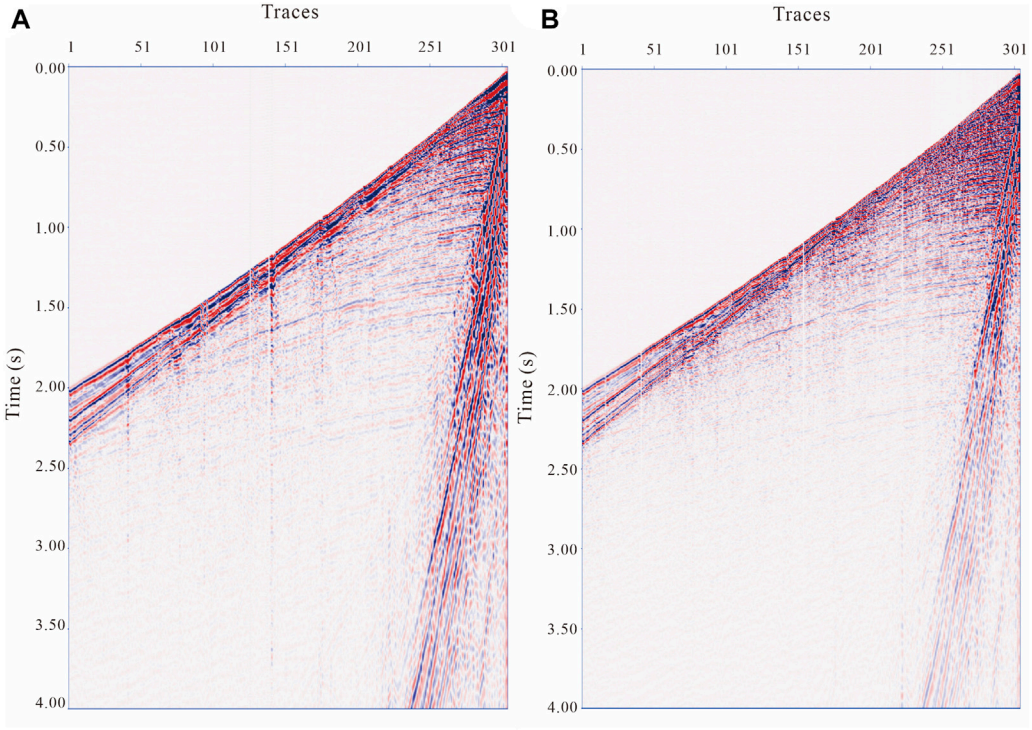

FIGURE 6
Shot gather **(A)**. Velocity shot gather; **(B)**. Acceleration shot gather.

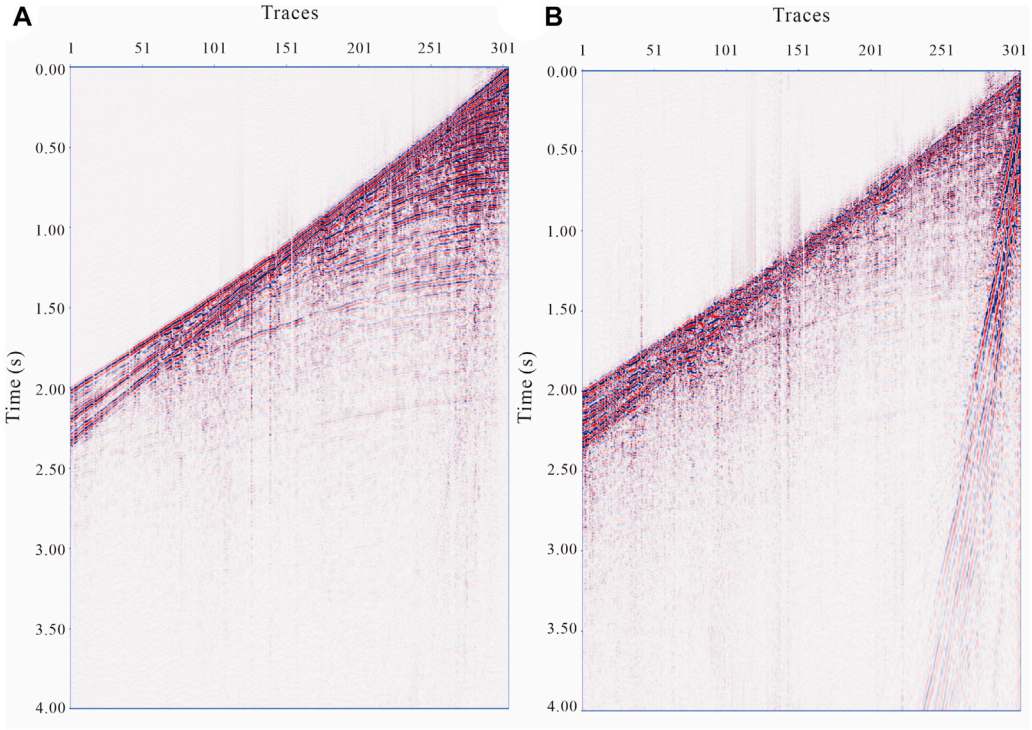

FIGURE 7
De-noising data **(A)**. Processed acceleration shot gather; **(B)**. Noise.

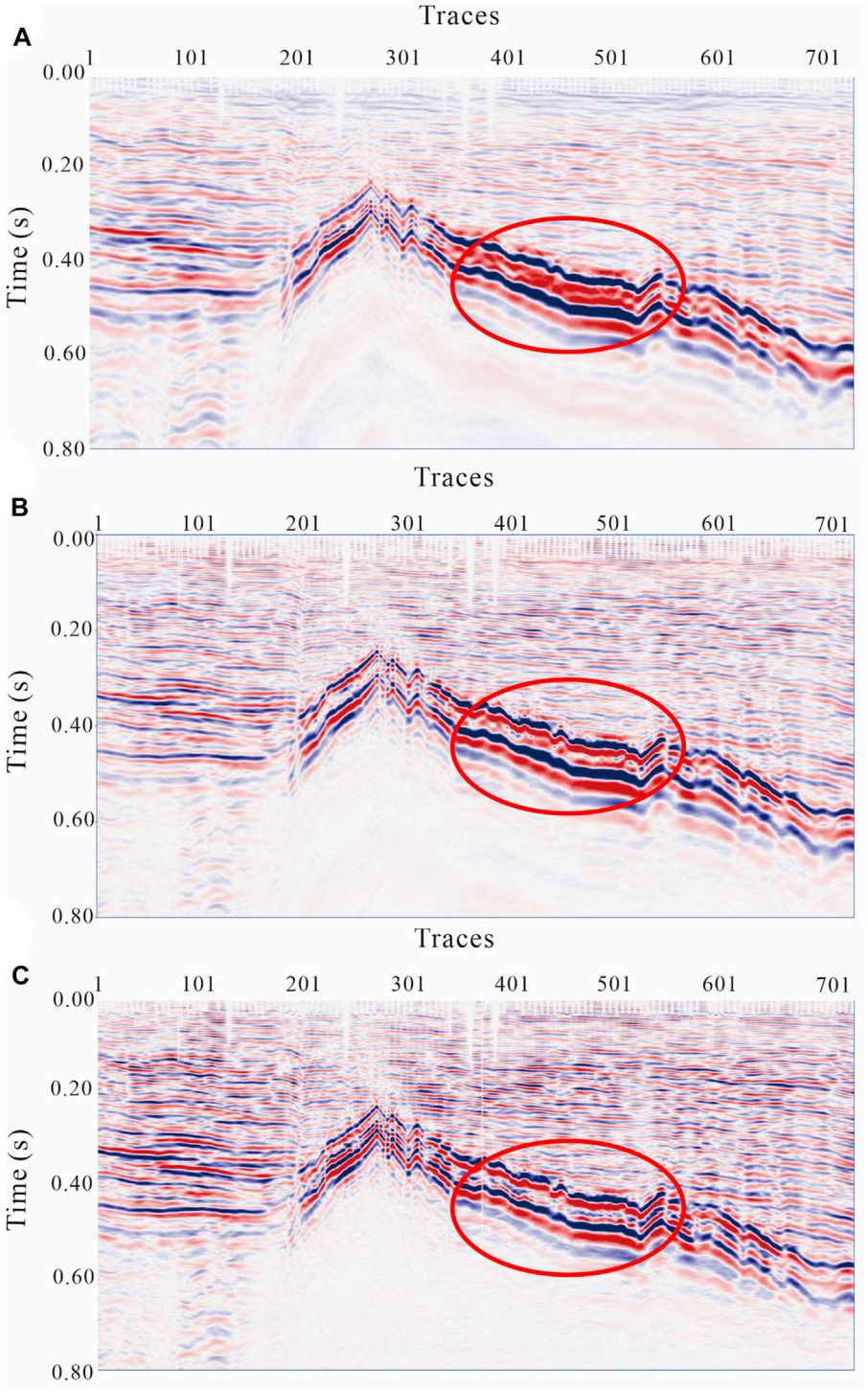

FIGURE 8
Joint processing results **(A)**. Original velocity profile; **(B)**. Original acceleration profile; **(C)**. Processed acceleration profile.

memory requirement, the order of the output vectors and the amplitude of the output signal are uncertain. The Kalman filter method has the problem of uncertainty of prior information. The decomposition components obtained by ICA of seismic records can provide Kalman filter components with more comprehensive prior information. Therefore, the Kalman filter method is used to denoise the acceleration and the original acceleration signals by using the information obtained from the ICA as the prior information.

The mathematical model of the Kalman filter method is divided into two types of equations: the state equation and observation equation. These two equations are used to describe the system. The state equation can be written as (Ott and Meder, 1972):

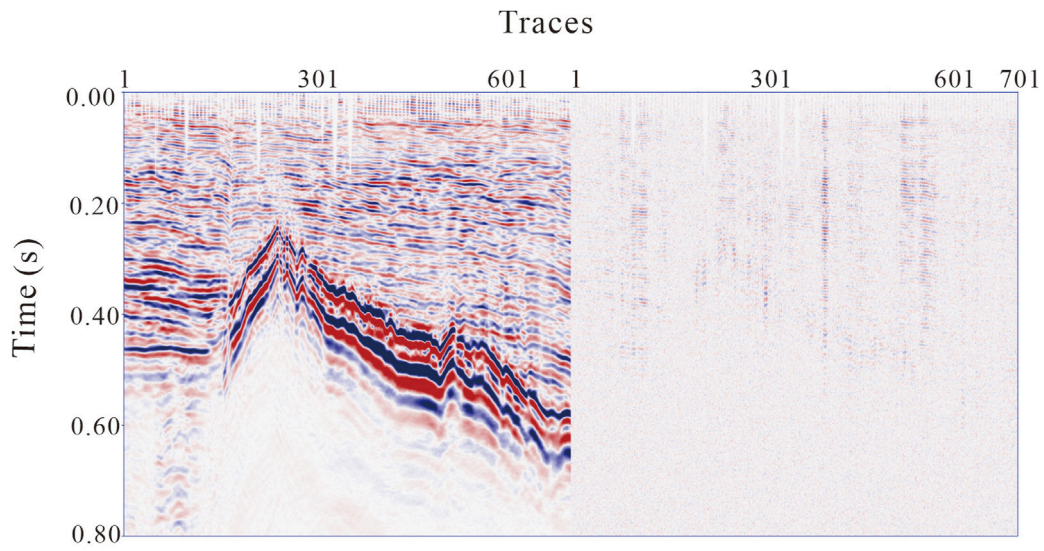

FIGURE 9
Comparison results before and after denoising (Left is the original acceleration signal; Right is noise removal).

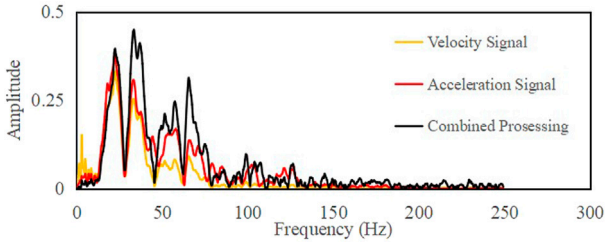

FIGURE 10
Spectrum of joint processing results (Yellow curve, original velocity profile spectrum; Red curve, original acceleration profile spectrum; Black curve, profile spectrum after combined processing).

$$X_k = \Phi_k X_{k-1} + W_k \tag{9}$$

where X_k is the n-dimensional column vector and is the state of the system at time k. Φ_k is a square matrix of order $n \times n$, which is the state transition square matrix of the system and describes the law of the system from k-1 time to k time. W_k is the n-dimensional column vector, which is also the system noise. The expression of the observation equation is

$$Z_k = H_k X_k + V_k \tag{10}$$

where Z_k is the m-dimensional column vector and observation vector. H_k is a matrix of order m×n. V_k is the m-dimensional column vector, which is the observation noise.

The state equation and observation equation applied to the seismic system can be rewritten as (Eikrem et al., 2019):

$$R_k = F_k R_{k-1} + W_k \tag{11}$$

$$S_k = B_k R_k + V_k \tag{12}$$

where R is the reflection coefficient sequence, B is the seismic wavelet sequence, S is the seismic record obtained by observation, F is the state transition matrix, W and V are the system noise and observation noise, respectively, and their variances are Q and C, respectively.

The core of the Kalman filter method is to obtain the state quantity in the state equation using the observed quantity.

The implementation process of the Kalman filter method is as follows.

First, calculate the initial state estimation and error covariance matrix as follows:

$$R_k = F_k R_{k-1} \tag{13}$$

$$P_k^{'} = F_k P_{k-1} F_k^T + Q_k \tag{14}$$

where R is the sequence of reflection coefficients, P is the initial error covariance estimate, k is the number of iterations, and T is the transpose of the matrix in the upper-right corner.

Then, calculate the gain matrix K:

$$K_k = P_k^{'} B_k^T \left[B_k P_k^{'} B_k^T + C_k \right]^{-1} \tag{15}$$

According to the gain matrix K, the state prediction and error covariance matrices are updated using the following equation:

$$R_k = R_{k-1} + K_k [S_k - B_k R_{k-1}] \tag{16}$$

$$P_k = [I - K_k B_k] P_k^{'} \tag{17}$$

where P is the updated error covariance matrix and I is the identity matrix.

The above equation shows that the result obtained from one use of the Kalman filter method becomes the prior information for the next use. Finally, the obtained state prediction R and wavelet can be reconstructed to obtain a denoised result.

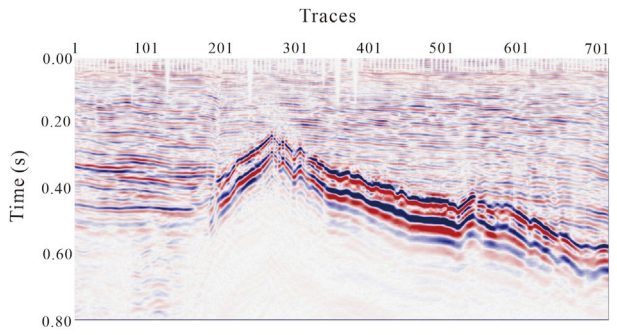

FIGURE 11
Separate processing result.

2.3 Assessment method

In this study, SNR and time resolution were used to evaluate the merits and practicability of the denoising method.

The equation for calculating SNR is as follows:

$$SNR = 10lg\frac{P_s}{P_n} \tag{18}$$

where P_s is the power of the signal, P_n is the power of the noise, and lg is the logarithm of base 10.

The power of discrete signal $x(n)$ can be expressed as:

$$P = \frac{\sum_{n=0}^{N-1} x(n)^2}{N} \tag{19}$$

where N is the length of discrete signal $x(n)$.

2.4 Joint denoising process

In this method, the initial normalized and whitened data were obtained using the original seismic velocity and acceleration signals. Then, ICA was performed to obtain the independent initial effective signal and separation noise. Finally, the initial processing data, initial effective signal, and noise were taken as the inputs of the Kalman filter, and the final joint denoising results were obtained. Figure 2 shows a flow chart of the denoising using seismic velocity and acceleration signals.

3 Results

3.1 Model data

A two-dimensional model was established (Figure 3A) to verify the joint denoising processing method for seismic velocity and acceleration signals. The wavelet of the velocity signal was the Riker wavelet with a dominate frequency of 20 Hz, and the wavelet of the acceleration signal was the derivative of the Riker wavelet with a dominate frequency of 20 Hz. Figure 3A shows the theoretical reflection coefficient, Figure 3B shows the synthesized velocity signal, Figure 3C shows the synthesized acceleration signal, and Figure 3D shows the acceleration signal obtained by this method. A comparison between shows that this method can obtain more accurate seismic signals without noise.

The combined denoising method proposed in this paper was used to process the synthesized seismic record by adding Gaussian white noise with a SNR of 5 dB to verify the anti-noise ability of the method. Figures 4A, B show the velocity and acceleration signals, respectively, after adding noise, and Figure 4C shows the seismic acceleration signal obtained by this method. Figure 4D shows the residual difference between the original and processed acceleration signals. The comparison between Figure 3C, Figures 4C, D shows that the joint denoising method proposed in this paper can still separate accurate effective signals with the same Gaussian white noise.

Based on Figure 4, additional Gaussian white noise with a SNR of 15 is added to the synthesized acceleration signal, and the proposed joint denoising processing method was used to verify the anti-noise capability of this method. Figures 5A, B show the velocity signal after noise is added, and the acceleration signal after noise is added twice. Figure 5C shows the seismic acceleration signal obtained using this method. Figure 4D shows the residual difference between the original and processed acceleration signals. From Figure 3C, Figure 4C, Figure 5C, D, it can be seen that the joint denoising method proposed in this study can still separate accurate and effective signals containing mixed noise. Additionally, the SNR of the signals in Figures 5B, C were calculated to be 14.5 dB and 20.5 dB respectively, indicating that the proposed joint denoising method can significantly improve the SNR of the signal.

3.2 Field data

To further analyze the accuracy of this method and verify its effectiveness, we applied it to the velocity and acceleration signals of an offshore engineering area belonging to Sinopec Petroleum Engineering Geophysics Co. Figures 6A, B show the seismic velocity and acceleration shot gathers, respectively. Velocity and acceleration shot gathers are the signals received at the same position and time using velocity and acceleration geophones respectively. Figures 7A, B show the effective acceleration signal and filtered noise obtained by denoising using the method proposed in this paper respectively. After denoising, the continuity of the events in the seismic data is better. And there are fewer effective signals in the filtered noise.

Figures 8A, B show the seismic velocity and acceleration profiles, respectively, while Figure 8C shows the seismic profile processed by the proposed method. Figure 9 shows the original acceleration profile and the noise filtered by the combined treatment. After processing, the continuity of the event in the seismic data is better, the event is compressed, and the structure is easy to recognize. Additionally, the weak seismic signal in the shallow layer of the seismic data was strengthened. The comparison results show the feasibility and practicability of this method for denoising seismic velocity and acceleration data. It can be seen from the filtered noise profile that although there are some effective signals in the noise filtered by this method, their amplitude is small, and their energy is

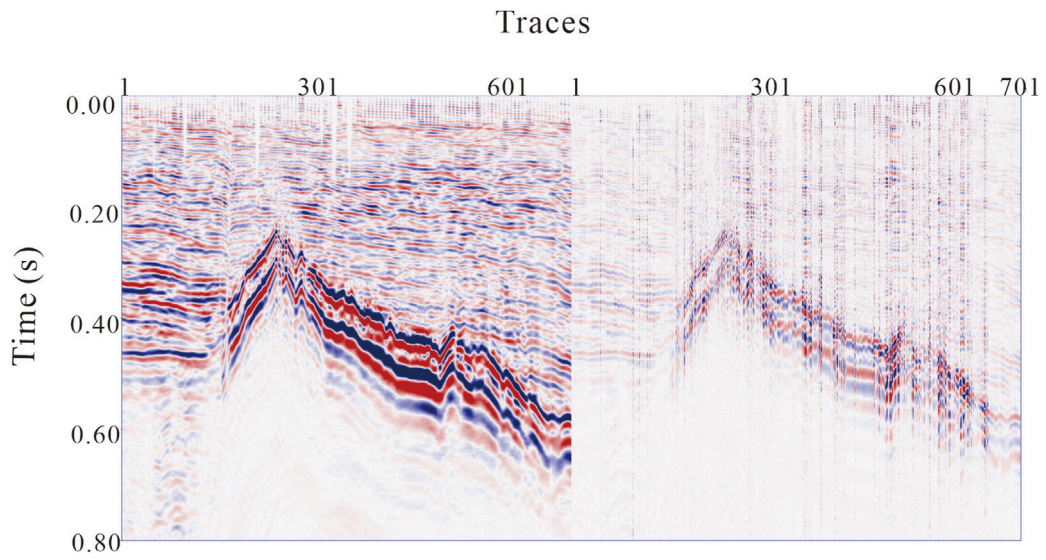

FIGURE 12
Comparison results before and after denoising (Left is the original acceleration signal; Right is noise removal).

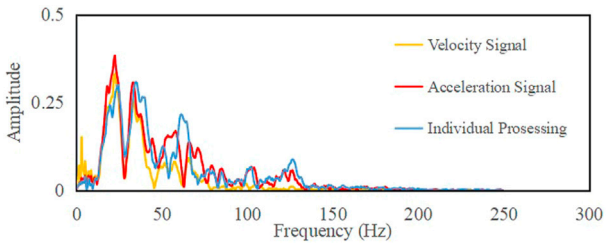

FIGURE 13
Spectrum of separate processing results (Yellow curve, spectrum of the original velocity profile; Red curve, original acceleration profile spectrum; Blue curve, profile spectrum alone after processing).

weak, and most of the filtered noise results were incoherent. Figure 10 shows the frequency spectra of the original velocity profile, original acceleration profile, and processed profile. The yellow curve represents the original velocity profile spectrum, the red curve the original acceleration profile spectrum, and the black curve the profile spectrum after combined processing. From the spectrum of the data before and after processing, it can be seen that the proposed joint denoising method has almost no loss at low frequency. The dominate frequency of the signal was increased from 20 Hz to 40 Hz. The results show that the time resolution of the original velocity profile, the original acceleration profile and the processed profile are 10.9 m, 8.5 ms and 6 8ms, respectively. The time resolution was improved by approximately 20%, indicating that this method can significantly improve the time resolution of seismic data.

To compare the advantages of joint processing, only a seismic acceleration signal was used for denoising. Figure 11 shows the seismic profile alone after noise removal; Figure 12 shows the original acceleration profile and filtered noise separately; and Figure 13 shows the spectrum of the seismic profile denoised using only acceleration signals. The time resolution of the seismic profile obtained using a single denoising processing method was 8 ms. This indicates that the effect of single denoising is weaker than that of combined denoising in terms of improving time resolution. Meanwhile, separate processing barely broadens the frequency band of the original data. Also, separate processing loses a part of the high-frequency information of the signal, while it can be observed that there are still many effective signals in the filtered noise profile. Finally, the joint denoising method is more sensitive to the identification of pinch-out points, and the event continuity is better.

4 Discussion and conclusion

The joint denoising method presented in this paper relies on the system and observation equations, which are represented by the state transition matrix in the Kalman filter. The state transition matrix can typically be determined using either the average value method or the white noise method. In this study, the white noise method was chosen to determine the state transition matrix, owing to its simplicity and efficiency in calculation. Furthermore, when dealing with significant interference and low-dimensional data, the denoising results obtained using the average-value method may not accurately reflect the true situation, whereas the state-transition matrix determined using the white-noise method provides more reliable results. However, in joint denoising, the effect of Kalman filter is more dependent on the establishment of the observation system, that is, the effect of denoising is affected by the establishment of the state transition matrix.

The test results of model seismic data both with and without noise demonstrate that the method outlined in this paper is capable

of effectively separating effective signals and enhancing the SNR. These results are consistent with the expected theoretical values. The processing of actual seismic data indicates that this method increases the signal bandwidth and time resolution. The proposed joint processing technique has numerous advantages over single-signal denoising, including a broadened bandwidth, improved time resolution, and greater continuity of events. Furthermore, this study highlights that combining different signal recording methods leads to a more accurate restoration of seismic wave signals, which will provide valuable insights for improving seismic acquisition techniques in the future.

Data availability statement

The data analyzed in this study is subject to the following licenses/restrictions: The dataset can be used with permission from the corresponding author. Requests to access these datasets should be directed to LY, youli@stu.cdut.edu.cn.

Author contributions

GZ, HbZ, LY, YY, and BZ developed and applied the method. GZ and HlZ supervised the funding for this study. All authors discussed the results and contributed to the final manuscript.

Conflict of interest

Author GZ was employed by the company Sinopec Petroleum Engineering Geophysics Co., Ltd. and Author HZ was employed by the company The Shengli Branch of the Sinopec Petroleum Engineering Geophysics Co., Ltd., and Author WC was employed by the company Sinopec Petroleum Engineering Geophysics Co., Ltd.

The remaining authors declare that the research was conducted in the absence of any commercial or financial relationships that could be construed as a potential conflict of interest.

This study was funded by the Research Project of Sinopec Petroleum Engineering Geophysics Co., Ltd. ("Research on seismic exploration technology based on acceleration signal," SGC-2021-08; "Research on imaging technology of primary reflection and multiple waves of viscoelastic media based on ocean double geophone data," SGC-2022-01). The funder was involved in the collection and processing of data.

Publisher's note

References

Bai, X. M., Yuan, S. H., Wang, Z. D., Chen, J. G., Wang, X. D., and Hu, Q. (2014). Digital geophones and exploration of tight Oil. A. 2014 SEG Annual Meeting.

Cao, J. J., Wang, Y. F., and Yang, C. C. (2012). Seismic data restoration based on compressive sensing using regularization and zero-norm sparse optimization. *J. Chin. J. Geophys.* 55 (2), 239–251. doi:10.1002/cjg2.1718

Cao, J. J., Zhao, J. T., and Hu, Z. Y. (2015). 3D seismic denoising based on a low-redundancy curvelet transform. *J. J. Geophys. Eng.* 12 (4), 566–576. doi:10.1088/1742-2132/12/4/566

Chen, Y. K., Zu, S. H., Wang, Y. F., and Chen, X. H. (2019). Deblending of simultaneous source data using a structure-oriented space-varying median filter. *J. Geophys. J. Int.* 216 (2), 1805–1823. doi:10.1093/gji/ggaa189

Damaševičius, R., Napoli, C., Sidekerskienė, T., and Woźniak, M. (2017). IMF mode demixing in EMD for jitter analysis. *J. J. Comput. Sci.* 22, 240–252. doi:10.1016/j.jocs.2017.04.008

Denis, M. (2004). *How digital sensors compare to geophones? A. CPS/SEG 2004 international geophysical conference*. Berlin, Germany: Springer.

Eikrem, K., Geir, J., and Morten, S. (2019). Iterated extended Kalman filter method for time-lapse seismic full-waveform inversion. *J. Geophys. Prospect.* 67 (2), 379–394. doi:10.1111/1365-2478.12730

Hajsadeghi, S., Asghari, O., Mirmohammadi, M., and Meshkani, S. A. (2020). Discrimination of mineralized rock types in a copper-rich volcanogenic massive sulfide deposit through fast independent component and factor analysis. *J. Nat. Resour. Res.* 29 (1), 161–171. doi:10.1007/s11053-019-09499-0

Han, J., and Van, D. B. M. (2013). Empirical mode decomposition for seismic time-frequency analysis. *J. Geophys.* 78 (2), 09–019. doi:10.1190/geo2012-0199.1

Hons, M., Stewart, R., Lawton, D., Bertram, M., and Hauer, G. (2008). Field data comparisons of MEMS accelerometers and analog geophones. *J. Lead. Edge* 27 (7), 896–903. doi:10.1190/1.2954030

Hons, M., Stewart, R., Lawton, D., and Malcolm, B. (2007). Ground motion through geophones and MEMS accelerometers: Sensor comparison in theory, modeling and field data. J. SEG Technical Program Expanded Abstracts.

Joachim, W. (1997). A review of nonlinear diffusion filtering. *J. Lect. Notes Comput. Sci.* 1252 (1), 1–28. doi:10.1007/3-540-63167-4_37

Lansley, M., Laurin, M., and Ronen, S. (2008). Modern land recording systems: How do they weigh up? *J. Lead. Edge* 27 (7), 888–894. doi:10.1190/1.2954029

Liu, X. W., Gao, W., Zhang, N., and Liu, W. Y. (2007). ICA with banded mixing matrix based seismic blind deconvolution. *J. Prog. Geophys.* 22 (4), 1153–1163.

Liu, Z. D., Lu, Q. T., Dong, S. X., and Chen, M. C. (2012). Research on velocity and acceleration geophones and their acquired information. *J. Appl. Geophys. Springer.* 9 (2), 149–158. doi:10.1007/s11770-012-0324-6

Meng, H. J., Su, Q., Zeng, H. H., Xu, X. R., Liu, H., and Zhang, X. M. (2021). Blind source separation of seismic signals based on ICA algorithm and its application. *J. Lithol. Reserv.* 33 (4), 93–100.

Mirko, B., and Maiza, B. (2009). Random and coherent noise attenuation by empirical mode decomposition. *J. Geophys.* 74 (5), 89–98. doi:10.1190/1.3157244

Morlet, J., Arens, G., Fourgeau, E., and Giard, D. (1982). Wave propagation and sampling theory—Part II: Sampling theory and complex waves. *J. Geophys.* 47, 222–236. doi:10.1190/1.1441329

Necati, G. (1986). F-X decon and complex wiener prediction filter. A. 1986 SEG Annual Meeting.

Nicolas, T., and Jérôme, L. (2017). Understanding MEMS based digital seismic sensors. *J. First Break.* 35 (1), 93–100.

Ott, N., and Meder, H. G. (1972). The Klaman filter as a prediction error filter. *J. Geophys. Prospect.* 20 (3), 549–560. doi:10.1111/j.1365-2478.1972.tb00654.x

Perona, P., and Malik, J. (1990). Scale-space and edge detection using anisotropic diffusion. *J. IEEE Trans. Pattern Analysis Mach. Intell.* 12 (7), 629–639. doi:10.1109/34.56205

Qin, F. L., Liu, J., and Yan, W. Y. (2018). The improved ICA algorithm and its application in the seismic data denoising. *J. J. Chongqing Univ.* 17 (4), 162–170.

Ren, L. G. (2018). Analysis and application of velocity and acceleration geophone's seismic response characteristic. *J. Prog. Geophys.* 33 (5), 2159–2165.

Saruwatari, H., Kawamura, T., Nishikawa, T., Lee, A., and Shikano, K. (2006). Blind source separation based on a fast-convergence algorithm combining ICA and beamforming. *J. Speech Lang. Process.* 14 (2), 666–678. doi:10.1109/TSA.2005.855832

Sergio, L. M. F., and Tad, J. U. (1988). Application of singular value decomposition to vertical seismic profiling. *J. Geophys.* 53 (6), 778–785. doi:10.1190/1.1442513

Spanias, A. S., Jonsson, S. B., and Stearns, S. D. (1991). Transform methods for seismic data compression. *J. IEEE Trans. Geoscience Remote Sens.* 29 (3), 407–416. doi:10.1109/36.79431

Wang, J., Zhang, J. H., Yang, Y., and Du, Y. S. (2021). Anisotropic diffusion filtering based on fault confidence measure and stratigraphic coherence coefficients. *J. Geophys. Prospect.* 69 (5), 1003–1016. doi:10.1111/1365-2478.13085

Wang, W., Gao, J. H., and Chen, W. C. (2012). Random seismic noise suppression via structure-adaptive median filter. *J. Chin. J. Geophys.* 55 (5), 1732–1741. doi:10.6038/j.issn.0001-5733.2012.05.030

Wei, J. D. (2018). Comparison of recording accuracy between analog geophone and MEMS accelerometer and their influence to the S/N ratio. *Prog. Geophys.* 33 (4), 1726–1733. doi:10.6038/pg2018CC0018

Zhang, H. B., Li, L. M., Zhang, G. D., Zhang, B. H., and Sun, M. M. (2020). Seismic acceleration signal analysis and application. *J. Appl. Geophys.* 17 (1), 67–80. doi:10.1007/s11770-020-0802-1

Zhang, H. L., Zhang, G., Xue, B., and Yuan, J. W. (2022). Mainlobe jamming suppression via improved BSS method for rotated array radar. *J. J. Syst. Eng. Electron.* 33 (6), 1151–1158.

frontiers | Frontiers in Earth Science

TYPE Original Research
PUBLISHED 09 June 2023
DOI 10.3389/feart.2023.1209433

OPEN ACCESS

EDITED BY
Lidong Dai,
Chinese Academy of Sciences, China

REVIEWED BY
Hao Rao,
China University of Geosciences Wuhan, China
Hongrui Xu,
Southwest Jiaotong University, China

*CORRESPONDENCE
Tianbin Li,
ltb@cdut.edu.cn

RECEIVED 20 April 2023
ACCEPTED 30 May 2023
PUBLISHED 09 June 2023

CITATION
Huang Y and Li T (2023), On the relationship between the mechanical strength and mineral microstructure of biotite granite under temperature influence.
Front. Earth Sci. 11:1209433.
doi: 10.3389/feart.2023.1209433

On the relationship between the mechanical strength and mineral microstructure of biotite granite under temperature influence

Yuyang Huang[1,2] and Tianbin Li[1,2]*

[1]College of Environment and Civil Engineering, Chengdu University of Technology, Chengdu, Sichuan, China, [2]State Key Laboratory of Geological Disaster Prevention and Geological Environment Protection, Chengdu University of Technology, Chengdu, Sichuan, China

Many studies are currently focusing on the mechanical properties of granite from macroscopic and microscopic perspectives, but only several studies on the influence of rock mineral composition on the mechanical properties using a combined macro-micro assessment. The biotite granite in the Gaoligong Mountains was selected as the research object, and the variation strength characteristics at 20–130°C were obtained through uniaxial compression experiments. The rock's uniaxial compressive strength and elastic modulus reached peak values at 40°C. The main mineral components of the rock determined by X-ray powder diffraction were quartz, biotite, albite, and potash feldspar. With Material Studio software, molecular dynamics simulations were carried out on the crystal models of quartz, biotite, albite, and potash feldspar at 20–130°C, and relevant mechanical parameters were calculated. The macroscopic and microscopic experimental data were compared and analyzed. The results show that: 1) due to the thermal expansion of minerals in the rock, the original cracks between particles are partially closed, and the sample strength is the largest at 40°C; 2) temperature mostly affects quartz and biotite phases, and the rock strength increases first and then decreases with the temperature increase. The mechanical properties of albite and potash feldspar are less affected by temperature; 3) macroscopic and microscopic experimental results show that the rock strength reaches the peak value in a certain temperature range. The obtained critical temperature is different because the rock sample also contains a small amount of argillaceous rock, siliceous rock, phyllite, and some siliceous and calcareous cement beside the main mineral composition; 4) The structural changes of quartz and biotite are affected by temperature. The bond length of the quartz crystal decreases while that of the biotite crystal first increases and then decreases with the temperature. The mechanism of the temperature influence on the increase of the rock strength is different for these two crystal phases, and it requires further exploration.

KEYWORDS

rock mechanics, granite, microstructure, numerical simulation, temperature

1 Introduction

Granite widely exists in crustal strata and is mainly composed of feldspar and quartz. It exhibits a high strength and stable structure, but under temperature influence, granite undergoes certain thermal damage, which changes the pore size, volume, rock composition, and microstructure of the original material, significantly affecting its mechanical properties. Exploring the impact of temperature-related microstructural changes of rocks on their macroscopic mechanical properties from a microscopic perspective and exploring the relationship between the microscopic mechanical properties and macroscopic mechanical properties can provide a theoretical foundation for predicting and preventing disasters such as rock bursts. Such studies have an important practical significance for solving rock engineering problems at high temperatures.

Chinese and foreign scholars have conducted studies on the mechanical properties of granite under different temperatures. In 1964, Lebedev and Khitaror studied the thermal physical properties of granite, including the determination of basic physical and mechanical parameters (Heuze, 1983; Lau et al., 1995), thermal cracking (Johnson et al., 1978), deformation mechanism (Vander Molen, 1981; Simpson, 1985), failure criterion, and constitutive equation (Heueckel et al., 1994). O Alm (Alm et al., 1985) analyzed the mechanical properties of granite after heat treatment at different temperatures and explored the micro-fracture process. Lin Muzeng (Lin, 1991) discovered that the Young's modulus of gradesite, quartz trachyte, and other rocks sharply decreases below 300°C as the temperature increases. Du et al. (Du et al., 2004) studied the mechanical properties of granite treated at different temperatures and obtained the variation law of mechanical parameters, such as peak stress, peak strain, elastic modulus, and Poisson's ratio of rocks with temperature. The results showed that a high temperature of up to 400°C subtly influenced the mechanical properties of granite. However, when the temperature exceeded 400°C, the mechanical properties of granite rapidly deteriorated, exhibiting a sharp decrease in peak stress (or strength) and elastic modulus and a rapid increase in peak strain. Xu (Xu, 2008) found that the mechanical properties of rock samples changed continuously under *in-situ* high-temperature treatment and showed a sudden change after heating and subsequent cooling, which was closely related to structural phase transformations. With the temperature increase, the brittleness of granite weakened, ductility increased, peak strength decreased, and the post-peak increased significantly. The mechanical properties of granite under high-temperature and low-temperature conditions are distinct. Tang Mingming (Tang et al., 2010) assessed the mechanical properties under low-temperature conditions. In uniaxial and triaxial tests, the compressive strength of slightly weathered granite increased as the temperature decreased in the low-temperature range, representing a nonlinear growth trend, a temperature limit value upon which the compressive strength tended to be stable was identified. The cohesion of micro-weathered granite increased with the temperature decrease under both dry and saturated conditions. The internal friction angle did not change significantly when the temperature decreased under dry conditions but increased with the temperature decrease under saturated conditions.

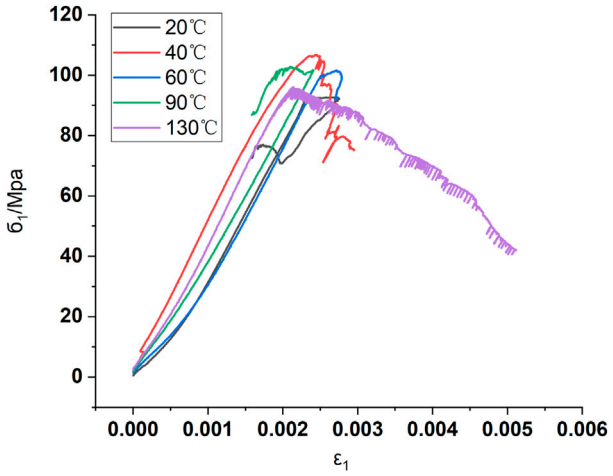

FIGURE 1
Stress-strain curves at different temperatures (20°C–130°C).

However, only several studies on the microstructural changes of granite under temperature influence are available in the literature. Gao (Gao et al., 2018) showed in the microscopic study of granite at different temperatures that the number of ink bottle-like pores in granite decreased while the number of parallel plate-like pores increased with the increase in temperature. The percentage of mesopores as a whole in the total pore volume showed an increasing trend. The total pore volume enlarged, and the connectivity was enhanced. Ji (Ji, 2008) determined the mechanical parameters, such as elastic modulus and hardness, of quartz and feldspar contained in the composition of Dagangshan granite minerals using micro- and nano-indentation tests, demonstrating that the elastic moduli of quartz and feldspar basically determine the overall elastic modulus of granite. Gao (Gao et al., 2021) analyzed the composition and micro-fracture characteristics of granite samples using X-ray diffraction and SEM tests, and the micro-fracture mechanism was correlated with the main mineral morphology.

The results of previous studies have largely promoted the research on the mechanical properties of granite rocks at different temperatures. However, the research mainly focused on the rock composition and strength changes, and less attention was paid to the microstructural changes of rock mineral components under temperature variation. Therefore, this paper investigates biotite granite at the Gaoligongshan tunnel site as the research object and addresses the relationship between the changes in the mineral composition structure of granite and mechanical properties at the micro-scale under high-temperature conditions.

2 Uniaxial compression experiments

Rock samples investigated in this study were prepared from biotite granite, and the uniaxial compression tests were performed using an MTS815Teststar program-controlled servo rigid testing machine. The whole stress-strain curves of rock samples were obtained.

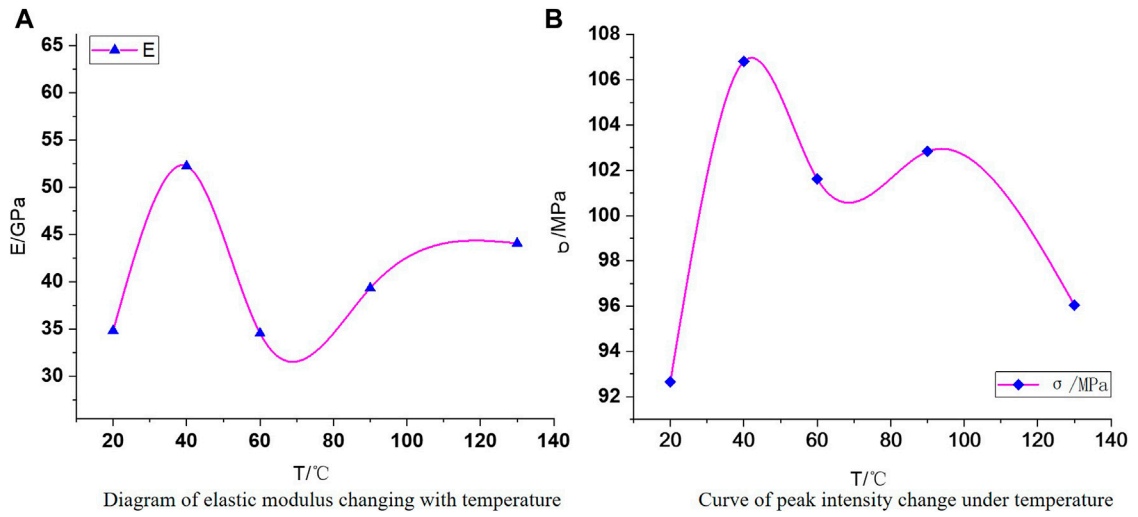

FIGURE 2
Changes in elastic modulus and peak strength with temperature.

The test temperature was set to 20, 40, 60, 90, and 130°C. The investigated sample was heated at a constant temperature in s DHG-9203A electric constant-temperature blast dryer. The sample was retained 2 h at the target temperature. At the beginning of the test, the axial displacement was controlled at a value of 0.1 mm/min. When deformation reached the yield stage, the loading rate was controlled by lateral deformation, and the value was 0.03 mm/min until the specimen was destroyed.

The mechanical and deformation parameters, such as compressive strength and elastic modulus, were determined through the stress-strain curve of the rock samples at different temperatures, and the failure mode and properties after reaching the peak were investigated.

2.1 The whole stress-strain process curve

From Figure 1 can be seen that the rock samples at 20°C and 60°C exhibit type II failure, while the rock samples at 40, 90, and 130°C show type I failure. Due to the inhomogeneity and discontinuity of the samples, brittle failure characteristics appear in the overall temperature range of 20°C–60°C. The test also shows that the same lithology exhibits different strength characteristics and failure modes at different temperatures, which is related to the influence factors, such as temperature, on the sample's storage capacity of elastic strain energy and stress environment.

2.2 Elastic modulus variation with temperature

Figure 2A shows that the elastic modulus first increases and then decreases with temperature. The elastic modulus increases by 17.4 GPa at 40°C relative to the value at 20°C, then decreases by 17.6 GPa at 60°C compared to the value at 40°C; further, the elastic modulus at 90°C is 4.8 GPa higher than at 60°C, and 5.0 GPa higher at 130°C than at 90°C. Thus, the elastic modulus of rock samples slowly increases with the temperature increase, while the structural stiffness gradually increases. The elastic modulus reaches the peak at 40°C.

2.3 Strength characteristics

The uniaxial compression test at different temperatures allowed for the determination of the temperature influence on the uniaxial compressive strength of rock samples, as shown in Figure 2B. The uniaxial compressive strength first increases and then decreases with temperature. At 40°C, the uniaxial compressive strength of rock increases by 15.54% compared with that at 20 °C; at 60, 90, and 130°C, it decreases by 4.67, 3.74, and 10.28% compared to that at 40°C, i.e., the rate of decrease gradually increases. These results imply that crystalline minerals inside rocks become softer as the temperature rises. At 40°C, the uniaxial compressive strength reaches the maximum. The comprehensive analysis shows that the thermal expansion of the rock's internal minerals at a certain temperature leads to the partial closure of original cracks between particles, practically densifying the rock and increasing the stiffness and strength compared to non-heated samples. These results need to be further verified via micro-mechanical assessment.

2.4 X-ray powder diffraction analysis

We selected five rock samples for testing test to determine the mineral composition of the rock using diffractometry. The results show the highest proportion of quartz, followed by plagioclase, mica, potash feldspar, tremolite, chlorite, pyrite, etc. According to the analysis report of rock and mineral identification, the plagioclase in

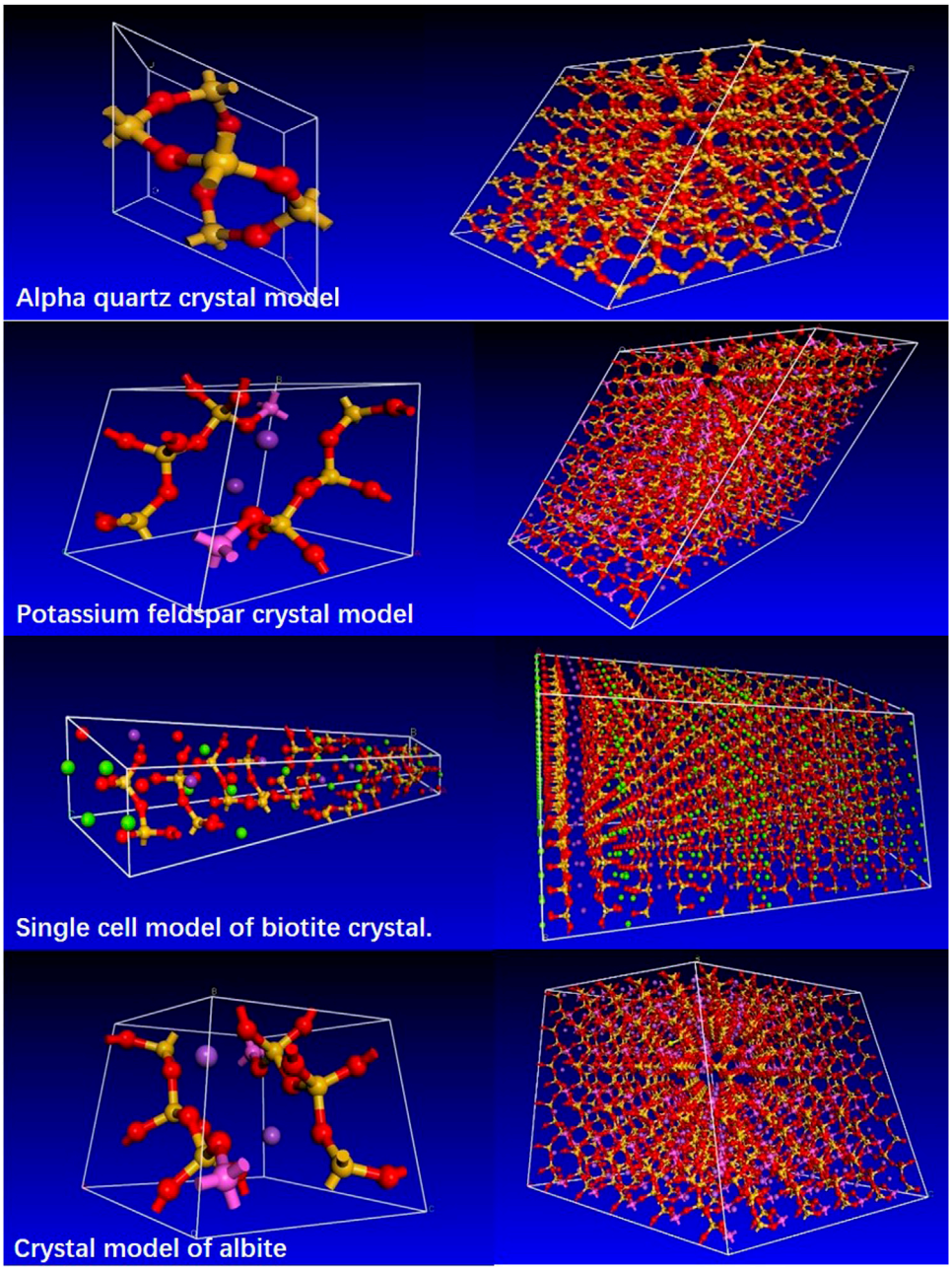

FIGURE 3
Crystal model.

the rock samples is mainly medium-acidic plagioclase, so it is concluded that it is mainly albite.

2.5 Microscopic simulations

The mineral composition of this group of samples was obtained from X-ray diffraction experiments. However, from the micro-perspective, the influence of temperature change on the mechanical properties of minerals needs to be explored. Therefore, we used the Forcite module in Material Studio, a material calculation software of Accelrys, to conduct molecular-scale mechanical numerical simulations of biotite, quartz, potash feldspar, and plagioclase in four main minerals of the tested rock samples.

The corresponding crystal model was first downloaded from the Material Projects crystal library, and the model *cif* file was imported into Material Studio software. Chemical keys were added while the structure was optimized. Then, the molecular dynamics simulations (Dynamic) of the model were carried out considering 20, 40, 60, 90, 130°C, and then the structure was optimized again. Finally, the mechanical properties of the model were calculated to get the final results.

TABLE 1 Parameters of crystal.

Formula	Spacegroup	Formation energy (eV)	E above hull (eV)	Band gap (eV)	Volume	Nsites	Density (gm/cc)
SiO_2	$P3_121$	−3.267	0.011	5.678	120.336	9	2.487
$KAlSi_3O_8$	P1	−3.256	0	4.934	376.251	26	2.457
$KMg_2AlFeSi_3(HO_6)_2$	P-1	−2.856	0.001	2.922	1055.554	88	2.824
$NaAlSi_3O_8$	P1	−3.224	0	4.876	347.661	26	2.505

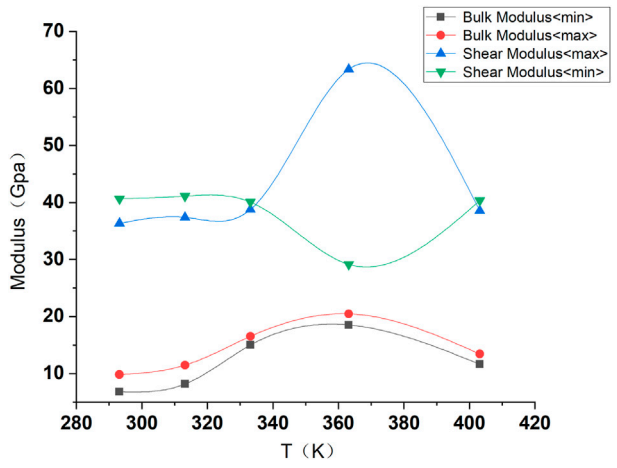

FIGURE 4
Volumetric modulus and Shear modulus change of quartz crystal at 20°C–130°C (293.15–403.15 K).

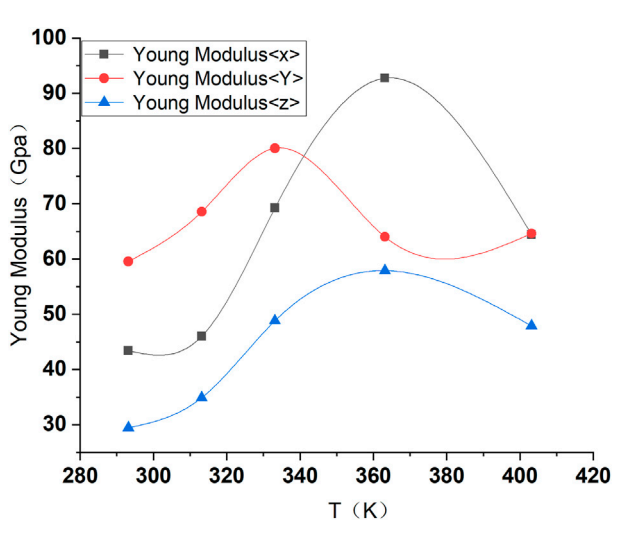

FIGURE 5
Young's modulus change of quartz crystal at 20°C–130°C (293.15–403.15 K).

During the modeling process, the supercell structure of each crystal 5*5*5 (biotite is 3*3*3) is established to clarify the crystal structure change. Figure 3 shows quartz, biotite, potassium feldspar, and albite crystal models. The NPT ensemble and COMPASS force field were used for calculation in the molecular dynamics simulation. The calculation step was 5000. The obtained results are convergent and reliable. Quartz, potassium feldspar, biotite, and albite crystal-related parameters are selected as follows (Table 1).

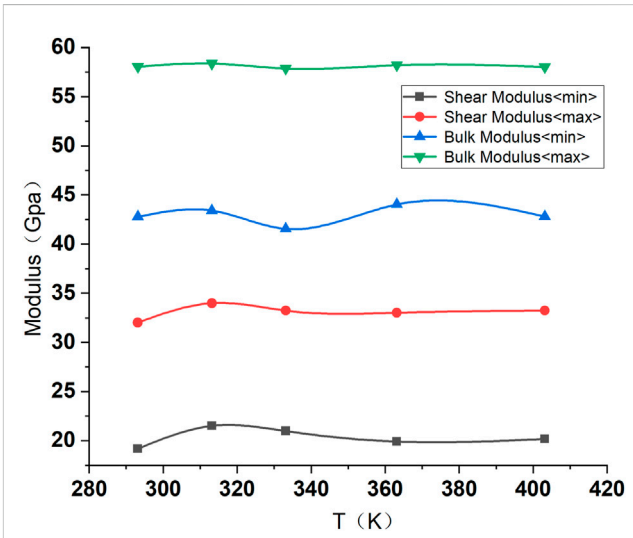

FIGURE 6
Change of volume modulus and Shear modulus of potassium feldspar crystal at 20°C–130°C (293.15–403.15 K).

2.5.1 α-Quartz crystal

Since α-quartz is ubiquitous in granite, the α-quartz crystal was selected as a simulation object. Figures 4, 5 show that the bulk modulus of quartz increases first and then decreases with temperature, reaching its maximum at 90°C (363.15 K). At this time, the volume change of the crystal is the smallest, while the rigidity is the greatest. The shear modulus does not change significantly during the heating process at 20°C–90°C, and the maximum value increases sharply at 90°C (363.15 K), indicating that the crystal adhesion is enhanced. The shear modulus decreases gradually after heating. The Young's modulus in the *y*-direction first increases and then decreases with temperature, reaching the peak value at 60°C (333.15 K). Young's moduli in x- and z-directions first increase and then decrease with temperature, reaching the peak value at 90°C (363.15 K), which indicates that the crystal stiffness is the largest at this temperature point.

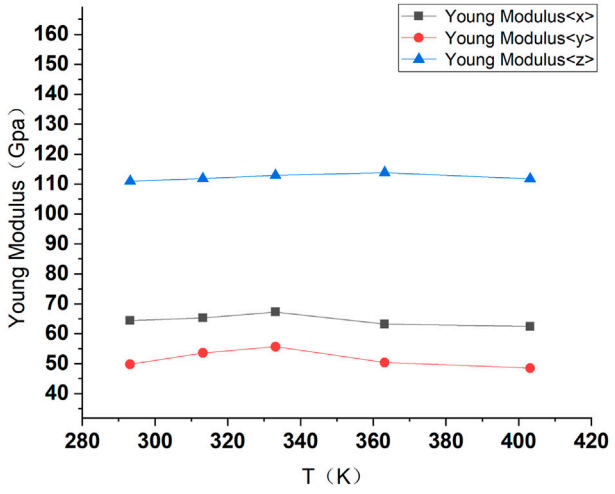

FIGURE 7
Change of Young's modulus of potassium feldspar crystal at 20°C–130°C (293.15–403.15 K).

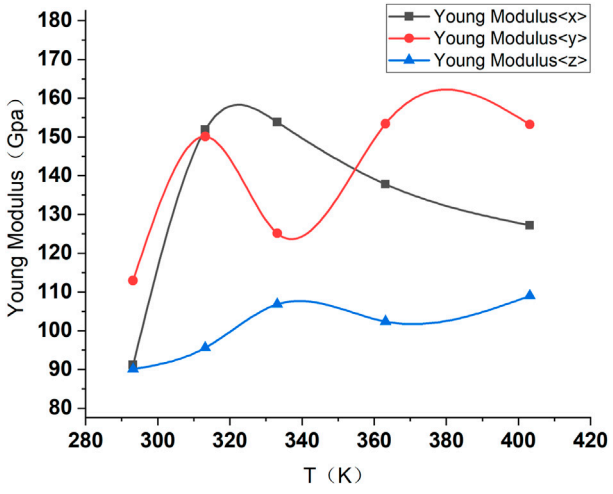

FIGURE 9
Young's modulus of biotite at 20°C–130°C (293.15–403.15 K).

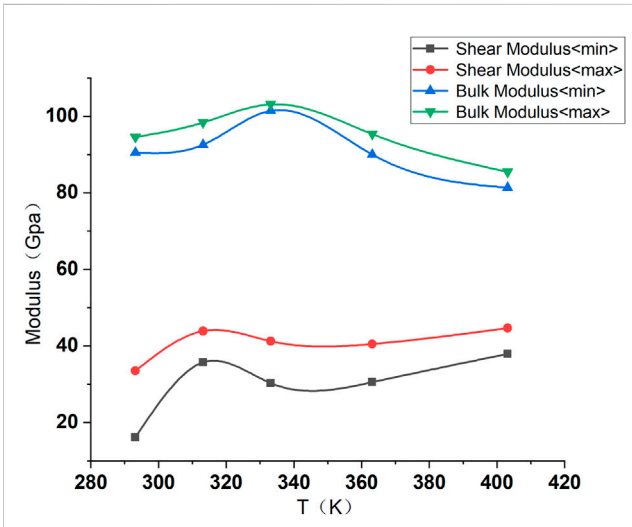

FIGURE 8
Change of volume modulus and Shear modulus of biotite crystal at 20°C–130°C (293.15–403.15 K).

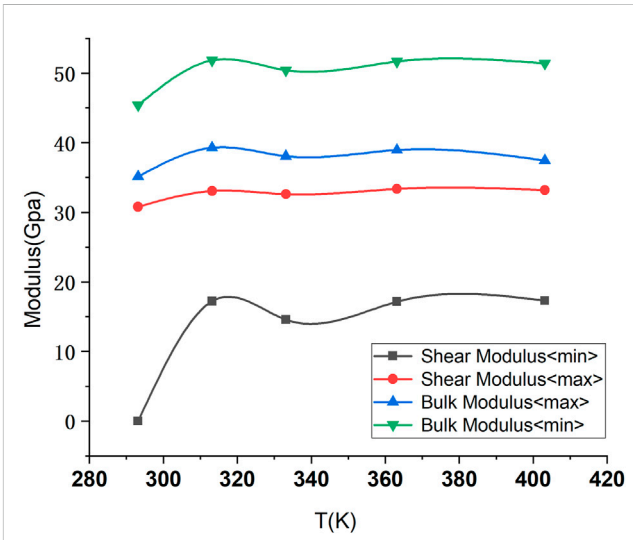

FIGURE 10
Change of Bulk modulus and Shear modulus of albite crystal at 20°C–130°C (293.15–403.15 K).

2.5.2 Potassium feldspar crystal

The related parameters of potassium feldspar are shown in Table 1. As shown in Figures 6, 7, the bulk modulus and Young's modulus of the potassium feldspar crystal have no obvious change with the increase in temperature. The crystal compressibility decreases in the range of 20°C–40°C (293.15–313.15 K) and increases between 40°C and 60°C (313.15–333.15 K).

2.5.3 Biotite crystals

The composition of biotite is complex, and it may easily undergo extensive isomorphic transformations. Therefore, the chemical composition of biotite produced in different rocks greatly varies. Most acidic and alkaline rocks contain biotite; generally, biotite in acidic and alkaline magmatic rocks has a high content of FeO and a low content of Mg. Since this group of rocks belongs to granite, and the content of Fe in rocks is relatively high, $KMg_2AlFeSi_3(HO_6)_2$ is selected as a research model. As shown in Figures 8, 9, the bulk modulus of the biotite crystal increases first and then decreases during the heating process, reaching the maximum at 60°C (333.15 K). Under such conditions, the crystal volume change is the smallest, while the rigidity is the highest. The shear modulus first increases, then decreases between 60°C and 90°C (333.15–363.15 K), and remains constant between 90°C and 130°C (333.15–403.15 K), demonstrating that the crystal bonding force rises initially, then falls, and rises again. The bonding force decreases at 60°C–90°C (333.15–363.15 K), exhibiting the lowest strength. In the *x*-direction, the Young's modulus first increases and then

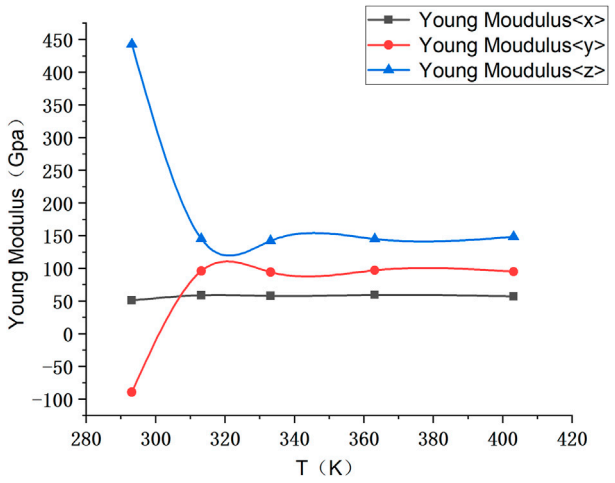

FIGURE 11
Change of Young's modulus of albite crystals at 20°C–130°C (293.15–403.15 K).

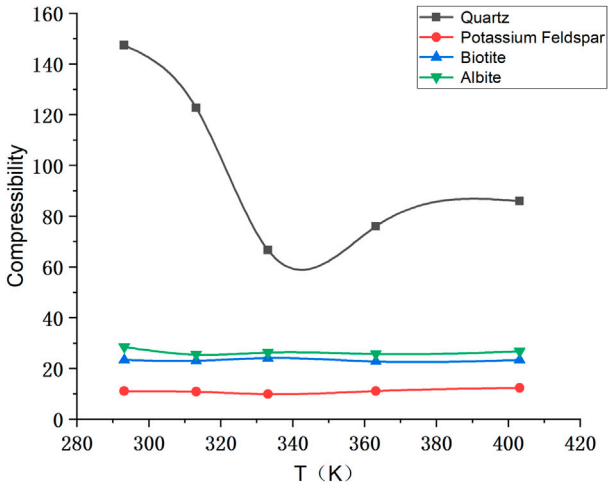

FIGURE 12
Crystal compressibility.

decreases, reaching the peak at 40°C–60°C (313.15–333.15 K). In the *y*-direction, the Young's modulus shows repetitive increasing-decreasing sequences and peaks at 90°C–130°C (363.15–403.15 K). In the *z*-direction, the Young's modulus increases slowly, and the change rate is not significant.

2.5.4 Albite crystal

According to the rock and mineral identification report, the granite in this group contains acidic and medium-acidic plagioclase, so it is preliminarily assessed as albite. As shown in Figures 10, 11, the volume modulus of the albite crystal remains stable after increasing during heating, being in the range of 50–52 GPa. There is no significant change in shear modulus. In the *x*-direction, the Young's modulus initially decreases and then remains stable. In the *y*-direction, the Young's modulus increases in the beginning and then remains stable. In the *z*-direction, the Young's modulus exhibits no obvious change.

3 Discussion

1) According to the results of the uniaxial compression experiments and mineral microscopic numerical simulations of the investigated rock samples, it can be seen that the elastic modulus first increases and then decreases with the increase of temperature, reaching the peak value at about 40°C (313.15 K). Similarly, the uniaxial compressive strength first increases and then decreases as the temperature rises, having the largest value at 40°C (313.15 K). The X-ray powder diffraction analysis indicated four main mineral components in the sample, namely, quartz, biotite, potash feldspar, and albite. In the microscopic numerical simulations of minerals, the mechanical properties of quartz and biotite change greatly under the influence of temperature. The strength reaches the peak value at 60°C–90°C. The albite and potash feldspar phases are less affected by temperature.
2) The crystal compressibility decreases to the minimum value when the temperature is 60°C–90°C (333.15–363.15 K), while the material stiffness has the maximum value (Figure 12). Therefore, the compressive strength and strength of quartz crystals are at their highest between 60°C and 90°C, and temperature fluctuations significantly affect the mechanical properties of quartz minerals. The compressibility of potassium feldspar, biotite, and albite is less affected by temperature.
3) Macroscopically, due to the temperature increase, the original cracks between particles are partially closed, which increases the overall stiffness and strength of the rock, with the mechanical strength peaking at 40°C. Microscopically, the two mineral components, i.e., quartz and biotite, are greatly affected by temperature, and the mechanical strength reaches the peak value at about 60°C. The reason for the difference between the two sets of experimental results is that the rock samples contain a small amount of argillaceous rock, siliceous rock, phyllite, and some siliceous and calcareous types of cement beside the main mineral components. The mechanical response mechanism of the entire rock and single minerals under temperature still differs, which needs further exploration.
4) The mechanism behind the influence of heating on the mechanical properties of granite is mainly related to the thermal expansion and different thermo-elastic properties of anisotropic particles in different crystallization directions, which causes uncoordinated thermal expansion across the particle boundaries, resulting in tensile or compressive stress between particles or within particles. As the temperature increases, the stress between particles or within particles increases further, resulting in microcrack formation or expansion and widening and connection of primary cracks in granite, which macroscopically shows the deterioration of the mechanical properties of granite.
5) Since quartz and biotite are greatly affected by temperature, according to the results of numerical simulation experiments, the

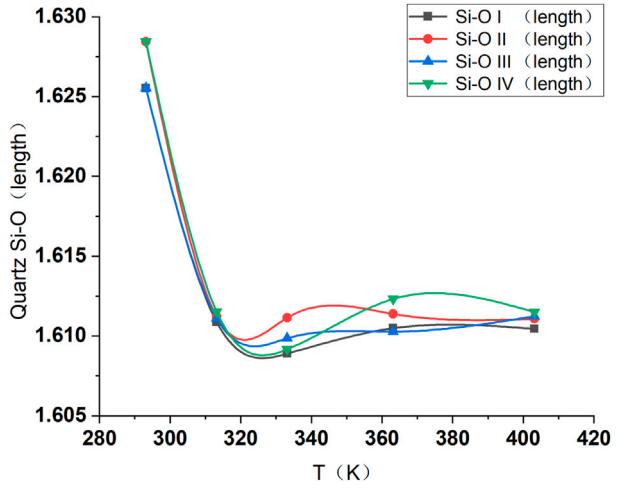

FIGURE 13
Variation trend of Si-O bond length in quartz minerals.

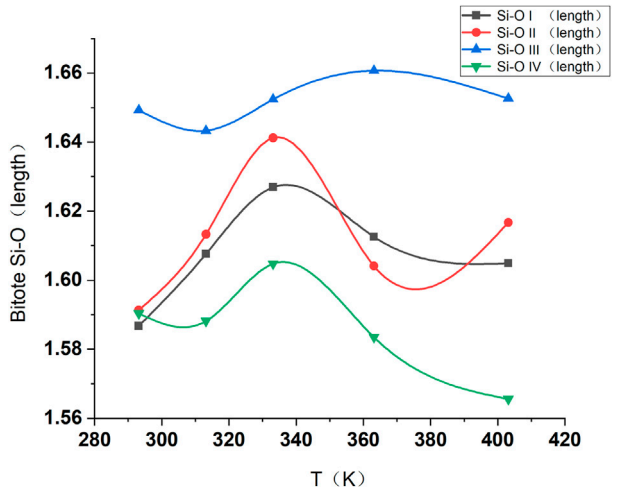

FIGURE 14
Trends of Si-O bond length in biotite minerals.

Si-O bond length in quartz minerals decreases with temperature, as shown in Figure 13. The Si-O bond length in biotite first increases and then decreases, as shown in Figure 14.

It shows that the bond length of quartz minerals decreases with temperature, and the spatial structure is changed. We conclude that the mineral crystal may be in a compression state during the heating process. The strength gradually grows because the quartz crystal is reasonably stable and the change in mechanical properties. With the temperature increase, the bond length of the biotite crystal first increases and then decreases, indicating that the spatial structure also changes. The difference is that the biotite crystal may undergo thermal expansion. During the heating process, the expansion of the interlayer structure favors densification. Macroscopically, it leads to a dense structure and increased rock strength.

4 Conclusion

1) According to the uniaxial compression test results, the elastic modulus first increases and then decreases with temperature, and the structural stiffness of rock samples gradually becomes higher. At 40°C, the elastic modulus reaches the peak value. Similarly, with the temperature increase, the uniaxial compressive strength first increases and then decreases because the thermal expansion of minerals inside the rock leads to the partial closure of original cracks between particles, increasing the overall stiffness and strength of the rock.
2) According to the numerical simulation results of the MS molecular dynamics module, the samples contain four minerals: quartz, albite, potash feldspar, and biotite. The strength of quartz and biotite is most affected by temperature, which first increases and then decreases with temperature. Albite and potassium feldspar are not affected by temperature.
3) In the uniaxial compression test, the strength reaches the peak temperature between 40°C–60°C; in the MS numerical simulation, the temperature peaks in the 60°C–90°C range. The difference originates from the fact that rock samples also contain other compositions, including a small amount of argillaceous rocks, siliceous rocks, phyllite, and some siliceous and calcareous types of cement.
4) The rock structure changes when quartz and biotite crystals are affected by temperature. The bond length of quartz crystals decreases, while the bond length of biotite crystals first increases and then decreases with temperature. The mechanism behind the influence of these two phenomena on the rock strength increase is different and needs further exploration.

Data availability statement

The raw data supporting the conclusions of this article will be made available by the authors, without undue reservation.

Author contributions

YH: Conceptualization, Methodology, Software, Investigation, Formal Analysis, Writing—Original Draft, TL: Conceptualization, Review and Editing. All authors contributed to the article and approved the submitted version.

Conflict of interest

The authors declare that the research was conducted in the absence of any commercial or financial relationships that could be construed as a potential conflict of interest.

Publisher's note

References

Alm, O., Jaktlund, L. L., and Shaoquan, K., The influence of microcrack density on the elastic and fracture mechanical properties of Stripa granite. *Phys. Earth Planet. Interiors*, 1985, 40(3): 161–179. doi:10.1016/0031-9201(85)90127-x

Du, Shouji, Liu, Hua, and Zhi, Hongtao, Experimental study on mechanical properties of granite after high temperatur. *J. Rock Mech. Eng.*, 2004, 23 (14): 2359–2359. doi:10.3321/j.issn:1000-6915.2004.14.010

Gao, M., Li, T., Zhu, J., Yin, H., and Yang, Y., An analysis of relationship between the microfracture features and mineral morphology of granite. *Adv. Civ. Eng.*, 2021, 2021(5): 1–6.doi:10.1155/2021/4765731

Gao, Hongmei, Meng, Liyan, and Yang, yue., Microstructure and pore size distribution characteristics of granite at different temperatures. *J. Heilongjiang Univ. Sci. Technol.*, 2018, 028 (002): 185–188. doi:10.3969/j.issn.2095-7262.2018.02.012

Heueckel, T., Peano, A., and Pellegrint, R., A constitutive law for ther-mo-plastic behavior of rocks: An analogy with clays. *Surv. Geophys*, 1994, 15: 643–671. doi:10.1007/BF00690178

Heuze, F. E., High-temperature mechanical, physical and thermalproperties of granitic rocks-a review. *Int. J. Rock Mech. Min. Sciand Geomech. Abstr.*, 1983, 20(1): 3–10.doi:10.1016/0148-9062(83)91609-1

Ji, Jingchen. 2008, *Physical and mechanical properties and macroscopic and microscopic mechanical properties of granite*. Anhui University of Technology. Ma'anshan, China

Johnson, B., Gangi, A. F., and Handin, J., Thermal cracking of rock sub-ject to slow, uniform temperature changes. *Proc. 19th U. S. SympRock Mech.*, 123 (3), 1978. 259–267.

Lau, J. S. O., Gorski, B., and Jackson, R., *The effects of temperature andwater saturation on mechanical properties of Lac du Bonnet pinkgranite*. 8th International congress on Rock Mech, Tokyo, Japan, 1995.

Lin, Muzeng. *Rock thermophysics and its engineering applications*. Chongqing University Press, Chongqing, China, 1991.

Simpson, C., Deformation of granitic rocks across the brittle-duc-tile transition. *J. Struct. Geol.*, 1985, 7: 503–511.doi:10.1016/0191-8141(85)90023-9

Tang, Mingming, Wang, Zhiyin, and Sun, Yili, Experimental study on mechanical properties of granite under low temperature. *Rock Mech. Eng.*, 2010, 29 (004): 787–794.

Vander Molen, I., The shift of the α-β transition temperature of quartz associated with the thermal expansion of granite at high pressure. *Tectonophysics*, 1981, 73: 323–342.doi:10.1016/0040-1951(81)90221-3

Xu, Xiaoli. *Study on mechanical properties evolution and microscopic mechanism of granite under temperature load*. China University of Mining and Technology, Beijing, China, 2008.

frontiers | Frontiers in Earth Science

TYPE Original Research
PUBLISHED 13 July 2023
DOI 10.3389/feart.2023.1223997

OPEN ACCESS

EDITED BY
Lidong Dai,
Chinese Academy of Sciences, China

REVIEWED BY
Lingyun Kong,
China University of Geosciences Wuhan, China
Peiqiang Zhao,
China University of Petroleum, Beijing, China

*CORRESPONDENCE
Liang Wang,
wangliang_swpu@163.com

RECEIVED 17 May 2023
ACCEPTED 29 June 2023
PUBLISHED 13 July 2023

CITATION
Guo Y, Sima L, Wang L, Miao X, Li A and Su S (2023), Saturation evaluation of tight sandstone in the Dayi structure, West Sichuan Depression.
Front. Earth Sci. 11:1223997.
doi: 10.3389/feart.2023.1223997

Saturation evaluation of tight sandstone in the Dayi structure, West Sichuan Depression

Yuhao Guo[1], Liqiang Sima[1], Liang Wang[2]*, Xiangxi Miao[3], Angxing Li[4] and Shute Su[2]

[1]School of Geoscience and Technology, Southwest Petroleum University, Chengdu, China, [2]College of Energy, Chengdu University of Technology, Chengdu, Sichuan, China, [3]Southwest Measurement and Control Company of Sinopec Jingwei, Chengdu, Sichuan, China, [4]China Petroleum Qinghai Oilfield Exploration and Development Research Institute, Qinghai, China

Tight sandstone reservoirs are characterized by poor physical properties, strong heterogeneity, and complex pore structures, resulting in low reservoir saturation calculation accuracy, and the log interpretations do not match the gas test results. In response to the aforementioned problems, the tight sandstone reservoir of the third member of the Xujiahe Formation of the Dayi structure in the Western Sichuan Depression was investigated through a series of experiments on petrophysical properties, casting thin-section identification, rock resistivity, nuclear magnetic resonance, and high-pressure mercury intrusion. Then, after a systematic analysis of the influence of different factors, including physical properties, mineral composition, and pore structure, on the rock-electric parameters, the parameters of the Archie model were appropriately corrected. The results showed that, for tight sandstone reservoirs, the cementation exponent was mainly affected by the physical properties and clay content, and the saturation exponent was controlled by the proportion of relatively large pore components in the total pore system. Therefore, the non-linear least squares method was used to construct the variable cementation index model; the pseudo-capillary pressure curve was constructed, and a new parameter "the large-pore proportion," which is used to optimize the saturation exponent, was proposed in combination with the fractal theory. Finally, an Archie model with variable parameters was used to process the actual logging data in the study area. The results show that this method can obtain more accurate gas saturation, providing a new idea and method for fine sandstone saturation logging evaluation.

KEYWORDS

Western Sichuan Depression, tight sandstone, petrophysics, fractal theory, saturation model

1 Introduction

Tight sandstone gas reservoirs are globally considered important for exploring and exploiting unconventional gas reservoirs, and accurately evaluating the saturation of reservoirs is crucial in this process (Jia et al., 2012; Zou et al., 2015; Zhao et al., 2016; Jia et al., 2022). In 1942, Archie, an expert at the Shell Company, published Archie's formula and proposed the first model for well logging to calculate the saturation of oil and gas in reservoirs (Archie G E, 1942). However, with the progressive deepening of exploration and exploitation, scholars have found that Archie's formula has poor applicability to unconventional reservoirs, as indicated by the mismatch between the log interpretation of the saturation and gas test results. The following are the causes of this situation: compared

with conventional sandstone reservoirs, tight sandstone reservoirs are characterized by poor physical properties, strong heterogeneity, diverse pore types, complex pore structure, etc., complicating the conductivity law of core and making the rock–electric relationship "non-Archie" (Sun, 2007; Li et al., 2015; Yan et al., 2015). To enhance the accuracy of calculating tight sandstone reservoir saturation, many scholars have conducted research that can be broadly categorized into the following two methods. First, a series of new saturation model based on the complex conductance mechanism of tight sandstone have been established (Zhang et al., 2010; Zhang et al., 2011; Tang et al., 2016; Hu et al., 2017). The second tunes the rock electric parameters of Archie's formula to improve its applicability to tight sandstone reservoir evaluations. In comparison, creating a new saturation model is more complicated, with many parameters to be determined, several of which are difficult to determine in practical applications, thereby challenging its applicability. Therefore, the Archie model with optimized parameters remains widely used in the evaluation of tight sandstone reservoir saturation (Xia et al., 2020).

The Upper Triassic Xujiahe Formation in Sichuan Basin is a key stratum for tight sandstone gas exploration and exploitation in China. For a long time, the Xu 2, 4, and 6 members have been the main focus, while the Xu 1, 3, and 5 members, as source rocks, have received less attention (Zhang and Yang, 2022). Recent studies have shown that the gas reservoir fullness of the Xu 2, 4, and 6 members is low, and gas-bearing abundance only increases in the structurally high part (Zhao

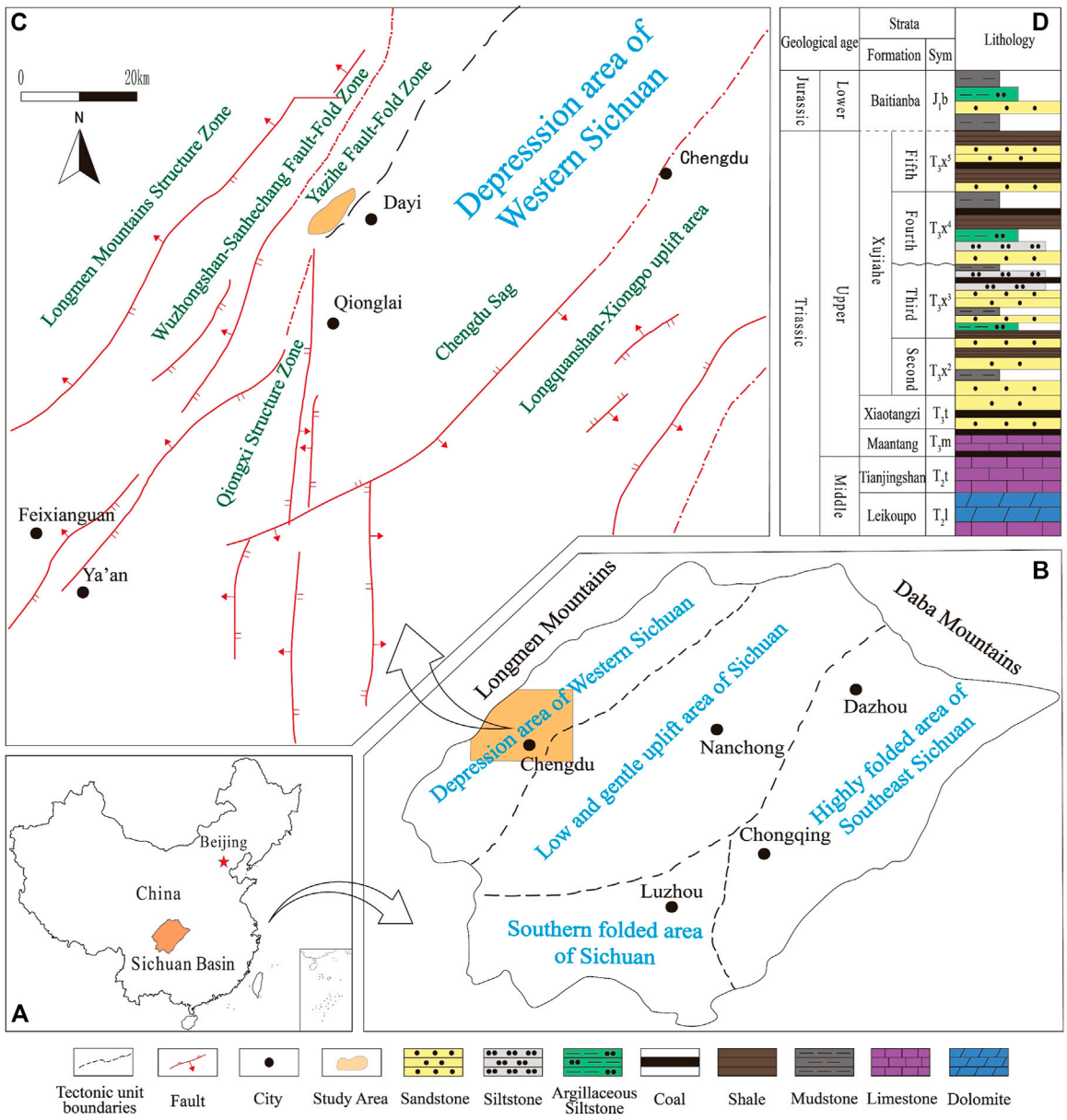

FIGURE 1
(A) Location of the Sichuan Basin in China. **(B)** Location of the Depression area of Western Sichuan in Sichuan Basin. **(C)** Location of Dayi structure in Depression area of Western Sichuan. **(D)** The stratigraphic division of Xujiahe Formation sequence (modified by Yang et al., 2021).

et al., 2011; Bian et al., 2012). In contrast, the source rock strata in the Xu 1, 3, and 5 members are developed with continuously distributed thick massive sandstone, with a sufficient gas supply for its coexistence with the source rock, which likely forms under suitable conditions, leading to their high exploration potential (Qin et al., 2007; Fan et al., 2018; Fu et al., 2020).

Taking tight sandstone reservoirs of the third Member of the Xujiahe Formation as the research object, the conductivity law of tight sandstone was systematically analyzed through petrophysical properties, cast thin section identification, nuclear magnetism, rock resistivity, and high-pressure mercury intrusion. A saturation model with variable rock electric parameters was constructed based on the analysis to improve the accuracy of tight sandstone saturation logging evaluation.

2 Methodology

2.1 Geological setting

Geographically, the Sichuan Basin, located in Southwest China with an area of approximately 260,000 km^2 is composed of a low and gentle uplift, a southern folded area, a highly folded southeast area, and a western depression area (Figures 1A, B), which is situated southwest of the West Sichuan Depression. The regional structure is the frontal hidden structural belt within the Longmenshan thrust belt in western Sichuan, adjacent to the Chengdu Depression in the southeast, the Wuzhongshan structural belt in the northwest, the Yazihe structure in the north obliquely, and the Qiongxi structure in the south (Figure 1C). The Dayi structure is a northwest-dipping monocline with traps controlled by local structures, faults, and trough faults as the main developed faults (Chen et al., 2013; Liu et al., 2014; Chen et al., 2016). Based on regional geological data, the Dayi structure of the Xujiahe Formation is a mega-thick continental coal-bearing clastic rock series, deposited in the Xu 2, 3, 4, and 5 members from the bottom up (Figure 1D); the sandstone reservoir of the Xu 3 member is one of the main gas-producing reservoirs.

Research has indicated that the tight sandstone in the Xu 3 Member underwent three stages of evolution. In the early diagenetic stage, because of the large burial depth, the porosity decreased significantly under compaction, and the primary porosity decreased from 30% to nearly 10%. In the middle diagenetic stage, the Anxian orogenic movement provided abundant carbonate cement for the Xujiahe Formation, leading to a further decrease in porosity, and tight reservoirs exhibited ultralow porosity, which dropped below 2%. In the late diagenetic period, the porosity of tight reservoirs increased under dissolution, but was still below 5% (Zhang, 2009; Luo, 2015; Liu et al., 2018; Liu et al., 2020).

2.2 Samples and experimental measurements

2.2.1 Sample source

The experimental cores were obtained from tight sandstone reservoirs in the study area. While collecting core samples, considering the length of the cores and the planar distribution of the core wells, 25 cores were drilled from five wells to ensure that the cores represented the characteristics of the block.

2.2.2 Experimental methods

To ensure the comparability of measurements between different experiments, each core sample was cut into plugs and chips, and the designed experimental procedure was strictly followed. The chips were grounded into powder for X-ray diffraction analysis, parts of the plugs were cut for casting thin section identification and the remaining plunger samples were used for petrophysical properties, nuclear magnetic resonance (NMR), rock resistivity, and high-pressure mercury intrusion (HPMI) experiments. The experiments were conducted in the following steps. (1) Before the experiment, both sides of the core samples were polished and cleaned to remove remnants of the reservoir fluids or drilling mud inside the sample. (2) The core was dried at 100°C until the quality of core samples remained stable, and the helium porosity and permeability were tested after cooling. (3) The core was placed in a vacuum dryer and vacuumized for 8 h under a vacuum of 133.3 Pa. Then, distilled water was added to the dryer, and external pressure was applied to the core and distilled water to fully saturate the core. (4) Fully water-saturated NMR T_2 spectra and porosities were obtained from core NMR experiments. A centrifuge was used to displace the mobile water in the core, and NMR measurements were performed again to obtain the centrifuge T_2 spectrum and porosity of the bound fluids. (5) After the NMR experiment, the core was dried again, and then vacuum and pressurization of a saturated formation water solution were performed to conduct the desaturated rock–electric experiment. (6) Finally, ten cores were screened for high-pressure mercury intrusion experiments.

3 Results

3.1 Petrophysical parameters of core sample

The results of the core physical property experiments indicated that the reservoir in the study area was highly dense, and the values of core porosity and permeability were small (Table 1). The porosity is between 2% and 4%, with an average value of 3.16%; permeability ranges from 0.01×10^{-3} to 0.1×10^{-3} μm^2, with an average value of 0.0235×10^{-3} μm^2. Porosity and permeability are positively correlated. With similar porosity values, the relative difference in permeability values was significant, implying strong heterogeneity of the reservoir pore structure (Figure 2).

3.2 Mineral components X-ray obtained from diffraction analysis

Whole-rock X-ray diffraction analysis of the core revealed that the mineral composition of the reservoir cores was mainly quartz (average value: 66.4%), followed by feldspar (average value: 20.77%) and clay minerals (average value: 8.24%), with minor amounts of dolomite and calcite (Table 1).

3.3 Pore structure parameters of core samples derived from HPMI and water-saturated NMR experiments

The HPMI curves of the ten core samples with different porosities and permeability are shown in Figure 3A. The mercury

TABLE 1 Petrophysical properties of core plug and their corresponding lithological components of chips.

Core no.	Porosity (%)	Permeability ($\times 10^{-3}$ μm^2)	Main mineral components			Cementation exponent	Saturation exponent
			Quartz content (%)	Feldspar content (%)	Clay content (%)		
D9-2	2.760	0.010	75.700	14.900	6.460	1.570	4.543
D3-1	3.120	0.010	58.500	25.690	12.600	1.554	4.788
D8-2	3.400	0.039	71.980	19.750	4.550	1.599	4.708
D9-1	2.590	0.014	76.740	17.230	4.500	1.606	4.772
D5-1	2.640	0.020	63.190	17.630	9.740	1.536	4.797
D10-1	3.970	0.050	58.740	26.570	11.130	1.583	4.923
D2-2	3.200	0.008	62.330	20.740	10.430	1.517	5.028
D7-1	2.730	0.017	64.390	22.040	9.980	1.584	5.082
D2-1	3.060	0.015	56.730	27.570	8.740	1.554	5.296
D5-2	2.290	0.022	66.300	17.070	8.740	1.532	5.417
D10-2	4.350	0.042	72.770	17.820	4.870	1.581	5.523
D15-2	3.280	0.032	70.040	18.160	8.420	1.621	5.602
D13-1	3.330	0.018	68.080	21.210	7.970	1.593	5.846
D7-2	3.190	0.015	60.530	26.410	7.590	1.598	6.105
D13-2	2.700	0.016	72.290	20.430	6.500	1.552	6.308
D4-2	2.140	0.016	63.720	20.090	11.760	1.528	7.260
D4-1	3.020	0.009	56.910	23.630	13.800	1.527	7.522

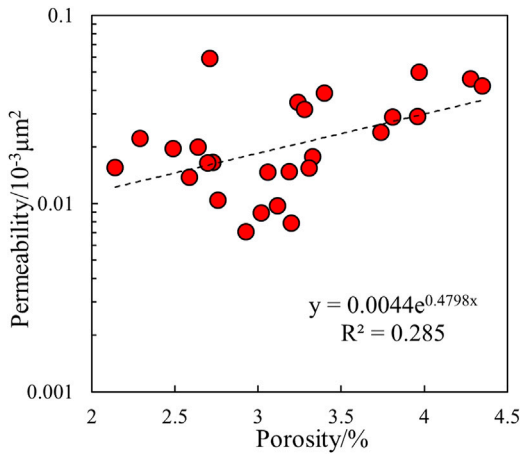

FIGURE 2
Cross-plots of porosity vs. permeability for all core samples.

intrusion curves indicate that the maximum mercury intrusion saturations for all core samples are less than 65%, that is, mercury cannot enter most of the pore systems when the injection pressure reaches 200 MPa. Moreover, the maximum relaxation time of the saturated T_2 spectrum exceeds 20,000 ms and presented a bimodal distribution, indicating strong core heterogeneity (Figure 3B).

Based on the HPMI curves and NMR T_2 spectra aforementioned displayed, quantitative pore structure parameters, such as maximum pore radius (R_a), average pore radius (R_p), median pore radius (R_{50}), structure coefficient (Φ), relative sorting coefficient (D), characteristic structural parameters (C), homogeneity coefficient (α), maximum mercury intrusion saturations (Shg_{max}), displacement pressure (Pd), median pressure (P_{50}), and saturated T_2 mean value (T_{2LM}), are calculated and shown in Table 2. The data show that the average pore radius of the reservoir core was between 22 and 96 nm, and the displacement pressure mainly ranged from 1.354 to 8.263 MPa. The maximum throat radius of the corresponding core was between 89 and 543 nm, indicating that the reservoirs of the Xu 3 Member in the study area were developed with nanoscale pore throats with a large difference in size.

3.4 Rock–electric parameters obtained from rock resistivity experiment

Twenty-five cores from the Xu 3 Member in the study area were selected as experimental samples, with porosity ranging from 2.298% to 4.153% and permeability ranging from 0.0071 × 10^{-3} to 0.0591 × 10^{-3} μm^2. Figure 2 shows the results of the rock resistivity

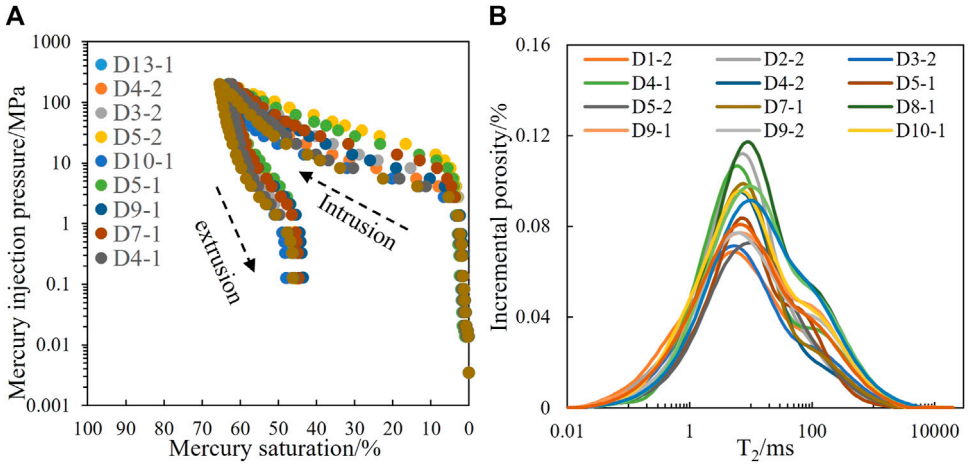

FIGURE 3
(A) Characteristics of HPMI curves and **(B)** water-saturated NMR T_2 spectra of core samples.

TABLE 2 Pore structure parameters of the core samples derived from the HPMI test and the NMR experiment.

Core no.	R_a (nm)	R_p (nm)	R_{50} (nm)	Φ	D	C	α	S_{Hgmax} (%)	Pd (MPa)	P_{50} (MPa)	T_{2LM} (ms)
D13-1	542.621	77.939	20.538	1.666	0.130	0.130	0.144	63.107	1.355	35.790	9.508
D4-2	88.946	21.959	5.914	0.022	0.154	0.154	0.247	59.034	8.263	124.290	7.556
D3-2	178.473	50.527	11.918	0.044	0.117	0.117	0.283	62.897	4.118	61.670	7.678
D5-2	88.978	21.912	7.487	0.048	0.142	0.142	0.246	62.964	8.260	98.170	10.317
D10-1	542.960	92.123	35.910	0.168	0.127	0.127	0.170	63.179	1.354	20.470	9.957
D5-1	133.687	29.150	9.184	0.005	0.112	0.112	0.218	63.120	5.498	80.030	9.272
D9-1	268.679	59.744	13.248	0.104	0.129	0.129	0.222	62.254	2.736	55.480	10.897
D7-1	133.706	34.088	12.779	0.028	0.153	0.153	0.255	62.586	5.497	57.520	8.038
D4-1	541.578	89.506	20.295	0.316	0.142	0.142	0.165	62.993	1.357	36.220	9.587
D10-2	542.431	96.139	29.187	0.296	0.141	0.141	0.177	65.398	1.355	25.180	12.542

experiment, indicating that the relationship between core formation factors and porosity in the study area is relatively concentrated, and when proportionality coefficient a=1, the distribution range of cementation exponent (m) is 1.4–1.7 (Figure 4A). For proportionality coefficient b=1, the distribution range of the saturation exponent (n) was 3–8, and the relationship between the resistivity index and water saturation was relatively scattered, which is non-linear when the water saturation is less than 40%, typical of the "non-Archie phenomenon" (Figure 4B).

4 Discussion

By applying Archie's formula to tight sandstone reservoirs, the parameters in the model must be collected, provided that a systematic and in-depth analysis of the response law of rock resistivity is conducted. Therefore, based on rock–electric experimental data analysis combined with petrophysical property analysis, casting thin section identification, and HPMI experiments, the influences of physical properties, mineral composition, and pore structure on the resistivity law of the core were analyzed.

4.1 Influence of mineral components on rock–electrical parameters

Although the absolute contents of both quartz and feldspar have no significant correlation with the rock–electrical parameters (Figures 5A, B), the clay content has a good negative correlation with the cementation exponent (Figure 5C), that is, the higher the clay content, the smaller the value of m. The analysis suggests that owing to the adsorption of clay minerals on water, a water film is easily formed on the surface of the particles, increasing the conductivity of the core and reducing the value of the formation factor. This results in a decrease in the fitted m value. Figure 5D shows that there was no significant correlation between the clay content and the saturation exponent.

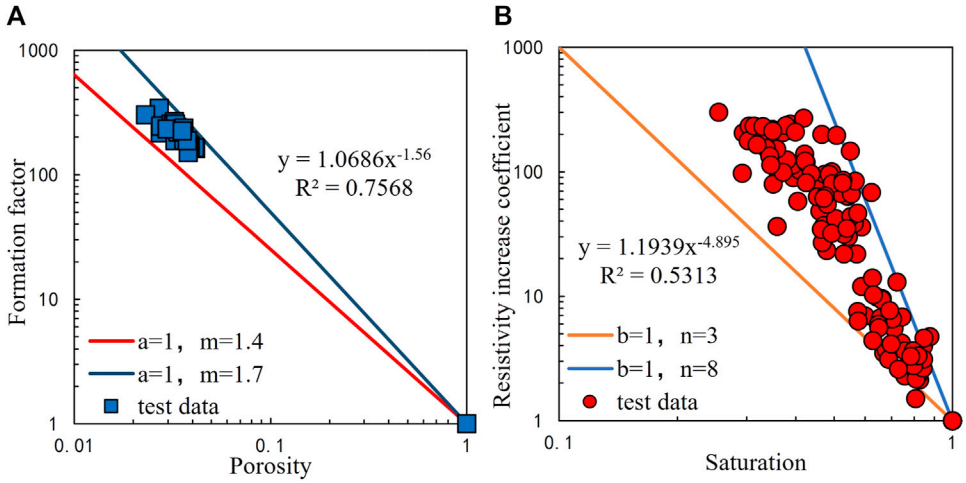

FIGURE 4
Results of rock resistivity experiment. **(A)** Cross-plots of porosity vs. formation factor and **(B)** Cross-plots of saturation vs. resistivity increase coefficient.

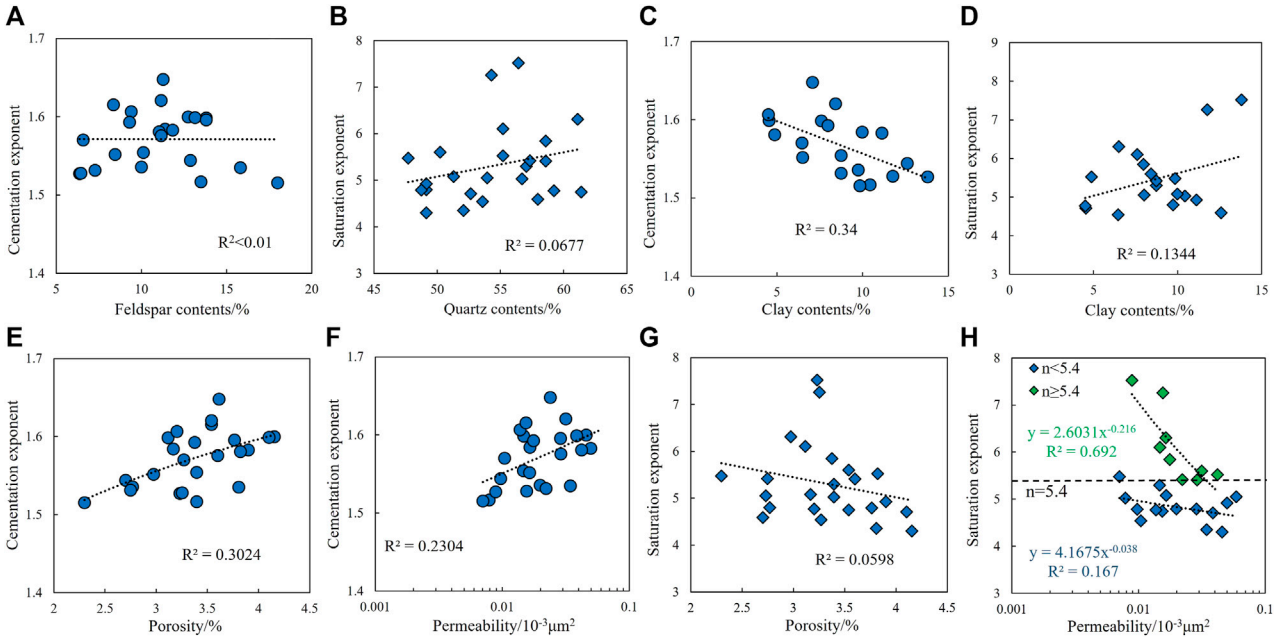

FIGURE 5
(A) Cross-plots of feldspar content vs. cementation exponent. **(B)** Cross-plots of quartz contents vs. saturation exponent. **(C)** Cross-plots of clay contents vs. cementation exponent. **(D)** Cross-plots of clay contents vs. saturation exponent. **(E)** Cross-plots of porosity vs. cementation exponent. **(F)** Cross-plots of permeability vs. cementation exponent. **(G)** Cross-plots of porosity vs. saturation exponent. **(H)** Cross-plots of permeability vs. saturation exponent.

4.2 Influence of physical properties on rock–electrical parameters

The cross-plot of the cementation exponent and physical property parameters shows that the value of *m* increases with an increase in porosity and permeability and is more correlated with porosity, indicating that the cementation index is more affected by porosity (Figures 5E, F). Similarly, the cross-plot of the saturation exponent and physical parameters indicated that the saturation exponent was negatively correlated with the porosity and permeability (Figures 5G, H). Further analysis revealed that the fitting trend between the saturation exponent and permeability

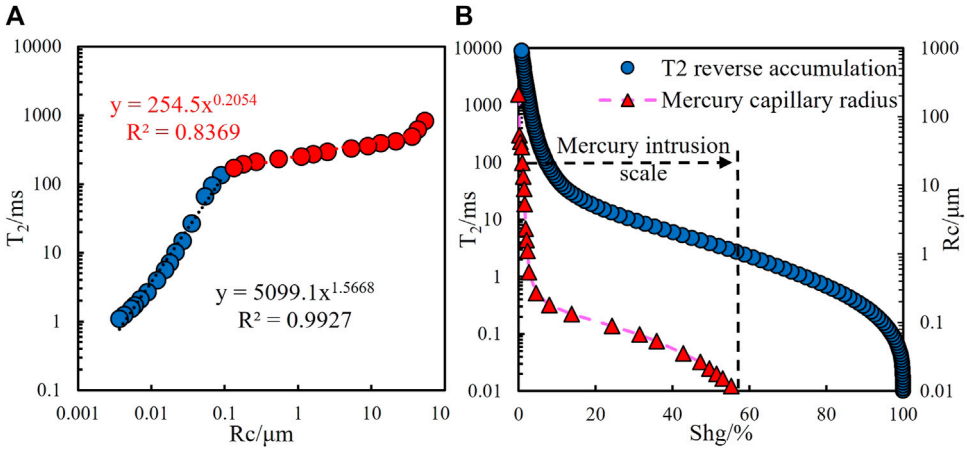

FIGURE 6
(A) Cross-plot of Rc vs. T_2 and **(B)** difference in measurement scales between NMR and mercury intrusion experiments.

exhibited two patterns. (1) When $n > 5.4$, n decreases rapidly with increasing permeability and (2) when $n < 5.4$, n decreases slowly with increasing permeability. In theory, the saturation exponent reflects the degree of uniformity of the fluid distribution in the core; the larger the n value, the more uneven the fluid distribution. The relationship between the saturation index and permeability reveals that, in an extremely complex fluid distribution, if there are preferential seepage channels, the fluid is distributed quickly and evenly, whereas when the fluid distribution is uniform, the change in permeability has no obvious effect (Gao, 2012; Cong and Hu, 2016; Zhang et al., 2017).

4.3 Influence of pore structure on rock–electrical parameters

The pore structure of the cores can be characterized quantitatively by HPMI experiments, but with limited pressure in the laboratory mercury intrusion apparatus, it is difficult to inject mercury into every pore of the cores; therefore, the capillary pressure curve cannot reflect the total pore system (Yakov V and Win L S, 2001; Liu et al., 2008; Li et al., 2015). However, the NMR experiment can measure the attenuation signal of all hydrogen nuclei of water-saturated core pores; therefore, the pore structure of tight sandstone cores was evaluated using pseudo-capillary pressure curves constructed through NMR (Figure 6A). Yudan et al. (2005) suggested that the relationship between the capillary pressure (Pc) and relaxation time (T_2) can be expressed as follows (He et al., 2005):

$$P_c = \frac{2\sigma \cos\theta}{\rho_2 \times F_s} \times \frac{1}{T_2}, \quad (1)$$

where σ represents the fluid interface tension, θ is the wetting contact angle, ρ_2 is the transverse surface relaxation time, and Fs is a geometry factor. The value of Fs was 2 for the cylindrical throat and 3 for the spherical throat. After non-linear interpolation of the T_2 spectrum, the relationship between the capillary pressure and pore radius (Rc) was fitted, and the results showed that a piecewise fitting relationship exists between the two variables, implying that the pore system can be divided into two parts (Figure 6B).

Finally, the characteristic pore structure parameters of the cores in the study area were extracted based on the construction of a pseudo-capillary pressure curve (Table 3).

The cross-plot of the cementation exponent and mercury intrusion characteristic parameters shows that, overall, the cementation exponent decreases with the increase of the relative sorting and homogenization coefficients, indicating that the stronger the throat homogeneity, the smaller the value of m (Figures 7A, B). The cross-plot of saturation exponent and mercury injection characteristic parameters shows that, in the overall trend, the saturation exponent has a strong negative correlation with the median radius and the average radius, suggesting that the larger the radius of the pore and throat, the more uniform the fluid saturation distribution (Figures 7C, D). The correlation analysis between the rock–electrical parameters and mercury intrusion characteristic parameters also showed that, compared with the cementation exponent, the correlation coefficient between the saturation exponent and mercury intrusion characteristic parameters was greater, indicating that the saturation exponent was more influenced by the pore structure.

A diagram of the saturation exponent and pseudo-capillary pressure curve characteristic parameters revealed that the index was controlled by the core–pore structure. Therefore, the influence of the pore structure on the index was further analyzed by combining it with the data from casting thin section identification, physical property analysis, and NMR experiments.

Four cores (D4-1, D7-1, D9-1, and D9-2) with similar porosities and different saturation exponents were selected for comparative analysis of the water-saturated NMR T_2 spectrum (Figure 8A).The saturation exponent is related to the signal amplitude at 100 ms of the T_2 spectrum, and the larger the signal amplitude at 100 ms, the smaller the value of n (Figure 8B), and a comparison of the casting thin sections from the four cores shows that, in general, the larger the maximum pore size and main pore size distribution interval, the smaller the saturation exponent (Figure 9). Therefore, in tight

TABLE 3 Pore structure parameters derived from the pseudo-capillary curve and their corresponding large porosity proportion.

Core no.	P_{50} (MPa)	R_{50} (nm)	Rp (nm)	α	D	Large porosity proportion (%)
D1-2	58.383	12.589	40.574	0.355	0.439	5.002
D2-1	46.260	15.888	27.247	0.349	0.429	5.022
D2-2	44.075	16.676	26.745	0.347	0.428	6.359
D3-1	51.076	14.390	65.994	0.346	0.437	5.815
D3-2	50.158	14.654	17.442	0.351	0.432	3.209
D4-1	45.151	6.279	17.627	0.350	0.427	1.532
D4-2	71.533	5.275	19.265	0.367	0.449	1.448
D5-1	56.843	12.930	58.357	0.357	0.435	5.551
D5-2	65.379	11.242	39.364	0.365	0.442	4.065
D7-1	55.588	13.222	35.929	0.355	0.435	5.491
D7-2	43.691	16.823	16.877	0.347	0.427	2.273
D8-1	20.108	36.552	66.125	0.333	0.400	8.707
D8-2	33.168	22.160	47.530	0.345	0.414	6.607
D9-1	56.824	12.935	38.728	0.359	0.434	5.866
D9-2	51.541	34.261	48.420	0.355	0.430	6.462
D10-1	25.907	28.371	26.115	0.337	0.409	5.856
D10-2	19.892	36.950	25.972	0.333	0.399	3.200
D11-1	36.943	19.895	57.800	0.348	0.417	7.449
D11-2	22.527	10.627	25.761	0.338	0.403	3.537
D13-1	38.173	9.255	17.048	0.345	0.421	2.948
D13-2	59.753	12.301	17.399	0.355	0.441	1.989
D14-1	25.985	28.285	17.040	0.341	0.407	7.286
D14-2	35.337	20.800	31.665	0.347	0.416	7.066
D15-1	27.580	26.649	56.403	0.339	0.411	6.670
D15-2	39.173	18.763	17.154	0.346	0.422	3.003

sandstone reservoirs, the saturation exponent is controlled by the pore structure, particularly by the development of large-size reservoir pores, that is, the more developed the large-size pores, the more uniform the core fluid saturation distribution and the smaller the saturation exponent. To describe the development of large-sized pores, the fractal dimension theory of pore throats was used to quantitatively evaluate the pore structure.

4.3.1 Determination of fractal dimension by high-pressure mercury injection experiment

The fractal theory is used to study the internal structure of an object based on self-similarity (Xie et al., 2010; Huang et al., 2018; Xia et al., 2018). Numerous studies have shown that the pore structure of tight sandstone has fractal features, and the complexity and heterogeneity of the pore structure can be characterized by the fractal dimension. In general, D in the fractal dimension is distributed between 2 and 3; the closer it is to 2, the smoother the pore surface and the more regular the pore throat structure.

Typically, the fractal dimension of a pore structure is obtained through HPMI experiments in the laboratory. According to the capillary model and the fractal geometry theory, the fractal dimension of a pore with a radius larger than r (a specific value) can be represented by the following function:

$$S_{Hg}(\geq r) = \frac{r_{max}^{3-D} - r^{3-D}}{r_{max}^{3-D}} = 1 - \left(\frac{r}{r_{max}}\right)^{3-D}, \quad (2)$$

where r_{max} is the maximum pore–throat radius in (μ)m and D is the fractal dimension.

Taking both sides of Eq. 2, we obtain

$$\log\left[1 - S_{Hg}(\geq r)\right] = (3 - D)\log r - (3 - D)\log r_{max}. \quad (3)$$

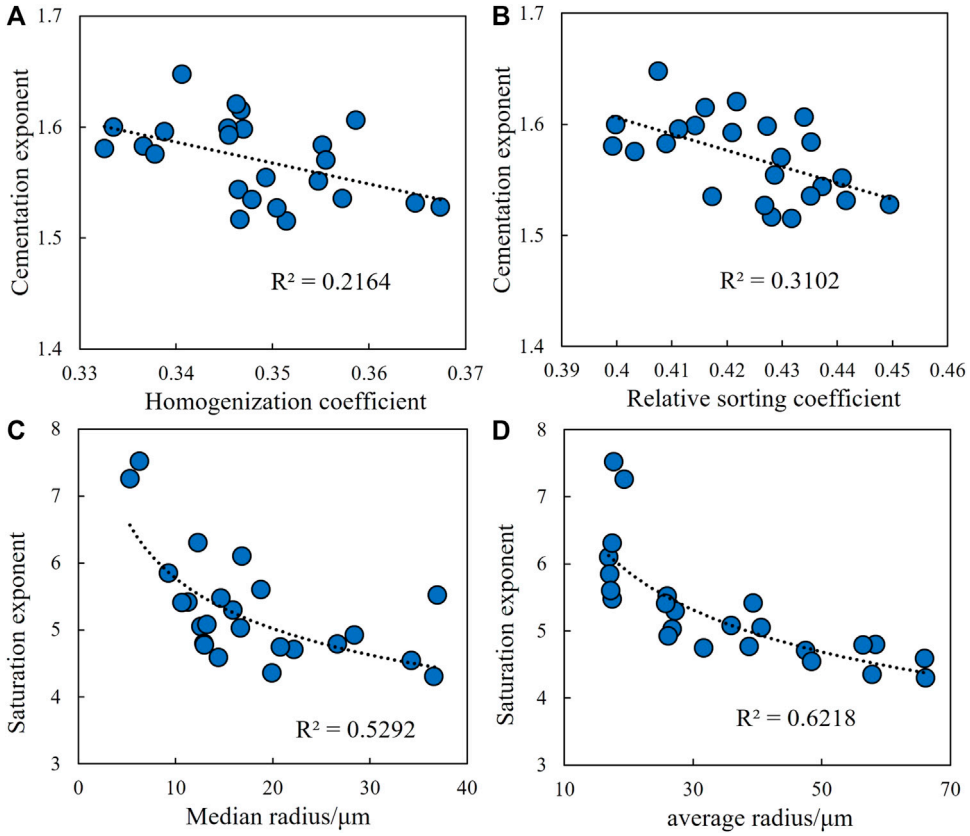

FIGURE 7
Relationship between pore structure parameters and rock–electrical parameters. **(A)** Cross-plots of homogenization coefficient vs. cementation exponent. **(B)** Cross-plots of relative sorting coefficient vs. cementation exponent. **(C)** Cross-plots of median radius vs. saturation exponent. **(D)** Cross-plots of average radius vs. saturation exponent.

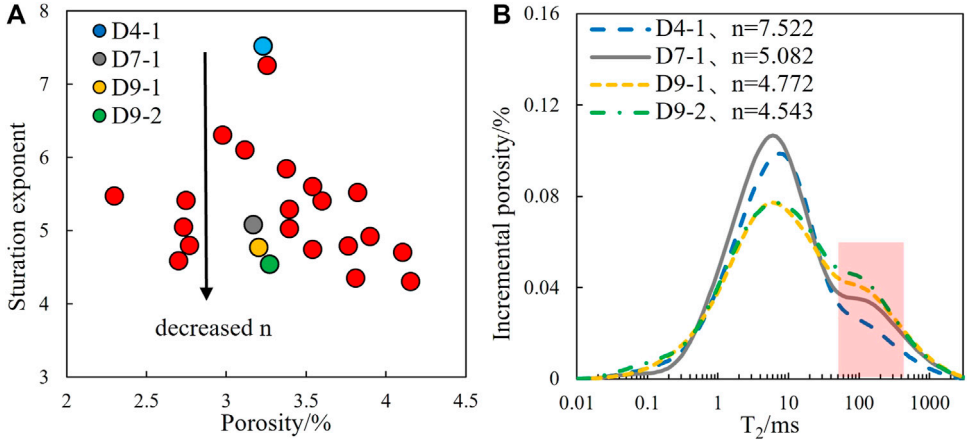

FIGURE 8
When the porosity is similar, the value of *n* decreases with the proportion of large pores increase. **(A)** Cross-plots of porosity vs. saturation exponent and **(B)** water-saturated NMR T_2 spectra of selected four cores.

Eq. 3 shows that fractal dimension D can be calculated using the relationship between log $[1-S_{Hg}(\geq r)]$ and log r.

Figure 10 shows the fitting results for the two reservoir cores in the study area obtained using Eq. 3. The relationship between $\log[1-S_{Hg}(\geq r)]$ and $\log r$ is expressed as a staged structure. The two segments of the fitted curve represent relatively large and small pores in the cores, and the slopes correspond to fractal dimensions D_1 of the large pores and D_2 of the small pores (Qu et al., 2020).

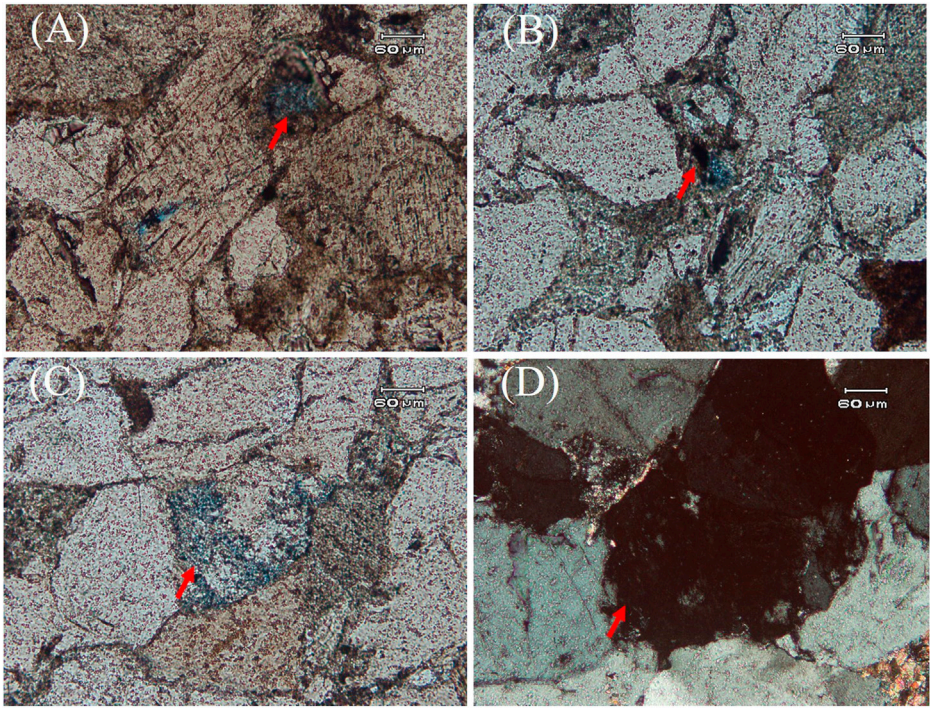

FIGURE 9
Casting thin section identification of cores with different saturation exponents. **(A)** Well-DY102, 4 585.605 m, fine lithic sandstone, maximum pore size is 0.2 mm, main pore size ranges from 0.05 to 0.1 mm. **(B)** Well-DY1, 4 590.375 m, feldspar lithic sandstone, maximum pore size is 0.1 mm, main pore size ranges from 0.01 to 0.05 mm. **(C)** Well-DY102, 4 597.865 m, medium lithic sandstone, maximum pore size is 0.26 mm, main pore size ranges from 0.02 to 0.21 mm. **(D)** Well-DY7, 4 597.875 m, medium feldspar lithic sandstone, maximum pore size is 0.38 mm, main pore size ranges from 0.02 to 0.22 mm.

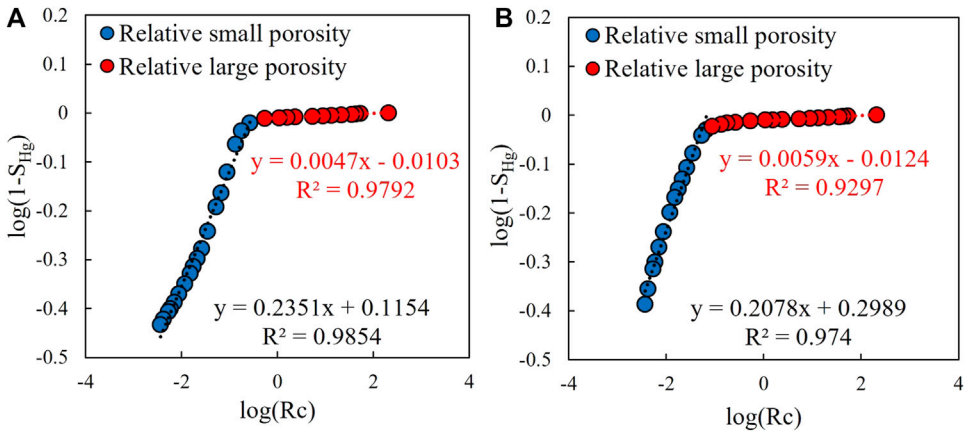

FIGURE 10
Fractal dimension fitting diagram of capillary mercury intrusion curves of core samples. **(A)** Cross-plot of log(Rc) vs. log(1–S_{Hg}) of D2-2 and **(B)** cross-plot of log(Rc) vs. log(1–S_{Hg}) of D3-2.

4.3.2 Determination of the proportion of large pores and optimization of the saturation exponent

Based on the relationship between permeability, relatively large pores, and saturation exponent, the development of large pores is shown to lead to a more uniform fluid distribution and a decrease in the saturation index. Thus, a relatively large pore size is a crucial factor affecting the saturation coefficient. To describe the development of large pores, the concept of large-pore proportion was introduced and defined as the ratio of large-pore components to the total pore system, denoted as *p*.

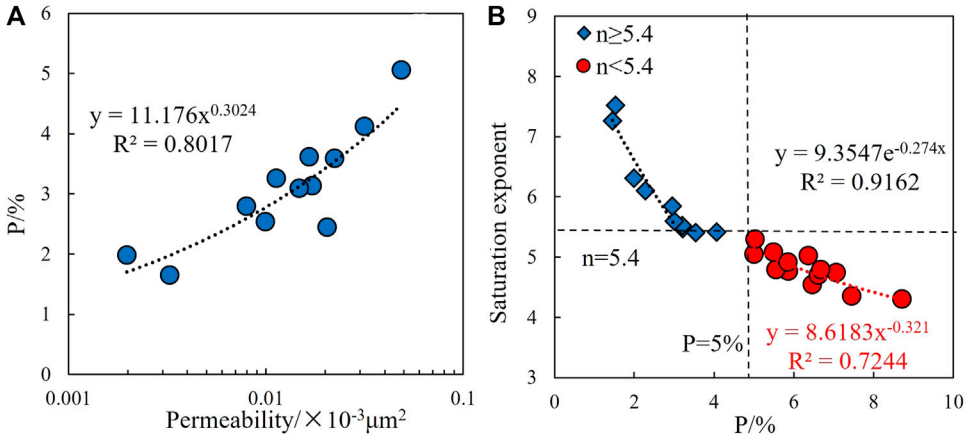

FIGURE 11
(A) Cross-plot of permeability vs. large porosity proportion and **(B)** cross-plot of large porosity proportion vs. saturation exponent.

The steps to determine the proportion of large pores in the lab are as follows: (1) determine the threshold pore radius of relatively large and small pores by the two-segment structure of capillary pressure curves; (2) calculate the ratio of large-pore components to the total pore system and construct the pseudo-capillary pressure curve with the water-saturated NMR T_2 spectrum; and (3) convert the threshold pore radius of relatively large and small pores into corresponding T_2 values, denoted as T_{2_C}, based on the fitting relationship between pore radius and T_2 distribution. Subsequently, the peak envelope area larger than T_{2_C} in the T_2 spectrum was divided by the entire spectrum envelope area, and a large pore proportion was obtained. In processing the actual well data, because no NMR logging data were collected in the study area, a calculation model of the large-pore proportion was indirectly constructed using the permeability scale (Figure 11A)

$$P = 0.1118 \times Perm^{0.3024}, \quad (4)$$

where P represents the proportion of large pores in % and $Perm$ is permeability in 10^{-3} μm^2.

The cross-plot of the large-pore proportion and the saturation exponent shows that the proportion is negatively correlated with the index, that is, the saturation exponent decreases as the proportion increases (Figure 11B). With n = 5.4 and p = 5% as limits, the fitting trends of the proportion and index can be roughly divided into two segments: when the proportion is less than 5%, the index was high, indicating that the cores contain mainly small pores, and the fluid saturation distribution is highly uneven. However, the distribution became rapid even with a slight increase in the number of large pores. When the proportion was greater than 5%, the saturation index was small, indicating that large pores developed well in the cores, resulting in a uniform fluid saturation distribution. However, with an increase in the proportion, the index decreased slowly, suggesting that the distribution did not change significantly.

5 Archie parameter model and application

5.1 Fixed rock–electrical parameters

Based on the basic theory of the Archie model, the relationships between porosity and formation factors as well as water saturation and electrical resistivity increase coefficients were fitted, and the fixed rock–electrical parameter values were obtained as a_1=1.0686, b_1=1.1939, m_1=1.56, and n_1=4.895.

5.2 Variable cementation index model

An analysis of the factors influencing the cementation exponent showed that m was controlled by the porosity and clay content. Therefore, the porosity and clay content were selected as independent variables, and linear multiple regression was used to construct the variable cementation index calculation model with a correlation coefficient R^2 of 0.7591. The variable cementation exponent is denoted as m_2, and the calculation model is as follows:

$$m_2 = 0.03 \times \varphi - 0.006 \times V_{clay} + 1.502, \quad (5)$$

where m_2 is the variable cementation exponent and V_{clay} is the clay content in percentage.

5.3 Variable saturation exponent model

Previous studies have shown that the saturation exponent is primarily controlled by the proportion of large pores in the core relative to the total pore system. The distribution of the core fluid saturation presented different rules, with a threshold proportion of large pores of 5%. Hence, the proportion-dependent variable saturation index model was constructed and denoted as n_2. The calculation model was

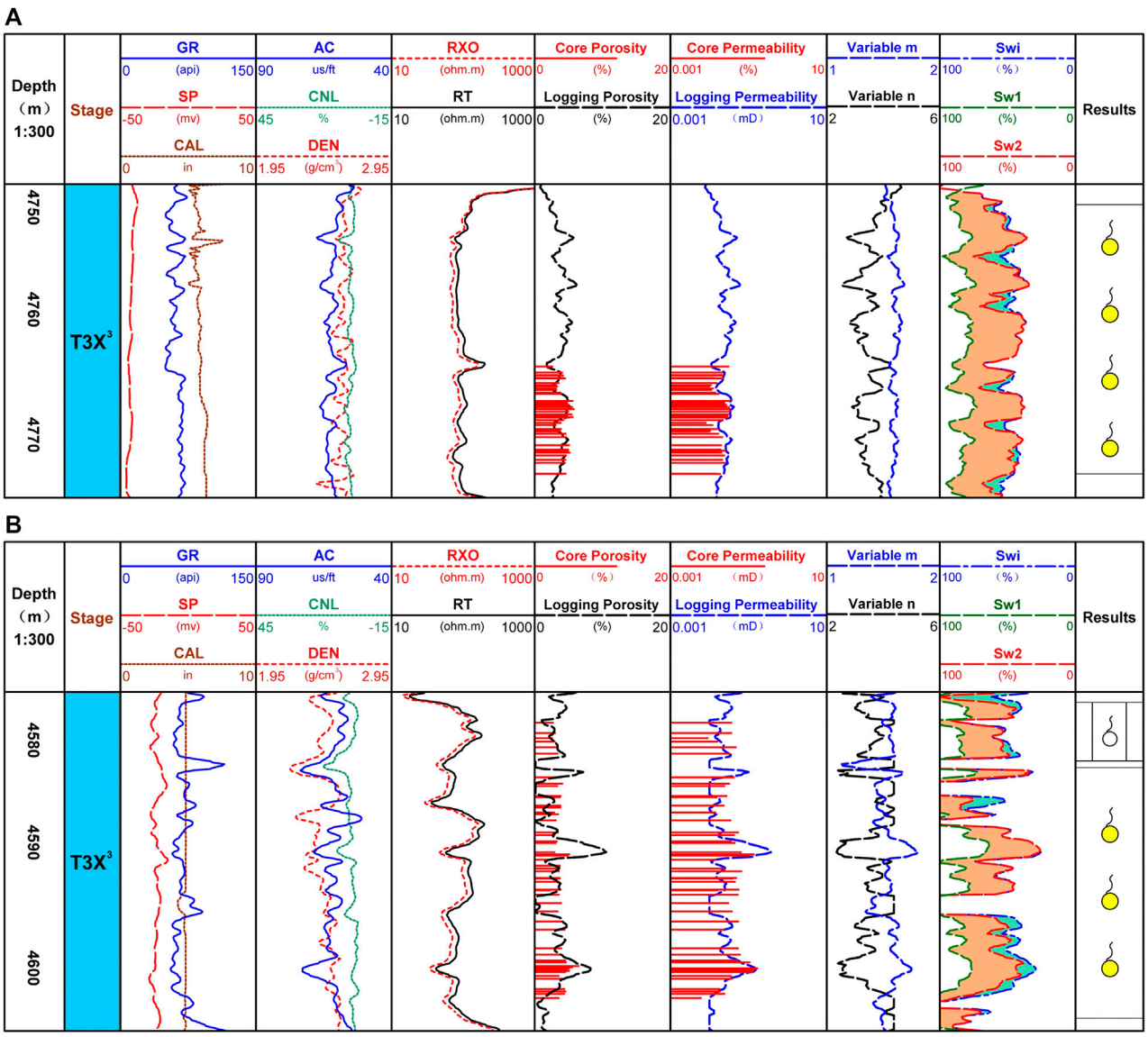

FIGURE 12
Comprehensive logging interpretation of wells of the Dayi structure. **(A)** Logging interpretation at 4 750 m–4 775 m and **(B)** logging interpretation at 4 580 m–4 605 m.

$$\begin{cases} n_2 = 9.3547 \times e^{-0.274 \times P}, P < 5\% \\ n_2 = 8.6183 \times P^{-0.321}, P \geq 5\% \end{cases} \quad (6)$$

5.4 Applications

Based on Archie's model with variable parameters, the reservoir saturation of the Xu 3 Member in Well X of the Dayi structure in the West Sichuan Depression was quantitatively evaluated. The green curve in the nine sections (Sw_1) represents the saturation calculation results for the fixed rock electrical parameters, and the red curve represents the saturation calculation results for the variable Archie parameter model (Sw_2).

Analysis of the comprehensive evaluation result map of the well logging data obtained from 4750 to 4775 m of this well suggests that this interval is an industrial gas reservoir, as determined by the gas testing results. The conventional logging curve shows that the natural gamma rays in the perforated interval are low, the well diameter is relatively stable, and the spontaneous potential curve presents an overall negative anomaly, indicating the good permeability of this interval. All three porosity curves show that the values of acoustics and neutrons increase, whereas the density value decreases, and the deep and shallow lateral resistivity has a slight positive difference. A comparison of the saturation calculation results in the perforated interval suggests that (1) the calculated water saturation from the fixed rock-electric parameter model is large and overlaps the bound water saturation, indicating that there

is a large amount of mobile water, and the calculation is inconsistent with the gas testing result and (2) the calculated water saturation from the variable Archie's model ranges from 40% to 70%, which is consistent with the bound water saturation. The overlapping results indicate the presence of gas in the interval, which is consistent with the gas test results (Figure 12A).

Based on the analysis of the comprehensive evaluation result map of well-logging data obtained from 4580 to 4605 m in this well, the calculated bound water saturation from the fixed rock–electric parameter model overlaps with the water saturation in the interval, indicating a large amount of mobile water, which is inconsistent with the gas testing result. However, the water saturation calculated from Archie's model was similar to the bound water saturation, which was consistent with the gas testing results, further proving the effectiveness of Archie's model with variable parameters in the application (Figure 12B).

6 Conclusion

The reservoir lithology of the Xu 3 Member in the West Sichuan Depression is dominated by the feldspar lithic sandstone, followed by lithic sandstone. The average porosity and permeability are 3.16% and 0.0235×10^{-3} μm^2, respectively, indicating reservoirs in the Xu 3 Member are typical tight sandstone reservoirs. Reservoirs are developed with nanoscale pore throats, with relatively large differences in size and complex pore structures.

The conductivity law of tight sandstone reservoirs in the study area shows that the cementation exponent is controlled by porosity and clay content, and the main factor affecting the saturation exponent is the ratio of the large-pore components to the total pore system. In this study, the fractal dimension was used, and through formula derivation, an obvious boundary was observed between the fractal dimensions of relatively large and small pores in tight sandstone. Therefore, the "large-pore proportion" concept is proposed, and the segmentation calculation model of saturation index is established.

Applying the saturation calculation model with variable Archie parameters to the actual well data processing in the study area shows that the calculation accuracy of tight sandstone reservoir saturation can be effectively improved, and the logging interpretation is made more consistent with the gas testing results.

Data availability statement

The original contributions presented in the study are included in the article/Supplementary material; further inquiries can be directed to the corresponding author.

Author contributions

All authors listed have made a substantial, direct, and intellectual contribution to the work and approved it for publication.

Conflict of interest

XM was employed by Southwest Measurement and Control Company of Sinopec Jingwei.

The remaining authors declare that the research was conducted in the absence of any commercial or financial relationships that could be construed as a potential conflict of interest.

Publisher's note

References

Archie, G. E. (1942). The electrical resistivity log as an aid in determining some reservoir characteristics. *Trans. AIME* 146, 54–62. doi:10.2118/942054-g

Bian, C., Wang, H., Wang, C., et al. (2012). Exploration status and resource potential evaluation of tight sandstone gas reservoirs in the Sichuan Basin. *Petroleum Eng. Sci.* 7, 74–80. doi:10.3969/j.issn.1009-1742.2012.07.011

Chen, Y., Hu, Y., Wang, Y., et al. (2016). Natural gas accumulation conditions of the 4th member in Leikoupo Formation of Dayi structure. *Special Oil Gas Reservoirs*. 2016(3), 25–29. doi:10.3969/j.issn.1006-6535.2016.03.006

Chen, Y., Zheng, B., Yuan, D., et al. (2013). Characteristics and main controlling factors of fractures in gas reservoir of Xujiahe Formation. *Dayi Struct. Petroleum Geol. Exp.* 35 (1), 30–35. doi:10.11781/sysydz201301029

Cong, Y., and Hu, K. (2016). Saturation model for tight sandstone based on complex pore structure and additional shaliness conductivity. *Well Logging Technol.* 40 (4), 466–471. doi:10.16489/j.issn.1004-1338.2016.04.016

Fan, Z., Liu, S., Fan, C., et al. (2018). Analysis of typical seismic profile and balanced cross-section recovery and tectonic evolution in the Longmenshan Fold – thrust Belt. *Geol. Rev.* 64 (2), 347–360. doi:10.16509/j.georeview.2018.02.004

Fu, Z., Dai, R., Wang, X., et al. (2020). The characteristics and main controlling factors of high quality tight sandstone reservoir in the 3th member of Xujiahe Formation in West Sichuan Depression. *Geol. China* 49 (1), 298–310. doi:10.12029/gc20220119

Gao, J. (2012). Influencing factors of rock-electrical parameters alternation causes after polymer flooding in high porosity and high permeability sand rock. *J. Southwest Petroleum Univ. Sci. Technol. Ed.* 34 (5), 114–118.

He, Y., Mao, Z., Xiao, L., et al. (2005). An improved method of using NMR T_2 distribution to evaluate pore size distribution. *Chin. J. Geophys.* 48 (2), 373–378. doi:10.3321/j.issn:0001-5733.2005.02.020

Hu, F., Zhou, C.;, Xia, L., et al. (2017). A tight sandstone trapezoidal pore oil saturation model. *Petroleum Explor. Dev.* 44 (5), 827–836. doi:10.11698/PED.2017.05.19

Huang, H., Lei, C., Sun, W., et al. (2018). Pore-throat structure and fractal characteristics of Shihezi Formation tight gas sandstone in the Ordos basin, China. *World Sci.* 26 (2), 1–22. doi:10.1142/S0218348X18400054

Jia, A., Yunsheng, W., Guo, Z., et al. (2022). Development status and prospect of tight sandstone gas in China. *Nat. Gas. Ind.* 42 (1), 83–92. doi:10.3787/j.issn.1000-0976.2022.01.008

Jia, C., Zou, C., Li, J., et al. (2012). Assessment criteria, main types, basic features and resource prospects of the tight oil in China. *Acta Pet. Sin.* 33 (3), 343–350. doi:10.7623/syxb201203001

Li, A., Ren, X., Wang, G., et al. (2015). Characterization of pore structure of low permeability reservoirs using a nuclear magnetic resonance method. *J. China Univ. Petroleum* 39 (6), 93–98. doi:10.3969/j.issn.1673-5005.2015.06.012

Liang, X., Shi, Y., Li, G., Guo, H., and Li, J. (2021). A method to predict the resistivity index for tight sandstone reservoirs from nuclear magnetic resonance data. *AAPG Bull.* 105 (5), 1009–1032. doi:10.1306/05222018269

Liu, C., Yan, D., and Li, S. (2014). Types and controlling factors of fractures for the third member of Xujiahe Formation in Dayi structure, West Sichuan depression. *Fault-Block Oil Gas Filed* 21 (1), 29–31. doi:10.6056/dkyqt201401006

Liu, S., Ren, X., Yao, S., et al. (2018). Relationship between gas reservoir distribution and structural system of upper triassic Xujiahe Fm in the Sichuan Basin. *Nat. Gas. Ind.* 38 (1), 1–14. doi:10.1016/j.ngib.2018.11.014

Liu, X., Liang, X., and Zhang, W. (2008). Construction method and application of reservoir capillary pressure curve. *J. Southwest Petroleum Univ. Sci. Technol. Ed.* 30 (6), 126–130. doi:10.3863/j.issn.1000-2634.2008.06.030

Liu, Z., Xu, S., Liu, J., et al. (2020). Enrichment laws of deep tight sandstone gas reservoirs in the Western Sichuan Depression, Sichuan Basin. *Nat. Gas. Ind.* 40 (2), 31–40. doi:10.3787/j.issn.1000-0976.2020.02.004

Luo, N. (2015). *Characteristics and genetic mechanism of tight reservoir in the second member of the upper triassic Xujiahe Formation in the middle part of western sichuan depression*. Chengdu: Chengdu University of Technology.

Qin, S., Tao, S., Tu, T., et al. (2007). Characteristics of natural gas geochemistry and accumulation in Western Sichuan Depression. *Petroleum Explor Dev*. 34(1), 34–38. doi:10.1016/S1872-5813(07)60034-6

Qu, Y., Sun, W., Tao, R., et al. (2020). Pore-throat structure and fractal characteristics of tight sandstone in Yanchang Formation, Ordos Basin. *Mar. Petroleum Geol.* 120, 2–15. doi:10.1016/j.marpetgeo.2020.104573

Sun, J. (2007). Archie's formula: Historical background and earlier debates. *Prog. Geophys.* 22 (2), 472–484. doi:10.3969/j.issn.1004-2903.2007.02.020

Tang, X., Song, Y., Fu, J., et al. (2016). Conductance mechanism and conduction model for tight shale-rich and calcite-rich sands. *Prog. Geophys.* 31 (4), 1660–1669.

Xia, L., Li, C., Bo, Li, Liu, X., and Yuan, C. (2020). Response laws of rock electrical property and saturation evaluation method of tight sandstone. *Petroleum Explor. Dev.* 47 (1), 214–224. doi:10.1016/s1876-3804(20)60020-9

Xia, Y., Cai, J., Wei, Wei, Hu, X., Wang, X., and Ge, X. (2018). A new method for calculating fractal dimensions of porous media based on pore size distribution. *World Sci.* 26 (1), 1850006–1850012. doi:10.1142/s0218348x18500068

Xie, S., Cheng, Q., Ling, Q., Li, B., Bao, Z., and Fan, P. (2010). Fractal and multifractal analysis of carbonate pore-scale digital images of petroleum reservoirs. *Mar. Petroleum Geol.* 27, 476–485. doi:10.1016/j.marpetgeo.2009.10.010

Yakov, V., and Win, L. S. (2001). A practical approach to obtain primary drainage capillary pressure curves from NMR core and log data. *Petrophysics* 42 (4), 334–343.

Yan, J;, Wen, D., Li, Z., et al. (2015). The influence of low permeable sandstone pore structure on rock electrical parameters and its application. *Nat. Gas. Geosci.* 26 (12), 2227–2233.

Yang, P;, Zhang, L., Liu, k., Cao, B., Gao, J., and Qiu, G. (2021). Diagenetic history and reservoir evolution of tight sandstones in the second member of the Upper Triassic Xujiahe Formation, Western Sichuan Basin, China. *J. Petroleum Sci. Eng.* 201, 108451. doi:10.1016/j.petrol.2021.108451

Zhang, D., and Yang, Y. (2022). Exploration potential and development direction of continental tight sandstone gas in the Sichuan Basin. *Nat. Gas. Ind.* 42 (1), 1–11. doi:10.3787/j.issn.1000-0976.2022.01.001

Zhang, F., Yan, J., Li, Z., et al. (2017). Analysis of rock electrical parameters and rw in arichie formula for clastic roch. *Well Logging Technol.* 41 (2), 127–134. doi:10.16489/j.issn.1004-1338.2017.02.001

Zhang, L, Pan, B, Li, Z., et al. (2010). New three-water conduction model and its application in evaluation of low porosity and low permeability reservoir. *Oil Geophys. Prospect.* 45 (3), 431–435. doi:10.13810/j.cnki.issn.1000-7210.2010.03.025

Zhang, L., Pan, B., Ning, L., et al. (2011). Reservoir classification method based on three-water model to evaluate low porosity and low permeability reservoir. *Well Logging Technol.* 35 (1), 31–35.

Zhang, S. (2009). Discussion on the diagenesis and timing of tight sandstone reservoir in Xujiahe Formation, western Sichuan Basin. *J. Mineralogy Petrology* 29 (4), 33–38. doi:10.19719/j.cnki.1001-6872.2009.04.005

Zhao, J., Cao, Q., Bai, Y., et al. (2016). Petroleum accumulation from continuous to discontinuous: Concept, classification and distribution. *Acta Pet. Sin.* 37 (2), 145–159. doi:10.7623/syxb201602001

Zhao, i, Bian, C., Xu, C., Wang, H., Wang, T., and Shi, Z. (2011). Assessment on gas accumulation potential and favorable plays within the xu-1, 3 and 5 members of the Xujiahe Formation in the Sichuan Basin. *Petroleum Explor. Dev.* 38 (4), 385–393. doi:10.1016/s1876-3804(11)60041-4

Zou, C., Zhai, G., Zhang, G., Wang, H., Li, J., et al. (2015). Formation, distribution, potential and prediction of global conventional and unconventional hydrocarbon resources. *Petroleum Explor. Dev.* 42 (1), 14–28. doi:10.1016/s1876-3804(15)60002-7

frontiers | Frontiers in Earth Science

TYPE Original Research
PUBLISHED 02 August 2023
DOI 10.3389/feart.2023.1132118

OPEN ACCESS

EDITED BY
Qiaomu Qi,
Chengdu University of Technology, China

REVIEWED BY
Hewu Liu,
Anhui University of Science and Technology, China
Yiming Yan,
China University of Petroleum, China
Jie Chi,
China University of Petroleum, China

*CORRESPONDENCE
R. Prioli,
prioli@vdg.fis.puc-rio.br

RECEIVED 26 December 2022
ACCEPTED 20 June 2023
PUBLISHED 02 August 2023

CITATION
de Lacerda DLP, Prioli R, Parizek-Silva YM and Vasquez GF (2023), Nanoscale identification and characterization of the shear strength of minerals and organic matter in shale.
Front. Earth Sci. 11:1132118.
doi: 10.3389/feart.2023.1132118

Nanoscale identification and characterization of the shear strength of minerals and organic matter in shale

D. L. P. de Lacerda[1,2], R. Prioli[2]*, Y. M. Parizek-Silva[2] and G. F. Vasquez[2]

[1]Departamento De Física, Pontifícia Universidade Católica Do Rio De Janeiro, Rio De Janeiro, Brazil, [2]Centro De Pesquisas Leopoldo Américo Miguez De Mello (CENPES), Rio De Janeiro, Brazil

Shales are composed of minerals and organic matter, whose individual properties are essential to determining the rock's macroscopical deformation and strength. Scanning electron microscopy combined with electron energy dispersive spectroscopy (EDS) has been extensively used to evaluate composition, while peak-force atomic force microscopy (AFM) has been used on the determination of elastic modulus with nanometric resolution. Still, there is a need for tools to conduct an in-depth study of the minerals' tribomechanical properties. Atomic force microscopy is a tool that can contribute to these studies, as it can simultaneously measure the tribomechanical properties and identify the phases. In this work, we propose using atomic force microscopy and energy dispersive spectroscopy to identify the shale components and to measure the *in situ* tribomechanical properties from the different phases. Friction images between the atomic force microscopy tip and the surface were acquired as a function of load. Minerals and organic matter were later identified by colocalized energy dispersive spectroscopy mapping. Then, the frictional characteristics of the major shale constituents were obtained by adjusting the Derjaguin-Muller-Toporov model to the selected components. Moreover, the identification of the different phases was performed. The results show that friction at the nanometer scale was observed to be higher for organic matter than for any other shale constituent, while shear strength was observed to be higher for quartz and lower for organic matter. These characteristics were used to differentiate shale constituents. It is shown that a careful comparison of friction can be used to differentiate the sulfite pyrite, tectosilicates (quartz, andesine, and albite), phyllosilicate biotite, and organic matter. The presented methodology gives novel information on friction properties in the nanoscale that are comparable to available centimetric characterization techniques contributing to the understanding of rock strength.

KEYWORDS

shear-strength, friction, shale, organic matter, minerals

1 Introduction

The lack of knowledge about the geochemical and physical properties of shales contributes to uncertainties on the amount of recoverable gas and oil available, preventing the full development of these resources, raising environmental concerns, and increasing economic unknowns (Kerr, 2010; Middleton et al., 2017). Shales are

heterogeneous, composed of a wide variety of minerals, clays, organic matter, and pores of complex characterization. They play an essential role in the frictional characteristics, fracture dynamics, and slip of rocks (Tembe et al., 2010; Fang et al., 2018; Zhang et al., 2020).

Fracture formation and movement are influenced by shear slip and moderated by the frictional strength of the fracture surface (Hu et al., 2016; Yan et al., 2016). The contact interface in a fracture surface is governed by a population of small asperities in contact. The slip of the rock occurs in a discontinuous manner governed by friction instabilities at the population of asperities in contact. Such instabilities may lead to a stick and slip movement at the interface (Scholz and Engelder, 1976; Dieterich and Kilgore, 1994; Ben-David et al., 2010; Li et al., 2011). For instance, when a high-pressure fluid is injected into the rock, as the pressure is increased, the shear forces at the asperities build up until critical stress is achieved, and a slip occurs. At the contact, the surface slip does not happen at once but propagates through the interface leading to fracture or further increase of preexisting cracks (Svetlizky and Fineberg, 2014; Shlomai et al., 2020).

Shear slip is influenced by rock composition. The amount of clay and organic matter plays a significant role in the mechanical strength of the rock (Ikari et al., 2011; Kohli and Zoback, 2013). As their content increases, the rock shear strength decreases. This trend is observed until a total amount of clay and organic matter achieves ~ 40 vol%, which becomes constant (Wang et al., 2019). Although mineralogy does influence the shear properties of faults, the direct correlation between the slip of the faults and the frictional properties of the individual phases present at the surface of the rock has not been investigated. In shales, due to their fine grain and porous structure in the nanoscale, high-resolution characterization techniques are required to measure the frictional properties of the minerals and organic matter. One instrument suitable for characterizing small-scale structures is the atomic force microscope (AFM).

AFM has been used for high-resolution imaging of pores (Javadpour, 2009; Javadpour et al., 2012; Zhu et al., 2017; Kumar et al., 2018; Zhao et al., 2019). Adhesion forces between the AFM microscope tip, organic matter, and minerals have been measured (Tian et al., 2018; Tian et al., 2019). Different AFM operational modes have also been explored to access mechanical properties of shale minerals and organic matter, such as AFM nanoindentation (Zeszotarski et al., 2004), atomic force acoustic microscopy (Prasad et al., 2002), and Peak-Force (Eliyahu et al., 2015; Emmanuel et al., 2016a; Emmanuel et al., 2016b; Khatibi et al., 2018; Li et al., 2018). Resistivity properties were studied using PF-TUNA mode (Wang et al., 2017).

Although there is a growing interest in the use of AFM for the microstructural and micromechanical characterization of rocks, few studies exploring the lateral force mode on the analysis of the geochemical composition and tribomechanical properties of rocks and minerals have been reported in the literature (Higgins and Hu, 2005; Higgins et al., 2007; Cubillas and Higgins, 2009; Hu et al., 2010). Our paper aims to contribute to these studies.

In this manuscript, the AFM has been used to produce friction maps, *in situ*, on the surface of shale rock, with high spatial resolution. With a mechanical contact model, adhesion and shear strength were obtained for the organic and inorganic components of the shale rock. These measurements bring new information on the behavior of the shale components under shear produced by a small asperity contact at the mineral scale.

2 Materials and methods

A diagram showing all steps, from sample preparation to analysis, performed in our experiment is presented in Figure 1. The shale samples were embedded in epoxy resin, polished, and studied with a combination of high-resolution microscopy. Digital imaging processing allowing image colocalization and data analysis were performed to extract the tribomechanical properties from the observed minerals and organic matter at the grain-scale.

2.1 Samples characteristics and preparation

Shale fragments from the Assistência Member, Irati Formation in the Paraná Basin, Brazil, were studied in this work. The deposition of the oil shale found in the Assistência Member has occurred in a hypersaline and marine environment leading to the formation of an organic-rich shale with a wide variety of minerals and a Type I organic matter (Zalán et al., 1990; Milani and Zalán, 1999). Characterization by x-ray diffraction has shown the occurrence of quartz, pyrite, feldspar, and phyllosilicates (Anjos et al., 2010; Nicolini et al., 2011). Geochemical characterization shows that the average total organic carbon content in Irati shales is around 3.8% of the mass, with peaks of 14.4% in the Irati Formation (Holanda et al., 2016).

Shale fragments were embedded in an epoxy resin from which cylindrical samples 1 inch in diameter were cut. The surface of the samples was ground using silicon carbide paper with grits up to 3200 and particle grain size of ~4.5 μm. The surfaces were further polished with diamond paste using finer abrasive particles with grain sizes of 0.25 μm. The samples were then rinsed with ethanol and dried with air spray.

2.2 Lateral force microscopy

The AFM can be used in a diversity of modes. In the AFM lateral force scanning mode (Meyer et al., 1998), a tip at the end of a cantilever scans the sample in close contact with the surface, while a normal repulsive contact force between the tip and the surface is kept constant by a closed loop feedback system. The scanning is performed perpendicularly to the cantilever´s main axis. The sample topography is registered from the vertical displacement of the piezoelectric ceramic necessary to keep the normal force constant during scanning. The difference between the expected vertical tip position and the real position is acquired in the error channel. Cantilever torsion produced by the friction forces between the tip and the surface is registered in the lateral force channel. The influence of the surface topography in the lateral force images is minimized by subtracting the lateral force backward images from the lateral force forward images (Liu et al., 1996). The resulting image is named friction force image throughout this manuscript. In our measurements, topography, error, and lateral force forward and

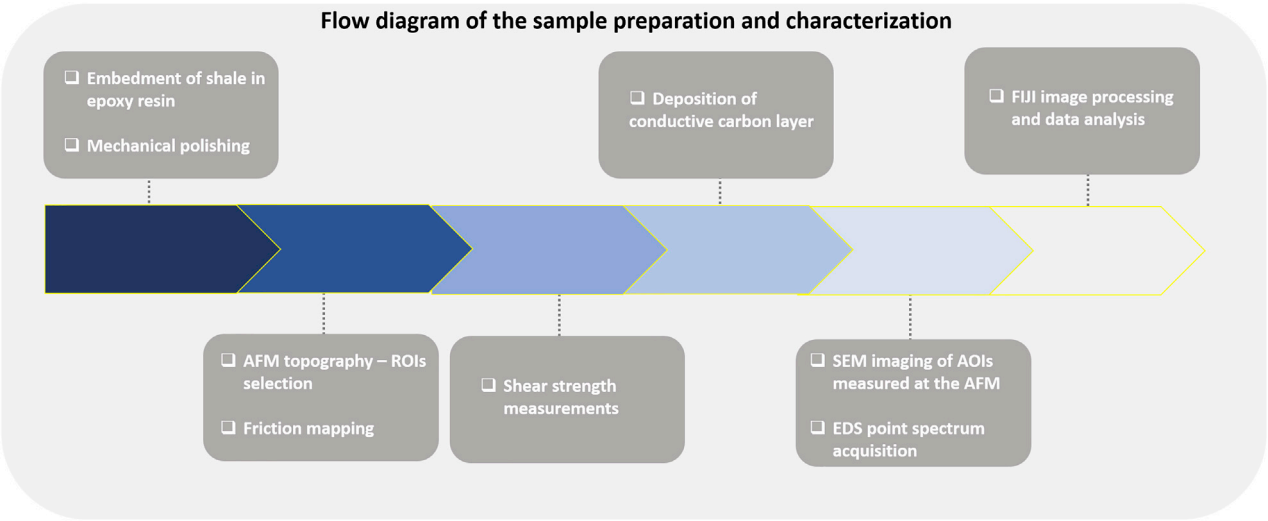

FIGURE 1
Flow chart outlining each step of our experiment, from sample preparation to analysis. The shale samples were embedded in epoxy resin and polished. The AFM analysis was performed followed by SEM and EDS characterization. The tribomechanical characteristics of the observed components of the rock were extracted using digital imaging processing.

backward images were simultaneously acquired. Figure 2 illustrates the AFM working principle.

The samples were brought to an AFM (Nx-10, Park Systems) for sample characterization. The microscope is on top of an active vibration isolation table and enclosed in an environmentally sealed acoustic enclosure box. The topography and lateral force images were obtained in the air at ~ 30°C and ~ 20% relative humidity. All images were acquired at a speed of 1 μm/s with a cantilever of 3.6 N/m bending constant (FESPW, Bruker), and load ranging from 0.1 to 1.0 μN. The sharp tip of the AFM is easily damaged when scanning the surface of the rock. That leads to variations in the tip-surface contact area, making the shear strength and adhesion analysis difficult to perform. Therefore, the tip was previously scratched on a silicon substrate to wear the tip apex, making it stable during image acquisition. The radius of curvature of the tip used in our experiments was measured by scanning a tip calibration grid and confirmed by SEM as 256 ± 13 nm.

Before the friction force measurements, the microscope photodetector was calibrated by measuring the lateral forces between the tip and an SiO_2 sample while scanning with the same normal forces and speeds used at the shale experiments in scanning directions parallel and perpendicular to the cantilever's main axis and considering a friction coefficient between silicon and SiO_2 (Liu et al., 1996). One set of calibrated images was acquired to measure the friction as a function of normal load, analogous to the high-speed procedure reported by Bosse et al., 2014.

2.3 Mineralogical SEM and EDS analysis

After AFM characterization, the samples were coated with a 10 nm thick conductive carbon layer. The layer was needed to prevent surface charging artifacts during the SEM analysis. After deposition, the samples were transferred to the SEM for characterization.

A scanning electron microscope (JSM-6490-LV, JEOL) was used to characterize the microstructure and mineralogical composition of the sample's surfaces. The images were acquired in low vacuum using an electron beam of 20 keV, a working distance of 10 mm, with a backscattering electron detector (BSE) and energy dispersive x-ray spectroscopy (EDS). The SEM and EDS images were acquired at the same location of AFM. EDS compositional point analysis was used to determine the chemical composition of selected grains.

2.4 Friction analysis and segmentation

The open-source image processing package FIJI was used to register the SEM to the AFM image, to extract data of selected minerals from the friction images, and to segment the organic matter from the mineral phase (Schindelin et al., 2012). Initially, the SEM image was registered into AFM topography correlating two pairs of manually defined landmarks. Next, histograms of friction were recovered from the maximum load friction image in the minerals previously identified with EDS analysis. The organic matter phase was segmented in the same image using a non-local means filter and manual segmentation (Buades et al., 2011).

2.5 Shear strength determination

The next step was analyzing the effect of applied normal force, $F_{n,}$, on friction, F_{f}, of the selected minerals. The FIJI was used to colocalize the set of friction images to reduce the image deformations and translations between acquisitions with different loads (Thevenaz et al., 1998; Schindelin et al., 2012). The average

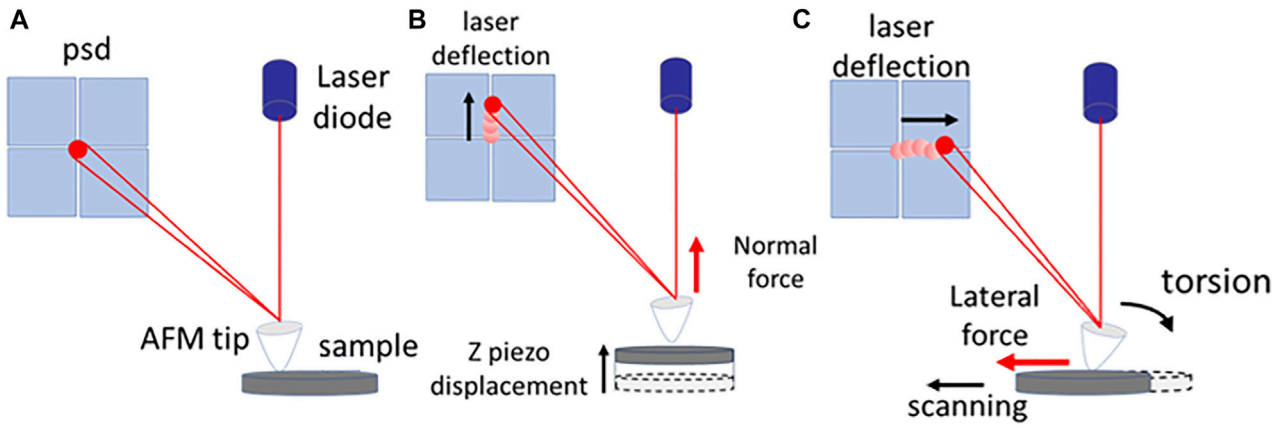

FIGURE 2
AFM working principle. **(A)** A cantilever tip probe interacts with the sample surface. The probe movement and forces are monitored by the deflection of a laser beam onto a position-sensitive photodetector (psd). **(B)** The vertical movement of the sample produces normal forces (F_N) that bend the probe, moving the laser beam upwards\downwards in the detector. **(C)** The lateral movement of the sample produces friction forces, and torsion of the probe, moving the beam laterally in the detector. During scanning, the vertical and horizontal movements of the sample are controlled by a piezoelectric scanner.

friction, and its standard deviation, was recovered from a square of 10x10 pixel inside the selected minerals and organic matter regions. The above experimental steps were executed following the flow diagram listed in Figure 1. At the end of the data analysis step, a friction map for each individual phase and the friction dependence with load was obtained.

The effect of normal force, $F_{n,}$, on friction, F_f, can be described from the contact theory equations (Meyer et al., 1998). On scanning, the contact area, A, between the tip and the surface was estimated with the use of the Derjaguin-Muller-Toporov (DMT) model where:

$$A = \pi\left(\frac{3R}{4E_r}\right)^{\frac{2}{3}}(F_n + F_{ad})^{\frac{2}{3}} \quad (1)$$

$$F_f = \eta(F_n + F_{ad})^{2/3} \quad (2)$$

$$\eta = \tau\pi\left(\frac{3R}{4E_r}\right)^{\frac{2}{3}} \quad (3)$$

Where R is the tip radius, E_r is the reduced elastic modulus, and F_{ad} is the adhesion between tip and surface, respectively (Derjaguin et al., 1975). The friction was obtained from shear strength τ following $F_f = \tau A$ (Carpick et al., 1999; Higgins et al., 2007; Cubillas and Higgins, 2009).

3 Results

3.1 Elemental mapping and mineralogy

The elemental distribution observed by EDS indicates that silicates are predominant in our samples. The presence of quartz with silicon and oxygen only and feldspar with silicon, oxygen, aluminum, sodium, and calcium are abundant. Biotie, verified by typical crystalline habit and cleavage added to silicon, oxygen, potassium, aluminum, magnesium, and iron in a characteristic ratio, is also observed. The morphology and presence of sulfur and iron indicated the presence of pyrites. The regions with high carbon concentrations were associated with organic matter.

Figure 3A shows EDS color mapping obtained by overlaying the selected elemental maps with the BSE image. In this image, we identify the different elements by their colors. White squares indicate selected regions of quartz (Qtz), pyrite (Py), the feldspars andesine (And) and albite (Alb), the phyllosilicate biotite (Bio), and organic matter (OM) from which the correspondent local EDS point analysis was acquired. The spectra are exhibited in Figure 3B. Multiple peaks can be seen. Each of them is associated with the occurrence of the elements indicated.

Figure 4 shows colocalized BSE, AFM topography, error, and friction force images of an ROI. The BSE image in Figure 4A shows minerals with different textures and gray levels. Dark gray is associated with organic matter, followed by gray, which includes tectosilicates and clay minerals. The light gray level is associated with pyrite. The AFM topography image in Figure 4B shows several grains with sizes ranging from the micron to the nanoscale. The error image in Figure 4C highlights the high spatial-frequency variations associated with intercrystallite pores and edges. The friction image in Figure 4D shows minerals with low friction (in red and green) embedded in a high friction matrix of clay and biotite (cyan) and organic matter (dark blue). The pyrite, biotite, and organic matter are seen only in BSE and Friction images, while quartz, andesine, and albite are seen in all modes. Topography and error identify the variations in surface height, including the ones associated with porosity.

3.2 Friction and shear at the grain scale

The friction force image and histograms for representative minerals and organic matter are shown in Figure 5. The data from each mineral and organic matter were obtained from the ROI

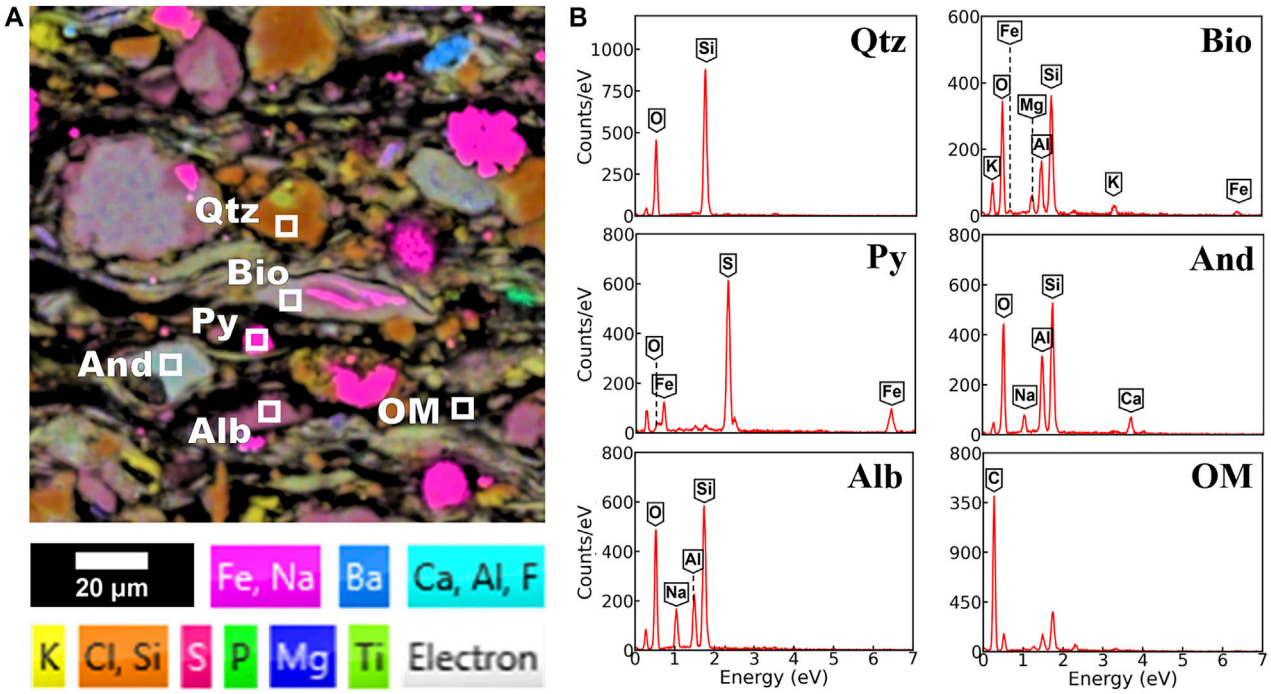

FIGURE 3
Mineralogical identification by SEM and EDS. **(A)** False color EDS mapping showing Fe, Na, Ba, Ca, Al, F, K, Cl, Si, P, Mg, and Ti elements distribution maps superimposed by a backscattering map and **(B)** EDS point analysis on quartz (Qtz), biotite (Bio), pyrite (Py), andesine (And), albite (Alb), and organic matter (OM).

indicated by the contour squares in Figure 5A. Histograms of friction forces from minerals and organic matter are presented in Figure 5B. The lowest friction force (200 ± 20 nN) was measured on the pyrite. Friction forces on andesine (275 ± 19 nN), quartz (293 ± 22 nN), and albite (293 ± 34 nN) were in the intermediate range. The higher friction forces were registered on biotite (365 ± 31 nN) and organic matter (562 ± 49 nN). The values reported are the mean ± standard deviation of the histograms in Figure 5.

Once the friction forces for the different minerals and organic matter were determined, a friction threshold 470 nN was used to separate organic from inorganic fractions all over the surface. For instance, Figure 6A shows a friction force map of our sample surface where all regions showing the presence of organic matter are identified in blue. As highlighted in Figure 6B, the friction forces measured for the organic matter at a 1 μN normal load varied between 400 nN and 700 nN, with a most frequent value at 456 nN. The segmentation shows that the organic matter is distributed over ~20% of the imaged area.

Figure 7 shows the load dependence of the friction forces for minerals and organic matter. The data was fitted (red dotted curve) by the $F_f = \eta(F_n + F_{ad})^{2/3}$ using η and F_{ad} as fitting parameters. The values obtained by fitting the friction data are summarized in Table 1. The E_r modulus was calculated for the AFM tip, minerals, and organic matter using mechanical parameters from the literature (Mavko et al., 2009). The adjusted parameters η and F_{ad}, the tip radius R, and E_r were used to determine the contact shear strength τ. As a general trend, friction is observed to be higher for organic matter and lower for pyrite at all normal forces.

4 Discussion

4.1 Frictional properties of shale components

Thousands of asperities may contact each other on a contact interface. Deformation of the asperities in contact occurs due to the applied load and depends on the material's elastic modulus. Shear stresses may lead to further elastic, plastic, and even fracture of the asperities in contact. As shear stress becomes high enough, the deformed or broken asperities may slide past each other, giving origin to the slip between the surfaces in contact.

In shale, a rock with a fine grain and rich composition, the asperities in contact may be formed by a large combination of materials with significantly different mechanical properties. Moreover, the contact interfaces may be mediated by gouges or even exogenous particles. Besides all that, the frictional strength observed for the surface of the rocks is in the range of 0.3–0.7 (Ikari et al., 2011; Kohli and Zoback, 2013; Kubo and Katayama, 2015; Yan et al., 2016; Wang et al., 2019). In good agreement, the measured friction coefficient between the AFM silicon tip and each of the individual shale constituents is within the same range. Our measurements show that the coefficient for the inorganic fraction

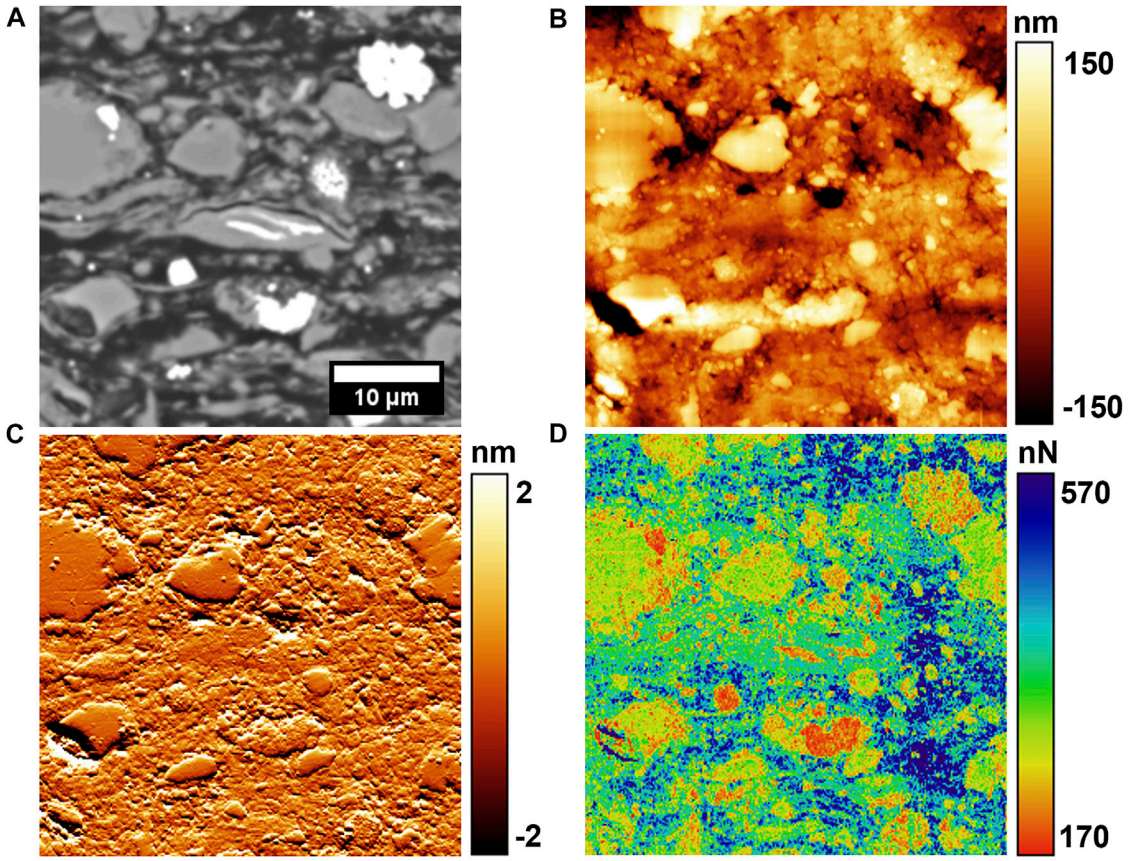

FIGURE 4
Scanning electron and force microscopy images of the same region from the shale surface. **(A)** Electron backscattering image, **(B)** surface topography, **(C)** error, and **(D)** friction force images measured by AFM. The friction image was acquired under a normal force of 1 μN.

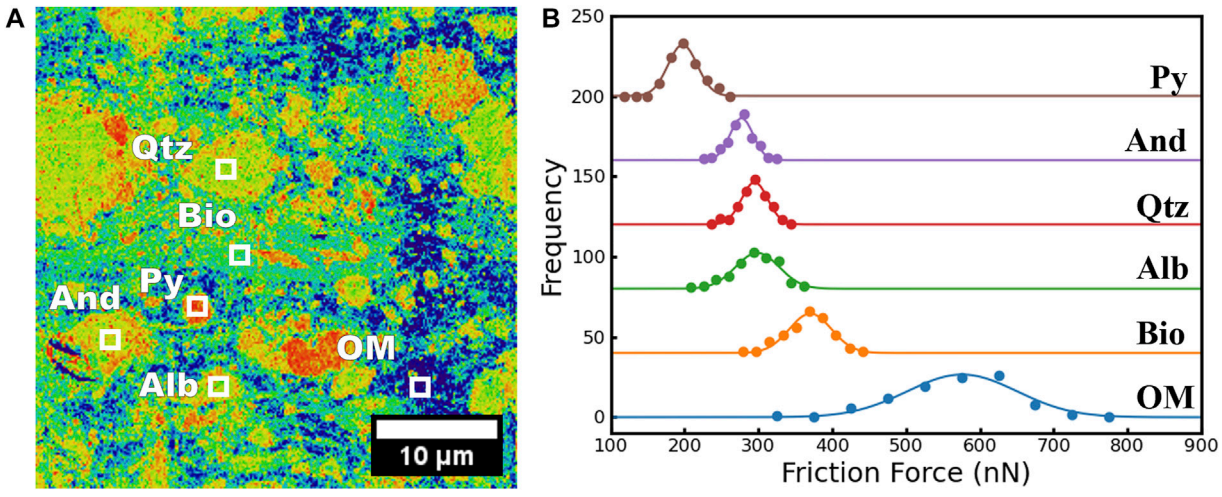

FIGURE 5
Friction measurements on minerals and organic matter. **(A)** Friction force image and identification of quartz (Qtz), biotite (Bio), pyrite (Py), andesine (And), albite (Alb), and organic matter (OM). **(B)** Distribution of friction forces observed on minerals and organic matter. The histograms were vertically offset to allow better visualization.

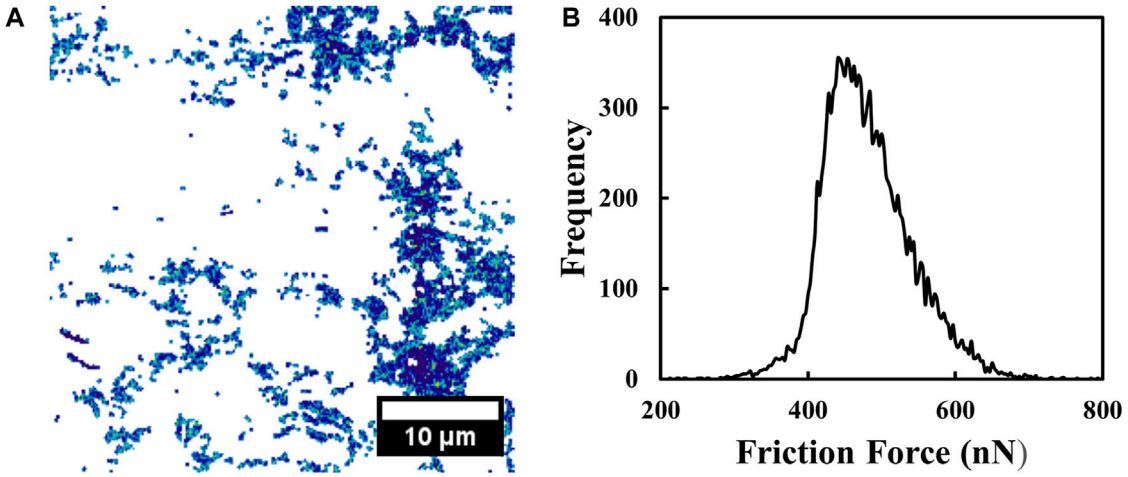

FIGURE 6
Distribution of organic matter. In 5 **(A)**, surface sites where organic matter was identified by the friction forces between the sample and the microscope tip are shown. In 5 **(B)**, the statistical distribution of friction forces observed for the organic matter is presented. A 1.0 μN normal force was used.

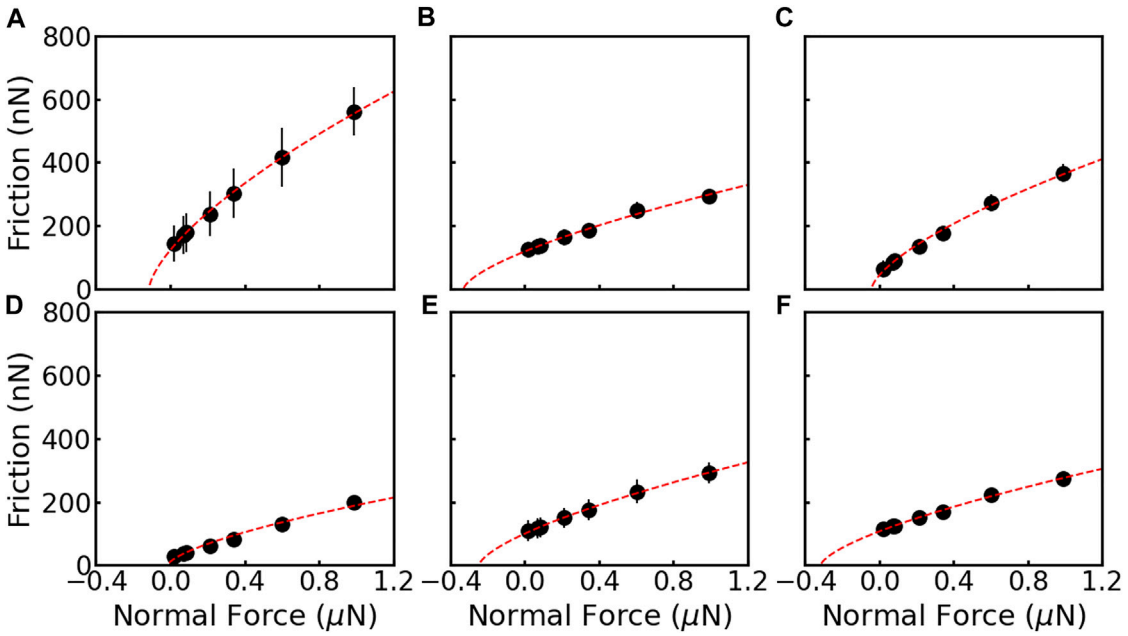

FIGURE 7
Friction force as a function of normal force for **(A)** organic matter, **(B)** quartz, **(C)** biotite, **(D)** pyrite, **(E)** albite, and **(F)** andesine grains. The black dots and error bars are average and standard deviation, respectively. The red dotted lines are the curves fitted using the DMT model.

of the shale ranges between 0.2 and 0.3, while for the organic matter is ~0.4.

The nonlinear DMT contact model describes the data well, allowing the adhesion and shear strength determination and indicating attractive long-range forces at the interface. Our data agree with the adhesion reported for kerogen, 100–120 nN (Tian et al., 2018; Tian et al., 2019). The results also indicate that the contact shear strength is independent of the applied normal force. The contact shear strength was higher for quartz, pyrite, and anorthite (~0.4 GPa) and low for albite, biotite, and organic matter (~0.3 GPa). The calculated shear strengths are in the same order as those estimated from nanoscale friction measurements (Carpick et al., 1997).

Considering that the mineralogical composition determines the frictional behavior of the interfaces, our shear strength

10.3389/feart.2023.1132118

TABLE 1 Frictional experiment parameters and data summary. The reduced modulus E_r, adjusted η parameter, the adhesion force F_{ad}, and the shear strength are presented.

Material	E_r (GPa)	η	F_{ad} (nN)	τ (GPa)
Quartz	63	2.46 ± 0.06	334 ± 25	0.37 ± 0.02
Albite	56	2.30 ± 0.05	316 ± 20	0.32 ± 0.02
Anorthite	70	2.54 ± 0.03	246 ± 11	0.41 ± 0.02
Biotite	32	3.53 ± 0.08	40 ± 10	0.34 ± 0.02
Pyrite	115	1.8 ± 0.1	21 ± 17	0.41 ± 0.04
Organic Matter	16	5.18 ± 0.07	116 ± 7.5	0.31 ± 0.01

results indicate that surfaces rich in quartz are less likely to initiate slip than surfaces rich in biotite and organic matter. However, once shear is initiated, the slip of surfaces rich in quartz is more likely to continue than those rich in biotite and organic matter due to the friction coefficient. Our results agree with the literature in that shear failure is less likely for fractures with higher tectosilicate content (Fang et al., 2018).

4.2 Organic matter identification

We demonstrate the *in situ* characterization of shale components with friction maps. These maps highlight that the measurement of frictional and shear strength give access to the mineralogical compositional of the surface with high spatial resolution. In our case, surface sites as small as ~15 nm could be unequivocally identified. This lateral resolution is comparable to the resolution observed using AFM mechanical modulus mapping techniques (Eliyahu et al., 2015; Emmanuel et al., 2016a; Emmanuel et al., 2016b; Yang et al., 2017; Khatibi et al., 2018; Li et al., 2018; Graham et al., 2020). The friction contrast allows the separation of the organic matter from the tectosilicates, phyllosilicates, and sulfide. Nevertheless, difficulties in separating the plagioclase and biotite with friction only are evident due to the partial overlap between the friction histograms (Figure 5). To overcome that, additional info from SEM, EDS, and correlative image techniques is needed. With the use of EDS, we were able to observe albite, anorthite, and biotite—materials with similar frictional strengths—in our sample.

Among the components of shale, organic matter is the one that attracts the most attention. It not only affects the sliding of fractured surfaces, as indicated by our results, but also their amount and type, which will be critical factors for the economic development of the rock. Our experiment demonstrates that the friction contrast measured in the lateral force mode by AFM may also contribute to identifying the organic matter fraction at the surface.

Histogram thresholding-based segmentation was used to separate the organic from inorganic components of the rock. The contrast observed in the friction image allows the accurate identification of the pixel ranges for the organic matter and a map, indicating the surface sites with the presence of the organic material, can be obtained, like the one shown in Figure 6. The sites where friction strengths correspond to the organic matter were observed covers 20% of the surface. Considering typical density values and mineralogical distributions we can expect a variation between 15% and 35% (Anjos et al., 2010; Nicolini et al., 2011; Holanda et al., 2016) for volumetric organic matter fraction, which agrees with our measures. In this map, the distribution of frictional strengths may be attributed to the local variation on the physical properties of the organic matter. These results show that the use of frictional contrast obtained with the use of the lateral force microscope mode, and available on any AFM, can accurately locate the organic components present at the surface of the rock.

5 Conclusion

In this work, we have explored atomic force microscopy in the lateral force mode to measure friction and shear strength at individual minerals and organic matter of a shale fragment from the Irati formation. The organic matter exhibits a lower shear strength than other materials. Moreover, its shear strength value at the nanoscale is in the same order as macroscale shear strengths observed for organic-rich shale rocks, contributing to understanding organic matter effects in slip propagation in shale rocks.

The use of the AFM, a high-resolution microscopy technique with the ability to simultaneously measure topography and tribological properties of the materials, has additional benefits on shale characterization. We demonstrate that friction force characteristics of minerals and organic matter of immature shale fragments can be used to examine the spatial distribution of shale composition. Friction between the microscope tip and shale compositional phases is higher for organic matter, followed by tectosilicates and pyrite. We have observed that the organic matter, tectosilicates, and pyrite were unambiguously identified by their friction forces. On the other hand, more than the AFM friction data is needed to identify quartz, albite, and anorthite phases. Identifying these phases demands a combination of AFM friction analysis with EDS spectroscopy performed at the SEM.

When compared with AFM elastic modulus measurements, the lateral force method, available in any commercial AFM, allows in one single image the geochemical and morphological characterization of individual minerals and organic matter in shale rocks with a wide range of elastic modulus, varying in two orders of magnitude.

Data availability statement

The original contributions presented in the study are included in the article/supplementary material, further inquiries can be directed to the corresponding author.

Author contributions

DLPL conception, design of the work, acquisition of AFM data, analysis, and interpretation of data. RP conception, design of the work, acquisition of AFM data, analysis, and interpretation of data. YMP-S acquisition and interpretation of SEM/EDS data. GFV conception, design of the work, and interpretation of data. All authors contributed to the article and approved the submitted version.

Funding

This study was financed in part by the Coordenação de Aperfeiçoamento de Pessoal de Nível Superior—Brasil (CAPES) and the Financiadora de Estudos e Projetos (FINEP).

Conflict of interest

The authors declare that the research was conducted in the absence of any commercial or financial relationships that could be construed as a potential conflict of interest.

Publisher's note

All claims expressed in this article are solely those of the authors and do not necessarily represent those of their affiliated organizations, or those of the publisher, the editors and the reviewers. Any product that may be evaluated in this article, or claim that may be made by its manufacturer, is not guaranteed or endorsed by the publisher.

References

Anjos, C. W. D. D., Meunier, A., Guimarães, E. M., and el Albani, A. (2010). Saponite-rich black shales and nontronite beds of the permian Irati Formation: Sediment sources and thermal metamorphism (Paraná Basin, Brazil). *Clays Clay Minerals* 58 (5), 606–626. doi:10.1346/ccmn.2010.0580503

Ben-David, O., Rubinstein, S. M., and Fineberg, J. (2010). Slip-stick and the evolution of frictional strength. *Nature* 463 (7277), 76–79. doi:10.1038/nature08676

Bosse, J. L., Lee, S., Andersen, A. S., Sutherland, D. S., and Huey, B. D. (2014). High speed friction microscopy and nanoscale friction coefficient mapping. *Meas. Sci. Technol.* 25 (11), 115401. doi:10.1088/0957-0233/25/11/115401

Buades, A., Coll, B., and Morel, J.-M. (2011). *Non-local means denoising. Image processing on line*, 208–212. doi:10.5201/ipol.2011.bcm_nlm

Carpick, R. W., Frank, O. D., and Salmeron, M. (1999). A general equation for fitting contact area and friction vs load measurements. *J. Colloid Interface Sci.*, 211(2), 395–400. doi:10.1006/jcis.1998.6027

Carpick, R. W., Ogletree, D. F., and Salmeron, M. (1997). Lateral stiffness: A new nanomechanical measurement for the determination of shear strengths with friction force microscopy. *Appl. Phys. Lett.* 70 (12), 1548–1550. doi:10.1063/1.118639

Cubillas, P., and Higgins, S. R. (2009). Friction characteristics of Cd-rich carbonate films on calcite surfaces: Implications for compositional differentiation at the nanometer scale. *Geochem. Trans.* 10 (1), 7. doi:10.1186/1467-4866-10-7

Derjaguin, B. V., Muller, V. M., and Toporov, Yu.P. (1975). Effect of contact deformations on the adhesion of particles. *J. Colloid Interface Sci.* 53 (2), 314–326. doi:10.1016/0021-9797(75)90018-1

Dieterich, J. H., and Kilgore, B. D. (1994). Direct observation of frictional contacts: New insights for state-dependent properties. *Pure Appl. Geophys. PAGEOPH* 143 (1-3), 283–302. doi:10.1007/bf00874332

Eliyahu, M., Emmanuel, S., Day-Stirrat, R. J., and Macaulay, C. I. (2015). Mechanical properties of organic matter in shales mapped at the nanometer scale. *Mar. Petroleum Geol.* 59, 294–304. doi:10.1016/j.marpetgeo.2014.09.007

Emmanuel, S., Eliyahu, M., Day-Stirrat, R. J., Hofmann, R., and Macaulay, C. I. (2016a). Impact of thermal maturation on nano-scale elastic properties of organic matter in shales. *Mar. Petroleum Geol.* 70, 175–184. doi:10.1016/j.marpetgeo.2015.12.001

Emmanuel, S., Eliyahu, M., Day-Stirrat, R. J., Hofmann, R., and Macaulay, C. I. (2016b). Softening of organic matter in shales at reservoir temperatures. *Pet. Geosci.* 23 (2), 262–269. doi:10.1144/petgeo2016-035

Fang, Y., Elsworth, D., Wang, C., and Jia, Y. (2018). Mineralogical controls on frictional strength, stability, and shear permeability evolution of fractures. *J. Geophys. Res. Solid Earth* 123 (5), 3549–3563. doi:10.1029/2017jb015338

Graham, S. P., Rouainia, M., Aplin, A. C., Cubillas, P., Fender, T. D., and Armitage, P. J. (2020). Geomechanical characterisation of organic-rich calcareous shale using AFM and nanoindentation. *Rock Mech. Rock Eng.* 54 (1), 303–320. doi:10.1007/s00603-020-02261-6

Higgins, S. R., Hu, X., and Fenter, P. (2007). Quantitative lateral force microscopy study of the dolomite (104)–Water interface. *Langmuir* 23 (17), 8909–8915. doi:10.1021/la700467q

Higgins, S. R., and Hu, X. (2005). Self-limiting growth on dolomite: Experimental observations with *in situ* atomic force microscopy. *Geochimica Cosmochimica Acta* 69 (8), 2085–2094. doi:10.1016/j.gca.2004.10.010

Holanda, W., Bergamaschi, S., Santosdos, A. C., Rodrigues, R., and Bertolino, L. C. (2016). Characterization of the Assistência member, Irati Formation, Paraná Basin, Brazil: Organic matter and mineralogy/caracterização do membro do Assistência, formação Irati, bacia do Paraná, Brasil: Matéria orgânica E mineralogia. *J. Sediment. Environ.* 3 (1), 36–45. doi:10.12957/jse.2018.33304

Hu, J., Yang, S., Fu, D., Rui, R., Yu, Y., and Chen, Z. (2016). Rock mechanics of shear rupture in shale gas reservoirs. *J. Nat. Gas Sci. Eng.* 36, 943–949. doi:10.1016/j.jngse.2016.11.033

Hu, X., Cubillas, P., and Higgins, S. R. (2010). Properties of Ca-rich and Mg-rich carbonate films on dolomite: Implications for compositional surface mapping with scanning force microscopy. *Langmuir* 26 (7), 4769–4775. doi:10.1021/la9035425

Ikari, M. J., Marone, C., and Saffer, D. M. (2011). On the relation between fault strength and frictional stability. *Geology* 39 (1), 83–86. doi:10.1130/g31416.1

Javadpour, F., Moravvej Farshi, M., and Amrein, M. (2012). Atomic-force microscopy: A new tool for gas-shale characterization. *J. Can. Petroleum Technol.* 51 (04), 236–243. doi:10.2118/161015-pa

Javadpour, F. (2009). Nanopores and apparent permeability of gas flow in mudrocks (shales and siltstone). *J. Can. Petroleum Technol.* 48 (08), 16–21. doi:10.2118/09-08-16-da

Kerr, R. A. (2010). Natural gas from shale bursts onto the scene. *Science* 328 (5986), 1624–1626. doi:10.1126/science.328.5986.1624

Khatibi, S., Ostadhassan, M., Tuschel, D., Gentzis, T., Bubach, B., and Carvajal-Ortiz, H. (2018). Raman spectroscopy to study thermal maturity and elastic modulus of kerogen. *Int. J. Coal Geol.* 185, 103–118. doi:10.1016/j.coal.2017.11.008

Kohli, A. H., and Zoback, M. D. (2013). Frictional properties of shale reservoir rocks. *J. Geophys. Res. Solid Earth* 118 (9), 5109–5125. doi:10.1002/jgrb.50346

Kubo, T., and Katayama, I. (2015). Effect of temperature on the frictional behavior of smectite and illite. *J. Mineralogical Petrological Sci.* 110 (6), 293–299. doi:10.2465/jmps.150421

Kumar, S., Das, S., Bastia, R., and Ojha, K. (2018). Mineralogical and morphological characterization of older cambay shale from north cambay basin, India: Implication for shale oil/gas development. *Mar. Petroleum Geol.* 97, 339–354. doi:10.1016/j.marpetgeo.2018.07.020

Li, C., Ostadhassan, M., Guo, S., Gentzis, T., and Kong, L. (2018). Application of PeakForce tapping mode of atomic force microscope to characterize nanomechanical properties of organic matter of the Bakken Shale. *Fuel* 233, 894–910. doi:10.1016/j.fuel.2018.06.021

Li, Q., Tullis, T. E., Goldsby, D., and Carpick, R. W. (2011). Frictional ageing from interfacial bonding and the origins of rate and state friction. *Nature* 480 (7376), 233–236. doi:10.1038/nature10589

Liu, E., Blanpain, B., and Celis, J. P. (1996). Calibration procedures for frictional measurements with a lateral force microscope. *Wear* 192 (1-2), 141–150. doi:10.1016/0043-1648(95)06784-1

Mavko, G., Mukerji, T., and Dvorkin, J. (2009). *The rock physics handbook: Tools for seismic analysis of porous media*. Cambridge, UK; New York: Cambridge University Press.

Meyer, E., Gyalog, T., Overney, R. M., and Dransfeld, K. (1998). *Nanoscience: Friction and rheology on the nanometer scale*. Singapore: World Scientific.

Middleton, R. S., Hyman, J. D., and Viswanathan, H. S. (2017). The shale gas revolution: Barriers, sustainability, and emerging opportunities. *Appl. Energy* 199, 88–95. doi:10.1016/j.apenergy.2017.04.034

Milani, E. J., and Zalán, P. V. (1999). An outline of the geology and petroleum systems of the Paleozoic interior basins of South America. *Episodes* 22 (3), 199–205. doi:10.18814/epiiugs/1999/v22i3/007

Nicolini, J., Pereira, B. F., Pillon, C. N., Machado, V. G., Lopes, W. A., de Andrade, J. B., et al. (2011). Characterization of Brazilian oil shale byproducts planned for use as soil conditioners for food and agro-energy production. *J. Anal. Appl. Pyrolysis* 90 (2), 112–117. doi:10.1016/j.jaap.2010.11.001

Prasad, M., Kopycinska, M., Rabe, U., and Arnold, W. (2002). Measurement of Young's modulus of clay minerals using atomic force acoustic microscopy. *Geophys. Res. Lett.*, 29(8), 13–14. doi:10.1029/2001gl014054

Schindelin, J., Arganda-Carreras, I., Frise, E., Kaynig, V., Longair, M., Pietzsch, T., et al. (2012). Fiji: An open-source platform for biological-image analysis. *Nat. methods* 9 (7), 676–682. doi:10.1038/nmeth.2019

Scholz, C. H., and Engelder, J. T. (1976). The role of asperity indentation and ploughing in rock friction — I. *Int. J. Rock Mech. Min. Sci. Geomechanics Abstr.* 13 (5), 149–154. doi:10.1016/0148-9062(76)90819-6

Shlomai, H., Kammer, D. S., Adda-Bedia, M., and Fineberg, J. (2020). The onset of the frictional motion of dissimilar materials. *Proc. Natl. Acad. Sci.* 117 (24), 13379–13385. doi:10.1073/pnas.1916869117

Svetlizky, I., and Fineberg, J. (2014). Classical shear cracks drive the onset of dry frictional motion. *Nature* 509 (7499), 205–208. doi:10.1038/nature13202

Tembe, S., Lockner, D. A., and Wong, T.-F. (2010). Effect of clay content and mineralogy on frictional sliding behavior of simulated gouges: Binary and ternary mixtures of quartz, illite, and montmorillonite. *J. Geophys. Res.* 115 (B3), B03416. doi:10.1029/2009jb006383

Thevenaz, P., Ruttimann, U. E., and Unser, M. (1998). A pyramid approach to subpixel registration based on intensity. *IEEE Trans. Image Process.* 7 (1), 27–41. doi:10.1109/83.650848

Tian, S., Dong, X., Wang, T., Zhang, R., Zhang, P., Sheng, M., et al. (2018). Surface properties of organic kerogen in continental and marine shale. *Langmuir* 34 (46), 13882–13887. doi:10.1021/acs.langmuir.8b03151

Tian, S., Wang, T., Li, G., Sheng, M., and Zhang, P. (2019). Nanoscale surface properties of organic matter and clay minerals in shale. *Langmuir* 35 (17), 5711–5718. doi:10.1021/acs.langmuir.9b00157

Wang, J., Ge, H., Wang, X., Shen, Y., Liu, T., Zhang, Y., et al. (2019). Effect of clay and organic matter content on the shear slip properties of shale. *J. Geophys. Res. Solid Earth* 129, 9505–9525. doi:10.1029/2018JB016830

Wang, W., Li, J., Fan, M., and Abedi, S. (2017). Characterization of electrical properties of organic-rich shales at nano/micro scales. *Mar. Petroleum Geol.* 86, 563–572. doi:10.1016/j.marpetgeo.2017.06.021

Yan, W., Ge, H., Wang, J., Wang, D., Meng, F., Chen, J., et al. (2016). Experimental study of the friction properties and compressive shear failure behaviors of gas shale under the influence of fluids. *J. Nat. Gas Sci. Eng.* 33, 153–161. doi:10.1016/j.jngse.2016.04.019

Yang, J., Hatcherian, J., Hackley, P. C., and Pomerantz, A. E. (2017). Nanoscale geochemical and geomechanical characterization of organic matter in shale. *Nat. Commun.* 8 (1), 2179. doi:10.1038/s41467-017-02254-0

Zalán, P. V., Wolff, S., Astolfi, M. A. M., Vieira, I. S., Concelção, J. C. J., Appi, V. T., et al. (1990). The Paraná Basin, Brazil. *Inter. Crat. Basins*. doi:10.1306/m51530c34

Zeszotarski, J. C., Chromik, R. R., Vinci, R. P., Messmer, M. C., Michels, R., and Larsen, J. W. (2004). Imaging and mechanical property measurements of kerogen via nanoindentation. *Geochimica Cosmochimica Acta* 68 (20), 4113–4119. doi:10.1016/j.gca.2003.11.031

Zhang, F., An, M., Zhang, L., Fang, Y., and Elsworth, D. (2020). Effect of mineralogy on friction-dilation relationships for simulated faults: Implications for permeability evolution in caprock faults. *Geosci. Front.* 11 (2), 439–450. doi:10.1016/j.gsf.2019.05.014

Zhao, S., Li, Y., Wang, Y., Ma, Z., and Huang, X. (2019). Quantitative study on coal and shale pore structure and surface roughness based on atomic force microscopy and image processing. *Fuel* 244, 78–90. doi:10.1016/j.fuel.2019.02.001

Zhu, H., Ju, Y., Lu, W., Han, K., Qi, Y., Neupane, B., et al. (2017). The characteristics and evolution of micro-nano scale pores in shales and coals. *J. Nanosci. Nanotechnol.* 17 (9), 6124–6138. doi:10.1166/jnn.2017.14529

frontiers | Frontiers in Earth Science

TYPE Original Research
PUBLISHED 24 August 2023
DOI 10.3389/feart.2023.1267522

OPEN ACCESS

EDITED BY
Qiaomu Qi,
Chengdu University of Technology, China

REVIEWED BY
Lin Zhang,
Hohai University, China
Hemin Yuan,
China University of Geosciences, China

*CORRESPONDENCE
Chao Sun,
kang2008ping2008@163.com

RECEIVED 26 July 2023
ACCEPTED 14 August 2023
PUBLISHED 24 August 2023

CITATION
Sun C, Fortin J, Tang G and Wang S (2023), Prediction of dispersion and attenuation on elastic wave velocities in partially saturated rock based on the fluid distribution obtained from three-dimensional (3D) micro-CT images. *Front. Earth Sci.* 11:1267522. doi: 10.3389/feart.2023.1267522

Prediction of dispersion and attenuation on elastic wave velocities in partially saturated rock based on the fluid distribution obtained from three-dimensional (3D) micro-CT images

Chao Sun[1]*, Jérôme Fortin[2], Genyang Tang[3] and Shangxu Wang[3]

[1]College of Resources and Geoscience, China University of Mining and Technology, Xuzhou, China, [2]Laboratoire de Géologie, Ecole Normale Supérieure/CNRS, UMR8538, PSL Research University, Paris, France, [3]State Key Laboratory of Petroleum Resources and Prospecting, Key Laboratory of Geophysical Prospecting, China National Petroleum Corporation, China University of Petroleum, Beijing, China

Elastic wave attenuation in partially saturated porous rock is primarily due to wave-induced fluid flow, which arises from the contrast in compressibility between air and water and is influenced by the water distribution within the rock. We propose a method for constructing a numerical model that predicts mesoscopic dispersion and attenuation. Initially, we use fluid distribution data sourced from 3D X-ray Computed Tomography images to construct the numerical model, utilizing Biot's poroelastic equations as the governing equations. Subsequently, we implement the finite element method to derive solutions for the numerical model. Our focus is centered on two key challenges: 1) reducing memory cost, and 2) efficiently handling element intersection during the meshing process. The solutions illustrate the evolution of fluid pressure distribution and the frequency-dependent advancement of the elastic moduli, coupled with their corresponding attenuation. Ultimately, we compare these numerical predictions with previously published experimental data from a study on partially saturated Indiana limestone. The considerable agreement between our numerical results and the experimental data confirms the validity of our method, which crucially incorporates the actual fluid distribution (captured from 3D CT images) as a vital input.

KEYWORDS

3D CT image, dispersion, attenuation, mesoscopic-flow, numerical modeling

1 Introduction

Characterization of fluid distribution in a reservoir is essential in several scenarios, such as monitoring CO_2 geological storage and gas and oil production exploration (Klimentos, 1995; Tester et al., 2007). Seismic waves are known to be affected by fluid; therefore, it is a valuable tool for detecting *in situ* fluid properties (Adelinet et al., 2011; Anwer et al., 2017; He et al., 2020). At the mesoscopic scale, for a biphasic saturated rock, like gas and water, seismic waves induce a pore pressure gradient due to the difference in the fluid bulk moduli, causing

diffusion between the different fluid phases and, thus, energy transfer (Pride et al., 2004; Wang Y. et al., 2022b). This diffusion process causes attenuation and dispersion of seismic waves, known as patchy-flow or mesoscopic-wave-induced fluid flow (Müller et al., 2010). The mesoscopic scale refers to heterogeneities in the fluid distribution and rock fabric (e.g., Ba et al., 2015; 2017; Sun, 2017; Zhao Luanxiao et al., 2021b) greater than the pore size but smaller than the wavelength. The mesoscopic scale serves as a crucial bridge between the microscopic and macroscopic levels, enabling the significant upscaling of properties from the pore level to a broader, macroscopic perspective. The effect of mesoscopic flow on the dispersion and attenuation has been reported in a lot of experiments (e.g., Cadoret et al., 1998; Tisato and Quintal, 2013; Chapman et al., 2016; 2021; Mikhaltsevitch et al., 2016; Cavallini et al., 2017; Zhao Liming et al., 2021a; Sun et al., 2022). If we focus on fluid heterogeneity at the mesoscale, many analytical and numerical models can quantitatively assess its effect. One classical analytical model is the White model (e.g., White, 1975; White et al., 1975; Dutta and Odé, 1979; Monachesi et al., 2020). It assumed that fluid patches are composed of periodic layers or spheres. The layer's thickness or the sphere's radius, i.e., the so-called patchy size, determines the critical frequency for dispersion and attenuation. A second kind of analytical model is to assume a random distribution of the fluid (e.g., Müller and Gurevich, 2004; 2005; Toms et al., 2007; Müller et al., 2008; Toms-Stewart et al., 2009; Qi et al., 2014; Zhang et al., 2022). It assumed that the fluid distribution is stochastic and characterized by a correlation length, which can be used to predict the critical frequency of dispersion and attenuation. However, the prediction of the correlation length, the key parameter in this model, is not straightforward. Another way to predict the effect of mesoscopic flow on dispersion/attenuation is to use numerical models. It usually takes the fluid distribution as an input, and uses the finite element method to obtain the solution (e.g., Santos et al., 2005; Rubino et al., 2009; 2016; Quintal et al., 2011; Santos et al., 2021). The numerical model is computationally expensive compared to the analytical model. However, there is no assumption regarding the fluid distribution, making it more widely applicable. Fluid distribution can be obtained, for instance, from CT scan techniques (e.g., Cadoret et al., 1995; Toms-Stewart et al., 2009; Zhu et al., 2017; 2023; Lin et al., 2021; Wang S. et al., 2022a). In a recent study, Chapman et al. (2021) measured the velocity dispersion and attenuation in a biphasic saturated sandstone (water and CO2 gas) and obtained the 3D fluid distribution using CT images. Their results indicate that the majority of the gas is situated towards the end of the sample, resembling a two-layer fluid distribution. Thus, they used an effective 1D numerical model and did not have to consider the cost of a 3D numerical simulation. More recently, Sun et al. (2022) measured the velocity dispersion and attenuation in a partially saturated (air/water) Indiana limestone. Sun et al. (2022) also obtained the 3D fluid distribution using the micro-CT image, and used the finite-element method to predict dispersion and attenuation. However, their numerical simulation was conducted in a 2D space due to unresolved memory consumption issues within the 3D numerical simulation. In addition, they observed a discrepancy between the 2D simulations and the experimental data, which they attributed to the difference between a 2D and 3D numerical simulation. A method for computing dispersion and attenuation in fully saturated rocks was presented by Lissa et al. (2021) to predict squirt flow using a 3D CT image as input. As Lissa et al. (2021) focused on squirt flow, the simulation was done on a cube containing several cracks leading to a cube size of (~300 μm^3), using 0.8 TB of RAM. This approach works perfectly for a local prediction, as for squirt flow; however, it is infeasible for mesoscopic flow: i) a very fine mesh would be needed to represent the distribution and geometry of the two fluid phases, ii) the simulation should be done at a larger scale (~cm^3).

The study describes a new and detailed method for numerically predicting dispersion and attenuation due to mesoscopic flow using a 3D fluid distribution obtained by a micro-CT image as an input. The finite element method solves the frequency-domain Biot's equations to predict the fluid diffusion process. We present a method to overcome the problems of the element intersections in meshing and memory cost in solving Biot's equations. Finally, the 3D numerical predictions are compared and discussed with experimental data published by Sun et al. (2022).

2 Methods

Our proposed method consists of five steps: 1) reconstruct the fluid distribution to make the numerical model; 2) mesh the numerical model; 3) apply Biot's equations as the governing equations; 4) set the boundary condition; 5) solve the numerical solution using the finite element method. These steps are tested on an Indiana specimen (Figure 1A). This carbonate rock has a porosity of 10.8% and a permeability of 2x10^{-17} m^2. The dispersion of elastic wave velocity under confining pressure was investigated under dry and water saturation by Borgomano et al. (2019) and under partial saturation (air/water) by Sun et al. (2022). Additionally, X-ray images under dry, fully water-saturated, and partially saturated conditions were obtained by Sun et al. (2022).

2.1 Fluid distribution reconstruction

The estimation of fluid distribution is the first step of the method. For an homogenous dry sample, the fluid distribution dominates the heterogeneity of the partial saturated sample. Following Cadoret et al. (1995), recent studies like Chapman et al. (2021), Sun et al. (2022), and Wang S. et al. (2022a), the 3D fluid distribution can be estimated using the CT gray image of dry, partially and fully saturated sample. The distribution of the fluid is obtained following two steps.

(i) The gray image of partially and fully saturated samples should be normalized, referring to the gray value of two reference materials, for example, aluminum and sleeve. The rescaled image for the fully water-saturated sample can be obtained following Eq. 1, which is adapted from Lin et al. (2017) and Wang S. et al. (2022a):

$$I_{cor} = \left(I - I_{ref1\_water}\right) * \frac{I_{ref2\_dry} - I_{ref1\_dry}}{I_{ref2\_water} - I_{ref1\_water}} + I_{ref1\_dry} \quad (1)$$

where I_{cor} is the normalized gray value, I is the gray value of the raw image, I_{ref1_water} and I_{ref2_water} are the average gray value of the two reference materials measured during the scan of the water-saturated

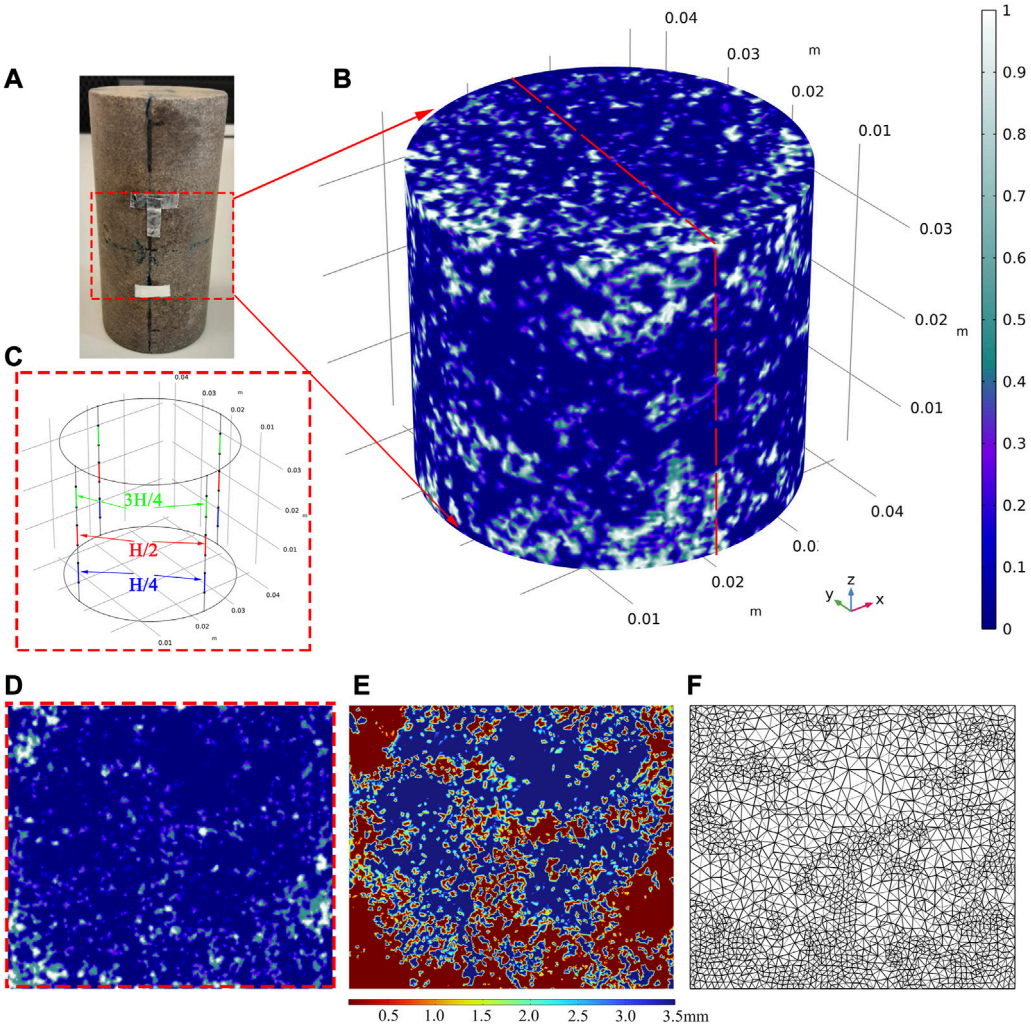

FIGURE 1
(A) Picture of the sample. The red dashed square indicates the volume that is investigated under the CT scan. The overall saturation is 88% obtained by the drainage method. More details can be found in Sun et al. (2022); **(B)** fluid distribution: blue zones represent regions of full water saturation. The white zones correspond to full air saturation; **(C)** Positions for strain gauges at 1/4 (blue), 1/2 (red), and 3/4 (green) of the sample's length; **(D)** the YZ section of the fluid distribution; **(E)** mesh scale *versus* the space coordinate; **(F)** the adaptive mesh calculated according to **(E)**.

sample. I_{ref1_dry} and I_{ref2_dry} are the average gray value of the two reference materials measured during the scan of the dry sample.

(ii) The images for the water-saturated sample I_{Water} and partially saturated sample $I_{water+air}$ are rescaled referring to the dry sample I_{Air} using Eq. 1. Then, the air saturation S_{Air} is calculated as:

$$S_{Air} = \frac{I_{water} - I_{water+air}}{I_{water} - I_{air}} \quad (2)$$

We use the CT data from Sun et al. (2022) obtained on an Indiana limestone partially saturated by the drainage method to calculate the fluid saturation distribution according to Eq. 1 and Eq. 2. The air saturation S_{Air} is shown in Figure 1B. In this sample, the global water saturation obtained by drainage is 88%. In Figure 1B, white zones correspond to full air saturation while blue zones to pure water saturation. Air patches are distributed over the entire sample with sizes in the range of 0.5 mm–10 mm.

2.2 Numerical model meshing

The second step of the method is to mesh the fluid heterogeneities (Figure 1B). Lissa et al. (2021) converted the CT images into a surface format in AVIZO to create triangular elements on every surface between solids and pores and on the boundaries of the investigated volume. Then, they imported the mesh '*.stl' in COMSOL Multiphysics. However, this procedure cannot be used for partial saturation, as shown in Figure 1B. Indeed, Figure 1B shows that the volume contains many air patches with complex geometries; in particular, the meshing process in AVIZO leads to too many intersections or overlap elements, which are difficult to remove.

We use a method presented by Cepeda et al. (2013) to overcome the limitation. This method was developed first for medical CT scan images and allows incorporating complex geometries with non-uniform material properties in COMSOL Multiphysics. It is a practical alternative, as no intersections or overlapping elements occur, and thus, it avoids the need for critical geometry

simplifications that may compromise the accuracy of the simulation. In our case (Figure 1B), the non-uniform property is the fluid saturation S_{Air}. The mesh must be refined at the water-air interfaces. We thus define an adaptive mesh using the following steps: first, a uniform 3D cylinder is constructed according to the size of the CT image and then divided with a coarse mesh; afterward, we refine the mesh at the water-air interfaces using a function *Airarea*:

$$Airarea = \frac{\left(\begin{array}{c} S_{Air}^{(x-d,y,z)} + S_{Air}^{(x+d,y,z)} + S_{Air}^{(x,y-d,z)} + S_{Air}^{(x,y+d,z)} + S_{Air}^{(x,y,z-d)} \\ + S_{Air}^{(x,y,z+d)} \end{array} \right)}{6} \tag{3}$$

where, y, and z are the space coordinates, d is the fine mesh size, that is fixed. $S_{Air}^{(x,y,z)}$ denotes the air saturation at a given spatial coordinate (x, y, z). For example, $S_{Air}^{(x-d,y,z)}$ signifies the air saturation at the location $(x - d, y, z)$, while $S_{Air}^{(x+d,y,z)}$ denotes the air saturation at the location $(x + d, y, z)$, and so forth. The function *Airarea* is 1 for the air-saturated zones and 0 for the water-saturated zones and varies in the partially saturated zones. Finally, considering the 5% uncertainty in the fluid distribution, the mesh size is defined as:

$$\text{Mesh size} = \begin{cases} d, 0.05 \le Airarea \le 0.95 \\ C, Airarea > 0.95 \text{ and } \quad Airarea < 0.05 \end{cases} \tag{4}$$

where d and C are the fine and coarse mesh sizes, respectively. Figure 1E shows the mesh size in the YZ section (Figure 1D) for the 3D fluid distribution given in Figure 1B according to Eq. 4, with C=3.5 mm and d=0.35 mm. Finally, a tetrahedral mesh is created and shown in Figure 1F. As expected, the mesh is coarse in the pure water saturation zone and refined in the partially saturated zone.

2.3 Governing equations

We use Biot's equations (Biot, 1956a; 1956b; 1962; Rubino et al., 2009; 2016) in the frequency-space domain:

$$-\omega^2\left(\rho_b - \frac{\rho_f^2}{\rho_c(\omega)}\right)\boldsymbol{u^s} - \nabla\cdot\boldsymbol{\sigma} = \frac{\rho_f}{\rho_c(\omega)}\nabla P_f \tag{5}$$

$$\nabla\cdot\left[-\frac{1}{\rho_c(\omega)}\left(\nabla P_f - \omega^2\rho_f\boldsymbol{u^s}\right)\right] - \frac{\omega^2\boldsymbol{P_f}}{\mathrm{M}} = \alpha\omega^2\nabla\cdot\boldsymbol{u^s} \tag{6}$$

where ∇ is the Hamiltonian operator, ω is the angle frequency, $\alpha = 1 - \frac{K_d}{K_g}$ is Biot-Willis coefficient, K_d is the drained bulk modulus, K_g is the bulk modulus of the grain. The density of the saturated sample is:

$$\rho_b = (1-\phi)\rho_s + \phi\rho_f \tag{7}$$

where the ρ_f and ρ_s are the densities of fluid and grain, respectively. ϕ is the porosity. The complex density is:

$$\rho_c(\omega) = \frac{\tau\rho_f}{\phi} + \frac{\eta}{\hat{i}\omega\kappa} \tag{8}$$

where τ is the tortuosity of the pore and can be estimated roughly by $\tau = \frac{1}{2}(1 + \frac{1}{\phi})$ according to Berryman (1982) and Rubino et al. (2009). η is the fluid viscosity, κ is the permeability, and $\hat{i}$ is the imaginary unit.

The displacement vector of the rock matrix is $\boldsymbol{u^s} = (u_i^s)$, and the corresponding strain tensor is defined as $\varepsilon_{ij} = \frac{1}{2}(u_{i,j}^s + u_{j,i}^s)$, where $i, j = 1, 2, 3$ are Euclidean space dimensions.

The stress tensor σ is related to the displacement of the matrix and fluid pressure P_f, and:

$$\sigma_{ij} = 2\mu\varepsilon_{ij} + \delta_{ij}\left(\lambda_m\nabla\cdot\boldsymbol{u^s} - \alpha P_f\right) \tag{9}$$

where the $\lambda_m = K_d - \frac{2}{3}\mu$, and the μ is the shear modulus, $\delta_{ij} = \begin{cases} 1\ i = j \\ 0\ i \neq j \end{cases}$ is Kronecker (delta) tensor. The so-called pore-space modulus (Gurevich et al., 2009) is defined as:

$$\mathrm{M} = \left(\frac{\phi}{K_f} + \frac{\alpha-\phi}{K_g}\right)^{-1} \tag{10}$$

For a biphasic saturated sample (air/water), the effective fluid bulk modulus K_f, density ρ_f and viscosity η are defined respectively as:

$$K_f = \left(\frac{S_{Air}}{K_{Air}} + \frac{1-S_{Air}}{K_w}\right)^{-1} \tag{11}$$

$$\rho_f = \rho_{Air}S_{Air} + \rho_w(1-S_{Air}) \tag{12}$$

$$\eta = \eta_{Air}\left(\frac{\eta_w}{\eta_{Air}}\right)^{1-S_{Air}} \tag{13}$$

where K_{Air} and K_w are the bulk modulus of water and air, respectively, S_{Air} is the air saturation. ρ_{Air} and ρ_w are the densities of air and water, respectively. Eq. 13 for the mixed-fluid viscosity η follows the work of Teja and Rice (1981), where η_{Air} and η_w are the viscosities of air and water, respectively.

2.4 Oscillatory relaxation test

The third step is the oscillatory relaxation test (e.g., Rubino et al., 2009; 2016; Chapman and Quintal, 2018; Santos et al., 2021).

For computing the P-wave modulus, the boundary conditions are defined as follows: i) an axial oscillation stress σ_{33} is loaded at the top boundary of the sample, with an amplitude of 0.1 MPa; ii) the vertical displacement at the bottom boundary of the sample is set to zero; iii) for the side boundaries, the normal displacement is set to zero, i.e., $u_1 = u_2 = 0$; iv) all the boundaries are impermeable for the fluid (no flow across the boundaries). The initial conditions for displacements are set to zero. The P-wave modulus M_P and P-wave attenuation Q_P^{-1} are obtained using the following:

$$\mathrm{M}_P = \sigma_{33}/\varepsilon_{33} \tag{14}$$

$$Q_P^{-1} = \mathrm{Imag}(\mathrm{M}_P)/\mathrm{Real}(\mathrm{M}_P) \tag{15}$$

where ε_{33} and σ_{33} are the axial strain and stress, respectively.

To compute the shear modulus (directly related to the S-velocity), the boundary conditions are defined as follows: i) an oscillation stress σ_{32} is loaded at the top boundary of the sample, with an amplitude of 0.1 MPa; ii) the horizontal displacement at the bottom boundary of the sample is set to zero; iii) for the side boundaries, the axial displacement is set to zero, i.e., $u_3 = 0$; iv) all the boundaries are impermeable for the fluid (no flow across the boundaries). The initial conditions for displacements are set to

TABLE 1 Rock properties and the elastic parameters for the numerical prediction. P_c is the confining pressure.

Properties	Indiana
Porosity ϕ(%)	10.8
Permeability-κ(m^2)	2x10^{-17}
Drained Bulk modulus-K_d (GPa)	24 (P_c = 5 MPa)
Bulk modulus of grain-K_g (GPa)	77
Undrained Bulk modulus -K_u (GPa)	32.5 (P_c = 5 MPa)
Shear modulus-μ (GPa)	15.2 (P_c = 5 MPa)
Biot-Willis coefficient-α	0.688
Skempton's coefficient-B	0.38
Density ρ (kg/m^3)	2,369.2

TABLE 2 Fluid properties for the numerical prediction.

Properties	Water	Air
Bulk modulus-K_d (GPa)	2.25	1x10^{-4}
Density ρ (kg/m^3)	1,000	1
Viscosity-η (Pa*s)	10^{-3}	2x10^{-5}

zero. The shear modulus μ and attenuation Q_S^{-1} are obtained using:

$$\mu = \sigma_{32}/(2\varepsilon_{32}) \tag{16}$$

$$Q_S^{-1} = \mathrm{Imag}(\mathrm{M_S})/\mathrm{Real}(\mathrm{M_S}) \tag{17}$$

where ε_{32} and σ_{32} are the shear strain and stress along the y direction, respectively. For both oscillatory relaxation tests, the physical properties of the rock sample and fluids used are deduced from Borgomano et al. (2019) and Sun et al. (2022) and shown in Table 1 and Table 2.

Finally, the complex bulk modulus (K) can be deduced from the complex P-wave modulus M_P and shear modulus μ by:

$$K = M_P - \frac{4}{3}\mu \tag{18}$$

$$Q_K^{-1} = \mathrm{Imag}(K)/\mathrm{Real}(\mathrm{K}) \tag{19}$$

2.5 Numerical solution

The method's fourth step is to solve Biot's equations numerically (Eq. 5 and Eq. 6). We adopt a hybrid method (Halimi Bin Ibrahim and Skote, 2013), i.e., Newton iteration method (NIM) and LU matrix factorization method (LUM). Eq. 5 and Eq. 6 are rewritten in the following form:

$$\boldsymbol{L}(\boldsymbol{X}) = \begin{pmatrix} L_1(u_1, u_2, u_3, P_f) \\ L_2(u_1, u_2, u_3, P_f) \\ L_3(u_1, u_2, u_3, P_f) \\ L_4(u_1, u_2, u_3, P_f) \end{pmatrix} = 0 \tag{20}$$

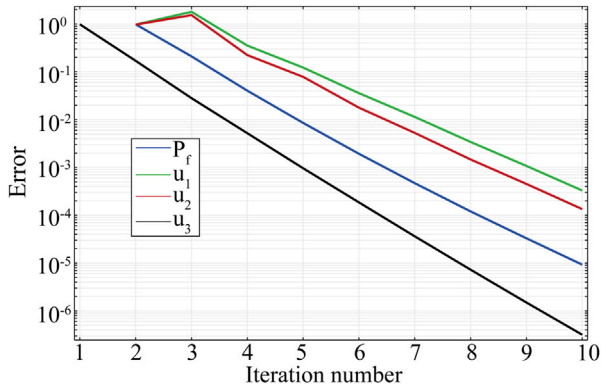

FIGURE 2
Relative error *versus* iteration number during the solving process. The blue line is the fluid pressure. The green, red, and black lines correspond to displacement components along x, y, and z, respectively.

where the variable $\mathbf{X} = \begin{pmatrix} u_1 \\ u_2 \\ u_3 \\ P_f \end{pmatrix}$, is composed of the solid displacement vector $\boldsymbol{u}^s = [u_1, u_2, u_3]$ and fluid pressure P_f. Here we drop the superscript s for the solid displacement vector to leave a space for a new superscript i counting the iteration number. We use a hybrid method to solve Equation 20: the displacement vector $[u_1, u_2, u_3]$ is solved using the NIM method, and the fluid pressure P_f is solved by the LUM method. The detailed steps for the hybrid method are as follows:

Step A: Set the initial condition, $\mathbf{X}^{i=0} = \begin{pmatrix} u_1^{i=0} \\ u_2^{i=0} \\ u_3^{i=0} \\ P_f^{i=0} \end{pmatrix} = 0$,
Do loop *on iteration number* $\boldsymbol{i}$:

Step B: Update the calculated variable u_1^i (u_1^0 =0 for i=0). u_1^{i+1} is achieved using the NIM method: The Jacobian of the linear equation L_1 with respect to the independent variable u_1 is $J_1 = \frac{\partial L_1}{\partial u_1}$; then $u_1^{i+1} = u_1^i + \Delta u_1$, where the updated term is $\Delta u_1 = -\frac{L_1}{J_1}$ (Ben-Israel, 1966).

Step C: Update the calculated variable u_2^i. u_2^{i+1} is estimated using the NIM method: Take the updated u_1^{i+1} into L_2, then calculate Jacobian $J_2 = \frac{\partial L_2}{\partial u_2}$; and finally $u_2^{i+1} = u_2^i + \Delta u_2$ where updated term $\Delta u_2 = -\frac{L_2}{J_2}$.

Step D: Update the calculated variable u_3^i. u_3^{i+1} is also estimated by the NIM method: Take the updated u_1^{i+1} and u_2^{i+1} into L_3, the corresponding Jacobian is $J_3 = \frac{\partial L_3}{\partial u_3}$; then $u_3^{i+1} = u_3^i + \Delta u_3$, where the updated term $\Delta u_3 = -\frac{L_3}{J_3}$.

Step E: Update the calculated variable P_f^i. Take u_1^{i+1}, u_2^{i+1} and u_3^{i+1} into L_4, then P_f^{i+1} is obtained using the LU matrix decomposition method (e.g., Bartels and Golub, 1969; Abbasbandy et al., 2006).

Step F: $\mathbf{X}^{i+1} = \begin{pmatrix} u_1^{i+1} \\ u_2^{i+1} \\ u_3^{i+1} \\ P_f^{i+1} \end{pmatrix}$, if $|\mathbf{X}^{i+1} - \mathbf{X}^i| < \epsilon$, ***end the*** **loop;**
Otherwise, go back to *step B* and $i = i + 1$. ϵ is a relative error, defined as 10^{-3}, which is a measure of the error relative to the size of each solution component.

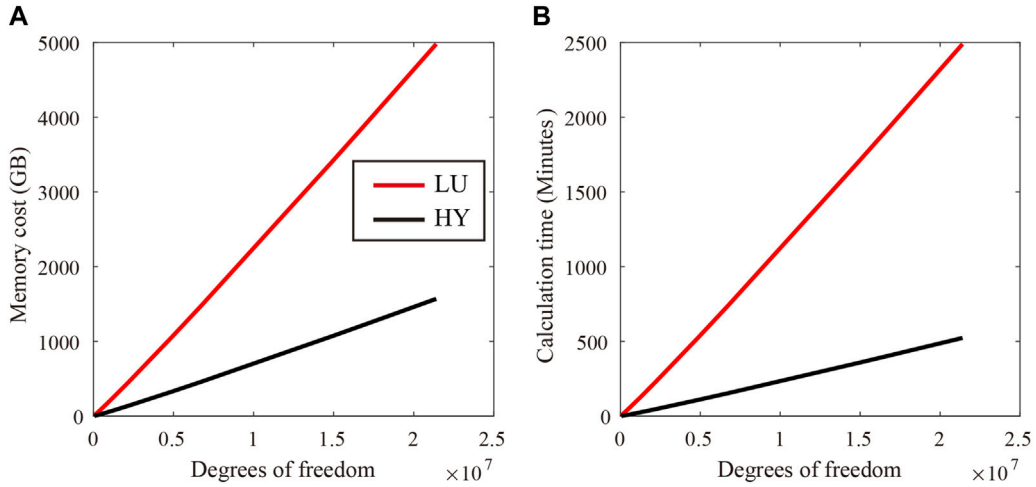

FIGURE 3
(A) Memory cost and **(B)** Calculation time cost. The degrees of freedom are determined by the product of the number of nodes in the mesh and the number of dependent variables (4 in our case). The black and red lines represent the hybrid method and the classical LU decomposition method, respectively.

Figure 2 shows the evolution of the relative error for displacements and fluid pressure as a function of the iteration number during the solving process. After ten iterations, Eq. 20 is solved with a relative error below 10^{-3}. In the case of the hybrid method, only one independent variable is considered in every step, thus reducing the memory cost and calculation time. For comparison, we solved Eq. 20 using the hybrid method and the classical LU decomposition method and show the results in Figure 3: With the hybrid method (see the black line in Figure 3A), the memory cost is divided by a factor of 3 in comparison with the conventional LU method (see the red line in Figure 3A), and the computation time is reduced by a factor of 5 (Figure 3B).

3 Results and discussion

3.1 Axial strain ε_{33}, fluid pressure P_f and local bulk modulus evolution

Using the physical properties (Table 1; Table 2) and the patchy air-water distribution (Figure 1B), we conducted an oscillatory-compressibility test (Section 2.4) to calculate the strain and fluid pressure as a function of the frequency oscillation. The distribution of the i) pore fluid pressure normalized to axial stress σ_{33} and ii) axial strain are shown in Figure 4 and Figure 5, respectively, for different frequencies. It can be observed that pore pressure gradients take their highest values at the air-water interfaces with higher values for frequencies above 10 Hz. However, at the low frequency of 1Hz, air and water pressures are equilibrated to a very low value (Figure 4A). We can refer to this state as a 'relaxed state' under undrained conditions. Indeed, during an axial oscillation of 1Hz, the pressure of the water increases due to the Skempton effect (Kümpel, 1991), but the frequency is sufficiently low to give time for water to diffuse in the air-saturated zone, as air is much more compressible than water. At the highest frequency of 1 kHz (Figure 4D), water is pressurized and has no time to flow in the air-saturated zone, i.e., the distribution of the overpressure (red color in Figure 4D) is close to the distribution of the water saturation zones. We refer to this state as an "unrelaxed state" under undrained conditions. To estimate the increase of water pressure at 1 kHz, we recall that under the P-wave boundary condition ($\varepsilon_{11} = \varepsilon_{22} = 0$), the ratio $\frac{P_f}{\sigma_{33}}$ in a representative elementary volume (REV) fully saturated with water is deduced as

$$\frac{P_f}{\sigma_{33}} = B\frac{K_u}{K_u + 4\mu/3} \tag{21}$$

where $B = \frac{1-\frac{K_d}{K_u}}{\alpha}$ is the Skempton's coefficient (Kümpel, 1991), μ is the shear modulus. K_u is the undrained bulk modulus obtained by Biot-Gassmann's equation (Gassmann, 1951):

$$K_u = K_d + \alpha^2\left(\frac{\phi}{K_f} + \frac{\alpha - \phi}{K_g}\right)^{-1} \tag{22}$$

Using the parameters given in Table 1, the Skempton's coefficient B =0.38 and $\frac{P_f}{\sigma_{33}} = 0.38 * \frac{32.5}{32.5+4*15.2/3} = 0.23$, which is consistent with values shown in the water-saturated zones (red color in Figure 4D). For the air-saturated zones, as the compressibility of air is large, $K_u \approx K_d$ (Eq. 22 using air bulk modulus for K_f) and no pressurization is expected in agreement with the blue color in Figure 4D. Figure 4B and Figure 4C give the results of the water pressurization at the intermediate frequencies of 10 Hz and 100 Hz and illustrate the evolution of the pore pressure gradient in the sample as the frequency increases.

The distribution of axial strain at different frequencies is given in Figure 5. At the low frequency of 1 Hz (Figure 5A), there is no pressurization of the pore fluid (Figure 5A), and the axial deformation is homogeneous and can be approximately estimated ($K_u \approx K_d$) as:

$$|\varepsilon_{33}| = \frac{|\sigma_{33}|}{K_d + 4\mu/3} \approx 2.3 \times 10^{-6} \tag{23}$$

which is consistent with the value predicted by the numerical simulation in Figure 5A. On the other hand, in the case of an unrelaxed state at a REV scale, the axial strain is approximately given by:

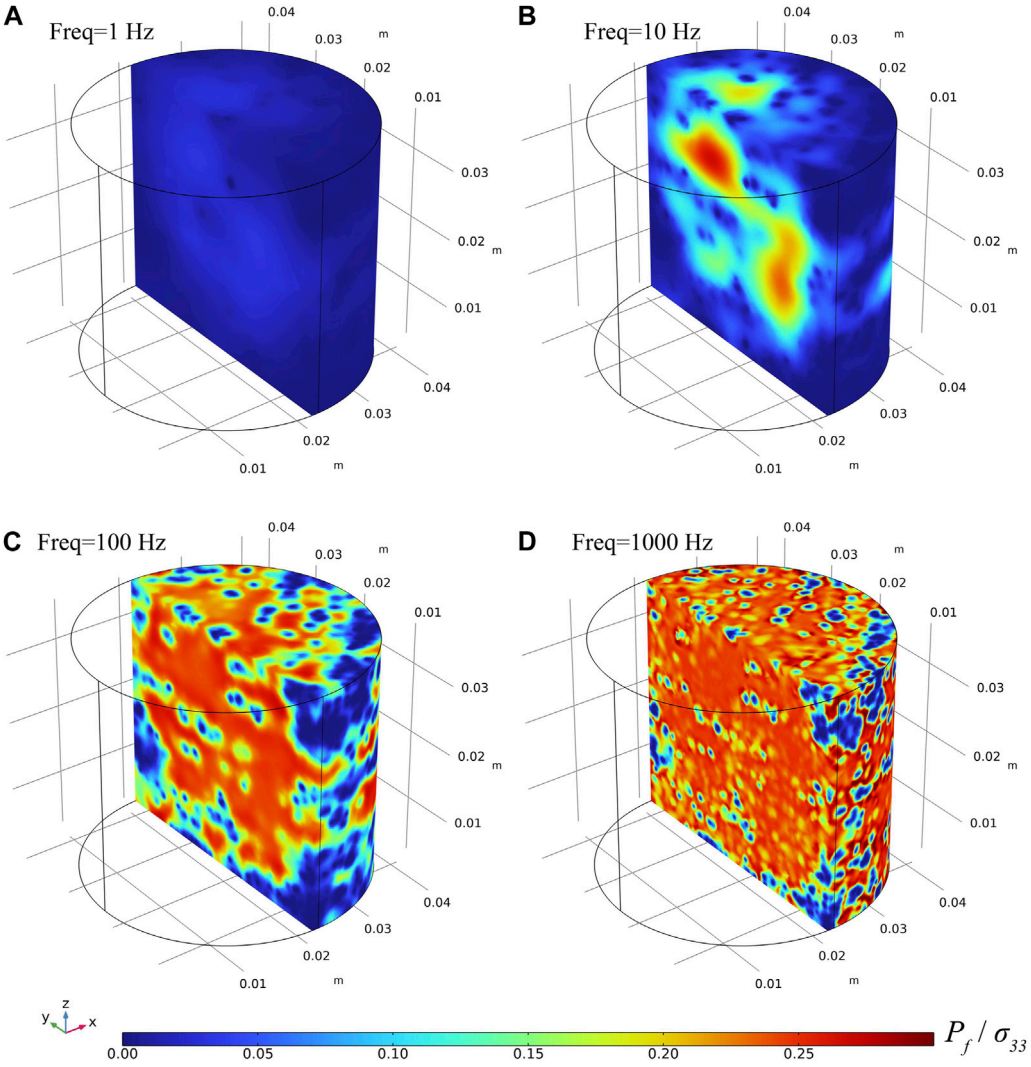

FIGURE 4
The normalized fluid pressure at frequencies of **(A)** 1Hz, **(B)** 10 Hz, **(C)** 100 Hz, and **(D)** 1,000 Hz. Total water saturation is 88% (Figure 1). The predictions are conducted using the fluid distribution shown in Figure 1 and the numerical model.

$$|\varepsilon_{33}| = \frac{|\sigma_{33}|}{K_u + 4\mu/3} \approx 1.8 \times 10^{-6} \tag{24}$$

As a result, the axial strain varies from 2.3×10^{-6} to 1.8×10^{-6} with an increase in frequency. This signifies that the behavior of porous rock shifts from a relaxed to an unrelaxed regime at the Representative Elementary Volume (REV) scale. With the rising frequency, the spatial distribution of the axial strain undergoes changes, which align with the evolution of the pore pressure (see Figure 4; Figure 5). Specifically, areas saturated with water exhibit less deformation compared to those saturated by air. Additionally, as the frequency increases, the count of less deformable patches escalates.

Finally, we performed an oscillatory-shear test to assess the influence of frequency on pore pressure, shear strain, and shear attenuation. As anticipated, the numerical simulations indicate that oscillatory-shear stress does not induce fluid pressurization. Furthermore, shear strain is found to be independent of frequency, and there is no observable shear attenuation. This corroborates the foundational assumption in poroelasticity theory: the fluid has no effect on the shear modulus.

3.2 Global P-wave, bulk, and shear moduli

We determined the global P-wave modulus and its corresponding attenuation (represented by black curves in Figure 6A; Figure 6B), shear modulus and its corresponding attenuation (black curves in Figures 6C,D), and bulk modulus with its associated attenuation (black curves in Figure 6E; Figure 6F) by the entire specimen. These are collectively referred to as the global modulus. The four frequencies (1, 10, 100, and 1,000 Hz) highlighted in Figure 4 and Figure 5 are illustrated as red lines in Figure 6A and Figure 6B.

Our initial observation revealed that the shear modulus (see Figure 6C) is independent of frequency, and there is no associated attenuation (indicating no water effect) (refer to Figure 6D). On the other hand, the bulk modulus (represented by the black curves in

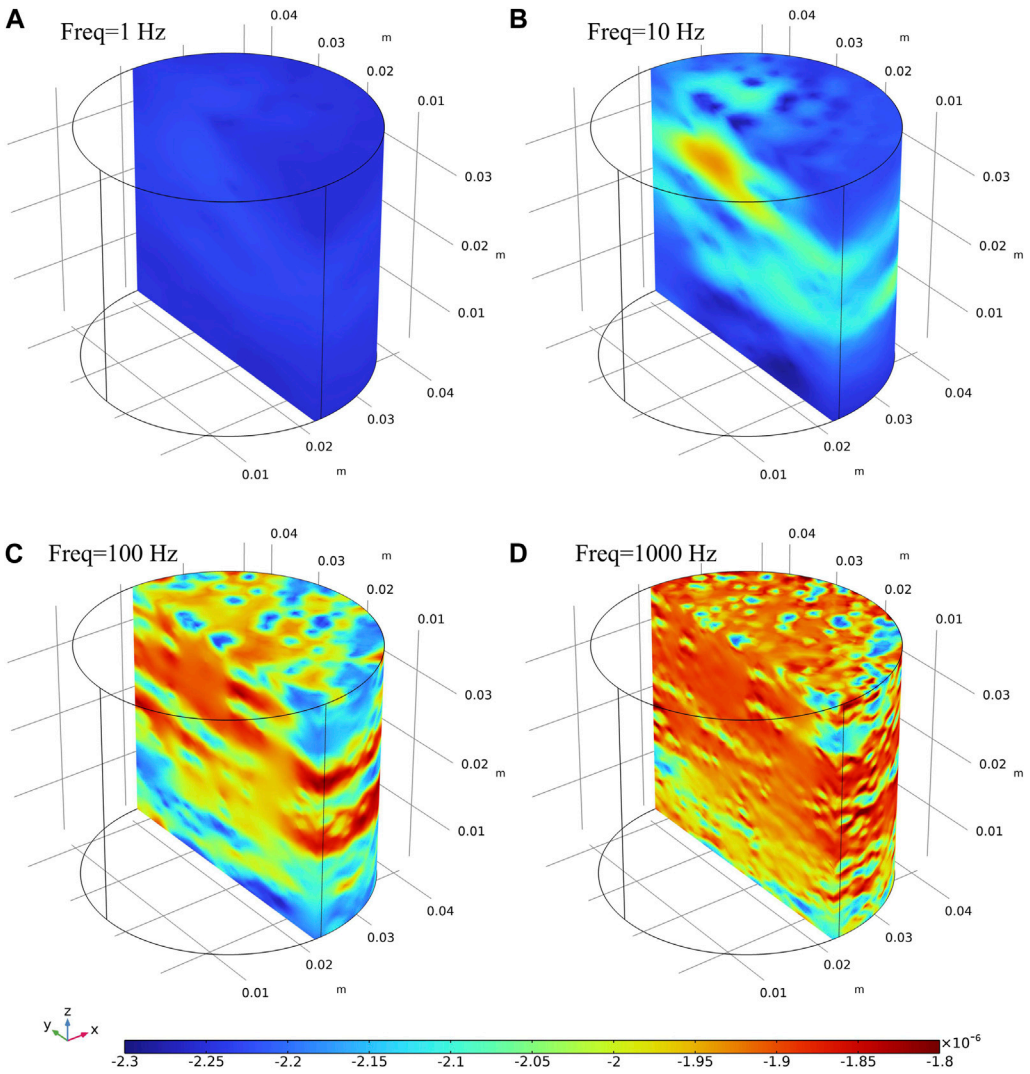

FIGURE 5
Distribution of axial strain at frequencies of **(A)** 1Hz, **(B)** 10 Hz, **(C)** 100 Hz and **(D)** 1,000 Hz. Simulations are done using the numerical test combing with the fluid distribution shown in Figure 1B.

Figure 6E) ranges from 24.2 GPa to 31.3 GPa. This span corresponds to the bulk modulus in both the relaxed and unrelaxed states under the undrained boundary condition (see Figure 6).

At lower frequencies, the fluid pressure has ample time to equilibrate, yielding a homogeneously mixed fluid. Consequently, the bulk modulus of this mixed fluid can be treated as a single-phase effective fluid bulk modulus by applying Wood's law (1946):

$$K_f^{LF} = \left(\frac{1-S}{K_{air}} + \frac{S}{K_{wat}}\right)^{-1} \tag{25}$$

Here, S represents the water saturation. S=0.88, K_{air} =10^{-4} GPa, and K_{wat} =2.25 GPa. This results in K_f^{LF} = 8x10^{-4} GPa, which is approximately equal to K_{air}. By extending Gassmann's theory (as per Eq. 22) with K_f^{LF}, we infer a bulk modulus (24.2 GPa) that closely mirrors the drained bulk modulus (24 GPa). This represents the minimum value for the bulk modulus, often referred to as the low-frequency limit or the Gassmann-Wood limit.

At higher frequencies, there is insufficient time for fluid flow and pressure equalization. Under these conditions, individual fluid phases are effectively isolated, allowing for the use of Eq. 22 to define an undrained bulk modulus for each region saturated by its respective fluid. Following this, Hill's law (1963) can be used to define an effective bulk modulus for the entire sample:

$$K^{HF} = \left(\frac{S}{K_u + 4/3\mu} + \frac{1-S}{K_d + 4/3\mu}\right)^{-1} - 4/3\mu \tag{26}$$

Here, K_d represents the drained bulk modulus and K_u is the undrained bulk modulus fully saturated with water (Mavko and Mukerji, 1998). This upper limit, referred to as the Gassmann-Hill limit, results in K^{HF} = 31.3 GPa in our case, which is less than K_u = 32.5 GPa. Both the drained bulk modulus and the Gassmann-Hill limit are depicted as dashed grey lines in Figure 6E.

In a short summary, the bulk modulus of the entire sample escalates from the Gassmann-Wood limit to the Gassmann-Hill limit with increasing frequency. The dispersion is associated with an

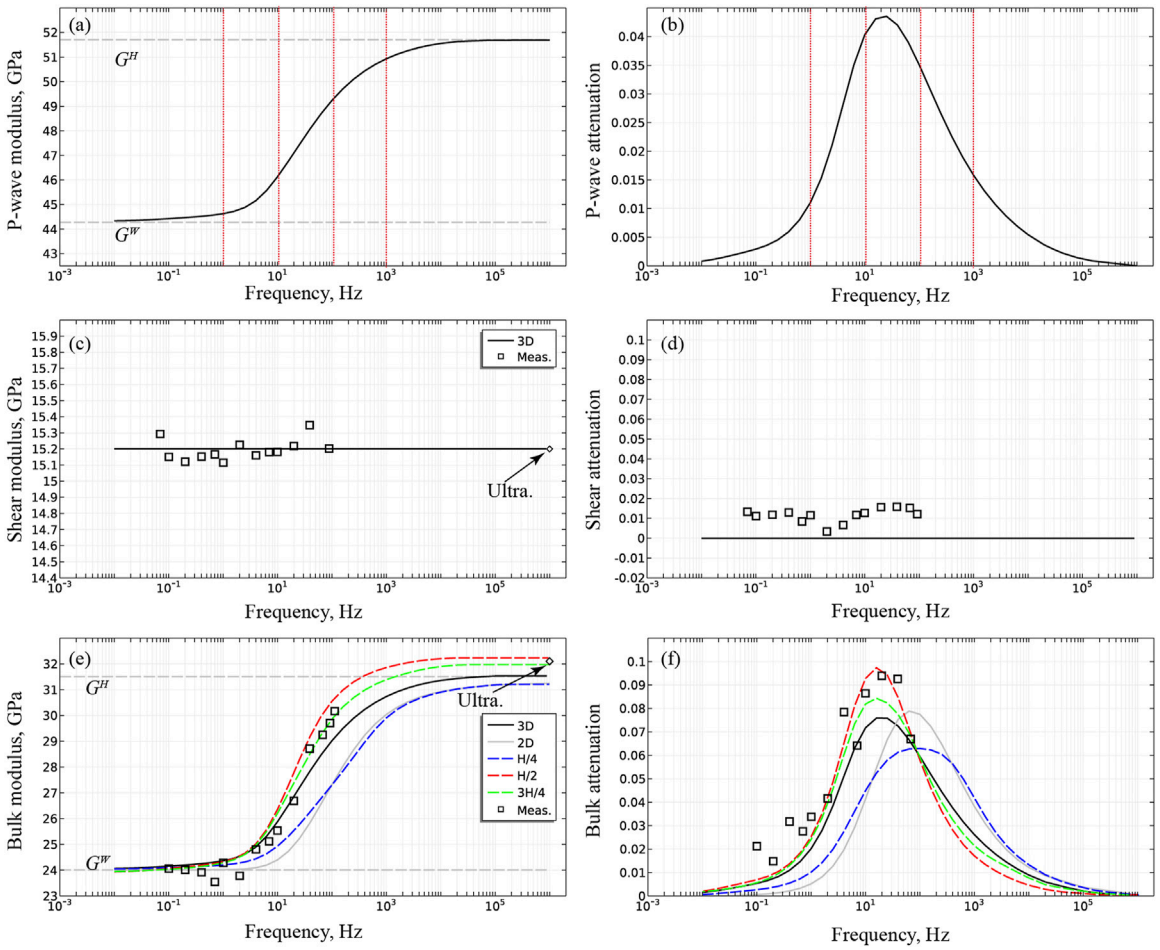

FIGURE 6
Elastic moduli of the entire sample and corresponding attenuation *versus* frequencies. **(A)** P-wave modulus; **(B)** P-wave attenuation; **(C)** shear modulus; **(D)** shear attenuation; **(E)** bulk modulus; **(F)** bulk attenuation. Experimental data from Sun et al. (2022) are plotted (square dots and diamond dots). The uncertainty of the measured bulk modulus is 6.4% in the seismic band and 2% at the ultrasonic frequency. In **(E)** and **(F)**, in addition to the bulk modulus of the entire sample, we simulate the local bulk modulus measured by strain gauges located at the middle of the sample (red dashed line), at a quarter length from the bottom (blue dashed line) and at a quarter length from the top (green dashed lines). The Gassmann-Hill and Gassmann-wood limits are shown in **(E)** as dashed lines. Finally, we add a 2D numerical simulation (grey lines in **(E)** and **(F)**) to highlight the mismatch between a 2D (grey curve) and a 3D (black curve) numerical simulation.

attenuation (represented by the black curve in Figure 6F) peaking at 0.075 at 20 Hz. Lastly, we plot the P-wave modulus and its corresponding attenuation as functions of frequency in Figures 6A,B. As the P-wave modulus is a linear amalgamation of the shear and bulk moduli, its behavior closely mirrors that of the bulk modulus. Specifically, the P-wave modulus increases from 44 GPa to 52 GPa, accompanied by a peak attenuation of 0.045 at 20 Hz.

3.3 Numerical prediction vs experimental measurements

In numerous laboratory experiments (e.g., Batzle et al., 2006; Adelinet et al., 2010; Mikhaltsevitch et al., 2015; Sun et al., 2018), researchers measure the strain's evolution with frequency under oscillatory stress using local strain gauges. This approach yields a locally measured bulk modulus. To emulate such experiments, we average strain over a span of 6 mm—the typical length of a strain gauge—and simulate four strain gauges that are averaged. These gauges are situated at the sample's half-length (represented by red lines in Figure 1C), a quarter-length from the bottom (blue lines in Figure 1C), and a quarter-length from the top (green lines in Figure 1C). The results are presented in Figure 6E: In general, the local bulk modulus and attenuation measured at the midpoint (50%, red curve) and three-quarters (75%, green curve) of the sample length closely align with the bulk properties of the entire sample (black curve). However, the frequency-dependent evolution of the local bulk modulus at one-quarter (25%, blue curve) of the sample deviates significantly from the evolution of the global bulk modulus (black curve). Furthermore, the high-frequency limit of local measurements differs from the Gassmann-Hill limit, as the strain gauges only capture the effects of local saturation. Consequently, high-frequency results may approach the undrained bulk modulus fully saturated with water, which surpasses the Gassmann-Hill limit. Interestingly, the disparity between local and global measurements in our study is not as marked as in Chapman and Quintal (2018). This reduced difference can likely

be attributed to i) our approach of consolidating local results from four strain gauges, which serves to lessen the discrepancy between local and global responses, and ii) a comparatively uniform air/water distribution in our experiment, as opposed to the more varied distribution seen in Chapman and Quintal's work (2018).

The progression of the moduli with frequency for the Indiana sample, saturated to 88% (Figures 1A,B), was studied by Sun et al., 2022. We chose the Indiana sample for this investigation due to its lack of micro-cracks, thus eliminating the squirt-flow mechanism (Borgomano et al., 2019). In these tests, strain measurements were taken by averaging readings from four strain gauges situated in the half-length of the specimen. We have represented the experimental data in Figure 6 with black square dots. Figures 6C,D juxtapose the projected and observed values of the shear modulus and attenuation. The frequency-independent shear modulus (depicted by the black curve in Figure 6C) aligns with the measurements (square dots in Figure 6C) spanning the seismic bands (0.1–100 Hz) and ultrasonic frequency (1 MHz). Additionally, the predicted shear attenuation (black curve in Figure 6D) aligns with the measurement (square dots in Figure 6D), given that the measurement error range for attenuation is within 0.02.

Figures 6E,F juxtapose the anticipated and actual measurements of the bulk modulus and attenuation. Generally, there's an excellent agreement between the measurements and the numerical predictions, as illustrated by the black square dots and red curves. The numerical simulation, based on the CT-scan images, accurately replicates i) the dispersion of the modulus and ii) both the low and high-frequency limit. There's also a strong correspondence between the measured attenuation and the numerical simulation. This comparison between the numerical simulation and experimental data confirms the efficacy of the method detailed in this paper in predicting mesoscopic dispersion and attenuation.

3.4 2D model vs 3D model

We now turn to comparing the results derived from 2D and 3D numerical simulations. Utilizing the YZ section of the CT image (Figure 1D), the bulk modulus and attenuation for the 2D model were computed. The global response of the 2D model is determined by averaging the strain across the entire section. As shown by the solid gray line in Figure 6F, the prediction using the 2D model exhibits a higher critical frequency (100 Hz) and peak attenuation (0.08) compared to the 3D model (black curve in Figure 6F). Furthermore, the bulk modulus derived from the 2D model (solid gray line in Figure 6E) deviates from the one obtained from the 3D model (black curve in Figure 6E). The discrepancy between the 2D and 3D results is attributed to the fluid flow in the ZX and ZY direction, which is not accounted for in the 2D numerical simulation. This finding elucidates the mismatch observed by Sun et al. (2022) between experimental data and numerical simulation, which can be attributed to their use of a 2D model.

4 Conclusion

In this paper, we introduce a novel method aimed at predicting velocity dispersion and attenuation attributable to mesoscopic flow, leveraging actual fluid distribution data derived from CT images. The numerical model is initially established by meshing CT images through a technique adept at handling intricate geometries and non-uniform material properties, thus effectively bypassing element intersections, a common issue associated with AVIZO. To find the solution for the numerical model governed by Biot's equations, we use a hybrid method that significantly curtails memory cost compared to the LU matrix factorization method.

The solution from the numerical model forecasts the evolution of pore pressure distribution with frequency, thereby anticipating the advancement of the elastic moduli and their attenuation. We also model the development of the moduli for the entire sample (global moduli) as well as those measured by a strain gauge (local moduli). The discrepancies observed between local and global responses can be attributed to the heterogeneity in fluid distribution. Importantly, the 3D model's predictions are validated by experimental data collected from Indiana limestone.

The presented method successfully addresses issues pertaining to memory consumption and calculation time, thereby setting the stage for quantifying the relationship between fluid distribution and seismic attenuation. This innovative approach holds the potential to serve as a robust tool for upscaling at the reservoir scale.

Data availability statement

The raw data supporting the conclusion of this article will be made available by the authors, without undue reservation.

Author contributions

CS: Methodology, Writing–original draft, Writing–review and editing. JF: Methodology, Writing–original draft, Writing–review and editing. GT: Supervision, Writing–review and editing. SW: Supervision, Writing–review and editing.

Funding

The author(s) declare financial supportwas received for the research, authorship, and/or publication of this article. This work is supported by the National Natural Science Foundation of China (42104111, 42274142, 41930425, 41774143, 41804104) and also supported by Open Fund (WX-KFJJ-2022-08) of SINOPEC Key Laboratory of Geophysics, and State Key Laboratory of Petroleum Resources and Prospecting, China University of Petroleum, and Xuzhou Science and Technology Bureau Young Talents Project (No. KC22018). The authors declare that this study received funding from SINOPEC Key Laboratory of Geophysics. The funder was not involved in the study design, collection, analysis, interpretation of data, the writing of this article, or the decision to submit it for publication.

Acknowledgments

We acknowledge the help of Dr. Jan V. M. Borgomano at Ecole Normale Supérieure for scanning the sample.

Conflict of interest

Authors GT and SW were employed by China National Petroleum Corporation.

The remaining authors declare that the research was conducted in the absence of any commercial or financial relationships that could be construed as a potential conflict of interest.

Publisher's note

References

Abbasbandy, S., Ezzati, R., and Jafarian, A. (2006). LU decomposition method for solving fuzzy system of linear equations. *Appl. Math. Comput.* 172 (1), 633–643. doi:10.1016/j.amc.2005.02.018

Adelinet, M., Dorbath, C., Ravalec, M. L., Fortin, J., and Guéguen, Y. (2011). Deriving microstructure and fluid state within the Icelandic crust from the inversion of tomography data. *Geophys. Res. Lett.* 38 (3). doi:10.1029/2010GL046304

Adelinet, M., Fortin, J., Guéguen, Y., Schubnel, A., and Geoffroy, L. (2010). Frequency and fluid effects on elastic properties of basalt: experimental investigations. *Geophys. Res. Lett.* 37 (2). doi:10.1029/2009GL041660

Anwer, H. M., Ali, A., and Alves, T. M. (2017). Bayesian inversion of synthetic AVO data to assess fluid and shale content in sand-shale media. *J. Earth Syst. Sci.* 126 (3), 42. doi:10.1007/s12040-017-0818-y

Ba, J., Carcione, J. M., and Sun, W. (2015). Seismic attenuation due to heterogeneities of rock fabric and fluid distribution. *Geophys. J. Int.* 202 (3), 1843–1847. doi:10.1093/gji/ggv255

Ba, J., Xu, W., Fu, L.-Y., Carcione, J. M., and Zhang, L. (2017). Rock anelasticity due to patchy saturation and fabric heterogeneity: A double double-porosity model of wave propagation. *J. Geophys. Res. Solid Earth* 122 (3), 1949–1976. doi:10.1002/2016JB013882

Bartels, R. H., and Golub, G. H. (1969). The simplex method of linear programming using LU decomposition. *Commun. ACM* 12 (5), 266–268. doi:10.1145/362946.362974

Batzle, M. L., Han, D.-H., and Hofmann, R. (2006). Fluid mobility and frequency-dependent seismic velocity — direct measurements. *GEOPHYSICS* 71 (1), N1–N9. doi:10.1190/1.2159053

Ben-Israel, A. (1966). A Newton-Raphson method for the solution of systems of equations. *J. Math. Analysis Appl.* 15 (2), 243–252. doi:10.1016/0022-247X(66)90115-6

Berryman (1982). "Elastic waves in fluid-saturated porous media (Vol 154)," in Macroscopic Properties of Disordered Media, Rome, June 1–3, 1981.

Biot, M. A. (1962). Mechanics of deformation and acoustic propagation in porous media. *J. Appl. Phys.* 33 (4), 1482–1498. doi:10.1063/1.1728759

Biot, M. A. (1956b). Theory of propagation of elastic waves in a fluid-saturated porous solid. II. Higher frequency range. *J. Acoust. Soc. Am.* 28 (2), 179–191. doi:10.1121/1.1908241

Biot, M. A. (1956a). Theory of propagation of elastic waves in a fluid-saturated porous solid. I. Low-Frequency range. *J. Acoust. Soc. Am.* 28 (2), 168–178. doi:10.1121/1.1908239

Borgomano, J. V. M., Pimienta, L. X., Fortin, J., and Guéguen, Y. (2019). Seismic dispersion and attenuation in fluid-saturated carbonate rocks: effect of microstructure and pressure. *J. Geophys. Res. Solid Earth* 124 (12), 12498–12522. doi:10.1029/2019JB018434

Chapman, S., and Quintal, B. (2018). "Numerical assessment of local versus bulk strain measurements to quantify seismic attenuation in partially saturated rocks," in *SEG technical program expanded abstracts 2018* (Texas, United States: Society of Exploration Geophysicists), 1–0, 3547–3551. doi:10.1190/segam2018-2992202.1

Cadoret, T., Mavko, G., and Zinszner, B. (1998). Fluid distribution effect on sonic attenuation in partially saturated limestones. *GEOPHYSICS* 63 (1), 154–160. doi:10.1190/1.1444308

Cadoret, T., Marion, D., and Zinszner, B. (1995). Influence of frequency and fluid distribution on elastic wave velocities in partially saturated limestones. *J. Geophys. Res. Solid Earth* 100 (B6), 9789–9803. doi:10.1029/95JB00757

Cavallini, F., Carcione, J. M., Vidal de Ventós, D., and Engell-Sørensen, L. (2017). Low-frequency dispersion and attenuation in anisotropic partially saturated rocks. *Geophys. J. Int.* 209 (3), 1572–1584. doi:10.1093/gji/ggx107

Cepeda, J. F., Birla, S., Subbiah, J., and Thippareddi, H. (2013). *A practical method to model complex three-dimensional geometries with non-uniform material properties using image-based design and COMSOL multiphysics*.

Chapman, S., Borgomano, J. V. M., Quintal, B., Benson, S. M., and Fortin, J. (2021). Seismic wave attenuation and dispersion due to partial fluid saturation: direct measurements and numerical simulations based on x-ray ct. *J. Geophys. Res. Solid Earth* 126 (4). doi:10.1029/2021JB021643

Chapman, S., Tisato, N., Quintal, B., and Holliger, K. (2016). Seismic attenuation in partially saturated berea sandstone submitted to a range of confining pressures: seismic attenuation in berea sandstone. *J. Geophys. Res. Solid Earth* 121 (3), 1664–1676. doi:10.1002/2015JB012575

Dutta, N. C., and Odé, H. (1979). Attenuation and dispersion of compressional waves in fluid-filled porous rocks with partial gas saturation (White model); Part II, Results. *Geophysics* 44 (11), 1789–1805. doi:10.1190/1.1440939

Gassmann, F. (1951). Über die elastizität poröser medien: vier. der natur. *Ges. Zürich* 96, 1–23.

Gurevich, B., Brajanovski, M., Galvin, R. J., Müller, T. M., and Toms-Stewart, J. (2009). P-wave dispersion and attenuation in fractured and porous reservoirs – poroelasticity approach. *Geophys. Prospect.* 57 (2), 225–237. doi:10.1111/j.1365-2478.2009.00785.x

Halimi Bin Ibrahim, I., and Skote, M. (2013). Effects of the scalar parameters in the Suzen-Huang model on plasma actuator characteristics. *Int. J. Numer. Methods Heat Fluid Flow* 23 (6), 1076–1103. doi:10.1108/HFF-05-2011-0108

He, Y.-X., Wang, S., Yuan, S., Tang, G., and Wu, X. (2020). An improved approach for hydrocarbon detection using Bayesian inversion of frequency- and angle-dependent seismic signatures of highly attenuative reservoirs. *IEEE Geoscience Remote Sens. Lett.* 19, 1–5. doi:10.1109/LGRS.2020.3017627

Hill, R. (1963). Elastic properties of reinforced solids: some theoretical principles. *J. Mech. Phys. Solids* 11 (5), 357–372. doi:10.1016/0022-5096(63)90036-X

Klimentos, T. (1995). Attenuation of P- and S-waves as a method of distinguishing gas and condensate from oil and water. *GEOPHYSICS* 60 (2), 447–458. doi:10.1190/1.1443782

Kümpel, H.-J. (1991). Poroelasticity: parameters reviewed. *Geophys. J. Int.* 105 (3), 783–799. doi:10.1111/j.1365-246X.1991.tb00813.x

Lin, Q., Bijeljic, B., Raeini, A. Q., Rieke, H., and Blunt, M. J. (2021). Drainage capillary pressure distribution and fluid displacement in a heterogeneous laminated sandstone. *Geophys. Res. Lett.* 48 (14), e2021GL093604. doi:10.1029/2021GL093604

Lin, Q., Bijeljic, B., Rieke, H., and Blunt, M. J. (2017). Visualization and quantification of capillary drainage in the pore space of laminated sandstone by a porous plate method using differential imaging X-ray microtomography: imaging of capillary drainage using dipp. *Water Resour. Res.* 53 (8), 7457–7468. doi:10.1002/2017WR021083

Lissa, S., Ruf, M., Steeb, H., and Quintal, B. (2021). Digital rock physics applied to squirt flow. *GEOPHYSICS* 86 (4), MR235–MR245. doi:10.1190/geo2020-0731.1

Mavko, G., and Mukerji, T. (1998). Bounds on low-frequency seismic velocities in partially saturated rocks. *GEOPHYSICS* 63 (3), 918–924. doi:10.1190/1.1444402

Mikhaltsevitch, V., Lebedev, M., and Gurevich, B. (2016). Laboratory measurements of the effect of fluid saturation on elastic properties of carbonates at seismic frequencies: effect of fluid saturation on carbonates. *Geophys. Prospect.* 64 (4), 799–809. doi:10.1111/1365-2478.12404

Mikhaltsevitch, V., Lebedev, M., and Gurevich, B. (2015). *A laboratory study of attenuation and dispersion effects in glycerol-saturated Berea sandstone at seismic frequencies*. Texas, United States: Society of Exploration Geophysicists, 3085–3089. doi:10.1190/segam2015-5898429.1

Monachesi, L. B., Wollner, U., and Dvorkin, J. (2020). Effective pore fluid bulk modulus at patchy saturation: an analytic study. *J. Geophys. Res. Solid Earth* 125 (1), e2019JB018267. doi:10.1029/2019JB018267

Müller, T. M., Toms-Stewart, J., and Wenzlau, F. (2008). Velocity-saturation relation for partially saturated rocks with fractal pore fluid distribution. *Geophys. Res. Lett.* 35 (9), L09306. doi:10.1029/2007GL033074

Müller, T. M., Gurevich, B., and Lebedev, M. (2010). Seismic wave attenuation and dispersion resulting from wave-induced flow in porous rocks A review. *Geophysics* 75 (5), 75A147–75A164. doi:10.1190/1.3463417

Müller, T. M., and Gurevich, B. (2004). One-dimensional random patchy saturation model for velocity and attenuation in porous rocks. *Geophysics* 69 (5), 1166–1172. doi:10.1190/1.1801934

Müller, T. M., and Gurevich, B. (2005). Wave-induced fluid flow in random porous media: attenuation and dispersion of elastic waves. *J. Acoust. Soc. Am.* 117 (5), 2732–2741. doi:10.1121/1.1894792

Pride, S. R., Berryman, J. G., and Harris, J. M. (2004). Seismic attenuation due to wave-induced flow. *J. Geophys. Res. Solid Earth* 109 (B1), B01201. doi:10.1029/2003JB002639

Qi, Q., Müller, T. M., Gurevich, B., Lopes, S., Lebedev, M., and Caspari, E. (2014). Quantifying the effect of capillarity on attenuation and dispersion in patchy-saturated rocks. *GEOPHYSICS* 79 (5), WB35–WB50. doi:10.1190/geo2013-0425.1

Quintal, B., Frehner, M., Madonna, C., Tisato, N., Kuteynikova, M., and Saenger, E. H. (2011). Integrated numerical and laboratory rock physics applied to seismic characterization of reservoir rocks. *Lead. Edge* 30 (12), 1360–1367. doi:10.1190/1.3672480

Rubino, J. G., Caspari, E., Müller, T. M., Milani, M., Barbosa, N. D., and Holliger, K. (2016). Numerical upscaling in 2-D heterogeneous poroelastic rocks: anisotropic attenuation and dispersion of seismic waves. *J. Geophys. Res. Solid Earth* 121 (9), 6698–6721. doi:10.1002/2016JB013165

Rubino, J. G., Ravazzoli, C. L., and Santos, J. E. (2009). Equivalent viscoelastic solids for heterogeneous fluid-saturated porous rocks. *GEOPHYSICS* 74 (1), N1–N13. doi:10.1190/1.3008544

Santos, J., Carcione, J., and Ba, J. (2021). Two-phase flow effects on seismic wave anelasticity in anisotropic poroelastic media. *Energies* 14 (20), 6528. doi:10.3390/en14206528

Santos, J. E., Ravazzoli, C. L., Gauzellino, P. M., and Carcione, J. M. (2005). Numerical simulation of ultrasonic waves in reservoir rocks with patchy saturation and fractal petrophysical properties. *Comput. Geosci.* 9 (1), 1–27. doi:10.1007/s10596-005-2848-9

Sun, C., Fortin, J., Borgomano, J. V. M., Wang, S., Tang, G., Bultreys, T., et al. (2022). Influence of fluid distribution on seismic dispersion and attenuation in partially saturated limestone. *J. Geophys. Res. Solid Earth* 127 (5). doi:10.1029/2021JB023867

Sun, C., Tang, G., Zhao, J., Zhao, L., and Wang, S. (2018). An enhanced broad-frequency-band apparatus for dynamic measurement of elastic moduli and Poisson's ratio of rock samples. *Rev. Sci. Instrum.* 89 (6), 064503. doi:10.1063/1.5018152

Sun, W. (2017). Determination of elastic moduli of composite medium containing bimaterial matrix and non-uniform inclusion concentrations. *Appl. Math. Mech.* 38 (1), 15–28. doi:10.1007/s10483-017-2157-6

Teja, A. S., and Rice, P. (1981). Generalized corresponding states method for the viscosities of liquid mixtures. *Industrial Eng. Chem. Fundam.* 20 (1), 77–81. doi:10.1021/i100001a015

Tester, J. W., Anderson, B. J., Batchelor, A. S., Blackwell, D. D., DiPippo, R., Drake, E. M., et al. (2007). Impact of enhanced geothermal systems on US energy supply in the twenty-first century. *Philosophical Trans. R. Soc. A Math. Phys. Eng. Sci.* 365 (1853), 1057–1094. doi:10.1098/rsta.2006.1964

Tisato, N., and Quintal, B. (2013). Measurements of seismic attenuation and transient fluid pressure in partially saturated berea sandstone: evidence of fluid flow on the mesoscopic scale. *Geophys. J. Int.* 195 (1), 342–351. doi:10.1093/gji/ggt259

Toms, J., Müller, T. M., and Gurevich, B. (2007). Seismic attenuation in porous rocks with random patchy saturation. *Geophys. Prospect.* 55 (5), 671–678. doi:10.1111/j.1365-2478.2007.00644.x

Toms-Stewart, J., Müller, T. M., Gurevich, B., and Paterson, L. (2009). Statistical characterization of gas-patch distributions in partially saturated rocks. *GEOPHYSICS* 74 (2), WA51–WA64. doi:10.1190/1.3073007

Wang, S., Ruspini, L. C., Øren, P.-E., Van Offenwert, S., and Bultreys, T. (2022a). Anchoring multi-scale models to micron-scale imaging of multiphase flow in rocks. *Water Resour. Res.* 58 (1), e2021WR030870. doi:10.1029/2021WR030870

Wang, Y., Zhao, L., Cao, C., Yao, Q., Yang, Z., Cao, H., et al. (2022b). Wave-induced fluid pressure diffusion and anelasticity in partially saturated rocks: the influences of boundary conditions. *Geophysics* 87 (5), MR247–MR263. doi:10.1190/geo2021-0809.1

White, J. E. (1975). Computed seismic speeds and attenuation in rocks with partial gas saturation. *Geophysics* 40 (2), 224–232. doi:10.1190/1.1440520

White, J. E., Mihailova, N., and Lyakhovitsky, F. (1975). Low-frequency seismic waves in fluid-saturated layered rocks. *J. Acoust. Soc. Am.* 57 (S1), S30. doi:10.1121/1.1995164

Wood, A. B. (1946). *A textbook of sound*. 2. New York: Macmillan. Available at: http://archive.org/details/in.ernet.dli.2015.15768.

Zhang, L., Ba, J., Carcione, J. M., and Wu, C. (2022). Seismic wave propagation in partially saturated rocks with a fractal distribution of fluid-patch size. *J. Geophys. Res. Solid Earth* 127 (2). doi:10.1029/2021JB023809

Zhao, L., Tang, G., Sun, C., Zhao, J., and Wang, S. (2021a). Dual attenuation peaks revealing mesoscopic and microscopic fluid flow in partially oil-saturated Fontainebleau sandstones. *Geophys. J. Int.* 224 (3), 1670–1683. doi:10.1093/gji/ggaa551

Zhao, L., Wang, Y., Yao, Q., Geng, J., Li, H., Yuan, H., et al. (2021b). Extended Gassmann equation with dynamic volumetric strain: modeling wave dispersion and attenuation of heterogeneous porous rocks. *Geophysics* 86 (3), MR149–MR164. doi:10.1190/geo2020-0395.1

Zhu, W., Zhao, L., and Shan, R. (2017). Modeling effective elastic properties of digital rocks using a new dynamic stress-strain simulation method. *Geophysics* 82 (6), MR163–MR174. doi:10.1190/geo2016-0556.1

Zhu, W., Zhao, L., Yang, Z., Cao, H., Wang, Y., Chen, W., et al. (2023). Stress relaxing simulation on digital rock: characterize attenuation due to wave-induced fluid flow and scattering. *J. Geophys. Res. Solid Earth* 128 (2), e2022JB024850. doi:10.1029/2022jb024850

frontiers | Frontiers in Earth Science

TYPE Original Research
PUBLISHED 07 September 2023
DOI 10.3389/feart.2023.1257481

OPEN ACCESS

EDITED BY
Qiaomu Qi,
Chengdu University of Technology, China

REVIEWED BY
Yang Zhou,
Chengdu University of Technology, China
Suzhen Shi,
China University of Mining and Technology, China

*CORRESPONDENCE
Yungui Xu,
yungui.xu@outlook.com
Libing Du,
dulibing0622@126.com

RECEIVED 12 July 2023
ACCEPTED 29 August 2023
PUBLISHED 07 September 2023

CITATION
Wang Y, Xu Y, Du L, Gai S, Yu W and Huang X (2023), DFN modelling constrained by multiple seismic attributes using the steering pyramid technology. *Front. Earth Sci.* 11:1257481. doi: 10.3389/feart.2023.1257481

DFN modelling constrained by multiple seismic attributes using the steering pyramid technology

Yudi Wang[1,2], Yungui Xu[1,2]*, Libing Du[1,2]*, Shanshan Gai[3], Wenzheng Yu[3] and Xuri Huang[1,2]

[1]State Key Laboratory of Oil and Gas Reservoir Geology and Exploitation, Southwest Petroleum University, Chengdu, China, [2]School of Geosciences and Technology, Southwest Petroleum University, Chengdu, China, [3]Geophysical Research Institute, Sinopec Shengli Oilfield Company, Dongying, China

Fracture modelling is essential for understanding fluid flow in fractured hydrocarbon reservoirs, particularly in the phase of production; however, traditional discrete fracture network (DFN) modelling methods lack constraints that reflect characteristics of fracture development. Fractures or fracture networks exhibit a high degree of randomness; as such, it is difficult to model fracture characteristics. This paper proposes a new approach for DFN modelling constrained by seismic attributes. Firstly, the steerable pyramid method is adopted to improve seismic data resolution; secondly, multiple seismic attributes are extracted and combined into a composite attribute to characterize fracture spatial distribution; finally, a DFN modelling method is established by using the composite attribute as a location constraint. To verify the effectiveness of the approach, a case study is conducted in the Bonan Depression, in East China. The results show that, compared with the traditional DFN modelling methods, the DFN modelling with the location constraint create a more realistic fracture model which accurately reflects fracture distribution characteristics. The application demonstrates the potential of wide application prospects in fractured reservoirs.

KEYWORDS

seismic attributes, seismic data decomposition, composite attribute, fracture modelling, discrete fracture network (DFN)

1 Introduction

Fractures including joints, faults, pressure solution seams, and deformation bands are pervasive in crustal rocks (Welch et al., 2022). These features interconnect to form complex fracture networks that provide crucial storage space for oil and gas reservoirs, as well as important channels for their transportation and exploitation. For example, Hardebol et al. (2015); Azim (2016) studied the impact of fracture network geometry on fluid flows in fractured reservoirs. Hunziker et al. (2018) studied the impact of stochastic fracture networks on seismic attenuation. Understanding the spatial distribution of fractures is essential for efficiently developing oil and gas reservoirs.

The Discrete Fracture Network (DFN) (Shi et al., 2021) method is an important tool for studying the spatial distribution patterns of fractures. This method directly uses fractures of various sizes and shapes to form a network, and then uses discrete data to characterize the fracture system. Since Baecher et al. (1977); Baecher, (1983) introduced the DFN method for evaluating reservoirs in 1977, many scholars have tried to improve it. For example, Mardia et al. (2007) used a Markov Monte Carlo method to update

fracture locations, achieving a dynamic simulation with a changing sampling distribution. Xu and Dowd (2010) and Dong et al. (2018b) created the shape of a random polygon with a fixed number of sides that more accurately follows geological laws. Singh et al. (2022) combined DFN with the discrete element method to improve fracture stability. Kolyukhin et al. (2023) perform the statistical analysis of model realization on different spatial scales to investigate the possibility to evaluate the corresponding correlation fractal dimension and power exponent. However, many of these methods focus on improving the fracture shape and probability distribution pattern, and for realistic fracture modeling, integrating more geological or geophysical knowledge is essential.

In recent years, many scholars have attempted to integrate various constraints to enhance DFN modelling accuracy. Dong et al. (2018a) introduced a fracture density-constrained cast point modelling method, which improved fracture modelling accuracy to a certain extent. However, the method has high randomness and low accuracy in measuring fracture density parameters. To further enhance fracture modelling accuracy, Lei et al. (2020) applied constraints using various parameters from well logs, such as ground stress, lithology, and permeability. However, obtaining these parameters directly from wells in real-world applications can be difficult as they are typically obtained by examining rock samples from wells in laboratories, which only reflect fractures at sparse well locations. Also, in this paper, we study the possibility of using seismic data to characterize the DFN. Seismic attributes have been used to determine the probability distribution of fault lengths (Torabi et al., 2017). Schneider et al. (2016) employed seismic attributes to estimate fracture orientation and intensity. To overcome the limitation of a possible wide spatial constraint, Yang et al. (2022) utilized a single seismic attribute for DFN fracture modelling, but this approach suffers from inaccuracy and large randomness because fracture characterization using a single seismic attribute tends to be incomplete and biased. Nevertheless, to achieve realistic DFN modelling, more robust constraints with less randomness and higher accuracy are required.

This paper presents a novel approach for DFN modelling by integrating a new location constraint of multiple seismic attributes extracted using the steerable pyramid technology. Firstly, the steerable pyramid method is employed to decompose seismic data and enhance its resolution. Secondly, multiple seismic attributes are meticulously integrated to create a high-resolution composite attribute that serves as both a fracture identification tool and a DFN location constraint. Finally, an accurate fracture model is established with the constraint to reflect the realistic fracture distribution and reproduce spatial fracture characteristics more accurately. To validate the effectiveness of this approach, a real case study is conducted in the Bonan Depression of East China.

2 Methodology

To overcome the problems addressed in the current DFN modelling technology, this paper developed an approach to constrain the DFN modelling with multiple seismic attributes extracted from high resolution seismic data obtained with the steerable pyramid method. The goal is to integrate different seismic attributes to identify spatial fracture distribution and characterize fracture network in a quantitative sense.

The basis of this approach lies in selecting the optimal seismic data and integrating multiple seismic attributes to identify fractures and fracture networks. Three major phases are involved in the method are as follows.

(1) Seismic data decomposition and data selection. The original seismic data are decomposed into 7 volumes with different dominant frequencies, or called 'Levels' using the steerable pyramid method. The method is able to decompose seismic data into different levels, while maintaining the geological structure information. Lower levels of higher dominant frequencies are stacked to produce a new seismic data of a high resolution for later stage processing.
(2) Composite attribute building and fracture identification. Multiple seismic attributes are carefully extracted from the lower levels data of high-resolution produced in the previous step. The selected attributes are merged with proper weights to form a composite seismic attribute, which holds advantages of each attribute to enhance the fracture representation and identification.
(3) DFN modelling with the location constraint of composite seismic attribute. The composite seismic attribute (holding high resolution content) is utilized as the constraint of DFN modelling, which is essentially the DFN modelling process constrained with multiple seismic attributes.

2.1 Seismic data decomposition and data selection

Before we go to the details of this study, a brief review of the steering pyramid method is given here. The steering pyramid method is an algorithm for multi-scale, multi-directional decomposition and reconstruction of seismic data. The method decomposes an image into a group of images (called Levels) of the same size as the original one but with different resolution or different frequency band (Mathewson and Hale, 2008). In the process of decomposition, different radial filters and directional filters are designed to enhance data intrinsic features of discontinuity as well as the original structure of the input image remain unchanged. The following filter formulas are defined based on different angles:

$$G_k = \sum_m \sum_n W_k G_{k-1}(2x+m, 2y+n) \tag{1}$$

$$f^{\theta}(x, y) = \sum_{j=1}^{M} k_j(\theta) f^{\theta_j}(x, y) \tag{2}$$

where G_k represents the k_{th} level of the pyramid, x, y represents an array of image pixels from different levels, and W_k represents a window function with low-pass characteristics. $f^{\theta}(x, y)$ is a function of the controllable filter in the θ direction, which can be obtained by combining the interpolation function $k_j(\theta)$ in the θ direction and the linear $f^{\theta_j}(x, y)$ of the basic function in the θ direction, and M is the number of the basic functions required for steering. $k_j(\theta)$ are the weighting functions.

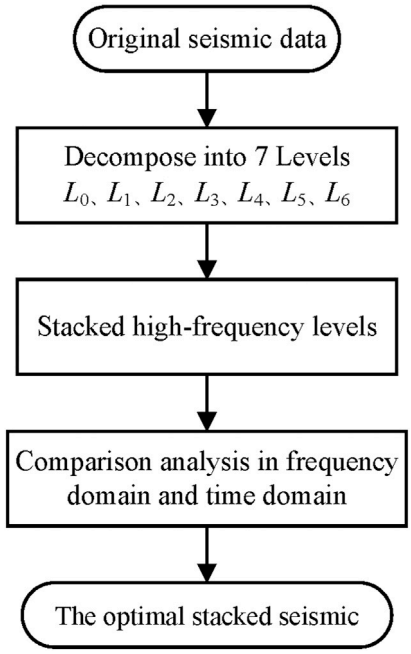

FIGURE 1
The processing workflow with the steerable pyramid method.

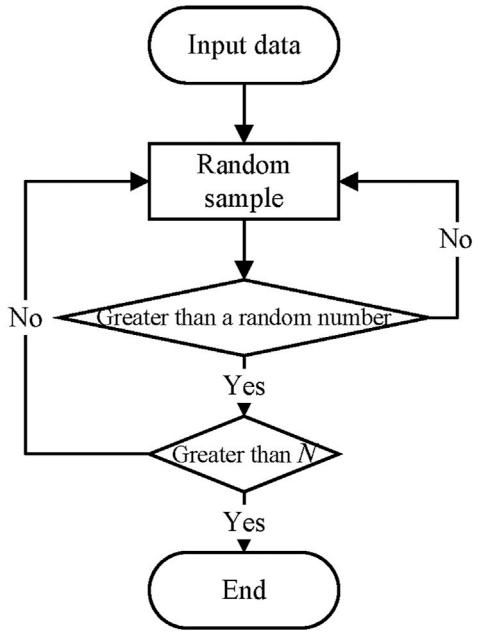

FIGURE 2
Flow chart of DFN fracture modelling.

In the seismic application of the decomposition method, seismic data are normally decomposed into 7 levels of different frequency band. The levels holding high-frequency can be stacked to one, and for example Level 0 and 1 are stacked to form a high-frequency stack, which improves seismic data resolution and enhances the discontinuity for the purpose of identification of edges, joints, faults, fractures or cavities. Zhao et al. (2021) used the steerable pyramid technology on seismic data to recognize geological structure. This method effectively removes background noise and enhances the potential geological structures.

Following the seismic decomposition and level stack, a comparison analysis is performed to evaluate the benefits of the process in both frequency domain and time domain, depending on the study objective. For example, high-resolution stacks can exhibit clearer or more consistent images of fault development in 3D space for fault interpretation. This process is shown in a workflow of Figure 1.

2.2 Composite attribute building and fracture identification

Once the seismic decomposition is complete, seismic attributes can be extracted from the stack with high resolution. For fracture identification in this paper, the seismic attributes, variance, curvature and mean consistent curvature are selected.

The variance attribute is a seismic attribute that describes the variability of seismic amplitudes in neighboring seismic traces. It is more sensitive to fractures caused by faults with strong discontinuities and is suitable for identifying faults at median-scale (Zhang et al., 2021). Curvature can provide information about the spatial distribution of structural features in a rock formation, and is most sensitive to fractures developed by fold; it is suitable for identifying large-scale fractures (Al-Dossary and Marfurt, 2006). The mean consistent curvature, a specific curvature derivative, is a type of seismic attribute that measures the curvature of a seismic horizon or event in a consistent manner throughout the entire seismic volume. The mean consistent curvature attribute is designed to be more sensitive to small-scale fractures and other subtle structural features, as it is able to capture variations in the seismic response that are not evident in the original seismic data (Chilès and Marsily, 1993).

The attributes above represents different characteristics of fractures or fracture networks (e.g., geometry, scales and accuracy). To combine the advantages of each of the seismic attributes, a composite seismic attribute with high accuracy is generated using a linear superposition method. The steps to achieve this are as follows.

① Seismic attributes are normalized to ensure that they be superposed.
② Giving each seismic attribute a weight. This weight is represented by the fracture-related fill ratio, which is the ratio of the fault area described by the seismic attribute to the existing geologically recognizable fault area. The closer to 1 the ratio is, the better the seismic attributes fit with the actual, and the higher the correlation is.
③ The linear superposition is applied to generate a composite attribute and the process can be represented with the mathematical relationships between multiple seismic attributes using the Eq. 3.

$$\begin{cases} r_i = \dfrac{S_i}{S} \\ \omega_i = \dfrac{r_i}{\sum_{i=1}^{3} r_i} \\ K = \omega_1 K_{\mathrm{Cur}} + \omega_2 K_{\mathrm{Con}} + \omega_3 K_{\mathrm{Var}} \end{cases} \tag{3}$$

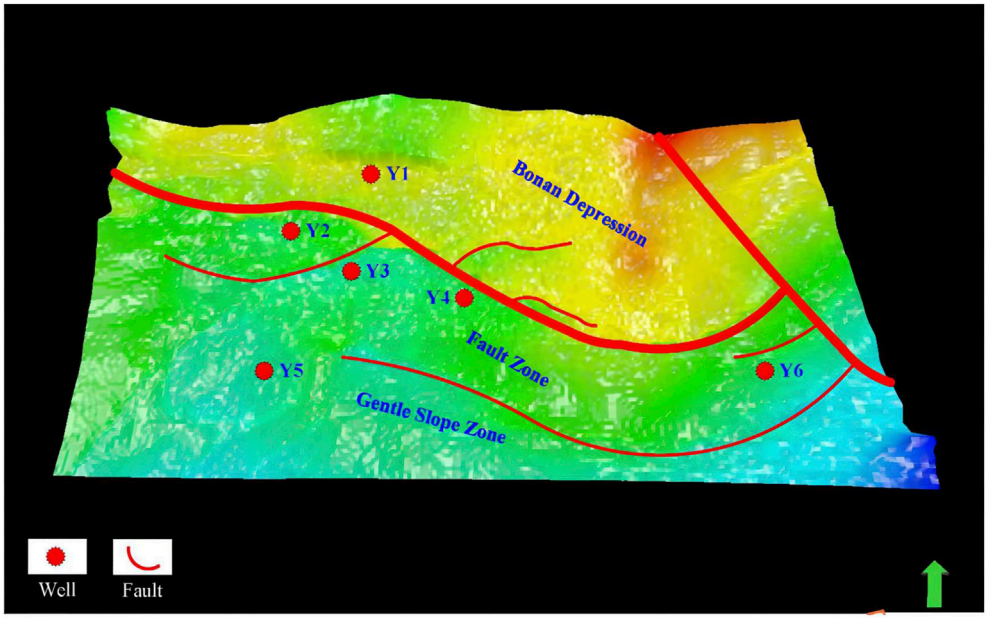

FIGURE 3
Study area map.

where K_{Cur} represents curvature; K_{Con} represents the mean consistent curvature; K_{Var} represents the seismic variance; r_i denotes the correlation between different seismic attributes and large faults; S_i is the area of large faults with different seismic attributes; S is the area of large faults for which existing geological measured; ω_i is the constraint weight; and ω_1、ω_2、ω_3 are the constraint weights, which are summed as 1.

Assuming that the geological survey large fault area S is 20 km^2. The curvature attribute calculation obtains the fault area S_1 as 10km^2, and the variance attribute calculation obtains the area S_2 as 18 km^2. Then the correlation r_1 between the curvature attribute and the fault is 0.5, and the correlation r_2 between the variance and the fault is 0.9. From the above equations, it can be deduced that the weight ω_1 of the curvature attribute is 0.357, and that of the variance ω_2 is 0.643.

2.3 DFN modelling with the constraint of composite seismic attribute

In this section, the composite seismic attribute generated from the previous section is utilized as the fracture location constraint in the DFN modelling (Chopra and Marfurt, 2013) by introducing the Poisson process. DFN modelling is a numerical modelling approach used to simulate fluid flow and transport in fractured rock masses.

The principle of the Poisson process is a mathematical model used to describe the occurrence of random events over time or space. It is particularly useful in modelling systems where events occur randomly, or in this paper, fractures distribute randomly. Therefore, the Poisson process can be used in DFN modelling to generate random fractures in a rock mass to create a DFN model simulate the development of natural fractures or fracture network in rocks.

When generating fractures in 3D space, the flow chart of the traditional approach is shown in Figure 2. In this paper, we use the composite seismic attribute to constraint fracture location distribution as the attribute is much related to the development of fractures or fracture network. The steps are as follows.

① The composite seismic attribute is regularized, shown in Eq. 4. The generation probability P_r of fractures per unit volume can be calculated as,

$$P_r = \frac{\mathrm{P} - \mathrm{P}_{\min}}{\mathrm{P}_{\max} - \mathrm{P}_{\min}} \tag{4}$$

where $\mathrm{P_r}$ is the generation probability of fractures; P is the input composite seismic attribute; $\mathrm{P}_{\min}$ is the minimum value of the input composite seismic attribute and $\mathrm{P}_{\max}$ is the maximum value of the input composite seismic attribute.

② With the composite seismic attribute, a fracture network can be generated by randomly placing fractures in rock mass according to the Poisson distribution. The Poisson process is used to generate the fracture center locations (x, y, z), where x, y, z are independent random coordinate values that obey the uniform distribution.

③ The probability values $P_r(x, y, z)$ are extracted. If $P_r(x, y, z) \geq rand$, the generated fracture center position is valid; otherwise, it is invalid. *rand* is a random value in the interval [0, 1].

④ When the value of effective fractures is less than the preset value N of the fractures, the above steps are repeated; otherwise, the process is terminated.

Overall, using the Poisson process as an input for DFN simulations can help create more realistic and representative models of fractured rock masses, which can be useful for understanding and predicting fluid flow and transport in geological systems.

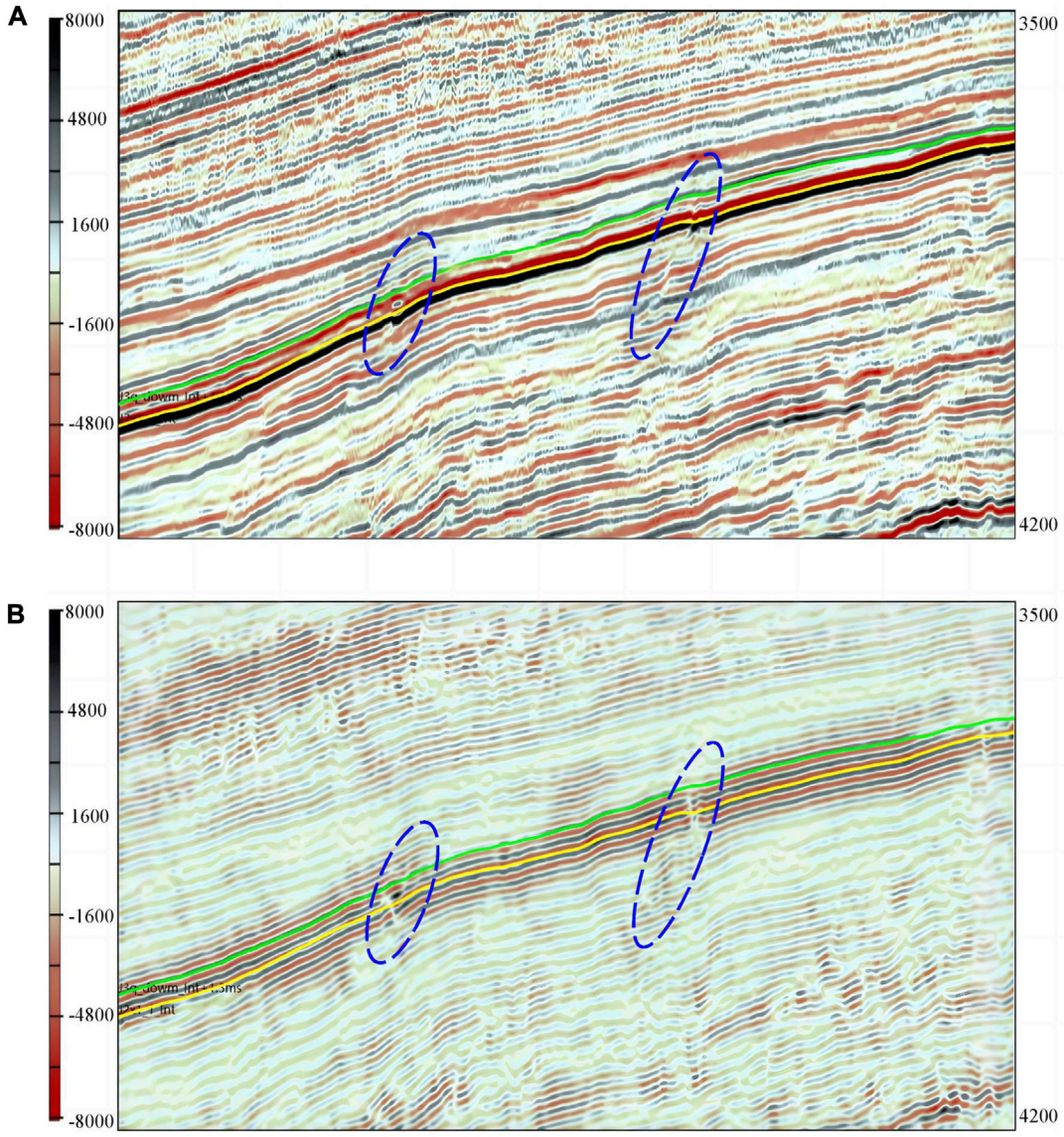

FIGURE 4
Seismic profiles: **(A)** original seismic profile, **(B)** stacked seismic profile.

3 Application

3.1 Geological background

The study area, the Bonan Depression, is located in the middle of the Zhanhua Oil field, in East China. In spite of the long production history, the geological structure and fault systems are not fully understood due to the presence of the complex faults and fault system. Seismic interpretation shows that the depression is crossed by two major faults indicated by two bold red curves (Kang et al., 2002; Wang and Zhang, 2023) shown in Figure 3. Many minor faults develop as branches of the two majors.

The study area is approximately 16.2 km from east to west and 9.2 km from north to south, and the thickness of the target layer, the Shasi Interval, is around 15 m. High-angle tectonic fractures are developed within the distance of hundreds of meters of the faults, and there are six wells in the study area. The reservoir model is not effective based on the traditional DFN modelling approach, and the workflow proposed in the previous section will be tested and verified in the study area in order to improve the understanding of the reservoir model.

3.2 Seismic data decomposition, seismic attribute computation and composite attribute generation

For the case application, seismic data from the Bonan Depression area were decomposed, and seismic attributes were extracted before the composite attribute was generated. The steerable pyramid technique decomposed the seismic data into seven levels, from Level 0 to 6. Level 0 contained much noise

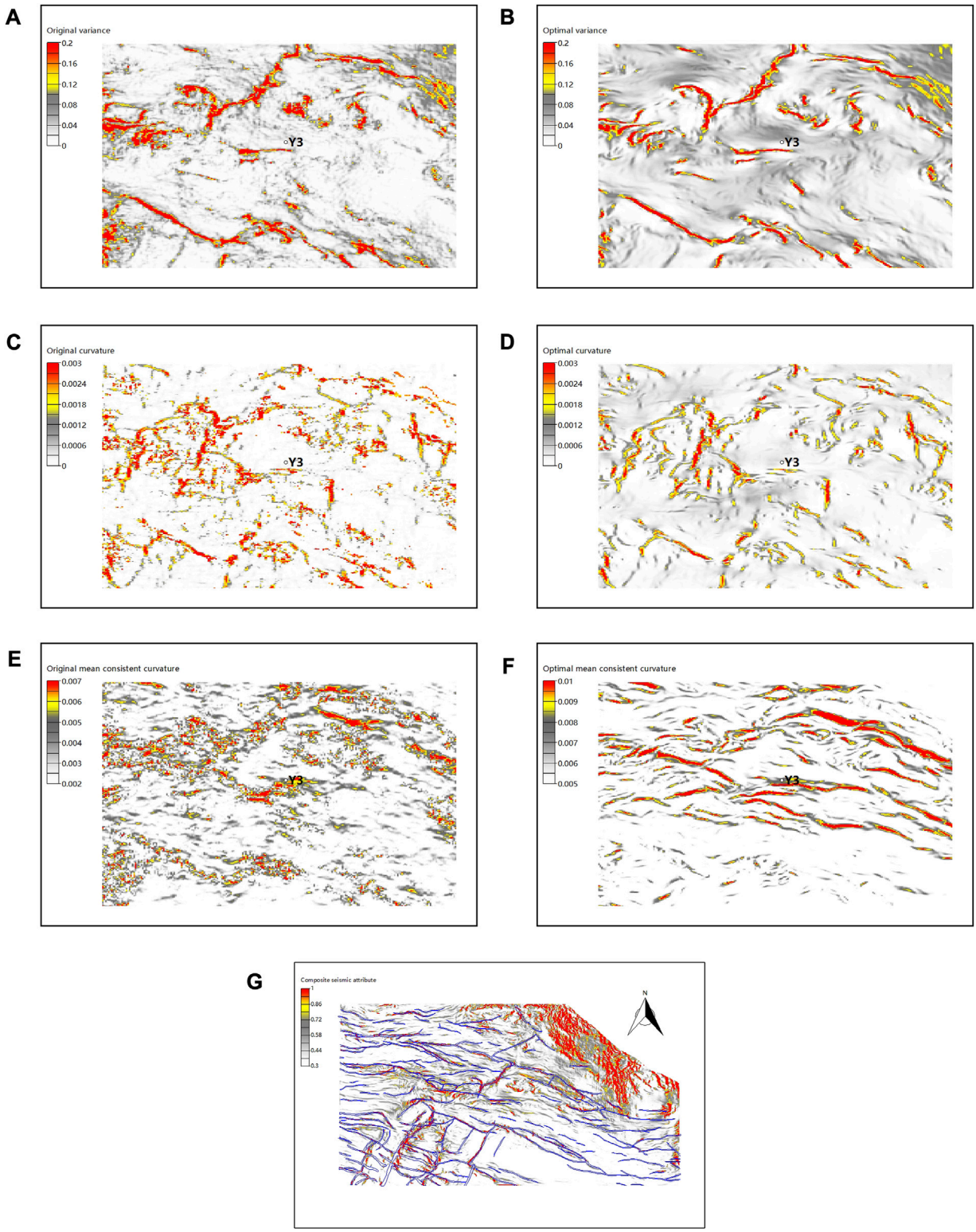

FIGURE 5
Map showing different seismic attributes: **(A)** original variance, **(B)** optimal variance, **(C)** original curvature, **(D)** optimal curvature, **(E)** original mean consistent curvature, **(F)** optimal mean consistent curvature, **(G)** composite seismic attribute map.

and was not considered. The higher levels (Level 4, 5, and 6), holding low-frequency content, indicated the large-scale trend of the fault system. The other levels (Level 1, 2, and 3) of the high-frequency band were stacked to improve the resolution and prediction of small-scale faults. To examine the workflow, crossline 803 was extracted and presented in Figure 4A. The section stacked with

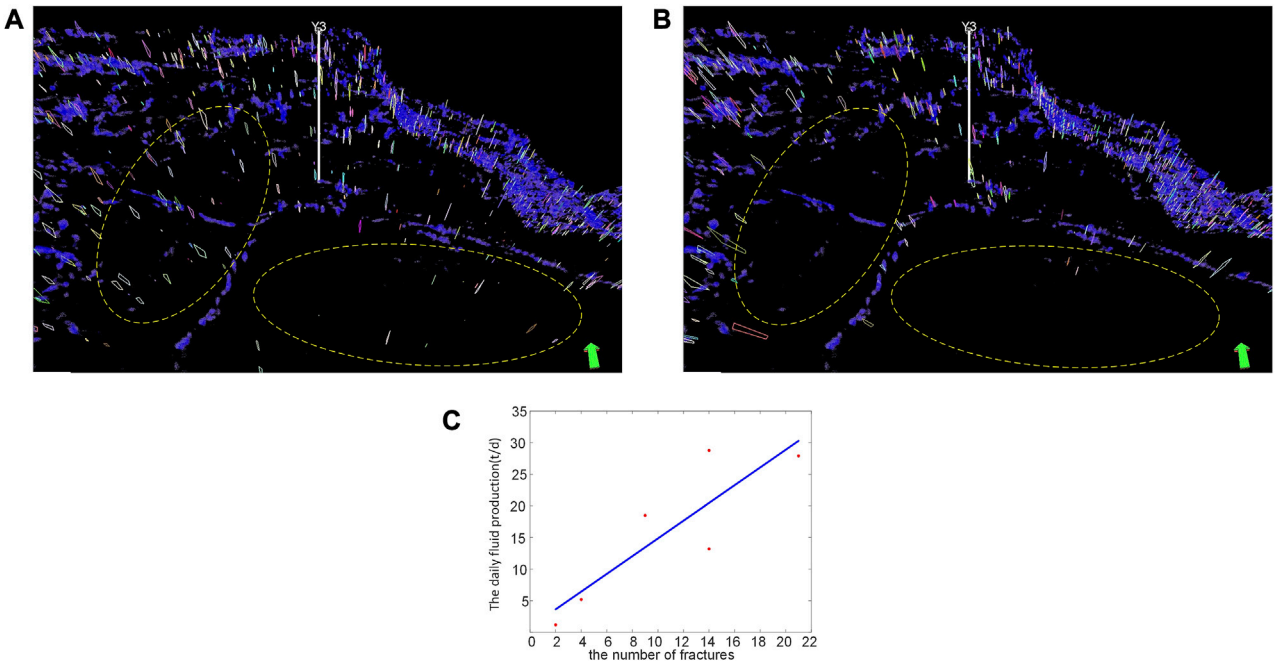

FIGURE 6
Fracture modelling and analysis in study area in the southern Bonan Depression: **(A)** fracture model constrained by fracture density, **(B)** fracture model constrained by composite seismic attribute, **(C)** number of fractures near the well in the model and the daily fluid production.

Level 1, 2, and 3 is shown in Figure 4B for comparison. The area highlighted in the ellipses indicates the improved clarity of the two faults (enhancement of the discontinuity), which facilitates seismic interpretation.

Following the decomposition, three seismic attributes, variance, curvature and mean consistent curvature are extracted using the stack. Figure 5B shows the variance for the window parameter of 3*3. Figure 5D shows the variancefor a vertical radius parameter of 12. Figure 5F shows the mean consistent curvature for the window parameter of 3*3. Figures 5A, C, E are the three attributes extracted from the original seismic using the same parameters. It can be seen that the attributes from the original seismic are much noisier, compared with the ones from the stack, from which the outlines of the faults and fault system are more clearly observed. Since fractures develop along the faults or within the fault system. These clear images will reflect more logical fracture distribution if they are utilized to constrain the DFN modelling in this area.

With the extracted seismic attribute, a composite attribute is computed according to the Eq. 3 in the previous section shown in Figure 5G. The composite attribute combines the advantage of the three, reflecting the potential fractures along the fault or within the fault system. And it will be used as the final resulting attribute constrain the DFN modelling in the next section.

3.3 Fracture modeling

With the composite attribute extracted, it is served as the location constraint of the DFN modelling in this section. The modelling process is constructed with the approach presented in the section II(C). In addition, Fracture density distribution (or the number of fractures in one location) is created from wells in the method presented in (Jian et al., 2021) and the details are not discussed here as we focus on the location constraint. By examining the fracture properties at the wells, its orientation is determined as 30° and 135° with the variance of 0.1. The fracture dip angle is mainly high-angle, and the mean value and variance are 75° and 0.5, respectively. In the process of fracture generating, each fracture is created with 4 edges, and the mean fracture length is 10 m, and its width is around 3–4 m.

With the parameters above, the DFN model created with the location constraint is shown in Figure 6B. Figure 6A is the model built without the constraint. By comparison, fractures in Figure 6A distribute across the full area; however, in tectonic sense, they should only emerge along the faults or within the fault system. Therefore, with the location constraint, Figure 6B indicates the consistency of the spatial relation between fractures and the regional faults. For example, many fractures develop in the two ellipses (see Figure 6A) there are no faults, which is not correct in geological sense; at the same locations (the two ellipses in Figure 6B), few fractures develop as the location constraint is applied.

As the same time, we compare the number of fractures near the well with the daily fluid production. The number of fractures within a square with the side length of 100 m, centered at the well. The number of fractures for Wells Y1–Y6 are 2, 4, 21, 14, 14 and 9, respectively. The corresponding daily fluid productions per well were 1.18, 5.19, 27.9, 28.77, 13.2 and 18.5. The fracture distribution at the wells is consistent with the production with the correction coefficient of 0.755 (Figure 6C). This demonstrates the effectiveness of the DFN method.

4 Conclusion

To improve DFN modelling, a new approach is developed by integrating high resolution seismic attributes as a location constraint into a more realistic modelling workflow in this paper. The steerable pyramid technology is able to enhance seismic resolution, which make it possible to generate a high-resolution fracture prediction map along with seismic attribute extraction techniques. For fractured reservoir modelling, DFN modelling provides a powerful tool for simulate fractured reservoir models, helping understand the characteristics of fractures or fracture network in rock masses. With the map as a spatial and geological constraint, DFN modelling is able to generate a more logical and realistic fracture models, promoting the ability of more fracture modelling. The correlation between the logging daily production rate and the fracture model is as high as 70%, and there is an obvious positive correlation. At the same time, the fracture model has a higher degree of overlap with the fracture development zones predicted by seismic attribute results. All the above real case application shows that the approach in this paper can effectively improve the accuracy of fracture modelling, reducing randomness in the traditional DFN modelling. Also, the real case demonstrates the potential of this approach in wide application prospect.

Data availability statement

The seismic data that support the findings of this study are available from the Sinopec Shengli Oilfield Company. Restrictions apply to the availability of these data, which were used under license for this study. The seismic data are available from the authors with the permission of the Sinopec Shengli Oilfield Company. Requests to access these datasets should be directed to YW, wangyudi0219@163.com.

Author contributions

YW: Writing–original draft. YX: Writing–review and editing. LD: Writing–review and editing. SG: Data curation, Writing–review and editing. WY: Data curation, Writing–review and editing. XH: Conceptualization, Writing–review and editing.

Funding

The authors declare financial support was received for the research, authorship, and/or publication of this article. This research was funded by the China Natural Science Foundation (42241206), and the China Natural Science Foundation (U20B2016).

Conflict of interest

Authors SG and WY were employed by the company Sinopec Shengli Oilfield Company.

The remaining authors declare that the research was conducted in the absence of any commercial or financial relationships that could be construed as a potential conflict of interest.

Publisher's note

All claims expressed in this article are solely those of the authors and do not necessarily represent those of their affiliated organizations, or those of the publisher, the editors and the reviewers. Any product that may be evaluated in this article, or claim that may be made by its manufacturer, is not guaranteed or endorsed by the publisher.

References

Al-Dossary, S., and Marfurt, K. J. (2006). 3D volumetric multispectral estimates of reflector curvature and rotation. *Geophysics* 71 (5), 41–51. doi:10.1190/1.2242449

Azim, R. A. (2016). Integration of static and dynamic reservoir data to optimize the generation of subsurface fracture map. *J. Petroleum Explor. Prod. Technol.* 6, 691–703. doi:10.1007/s13202-015-0220-8

Baecher, G. B., Lanney, N. A., and Einstein, H. H. (1977). "Statistical description of rock properties and sampling," in *The 18th U.S. Symposium on rock mechanics (USRMS)*).

Baecher, G. B. (1983). Statistical analysis of rock mass fracturing. *Math. Geol.* 15 (2), 329–348. doi:10.1007/BF01036074

Chilès, J.-P., and Marsily, G. d. (1993). Stochastic models of fracture systems and their use in flow and transport modeling. *Flow Contam. Transp. Fract. Rock*, 169–236. doi:10.1016/b978-0-12-083980-3.50008-5

Chopra, S., and Marfurt, K. J. (2013). Structural curvature versus amplitude curvature. *Lead. Edge* 32 (2), 178–184. doi:10.1190/tle32020178.1

Dong, S., Zeng, L., Cao, H., Xu, C., and Wang, S. (2018a). Principle and implementation of discrete fracture network modeling controlled by fracture density. *Geol. Rev.* 64 (5), 1302–1314. doi:10.16509/j.georeview.2018.05.020

Dong, S., Zeng, L., Xu, C., Cao, H., Wang, S., and Lü, W. (2018b). Some progress in reservoir fracture stochastic modeling research. *Oil Geophys. Prospect.* 3, 625–641. doi:10.13810/j.cnki.issn.1000-7210.2018.03.023

Hardebol, N. J., Maier, C., Nick, H., Geiger, S., Bertotti, G., and Boro, H. (2015). Multiscale fracture network characterization and impact on flow: A case study on the latemar carbonate platform. *J. Geophys. Res. Solid Earth* 120 (12), 8197–8222. doi:10.1002/2015JB011879

Hunziker, J., Favino, M., Caspari, E., Quintal, B., Rubino, J. G., Krause, R., et al. (2018). Seismic attenuation and stiffness modulus dispersion in porous rocks containing stochastic fracture networks. *J. Geophys. Res. Solid Earth* 123 (1), 125–143. doi:10.1002/2017JB014566

Jian, S., Fu, L., Cao, C., Han, T., and Du, Q. (2021). 3D finite-element modeling of effective elastic properties for fracture density and multiscale natural fractures. *J. Geophys. Eng.* 18 (4), 567–582. doi:10.1093/jge/gxab036

Kang, R., Liu, K., Zhao, C., Jin, P., Peng, D., Luo, S., et al. (2002). Sedimentary facies of the shahejie formation of paleogene in bonan sag of jiyang depression. *J. Palaeogeogr.* 4 (4), 19–29.

Kolyukhin, D., Protasov, M. J. C., and Geosciences, (2023). Multiscale study of statistical fractal DFN model and corresponding seismic images. *Comput. Geosciences* 171, 105285. doi:10.1016/j.cageo.2022.105285

Lei, C., Xu, Q.-y., Yuan, X.-t., Kang, C.-j., and He, F. (2020). "The method of DFN in granite buried hill reservoir based on multiple attribute constraints: A case study of B field, Chad," in *Proceedings of the international field exploration and development conference 2019* (Springer Singapore), 1934–1946.(

Mardia, K., Nyirongo, V., Walder, A., Xu, C., Dowd, P., Fowell, R., et al. (2007). Markov chain Monte Carlo implementation of rock fracture modelling. *Math. Geol.* 39 (4), 355–381. doi:10.1007/s11004-007-9099-3

Mathewson, J., and Hale, D. (2008). "Detection of channels in seismic images using the steerable pyramid," in *SEG international exposition and annual meeting: SEG)*. SEG-2008-0859.

Schneider, S., Eichkitz, C., Schreilechner, M., and Davis, J. (2016). Interpretation of fractured zones using seismic attributes—case study from teapot dome, Wyoming, USA. *InterpreCtation* 4 (2), T249–T260. doi:10.1190/INT-2015-0210.1

Shi, C., Jiang, X., Kou, Y., and Zhang, Z. (2021). Research status and prospect of theoretical model of shale gas seepage. *Petrochem. Ind. Appl.* 40 (8), 10–16. doi:10.3969/j.issn.1673-5285.2021.08.003

Singh, J., Pradhan, S. P., Singh, M., and Hruaikima, L. (2022). Control of structural damage on the rock mass characteristics and its influence on the rock slope stability along national highway-07, garhwal himalaya, India: an ensemble of discrete fracture network (DFN) and distinct element method (DEM). *Bull. Eng. Geol. Environ.* 81 (3), 96. doi:10.1007/s10064-022-02575-5

Torabi, A., Alaei, B., and Kolyukhin, D. (2017). Analysis of fault scaling relations using fault seismic attributes. *Geophys. Prospect.* 65 (2), 581–595. doi:10.1111/1365-2478.12440

Wang, Y., and Zhang, S. (2023). Formation mechanism of high-quality reservoirs in deep strata of paleogene, bonan subsag, Zhanhua sag, bohai bay basin. *Petroleum Geol. Exp.* 45 (1), 11–19. doi:10.11781/sysydz202301011

Welch, M. J., Lüthje, M., and Oldfield, S. J. (2022). DFN generator v2.0: A new tool to model the growth of large-scale natural fracture networks using fundamental geomechanics. *Geosci. Model Dev. Discuss.*, 1–42. doi:10.5194/gmd-2022-22

Xu, C., and Dowd, P. (2010). A new computer code for discrete fracture network modelling. *Comput. Geosciences* 36 (3), 292–301. doi:10.1016/j.cageo.2009.05.012

Yang, Z., Zhao, H., Huang, Y., Yang, H., Tang, X., Wang, T., et al. (2022). A small heat shock protein, GmHSP17.9, from nodule confers symbiotic nitrogen fixation and seed yield in soybean. *Petroleum Geol. Oilfield Dev. Daqing* 41 (3), 103–115. doi:10.1111/pbi.13698

Zhang, X., Yu, J., Li, N., and Wang, C. (2021). Multi-scale fracture prediction and characterization method of a fractured carbonate reservoir. *J. Petroleum Explor. Prod. Technol.* 11 (1), 191–202. doi:10.1007/s13202-020-01033-w

Zhao, Y., Huang, X., Chen, Y., Song, H., Zhang, D., Cui, X., et al. (2021). Application of the directionally steerable pyramid method to identify geological boundaries in a conglomerate sand reservoir. *Geophys. Prospect. Petroleum* 60 (3), 414–420. doi:10.3969/j.issn.1000-1441.2021.03.007

frontiers | Frontiers in Earth Science

TYPE Original Research
PUBLISHED 12 October 2023
DOI 10.3389/feart.2023.1267211

OPEN ACCESS

EDITED BY
Lidong Dai,
Chinese Academy of Sciences, China

REVIEWED BY
Maining Ma,
University of Chinese Academy of Sciences, China
Xiaoge Huang,
Chinese Academy of Sciences (CAS), China
Chang Su,
Institute of Disaster Prevention, China

*CORRESPONDENCE
Haoran Zhang,
iggcaszhanghr@163.com
Xiwei Xu,
xiweixu@vip.sina.com

RECEIVED 26 July 2023
ACCEPTED 20 September 2023
PUBLISHED 12 October 2023

CITATION
Zhang H, Xu X and Yang S (2023), Ultramafic pseudotachylytes in high-pressure metamorphogenic peridotite from Luobusha, Tibet: a record of crustal paleo-earthquakes.
Front. Earth Sci. 11:1267211.
doi: 10.3389/feart.2023.1267211

Ultramafic pseudotachylytes in high-pressure metamorphogenic peridotite from Luobusha, Tibet: a record of crustal paleo-earthquakes

Haoran Zhang[1]*, Xiwei Xu[2]* and Saihong Yang[3]

[1]State Key Laboratory of Earthquake Dynamics, Institute of Geology, China Earthquake Administration, Beijing, China, [2]School of Earth Sciences and Resources, China University of Geosciences, Beijing, China, [3]Key Laboratory of Lunar and Deep Space Exploration, National Astronomical Observatories, Chinese Academy of Sciences, Beijing, China

In this paper, we report an occurrence of ultramafic pseudotachylytes, providing fault-rock evidence of paleo-earthquakes, from the Luobusha ophiolite complex in the Yarlung Zangbo suture zone. The pseudotachylytes form hairline-thin aphanitic veinlets and vein networks bounded by micro-damage zones cutting through the host harzburgite, forming flow banding in some places. The pseudotachylyte veins are dominated by close-knit ultrafine-grained minerals consisting of olivine, orthopyroxene, serpentine, spinel, and magnetite, cemented by an extremely fine matrix. As the primary component of the pseudotachylyte veins, olivine occurs as microphenocryst showing zoning from core to rim and as irregularly shaped microlite immersed in the interstitial material. Zoned crystals of olivine developed with Mg-rich cores and more Fe-rich rims. Microlite diagnosis of crystallization in a quenched melt includes dendritic, skeletal, and poikilitic olivine crystals, which are typical of ultramafic pseudotachylyte. The olivine microlites contain higher amounts of Ca, Al, and Cr but a lower Ni content compared with the host harzburgite olivine. Irregularly shaped chrome-spinel crystals are chemically zoned as well, indicating an Fe-rich rim overgrowth. Ni sulfide droplets interspersing among the matrix imply melt occurrence. The presence of a micro-fibrous and micro-vesicular interstitial matrix also indicates a melting-related origin. Ultracataclastite veins associated with pseudotachylyte transecting serpentine are observed, which convey that heat was generated during rapid comminution and injection. The characteristic petrography, microtextures, and chemical inhomogeneities meet the criteria of ultramafic pseudotachylyte and reveal a mixed genesis via a combination of crushing and melting. The development of extremely tiny globular prograde serpentine inclusions (~100 nm) in the olivine microlites is ascribed to the dehydration reaction of serpentine to olivine within the pseudotachylyte. The Luobusha metamorphogenic peridotite was subjected to serpentinization after having emplaced in the crust and subsequently to high-pressure metamorphism. The pseudotachylytes were generated in the crust after the high-pressure metamorphism and did not descend to a greater depth. Flash ultra-comminution associated with frictional heating may release fluids via localized heat-driven prograde reactions in the crust.

KEYWORDS

pseudotachylyte, quench, melt, dehydration, high-pressure metamorphism, Luobusha

1 Introduction

It is known that pseudotachylytes can be generated during earthquakes, meteoritic impacts, and large-scale landslides (Lin, 2008). Tectonogenetic pseudotachylytes that are related to seismic activities have generally been considered as products formed under the condition of high strain rates within shear zones and/or seismic fault zones (McKenzie and Brune, 1972; Sibson, 1975; Spray, 1987; 1995; Magloughlin, 1992; McNulty, 1995; Lin and Shimamoto, 1998). Frictional heating and strong abrasion that are generated during rapid seismic faulting are sufficient to melt and/or crush rock within the fault zone and fluidize ultrafine-grained materials (Kano et al., 2004), which eventually give rise to pseudotachylytes. More pseudotachylytes recognized from crustal sialic protoliths, such as crystalline rocks of intermediate and granitoid composition, have been reported in the literature, but cases of pseudotachylytes derived from peridotite are less common. The possible reasons why ultramafic pseudotachylyte has rarely been spotted are that peridotite is not a major constituent of the crust, its required melting temperatures are high, and its density inhibits uprise from great depths in the subduction zone (Evans and Cowan, 2012). However, the lower creep strength of silica-rich rocks compared with ultramafic rocks at the same melting temperatures would make it difficult to realize the high-stress conditions needed for frictional melting of silicic or basic rocks. In addition, the thermal feedback effect that may cause frictional melting may be easier for ultramafic rocks because of the higher activation energies of creep (Tullis and Yund, 1982; Karato, 1989). Hence, a relatively reasonable explanation for this scarcity of ultramafic pseudotachylyte is that evidence of possible ultramafic melts may be easily obscured by more rapid grain growth and recrystallization in ultramafic rocks than in silicic rocks (Karato, 1989). Research studies concerning ultramafic pseudotachylyte from the Balmuccia lherzolite, Ivrea–Verbano zone, North Italy, have demonstrated that shear heating can cause high-degree heating so that ultramafic rocks, which have a much higher melting temperature than other crustal rocks, undergo a significant degree of melting, followed by rapid crystallization on a time scale of 100 s or less, conditions consistent with an earthquake that may occur mainly in the oceanic upper mantle (Obata and Karato, 1995; Jin et al., 1998). Near-complete melting of peridotite took place during exhumation of the lithospheric mantle in the early stages of the formation of the Ligurian Tethys oceanic basin, which resulted in the formation of pseudotachylytes from the Mt. Moncuni ultramafic in the western Alps of Italy (Piccardo et al., 2010). Pseudotachylytes also developed in mantle peridotite at the Alpine subduction complex of Corsica during subduction-related faulting of metabasites and metaperidotites under lawsonite–blueschist facies conditions were described in detail (Austrheim and Andersen, 2004; Andersen and Austrheim, 2006; Andersen et al., 2008; Deseta et al., 2014). In the upper part of the Alpine subduction zone, frictional heating on co-seismic faults raised the temperature from ambient blueschist facies conditions to more than 1,700°C, which resulted in disequilibrium melting of spinel peridotite (Andersen and Austrheim, 2006).

The typical mineralogy and texture of most field examples of ultramafic pseudotachylyte reported to date have been generalized and summarized in detail, which could provide us much valuable references to aid the recognition of ultramafic pseudotachylyte. Moreover, a genetic association between co-seismic deformation and high-pressure metamorphism has been proposed and realized at some localities worldwide (Austrheim and Boundy, 1994; Austrheim et al., 1997; Lund and Austrheim, 2003; Austrheim and Andersen, 2004; John and Schenk, 2006; Angiboust et al., 2012; Austrheim, 2013; Andersen et al., 2014; Yang J.- et al., 2014; Yang et al., 2014 J.-J., 2016). It is considered that the role of faults or shear zones is to introduce a fluid that enhances metamorphic reactions at depths in the subducted slab through studies on eclogite pseudotachylyte that indicates fossil earthquake (Austrheim and Boundy, 1994; Austrheim, 2013). However, eclogite facies, such as breccia and cataclasite dykes, as well as the quench textures in a variably eclogitized gabbro at Yangkou in the Chinese Su-Lu ultrahigh-pressure metamorphic belt, are interpreted to be the result of co-seismic high-pressure metamorphism in the crust instead of high-pressure crystallization in subducted dry rocks when fluid becomes available (Yang J.- et al., 2014; Yang et al., 2014 J.-J., 2016). If the rocks were held at great depths for millions of years after the seismic events, then the quenching textures would have been erased owing to continuous mineral growth and equilibration in the stability of the eclogite (Yang J.-J. et al., 2014). In addition, the wall rock to the pseudotachylyte and associated ultracataclastite was subjected to serpentinization after having emplaced in the shallow crust and then transformed back into peridotite by subsequent high-pressure metamorphism (Huang et al., 2014). In several similar observations reported in the study of orogenic belts worldwide (Evans and Trommsdorff, 1978; Trommsdorff et al., 1998; Yang, 2003; Bucher, 2005; Ravna et al., 2006; Yang and Powell, 2008; Naemura et al., 2009; Morgunova and Perchuk, 2012; Rebay et al., 2012; Debret et al., 2013), it is proposed that a similar process may be experienced by all orogenic peridotites (Yang et al., 2013). Therefore, a research issue to be tackled is whether the earthquake in peridotite and associated high-pressure metamorphism occurred at mantle depth (Obata and Karato, 1995; Jin et al., 1998; Austrheim and Andersen, 2004), as has been assumed, or whether they took place in the brittle regime of the crust.

The present study documents some types of ultra-thin dark-brown aphanitic veinlets and vein networks occurring in harzburgite at the Luobusha ophiolite complex in the Yarlung Zangbo suture zone. The detailed petrographic observation shows that they are composed of fine- and ultrafine-grained minerals and take the form of tenuous branches parallel to or intersected with each other at small angles. The microtextures of these dark-brown veinlets obtained from scanning electron microscopy observation and their mineral chemistry are similar to some natural ultramafic pseudotachylytes described in previous papers (Obata and Karato, 1995; Andersen and Austrheim, 2006; Piccardo et al., 2010; Deseta et al., 2014) and to the run products generated during the high-velocity friction experiments (Lin et al., 2013), which make us fully convinced that these melanocratic veinlets are ultramafic pseudotachylyte formed in harzburgite at this locality. It is for the first time that ultramafic pseudotachylyte has been recognized in the Yarlung Zangbo suture zone. This study presents petrographic, microtextural, and mineral chemical data for the ultramafic pseudotachylyte at Luobusha. In addition, the ultramafic pseudotachylyte within the high-pressure metamorphogenic peridotite at this locality, thus, provides an opportunity to examine the interaction mechanism of co-seismic deformation and high-pressure metamorphism.

2 Geological setting

The Luobusha ophiolite (Figure 1) lies approximately 200 km southeast of Lhasa along the Yarlung Zangbo suture zone—a major tectonic boundary that separates the Lhasa Block to the north from the Indian plate to the south (Allégre et al., 1984). The ophiolite in this part of the suture zone extends for about 42 km in an east–west direction, with an outcrop area of approximately 70 square kilometers (Zhou et al., 1996; Robinson et al., 2004). The mantle peridotite mainly consists of harzburgite, in which there are a large number of dunite and podiform chromitite blocks, as well as a small amount of lherzolite, distributed in the southern ophiolite belt and in fault contact with the southern flysch formation (Zhang et al., 1996). According to the vertical variation of rock assemblage and chemical composition in the section sequence, the mantle peridotite can be divided into upper and lower subzones (Chen et al., 2011). The upper subzone is distinguished from other bodies in the Yarlung Zangbo ophiolite belt by the obvious increase of ductility (the main chromite metallogenic belt). In the strongly deformed peridotite, most dunite rocks are long, lenticular, and plate-like bodies with the same orientation and occurrence as the peridotite body. In addition, there are a few dunite rocks with various forms, weak directionality, and irregular boundaries, which form a sharp or gradual transition with harzburgite. The lower subzone is characterized by less dunite and more harzburgite, which is in a transitional relationship with the upper subzone. This zonation in the profile is considered to be a reflection of the zonation melting of the upper mantle rather than the result of magmatic differentiation (Chen et al., 2011). The cumulate rocks mainly include wehrlite, pyroxenite, dunite, and gabbro. To the south, the ophiolite underlies a thick sequence of Triassic flysch-type sedimentary rocks through a steep thrust fault; to the north, it thrusts over the Gangdese granitic batholith of the Lhasa Terrane and the Luobusha Formation, which is a Tertiary Oligo–Miocene molasse deposit (Huang et al., 2014).

Studies on the entire Yarlung Zangbo ophiolite proposed that the mantle peridotites outcropped in the Yarlung Zangbo ophiolite belt are probably subcontinental lithospheric mantle beneath the Asian plate (Wu et al., 2014). During the Early Cretaceous, extension of the leading edge of the Asian continent resulted in the exhumation of the subcontinental lithospheric mantle and the formation of an oceanic basin. Exhumation and thinning of the lithosphere resulted in upwelling and melting of the asthenosphere, which led to the eruption of basalt and intrusion of gabbro and dolerite. During the maximum extension, partial melting of the metasomatized refractory lithosphere mantle gave rise to some amount of boninitic melts. Yarlung Zangbo ophiolite is much different from the ideal ophiolite section defined by the Penrose Conference, and it could not be considered a remnant of the Neo-Tethyan Ocean between the Indian and Asian continents. Yarlung Zangbo ophiolite represents an oceanic lithosphere formed at an ultraslow spreading center with a spreading rate much lower than that in Western Alps (Wu et al., 2014).

3 Materials and methods

Thin sections were examined using a polarizing microscope and by scanning electron microscopy. Optical analyses were performed using a standard polarized light microscope (Leica DM2700P). Backscattered electron (BSE, atomic Z-contrast) analyses were carried out using an FEI Nova NanoSEM 450 equipped with a Nordlys Nano detector at the Institute of Geology and Geophysics, Chinese Academy of Sciences (IGGCAS), Beijing. Mineral chemistry analysis was performed using a wavelength-dispersive (WDS)

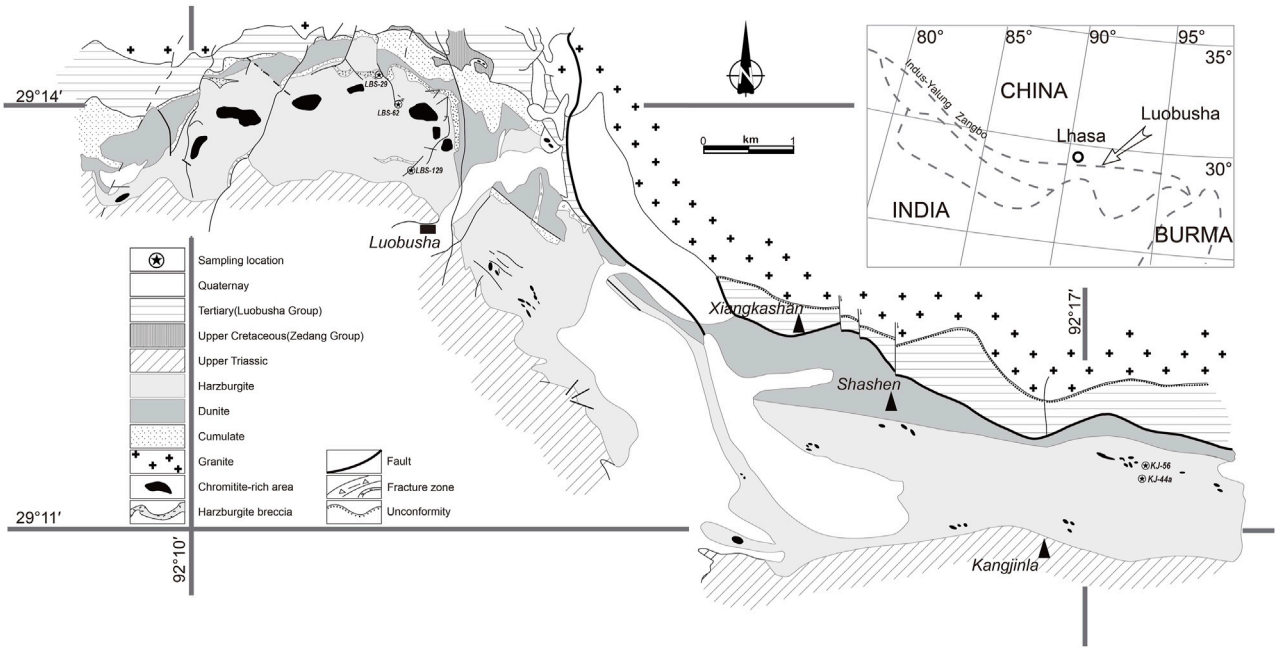

FIGURE 1
Geological map of the Luobusha ophiolite, Tibet, SW China [simplified from the work of Zhang et al. (1996)].

TABLE 1 Mineral composition of zoned olivine and the matrix from the pseudotachylyte veins. Listed cations follow the formula with Fe^{3+} corrected according to the work of Droop (1987), Mineralogical Magazine, v. 51, pp. 431–435. Total*s: Recalculated on an anhydrous basis to a total of 100%. Mineral abbreviations are according to the work of Whitney and Evans, 2010, with ol referring to olivine.

PST zoned olivine core						PST zoned olivine rim					PST matrix							
Sample	KJ-44a	KJ-44a	KJ-56	KJ-56	LBS-29	KJ-44a	KJ-44a	KJ-56	KJ-56	LBS-29		KJ-44a	KJ-44a	KJ-56	KJ-56	LBS129	LBS-62	12LBS29
SiO_2	41.19	41.11	41.09	40.94	40.91	40.10	40.96	40.27	40.23	41.04	SiO_2	40.98	41.11	42.55	41.87	38.94	39.92	41.19
TiO_2	0.00	0.00	0.02	0.00	0.03	0.01	0.00	0.01	0.02	0.00	TiO_2	0.01	0.02	0.00	0.00	0.02	0.04	0.02
Al_2O_3	0.06	0.02	0.03	0.00	0.00	0.07	0.10	0.07	0.44	0.30	Al_2O_3	0.02	0.07	0.09	0.21	0.16	0.10	0.00
Cr_2O_3	0.05	0.05	0.03	0.02	0.03	0.08	0.06	0.14	0.24	0.22	Cr_2O_3	0.00	0.01	0.00	0.01	0.10	0.08	0.04
FeO	8.27	8.50	8.53	8.93	9.34	11.50	11.28	12.89	11.69	12.68	FeO	5.30	4.41	3.82	3.62	6.76	5.94	4.86
MnO	0.11	0.11	0.10	0.13	0.16	0.19	0.24	0.22	0.25	0.19	MnO	0.10	0.06	0.07	0.02	0.16	0.10	0.08
NiO	0.39	0.38	0.38	0.34	0.37	0.36	0.35	0.36	0.36	0.31	NiO	0.07	0.07	0.22	0.10	0.16	0.13	0.05
MgO	50.04	51.00	49.75	49.89	49.24	47.82	47.47	46.55	45.74	46.39	MgO	40.52	39.08	39.89	39.58	40.44	42.62	39.76
CaO	0.04	0.00	0.04	0.01	0.03	0.02	0.02	0.03	0.05	0.05	CaO	0.02	0.02	0.03	0.04	0.14	0.08	0.03
Total	100.16	101.18	99.98	100.30	100.16	100.17	100.50	100.57	99.03	101.19	Total	87.05	84.90	86.69	85.49	87.05	89.05	86.05
O = 4											H_2O	12.59	12.37	12.69	12.53	12.39	12.75	12.49
											Total*	99.61	97.22	99.35	97.97	99.27	101.74	98.51
											O = 7							
Si	1.00	0.99	1.00	1.00	1.00	0.99	1.01	1.00	1.01	1.01	Si	1.93	1.99	2.02	2.01	1.84	1.83	1.97
Ti	0.00	0.00	0.00	0.00	0.00	0.00	0.00	0.00	0.00	0.00	Ti	0.00	0.00	0.00	0.00	0.00	0.00	0.00
Al	0.00	0.00	0.00	0.00	0.00	0.00	0.00	0.00	0.01	0.01	Al	0.00	0.00	0.01	0.01	0.01	0.01	0.00
Cr	0.00	0.00	0.00	0.00	0.00	0.00	0.00	0.00	0.00	0.00	Cr	0.00	0.00	0.00	0.00	0.00	0.00	0.00
Fe^{3+}	0.00	0.02	0.00	0.01	0.00	0.02	0.00	0.00	0.00	0.00	Fe^{3+}	0.13	0.01	0.00	0.00	0.27	0.23	0.06
Fe^{2+}	0.17	0.15	0.17	0.18	0.19	0.22	0.23	0.27	0.25	0.26	Fe^{2+}	0.08	0.17	0.15	0.14	0.00	0.00	0.13
Mn	0.00	0.00	0.00	0.00	0.00	0.00	0.00	0.00	0.01	0.00	Mn	0.00	0.00	0.00	0.00	0.01	0.00	0.00
Ni	0.01	0.01	0.01	0.01	0.01	0.01	0.01	0.01	0.01	0.01	Ni	0.00	0.00	0.01	0.00	0.01	0.00	0.00
Mg	1.82	1.83	1.81	1.81	1.80	1.76	1.74	1.72	1.71	1.70	Mg	2.85	2.82	2.82	2.83	2.85	2.92	2.83
Ca	0.00	0.00	0.00	0.00	0.00	0.00	0.00	0.00	0.00	0.00	Ca	0.00	0.00	0.00	0.00	0.01	0.00	0.00
Total	3.00	3.00	3.00	3.00	3.00	3.00	3.00	3.00	3.00	3.00	Total	5.00	5.00	5.00	5.00	5.00	5.00	5.00
											OH	4.00	4.00	4.00	4.00	4.00	4.00	4.00
X_{Mg}	0.91	0.92	0.91	0.91	0.90	0.89	0.88	0.86	0.87	0.87		0.97	0.94	0.95	0.95	1.00	1.00	0.95

10.3389/feart.2023.1267211

electron microprobe analyzer (JEOL JXA-8100) at IGGCAS. Well-characterized natural samples were used as standards. The operating conditions for the analyses are as follows: the accelerating voltage was 15 kV for silicates and 20 kV for sulfides; beam current was 10 or 20 nA for silicates and 20 nA for sulfides; focus beam diameter was 3 μm for matrix and big inclusions but 1–2 μm for tiny inclusions; and counting time was 20 s for Na, Mg, Al, Si, Ca, and Fe, 30 s for Cr, and 10 s for K, Mn, Ti, Ni, F, Cl, and S. The JEOL ZAF program was used for matrix correction. Light elements (F, Cl, and Na) were analyzed first during the analytical sequence to minimize the effect of migration. Representative analyses are presented in Figures 5, 6; Table 1.

4 Petrography

Our samples of pseudotachylytes derived from harzburgite were collected at the ore districts of Luobusha and Kangjinla, which, together with the Xiangkashan ore district, are commonly called Luobusha. In outcrop, it is not easy to distinguish between pseudotachylyte veins and the commonly present serpentine veins, which became a huge disadvantage for our recognition. Further identifications were carried out through detailed petrographic observations on a thin-section scale and analysis in the laboratory.

In most cases, the ultramafic pseudotachylytes found in Luobusha formed simple veins and complex networks (Figures 2A–D) within micro-damage zones. The thin-section examination showed that the micro-damage zones containing hairline-thin ultramafic pseudotachylyte veins formed in the harzburgites were less than 2 mm wide in general. A characteristic feature of individual damage zones containing pseudotachylyte veins was that they form an asymmetrical network composed of highly fractured and net-veined host rock fragments. Simple pseudotachylyte veins occurred as the core of the micro-damage zones (Figures 2A–D) and varied in thickness of a small range from ca. 50 μm to an observed width of 200 μm in thin sections. Transmitted light microscopy revealed that the simple pseudotachylyte veins, which occasionally branched off on the local scope, are darker than the host rock fragments. Some opaque mineral assemblages occurred as contact with the dominant transparent minerals with different levels of granularity. These opaque minerals were magnetite and, in general, cemented with serpentine that came into being on account of the hydration of the olivine fragments at a later stage. So, the serpentine takes on banded occurrence stretching parallel to the micro-damage zones (Figures 2A, B, D). Flow structures (Figure 2C) were seen in places, indicating the presence of flow along the fracture. The pseudotachylytes were also associated with cataclasite and ultra-cataclasite veins consisting of ultrafine-grained pulverized lithic fragments and clasts, which make them seem like an “ultrafine fracture zone” across the entire thin section under the optical microscope (Figures 2G, H). The high-magnification microscopic observation roughly revealed that the pseudotachylyte veins are composed of close-knit ultrafine-grained minerals, but their boundary could not be discerned even with the aid of the highest microscopic power (Figure 2D). In view of the petrographic feature described above, in our pilot case study of the pseudotachylyte veins from Luobusha, only via optical microscopy, we recognized these veins just as micro-damage zones or ultra-cataclasites before we were fully convinced that these veins were ultrafine pseudotachylyte by scanning electron microscopy.

For these micro-pseudotachylyte veins, polarizing microscopy can only reveal their rough geometric and morphological features. When we used the eyepiece of ×10 combined with the objective of ×50, the morphology and size of the ultrafine minerals in the pseudotachylyte veins were hardly discerned because the view area was fairly fuzzy and gloomy. As a result, we could not make out the detailed structures of these veins by polarizing microscopy, let alone discover the types of minerals in the veins. Further works have been carried out by scanning electron microscopy and electron microprobe analyses. High-resolution scanning electron microscopy examination and analyses of chemical compositions show that the ultrafine granules in the pseudotachylyte veins are mainly olivine, orthopyroxene, serpentine, spinel, and magnetite. These fine-grained minerals are less than 10 μm, and very few are more than 50 μm, generally cemented by an extremely fine interstitial material. Olivine is the primary component of the pseudotachylyte veins occurring as microphenocrysts, showing zoning from core to rim and as extremely irregular-shaped microlite immersed in the interstitial material (Figures 3A–D). They are less variable in grain size (<10–20 μm). The olivine microphenocrysts in the pseudotachylyte veins are distinctly zoned with darker cores and bright rims, and some grain boundaries are jagged, indicating obvious geochemical zoning (Figures 3B–D). The olivine microlites (<1 μm) are granular and vermicular in shape. In some samples, the olivine microlites within the pseudotachylyte vein are extremely irregular, which can be referred to as dendritic and skeletal crystals (Figures 4A–D). Most of the crystal boundaries are serrated and flame-like. Tabular and fibrous microcrystals developed as interstitial material in the space between poikilitic olivine grains (Figure 4A). The interstitial matrix between microphenocrysts and microlites has a lower average atomic weight and low total oxide analyses (<90%), exhibiting micro-fibers and micro-pores in the BSE images obtained under a high magnification of field emission high-resolution scanning electron microscopy, and the black domains represent micro-cavities in the interstitial matrix between the new-formed crystallites (Figure 3H and Figures 4E, F). Minor orthopyroxene porphyroclasts were cemented by the fine-grained variable amounts of olivine crystallites. Small irregularly shaped chrome-spinel can be spotted among the interstitial matrix. These chrome-spinel crystals are snowflake- or coral-like in form and have a higher average atomic number (bright) along the rims, indicating chemical zonation (Figures 3B, E, G). They are less than 10 μm across and may represent Fe-rich rim overgrowth. In addition, the interstitial matrix contains nanoparticles of Ni sulfide grains. These Ni sulfide grains identified via electron probe microanalysis are often ~1–2 μm across and intersperse among the matrix like a droplet (fine bright spots) and may imply melt occurrence (Figures 4A, C). The pseudotachylyte veins are marked by streaks and bands, indicating compositional variation and textural zoning (Figures 2B, D). BSE (backscattered electron) imaging shows that these pseudotachylyte veins feature the average atomic contrast (zones of different brightness) (Figures 2E, F, 3A). The distribution character of the olivine grains in the bright parts is

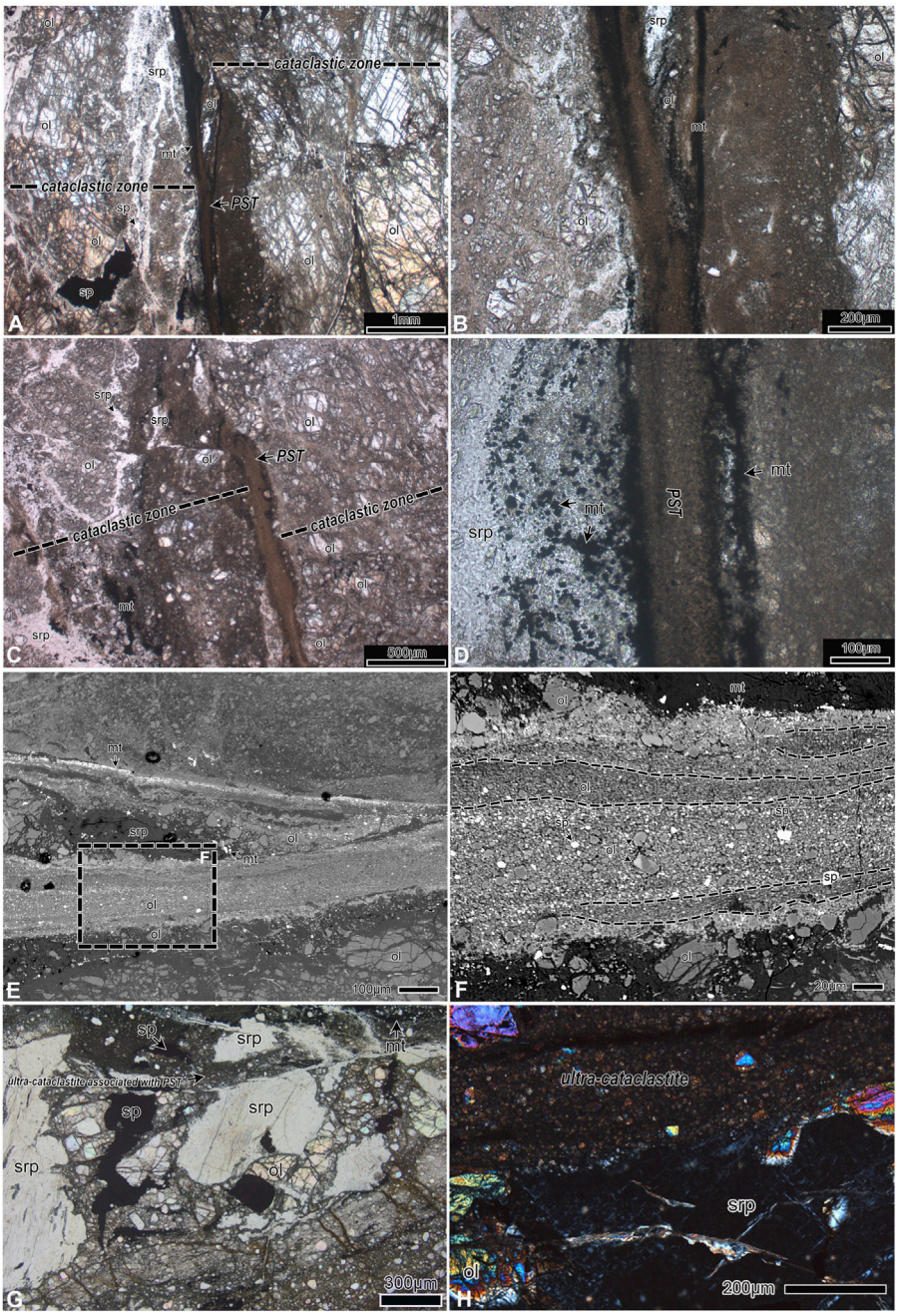

FIGURE 2
Optical and backscattered electron images of pseudotachylyte veins in harzburgites. **(A, B)** Opitcal photomicrograph (plane-polarized light). Hairline-thin pseudotachylyte vein occurred at the central part of the micro-damage zone that is less than 2 mm (max 1.8 mm) wide. The vein can be traced almost continuously across the entire thin section. It should be noted that the vein branched off but did not change the extending direction. The wall rock surfaces are rough with a fractured appearance. The serpentites of the later stage take on banded occurrence stretching parallel to the micro-damage zones. **(C)** Flow banding pseudotachylyte veins occurred within the micro-damage zone. The vein is also hairline-thin and looks like a rivulet making a bend locally under plane-polarized light. **(D)** Microscope examination (plane-polarized light) at high power shows that the pseudotachylyte veins are composed of close-knit ultrafine-grained minerals, but their boundary could not be discerned. Plenty of pulverized minerals are located on both sides of the pseudotachylyte vein. Some opaque mineral assemblages (magnetite) occur as contacts of the dominant transparent minerals with different levels of granularity and are, in general, cemented with serpentites, which were formed by later hydration of the olivine fragments. **(E)** BSE photographs show that pseudotachylyte veins feature the average atomic contrast (zones of different brightness) representing the streaks spotted under the optical scope. **(F)** Framed detail in (E) displays compositional variation and textural zoning of pseudotachylyte veins. **(G, H)** Optical photomicrographs showing that ultracataclastite associated with pseudotachylyte veins and ultracataclastite transecting serpentine porphyroclast under plane-polarized light and cross-polarized light, respectively. Mineral abbreviations are according to the work of Whitney and Evans (2010), with ol referring to olivine, srp to serpentite, mt to magnetite, sp to spinel, and cmt to chromite.

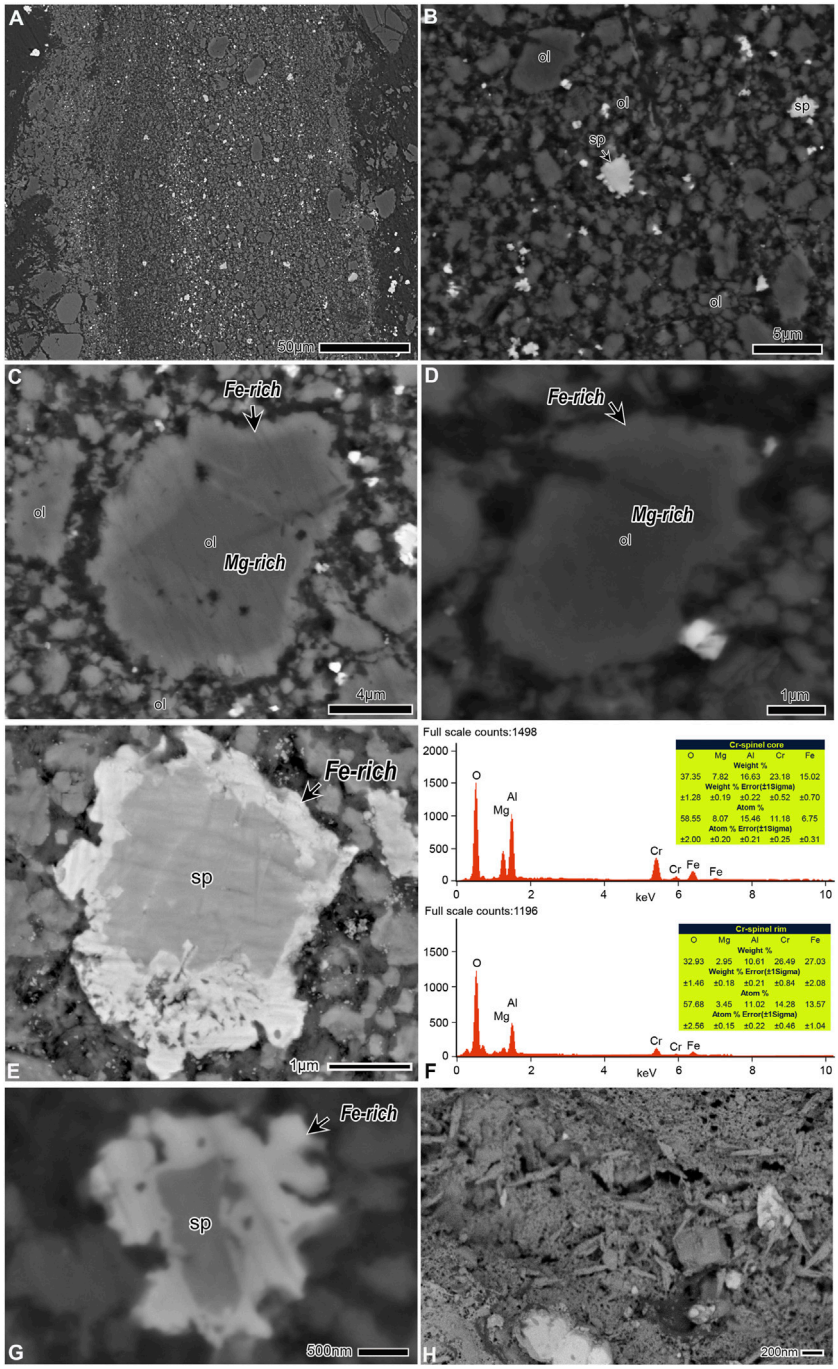

FIGURE 3
Back-scattered electron images obtained using field emission electron microscopy. **(A)** The average atomic contrast is evident. The darker part is attributed to a cluster of densely packed olivine microlites and interstitial material. Spinel and magnetite particles arranged along the extension direction of the pseudotachylyte vein forming a narrow bright stripe. **(B)** Sub-idiomorphic olivine microphenocrysts and vermicular olivine microlites are cemented by interstitial material. **(C, D)** Zoning texture of olivine grains. The darker core is relatively rich in Mg, whereas the bright rim is relatively rich in Fe. It should be noted that the grain boundaries are uneven and serrated. **(E, G)** Chemically zoned chrome-spinel with an Fe-rich rim overgrowth. **(F)** Energy-dispersive spectrometry result reveals that the rim of the chrome-spinel in **(E)** is rich in Fe compared to the core. **(H)** The micro-cavities are visible in the micro-fibrous and micro-porous interstitial material.

that the microphenocrysts are surrounded by densely packed irregularly shaped crystals. These crystals are very tiny, generally not more than 5 microns, which are recognized as olivine microlites. However, some of the microphenocrysts are more than 10 microns across. The matrix in the gap between the particles is composed of serpentine minerals (Figures 2F, 3A). The darker part of these pseudotachylytes consists of worm-like olivine microlites densely interconnected with each other. The interspace matrix also features a lower average atomic weight (Figures 3A, B). Ultracataclastite and ultracataclastite associated with pseudotachylyte veins transected serpentine (Figures 2G, H). Within the

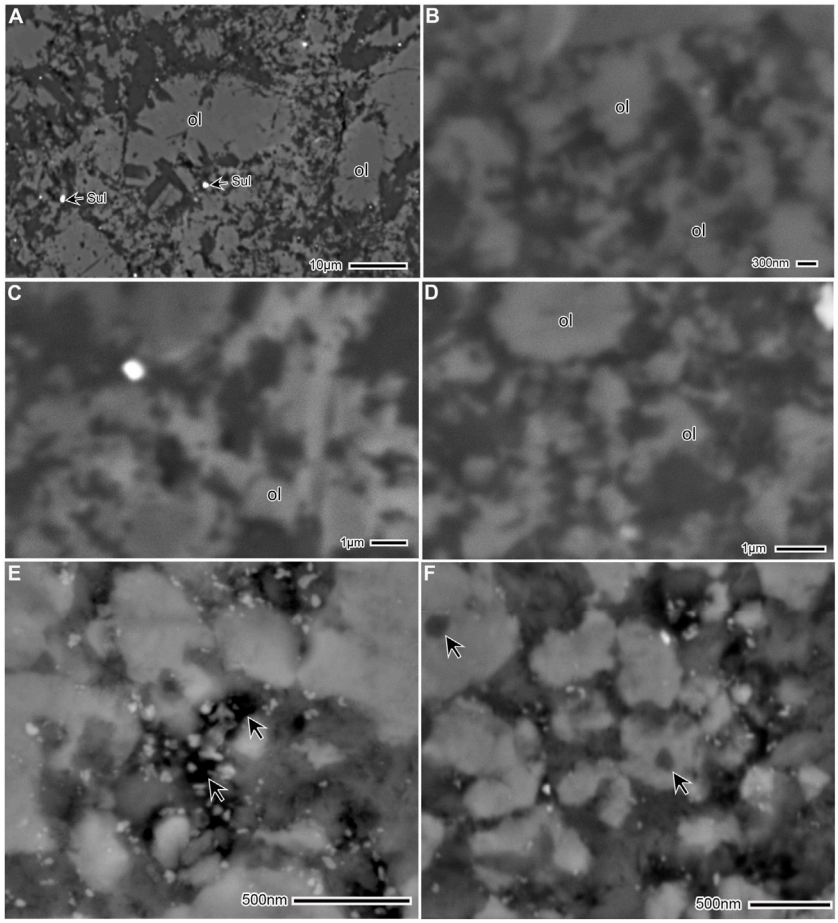

FIGURE 4
Back-scattered electron images showing the microtexture of microlites of olivine and the interstitial matrix. **(A)** Poikilitic and skeletal olivine microlites and interstitial matrix. Most of the crystal boundaries are serrated and flame-like. The Ni sulfide (Sul) granules should also be noticed. **(B–D)** High-resolution scanning electron microscopy photographs of micro-dendritic and skeletal microlites of olivine and the interstitial matrix. **(E, F)** The olivine microlites are cemented by flocculent and spongiform interstitial materials. Extremely tiny globular inclusions (arrowed) in the core of the olivine microlites are shown. They have a lower average atomic weight compared to host olivine microlites and are speculated to be prograde serpentine inclusions. The arrows in **(E)** indicate miniscule micro-cavities.

pseudotachylyte, it is visible that some punctiform inclusions developed in the olivine microlites and might be serpentine presumably (Figures 4E, F).

5 Mineral chemistry

The comparative study of chemical composition between pseudotachylyte veins and host rock is a common analytical method used by researchers. Representative analyses are presented in Figures 5, 6; Table 1. Mineral formulae were calculated by assuming stoichiometry and charge balance (Droop, 1987). Electron microprobe (EMP) analyses show that the olivine in the host harzburgite is homogeneous (Fo_{90-92}) (Figure 5), whereas olivine microphenocrysts in the pseudotachylyte are quite heterogeneous, ranging from Fo_{85}–Fo_{92}, and display chemical zonation characteristics with Mg-rich cores (Fo_{90-92}) and higher Fe-content along the margins (Fo_{86-89}) (Table 1). The forsterite contents of the microlites fall in between the former two occurrences of olivine in the diagrams (Figure 5), ranging from Fo_{87}–Fo_{92}. The significant feature of the olivine microlites is that they contain significant amounts of Ca, Al, and Cr compared with the olivine in the host harzburgite recognized from the diagrams (Figures 5, 6). However, it is noted that olivine microlites and the microphenocrysts in pseudotachylyte have a lower Ni content compared to the host harzburgite olivine (Figures 5, 6).

The pseudotachylyte micro-fibrous and micro-porous interstitial matrix between microphenocrysts and microlites contains a large number of extremely fine materials below the spatial resolution of our instrumentation, which makes it difficult to accurately determine the chemical composition. BSE images show that the interstitial matrix has a low average atomic weight. EMP analyses give a range of ultramafic compositions with SiO_2 and MgO contents from 38.9%–42.5% and 39.0%–42.62%, respectively. The analyses give low totals ranging from 84.9%–89.05% and total*s 97.2%–101.74% recalculated on an anhydrous basis to a total of 100% (see Table 1). It can be interpreted that the analyses represent mixed data and do not reconcile with real mineral compositional variations.

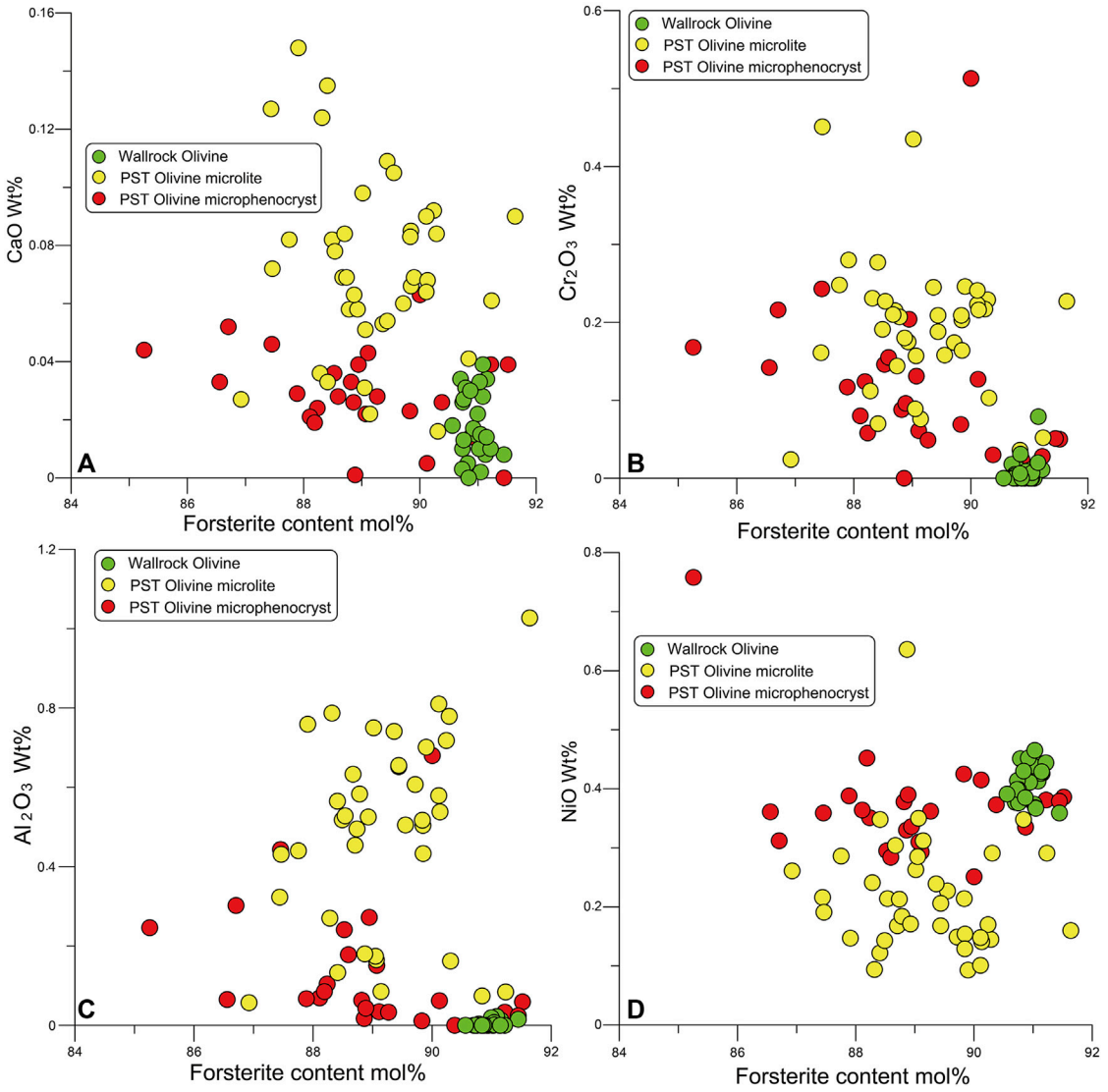

FIGURE 5
Ca **(A)**, Cr **(B)**, Al **(C)**, and Ni **(D)** contents versus the Fo content of olivine in three main occurrences from the pseudotachylyte veins obtained by electron microprobe analysis.

In addition, the rims of zoned irregularly shaped chrome-spinel are higher in Fe (27.03 wt%) and lower in Mg (2.95 wt%) than their cores that contain lower Fe (15.02 wt%) but higher Mg (7.82 wt%) obtained by using an energy-dispersive spectrometer (EDS) equipped on the scanning electron microscope (Figure 3F). Despite a semi-quantitative analysis, the Mg–Fe zoning from core to rim has been well revealed.

6 Discussion

6.1 Type of injection vein

Most of the sampled veinlets with dark-brown color, dense and aphanitic appearance, and occurrence as both simple veins and irregular networks are typically very thin (~2 cm), similar to the ultramafic pseudotachylyte from a spinel lherzolite mass in the Ivrea–Verbano zone, Northern Italy (Obata and Karato, 1995). Most pseudotachylyte veins in mantle peridotite from the Alpine subduction complex of Corsica are less than 2 cm thick (Andersen and Austrheim, 2006). The pseudotachylyte veins from the Luobusha peridotite complex are so hairline-thin that they can only be identified in thin sections and can hardly be discerned in outcrop. Very thin injection veins require extremely low viscosity for the melt. High-pressure experiments showed that ultramafic melts have very low viscosities of 10^{-1} Pa·s or less (Suzuki et al., 2001). Such low viscosity is consistent with the intrusive features associated with the mm-thin ultramafic pseudotachylytes. The mm-to-cm-thin veins must have been emplaced and solidified in seconds and ca 10–15 min, respectively (Andersen and Austrheim, 2006). The experimentally generated injection veins of ultramafic pseudotachylyte that formed during the serpentinite high-velocity friction experiments ranged in width from 0.1 to 0.5 mm (Lin et al., 2013). Based on vein geometry, the individual veins and network veins within Luobusha peridotite are

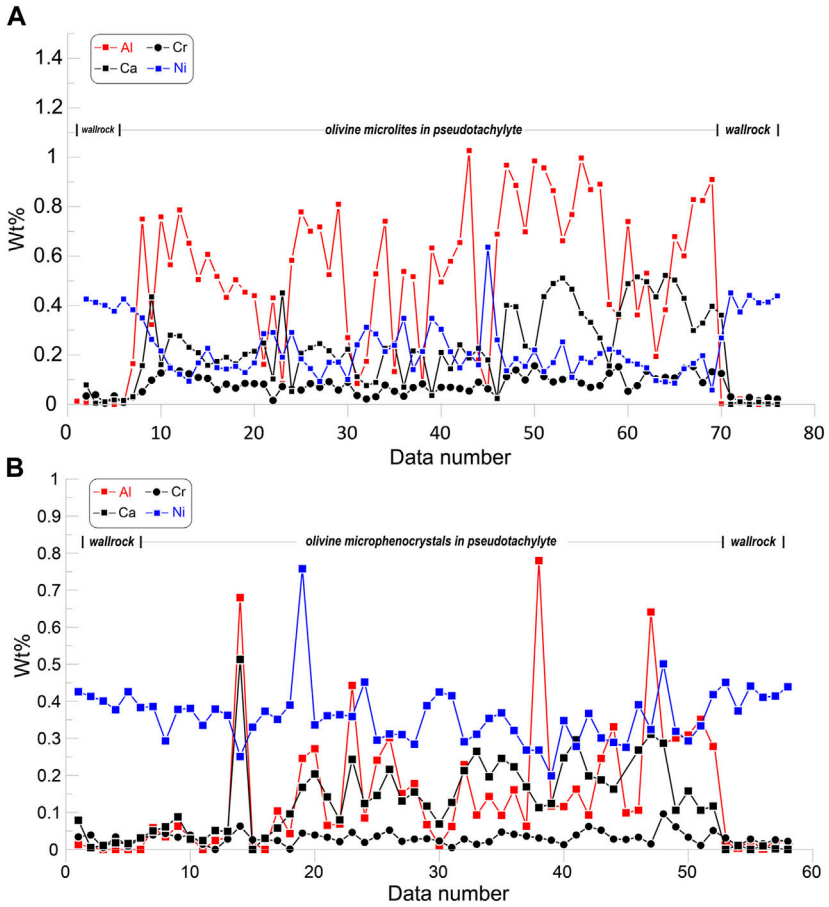

FIGURE 6
Compositional profiles of olivine microlites **(A)**, microphenocrysts **(B)**, and wall rock olivine within a transect spanning the pseudotachylyte and wall rock on each side.

injection veins. The fragment-bearing frictional melt moves rapidly from the generation zone to the void spaces within dilational fractures that formed at the same time as the pseudotachylyte. Rapid injection under thermal pressurization of the melt associated with expansion is related to frictional heating within the pseudotachylyte generation zone and syn-dilational fractures formed by seismic rupture (Lin, 2008). Dilational fractures often contain a zone of cataclasite (Lin, 2008), which can account for the occurrence that pseudotachylyte veins are bound by micro-damage zones.

6.2 Diagnostic quenching microtextures and chemical inhomogeneties

The microlites in the pseudotachylyte veins are extraordinarily fine-grained, showing certain melting and recrystallization characteristics. In particular, some olivine microphenocrysts display characteristic textures of minerals crystallized from the melt and chemical zonation generated at high temperatures. The olivine crystals are zoned with Mg-rich cores and more Fe-rich margins. This zoning pattern is typical evidence of crystallization from friction melts (Obata and Karato, 1995; Andersen and Austrheim, 2006). The preservation of Fe–Mg zoning at the scale of ~1 μm indicates that the cooling time was shorter than 10^2 s, which suggests that the formation of the pseudotachylyte was associated with co-seismic faulting (Buening and Buseck, 1973; Obata and Karato, 1995). In addition, snowflake- and coral-like chrome-spinel are chemically zoned as well. The spinel crystals have Mg–Fe zoning from core to rim, indicating Fe-rich rim overgrowth, which are similar to those described by Andersen in Corsica ultrabasic pseudotachylyte veins (Andersen and Austrheim, 2006). The compositional variations between the wall rock and the pseudotachylyte minerals are blindingly obvious. Olivine in the host harzburgite is more restricted (Fo_{90-92}), whereas the microphenocrysts in the pseudotachylytes are very heterogeneous, ranging from Fo_{85}–Fo_{92}. The forsterite contents of the microlites fall in between the former two occurrences of olivine in the diagrams (Figure 5), ranging from Fo_{87}–Fo_{92}. The microphenocrysts, especially some microlites in the pseudotachylyte, have higher CaO contents than the host harzburgite olivine and also have higher Cr_2O_3 and Al_2O_3 (Figures 5, 6). The high Cr content of the olivine microcrystals supports the hypothesis of a high-temperature origin for the pseudotachylyte. High abundances of Ca and Cr in olivine are often observed for rapidly grown crystals from high-temperature ultramafic magmas, such as komatiites (Arndt et al., 1977; Obata and Karato, 1995). Olivine crystals can

accommodate significant amounts of Cr^{2+} at high temperatures, even at typical terrestrial oxidation conditions, and the solubility of Cr^{2+} increases effectively with an increase in temperature (Li et al., 1995; Obata and Karato, 1995). The high Ca and Cr contents of olivine microphenocrysts support the view that their zoning pattern is consistent with interpreting that the olivine is precipitated as crystal from the melt. However, it is noted that the olivine microlites and the microphenocrysts in pseudotachylyte have a lower Ni content compared to the host harzburgite olivine. Some nanoparticles of Ni sulfide droplets have been observed in the interstitial matrix, which is akin to the previously described examples of pseudotachylyte from the Balmuccia peridotite (Ueda et al., 2008) and the Alpine Corsica complex (Andersen and Austrheim, 2006). Both of them were interpreted to crystallize directly from the frictional melt. The loss of Ni in the olivine during the melting process results in the formation of sulfide in the newly crystallized pseudotachylyte matrix, which may account for observed lower Ni contents in the newly formed microcrystalline olivine. As a consequence, we interpret the high Ca and Cr contents and lower Ni contents of olivine grains to be crystallized directly from the friction melt. The chemical inhomogeneties, that is to say, the zoning patterns as well as the compositional variations between the host harzburgite and the pseudotachylyte minerals, are very similar to those of the pseudotachylyte from the Balmuccia peridotite and the Alpine Corsica complex (Obata and Karato, 1995; Andersen and Austrheim, 2006).

The interstitial matrix between microphenocrysts and microlites appears micro-fibrous and micro-porous. The micro-cavities are visible when observed by field emission high-resolution scanning electron microscopy (SEM) in the interstitial matrix between the newly formed crystallites. SEM examination shows that the interstitial matrix between microphenocrysts and microlites has a lower average atomic weight and low total oxide analyses (<90%) exhibiting fibrous and cotton-like in the BSE image obtained under high magnification of SEM, and the black domains represent cavities (Figures 3H, 4E, F). These cavities probably represent vesicles present at the melt stage since olivine crystals have crystallized into the cavities. The presence of a micro-vesicular interstitial matrix suggests that the frictional melting was accompanied by high fluid pressures, which, at least locally, was sufficient to release a free gas phase from the melt. The fibrous domains of the matrix were probably formed via the devitrification of the original glass to serpentine (Andersen and Austrheim, 2006).

6.3 Rate of deformation and co-seismic transient high-pressure metamorphism (dehydration) in the crust

Rock textures and microstructures can be used to infer the rate of deformation and associated high-pressure metamorphism. For instance, quench textures formed by spherulites, dendrites, and skeletal, acicular, or poikilitic microlites can be recognized in rocks crystallized from volcanic and friction or shock melts (Sibson, 1975; Lin, 2008; Yang et al., 2016). The dendritic textures are formed by rapid cooling only under limited conditions where the growth rate of crystals is fast in comparison to the nucleation rate (Chalmers, 1964). The crystallization of microlites from friction melt would imply that the duration of the high-pressure metamorphism was very brief owing to the co-seismic nature of the melt (Yang et al., 2016). Furthermore, porphyroclasts dominated by thermally rounded olivine and minor orthopyroxene can be observed. The disequilibrium feature of the clasts suggests that there exists very rapid heating (Swanson, 1992).

It is observed that ultracataclastite veins are associated with pseudotachylyte transecting serpentine. In the sampled pseudotachylytes, some extremely tiny globular inclusions (~100 nm) can be observed in the core of the olivine microlites under a high-resolution scanning electron microscope. These inclusions have a lower average atomic weight compared to host olivine microlites (Figures 4E, F). As they are extremely minuscule with a nanometer scale of particle size, existing analytical methods are not suitable for mineral identification and chemical composition analysis. Based on the lower average atomic number, these tiny inclusions would be prograde serpentine. For complete reaction, serpentine disappears before olivine is crystallized during prograde metamorphism, simulated by P-T pseudosection for the harzburgite in the system $CaO–FeO–MgO–SiO_2–H_2O$ (Huang et al., 2014). Reaction kinetics has played a role in the preservation of portions of the serpentinite minerals in the peridotite minerals. The preservation of serpentine (lizardite) as inclusions in the high-pressure minerals implies that the breakdown of lizardite was slower than the P-T increase such that olivine started to grow while a portion of lizardite persisted (Huang et al., 2014), which means that the high-pressure metamorphism took place rapidly. Frictional heating in ultracataclastite associated with pseudotachylyte veins would dehydrate hydrous minerals (serpentine) to their corresponding products (olivine) of high-pressure metamorphism. This characteristic and attractive feature was also observed in pseudotachylyte-like veins from Corsica, where serpentine inclusions were partly surrounded by neoblastic olivine (Austrheim and Andersen, 2004).

A question arises then as to how a prograde serpentine could be enclosed in the olivine microlites quenching from the melt. High-velocity friction experiments on serpentinite under conditions equivalent to large amounts of earthquake slip show that both serpentine and olivine minerals were melted by friction heating. Rapid serpentine dehydration occurred in a zone of up to ~3 mm wide. Dehydration reactions of serpentine can be caused by frictional heating that accompanies frictional melting in the slip zone and its bounding zones (Lin et al., 2013). The microtexture shown in Figure 4F implies a partial melting and multiple stages of co-seismic friction. The serpentine minerals were melted during the formation of the former pseudotachylyte and then quenched into microlites of serpentine. Further frictional heating overprinting pre-existing pseudotachylyte resulted in the breakdown (dehydration) of serpentine into high-pressure microlites of olivine.

The wall rock to the pseudotachylyte and associated ultracataclastite was subjected to serpentinization after having emplaced in the crust and then transformed back into peridotite by subsequent high-pressure metamorphism at Luobusha (Huang et al., 2014). The pseudotachylytes were generated in the crust after the high-pressure metamorphism and did not recede to a greater depth. If the rocks were held at great depths after the seismic events, then the quenching textures would have been erased due to

continuous mineral growth. So, we hold the opinion that flash ultra-comminution and frictional heating may release fluids by localized heat-driven prograde reactions in the crust, which appears to be the more likely process for the preservation of the petrographic features in the present study.

6.4 Physical origin of pseudotachylyte in Luobusha peridotite

Clarification of the physical origin of pseudotachylyte is complicated by its very fine-grained nature, the common presence of devitrified and recrystallized material and rock fragments, and the obscuring effects of subsequent deformation, alteration, and metamorphism (Lin, 2008). It is clear that glass or glassy material within pseudotachylyte indicates the generation of melt during its formation, but the converse is not true: the absence of glass or glassy material is not a diagnostic test for the melting origin for pseudotachylyte because primary glass or glassy material can be devitrified during subsequent alteration and/or metamorphism (Lin, 2008). In addition to the melting-origin pseudotachylyte, crushing-origin pseudotachylytes, which are generated by rapid comminution and injection during seismic faulting, are also considered to represent fossil earthquakes, as with melt-origin pseudotachylytes (Kano et al., 2004; Lin, 2008). Such veins are mainly composed of fine-grained fragments of the wall rock, with little or no evidence of melting (Lin, 2008). However, there exists a gradation from melting-origin pseudotachylyte, which is mostly composed of glass or glass-derived material, to crushing-origin pseudotachylyte (Lin, 2008). The pseudotachylytes in Luobusha peridotite are often associated with ultracataclastite veinlets and are of injection vein type. The pseudotachylytes occurred as thin layers in the core of micro-damage zones. In the immediate vicinity of the pseudotachylyte veins, it is visible that the olivine, pyroxene, and serpentine display strong brittle deformation, and a large number of network cracks developed in the harzburgite wall rock. The cracks are filled with extremely fine crushed minerals of irregular shape. Banding defined by clusters of microphenocryst, microlites, and interstitial material and variable content of thermally rounded olivine in the pseudotachylytes indicate inefficient mixing of the melt, which implies mixed genesis of a combination of crushing and melting. Flash ultra-comminution was associated with frictional heating. It follows from the description and interpretations stated earlier that strong abrasion and ultra-comminution generated during rapid seismic faulting melted rock within the fault zone and fluidized ultrafine-grained material, ultimately producing pseudotachylyte in the studied peridotite rocks.

7 Conclusion

Large paleo-earthquakes have been frozen in ultramafic pseudotachylyte from the Luobusha ophiolite complex in the Yarlung Zangbo suture zone, evidenced by the petrography and mineral chemistry data presented here. The hairline-thin pseudotachylyte veins were formed by rapid injection along dilational fractures from the generation zone produced by strong abrasion and ultra-comminution revealed by the characteristic microtextures and chemical inhomogeneties. Quenching microtextures of olivine and localized shear heat-driven prograde reaction textures demonstrate that the duration of frictional heating within seismic slip zones and associated dehydration reaction of serpentine to olivine was very brief. The Luobusha peridotite is metamorphogenic, which was subjected to serpentinization after having emplaced in the crust, followed by transformation back into peridotite during subsequent high-pressure metamorphism. The pseudotachylytes were generated in the crust after the high-pressure metamorphism and did not recede to a deeper depth. Flash ultra-comminution associated with frictional heating may release fluids via localized heat-driven prograde reactions in the crust.

Data availability statement

The original contributions presented in the study are included in the article/Supplementary Material; further inquiries can be directed to the corresponding authors.

Author contributions

HZ: conceptualization, data curation, investigation, methodology, software, and writing–original draft. XX: conceptualization, funding acquisition, supervision, and writing–review and editing. SY: investigation, methodology, software, and writing–review and editing.

Funding

The authors declare financial support was received for the research, authorship, and/or publication of this article. This work was financially supported by the National Natural Science Foundation of China (Grant 41941016).

Acknowledgments

The authors are very grateful to Tsering Norbu, Lobsang, Tenzin, Nyima Tashi, and Phuntsok for providing great help with field works and sampling at a high altitude.

Conflict of interest

The authors declare that the research was conducted in the absence of any commercial or financial relationships that could be construed as a potential conflict of interest.

Publisher's note

References

Allégre, C. J., Courtillot, V., Tapponnier, P., Hirn, A., Mattauer, M., Coulon, C., et al. (1984). Structure and evolution of the Himalaya–Tibet orogenic belt. *Nature* 307, 17–22. doi:10.1038/307017a0

Andersen, T. B., Austrheim, H., Deseta, N., Silkoset, P., and Ashwal, L. D. (2014). Large subduction earthquakes along the fossil moho in alpine Corsica. *Geology* 42, 395–398. doi:10.1130/G35345.1

Andersen, T. B., and Austrheim, H. (2006). Fossil earthquakes recorded by pseudotachylytes in mantle peridotite from the Alpine subduction complex of Corsica. *Earth Planet. Sci. Lett.* 242, 58–72. doi:10.1016/j.epsl.2005.11.058

Andersen, T. B., Mair, K., Austrheim, H., Podladchikov, Y. Y., and Vrijmoed, J. C. (2008). Stress release in exhumed intermediate and deep earthquakes determined from ultramafic pseudotachylyte. *Geol* 36, 995. doi:10.1130/G25230A.1

Angiboust, S., Agard, P., Yamato, P., and Raimbourg, H. (2012). Eclogite breccias in a subducted ophiolite: A record of intermediate-depth earthquakes? *Geology* 40, 707–710. doi:10.1130/G32925.1

Arndt, N. T., Naldrett, A. J., and Pyke, D. R. (1977). Komatiitic and iron-rich tholeiitic lavas of munro township, northeast ontario. *J. Petrology* 18, 319–369. doi:10.1093/petrology/18.2.319

Austrheim, H., and Andersen, T. B. (2004). Pseudotachylytes from Corsica: fossil earthquakes from a subduction complex. *Terra nova.* 16, 193–197. doi:10.1111/j.1365-3121.2004.00551.x

Austrheim, H., and Boundy, T. M. (1994). Pseudotachylytes generated during seismic faulting and eclogitization of the deep crust. *Sci. New Ser.* 265, 82–83. doi:10.1126/science.265.5168.82

Austrheim, H., Erambert, M., and Engvik, A. K. (1997). Processing of crust in the root of the caledonian continental collision zone: the role of eclogitization. *Tectonophysics* 273, 129–153. doi:10.1016/S0040-1951(96)00291-0

Austrheim, H. (2013). Fluid and deformation induced metamorphic processes around moho beneath continent collision zones: examples from the exposed root zone of the caledonian mountain belt, w-norway. *Tectonophysics* 609, 620–635. doi:10.1016/j.tecto.2013.08.030

Bucher, K. (2005). Blueschists, eclogites, and decompression assemblages of the zermatt-saas ophiolite: high-pressure metamorphism of subducted tethys lithosphere. *Am. Mineralogist* 90, 821–835. doi:10.2138/am.2005.1718

Buening, D. K., and Buseck, P. R. (1973). Fe-Mg lattice diffusion in olivine. *J. Geophys. Res.* 78, 6852–6862. doi:10.1029/JB078i029p06852

Chalmers, B. (1964). *Principles of solidification*. New York: Robert E. Krieger Pub, 319.

Chen, X.-Z., Xia, B., Li, J.-F., Yu, M., Zhang, L.-F., Huang, Q.-T., et al. (2011). Isotopic characteristics and genesis of mantle peridotite from the Luobusha ophiolite. *Geotect. Metallogenia (in Chinese)* 35, 85–94. doi:10.16539/j.ddgzyckx.2011.01.007

Debret, B., Nicollet, C., Andreani, M., Schwartz, S., and Godard, M. (2013). Three steps of serpentinization in an eclogitized oceanic serpentinization front (lanzo massif - western alps): eclogitized serpentinization front (lanzo). *Journal of Metamorphic Geology* 31, 165–186. doi:10.1111/jmg.12008

Deseta, N., Andersen, T. B., and Ashwal, L. D. (2014). A weakening mechanism for intermediate-depth seismicity? Detailed petrographic and microtextural observations from blueschist facies pseudotachylytes, cape corse, Corsica. *Tectonophysics* 610, 138–149. doi:10.1016/j.tecto.2013.11.007

Droop, G. T. R. (1987). A general equation for estimating Fe $^{3+}$ concentrations in ferromagnesian silicates and oxides from microprobe analyses, using stoichiometric criteria. *Mineral. mag.* 51, 431–435. doi:10.1180/minmag.1987.051.361.10

Evans, B. W., and Cowan, D. S. (2012). A Melt origin for spinifex-textured metaperidotite in the Cerro del Almirez massif, southern Spain. *American Journal of Science* 312, 967–993. doi:10.2475/09.2012.01

Evans, B. W., and Trommsdorff, V. (1978). Petrogenesis of garnet lherzolite, cima di Gagnone, lepontine alps. *Earth and Planetary Science Letters* 40, 333–348. doi:10.1016/0012-821X(78)90158-9

Huang, M.-X., Yang, J.-J., Powell, R., and Mo, X. (2014). High-pressure metamorphism of serpentinized chromitite at Luobusha (southern Tibet). *American Journal of Science* 314, 400–433. doi:10.2475/01.2014.11

Jin, D., Karato, S., and Obata, M. (1998). Mechanisms of shear localization in the continental lithosphere: inference from the deformation microstructures of peridotites from the ivrea zone, northwestern italy. *Journal of Structural Geology* 20, 195–209. doi:10.1016/S0191-8141(97)00059-X

John, T., and Schenk, V. (2006). Interrelations between intermediate-depth earthquakes and fluid flow within subducting oceanic plates: constraints from eclogite facies pseudotachylytes. *Geol* 34, 557. doi:10.1130/G22411.1

Kano, K., Lin, A., Fukui, A., and Tanaka, H. (2004). Pseudotachylytes of crushing origin from the Shimotsuburai fault of the Itoigawa-Shizuoka Tectonic Line active fault system, central Japan. *Jour. Geol. Soc. Japan* 110, 779–790. doi:10.5575/geosoc.110.779

Karato, S. (1989). Grain growth kinetics in olivine aggregates. *Tectonophysics* 168, 255–273. doi:10.1016/0040-1951(89)90221-7

Li, J.-P., O'Neill, H. S. C., and Seifert, F. (1995). *Subsolidus phase relations in the system MgO-S⅄ -Cr-0 in equilibrium with metallic Cr, and their significance for the petrochemistry of chromium*. 36.

Lin, A. (2008). *Fossil earthquakes: The formation and preservation of pseudotachylytes*. Berlin, Heidelberg: Springer Berlin Heidelberg. doi:10.1007/978-3-540-74236-4

Lin, A., and Shimamoto, T. (1998). Selective melting processes as inferred from experimentally generated pseudotachylytes. *Journal of Asian Earth Sciences* 16, 533–545. doi:10.1016/S0743-9547(98)00040-3

Lin, A., Takano, S., Hirono, T., and Kanagawa, K. (2013). Coseismic dehydration of serpentinite: evidence from high-velocity friction experiments. *Chemical Geology* 344, 50–62. doi:10.1016/j.chemgeo.2013.02.013

Lund, M. G., and Austrheim, H. (2003). High-pressure metamorphism and deep-crustal seismicity: evidence from contemporaneous formation of pseudotachylytes and eclogite facies coronas. *Tectonophysics* 372, 59–83. doi:10.1016/S0040-1951(03)00232-4

Magloughlin, J. F. (1992). Microstructural and chemical changes associated with cataclasis and frictional melting at shallow crustal levels: the cataclasite-pseudotachylyte connection. *Tectonophysics* 204, 243–260. doi:10.1016/0040-1951(92)90310-3

McKenzie, D., and Brune, J. N. (1972). Melting on fault planes during large earthquakes. *Geophysical Journal International* 29, 65–78. doi:10.1111/j.1365-246X.1972.tb06152.x

McNulty, B. A. (1995). Pseudotachylyte generated in the semi-brittle and brittle regimes, Bench Canyon shear zone, central Sierra Nevada. *Journal of Structural Geology* 17, 1507–1521. doi:10.1016/0191-8141(95)00052-F

Morgunova, A. A., and Perchuk, A. L. (2012). Petrology of precambrian metaultramafites of the gridino high-pressure complex (*karelia*). *Russian Geology and Geophysics* 53, 131–146. doi:10.1016/j.rgg.2011.12.011

Naemura, K., Hirajima, T., and Svojtka, M. (2009). The pressure–temperature path and the origin of phlogopite in spinel–garnet peridotites from the blanský les massif of the moldanubian zone, Czech republic. *Journal of Petrology* 50, 1795–1827. doi:10.1093/petrology/egp052

Obata, M., and Karato, S. (1995). Ultramafic pseudotachylite from the Balmuccia peridotite, Ivrea-Verbano zone, northern Italy. *Tectonophysics* 242, 313–328. doi:10.1016/0040-1951(94)00228-2

Piccardo, G. B., Ranalli, G., and Guarnieri, L. (2010). Seismogenic shear zones in the lithospheric mantle: ultramafic pseudotachylytes in the lanzo peridotite (western alps, nw italy). *Journal of Petrology* 51, 81–100. doi:10.1093/petrology/egp067

Ravna, E., Kullerud, K., and Ellingsen, E. (2006). Prograde garnet-bearing ultramafic rocks from the tromsø nappe, northern scandinavian Caledonides☆. *Lithos* 92, 336–356. doi:10.1016/j.lithos.2006.03.058

Rebay, G., Spalla, M. I., and Zanoni, D. (2012). Interaction of deformation and metamorphism during subduction and exhumation of hydrated oceanic mantle: insights from the western alps: deformation-metamorphism of hp serpentinites. *Journal of Metamorphic Geology* 30, 687–702. doi:10.1111/j.1525-1314.2012.00990.x

Robinson, P. T., Bai, W.-J., Malpas, J., Yang, J.-S., Zhou, M.-F., Fang, Q.-S., et al. (2004). Ultra-high pressure minerals in the Luobusa Ophiolite, Tibet, and their tectonic implications. *SP* 226, 247–271. doi:10.1144/GSL.SP.2004.226.01.14

Sibson, R. H. (1975). Generation of pseudotachylyte by ancient seismic faulting. *Geophys J Int* 43, 775–794. doi:10.1111/j.1365-246X.1975.tb06195.x

Spray, J. G. (1987). Artificial generation of pseudotachylyte using friction welding apparatus: simulation of melting on a fault plane. *Journal of Structural Geology* 9, 49–60. doi:10.1016/0191-8141(87)90043-5

Spray, J. G. (1995). Pseudotachylyte controversy: fact or friction? *Geol* 23, 1119. doi:10.1130/0091-7613(1995)023<1119:PCFOF>2.3.CO;2

Suzuki, A., (2001). Viscosity of komatiite magma at high pressure. Bayerishes Geoinstitut Annual Report Available at: http://www.bgi.uni-bayreuth.de/annual_report/navigat.php3?year=2001.

Swanson, M. T. (1992). Fault structure, wear mechanisms and rupture processes in pseudotachylyte generation. *Tectonophysics* 204, 223–242. doi:10.1016/0040-1951(92)90309-t

Trommsdorff, V., Sánchez-Vizcaíno, V. L., Gómez-Pugnaire, M. T., and Müntener, O. (1998). High pressure breakdown of antigorite to spinifex-textured olivine and orthopyroxene, SE Spain. *Contributions to Mineralogy and Petrology* 132, 139–148. doi:10.1007/s004100050412

Tullis, J., and Yund, R. A. (1982). Grain growth kinetics of quartz and calcite aggregates. *The Journal of Geology* 90, 301–318. doi:10.1086/628681

Ueda, T., Obata, M., Di Toro, G., Kanagawa, K., and Ozawa, K. (2008). Mantle earthquakes frozen in mylonitized ultramafic pseudotachylytes of spinel-lherzolite facies. *Geol* 36, 607. doi:10.1130/G24739A.1

Whitney, D. L., and Evans, B. W. (2010). Abbreviations for names of rock-forming minerals. *American Mineralogist* 95, 185–187. doi:10.2138/am.2010.3371

Wu, F.-Y., Liu, C.-Z., Zhang, L.-L., Zhang, C., Wang, J.-G., Ji, W.-Q., et al. (2014). Yarlung Zangbo ophiolite:A critical updated view. *Acta Petrol Sinica (in Chinese with English abstract)* 30, 293–325. doi:10.3986/AGS48106

Yang, J.-J., Fan, Z.-F., Yu, C., and Yan, R. (2014a). Coseismic formation of eclogite facies cataclasite dykes at Yangkou in the Chinese Su-Lu UHP metamorphic belt. *J. Meta. Geol.* 32, 937–960. doi:10.1111/jmg.12101

Yang, J.-J., Huang, M.-X., and Naemura, K. (2013). Towards a law for the metamorphic evolution of mantle-derived orogenic peridotites. *Acta Petrologica Sinica (in Chinese with English abstract)* 29 (5), 1479–1485.

Yang, J.-J., Huang, M.-X., Wu, Q.-Y., and Zhang, H.-R. (2014b). Coesite-bearing eclogite breccia: implication for coseismic ultrahigh-pressure metamorphism and the rate of the process. *Contrib Mineral Petrol* 167, 1013. doi:10.1007/s00410-014-1013-7

Yang, J.-J., and Powell, R. (2008). Ultrahigh-pressure garnet peridotites from the devolatilization of sea-floor hydrated ultramafic rocks. *Journal of Metamorphic Geology* 26, 695–716. doi:10.1111/j.1525-1314.2008.00780.x

Yang, J.-J. (2003). Relict edenite in a garnet lherzolite from the Chinese Su.Lu UHP metamorphic terrane: implications for metamorphic history. *American Mineralogist* 88, 180–188. doi:10.2138/am-2003-0121

Yang, J.-J., Zhang, H.-R., Chen, A.-P., and Huang, M.-X. (2016). Petrological evidence for shock-induced high- *P* metamorphism in a gabbro. *J. Metamorph. Geol.* 35, 121–140. doi:10.1111/jmg.12223

Zhang, H.-Y., Ba, D.-Z., Guo, T.-Y., Mo, X.-X., Xue, Y.-Z., Ruan, G.-F., et al. (1996). *Study of Luobusha typical chromite ore deposit Qusong county (in Chinese)*. Tibet (Xizang), Lhasa: Xizang People Press, 1–181.

Zhou, M.-F., Robinson, P. T., Malpas, J., and Li, Z. (1996). Podiform chromitites in the Luobusa ophiolite (southern Tibet): implications for melt-rock interaction and chromite segregation in the upper mantle. *J Petrology* 37, 3–21. doi:10.1093/petrology/37.1.3

frontiers | Frontiers in Earth Science

TYPE Original Research
PUBLISHED 09 January 2024
DOI 10.3389/feart.2023.1346880

OPEN ACCESS

EDITED BY
Lidong Dai,
Chinese Academy of Sciences, China

REVIEWED BY
Zhankun Liu,
Central South University, China
Kai Zheng,
Gannan Normal University, China
Kai Luo,
Yunnan University, China

*CORRESPONDENCE
Dongsheng Ren,
dongshengren@foxmail.com

RECEIVED 07 December 2023
ACCEPTED 27 December 2023
PUBLISHED 09 January 2024

CITATION
Ren D (2024), Friction stabilities of gypsum and kaolinite/calcite mixture fault gauges under high pressure.
Front. Earth Sci. 11:1346880.
doi: 10.3389/feart.2023.1346880

Friction stabilities of gypsum and kaolinite/calcite mixture fault gauges under high pressure

Dongsheng Ren*

State Key Laboratory of Earthquake Dynamics, Institute of Geology, China Earthquake Administration, Beijing, China

Various lab-scale friction tests and seismic observations have highlighted the role of fault gauges in earthquake initiation in geological faults. These fault gauges consist of particles accumulated over thousands of years due to surface wear caused by friction. Understanding their properties is crucial as they significantly influence both the frictional strength and sliding stability of faults. This study investigates the friction stability parameter (a-b) under loading rates of 0.2–25 μm/s using velocity step tests on gypsum fault gauges under a low normal stress condition (0.9 MPa) and steady-state velocity step tests on fault gauges composed of varying ratios of kaolinite/calcite mixture under an effective normal stress of 3 MPa. The conclusions drawn from this study are as follows: 1) The (a-b) values obtained from near steady-state velocity step tests on gypsum fault gauges and those reported in previous studies under similar conditions were both negative. However, our results show that the former values were one order of magnitude lower than the latter, indicating a higher susceptibility to velocity weakening. 2) Steady-statevelocity steptests on the kaolinite/calcite mixture fault gauges demonstrated positive (a-b) values for all mixtures with varying kaolinite contents. Moreover, the (a-b) values were proportional to the kaolinite content. We established a functional relationship between the (a-b) values of the mixture fault gauge and the mass fraction of kaolinite, providing valuable insights for future experiments and numerical simulations related to fault stability.

KEYWORDS

friction stabilities, gypsum, kaolinite/calcite mixture, high pressure, fault gauges

1 Introduction

Earthquakes are natural phenomena resulting from abrupt accelerated sliding on tectonic faults. This sliding releases energy through seismic waves and heat (Niemeijer et al., 2012). Seismic waves propagate through the earth's crust, causing surface vibrations, and earthquakes with significant magnitudes can result in substantial loss of life and property. Therefore, comprehending earthquake formation processes and mechanisms has become a relentless pursuit for numerous scientific researchers (Scholz, 1989; He et al., 1998; Marone, 1998; Mair et al., 2002; West et al., 2005; BenDavid et al., 2010; Kaproth and Marone, 2013). Brace and Byerlee (1966) introduced one crucial understanding of earthquake mechanisms, who suggested that the stick-slip phenomenon observed during the relative sliding of two rocks in laboratory experiments might be a mechanism for shallow earthquakes.

Since then, extensive laboratory friction experiments have been conducted to investigate the sliding properties of rock-rock interfaces (Johnson and Scholz, 1976; Scholz and Engelder, 1976; Engelder, 1978; Dieterich, 1979; Lockner and Okubo, 1983; Weeks and

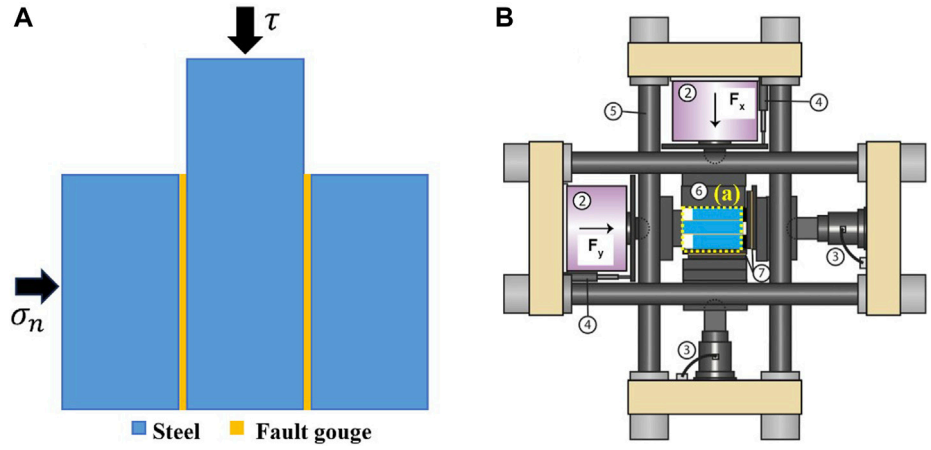

FIGURE 1
(A) Sample assembly diagram; **(B)** sample assembly and loading schema diagram, (1) Sample assembly; (2) Loading piston, (3) Fixed piston, (4) LVDT, (5) Loading frame, (6) Steel spacers, (7) Slide-bearing steel plates.

Tullis, 1985; Tullis, 1988; Kato et al., 1992; Karner and Marone, 2000). Nevertheless, lab-scale friction tests and seismic observations revealed that fault gauges in geological faults may play a critical role in earthquake initiation. These fault gauges consist of particles accumulated through surface wear over thousands of years due to friction.

The properties of fault gauges have a decisive influence on both the frictional strength and sliding stability of faults (Brace and Byerlee, 1966; Johnson et al., 1973; Sammis and Biegel, 1989; Frye and Marone, 2002; Mair et al., 2002; Anthony and Marone, 2005; Marone et al., 2008; Ikari et al., 2015; Scuderi et al., 2015; Jiang et al., 2016; Lieou et al., 2017; Hedayat et al., 2018). However, acquiring natural deep fault gauges without compromising their micromorphs and loading history is nearly impossible. To study the sliding properties of fault gauges, some scholars have used fault gauge samples collected from outcrops of fault surfaces (He et al., 2007). Various granular materials have also been used as simulants for fault gauges, assembled into the sliding surface of simulated faults in laboratories. These include pulverized particles obtained by manually grinding various rocks (Byerlee, 1978; Engelder, 1978; Morrow and Byerlee, 1989; Moore et al., 1997; He et al., 2007; Togo et al., 2011; Lu and He, 2014), industrially produced granular materials like finely ground glass beads (Géminard et al., 1999; Albert et al., 2001; Adjemian and Evesque, 2004; Härtl and Ooi, 2008; Johnson et al., 2013; Lastakowski et al., 2015; Rivière et al., 2018), MgO nanoparticles (Han et al., 2011; Yao et al., 2016), and even kitchen flour (Shinbrot et al., 2012; Leeman et al., 2015).

Within the framework of the rate- and state-dependent friction criterion, velocity weakening is a necessary condition for earthquakes to occur, while velocity strengthening typically cannot cause earthquakes (Scholz, 1998). Recent studies have shown that on some naturally seismogenic faults, creep on the fault during the seismic gap is unevenly distributed across the fault (Freymueller et al., 2000; Chlieh et al., 2008). This means that while some areas inside the fault are self-locking and undergoing stress recovery to prepare for the next earthquake, others are slowly creeping. These observations suggest the simultaneous existence of speed enhancement and velocity weakening on the same fault. In laboratory settings, some scholars have explored the influence of material inhomogeneity on fault belts' sliding properties (Buijze et al., 2021; Bedford et al., 2022). Consequently, investigating the friction stability of fault gauges with different attributes greatly aids related research on laboratory earthquakes. Prior studies have indicated that gypsum behaves as a speed-weakening material at room temperature (Buijze et al., 2021), meaning that (a-b) < 0. As such, (a-b) of gypsum is fitted through stick-slip experiments and cannot be obtained by steady-state tests of speed steps. Conversely, calcite and kaolinite are velocity-enhanced materials at room temperature (Buijze et al., 2021), signifying that (a-b) > 0. However, the friction properties of their mixtures have not been systematically reported to date. Given these reasons, it holds significant scientific importance to study the changes in friction stability parameters (a-b) throughvelocity steptests of gypsum fault gauges under low normal stress conditions and steady-state tests of speed steps of kaolinite/calcite mixture fault gauges with different proportions.

2 Experimental

The experiment was conducted at the Structural Physics Laboratory of the Institute of Geology, China Earthquake Administration. Gypsum, calcite, and kaolinite were purchased from Aladdin Company. We controlled the particle size of the gypsum fault gauge to 100–150 μm and that of kaolinite and calcite to 75–100 μm through grinding and sieving. To enhance the rigidity of the entire system and promote stable fault sliding, we used steel blocks for the surrounding rock of the fault. The steel blocks on both sides measured 100 × 50 × 50 mm^3, while the middle steel block measured 150 × 50 × 50 mm^3. The thickness of the fault gauge was 1.5 mm. Figure 1A shows the specific sample loading mode. Initially, we placed the assembled samples on the horizontal biaxial press, which had a maximum single-axis load capacity of 150 t and could be driven by either displacement or load control. We first loaded pressure in the F_x direction to the predetermined pressure, which was

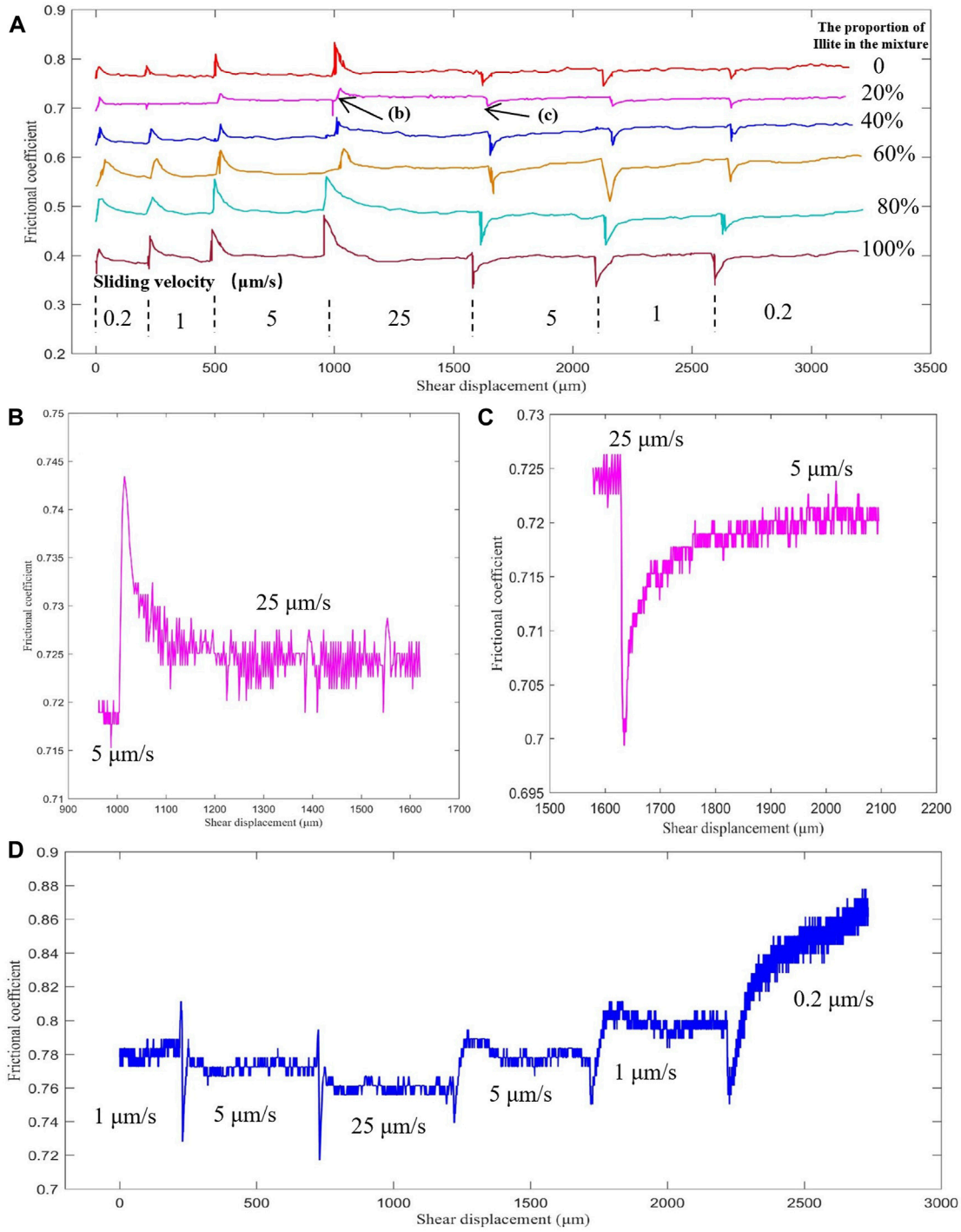

FIGURE 2
(A) Curves of the fault gauge frictional coefficient changing with displacements of different proportions of kaolinite/calcite mixture under the condition of room temperature and 3 MPa effective normal stress, **(B)** and **(C)** enlarged images of the black arrow in **(A)**, **(D)** variation curve of gypsum fault gauge frictional coefficient with displacement under the condition of room temperature and 0.9 MPa effective normal stress.

0.9 MPa for the gypsum fault gauge experiment and 3 MPa for the kaolinite/calcite mixture experiment. Once the F_x direction reached the predetermined pressure, we controlled the F_y direction using displacement and performed shear experiments at speeds of 0.2, 1, 5, and 25 μm/s, allowing approximately 0.5 mm of slip under each speed condition until the sliding reached a steady state.

After completing the experiment, we determined the values of the friction stability parameters (a-b) based on the rate-state friction constitutive relation. Rate- and state-dependent friction is described using τ and refers to the conditions under which materials either strengthen or weaken with an imposed velocity step (Dieterich, 1979; Ruina, 1983). The Dieterich-Ruina formulation allows us to

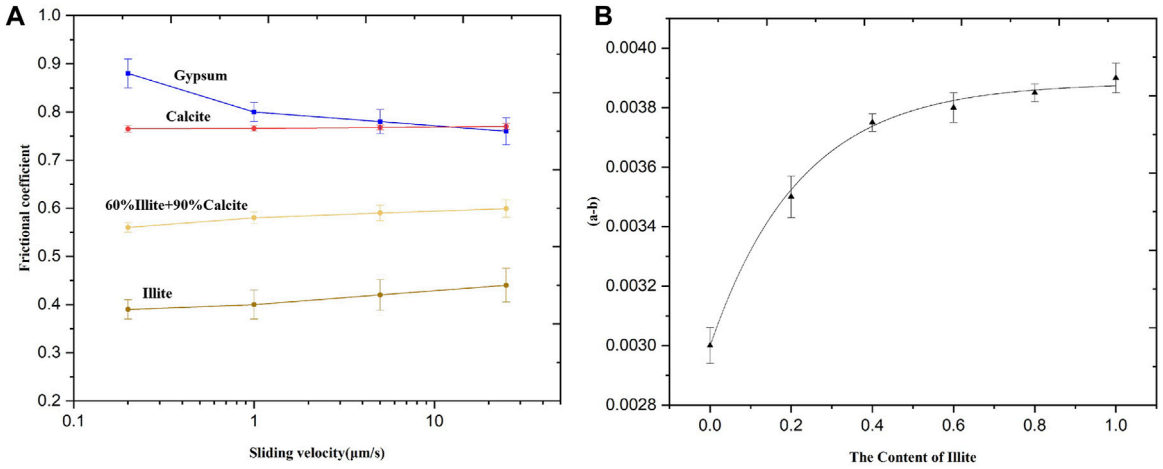

FIGURE 3
(A) Variation of frictional coefficient with loading rate for different fault gauge, **(B)** variation of kaolinite/calcite mixture fault gauge **(A, B)** with the mass fraction of kaolinite.

calculate τ as follows: $\tau = \sigma\left(\mu_0 + aln\frac{v}{v_0} + bln\frac{\theta v_0}{D_c}\right)$, where σ represents the effective normal stress, and μ_0 is the friction coefficient when the slip velocity (V) equals the reference velocity (v_0). The direct effect term ($aln\frac{v}{v_0}$) accounts for the initial increase in frictional strength, while the evolution term ($bln\frac{\theta v_0}{D_c}$) accounts for the reduction in frictional strength with slip distance and time, where D_c denotes the critical slip distance, and θ denotes the state variable. The parameters a and b are empirical, dimensionless quantities that govern these terms. The term $(a - b)$ represents the velocity dependence of the material under specific environmental conditions, such as stress, temperature, slip velocity, and fluid effects (Marone, 1998). When the sliding reached a steady state, $(a - b) = \Delta\mu_s/\Delta\, Ln\,(V)$.

3 Results and discussion

Figure 2A illustrates the stable sliding behavior of different kaolinite/calcite mixtures under various loading rates (0.2–25 μm/s). As the proportion of kaolinite mass increases, the overall mixed fault gauge's frictional coefficient gradually decreases. The frictional coefficient exhibits sudden changes during the experimental loading rate switching process, where an increase in loading rate results in a sudden increase in the frictional coefficient (Figure 2B), and a decrease in loading rate leads to a sudden decrease in the friction coefficient (Figure 2C).

Previous studies suggested that gypsum exhibits stick-slip behavior under different normal stress conditions at room temperature (Buijze et al., 2021). However, using steel blocks as the surrounding rock and a low effective normal stress of 0.9 MPa in our experimental design is not conducive to stick-slip in the gypsum fault gauge. Therefore, we observe a more stable sliding behavior in the gypsum fault gauge. The accuracy of the gypsum fault gauge's (a-b) obtained through the steady-statevelocity steptest is superior to the value obtained by fitting the stick-slip data (Dieterich, 1979; Ruina, 1983). Additionally, the friction coefficient exhibits sudden changes during the experimental loading rate switching process, where an increase in loading rate leads to a sudden decrease in the friction coefficient, while a decrease in loading rate causes a sudden increase.

Based on the data, we derived the variation curves of different fault gauge frictional coefficients with loading rate, as shown in Figure 3A. Using the formula $(a - b) = \Delta\mu_s/\Delta\, Ln\,(V)$, we determined that the slope of the curve in Figure 3 (middle) represents the (a-b) value of the fault gauge. The slope of the gypsum fault gauge is less than 0, indicating velocity weakening under this loading condition, with (a-b) approximately −0.01. Compared with the (a-b) value of −0.0031 (deMeer and Spiers, 1997) obtained through fitting the gypsum fault gauge under similar particle size conditions, our results show stronger velocity weakening. In contrast, the slopes of the kaolinite/calcite mixture fault gauges are all positive, indicating speed enhancement characteristics. Furthermore, as the kaolinite content increases, the slope of the curve becomes larger, suggesting that the (a-b) value of the material increases with the proportion of kaolinite. Additionally, we calculated the mixed fault gauge's (a-b) for different kaolinite content, as shown in Figure 3B. This allowed us to establish the relationship between the mixed fault gauge's (a-b) and kaolinite content. Through this relationship, we can estimate the mixed fault gauge's (a-b) for different kaolinite mass fractions, providing a basis for future experiments and numerical simulations.

4 Conclusion

By designing a well-designed steady-state velocity step test, we successfully determined the values of (a-b) for both the gypsum fault gauge and the fault gauge consisting of different components of the kaolinite/calcite mixture. For the gypsum fault gauges, the (a-b) values obtained through near steady-statevelocity steptests and those reported in previous studies under similar conditions were negative. However, the (a-b) values obtained in our tests were one order of magnitude lower than those reported in previous studies, indicating that the gypsum fault gauge in our experimental setup

exhibits a stronger tendency toward velocity weakening. Our steady-state velocity step tests on the kaolinite/calcite mixture fault gauges revealed that all mixtures, regardless of their kaolinite contents, exhibited positive (a-b) values. Furthermore, we observed a proportional relationship between (a-b) and the kaolinite content. As a result, we established a functional relationship between the (a-b) values of the mixture fault gauge and the mass fraction of kaolinite.

Author contributions

DR: Conceptualization, Funding acquisition, Writing–original draft, Writing–review and editing.

Funding

The author(s) declare financial support was received for the research, authorship, and/or publication of this article. This study is supported by the National Nonprofit Fundamental Research Grant of China, Institute of Geology, China Earthquake Administration (Grant No. IGCEA-22-19), the National Key R&D Program Project, Rock Physical Properties, Friction Parameters, and Mechanical Mechanisms of Fault Zones in the Sichuan Yunnan Region (Project No. 2021YFC3000603) and the National Natural Science Foundation of China (Project No. 42104176).

Conflict of interest

The author declares that the research was conducted in the absence of any commercial or financial relationships that could be construed as a potential conflict of interest.

Publisher's note

References

Adjemian, F., and Evesque, P. (2004). Experimental study of stick-slip behaviour. *Int. J. Numer. Anal. Methods Geomechanics* 28 (6), 501–530. doi:10.1002/nag.350

Albert, I., Tegzes, P., Albert, R., Sample, J. G., Barabási, A. L., Vicsek, T., et al. (2001). Stick-slip fluctuations in granular drag. *Phys. Rev. E* 64 (3), 031307. doi:10.1103/physreve.64.031307

Anthony, J. L., and Marone, C. (2005). Influence of particle characteristics on granular friction. *J. Geophys. Res. Solid Earth* 110 (B8). doi:10.1029/2004jb003399

Bedford, J., Faulkner, D., and Lapusta, N. (2022). Fault rock heterogeneity can produce fault weakness and reduce fault stability. *Nat. Commun.* 13, 326. doi:10.1038/s41467-022-27998-2

Bendavid, O., Cohen, G., and Fineberg, J. (2010). The dynamics of the onset of frictional slip. *Science* 330 (6001), 211–214. doi:10.1126/science.1194777

Brace, W. F., and Byerlee, J. D. (1966). Stick-slip as a mechanism for earthquakes. *Science* 153 (3739), 990–992. doi:10.1126/science.153.3739.990

Buijze, L., Guo, Y., Niemeijer, A. R., Ma, S., and Spiers, C. (2021). Effects of heterogeneous gouge segments on the slip behavior of experimental faults at dm scale. *Earth Planet. Sci. Lett.* 554, 116652. doi:10.1016/j.epsl.2020.116652

Byerlee, J. (1978). "Friction of rocks," in *Rock friction and earthquake prediction* (Basel: Birkhäuser), 615–626.

Chlieh, M., Avouac, J. P., Sieh, K., Natawidjaja, D. H., and Galetzka, J. (2008). Heterogeneous coupling of the sumatran megathrust constrained by geodetic and paleogeodetic measurements. *J. Geophys. Res. Solid Earth* 113. doi:10.1029/2007jb004981

de Meer, S., and Spiers, C. J. (1997). Uniaxial compaction creep of wet gypsum aggregates. *J.Geophys. Res. Solid Earth102 (B1)* 102, 875–891. doi:10.1029/96jb02481

Dieterich, J. H. (1979). Modeling of rock friction: 1. Experimental results and constitutive equations. *J. Geophys. Res.* 84 (B5), 2161–2168. doi:10.1029/jb084ib05p02161

Engelder, T. (1978). Aspects of asperity-surface interaction and surface damage of rocks during experimental frictional sliding. *pure Appl. Geophys.* 116 (4-5), 705–716. doi:10.1007/bf00876533

Freymueller, J. T., Cohen, S. C., and Fletcher, H. J. (2000). Spatial variations in present-day deformation, kenai peninsula, Alaska, and their implications. *J. Geophys. Res.* 105 (B4), 8079–8101. doi:10.1029/1999jb900388

Frye, K. M., and Marone, C. (2002). The effect of particle dimensionality on granular friction in laboratory shear zones. *Geophys. Res. Lett.* 29 (19), 22. doi:10.1029/2002gl015709

Géminard, J. C., Losert, W., and Gollub, J. P. (1999). Frictional mechanics of wet granular material. *Phys. Rev. E* 59 (5), 5881–5890. doi:10.1103/physreve.59.5881

Han, R., Hirose, T., Shimamoto, T., Lee, Y., and Ando, J. i. (2011). Granular nanoparticles lubricate faults during seismic slip. *Geology* 39 (6), 599–602. doi:10.1130/g31842.1

Härtl, J., and Ooi, J. Y. (2008). Experiments and simulations of direct shear tests: porosity, contact friction and bulk friction. *Granul. Matter* 10 (4), 263–271. doi:10.1007/s10035-008-0085-3

He, C., Ma, S., and Huang, J. (1998). Transition between stable sliding and stick-slip due to variation in slip rate under variable normal stress condition. *Geophys. Res. Lett.* 25 (17), 3235–3238. doi:10.1029/98gl02518

He, C., Wang, Z., and Yao, W. (2007). Frictional sliding of gabbro gouge under hydrothermal conditions. *Tectonophysics* 445 (3-4), 353–362. doi:10.1016/j.tecto.2007.09.008

Hedayat, A., Haeri, H., Hinton, J., Masoumi, H., and Spagnoli, G. (2018). Geophysical signatures of shear-induced damage and frictional processes on rock joints. *J. Geophys. Res. Solid Earth* 123 (2), 1143–1160. doi:10.1002/2017jb014773

Ikari, M. J., Niemeijer, A. R., and Marone, C. (2015). Experimental investigation of incipient shear failure in foliated rock. *J. Struct. Geol.* 77, 82–91. doi:10.1016/j.jsg.2015.05.012

Jiang, Y., Wang, G., Kamai, T., and McSaveney, M. J. (2016). Effect of particle size and shear speed on frictional instability in sheared granular materials during large shear displacement. *Eng. Geol.* 210, 93–102. doi:10.1016/j.enggeo.2016.06.005

Johnson, P. A., Ferdowsi, B., Kaproth, B. M., Scuderi, M., Griffa, M., Carmeliet, J., et al. (2013). Acoustic emission and microslip precursors to stick-slip failure in sheared granular material. *Geophys. Res. Lett.* 40 (21), 5627–5631. doi:10.1002/2013gl057848

Johnson, T., Wu, F. T., and Scholz, C. H. (1973). Source parameters for stick-slip and for earthquakes. *Science* 179 (4070), 278–280. doi:10.1126/science.179.4070.278

Johnson, T. L., and Scholz, C. H. (1976). Dynamic properties of stick-slip friction of rock. *J. Geophys. Res.* 81 (5), 881–888. doi:10.1029/jb081i005p00881

Kaproth, B. M., and Marone, C. (2013). Slow earthquakes, preseismic velocity changes, and the origin of slow frictional stick-slip. *Science* 341 (6151), 1229–1232. doi:10.1126/science.1239577

Karner, S. L., and Marone, C. (2000). Effects of loading rate and normal stress on stress drop and stick-slip recurrence interval. *Geophys. Monograph-American Geophys. Union* 120, 187–198. doi:10.1029/GM120p0187

Kato, N., Yamamoto, K., Yamamoto, H., and Hirasawa, T. (1992). Strain-rate effect on frictional strength and the slip nucleation process. *Tectonophysics* 211 (1-4), 269–282. doi:10.1016/0040-1951(92)90064-d

Lastakowski, H., Géminard, J. C., and Vidal, V. (2015). Granular friction: triggering large events with small vibrations. *Sci. Rep.* 5, 13455. doi:10.1038/srep13455

Leeman, J., Scuderi, M. M., Marone, C., and Saffer, D. (2015). Stiffness evolution of granular layers and the origin of repetitive, slow, stick-slip frictional sliding. *Granul. Matter* 17 (4), 447–457. doi:10.1007/s10035-015-0565-1

Lieou, C. K. C., Daub, E. G., Guyer, R. A., Ecke, R. E., Marone, C., and Johnson, P. A. (2017). Simulating stick-slip failure in a sheared granular layer using a physics-based constitutive model. *J. Geophys. Res. Solid Earth* 122 (1), 295–307. doi:10.1002/2016jb013627

Lockner, D. A., and Okubo, P. G. (1983). Measurements of frictional heating in granite. *J. Geophys. Res. Solid Earth* 88 (B5), 4313–4320. doi:10.1029/jb088ib05p04313

Lu, Z., and He, C. (2014). Frictional behavior of simulated biotite fault gouge under hydrothermal conditions. *Tectonophysics* 622, 62–80. doi:10.1016/j.tecto.2014.03.002

Mair, K., Frye, K. M., and Marone, C. (2002). Influence of grain characteristics on the friction of granular shear zones. *J. Geophys. Res. Solid Earth* 107 (B10), ECV 4-1. doi:10.1029/2001jb000516

Marone, C. (1998). Laboratory-derived friction laws and their application to seismic faulting. *Annu. Rev. Earth Planet. Sci.* 26 (1), 643–696. doi:10.1146/annurev.earth.26.1.643

Marone, C., Carpenter, B. M., and Schiffer, P. (2008). Transition from rolling to jamming in thin granular layers. *Phys. Rev. Lett.* 101 (24), 248001. doi:10.1103/physrevlett.101.248001

Moore, D. E., Lockner, D. A., Ma, S., Summers, R., and Byerlee, J. D. (1997). Strengths of serpentinite gouges at elevated temperatures. *J. Geophys. Res. Solid Earth* 102 (B7), 14787–14801. doi:10.1029/97jb00995

Morrow, C. A., and Byerlee, J. D. (1989). Experimental studies of compaction and dilatancy during frictional sliding on faults containing gouge. *J. Struct. Geol.* 11 (7), 815–825. doi:10.1016/0191-8141(89)90100-4

Niemeijer, A., Di Toro, G., Griffith, W. A., Bistacchi, A., Smith, S. A., and Nielsen, S. (2012). Inferring earthquake physics and chemistry using an integrated field and laboratory approach. *J. Struct. Geol.* 39 (0), 2–36. doi:10.1016/j.jsg.2012.02.018

Rivière, J., Lv, Z., Johnson, P. A., and Marone, C. (2018). Evolution of b-value during the seismic cycle: insights from laboratory experiments on simulated faults. *Earth Planet. Sci. Lett.* 482, 407–413. doi:10.1016/j.epsl.2017.11.036

Ruina, A. (1983). Slip instability and state variable friction laws. *J. Geophys. Res.* 88 (B12), 10359–10370. doi:10.1029/jb088ib12p10359

Sammis, C. G., and Biegel, R. L. (1989). Fractals, fault-gouge, and friction. *Pure Appl. Geophys.* 131 (1-2), 255–271. doi:10.1007/bf00874490

Scholz, C. H. (1989). The mechanics of earthquakes and faulting. *Geol. Curtain Engl. version* 17 (1), 49.

Scholz, C. H. (1998). Earthquakes and friction laws. *Nature* 391, 37–42. doi:10.1038/34097

Scholz, C. H., and Engelder, J. T. (1976). The role of asperity indentation and ploughing in rock friction—I: asperity creep and stick-slip. *International Journal of Rock Mechanics and Mining Sciences & Geomechanics Abstracts* 13 (5), 149–154. doi:10.1016/0148-9062(76)90819-6

Scuderi, M. M., Carpenter, B. M., Johnson, P. A., and Marone, C. (2015). Poromechanics of stick-slip frictional sliding and strength recovery on tectonic faults. *J. Geophys. Res. Solid Earth* 120 (10), 6895–6912. doi:10.1002/2015jb011983

Shinbrot, T., Kim, N. H., and Thyagu, N. N. (2012). Electrostatic precursors to granular slip events. *Proc. Natl. Acad. Sci.* 109 (27), 10806–10810. doi:10.1073/pnas.1121596109

Togo, T., Shimamoto, T., Ma, S., and Hirose, T. (2011). High-velocity frictional behavior of Longmenshan fault gouge from Hongkou outcrop and its implications for dynamic weakening of fault during the 2008 Wenchuan earthquake. *Earthq. Sci.* 24 (3), 267–281. doi:10.1007/s11589-011-0790-6

Tullis, T. E. (1988). Rock friction constitutive behavior from laboratory experiments and its implications for an earthquake prediction field monitoring program. *Pure Appl. Geophys.* 126 (2-4), 555–588. doi:10.1007/bf00879010

Weeks, J. D., and Tullis, T. E. (1985). Frictional sliding of dolomite: a variation in constitutive behavior. *J. Geophys. Res. Solid Earth* 90 (B9), 7821–7826. doi:10.1029/jb090ib09p07821

West, M., Sánchez, J. J., and Mcnutt, S. R. (2005). Periodically triggered seismicity at mount wrangell, Alaska, after the sumatra earthquake. *Science* 308 (5725), 1144–1146. doi:10.1126/science.1112462

Yao, L., Ma, S., Niemeijer, A. R., Shimamoto, T., and Platt, J. D. (2016). Is frictional heating needed to cause dramatic weakening of nanoparticle gouge during seismic slip? Insights from friction experiments with variable thermal evolutions. *Geophys. Res. Lett.* 43 (13), 6852–6860. doi:10.1002/2016gl069053

frontiers | Frontiers in Earth Science

TYPE Original Research
PUBLISHED 15 January 2024
DOI 10.3389/feart.2023.1331391

OPEN ACCESS

EDITED BY
Qiaomu Qi,
Chengdu University of Technology, China

REVIEWED BY
Xu Dong,
Northeast Petroleum University, China
Weichao Yan,
Ocean University of China, China
Jianping Yan,
Southwest Petroleum University, China

*CORRESPONDENCE
Yu Zeng,
zyng886@163.com
Fuqiang Lai,
laifq1982@163.com

RECEIVED 01 November 2023
ACCEPTED 21 December 2023
PUBLISHED 15 January 2024

CITATION
Lai Q, Wu Y, Zeng Y, Xie B, Jiang Y, Chen L, Tang M and Lai F (2024), Quantitative characterization of fractures and holes in core rolling scan images based on the MFAPNet deep learning model.
Front. Earth Sci. 11:1331391.
doi: 10.3389/feart.2023.1331391

Quantitative characterization of fractures and holes in core rolling scan images based on the MFAPNet deep learning model

Qiang Lai[1], Yuyu Wu[1], Yu Zeng[2]*, Bing Xie[1], Yuanke Jiang[2], Li Chen[1], Mingzheng Tang[2] and Fuqiang Lai[2]*

[1]Exploration and Development Research Institute, PetroChina Southwest Oil & Gas Field Company, Chengdu, China, [2]School of Petroleum and Natural Gas Engineering, Chongqing University of Science and Technology, Chongqing, China

The exploration and comprehensive assessment of fractured-vuggy reservoir information have perennially constituted focal points and challenges within the domain of oil and gas reservoir evaluation. The verification of geological phenomena, identification of various fracture and hole types, and the quantitative characterization thereof currently present pressing challenges. This study meticulously examines the deep carbonate reservoirs within the Dengying Formation in the Penglai gas region of the Sichuan Basin. The Core Rolling Scan images reveal five discernible features: unfilled holes, filled holes, filled fractures, open fractures, and algae. The analysis pinpoints three primary challenges in semantic segmentation recognition: the amalgamation of feature scales, class imbalance, and the scarcity of datasets with substantial sample sizes. To address these challenges, this paper introduces a Multi-Scale Feature Aggregation Pyramid Network model (MFAPNet), achieving a pixel accuracy of 68.04% in recognizing the aforementioned five types. Lastly, the model is employed in calculating core porosity, exposing a scaling relationship between wellbore image porosity and core porosity ranging from 1.5 to 3 times. To a certain extent, it reveals the correlation between the wellbore image logging data and the actual formation of the Dengying Formation in the Penglai Gas Field of the Sichuan Basin, and also provides a basis for the subsequent logging evaluation of the formation. The partial code and CHA355 dataset are publicly available at https://github.com/zyng886/MFAPNet.

KEYWORDS

carbonate rock, wellbore image, core rolling scan image, fracture and hole types, semantic segmentation, parameter calculation

1 Introduction

Due to rising global energy demands and the intensified oil and gas exploration activities, the exploration of deep carbonate oil and gas reservoirs in Tarim Basin, Sichuan Basin, and Ordos Basin has witnessed significant achievements since 2010. The proven reserves were estimated to be approximately $356.63*10^8$ tons of oil equivalent (Zou et al., 2014; Ma et al., 2019; Ma et al., 2022; Ma et al., 2023). The potential for deep carbonate rock natural gas exploration in China is promising. Nonetheless, due to the diversity and strong heterogeneity of storage spaces in deep carbonate rocks, the challenges always exist in identification of fracture and hole types, parameter extraction, and parameter calibration.

Traditional machine learning algorithms lack the capacity to accommodate arbitrary feature functions, such as those found in deep neural networks, thereby impeding the identification of multiscale geological features. The acquisition of core data poses considerable challenges, necessitating exploration into the correlation between well logging instrument data and core data. This challenge demands the implementation of a deep learning model with the ability to assimilate arbitrary geological features, enabling the swift and accurate prediction of subsurface conditions. The primary contributions of this study can be summarized as follows.

1. Articulated the three pivotal challenges in core image recognition, the amalgamation of feature scales, class imbalance, and the scarcity of datasets with substantial sample sizes.
2. In response to the aforementioned challenges, crafted a multiscale feature aggregation pyramid network model, achieving a pixel accuracy of 68.04% for identifying five distinct types.
3. To mitigate the time-consuming and labor-intensive aspects of traditional dataset labeling, introduced the 'segment anything' model, facilitating semi-automatic dataset annotation with significantly enhanced efficiency and accuracy.
4. Formulated a method for calculating core porosity based on the aforementioned algorithm, revealing the scaling relationship between them: the electrical imaging porosity is 1.5–3 times that of the core porosity. It also provides a theoretical foundation for the subsequent logging evaluation of the Dengying Formation in the Penglai Gas Field of the Sichuan Basin.

2 Related work

In traditional characterization methods of fracture and hole parameters, based on conventional logging curves, wellbore imaging, and core data, some algorithms such as Canny edge detection, threshold segmentation, and watershed transformation are employed in standard image recognition to discern fracture and hole parameters (Tian and Zhang, 2010; Lai, 2011; Ren et al., 2023). Although the segmentation results of these methods seem to be consistent with human visual perception, only basic color differences can be discerned and the genuine geological significance of fractures or holes are not considered. Consequently, the complete geological semantic information cannot be extracted from segmented images. For example, induced fractures, conductive minerals, clay aggregates, and calcium clusters in carbonate rock reservoirs are displayed as dark features in wellbore imaging results. These geological elements can be visually indistinguishable from fractures and holes, thus leading to different interpretation results. It is extremely difficult to interpret these geological data with traditional methods.

In recent years, deep learning has made significant achievements in image segmentation and has been applied in the classification and segmentation of geological images. Delhomme, (1992) proposed an imaging threshold method to visualize fracture shapes and depths (Hall et al., 1996). employed Hough transform to calculate sinusoidal fracture information and geological data and finally yielded effective fracture results with a sinusoidal distribution pattern. With the DeepLabv3+ semantic image segmentation model based on TensorFlow, Li B T et al. (2019) segmented and extracted fracture data calibrated with Labelme tool. Wang et al. (2021) introduced an automatic recognition method for wellbore imaging fractures and holes based on path morphology and sinusoidal function family matching. The introduced method could extract the data of single-scale fractures and dissolved holes, but the adaptive parameter selection for varied shapes or sizes had not been adopted in the method. Chen et al. (2023) identified main minerals, organic matters, and holes in shale with deep learning models such as Mask-RCNN, FCN, and U-Net and compared the runtime and accuracy of different deep learning models in processing geological images. Despite the commendable achievements of these methods, some challenges like mixed feature scales, class imbalance, and the unique nature of core datasets existed. To address these challenges, this paper introduced a multi-scale feature aggregation pyramid network model (MFAPNet).

3 Geology

3.1 Geological overview

The study area is situated in the northern slope of the Central Sichuan Uplift, displaying a significant northward-dipping monocline structure. It borders the Anyue gas field in the south and the Deyang-Anyue Sag in the west and is delimited by Jiulongshan to the north. It covers an approximate area of 2×10^4 km^2. Penglai Gas Region has exceptional geological conditions conducive to oil and gas accumulation. The Cambrian to Permian Maokou Formation serves as the host for four gas-bearing intervals, namely, Deng II, Deng IV, Cangchang I, and Maoyi II, arranged from the base to the summit. These intervals indicated well-developed lithologic reservoirs for oil and gas set against the backdrop of the monocline structure.

Deng II and Deng IV intervals predominantly comprise high-quality reservoir rocks, encompassing reef-flat facies such as algal boundstone dolomite, algal laminated dolomite, and algal sandstone dolomite. In Deng IV, the upper subinterval is characterized by dominant algal dolomite, whereas the lower subinterval is distinguished by powdery to fine-crystalline dolomite and mud-crystal dolomite. The lower subinterval of Deng IV showcases underdeveloped reef-flat bodies. The upper subinterval of Deng IV presents well-developed reef-flat deposits with a stable lateral distribution and is the principal reservoir in Deng IV interval.

3.2 Feature analysis

Fractures, holes, and algal laminations present distinct characteristics and often pose challenges in segmentation tasks:

Firstly, feature scales of the above hole types overlap and are complex. Fractures, algae, and holes exhibit diverse topological structures with different lengths and widths. Open fractures and filled fractures have similar macroscopic shapes and different microscopic details, so do the unfilled and filled dissolved holes. Conventional convolutional kernels have limited receptive fields and primarily capture proximate contextual information, so they cannot simultaneously extract the multi-scale semantic nuances of thin lines, broad fractures, small holes, and large holes, or distinguish genuine holes from spurious holes.

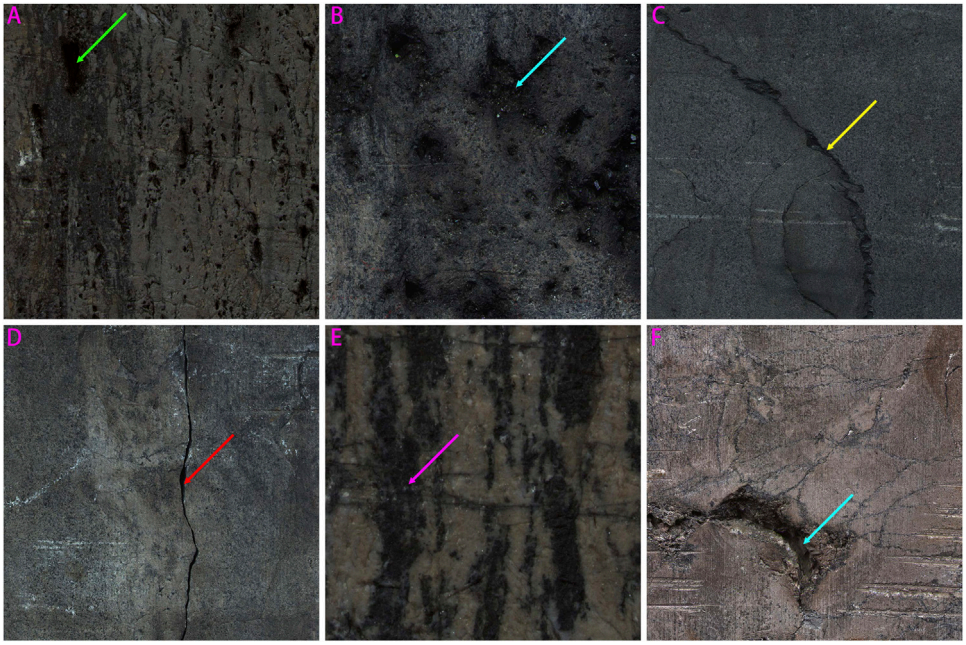

FIGURE 1
Typical fracture and hole types in core rolling scan images: **(A)** Bitumen-filled dissolved hole; **(B)** Unfilled dissolved hole; **(C)** Filled fracture; **(D)** Open fracture; **(E)** Algae; **(F)** Unfilled honeycomb-like dissolved hole.

Secondly, class imbalance is serious. Foreground pixels representing the target area, account for a minor part of the entire image. Moreover, the classes of pixels within dataset labels are markedly unbalanced. The utilization of the conventional cross-entropy loss function would cause the prevalent background and the identification loss of smaller fractures and holes.

Thirdly, the dataset volume is constrained, but the sample size is large. Unlike common datasets, oil and gas datasets should be annotated by experts and the number of related datasets is less. The procured raw core rolling scan images encompass tens of millions of pixels and contain assorted obstructions and shaded regions. The difference in the pixel quantity between the targeted region and the entire sample spans is about 1–2 orders of magnitude. Excessive image sizes are bounded by memory limitations, whereas smaller sizes may lead to the ignorance of small target areas, thus hindering accurate labeling.

We categorize the geological features observed in core rolling scan images into five distinct classes: unfilled holes, filled holes, filled fractures, open fractures, and algae.

Among all samples, unfilled dissolved holes and bitumen-filled dissolved holes were the dominant hole types. The two hole types had the similar characteristics. In the darker parts in the images, the bitumen-filled dissolved holes were obviously partly filled with or enriched with bitumen (Figure 1A). In contrast, dissolved holes without bitumen were displayed as separated or interconnected voids of different dimensions (Figures 1A, F). The fractures in the core rolling scan images were identified based on their morphology, size, and color. Those fractures with uneven contours, broader spans, and more saturated hues, which suggested the existence of bitumen, were classified as filled fractures (Figure 1C). Linear, elongated, and slender unfilled fractures were labeled as open fractures (Figure 1D). The assessment of algal laminations involved hue, texture, and geological conditions. Algal laminations were displayed as color gradients in rocks. Stratified or undulating textures accompanied by noticeable color transitions in the images could be identified as algal laminations (Figure 1E).

3.3 Dataset creation

Core images present diverse types of fractures and holes with different characteristics. Traditional manual labeling methods are limited by subjectivity, extended duration, and high expertise. By incorporating the segment anything model (SAM) (Kirillov et al., 2023) into dedicated geological annotation software, a semi-automatic segmentation of target regions (i.e., fractures and holes) from the image background can be realized. A unique technology named "segment anything" empowers SAM to execute zero-shot generalization on previously unseen objects and imagery without the prerequisite of further training. With the conventional polygon approximation technique, a multi-point polygon is marked around the target circle for approximation. However, with SAM, a singular point is marked within the target circle for automate the annotation. In comparison to conventional methods, the SAM has demonstrated a substantial improvement, achieving significantly enhanced levels of both speed and accuracy.

4 Methods

To address the three major challenges in traditional core rolling scan images datasets, we have constructed a multiscale feature aggregation pyramid network model:

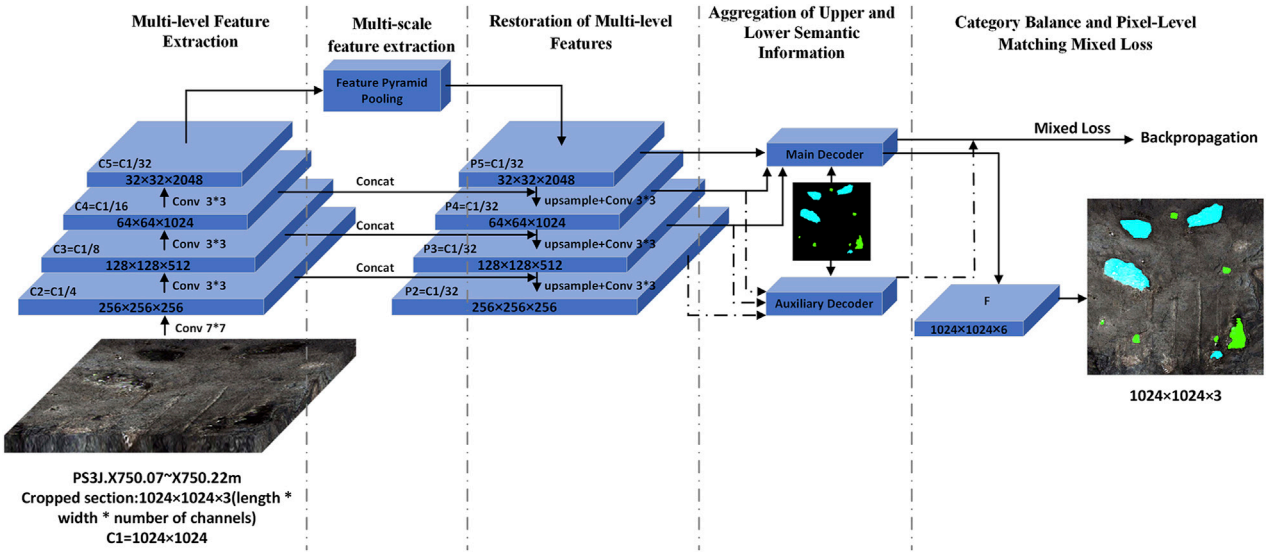

FIGURE 2
Framework of MFAPNet.

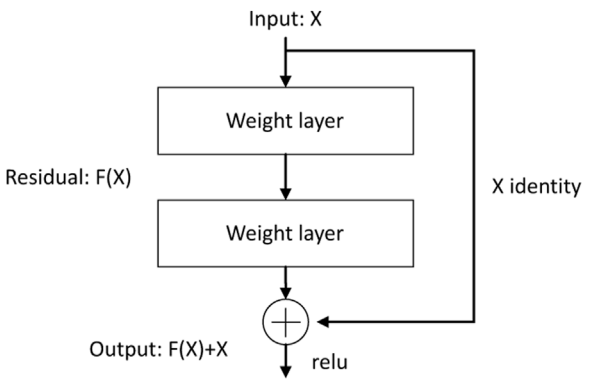

FIGURE 3
Residual module.

FIGURE 4
Segment from PS3J.X750.07-X750.22m.

The architecture of MFAPNet model is shown in Figure 2. Based on the encoder-decoder framework of U-Net (Ronneberger et al., 2015), an intermediate feature layer, termed "Bottleneck", is introduced. With the model, through a series of ResNet (He et al., 2016) convolutional operations, the dimensions of the feature map is gradually decreased based on the input image and then a tiered set of hierarchical feature maps are extracted. Subsequently, with a feature pyramid pooling module and an array of differently sized kernels, the feature maps with multi-scale semantic insights are obtained. In the decoding phase, Low resolution feature maps are subjected to upsampling and then integrated with high resolution maps. The subsequent convolution processes yield pyramid feature maps corresponding to those in the encoding phase. The semantic features drawn from the upper three mid-high layers and the lower three mid-low layers converge through primary and secondary decoding heads to produce high- and mid-layer semantic feature maps. Finally, these maps are juxtaposed against annotated versions to compute both primary and auxiliary loss metrics and the predictive image mask is ultimately generated through backpropagation and iteration.

4.1 Multi-level feature extraction

The extraction of multi-level features enables the model to extract high-order attributes from raw data, including edges, textures, shapes, and object components. The in-depth analysis and representation of intricate data structures empower the model to comprehend and depict detailed elements contained in input images. Through the extraction of multi-level features, the model can discern complex and abstract attributes and grasp data variances and non-linear interrelationships.

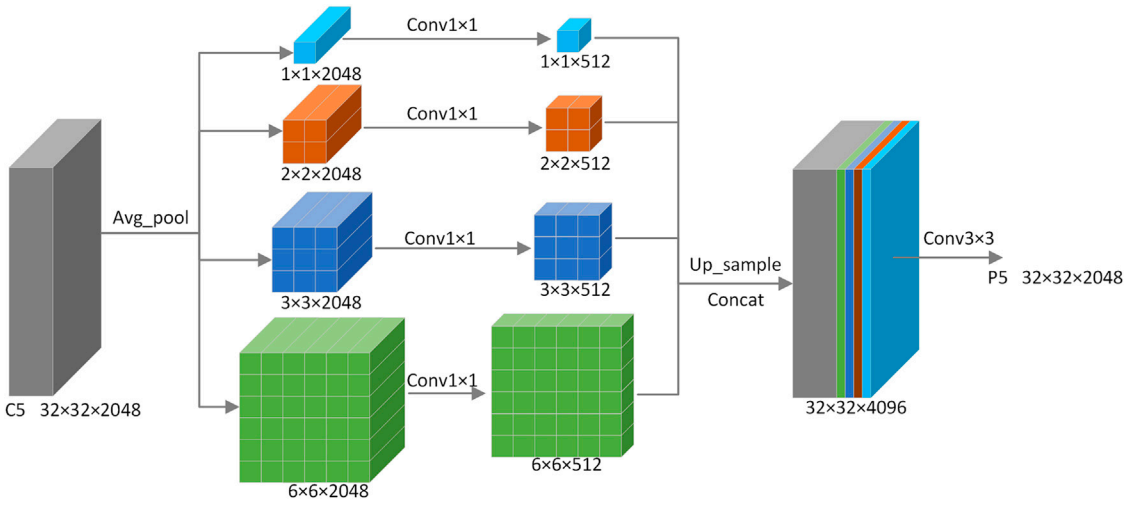

FIGURE 5
Pyramid pooling module (PPM).

For deep neural networks, key challenges like the gradient vanishing and exploding problem are solved through the incorporation of regularized initialization and intermediary regularization layers, notably, Batch Normalization (Ioffe and Szegedy, 2015). Degradation quandaries inherent to deep networks are addressed with residual modules. As illustrated in Figure 3, with an input denoted by x and its corresponding residual function F(x), the output generated by the residual module is defined as x + F(x). With this module, the input x is subjected to the transformation F and then the residual information is extracted to augment the foundational input x. This addition process indicates skip connections, namely, the integration of residual data with the original input, and can ensure refinement and adjustment. Such an architecture empowers neural networks to internalize the identity function I(x) = x throughout the training process. If it is the optimal solution, the module can discern an almost null residual, thereby retaining the integrity of the initial input. Conversely, in the presence of substantial discrepancies, the module can ascertain a more pronounced residual to refine the input data.

As depicted in Figure 2; Figure 4, a segment from PS3J.X750.07-X750.22 is selected. With the input data of 1024×1024×3 (C1 = 1024×1024), based on the ResNet primary feature extraction network, through 7x7 convolution, the feature map C2 with a quarter of its original size is obtained and its channels is increased to 256. Subsequently, the image undergoes a series of three analogous operations employing three 3x3 residual convolution to produce three distinct feature maps labeled as *C*3, *C*4, and *C*5. Their sizes respectively decrease to 1/8, 1/16, and 1/32 of the original size, whereas their channel increases to 512, 1024, and 2048.

4.2 Multi-scale feature extraction

In the fields of deep learning and computer vision, multi-scale feature extraction refers to capturing features from the data at different scales for the comprehensive information acquisition. The feature extraction approach performs well in handling the data at different scales, such as images, videos, and texts. The data at different scales correspond to structures and features with spatial or temporal scales. Harnessing multi-scale features allows models to encompass both granular and macroscopic characteristics and obtain a more profound comprehension of the data.

In deep convolutional networks, the realized receptive field is often far shorter than theoretical expectations. To counteract this discrepancy, the pyramid pooling module from PSPNet (Zhao et al., 2017) is incorporated into the terminal layer of the primary network. This integration ensures pyramid-style multi-scale feature extraction, as illustrated in Figure 5 and expressed as:

$$P5 = Conv_{3\times3}\left[\sum_{i=1\times1、\ 2\times2、\ 3\times3、\ 6\times6}^{Upsample、\ Concat} AvgPool_i + \mathrm{Conv}_{1\times1}(C5)\right] \quad (1)$$

Through average pooling (AvgPool) with four distinct sizes, the C5 layer captures multi-scale semantic feature insights. Subsequently, through the 1x1 convolution, the channels are reduced to a quarter of their initial size. After these features are upsampled to their original dimensions, they are concatenated and processed with the 3x3 convolution so as to integrate the multi-scale features into P5 and obtain comprehensive global information.

4.3 Restoration of multi-level features

To acquire multi-level semantic information with minimal interference, high-level features are realigned to the spatial resolution of the low-level features. This realignment, as expressed in Eq. 2, facilitates the restoration of features.

$$P_i = \mathrm{Conv}_{1\times1}\left(Upsample(P_{i-1}) + C_i\right), i = 4, 3, 2 \quad (2)$$

The feature layer P5 is upsampled to match the resolution of the C4 feature layer. Subsequently, it is concatenated and convolved with the C4 feature map to yield P3. This operation is reiterated twice to obtain the feature maps across various semantic levels: P5, P4, P3, and P2. By integrating high-level semantic information with low-level features, the details and

semantics in high-resolution images are captured. This integration enhances the performance of the model in intricate tasks like object detection and image segmentation through a robust and precise feature representation.

4.4 Aggregation of upper and lower semantic information

As the depth of a convolutional neural network increases, the semantic information extracted at each layer becomes increasingly rich, so that more global features are obtained. Analogously, the human visual system operates in a comparable way, in which global features as initial features are progressively refined for precise decision-making. Such a hierarchical processing way of features allows the sequential consideration of various levels of abstract features during data processing so as to facilitate a more comprehensive understanding and representation of intricate data, as expressed in Eqs 3, 4:

$$F = Conv_{3\times3}\left(\sum_{i=2、3、4、5}^{Upsample、Concat} P_i\right) \tag{3}$$

$$F_2 = Conv_{3\times3}\left[Upsample\left(P4\right)\right] \tag{4}$$

The main decoding head receives (P5, P4, P3) as the input, whereas the auxiliary decoding head processes (P4, P3, P2). After the obtained feature maps are restored to their original dimensions through upsampling, these features are concatenated into coherent feature maps. A subsequent 3x3 convolutional operation is performed to modulate the channel count so as to obtain the main and auxiliary feature segmentation maps, respectively denoted as F and F2. F is then superimposed onto the original image to generate the final prediction. The primary and auxiliary losses are amalgamated through weighted summation and applied in backpropagation for model optimization.

4.5 Class balance and pixel-level matching mixed loss

To deal with the unequal class distribution and ensure the matching between prediction results and actual labels, a class-balanced and pixel-level matched hybrid loss function is used in the study. The mixed loss function considering class-balanced cross-entropy loss and Dice Loss (Li X et al., 2019) is adopted:

$$CBCED\_LOSS = \alpha^{*}CBCE\_Loss + \beta^{*}Dice\_Loss \tag{5}$$

where CBCE_Loss denotes the class-balanced cross-entropy loss; Dice_Loss indicates Dice loss; *CBCED_LOSS* considers both class imbalance and pixel-level matching; α and β can be tuned according to the properties of tasks and datasets for the balance between the two loss types. In our work, a large weight is assigned to Dice Loss for pixel-level matching. A ratio of 1:3 (α=1 and β=3) is adopted. For *CBCE_LOSS*, it is assumed that *C* distinct classes exist and a weight, w_i, is assigned to a class and indicates its significance (i is the class index). Given a collection of samples, each sample has a true label Y and a predicted probability distribution P from the model. Then, the class-balanced cross-entropy loss is expressed as:

$$CBCE\left(P,Y\right) = -\sum_{i=1}^{C} w_i \times Y_i \times log\left(P_i\right) \tag{6}$$

where Y_i is the i-th element of the true label; P_i is the i-th element from the predicted probability distribution; w_i is the weight associated with the class. These weights can be modulated according to the importance of different classes so as to further address class imbalances. The ultimate loss is the mean loss across all samples:

$$CBCE\left(P,Y\right) = \frac{1}{N}\sum_{n=1}^{N} CBCE\left(P\left(s_n\right),Y_n\right) \tag{7}$$

where N indicates the total number of samples. The class-balanced cross-entropy loss allows different importance levels for different classes and can be used to deal with many computer vision tasks, especially class-imbalanced problems.

For Dice Loss, two sets (A and B) are considered. The size of their intersection is represented by $|A \cap B|$ and the size of their union is depicted as $|A \cup B|$ Then, Dice Loss can be defined as:

$$DiceLoss = 1 - \frac{2^{*}|A| \cap |B|}{|A| + |B|} \tag{8}$$

where $|A|$ and $|B|$ respectively indicate the sizes of sets A and B; $|A \cap B|$ represents the size of their intersection. Dice Loss value is between 0 and 1. The smaller the value is, the less the consistency between the predicted and actual segmentation results is.

In tasks involving semantic segmentation, Dice Loss is often used to indicate the resemblance between predicted and actual segmentation outcomes. Unlike cross-entropy loss, Dice Loss is focuses on pixel-level matching and performs better in dealing with class imbalances.

The gradient data from both primary and auxiliary losses calculated from F and F2 can be used to update network parameters through backpropagation. During backpropagation, the gradient information from the loss function flows backwards through network layers so as to guide weight adjustment. In this way, the model is adapted to training data and yields precise predictions for new data.

5 Experiments

5.1 Experimental parameter setting

To guarantee the precision of experimental results, the control variates method was used. In this method, all parameters remained constant except that the test variable was changed. Our experiments were executed on Windows 11 22H2 Professional Edition system and NVIDIA RTX A6000 48G GPU was used for training. The size of input images was 1024×1024 (Table 1).

The principal evaluation metric was mIoU. Additionally, Accuracy (Acc) and F-score (Wang et al., 2020) were used to indicate the performance of the network model in defect segmentation. mIoU is the average IoU value of all images or segmentation results. IoU (Intersection over Union) quantifies the relationship between the intersection and union areas of segmentation results and actual results as follows:

$$IoU = \frac{Intersection}{Union} \tag{9}$$

TABLE 1 Experimental parameter setting.

Experimental parameters	Values
System Platform	Windows 11 22H2
Python	3.10.12
CPU	I9 13900 KF
GPU	NVIDIA RTX A6000
Pytorch	2.0.1+cu118
CUDA	11.8
CuDNN	8.7
Optimizer	Adam
Learning_rate	0.0006
Batch_Size	4
Train_P	0.75 (266 photos)
Val_P	0.20 (71 photos)
Test_P	0.05 (18 photos)

Accuracy is the ratio of the number of the pixels correctly classified by the model to the total number of pixels:

$$Accuracy = \frac{Number\ of\ Correctly\ Classified\ Pixels}{Total\ Number\ of\ Pixels} \quad (10)$$

F-Score is the weighted average of precision and recall and can be used to evaluate the comprehensive efficacy of the classification model. F-Score indicates the balance between model precision and recall and can be expressed as:

$$Fscore = \frac{2 \cdot Precision \cdot Recall}{Precision + Recall} \quad (11)$$

5.2 Experimental dataset setting

In this study, the data of the core samples from the deep carbonate rock reservoir of the Dengying Formation located in Penglai Gas Area of Sichuan Basin. After screening the core data from various wells, FracturesHoleAlgae Dataset (CHA355) was derived. This dataset contained 266 training images, 71 validation images, and 18 testing images. As shown in Figure 6, the name of an image is composed of well sequence, depth range, and core number. The dimension of each image is 1024×1024 pixels and the sections indicate the representative areas from the initial core rolling scan images.

Figure 7 shows various colors for segmentation. Green indicates unfilled dissolved holes; cyan indicates filled dissolved holes; red indicates open fractures; yellow denotes filled fractures; purple indicates algae; black indicates the background. These annotated images are displayed in VOC format.

5.3 Comparison of experimental results obtained with different algorithms

In the section, the proposed MFAPNet was compared with renowned segmentation techniques such as FCN (Long et al., 2015),

FIGURE 6
Partial original images in the dataset.

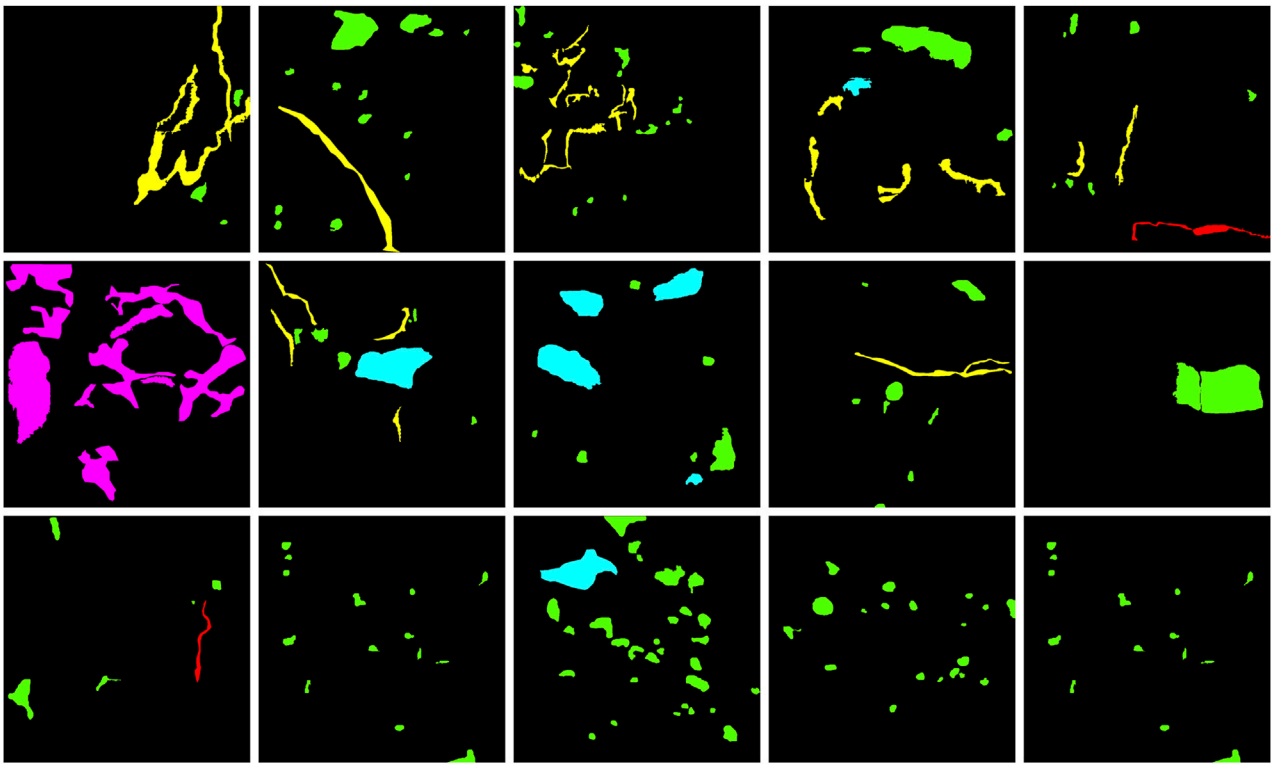

FIGURE 7
Partial labeled images in the dataset.

TABLE 2 Comparison of the results obtained with different algorithms from CHA355 dataset.

Method	Backbone	mIoU/%	mAcc/%	mFscore/%	mPrecision/%
FCN	ResNet-50	39.85	48.05	51.55	68.42
Unet	Unet	46.81	54.66	60.15	70.72
PSPNet	ResNet-50	49.31	62.90	63.40	70.77
DeepLabV3	ResNet-50	47.49	55.85	59.90	77.06
UperNet	ResNet-50	53.69	64.98	67.35	72.68
MFAPNet	ResNet-50	54.34	68.04	68.00	70.72

Note: Underlined numbers indicate the best result in terms of corresponding metric.

UNet, PSPNet, DeepLabV3 (Chen et al., 2017), and UperNet (Xiao et al., 2018). In FCN, the fully connected layer is replaced with a convolutional one so that it is feasible to input an image in any size. In UNet with an encoder-decoder design, an encoder is used to grasp image information, whereas the decoder is used to generate pixel-level segmentation results. In PSPNet, with a pyramid pooling module, the data at different scales are extracted. In DeepLabV3, dilated convolution is used to widen the receptive field and thus grasp more information. UperNet integrates UNet with pyramid structure and can enhance the multi-scale performance.

The segmentation results from CHA355 dataset are presented in Table 2. The mIoU value of MFAPNet was 14.49%, 7.53%, 5.03%, 6.85%, and 0.65% larger than that of FCN, UNet, PSPNet, DeepLabV3, and UperNet, respectively. Similarly, its mAcc was the mentioned models by 19.99%, 13.38%, 5.14%, 12.19%, and 3.06% larger than that of FCN, UNet, PSPNet, DeepLabV3, and UperNet, respectively. The mFscore of MFAPNet was 16.45%, 7.85%, 4.6%, 8.1%, and 0.65% larger than that of FCN, UNet, PSPNet, DeepLabV3, and UperNet, respectively. The mPrecision, of MFAPNet was 2.3% larger than that of FCN, equal to that of UNet, and reached 99.93%, 91.77%, and 97.30% of that of PSPNet, DeepLabV3, and UperNet, respectively. In conclusion, although MFAPNet lagged behind PSPNet, DeepLabV3, and UperNet in terms of

TABLE 3 Comparison of the results obtained with different algorithms from VOC2012 dataset.

Method	Backbone	mIoU/%	mAcc/%	mFscore/%	mPrecision/%
FCN	ResNet-50	66.27	77.61	82.67	83.37
Unet	Unet	69.32	83.31	86.00	81.43
PSPNet	ResNet-50	71.18	81.38	86.88	85.46
DeepLabV3	ResNet-50	70.59	81.33	86.52	84.72
UperNet	ResNet-50	73.85	82.43	88.66	88.05
MFAPNet	ResNet-50	73.89	81.96	88.73	88.62

Note: Underlined numbers indicate the best result in terms of corresponding metric.

TABLE 4 Comparison of the results obtained with different loss functions from CHA355 dataset.

Loss functions	mIoU/%	mAcc/%	mFscore/%	mPrecision/%
CrossEntropyLoss	52.58	64.75	66.44	72.72
DiceLoss	49.93	63.90	63.85	66.33
FocalLoss	50.89	63.56	63.91	69.67
TverskyLoss	46.81	54.66	60.15	70.72
CBCED_Loss	54.34	68.04	68.00	70.72

Note: Underlined numbers indicate the best result of corresponding metric.

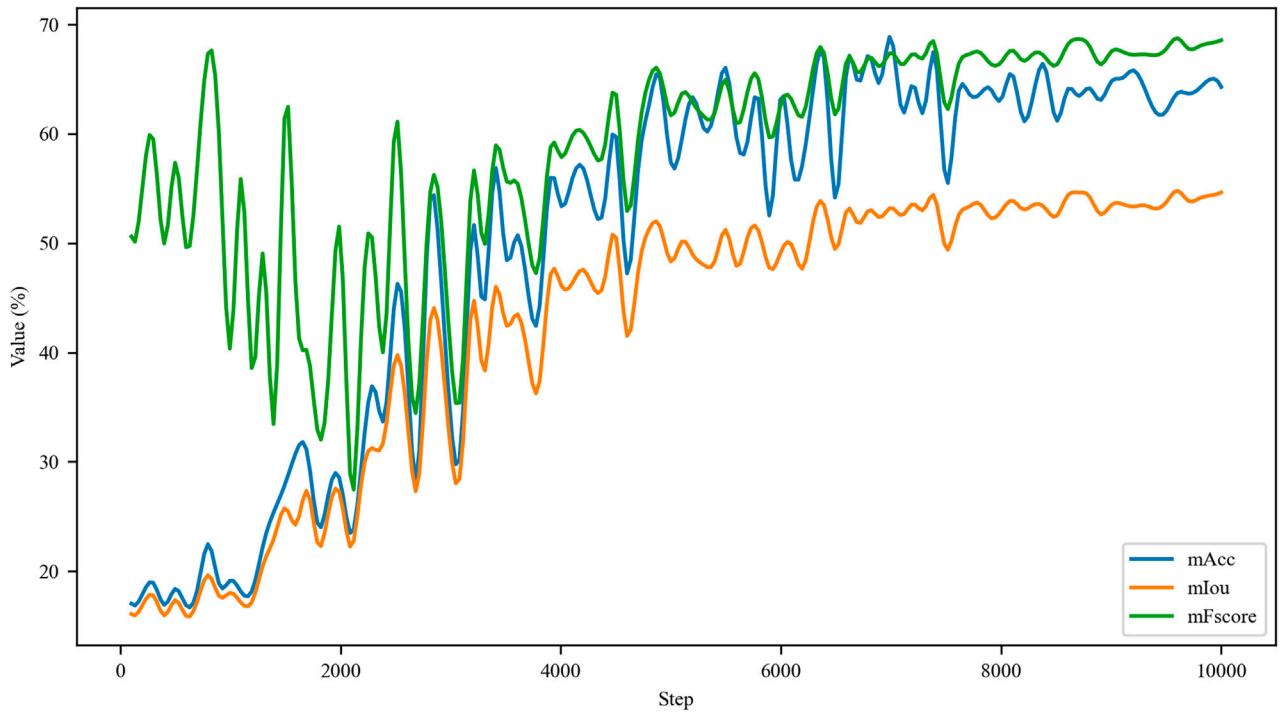

FIGURE 8
Training process.

mPrecision, its overall performance was better than that of the other five models in image segmentation.

The segmentation results obtained with various algorithms from VOC2012 dataset are shown in Table 3. The mIoU value of MFAPNet was 7.62%, 4.57%, 2.71%, 3.30%, and 0.04% larger than that of FCN, UNet, PSPNet, DeepLabV3, and UperNet, respectively. The mAcc value of MFAPNet was respectively 4.35%, 0.58%, and 0.63% larger than that of FCN, PSPNet, and DeepLabV3 and 1.62% and 0.57%

TABLE 5 Comparison of the results obtained with MFAPNet from CHA355 dataset.

Types	IoU/%	Acc/%	Fscore/%	Precision/%
Background	96.53	98.63	98.23	97.84
Unfilled holes	42.06	51.39	59.21	69.85
Filling holes	25.07	57.33	40.09	30.82
Filled fractures	48.64	60.71	65.45	70.98
Open fractures	57.81	78.81	73.27	68.45
Algae	55.95	61.37	71.76	86.37

Note: Underlined numbers indicate the best results of corresponding metric except the values of the background.

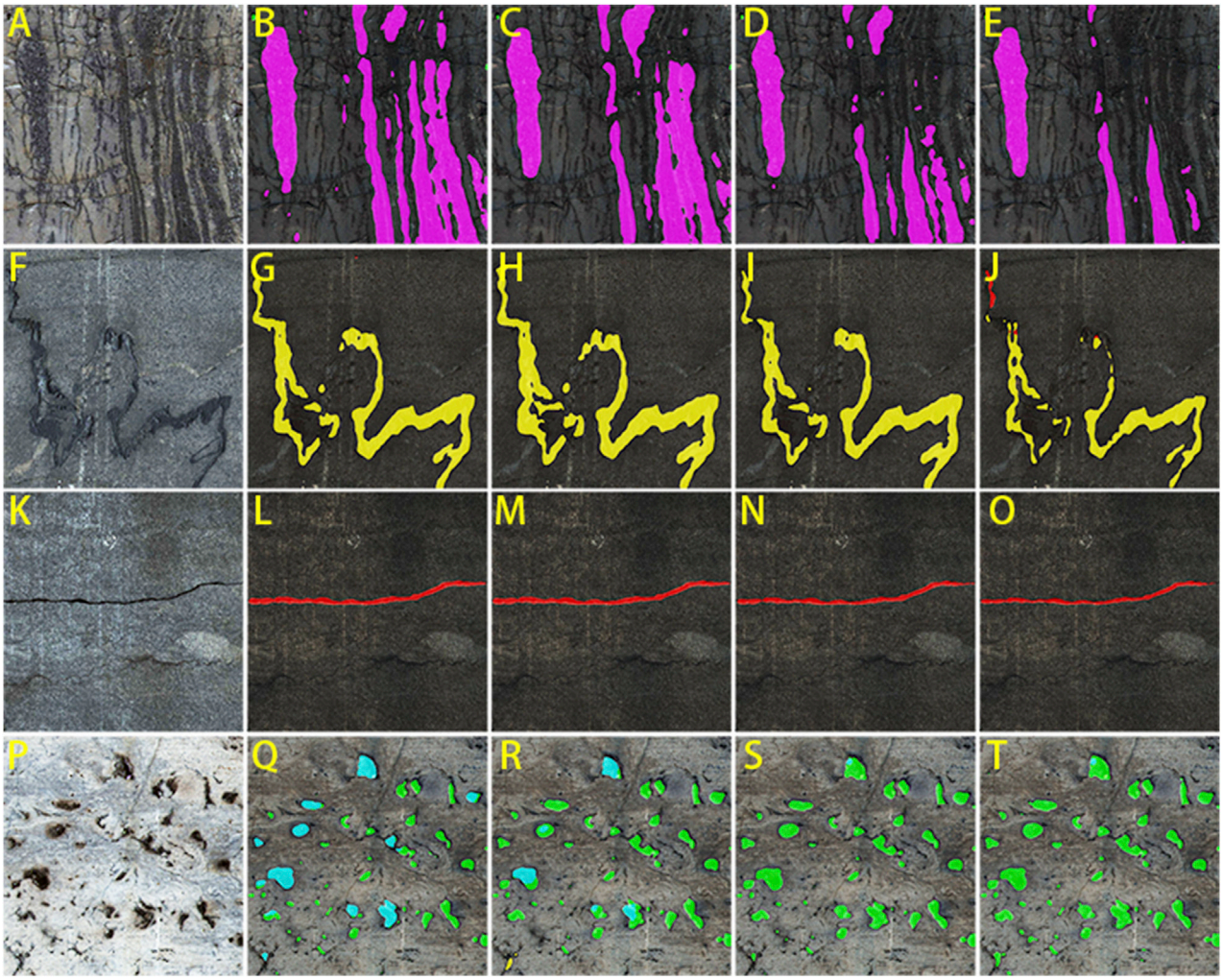

FIGURE 9
(**A, F, K, P**) are original images; (**B, G, L, Q**) are prediction results of MFAPNet; (C,H,M,R) are prediction results of PSPNet; (**D, I, N, S**) are prediction results of UperNet; (**E, J, O, T**) are prediction results of FCN. (**A**): Dominated by developmental algae, the algal layers are clearly visible; (**F**): Dominated by filled fractures, they pervade the entire image; (**K**): In the middle of the image, there is a open fracture that runs through the entire image; (**P**): Dominated by dissolved holes, some are unfilled while others are filled.

smaller than that of Unet and UperNet. The mFscore of MFAPNet was 6.06%, 2.73%, 1.85%, 2.21%, and 0.07% larger than that of FCN, UNet, PSPNet, DeepLabV3, and UperNet, respectively. The mPrecision of MFAPNet was 5.25%, 7.19%, 3.16%, 3.9%, and 0.576% larger than that of FCN, UNet, PSPNet, DeepLabV3, and UperNet, respectively.

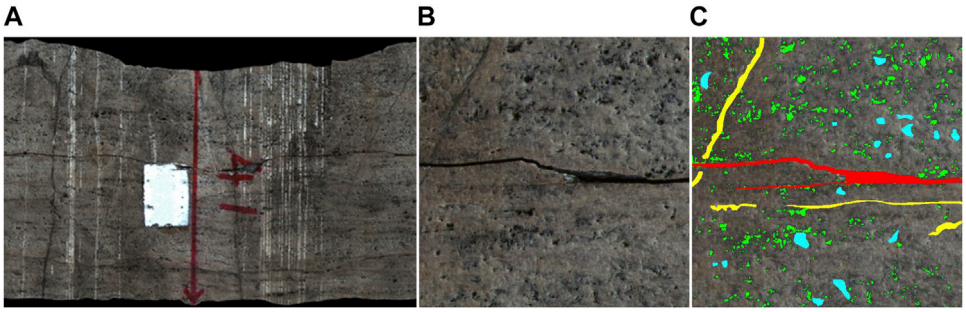

FIGURE 10
Comparison diagram: **(A)** original core rolling scan photo; **(B)** selected area; **(C)** predicted results.

5.4 Comparison of different loss functions

In this section, CBCED_Loss was compared with other loss functions: CrossEntropyLoss, DiceLoss, FocalLoss (Lin et al., 2017) and TverskyLoss (Milletari et al., 2016). CrossEntropyLoss quantifies the discrepancy between the predicted classification results of the model and actual labels and is commonly applied in multi-class classification scenarios. DiceLoss indicates the consistency of overlapping regions between predictions and actual labels and can address data imbalances. FocalLoss was designed to mitigate the class imbalance issue. In FocalLoss, in order to reduce the influence of easily classified samples, a larger weight is assigned to the samples which are difficult to be classified. In TverskyLoss, weight can be adjusted in the loss calculation so as to reach the balance between precision and recall.

Table 4 presents the results from CHA355 dataset. The mIoU value of CBCED_Loss was 1.76%, 4.41%, 3.45%, and 7.53% larger than that of CrossEntropyLoss, DiceLoss, FocalLoss, and TverskyLoss, respectively. Similarly, the mAcc value of CBCED_Loss was 3.29%, 4.14%, 4.48%, and 13.38% larger than that of CrossEntropyLoss, DiceLoss, FocalLoss, and TverskyLoss, respectively. The mFscore of CBCED_Loss was 1.56%, 4.15%, 4.09%, and 7.85% larger than that of CrossEntropyLoss, DiceLoss, FocalLoss, and TverskyLoss, respectively. The mPrecision, value of CBCED_Loss was 4.39% and 1.05% larger than that of DiceLoss and FocalLoss, equal to that of TverskyLoss, and 2.00% smaller than that of CrossEntropyLoss, respectively. In summary, even though the mPrecision of CBCED_Loss was slightly smaller than that of CrossEntropyLoss, its overall performance was more uniform and stable than the other four loss functions.

5.5 Training process and results

As shown in Figure 8, both mAcc (blue curve) and mIoU (orange curve) firstly display the consistent rising and stable trend and then converge. Notably, due to the utilization of pre-trained parameters from ImageNet-22K in this study, mFscore (orange curve) was large in the initial training phase. Then, these parameters were increasingly consistent with the dataset used in this study. After 4,000 iterations, the model was fully consistent with the parameters from the pre-trained model. The mFscore firstly increased and then converged.

As shown in Table 5, the model exhibited the optimal performance in recognizing filled fractures in the image except the background region. It distinguished open fractures from filled fractures better, but it could not distinguished unfilled holes from filled holes well. Furthermore, the model identified algae well.

5.6 Comparison of visualization results

Figure 9 shows the segmentation results obtained with various network models from CHA355 dataset. In the first row, due to the heterogeneity in algae features and considerable interference, the algal segmentation results of various network models were different. Notably, MFAPNet identified discrete algal layers better than other algorithms. The second row, characterized by white scratch interference, revealed that MFAPNet, PSPNet, and UperNet discerned filled fractures. In the third row, when obvious fractures could be observed without other interferences, every network model segmented the fractures well. In the fourth row, when mixed filled and unfilled holes could be observed, all models yielded false identification results of some holes. However, MFAPNet and UperNet could discriminate unfilled holes from filled holes. On the whole, the MFAPNet model developed in this study offered better segmentation results, outperformed other models in dealing with interferences and distinguishing filled regions from unfilled regions.

6 Application

In the study, the deep carbonate rock reservoir of the Dengying Formation in the Penglai Gas Field, Sichuan Basin was selected for porosity calibration. Figure 10A shows the original core rolling scan image of the segment PS9J.X977.10-X977.22. A representative area was selected (Figure 10B). This selected image was then input into MFAPNet to output the prediction result (Figure 10C).

Unfilled structures have no geological significance for oil and gas exploration, so only these parts were considered for further analysis. The porosity is calculated as:

$$Porosity = \frac{np.sum(\mathrm{Mask} == \mathrm{n})}{\mathrm{Mask}.size} \times 100\% \tag{12}$$

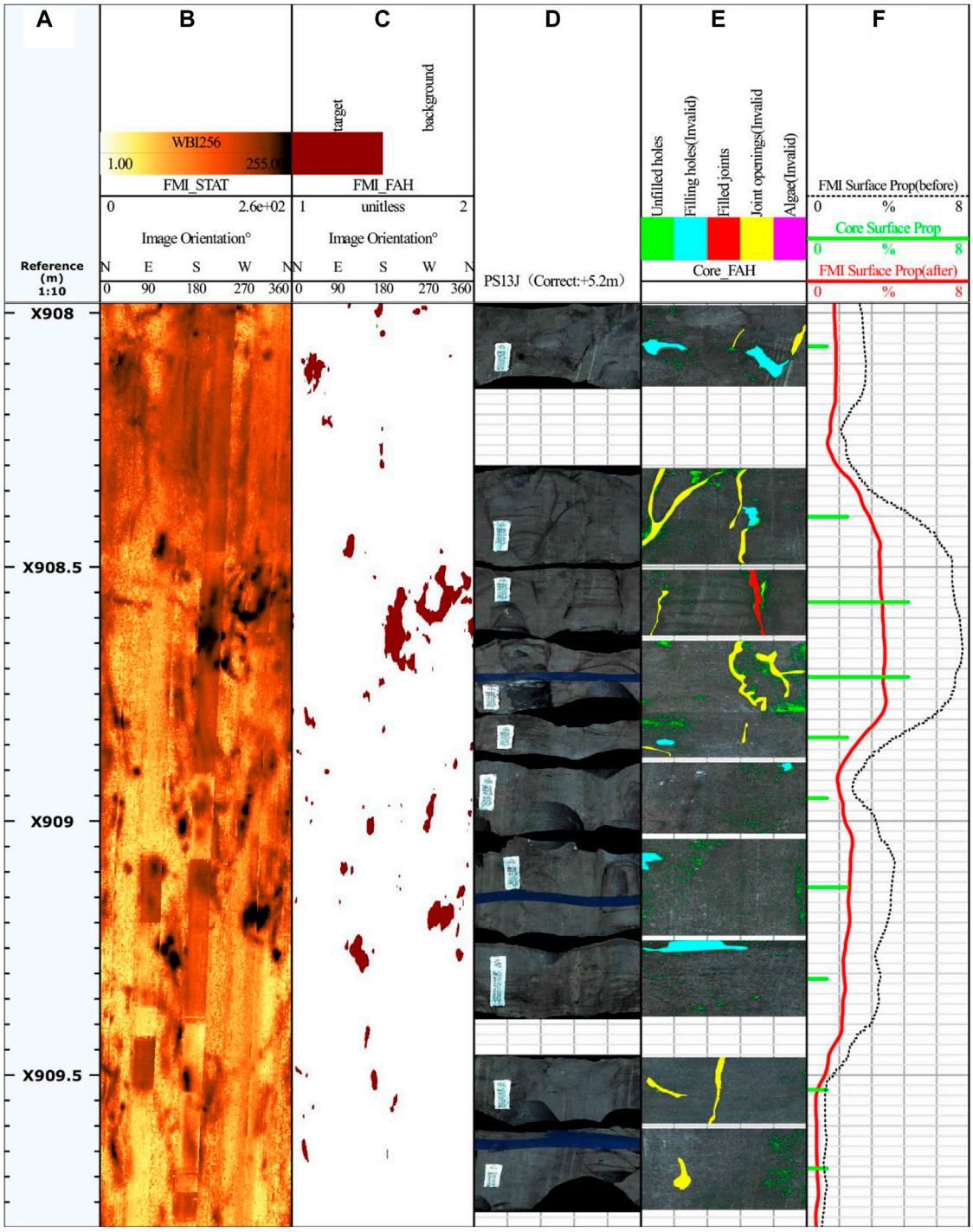

FIGURE 11
PS13J Comparison chart. **(A)** signifies a depth trace utilized for depth indexing. **(B)** represents a statically enhanced image derived from the Wellbore image. **(C)** displays an image capturing fractures and holes. **(D)** depicts a core rolling scan image at the specified depth. **(E)** denotes the outcomes following model segmentation. In **(F)**, a comparison of surface porosity is presented, with the black curve representing the surface porosity calculated based on the image of fractures and holes from the third trace. The green discrete columnar points correspond to the surface porosity derived from the respective core rolling scan image, and the red curve portrays the predicted core surface porosity post-calibration.

where *Mask* indicates the MFAPNet's prediction output; *np.sum*(*Mask* == n) indicates the summation of the values of the pixels with the predicted result equal to *n* (the value of unfilled fractures and holes); *Mask.size* indicates the cumulative value of the pixels in the predicted image. With Eq. 12; Figure 10C, the proportion of unfilled holes was calculated to be 4.48% and the proportion of open fractures was 2.41%. Consequently, core porosity for the segment shown in Figure 10A was 6.89%.

With this method, the porosity of PS13 core was determined, as illustrated in the porosity histogram (the sixth track in Figure 11).

Subsequent image segmentation enabled the extraction of wellbore imaging porosity (the third track), in which the wellbore imaging porosity curve was computed with a window length of 1 ft and a step of 0.1 in. When the logging tool's button electrode was close to an unfilled natural fracture, the resistivity of the drilling fluid within fractures was substantially lower than that of adjacent rock, thus leading to the large current of the electrode. As a result, the apparent width of fractures in imaging results was several times of their actual width (Nian et al., 2021). This phenomenon might also lead to the enlarged boundaries of dissolved holes. For a more precise representation of porosity, the curve was mathematically adjusted in this study. The refined curve was well consistent with the core porosity histogram. The curves in Figure 11 (sixth track) revealed that the porosity derived from wellbore imaging was 1.5–3 times of that obtained from core rolling scan images. Moreover, the difference increased with the decrease in porosity. This result, to some extent, reveals the correlation between the wellbore image logging data and the actual characteristics of the Dengying Formation in the Penglai Gas Field of the Sichuan Basin. It also provides a certain basis for the subsequent logging evaluation of the formation.

7 Conclusion

1. Based on the detailed descriptions of the core rolling scan images of the deep carbonate rock reservoir of the Dengying Formation in Penglai Gas Field, Sichuan Basin, we successfully acquired the distinct features of various fractures and holes and formulated a robust classification framework for these types. We highlighted three primary challenges in segmenting datasets comprising fractures, holes, and algae: variance in feature scales, class imbalance, and a limited dataset number with larger samples.
2. After the introduction of SAM segmentation model, we facilitated semi-automatic delineation of the target regions (fractures and holes) from the background in images and markedly accelerated the geological dataset compilation process.
3. We developed the MFAPNet semantic segmentation deep learning model, which ensured swift and high-fidelity intelligent recognition of fracture types as well as the quantitative analysis of fractures and holes.
4. We explored the porosity of wellbore imaging results and core rolling scan images and further validated the calibration relationship between electric imaging results and core rolling image porosity.

Data availability statement

The datasets presented in this study can be found in online repositories. The names of the repository/repositories and accession number(s) can be found below: https://github.com/zyng886/MFAPNet.

Author contributions

QL: Funding acquisition, Writing–review and editing. YW: Funding acquisition, Writing–review and editing. YZ: Writing–original draft. BX: Data curation, Investigation, Writing–review and editing. YJ: Data curation, Investigation, Writing–review and editing. LC: Data curation, Investigation, Writing–review and editing. MT: Data curation, Writing–review and editing. FL: Funding acquisition, Methodology, Resources, Writing–review and editing.

Funding

The author(s) declare financial support was received for the research, authorship, and/or publication of this article. The authors declare financial support was received for the research, authorship, and/or publication of this article. This work was financially supported by the National Natural Science Foundation of China (Grant 41402118) and also supported by Chongqing Municipal Education Commission Science and Technology Research Projects (KJZD-K202301508 and KJON202301535).

Acknowledgments

The authors are grateful to Yuejiao Liu for his invaluable assistance with scanning the sample.

Conflict of interest

Authors QL, YW, BX, and LC were employed by PetroChina Southwest Oil & Gas Field Company.

The remaining authors declare that the research was conducted in the absence of any commercial or financial relationships that could be construed as a potential conflict of interest.

Publisher's note

References

Chen, L. C., Papandreou, G., Schroff, F., and Adam, H. (2017). Rethinking atrous convolution for semantic image segmentation. arXiv preprint arXiv:1706.05587. Available at: https://doi.org/10.48550/arXiv.1706.05587.

Chen, Z. M., Tang, X., Liang, G. D., and Guan, Z. H. (2023). Identification and comparison of organic matter pores in shale scanning electron microscope images based on deep learning. *Earth Sci. Front.* 2023 (03), 208–220. doi:10.13745/j.esf.sf.2022.5.45

Delhomme, J. P. (1992). "A quantitative characterization of formation heterogeneities based on borehole image analysis," in Trans 33rd Symp Soc Prof Well Log Analysts, Oklahoma City, Oklahoma, June 1992. Paper T.

Everingham, M., Van Gool, L., Williams, C. K. I., Winn, J., and Zisserman, A. (2012). *The PASCAL visual object classes challenge 2012 (VOC2012) results*.

Hall, J., Ponzi, M., Gonfalini, M., and Maletti, G. (1996). "Automatic extraction and characterization of geological features and textures from borehole images and core photographs," in Trans 37th Symp Soc Prof Well Log Analysts, New Orleans, Louisiana, June 1996. Paper CCC.

He, K., Zhang, X., Ren, S., and Sun, J. (2016). "Deep residual learning for image recognition," in Proceedings of the IEEE conference on computer vision and pattern recognition, Las Vegas, NV, USA, 27-30 June 2016, 770–778.

Ioffe, S., and Szegedy, C. (2015). "Batch normalization: accelerating deep network training by reducing internal covariate shift," in International conference on machine learning, 448–456. pmlr.

Kirillov, A., Mintun, E., Ravi, N., Mao, H., Rolland, C., and Gustafson, L. (2023). Segment anything. arXiv preprint arXiv:2304.02643. Available at: https://doi.org/10.48550/arXiv.2304.02643.

Lai, F. Q. (2011). *Study on the processing and interpretation methods of electric imaging logging*. Beijing: China University of Petroleum.

Li, B. T., Wang, Z. Z., Kong, C. X., Jiang, Q. P., Wang, W. F., Lei, X. H., et al. (2019). New method for intelligent identification of fractures based on imaging logging. *Well Logging Technol.* 2019 (03), 257–262. doi:10.16489/j.issn.1004-1338.2019.03.007

Li, Z. H., Zhang, X., Luo, L., Mao, Y. X., and Li, M. (2016). Automatic identification and parameter calculation of holes in carbonate rock with a complex background. *Fract. Oil Gas Fields* 2016 (03), 314–323.

Lin, T. Y., Goyal, P., Girshick, R., He, K., and Dollár, P. (2017). "Focal loss for dense object detection," in Proceedings of the IEEE international conference on computer vision, Venice, Italy, 22-29 October 2017, 2980–2988.

Li X, X., Sun, X., Meng, Y., Liang, J., Wu, F., and Li, J. (2019). Dice loss for data-imbalanced NLP tasks. arXiv preprint arXiv:1911.02855. Available at: https://doi.org/10.48550/arXiv.1911.02855.

Long, J., Shelhamer, E., and Darrell, T. (2015). "Fully convolutional networks for semantic segmentation," in Proceedings of the IEEE conference on computer vision and pattern recognition, Boston, MA, USA, 07-12 June 2015, 3431–3440.

Ma, Y. S., Cai, X. Y., Li, H. L., Zhu, D. Y., Zhang, J. T., Yang, M., et al. (2023). New understanding of the development mechanism of deep-super deep carbonate reservoirs and the direction of ultra-deep oil and gas exploration. *Geol. J.* 30.06 (2023), 1–13. doi:10.13745/j-esf.sf.2023.2.35

Ma, Y. S., Cai, X. Y., Yun, L., Li, Z. J., Li, H. L., Deng, S., et al. (2022). Exploration and development practices and theoretical and technical advancements in the Shunbei ultra-deep carbonate oil and gas field in the Tarim Basin. *Petroleum Explor. Dev.* 01, 1–17.

Ma, Y. S., He, Z. L., Zhao, P. R., Zhu, H. Q., Han, J., You, D. H., et al. (2019). New progress in the formation mechanism of deep-super deep carbonate reservoirs. *Acta Pet. Sin.* 2019 (12), 1415–1425.

Milletari, F., Navab, N., and Ahmadi, S. A. (2016). "V-net: fully convolutional neural networks for volumetric medical image segmentation," in 2016 fourth international conference on 3D vision (3DV), Stanford, CA, USA, 25-28 October 2016, 565–571.

Nian, T., Wang, G. W., Fan, X. Q., Tan, C. Q., Wang, S., Hou, T., et al. (2021). Progress in fracture and cave interpretation evaluation based on imaging logging. *Geol. Rev.* 2021 (02), 476–488. doi:10.16509/j.georeview.2021.02.016

Ren, X. F., Wen, X. F., Lin, W. C., Liu, A. P., Yu, B. C., and Cai, F. (2023). Quantitative characterization technology and its application based on micro-resistivity imaging logging of tight carbonate rock pore space parameters. *Well Logging Technol.* 47 (01), 48–54.

Ronneberger, O., Fischer, P., and Brox, T. (2015). "U-net: convolutional networks for biomedical image segmentation," in Medical Image Computing and Computer-Assisted Intervention–MICCAI 2015: 18th International Conference, Munich, Germany, October 5-9, 2015, 234–241. Proceedings, Part III 18.

Tian, F., and Zhang, C. G. (2010). Fracture identification technology of electric imaging logging data and its application. *J. Geophys. Eng.* 7 (6), 723–727.

Wang, L., Shen, J. S., Heng, H. L., and Wei, S. S. (2021). Research on automatic identification and separation of fractures and caves in electric imaging logging based on path morphology and sine function family matching. *Petroleum Sci. Bull.* 6 (03), 380–395.

Wang, Q., Wu, B., Zhu, P., Li, P., Zuo, W., and Hu, Q. (2020). "ECA-Net: efficient channel attention for deep convolutional neural networks," in Proceedings of the IEEE/CVF conference on computer vision and pattern recognition, 11534–11542.

Xiao, T., Liu, Y., Zhou, B., Jiang, Y., and Sun, J. (2018). "Unified perceptual parsing for scene understanding," in Proceedings of the European conference on computer vision (ECCV), 418–434.

Zhao, H., Shi, J., Qi, X., Wang, X., and Jia, J. (2017). "Pyramid scene parsing network," in Proceedings of the IEEE conference on computer vision and pattern recognition, 2881–2890.

Zou, C. N., Du, J. H., Xu, C. C., Wang, Z. C., Zhang, B. M., Wei, G. Q., et al. (2014). *Formation distribution, resource potential, and exploration discoveries of the Sinian-Cambrian in the Sichuan Basin*. Petroleum Exploration and Development.

frontiers | Frontiers in Earth Science

TYPE Original Research
PUBLISHED 16 January 2024
DOI 10.3389/feart.2023.1325094

OPEN ACCESS

EDITED BY
Lidong Dai,
Chinese Academy of Sciences, China

REVIEWED BY
Zhihao Jiang,
Xi'an Shiyou University, China
Mehdi Ostadhassan,
Northeast Petroleum University, China

*CORRESPONDENCE
Liang Wang,
wangliang_swpu@163.com

RECEIVED 20 October 2023
ACCEPTED 23 November 2023
PUBLISHED 16 January 2024

CITATION
Su S, Wang L, Li J, Lu J, Luo Y and Jia J (2024), Research on porosity characterization methods of shale oil reservoirs in Lianggaoshan Formation, Sichuan Basin.
Front. Earth Sci. 11:1325094.
doi: 10.3389/feart.2023.1325094

Research on porosity characterization methods of shale oil reservoirs in Lianggaoshan Formation, Sichuan Basin

Shute Su[1,2], Liang Wang[1,2]*, Jun Li[1], Jing Lu[1], Yang Luo[2] and Jun Jia[3]

[1]Sinopec Key Laboratory of Shale Oil/Gas Exploration and Production Technology, Beijing, China, [2]College of Energy, Chengdu University of Technology, Chengdu, China, [3]College of Resource and Environmental Engineering, Mianyang Normal University, Mianyang, China

Shale oil, an important component of unconventional oil and gas resources, mainly exists in the storage spaces such as shale pores, microfractures, etc. Porosity is commonly used to quantitatively describe the storage space of shale oil and is a key parameter in reservoir evaluation. However, there are significant differences in the results by existing experimental methods for porosity measurement, and moreover, it is difficult to compare the porosity obtained by the experimental measurement method with the logging calculation method. It is urgent to explore reasons for the differences in porosity measurement between various porosity experiments and logging calculations of the shale oil reservoir, and propose an effective method for shale oil reservoir to characterize porosity. In this research, core samples of shale oil reservoirs from the Lianggaoshan Formation of the Sichuan Basin were selected to measure the porosity by means of experimental methods including helium gas charging, saturation liquid method, nuclear magnetic resonance (NMR), etc. Meanwhile, porosity was calculated using the combination method of lithology scanning (LS) logging and conventional logging as well as the NMR logging method. Subsequently, porosity experimental results and logging calculation results were compared to clarify the applicability of various porosity characterization methods. The research results indicate that: 1) The porosity measurement results by the saturation liquid method and the NMR experimental method are close, both greater than that using the helium gas charging method; 2) The hydrogen signal of the dry-state sample is significant in the NMR experiment, mainly originating from organic matter and clay minerals; 3) The NMR short relaxation component in the water-saturated state primarily reflects the signal of organic matter and clay mineral matrix, while the long relaxation component reflects the pore fluid component; 4) After deducting the NMR signal of the dry-state core, the core NMR porosity measurement results under the water-saturated state agree well with that using the saturation liquid method, which is an indicative of effective reservoir porosity; 5) The NMR logging is limited by its echo spacing and cannot reflect the signal from organic matter and the crystal water in clay minerals at $T_2 < 0.3$ ms. Taken together, the porosity

measurement method of subtracting the dry-state NMR signal from the water-saturated state NMR signal is considered effective and can be used to reflect the porosity of shale oil reservoirs in the Lianggaoshan Formation of the Sichuan Basin.

KEYWORDS

Sichuan Basin, Lianggaoshan Formation, shale oil, porosity, NMR experiment, logging

1 Introduction

With the continuous growth in global oil and gas demand and advancements in horizontal well drilling and fracturing technology, the exploration and development of shale oil reservoirs have become the focus of academic and industrial interest in recent years (Liu and Liu, 2006; Zhang et al., 2014; Jin et al., 2019; Li et al., 2019). Shale oil, as a type of unconventional oil and gas with enormous potential, has been recognized by geologists worldwide as an important supplement to the growth of oil and gas reserves in major basins (Schmoker, 2002; Zhang et al., 2015; Hu et al., 2020). Currently, the United States has been the most successful in the exploration and development of shale oil and gas, with a production accounting for over 60% of its total crude oil production (Zou et al., 2014; Zou et al., 2020). Shale oil explorations such as Barnett (Zeng et al., 2011; Modica and Lapierre, 2012), Eagle Ford (Domovan et al., 2016), and Bakken (Pollastro et al., 2012)in the United States have become the subject of study for various countries. Additionally, shale oil regions such as Montney and Horn River in Canada (Chalmers and Bustin, 2012) and the Bazhenov shale formation in Russia (Kontorovich et al., 2018) have also seen relatively successful exploration and development of shale oil. In recent years, the shale oil exploration in China has primarily focused on continental shale oil (Zou et al., 2010). As of 2023, significant discoveries of shale oil and gas formations have been made in various regions in China, including the Gulong shale oil area in Daqing (Sun et al., 2021), the Lucaogou Formation shale oil in the Junggar Basin (Yang et al., 2018; Zhi et al., 2019), and the Yanchang formation shale oil in the Ordos Basin (Cui et al., 2019; Fu et al., 2020).

The samples analyzed in this study were collected from the Lianggaoshan Formation located in the northeastern part of the Sichuan Basin. The Lianggaoshan Formation, which is part of the lacustrine sedimentary system, can be divided into three distinct members from bottom to top. The lithology of the formation exhibits strong heterogeneity, comprising pure shale assemblages, shell shale assemblages, and silt-type shale assemblages. Additionally, six thick sets of shale have been identified and documented (Rui et al., 2023). In 2020, significant breakthroughs were made in the exploration of shale oil in the Jurassic Lianggaoshan Formation of the Sichuan Basin (He et al., 2022a; 2022b). On-site tests conducted at the Ping'an 1 Well in the northeastern part of the basin revealed a daily oil production rate of 112.8 m^3 and a daily gas production rate of 11.45 × 104 m^3, highlighting the significant potential for shale oil and gas exploration in the Lianggaoshan Formation.

Porosity is the most critical parameter for evaluating shale oil reservoirs. The accurate characterization of porosity directly impacts the calculation of shale oil and gas reserves as well as the selection of development plans (Jian-fei et al., 2012). The porosity of shale oil reservoirs can be divided into two main aspects based on different characterization methods: geophysical (seismic and logging) calculations (Yang et al., 2015; Xiu-wen et al., 2011; Zhang et al., 2012; Li et al., 2017; Li et al., 2017) and core experiments (Tian et al., 2012; Jiao et al., 2014; Wang et al., 2014). Due to the influence of seismic data accuracy and resolution, the accuracy of porosity characterization by seismic methods is relatively low and is commonly used to predict the trend of macroscopic porosity changes (Ma et al., 2020). According to the rock physics volume model, conventional logging measurements such as acoustic, density, and neutron loggings can be used to calculate reservoir porosity (Shihe and Zhang, 1996). However, the key to accurately calculating reservoir porosity based on the rock volume physics model is the accurate determination on parameters such as reservoir rock matrix density, neutron, acoustic, etc. The direct acquisition of these reservoir rock matrix parameters relies on lithology scanning (LS) logging (Litho Scanner). The LS logging is based on the inelastic scattering of fast speed neutrons with the atomic nuclei of formation elements to accurately capture the continuous elements and mineral composition of the formation and obtain the matrix density and matrix neutron values with continuous depths (Yan et al., 2018). The obtained signal by nuclear magnetic resonance (NMR) logging is proportional to the quantity of hydrogen nuclei in the detecting formation. Through calibration, the NMR logging signal can accurately reflect the formation porosity. Furthermore, based on the accurately obtained NMR T_2 cutoff value, porosity can be divided into clay bound water porosity, capillary bound water porosity, and movable fluid porosity (Zhi-qiang et al., 2010).

The methods for determining porosity in shale oil and gas reservoirs mainly include gas charging, saturation liquid, and NMR methods. Shale oil and gas reservoirs are rich in organic matter, with pores primarily in the nano to micrometer range. To prevent gas medium adsorption, the gas charging method often uses inert helium gas as the medium when measuring porosity (Fu, 2018). The results of this method are mainly influenced by factors such as the degree of sample crushing, gas equilibrium pressure, and equilibrium time. The saturation liquid method is mainly based on the Archimedes' buoyancy principle. It calculates the porosity through measuring the dry weight of the core and its weight in both air and a known density fluid after saturated with the known fluid, and then calculating the total volume and matrix volume of the core (Zhou et al., 2021). This method may be influenced by clay expansion, wetting properties, the type of saturation fluid, and the degree of saturation. The NMR method has the advantages of fast, accurate, and high resolution, and can effectively reflect the "*in situ*" and "integrity" of reservoir pores. The intensity of NMR signals in conventional reservoirs depends on the total amount of pore fluid. However, in shale oil and gas reservoirs, hydrogen atoms in clay mineral crystal water and organic matter contain NMR signals, which in turn affect porosity measurement (Wang et al., 2018). Ramirez et al. (2011) applied the NMR method to measure the

10.3389/feart.2023.1325094

porosity value of Haynesville shale in Texas, United States. The measured value was obviously different from the porosity measured by the GRI method on crushed core samples. The interpretation of the data involves uncommon specific reservoir evaluation parameters, leading to greater uncertainty. Han et al. (2020) conducted porosity measurements on the Longmaxi Formation shale in the Sichuan Basin and found that different magnetic fields and echo spacings had an impact on the porosity measurement results. Yang et al. (2015) demonstrated through experimental research that, comparing the use of real density and apparent density method, low-temperature nitrogen adsorption method, and helium gas expansion method on both crushed samples and plunger samples, plunger sample porosity determination yielded the most accurate results (Yang et al., 2015). Renyan (2016) used the GRI method, low-pressure nitrogen adsorption method, and NMR method, respectively to measure the shale porosity of the Longmaxi Formation (Renyan, 2016). They concluded that the nitrogen adsorption method yielded the smallest porosity, which was not suitable for shale porosity measurement, and that the NMR measured porosity was greater than the GRI measured porosity. Tian Chong et al. studied the porosity measurement results using the helium gas method under different drying temperatures, vacuum extraction times, and helium gas saturation equilibrium pressures, and found that the helium gas method for porosity measurement based on shale plunger samples under the vacuum extraction and strict equilibrium conditions was relatively accurate and could reflect the effective porosity of shales (Tian et al., 2023).

Literature research shows that the study of porosity in shale oil and gas reservoirs primarily focuses on the shale gas reservoir, with relatively fewer studies on the porosity characterization in shale oil reservoirs. In addition, there are also rare comparative studies between the experimentally measured porosity and the logging-calculated porosity. Under such a condition, this paper conducts research on the core samples of shale oil reservoirs in the Lianggaoshan Formation of the Sichuan Basin. Specifically, experimental methods including helium gas charging, saturation liquid method, and NMR method are used for porosity measurement. Meanwhile, porosity is calculated using the combination method of LS logging and conventional logging as well as the NMR logging method. Next, comparative analysis of differences between experimentally measured porosity and logging-calculated porosity is performed to clarify the applicability of each method. Finally, an effective porosity characterization method for shale oil and gas reservoirs in the Lianggaoshan Formation of the Sichuan Basin is proposed.

2 Sample characteristics and experimental methods for porosity characterization

2.1 Sample characteristics

The experimental samples for core porosity measurement were taken from the shale oil reservoir section of Well A in the Lianggaoshan Formation of the central Sichuan Basin (Table 1). To avoid water-induced clay expansion commonly occurred in

TABLE 1 Basic sample information.

Sample	Depth (m)	Length (cm)	Diameter (cm)	TOC (%)	Clay (%)	POR_Helium (%)	POR_Water (%)	POR_NMR (%)		POR_Logging (%)		POR_CMR (%)	
								Dry	Water-saturated	Density	Neutron	PHIT	PHIE
1	X6 58.6	5.842	2.492	1.529	41.626	2.860	4.387	8.499	12.950	9.254	15.119	7.202	3.816
2	X6 61.5	6.188	2.504	1.646	48.118	3.380	5.083	8.807	14.408	9.875	16.554	7.978	3.570
3	X7 11.9	5.198	2.502	0.712	45.294	1.220	2.774	6.930	9.854	7.712	18.232	6.614	3.616
4	X7 17.2	6.454	2.482	1.465	58.061	2.870	5.297	10.454	16.561	15.739	17.949	10.293	5.520
5	X7 21.9	6.554	2.486	1.452	43.791	2.820	9.245	9.138	19.336	13.614	18.221	11.856	10.861
6	X7 26.7	6.812	2.502	0.771	44.247	1.890	2.592	5.435	7.970	3.598	7.028	5.095	2.538
7	X7 38.8	6.288	2.502	1.405	40.630	3.460	7.996	8.582	16.136	4.942	13.497	13.731	8.564
8	X7 43.8	6.686	2.502	1.012	39.631	3.100	4.122	5.287	9.716	7.983	14.082	10.595	5.329
9	X7 48.8	6.422	2.502	0.753	35.282	2.310	2.217	5.518	7.806	6.631	16.483	6.405	3.54
10	X7 53.8	6.088	2.502	0.811	45.593	1.050	1.721	2.192	5.632	3.519	9.859	8.197	4.592

conventional core drilling and the damage to samples caused by hydration (Fu et al., 2012), water-free and wire-cutting methods were taken to prepare the standard plunger samples before experiment. The sample depth, length, diameter, and other information are detailed in Table 1. The TOC of samples ranges from 0.712% to 1.646%, with an average of 1.156%; the clay mineral content ranges from 35.282% to 58.061%, with an average of 44.227%.

2.2 Experimental methods for porosity characterization

2.2.1 Helium gas charging method

The rock matrix volume was measured according to Boyle's law, and the formula for calculating the sample rock matrix volume is as follows:

$$V_g = V_s - V_r\left(\frac{P_1 Z_2}{P_2 Z_1} - 1\right) \quad (1)$$

where P_1 is the pressure of the reference chamber before expansion, and P_2 is the equilibrium pressure of the system after expansion, in MPa; V_r, V_s, and V_g represent the volumes of the reference chamber, sample chamber, and sample matrix, respectively, in cm^3; Z_1 represents the compressibility factor of the gas under the pressure condition P_1; Z_2 represents the compressibility factor of the gas under the pressure condition P_2. After measuring the rock matrix volume, the rock's total volume was obtained using the water immersion method, and then the porosity of the cylindrical shale can be calculated as follows:

$$\varnothing_{GIP} = \frac{V_t - V_g}{V_t} \times 100\% \quad (2)$$

where $\varnothing_{GIP}$ is the sample porosity by the gas measurement method, and V_t is the total volume of the sample, in cm^3. The experimental process complied with the national standard, i.e., Measurement of helium porosity and pulse decay permeability of shale (GB/T 34533-2017), and the Chinese petroleum industry standard, i.e., Practices for core analysis (SY/T 5336-2016).

2.2.2 Saturated liquid method

The saturated deionized water method was used to measure the porosity of core samples. Firstly, the mass of the dried sample was measured and recorded as m_1, and then the rock sample was weighed after being vacuumed and saturated with distilled water, recording the weight as m_2. The porosity measured by the saturated liquid method was calculated as:

$$\varnothing_W = \frac{\rho_B - \rho_G}{\rho_L - \rho_G} \times 100\% \quad (3)$$

where $\varnothing_W$ is the porosity obtained by the liquid measurement method; ρ_B, ρ_G, and ρ_L are the dry weight of the sample, the weight of the sample after being saturated with water, and the density of the saturated fluid in g/cm^3; ρ_{H_20} is the density of distilled water. The experimental process followed the Chinese petroleum industry standard, Practices for core analysis (SY/T 5336-2016).

2.2.3 NMR method

In the NMR experiment, a sample was placed in a uniform magnetic field, and the hydrogen nuclei in the fluid were polarized by the field. At this moment, a RF field of a certain frequency was applied to the sample. Then the RF field was turned off, and energy was released as the hydrogen nuclei changing from a polarized state to a stable state. In this experiment, the longitudinal relaxation time T_1 and the transverse relaxation time T_2 were measured by instrument. The relationship between the transverse relaxation time T_2 and the semaphore reflected the content and distribution of hydrogen-containing fluids in the formation, and it, after calibration, could also reflect the porosity and pore structure of the formation. The experimental procedure followed the Chinese petroleum industry standard, Specification for measurement of rock NMR parameter in laboratory (SY/T 6490-2014).

2.3 Experimental process of porosity measurement and its parameters

The experimental process is as follows. First, the plunger samples were dried to a constant weight in an oven set at 105°C. Subsequently, the experimenter measured the helium porosity of the dried core samples in a laboratory with a room temperature of 25°C and atmospheric pressure of 1 standard atmosphere. Next, measurements were conducted on some of the dried core samples to obtain the one-dimensional NMR T2 and two-dimensional NMR T1-T2 spectra. Next, the dried core samples were pressurized at 20 MPa and saturated with 6,000 ppm water for 24 h. Eventually, the one-dimensional NMR T_2 spectra and the two-dimensional NMR T_1-T_2 spectra of the core samples at the saturated water state were measured, and at the same time, the porosity of the saturated liquid method is measured. In this experiment, a low-field (2 MHz) NMR core analyzer was used as the experimental instrument, the echo spacing was 0.06 ms, the relaxation delay was 3 s, with a total of 2,000 echoes and 256 times of scanning.

3 Porosity logging calculation method

Well A has a complete logging suite, including both conventional and unconventional logging data. The conventional loggings include natural gamma ray (GR), spontaneous potential (SP), caliper (CAL), compensated acoustic wave (AC), compensated density (DEN), compensated neutron (CNL), deep lateral resistivity (RD), shallow lateral resistivity (RS), etc. The unconventional loggings include the LS logging and the NMR logging (CMR-NG).

3.1 Porosity calculation method by combining LS logging with conventional logging

The LS logging result showed that the mineral composition of the shale oil and gas reservoir in the Lianggaoshan Formation was complex, including chlorite, illite, quartz, feldspar, dolomite, calcite, and others. Different elemental contents in each mineral component

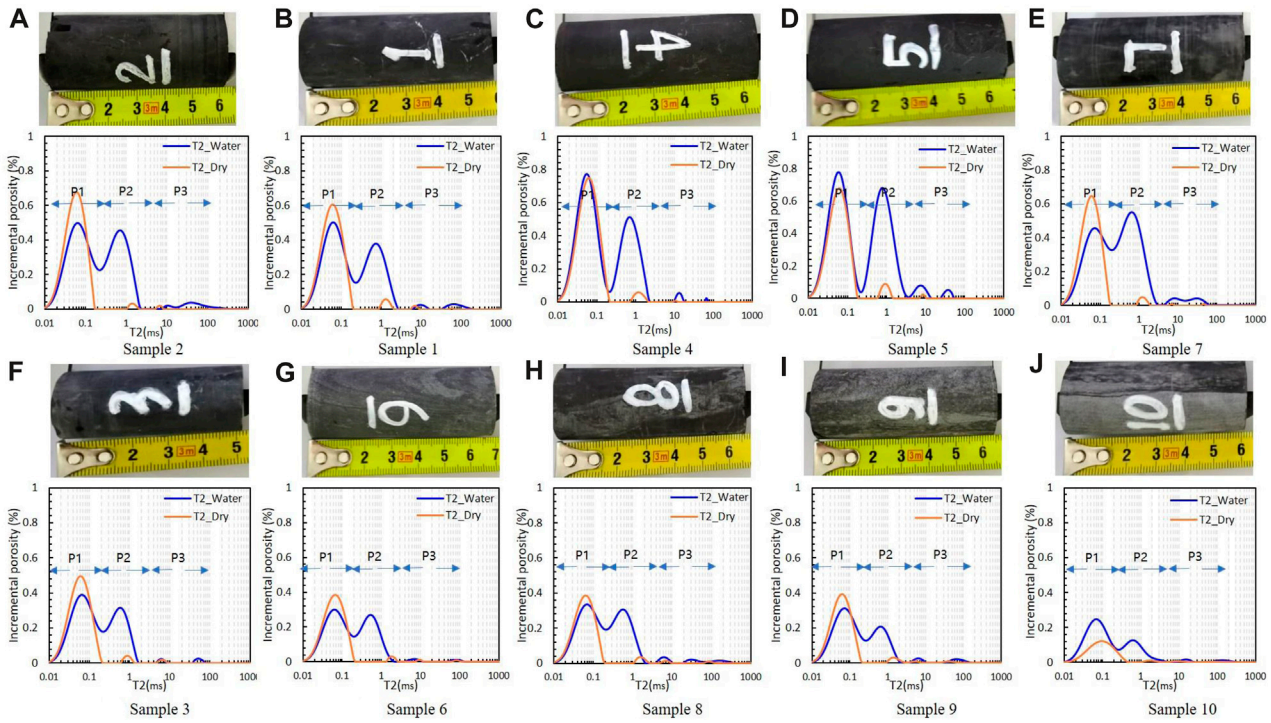

FIGURE 1
The 1D NMR experimental results of core samples under dry and water-saturated states.

have a significant impact on the rock matrix density and matrix neutron. With regard to the LS logging, the elemental contents were measured to calculate the rock matrix density RHGE and the matrix neutron TNGE (Liu et al., 2004). Based on the rock matrix neutron and matrix density loggings, the porosity of the shale oil and gas reservoir could be calculated according to the conventional density and neutron loggings by using the rock physics volume model. The formula for calculating porosity based on the neutron and density loggings can be expressed as:

$$PORD = \frac{DEN - RHGE}{DEN_f - RHGE} \tag{4}$$

$$PORN = \frac{CNL - TNGE}{CNL_f - TNGE} \tag{5}$$

where *PORD* and *PORN* are the logging-calculated density porosity and neutron porosity, respectively, in decimal form; *DEN* and DEN_f are the density logging values and fluid density values, respectively, in g/cm^3; *CNL* and CNL_f are the neutron logging values and neutron fluid values, respectively, in %; *RHGE* is the formation matrix density obtained by LS logging, in g/cm^3; *TNGE* is the formation matrix neutron obtained by LS logging, in %.

3.2 Porosity calculation with NMR logging

The principle of porosity calculation with NMR logging is similar to that of the NMR experimental porosity measurement. However, due to factors such as measurement environment, measurement efficiency, and measurement instrument precision, there are certain differences between the obtained parameters by NMR loggings and NMR experiments. The NMR logging for Well A adopted the CMR-NG instrument with a minimum echo spacing of 0.2 ms, which is greater than the 0.06 ms echo spacing in NMR experiments. As the echo spacing increased, the NMR logging became less effective in detecting signals from small pore fluids in the short relaxation section, making its resolution for small pores weaker than that of in the NMR experiment. The NMR logging signal was directly proportional to the number of hydrogen nuclei detected in the formation. With proper calibration, the NMR logging signal could accurately reflect the formation porosity (Xiao et al., 2001). The NMR porosity model for conventional formation includes matrix, dry clay, clay-bound water, irreducible fluid, and movable fluid. Using different T_2 cutoff values, the total porosity PHIT, effective porosity PHIE, and movable fluid volume FFI of the rock can be calculated according to Eqs 6–8, respectively and the NMR logging data.

$$\mathrm{PHIT} = \int_{T_{2min}}^{T_{2max}} \boldsymbol{S}(\boldsymbol{T_2})\boldsymbol{dT_2} \tag{6}$$

$$\mathrm{PHIE} = \int_{T_{2c}}^{T_{2max}} \mathbf{S}(\mathbf{T_2})\mathbf{dT_2} \tag{7}$$

$$\boldsymbol{FFI} = \int_{T_{2cutoff}}^{T_{2max}} \boldsymbol{S}(\boldsymbol{T})\boldsymbol{dt} \tag{8}$$

where $T_{2\mathrm{min}}$ is the minimum T_2 value observed by the NMR logging instrument, in ms, and this value for the CMR-NG instrument was

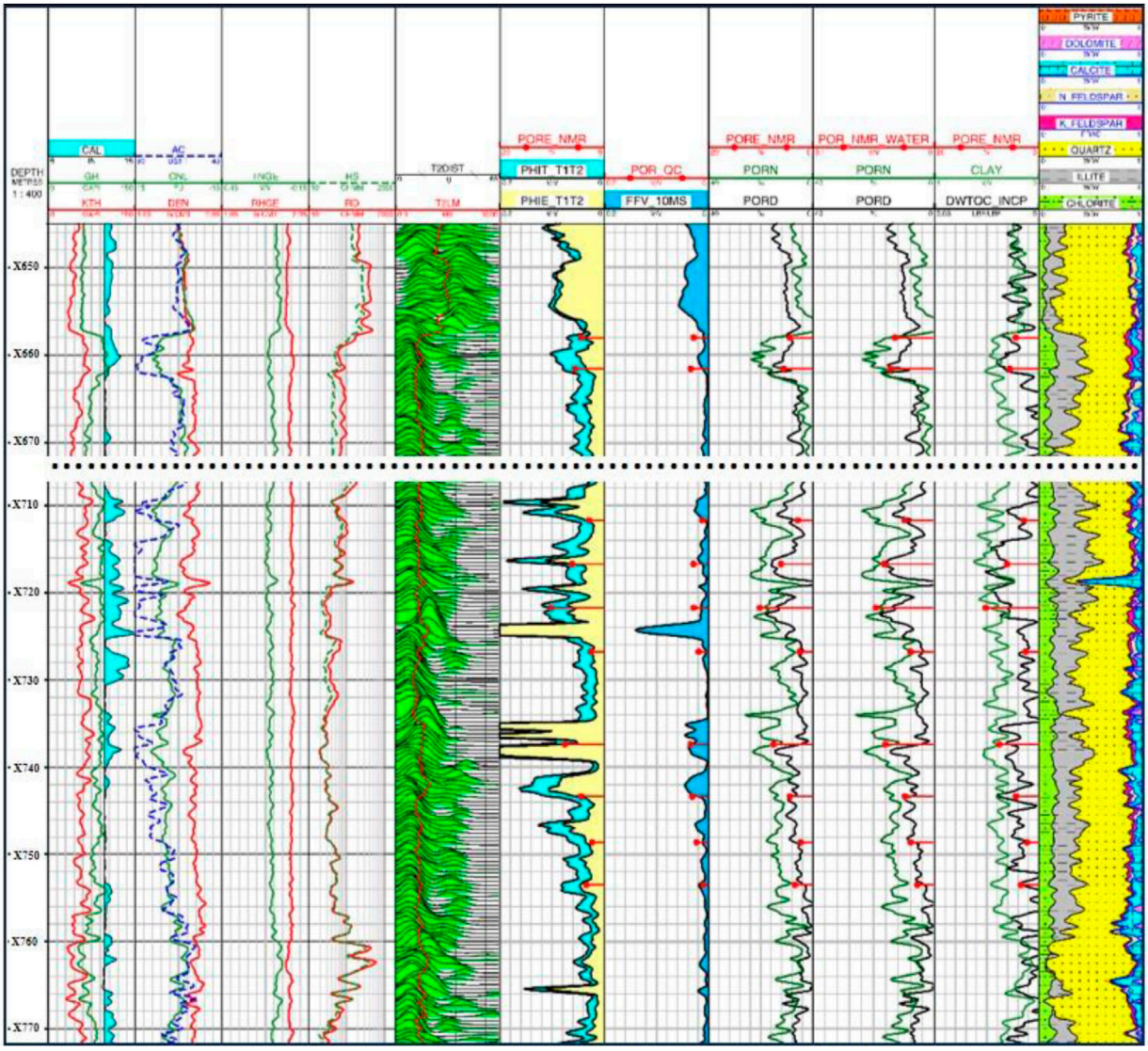

FIGURE 2
The calculated porosity using the combination method of conventional logging and LS logging as well as the NMR logging method.

0.3 ms; T_{2max} is the maximum T_2 value observed by the NMR logging instrument, and this value for the CMR-NG instrument was 3000 ms; T_{2c} is the cutoff value of T_2 for clay-bound water, in ms; $T_{2cutoff}$ is the cutoff value of T_2 for capillary-bound water, in ms.

4 Porosity experimental measurement results and logging calculation results

4.1 Experimental measurement results of porosity for shale oil reservoir

From Table 1, the porosity measured by the helium gas method ranges from 1.05% to 3.46%, with an average of 2.5%, in which sample 10 shows the minimum porosity value of 1.05% and sample 7 shows the maximum porosity value of 3.46%. The porosity measurement results by the saturation liquid method show that the porosity ranges from 1.721% to 9.245%, with an average of 4.543%, in which sample 10 exhibits the minimum value of 1.721% and sample 5 exhibits the maximum value of 9.245%.

The NMR experimental results of the core samples, both under dry and water-saturated states, are depicted in Figure 1. The arrangement of the samples in the figure is based on the TOC (Total Organic Carbon) content of each sample. Under the dry state, the sample NMR T_2 spectrum shows a single peak, with the peak ranging between 0.01 and 0.2 ms. Sample 10 shows the minimum porosity of 2.192% and sample 4 shows the maximum of 10.454%, with an average of 7.084%. Under the water-saturated state, the sample NMR T_2 spectrum shows a doublet peaks distribution, with the spectrum peak (P_1) during the short relaxation time almost overlapping the spectrum peak under the dry state, ranging between 0.01 and 0.2 ms. The spectrum peak (P_2) during the long relaxation time ranges between 0.2 and 3 ms. Some samples exhibit a peak (P_3) of 10~100 ms due to the impact by cracks.

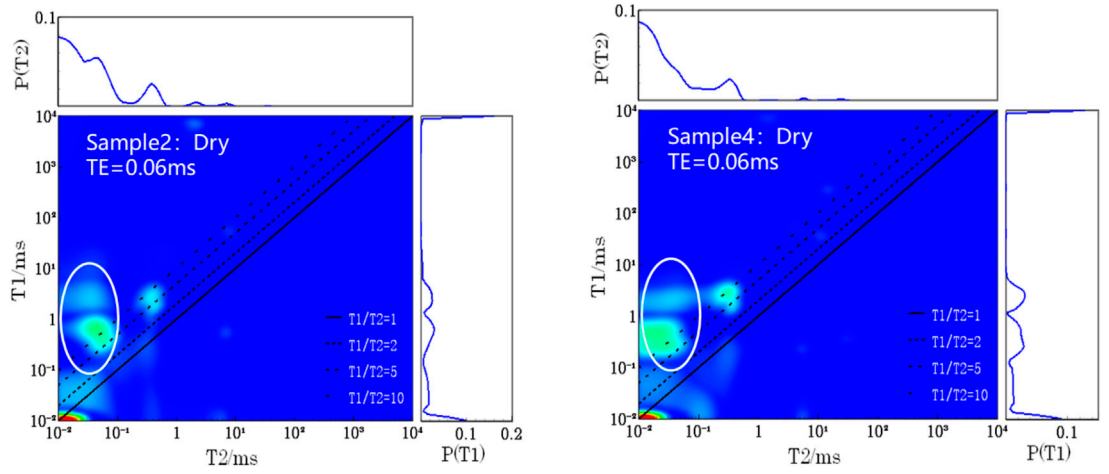

FIGURE 3
2D NMR experimental results of sample 2 and sample 4 under the dry state.

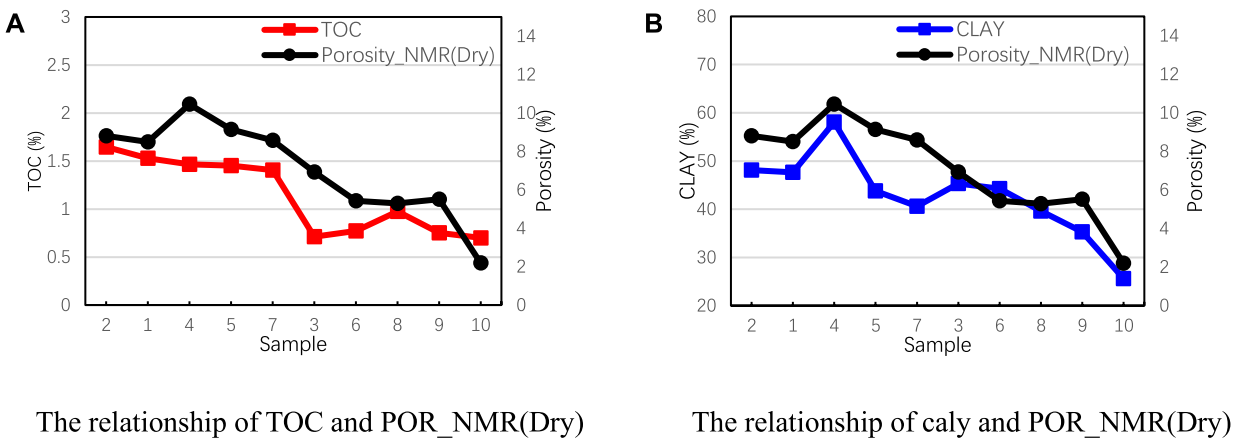

FIGURE 4
Relationship between POR_NMR (dry) and TOC and clay content. **(A)** The relationship of TOC and POR_NMR(Dry). **(B)** The relationship of clay and POR_NMR(Dry).

4.2 Logging calculation results of porosity for shale oil and gas reservoirs

Figure 2 shows the calculated porosity using the combination method of conventional logging and LS logging as well as the NMR logging method. In Figure 2, the first track is the depth track, the second track includes the CAL, natural GR, and uranium-free natural GR (KTH). The third track comprises acoustic logging (AC), density logging (DEN), and neutron logging (CNL). The fourth tracks are the matrix density curve (RHGE) and the matrix neutron curve (TNGE) by LS logging, respectively. The fifth track includes the deep resistivity (RD) and the shallow resistivity (RS). The sixth track displays the NMR logging T_2 spectrum. The seventh track includes the total porosity (PHIT) and effective porosity (PHIE) by NMR loggings, and the comparison with the effective porosity (PORE_NMR) by NMR experiments. The eighth track compares the helium porosity (POR_QC) with the NMR movable fluid porosity (FFV). The ninth and tenth tracks display the comparison between NMR logging neutron porosity (PORN) and density porosity (PORD) with the NMR experimental effective porosity (PORE_NMR) and the NMR porosity under the water-saturated state (POR_NMR_WATER). The eleventh track presents the clay content (CLAY), total organic carbon content (DWTOC), and the comparison with the NMR experimental effective porosity (PORE_NMR). The twelfth track shows the lithology profile obtained by LS logging.

The porosity logging calculation results at the corresponding depth of the 10 core samples are shown in Table 1. From the table, sample 10 shows the minimum density porosity of 3.519%, and sample 4 shows the maximum value of 15.739%, with an average of 8.287%; sample 6 displays the minimum neutron porosity of 7.028%, and sample 3 displays the maximum value of 18.232%, with an average of 14.702%; sample 6 exhibits the minimum NMR logging total porosity PHIT of 5.095%, and sample 5 exhibits the maximum value of 13.731%,

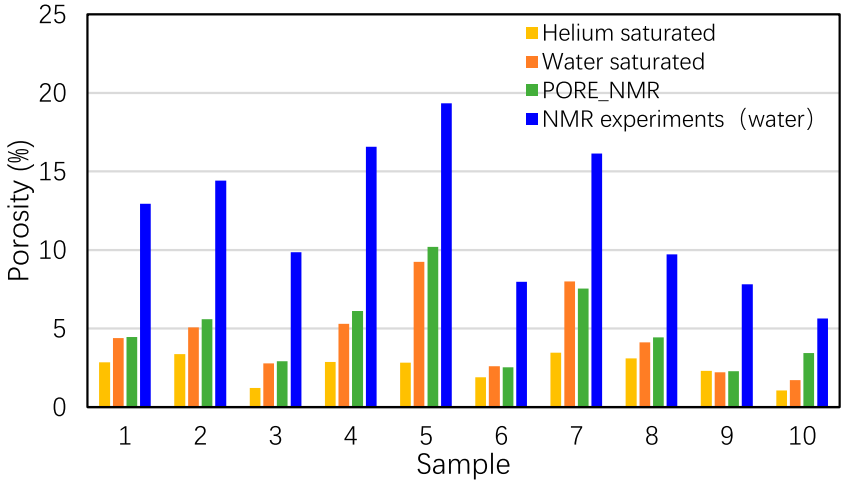

FIGURE 5
Comparison of sample porosity experimental measurements.

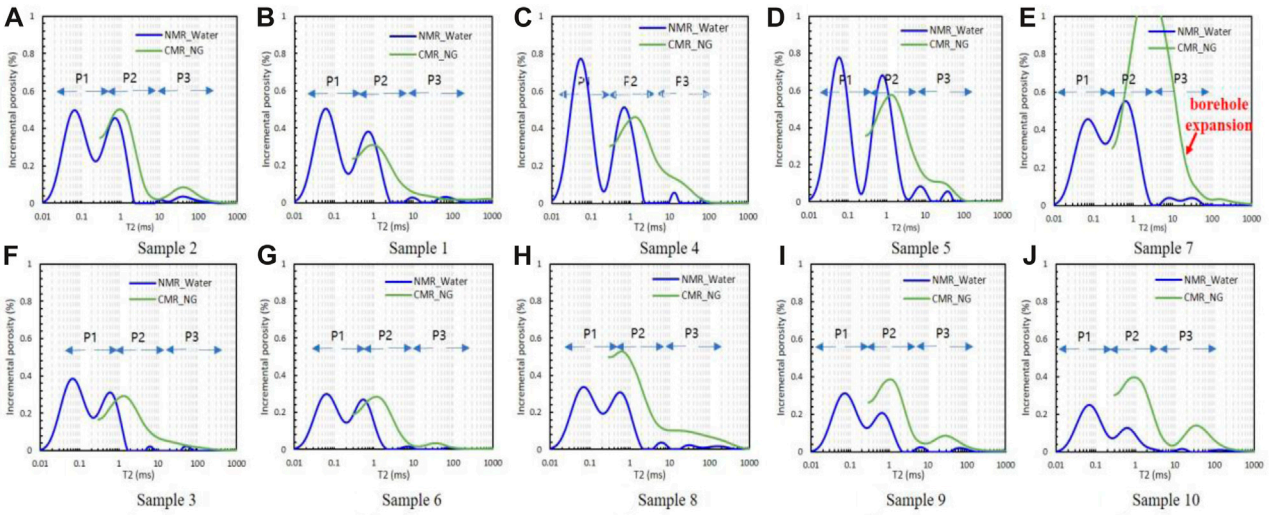

FIGURE 6
Comparison of POR_NMR (water) and POR_CMR.

with an average of 8.797%; sample 6 indicates the minimum NMR logging effective porosity PHIE of 2.538%, and sample 7 indicates the maximum value of 10.861%, with an average of 5.196%. Due to the borehole expansion of at the corresponding depth, sample 7 shows larger measurement values of both NMR logging total porosity and NMR logging effective porosity.

5 Discussions

5.1 Analysis of NMR experimental results under dry and water-saturated states

The dry-state NMR experimental results revealed significant NMR signals of the cores. The dry-state NMR T_2 spectrum exhibited a distinct single-peak feature, and signals at T_2 < 0.2 ms showed a significant amplitude. Additionally, there existed minor amplitude of spectrum peaks during the 1–3 ms T_2 relaxation time. Figure 1 shows the comparison between the amplitudes of the dry-state NMR T_2 spectrum peaks and the color of cores. From the figure, cores with darker colors (samples 1, 2, 4, 5, and 7) exhibit larger T_2 spectrum peak amplitudes, while cores with lighter colors (samples 3, 6, 8, 9, and 10) exhibit smaller T_2 spectrum peak amplitudes. The T_1-T_2 two-dimensional NMR experiments under the dry state showed that signals were concentrated in the regions of 0.01 ms < T_1 < 10 ms, 0.01 ms < T_2 < 0.1 ms, and T_1/T_2 > 5, as shown in Figure 3. Studies by Fleuery M and GE Xinmin et al. suggested that these signals could be caused by organic matter and the crystal water in clay minerals (Ge et al., 2015; Fleuery and Romero-Sarmiento, 2016).

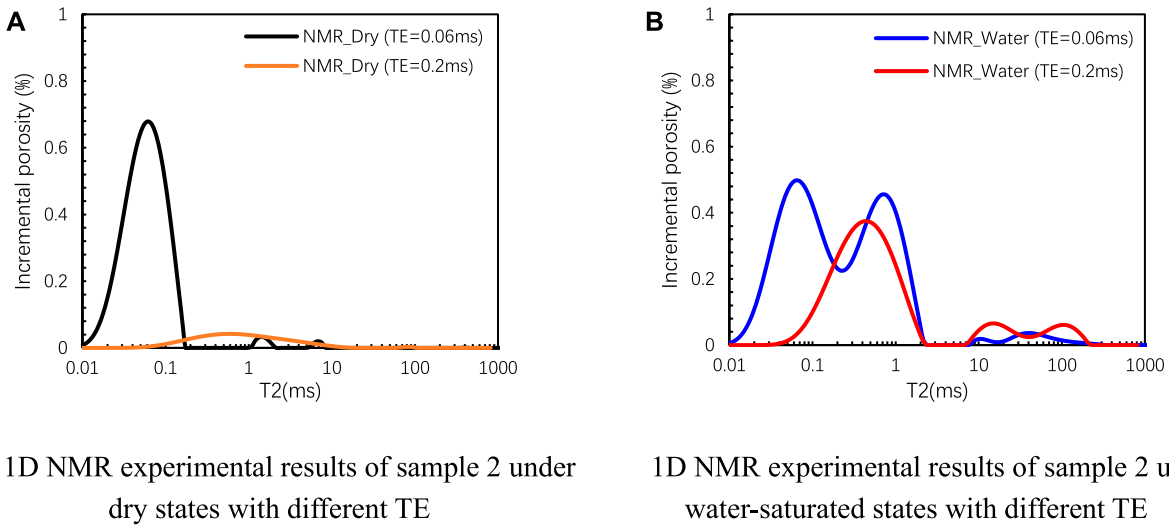

FIGURE 7
1D NMR experimental results of sample 2 under dry and water-saturated states with different TE. **(A)** 1D NMR experimental results of sample 2 under dry states with different TE. **(B)** 1D NMR experimental results of sample 2 under water-saturated states with different TE.

Comparing the dry-state NMR porosity (Porosity_NMR_Dry) with the TOC and clay mineral content (CALY) of the cores, the TOC and clay mineral content decreased, the dry-state NMR porosity decreased, as depicted in Figure 4. From the figure, sample 4 exhibits the highest NMR porosity in the dry state, primarily due to its highest clay mineral content. The aforementioned analysis indicated that the dry-state NMR signal was likely attributed to the organic matter and clay minerals.

After the core was saturated with water, the NMR T_2 spectrum showed doublet peaks, and the short relaxation component spectrum peaks basically coincided with the dry-state spectrum peaks. Therefore, it can be concluded that the 0.01–0.2 ms spectrum peaks in the saturated water state were caused by organic matter and clay mineral crystal water, while the spectrum peaks with a relaxation time greater than 0.2 ms, i.e., P_2 and P_3, could reflect the core porosity. The determination of core porosity should eliminate the influence of crystal water in clay minerals and hydrogen signals in organic matter. That is, the difference between the water-saturated state porosity and the dry-state NMR porosity was the size of core pores.

5.2 Comparative analysis between experimental NMR porosity and porosity measurement results by gravimetric and helium gas methods

Figure 5 presents a comparative illustration of the porosity measurement results using the helium gas charging method, the saturation liquid method, and the method of calibrating NMR hydrogen signals under the water-saturated and dry states. From the figure, the porosity can be ranked as helium porosity < porosity by saturation liquid method < porosity by NMR method under the water-saturated state. The helium porosity is notably lower than that using the saturation liquid method and the NMR method under the water-saturated state. Weng Jianqiao et al. suggested that the micro-nano

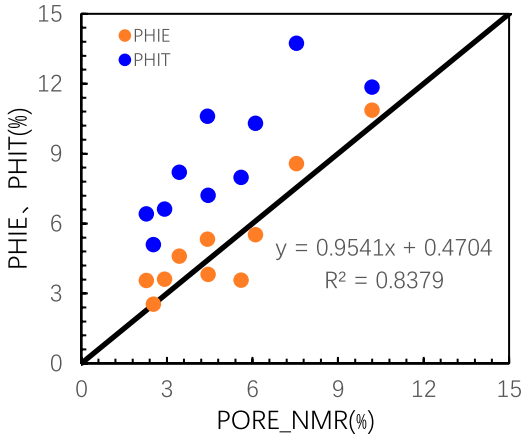

FIGURE 8
Comparison of PORE-NMR and POR_CMR.

shale pores make it difficult for helium gas molecules to enter the micropores through gas expansion, leading to underestimated porosity measurements (Weng et al., 2022). The difference value between the NMR signals in the water-saturated and dry states reflected the amount of water charging in the core. The difference value (PORE_NMR) between the NMR porosity in the water-saturated and dry states was close to the porosity by saturation liquid method. Except for sample 10, the difference in obtained porosities between the two methods was within 1%, confirming the accuracy of the NMR measurements.

5.3 Comparison of porosity between NMR experiments and NMR loggings

Figure 6 shows the comparison between the water-saturated core NMR T_2 spectrum (NMR_Water) and the NMR logging T_2

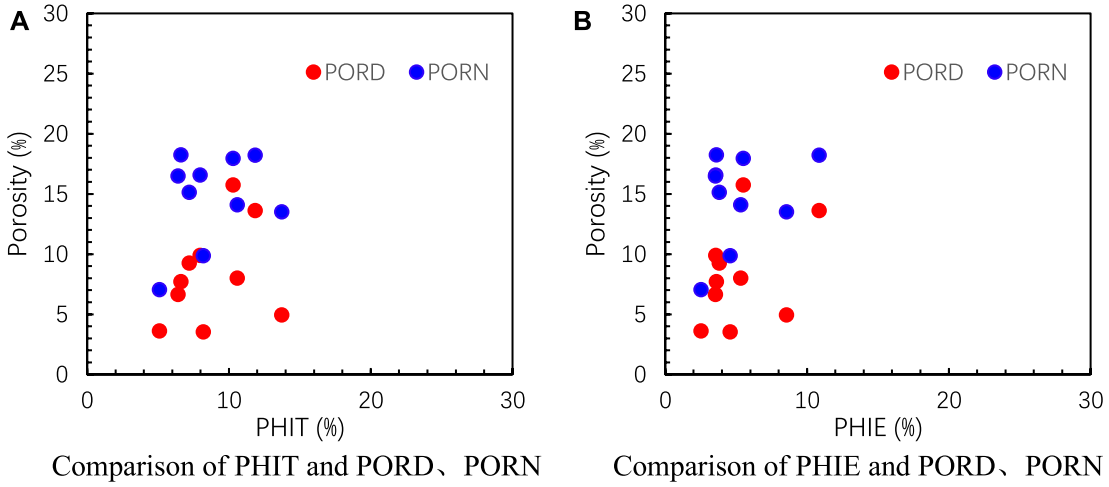

FIGURE 9
Comparison of POR_CMR and PORD, PORN. **(A)** Comparison of PHIT and PORD, PORN. **(B)** Comparison of PHIE and PORD, PORN.

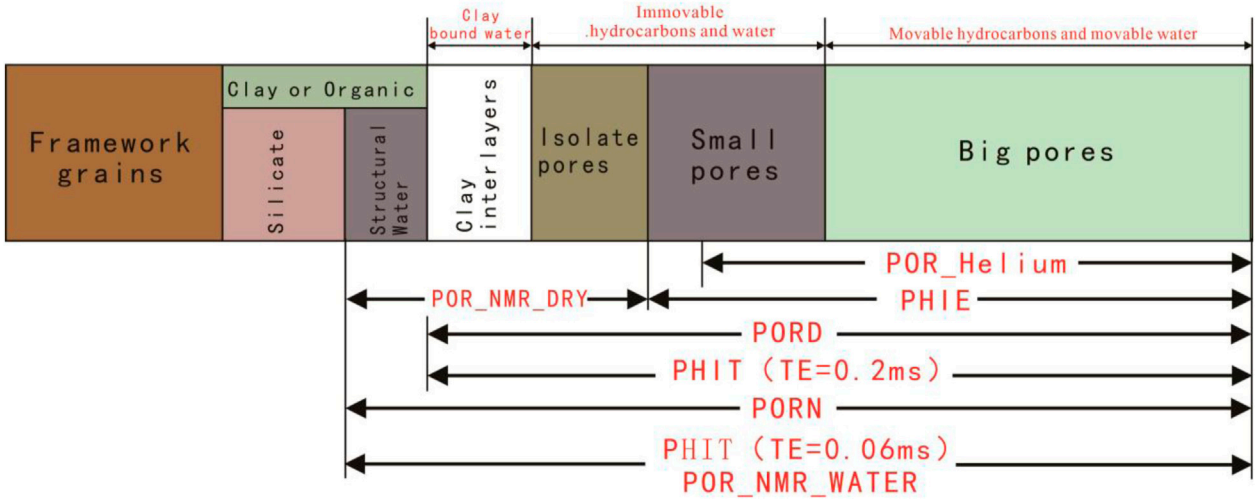

FIGURE 10
Schematic diagram of the porosity measurement range of various methods.

spectrum (CMR_NG) at the same depth. From the figure, the NMR logging T_2 spectrum exhibits a doublet peaks characteristic. The spectrum peaks are distributed in the range of 0.3–10 ms and 10–100 ms, respectively. The amplitude of the peak corresponding to 0.3–10 ms is much larger than that corresponding to 10–100 ms. Compared with NMR loggings, water-saturated NMR experiments mainly showed the three-peaks or multi-peaks distribution characteristic, and the main spectrum peaks P_1 and P_2 were distributed in the range of 0.01–0.2 ms and 0.2–2 ms. Compared to the NMR logging, during NMR experiments we obtained the NMR spectrum at a T_2 range of 0.01–0.3 ms, primarily due to the difference in the selected echo spacing. The NMR logging of CMR-NG had a minimum echo spacing (T_E) of 0.2 ms, while the echo spacing in the core NMR instrument was as low as 0.06 ms. The distribution range of the spectrum peaks corresponding to 0.3–10 ms in NMR loggings overlapped with the range of spectrum peaks corresponding to 0.2–2 ms in NMR experiments, but there were differences in their amplitudes. This discrepancy might be attributed to the differences in the contained fluids. Unlike the fully water-saturated cores in NMR experiments, the pores detected in NMR loggings of the actual formation contained not only clay and capillary-bound water but also adsorbed oil and movable oil. Samples 1, 2, 4, 5, and 7, which appeared darker colors and have higher TOC contents, were presumed to have developed organic pores, with oil mainly exhibiting surface relaxation and no significant peaks in the 10–100 ms range. Samples 3, 6, 8, 9, and 10, which had a lighter color and a lower TOC content, were

speculated to have developed inorganic pores, with oil in inorganic pores exhibiting volume relaxation and showing distinct peaks in the 10–100 ms range. The abnormally high peak amplitude of sample 7 was attributed to borehole expansion. Typically, when using a large NMR echo interval (TE), the signal from the short relaxation component tends to be attenuated before the acquisition of the first echo. As a result, these signals become unobservable (Fan et al., 2005; Zhang et al., 2023). In terms of sample 2, the NMR T_2 spectra in the dry and water-saturated states at different echo spacings of 0.2 and 0.06 ms respectively indicated that as the echo spacing increased, the spectrum peaks in the 0.01–0.2 ms range disappeared. This demonstrates that the 0.2 ms echo spacing was unable to obtain the signals from organic matter and the crystal water in clay minerals at $T_2 < 0.3$ ms, as shown in Figure 7.

The aforementioned analysis showed that the P_1 peak in the water-saturated state was mainly caused by organic matter and the crystal water in clay minerals. Therefore, when determining the core porosity, it needs to be subtracted as a background signal to obtain the core NMR porosity (PORE_NMR). Intersecting the core NMR porosity (PORE-NMR) with NMR logging total porosity (PHIT) and NMR logging effective porosity (PHIE), the PORE_NMR was slightly smaller than PHIT. The reason is that PORE_NMR could not reflect the water in disconnected pores. There was an obvious positive correlation between the NMR experimental effective porosity PORE_NMR and NMR logging effective porosity PHIE, with a correlation of 0.84, as shown in Figure 8. Therefore, the NMR experimental effective porosity mainly reflects the effective pores of the core.

5.4 Comparison of porosity calculations by NMR logging and conventional LS logging

Comparing the density porosity (PORD) and neutron porosity (PORN) by conventional loggings separately with the total porosity (PHIT) and effective porosity (PHIE) by NMR loggings, it is evident that the PORN is significantly higher than the PORD, PHIT, and PHIE. The higher neutron porosity is due to that in the neutron logging, the hydrogen atoms not only in the pore fluids but also in the rock matrix were measured. This led to an overestimation of porosity results due to the presence of organic matter and clay minerals in the shale oil reservoir. Both the PORD and PHIT represent the total porosity, and their values are quite close, both being higher than PHIE, as shown in Figure 9.

5.5 Comprehensive comparison of porosity measurement by NMR experiments and logging calculation

The classical rock physics volume model indicates that rocks consist of three major components: mineral matrix particles, clay and organic matter, and pores. The neutron porosity by logging calculation is greater than that using other methods, which is due to the principle of neutron logging. From the perspective of logging principles, due to the influence of resolution and performance of the instruments, the density logging can only detect signals from the reservoir's matrix pores and some clay mineral micropores. Whereas the neutron logging is based on the non-elastic and elastic scattering of high-energy neutrons emitted by the neutron source colliding with various elements in the formation. During this process, fast speed neutrons gradually lose energy and decrease in speed, and at this moment, the instrument can detect the intensity of the thermal and epithermal neutrons to calculate the formation porosity. Among various elements, hydrogen element has the strongest ability to slow down neutrons, making its impact significant in neutron logging. Neutron logging can detect signals not only from matrix pores and clay mineral micropores but also from some clay minerals and solid organic matter, leading to the neutron logging porosity calculation being greater than the actual formation porosity, as shown in Figure 10. The NMR measurement experiments ($T_E = 0.06$ ms) were similar to the neutron logging as they directly detect the hydrogen atom signals in the formation, allowing for the measurement of matrix pores and clay mineral micropores. However, the NMR logging ($T_E = 0.2$ ms) lost the signal from structural water, and the obtained NMR logging total porosity (PHIT) included the movable water porosity, clay-bound water porosity, and capillary-bound water porosity. The NMR logging effective porosity (PHIE) included the capillary-bound water porosity and the movable water porosity.

6 Conclusion

1) The measurement results by saturated liquid method were relatively consistent with that using the NMR experimental method, and it could also reflect the effective porosity of the formation. However, the helium gas charging method was affected by the complex pore structure of the shale, and it showed a significantly smaller measurement result than the saturated liquid method and the NMR experimental method.
2) In the shale oil reservoir of the Lianggaoshan Formation, Sichuan Basin, the signals from dry-state cores by the NMR experiment mainly came from clay mineral crystal water and organic matter in the formation. Under the water-saturated state, the short relaxation peaks in the core NMR experiment reflected the crystal water in clay minerals and organic matter, while the long relaxation peaks reflected the pore fluids in the formation. By subtracting the dry-state core NMR signal from the water-saturated core NMR signal, the effective porosity of the formation could be obtained.
3) Compared with NMR experiments ($T_E = 0.06$ ms), the NMR logging ($T_E = 0.2$ ms) was unable to reflect the signals from organic matter and the crystal water in clay minerals at $T_2 < 0.3$ ms.
4) The combination of LS logging and neutron logging calculated a too high porosity, whereas the density porosity was close to the total porosity of the formation.

Data availability statement

The raw data supporting the conclusion of this article will be made available by the authors, without undue reservation.

Author contributions

SS: Data curation, Formal Analysis, Investigation, Writing–original draft. LW: Conceptualization, Data curation, Funding acquisition, Project administration, Resources, Supervision, Writing–review and editing. JuL: Formal Analysis, Writing–review and editing. JiL: Formal Analysis, Writing–review and editing. YL: Formal Analysis, Writing–review and editing. JJ: Formal Analysis, Writing–review and editing.

Funding

The author(s) declare financial support was received for the research, authorship, and/or publication of this article. This study was supported by the Open foundation of the Sinnpec Key Laboratory of Shale Oil/Gas Exploration and Production Technology (No. 33550000-22-ZC0613-0209), the Natural Science Foundation of Sichuan Province (No. 2023NSFSC0260).

Conflict of interest

The authors declare that the research was conducted in the absence of any commercial or financial relationships that could be construed as a potential conflict of interest.

Publisher's note

All claims expressed in this article are solely those of the authors and do not necessarily represent those of their affiliated organizations, or those of the publisher, the editors and the reviewers. Any product that may be evaluated in this article, or claim that may be made by its manufacturer, is not guaranteed or endorsed by the publisher.

References

Chalmers, G. R. L., and Bustin, R. M. (2012). Light volatile liquid and gas shale reservoir potential of the Cretaceous Shaftesbury Formation in northeastern British Columbia,Canada. *AAPG* 97 (7), 1333–1367. doi:10.1306/10041111041

Cui, J., Zhu, R., Zhiguo, M. A. O., and Shixiang, L. I. (2019). Accumulation of unconventional petroleum resources and their coexistence characteristics in Chang7 shale formations of Ordos Basin in central China. *Front. Earth Sci.* 13 (3), 575–587. doi:10.1007/s11707-019-0756-x

Domovan, A. D., Sterker, T. S., Gardner, R. M., et al. (2016). *Find-ings from the Eagle Ford outcrops of west Texas&implication tothe subsurface of south Texas//BRYER J A.the Eagle FordShale-A renaissance in U. S. Oil production: AAPG Memoir110*. Tulsa, Oklahoma: Tulsa:American Association of Petroleum Geologists, 301–336.

Fan, Y., Ni, Z., Deng, S., et al. (2005). Experimental study on NMR measurement parameers and reservoir properties. *Petroleum Geol. Exp.* 27 (6), 624–626. doi:10.11781/sysydz200506624

Fleuery, M., and Romero-Sarmiento, M. (2016). Characterization of shales using T1-T2 NMR maps. *J. Petroleum Sci. Eng.* 137, 55–62. doi:10.1016/j.petrol.2015.11.006

Fu, J., Li, S., Niu, X., Deng, X., and Zhou, X. (2020). Geological characteristics and exploration of shale oil in chang 7 member of triassic Yanchang formation, Ordos Basin, NW China. *Petroleum Explor. Dev.* 47 (5), 931–945. doi:10.1016/s1876-3804(20)60107-0

Fu, Y. (2018). *Research on porosity measurement method of shale gas reservoir*. Chengdu, China: SouthWest Petreleum University.

Fu, Y., Zeng, L., Ma, F., et al. (2012). An experimental analysis of expansibility and diffusion of shale rocks. *Nat. Gas. Ind.* 32 (09), 48–51. doi:10.3787/j.issn.1000-0976.2012.09.011

Ge, X., Fan, Y., Chen, H., Deng, S., Cao, Y., and Zahid, M. A. (2015). Probing the influential factors of NMR T1-T2 spectra in the characterization of the kerogen by numerical simulation. *J. Magnetic Reson.* 260, 54–66. doi:10.1016/j.jmr.2015.08.026

Han, Bo, Nan, Li, Xin, Li, et al. (2020). Study on shale porosity in different NMR measurement pattern. *IFEDC* 2020, 1805–1814. doi:10.26914/c.cnkihy.2020.042435

He, W., Bai, X., Meng, Q. 'an, et al. (2022a). Accumulation geological characteristics and major discoveries of lacustrine shale oil in Sichuan Basin. *Acta Pet. Sin.* 43 (7), 885–898. doi:10.7623/syxb202207001

He, W., He, H., Wang, Y., et al. (2022b). Major breakthrough and significance of shale oil of the jurassic Lianggaoshan Formation in well ping'an 1 in northeastern Sichuan Basin. *China Pet. Explor.* 27 (1), 40–49.

Hu, S., Zhao, W., Hou, L., Yang, Z., Zhu, R., Wu, S., et al. (2020). Development potential and technical strategy of continental shale oil in China. *Petroleum Explor. Dev.* 47 (4), 877–887. doi:10.3969/j.issn.1672-7703.2022.01.004

Jian-fei, H., Can-can, Z., Xia, Li, et al. (2012). Summary of shale gas evaluation applying geophysical logging. *Prog. Geophys.* (4), 1624–1632. doi:10.6038/j.issn.1004-2903.2012.04.040

Jiao, K., Yao, S., Wu, H., et al. (2014). Advances in characterization of pore system of gas shales. *Geol. J. China Univ.* 20 (1), 151–161.

Jin, Z., Bai, Z., Gao, Bo, et al. (2019). Has China ushered in the shale oil and gas revolution? *Oil Gas Geol.* 40 (3), 451–458. doi:10.3969/j.issn.1006-7493.2014.03.015

Kontorovich, A. E., Ponomareva, E. V., Burshtein, L. M., Glinskikh, V., Kim, N., Kostyreva, E., et al. (2018). Distribution of organic matter in rocks of the Bazhenov horizon (West Siberia). *Russ. Geol. Geophys.* 59, 285–298. doi:10.1016/j.rgg.2018.03.007

Li, J., Wu, Q., Lu, J., et al. (2017). Measurement and logging evaluation of total porosity and effective porosity of shale gas reservoirs:A case from the Silurian Longmaxi Formation shale in the Sichuan Basin. *Oil Gas Geol.* 38 (3), 602–609. doi:10.11743/ogg20170320

Li, M., Ma, X., Jiang, Q., et al. (2019). Enlightenment from formation conditions and enrichment characteristics of marine shale oil in North America. *Petroleum Geol. Recovery Effic.* 26 (1), 13–28. doi:10.13673/j.cnki.cn37-1359/te.2019.01.002

Liu, R., and Liu, Z.-jun (2006). Oil shale resource situation and multi purpose development potential in China and abroad. *China's shale gas shale oil Resour.* 36 (6), 892–0898.

Liu, X., Sun, J., and Guo, Y. (2004). Application of elemental capture spectroscopy to reservoir evaluation. *Well Logging Technol.* 1, 26–30. doi:10.3969/j.issn.1671-5888.2006.06.005

Ma, Y., Li, M., Cai, X., et al. (2020). Mechanisms and exploitation of deep marine petroleum accumulations in China: advances, technological bottlenecks and basic scientific problems. *Oil Gas Geol.* 41 (4), 655–672. doi:10.3969/j.issn.1004-1338.2005.03.016

Modica, C. J., and Lapierre, S. G. (2012). Estimation of kerogen porosity in source rocks as a function of thermal transformation: example from the Mowry shale in the Powder River Basin of Wyoming. *AAPG Bull.* 96 (1), 87–108. doi:10.1306/04111110201

Ning, Li, Zhou, F., Wu, H., et al. (2023). New advances in methods and technologies for well logging evaluation of continental shale oil in China. *Acta Pet. Sin.* 44 (1), 28–44. doi:10.7623/syxb202301003

Pollastro, R. M., Roberts, L. N. R., and Cook, T. A. (2012). *Geologic model for the assessment of technically recoverable oil in the DevonianMississippian bakken Formation,Williston basin//BREYER J A.shale reservoirs-giant resources for the 21st century: AAPG Memoir97*. Tulsa, Oklahoma: Tulsa:American Association of Petroleum Geologists, 205–257. doi:10.1306/13321469M97948

Ramirez, T. R., Klein, J. D., Ron, J. M., et al. (2011). *Comparative study of formation evaluation methods for unconventional shale gas reservoirs: application to the Haynesville shale (Texas)*. The Woodlands, Texas, USA: Society of Petroleum Engineers, 332–362. doi:10.5724/gcs.09.29.0150

Renyan, Z. (2016). *Experimental study on physical parameters of shale gas reservoirs*. Chengdu, China: SouthWest Petreleum University.

Rui, F., Jiang, Y., Yang, C., et al. (2023). Geological characteristics of shale oil in the jurassic Lianggaoshan Formation in Sichuan Basin. *China Pet. Explor.* 28 (4), 66–78. doi:10.3969/j.issn.1672-7703.2023.04.007

Schmoker, J. W. (2002). Resource-assessing perspectives for unconventional gas systems. *AAPG Bull.* 86 (11), 1993–2000. doi:10.3969/j.issn.1672-7703.2023.04.007

Shihe, Y., and Zhang, C. (1996). *Logging data processing and comprehensive interpretation*. Dong Ying, China: China University of Petroleum Press.

Sun, L., Liu, He, He, W., Zhang, S., Zhu, R., et al. (2021). An analysis of major scientific problems and research paths of Gulong shale oil in Daqing Oilfield, NE China. *Petroleum Explor. Dev.* 48 (3), 527–540. doi:10.1016/s1876-3804(21)60043-5

Tian, C., Yi, Li, Li, D., et al. (2023). Selection and recommendation of shale reservoir porosity measurement methods. *Nat. Gas. Ind.* 43 (06), 57–65. doi:10.3787/j.issn.1000-0976.2023.06.005

Tian, H., Zhang, S., Liu, S., et al. (2012). Determination of organic-rich shale pore features by mercury injection and gas adsorption methods. *Editor. office Acta Petrolei Sinica* 33 (3), 419–427. doi:10.7623/syxb201203011

Wang, L., Yin, R., Liqiang, S., Fan, L., Wang, H., Yang, Q., et al. (2018). Insights into pore types and wettability of a shale gas reservoir by nuclear magnetic resonance: Longmaxi Formation, Sichuan Basin, China. *Energy Fuel* 32, 9289–9303. doi:10.1021/acs.energyfuels.8b02107

Wang, Y. M., Dong, D. Z., Yang, H., Wang, S., Huang, J., et al. (2014). Quantitative characterization of reservoir space in the lower silurian Longmaxi shale, southern sichuan, China. *Sci. China Earth Sci.* 57, 313–322. doi:10.1007/s11430-013-4645-y

Weng, J., Li, X., Qi, M., et al. (2022). Study on porosity measurement determination methods of a shale reservoir in the Longmaxi Formation, Sichuan Basin. *Rock Mineral Analysis* 41 (4), 598–605. doi:10.15898/j.cnki.11-2131/td.202012270173

Wu-yang, Y., and Wang, C.-bin (2010). Utilizing pre-stack simultaneous inversion to predict reservoir physical properties. *OGP* 45 (3), 414–417. doi:10.1306/07021413140

Xiao, lizhi, et al. (2001). *NMR logging interpretation and China case studies*. Beijing, China: Petroleum Industry Press. doi:10.1306/02221615104

Xiu-wen, Mo, Zhou-bo, Li, and Bao-zhi, P. (2011). Method and advance of shale gas formation evaluation by means of well logging. *Geol. Bull. China* 30 (0203), 400–405. doi:10.3969/j.issn.1671-2552.2011.02.027

Yan, X., Cao, C., and Wang, H. (2018). Research and application on processing and interpretation of litho scanner logging data. *Well Logging Technol.* 42 (05), 503–508. doi:10.16489/j.issn.1004-1338.2018.05.003

Yang, W., Xue, L. H., Tang, J., et al. (2015). Analysis and evaluation of different measuring methods for shale porosity. *Acta Sedimentol. Sin.* 33 (6), 1258–1264. doi:10.14027/j.cnki.cjxb.2015.06.018

Yang, Z., Hou, L., Lin, S., et al. (2018). Geologic characteristics and exploration potential of tight oil and shale oil in Lucaogou Formation in Jimsar sag. *China Pet. Explor.* 23 (4), 76–85. doi:10.3969/j.issn.1672-7703.2018.04.009

Zeng, X.-liang, Shu-gen, L., Huang, W.-ming, et al. (2011). Comparison of silurian Longmaxi Formation shale of Sichuan Basin in China and carboniferous Barnett Formation shale of fort worth basin in United States. *Geol. Bull. China* 30 (0203), 372–384. doi:10.3969/j.issn.1671-2552.2011.02.024

Zhang, J.-yan (2012). Well logging evaluation method of shale oil reservoirs and its applications. *Prog. Geophys.* 27 (3), 1154–1162. doi:10.6038/j.issn.1004-2903.2012.03.040

Zhang, L., Li, J., Zheng, Li, et al. (2014). Advancements in shale oil/gas research in north American and considerations on exploration for lacustrine shale oil/gas in China. *Adv. Earth Sci.* 29 (06), 700–711. doi:10.11867/j.issn.1001-8166.2014.06.0700

Zhang, R., Wang, W., Gao, Yi, et al. (2023). Sensitivity analysis of T2-T1 2D NMR measurement parameters in shale oil reservoirs[J]. *Chin. J. Magnetic Reson.*, 40(2): 122–135. doi:10.11938/cjmr20223025

Zhang, T., Peng, Z., Yang, W., et al. (2015). Enlightenments of American shale oil research towards China. *Lithol. Reserv.* 27 (3), 1–10. doi:10.3969/j.issn.1673-8926.2015.03.001

Zhi, D., Tang, Y., Yang, Z., et al. (2019). Geological characteristics and accumulation mechanism of continental shale oil in Jimusaer sag,Junggar Basin. *Oil Gas Geol.* 40 (3), 524–534. doi:10.11743/ogg20190308

Zhi-qiang, M., Zhang, C., and liang, X. (2010). A NMR-based porosity calculation method for low porosity and low permeability gas reservoir. *OGP* 45 (1), 105–109. doi:10.13810/j.cnki.issn.1000-7210.2010.01.026

Zhou, S., Dong, D., Zhang, J., et al. (2021). Optimization of key parameters for porosity measurement of shale gas reservoirs. *Nat. Gas. Ind.* 41 (05), 20–29. doi:10.3787/j.issn.1000-0976.2021.05.003

Zou, C., Dong, D., Wang, S., et al. (2010). Geological characteristics, formation mechanism and resource potential of shale gas in China. *Petroleum Explor. Dev.* 37 (6), 1875.

Zou, C., Pan, S., Jing, Z., et al. (2020). Shale oil and gas revolution and its impact. *Acta Pet. Sin.* 41 (1), 1–12. doi:10.7623/syxb202001001

Zou, C., Tao, S., Hou, L., et al. (2014). *Unconventional oil and gas geology*. Beijing, China: Geological Publishing House.

frontiers | Frontiers in Earth Science

TYPE Original Research
PUBLISHED 22 January 2024
DOI 10.3389/feart.2024.1340523

OPEN ACCESS

EDITED BY
Maxim Lebedev,
Edith Cowan University, Australia

REVIEWED BY
Haihai Hou,
Liaoning Technical University, China
Qian Zhang,
Peking University, China
Longyi Shao,
China University of Mining and Technology, Beijing, China

*CORRESPONDENCE
Ruikang Cui,
ruikang_cui@163.com

RECEIVED 18 November 2023
ACCEPTED 08 January 2024
PUBLISHED 22 January 2024

CITATION
Shi Y, He Y, Wan J, Sun J, Zeng J and Cui R (2024), The primary controlling factors of the occurrence state of deep high-rank coalbed methane in eastern Ordos Basin.
Front. Earth Sci. 12:1340523.
doi: 10.3389/feart.2024.1340523

The primary controlling factors of the occurrence state of deep high-rank coalbed methane in eastern Ordos Basin

Yujiang Shi[1], Yufei He[1], Jinbin Wan[1], Jianmeng Sun[2], Jingbo Zeng[1] and Ruikang Cui[2]*

[1]China National Logging Corporation, Xi'an, Shaanxi, China, [2]School of Geosciences, China University of Petroleum (East China), Qingdao, China

Introduction: This study investigates the key controlling factors of the occurrence state of deep coalbed methane (CBM). CBM is an abundant energy resource in China, particularly in deep coal seams. However, the exploration and development of deep CBM face numerous challenges, and the understanding of the controlling factors of its occurrence state is still limited.

Methods: The study reveals that deep CBM primarily exists in the form of adsorbed gas and free gas within the pore-fracture system of coal. Factors such as formation temperature, formation pressure, pore structure, and water saturation collectively influence the occurrence state of deep CBM. By employing the Simplified Local Density (SLD) model and molecular simulation methods.

Results and discussion: This study examines the impact of two external geological control factors (formation temperature, formation pressure) and three internal geological control factors (pore size, water saturation, Specific surface area) on deep CBM and establishes a theoretical model for gas content. Finally, the relationship between the adsorbed gas, free gas, total gas content, and burial depth is calculated using the model, uncovering the primary factors controlling the occurrence state of deep CBM. This research is of significant importance in providing key parameters for gas content in deep coal and optimizing deep CBM exploration.

KEYWORDS

deep coalbed methane, occurrence state, controlling factors, simplified local density model, molecular simulation

1 Introduction

China possesses abundant CBM resources, particularly in deep coal seams. CBM resources with depths exceeding 1,000 m account for 63% of the total proven resources (Geng et al., 2018). However, the exploration of deep CBM poses significant challenges, and the theoretical foundation for its development is relatively weak. There is insufficient understanding of the key controlling factors of the occurrence state of deep CBM. Deep CBM primarily exists in the coal matrix's pore-fracture system in the forms of adsorbed gas, free gas, and dissolved gas (Yao et al., 2014; Liu et al., 2018; Li et al., 2022). Therefore, it is

crucial to identify the primary controlling factors of the occurrence state of deep CBM for the optimal selection of sweet spots in deep CBM development.

Deep CBM reservoirs exhibit significant high-temperature and high-pressure characteristics. Moisture is also commonly present in CBM reservoirs, which can influence the occurrence state of coalbed gas. Furthermore, compared to shallow CBM reservoirs, deep CBM reservoirs are primarily dominated by micropores. Under the combined effects of high temperatures and formation pressures in deep geological formations, microfractures close, porosity decreases, and the heterogeneity of pore structures diminishes (Shen et al., 2014). Over the past few decades, researchers have been studying various controlling factors that impact CBM (Qin and Shen, 2016; Wang and Zhang, 2021; Ye et al., 2021; Tambaria et al., 2022) proposed that in deep CBM reservoirs, the coupling relationship between formation pressure and temperature controls the adsorption characteristics of coal seams as the burial depth increases. Specifically, in shallow depths, the positive effect of pressure on the adsorbed gas content in coal seams is observed. However, as the burial depth increases, the negative effect of temperature on the adsorbed gas content outweighs the positive effect of pressure. Sun et al. (2017) discovered that in the interior of the Baijiahai uplift in the Junggar Basin, deep CBM reservoirs with large, medium, small, and micropores are developed. The coal matrix exhibits strong adsorption energy and can accommodate a considerable amount of adsorbed gas, resulting in the coexistence of adsorbed and free gas reservoirs. Wang et al. (2020) found that moisture has a negative impact on the adsorption characteristics of coal seams. Moisture within the coal occupies methane adsorption sites and blocks the pores. In general, the occurrence state of deep CBM is influenced by factors such as formation temperature, formation pressure, pore structure, and water saturation. Currently, many researchers have studied the impact of specific controlling factors on deep CBM through experimental methods (Wang et al., 2020). However, due to the heterogeneity of experimental samples and limitations of the experimental methods, it is challenging to quantitatively characterize the influence of various controlling factors on the occurrence state of deep CBM using experimental approaches.

In recent years, with the advancement of numerical simulation methods, various theoretical approaches have been developed to study the adsorption characteristics of CBM, such as the Simplified Local Density (SLD) model (Qi et al., 2019; Huang et al., 2022; Pang et al., 2022), molecular simulation (Meng et al., 2018; Bai et al., 2021), and density functional theory (Yan and Yang, 2005). The SLD model, proposed by Rangarajan et al. (1995), considers that the adsorption effect is jointly influenced by the fluid-fluid interactions among adsorbate molecules and the fluid-solid interactions between adsorbate molecules and the adsorbent. To improve the accuracy of the model under high pressures, (Fitzgerald et al., 2003) introduced an empirical parameter to correct the excess volume parameter. With this modification, the SLD model has been widely used to investigate gas adsorption behavior in porous media.

Many researchers have successfully applied molecular simulation methods to investigate the distribution of methane molecules in different pore structures and the influence of various controlling factors, such as water saturation, on the occurrence state of CBM (Zhang et al., 2017; Hao et al., 2022; Yao et al., 2023).

Although researchers have made significant explorations using SLD model or molecular simulation methods to study the occurrence state of coalbed methane, these individual methods still have some limitations when studying the influence of different controlling factors on the occurrence state of coalbed methane. For example, the SLD model cannot accurately characterize the distribution of methane in different coal pore structures and the effect of water saturation, which are important external controlling factors on the occurrence state of coalbed methane. Molecular simulation methods involve complex calculations and idealized microscopic conditions, which may not be applicable at a macroscopic level for gas adsorption in coalbeds, as they differ from the actual coalbed environment. Therefore, it is necessary to combine the strengths of both methods to conduct related research and provide a diversified approach for studying the primary controlling factors of the occurrence state of deep coalbed methane.

This study investigated the impact of two external geological controlling factors and two internal geological controlling factors on the occurrence state of deep CBM using the SLD model and molecular simulation, respectively. Subsequently, considering the formation temperature, formation pressure, pore structure, water saturation, and previous research findings, a theoretical model for gas content was established. Finally, based on the theoretical gas content model, the relationship between the adsorbed gas, free gas, total gas content, and burial depth of the coal seam was calculated, and the main controlling factors influencing the occurrence state of deep CBM were discussed. This research provides guidance for determining key parameters of gas content in deep coal seams and optimizing sweet spots for deep CBM.

2 Simulation methodology

2.1 The simplified local density (SLD) model

Rangarajan et al. (1995) proposed a Simplified Local Density (SLD) model by employing the mean-field approximation to simplify the general density functional theory. The SLD model considers that the adsorption effects arise from the collective interactions between adsorbate-adsorbate and adsorbate-adsorbent interfaces. Specifically, the fluid-fluid interactions between adsorbate molecules and the fluid-solid interactions between adsorbate molecules and the adsorbent are assumed to jointly contribute to the adsorption effects. The fluid-fluid interactions between adsorbate molecules are characterized using a gas state equation, while the fluid-solid interactions between adsorbate molecules and the pore walls are described by a potential energy function. As depicted in Figure 1, the SLD model simplifies the pores of the adsorbent into slit-like pores, where an adsorbate molecule located at a distance of z from one pore wall is positioned between the pore walls of a pore with a width of L. The adsorbate molecule experiences collective forces from both pore walls and the remaining adsorbate molecules.

At adsorption equilibrium, the chemical potential of an adsorbate molecule at position z is the sum of the fluid-fluid

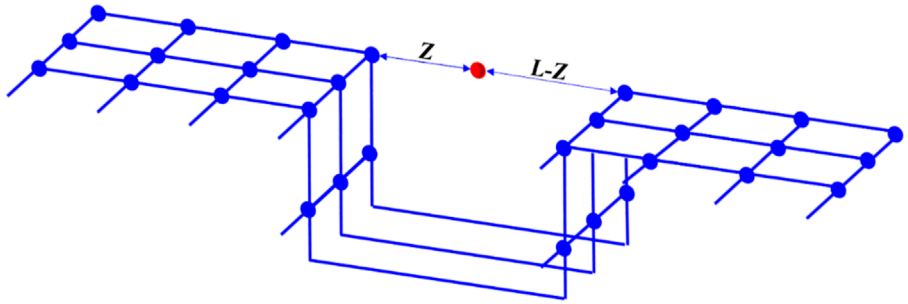

FIGURE 1
The Simplified Local Density (SLD) model.

chemical potential and the fluid-solid chemical potential, and it is equal to the chemical potential in the bulk phase.

$$\mu(z) = \mu_{ff}(z) + \mu_{fs}(z) = \mu_{bulk} \tag{1}$$

Where μ(z) is the chemical potential at the z position in the pore, J·mol^{-1}; z is the distance between the adsorbates and the pore wall, nm; μ_{ff}(z) is the fluid-fluid interaction chemical potential at position z in the pore, J·mol^{-1}; μ_{fs}(z) is the fluid-solid interaction chemical potential at position z in the pore, J·mol^{-1}; μ_{bulk} is the bulk chemical potential in the pore, J·mol^{-1}.

According to thermodynamic equilibrium, chemical potential can be expressed by fugacity in nanopores:

$$\mu_{bulk} = \mu_0(T) + RT\ln\left(\frac{f_{bulk}}{f_0}\right) \tag{2}$$

$$\mu_{ff}(z) = \mu_0(T) + RT\ln\left(\frac{f_{ff}(z)}{f_0}\right) \tag{3}$$

Where μ_0(T) represents any reference state chemical potential, J·mol^{-1}; f_0 refers to the fugacity of any reference state, Pa; f_{bulk} and f_{ff}(z)are respectively the bulk fugacity and the adsorption phase fugacity at z position in the pore, Pa.

In nanopores, the adsorbates are subjected to the force of the pore walls on both sides, and the chemical potential generated can be expressed as follows (Rangarajan et al., 1995):

$$\mu_{fs}(z) = N_A\left[\psi^{fs}(z) + \psi^{fs}(L-z)\right] \tag{4}$$

Where NA is Avogadro's number; Ψ^{fs}(z) and Ψ^{fs}(L-z) are the potential energy generated by the interaction between adsorbates at position z in the pore and the pore walls on both sides, J.

Eqs 2–5 can be obtained simultaneously:

$$f_{ff}(z) = f_{bulk}\exp\left(-\frac{\psi^{fs}(z) + \psi^{fs}(L-z)}{kT}\right) \tag{5}$$

Where k refers to Boltzmann's constant, $1.3806505 \times 10^{-23}$ J K^{-1}.

The fugacity of the bulk phase and the adsorbed phase can be calculated using the Peng-Robinson (PR) equation of state in academic terms (Qi et al., 2019; Huang et al., 2022).

The expression of excess adsorption amount is as follows:

$$n_{ex} = 11.2ZA\int_{lower}^{upper}[\rho(z) - \rho_b]dz \tag{6}$$

Where n_{ex} is the excess adsorption amount, m^3·g^{-1}; A is BET specific surface area, m^2·kg^{-1}; The lower limit and upper limit of the integral are respectively $3/8\sigma_{ff}$ and L-$3/8\sigma_{ff}$; Z is the gas compression factor.

2.2 Molecular simulation methods

Coal is an anisotropic porous material with a complex physicochemical structure, abundant micro- and nano-scale pores, and a high specific surface area, serving as the primary reservoir for CBM. The study area is deep coal in the eastern Ordos Basin. The main coal seam is developed in Taiyuan Formation, numbered 8#, and the coal rank is higher-rank. The molecular structure model of high-rank coal (C184H155O20N3S3) constructed by Wiser et al. (1967) is considered to best reflect the molecular structure of higher-rank coal (Long et al., 2022; Lin et al., 2023). The crystal cell model was established using the Amorphous Cell module and molecular dynamics simulation. Geometric optimization and annealing techniques were employed to achieve global energy minimization of the crystal cell. The optimized cell parameters were a = b = c = 26.77 Å, α = β = γ = 90°. The process of cell construction is illustrated in Figure 2. Subsequently, the cell was expanded to a 1 × 2 × 2 supercell, and a vacuum layer of 5–80 Å was added to obtain the slit model of the coal molecule. The establishment process of the slit model is depicted in Figure 2. It should be noted that in the diagram of methane density distribution in the slit pore, we adopted the center of the pore as the origin, and the distance on both sides of the pore was expressed by positive and negative values, which is a common method to describe the structure and properties of the pore (Mosher et al., 2013; Xiong et al., 2017).

3 Samples and experiments

The samples are deep coal from the eastern Ordos Basin, and the sampling depth is greater than 2000 m. According to various test standards, porosity was measured by helium method, specific surface area and pore diameter were obtained by low temperature CO_2 adsorption experiment and low temperature N_2 adsorption experiment, respectively. The low temperature CO_2 adsorption experiment is to calculate the specific surface area of CO_2 adsorption in coal pores at low temperature (273.15 K) and low pressure. The

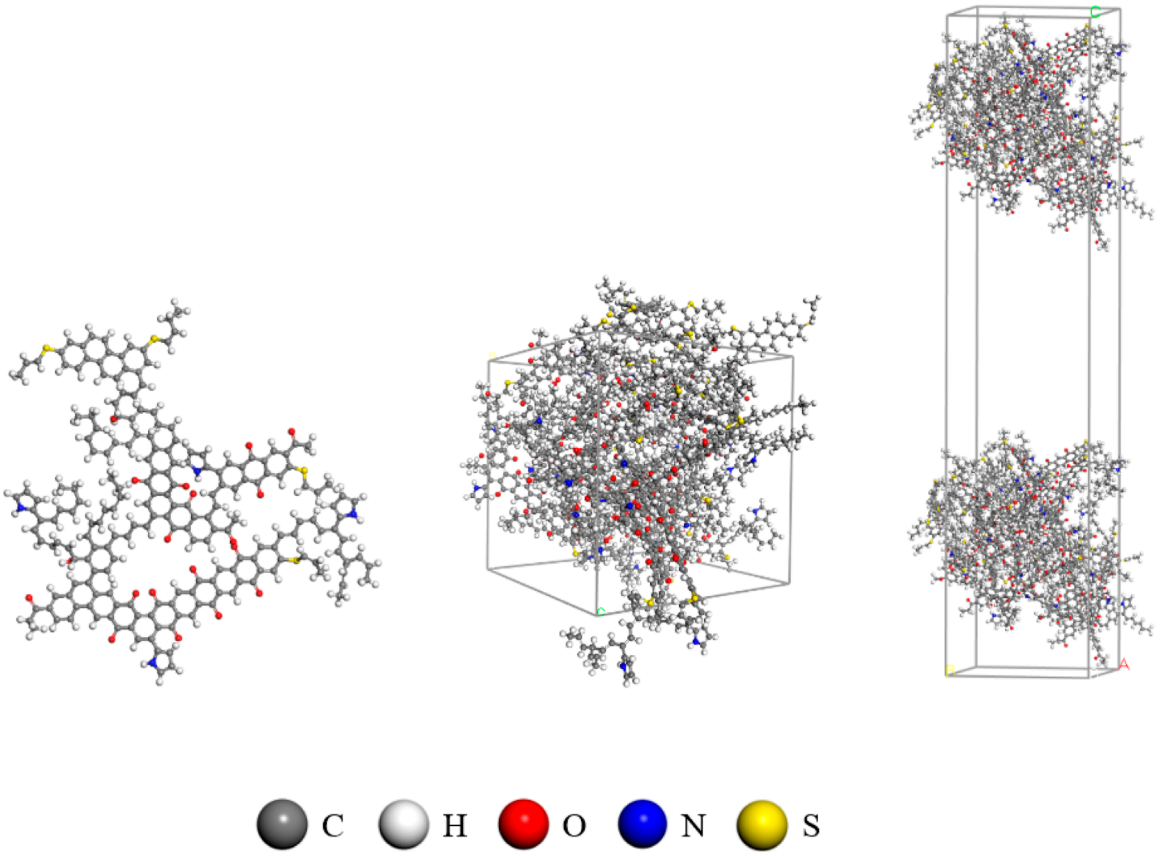

FIGURE 2
Coal molecular matrix model and slit pore model.

TABLE 1 Sample basic data.

Sample	Porosity %	Mad %	Aad %	Vad %	FCad %	BET specific surface area m^2/g	Pore size nm
1	7.9	1.47	3.77	6.43	88.33	78.11	4.97
2	8.9	0.69	9.06	6.55	82.58	112.92	8.62

TABLE 2 Gas content theoretical model parameters.

Porosity	φ = 7%
Water saturation	S_w = 20%
Density	ρ_b = 1.35 g/cm^3
Ground standard temperature	T_{sc} = 30 °C
Temperature gradient	TH = 2.0, 3.0, 4.0 °C/100m
Pressure gradient	PH = 0.85, 0.95, 1.05 MPa/100m

adsorption and desorption curves of N_2 in coal pores under low temperature (77.4 K) and low pressure were used to calculate the pore diameter. BET equation was used to calculate the specific surface area (Brunauer et al., 1938) and BJH equation was used to calculate the pore diameter (Barrett et al., 1951). Table 1 lists the basic information of the samples.

4 Results and discussions

The occurrence state of deep CBM is controlled by various geological factors, which can be broadly categorized into external controlling factors (formation temperature, formation pressure) and internal controlling factors (pore size, water saturation, Specific surface area). In this study, the SLD model is employed to simulate the adsorbed gas content of deep CBM under the influence of both external and internal geological factors. Additionally, molecular simulation methods are utilized to calculate the adsorbed gas and free gas densities under the influence of various controlling factors, as well as their occurrence state within the coal pores.

4.1 External geological controlling factors on the occurrence state of deep CBM

Temperature and pressure are significant external geological controlling factors that influence the content of deep CBM. As

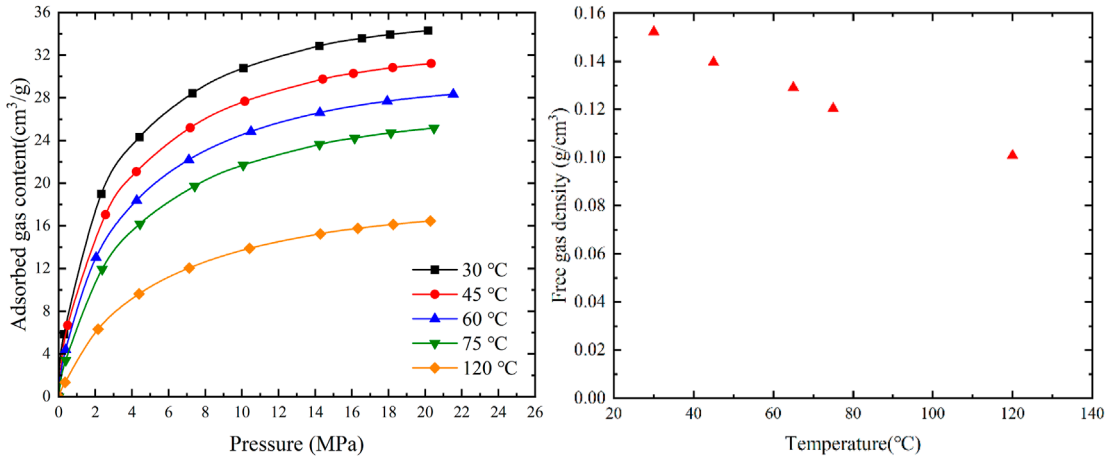

FIGURE 3
The response of gas content in different occurrence states of coal seams to temperature.

the coal seam depth increases, the formation temperature and pressure also increase, leading to a change in the dominant controlling factors for the occurrence state of deep CBM. Consequently, the proportion of adsorbed gas to free gas content is altered.

As shown in Figure 3, when the pressure is 20 MPa and remains unchanged, the adsorbed gas content gradually decreases with increasing temperature. The adsorbed gas content at 120°C is 48% lower than at 30°C. This is due to the physical adsorption of methane, which is an exothermic process. With increasing temperature, the kinetic energy of the adsorbed methane molecules increases, leading to a decrease in the interaction force between methane and the solid surface. Consequently, the adsorption capacity of coal weakens. As shown in Figure 3, at a pressure of 20 MPa, the free gas content also decreases gradually with increasing temperature. The free gas density at 120°C is 31% lower than at 30°C. The influence of temperature on the free gas is relatively smaller compared to the influence on the adsorbed gas.

As shown in Figure 4, the response of Langmuir pressure and Langmuir volume to temperature can be observed. It is evident from the graph that temperature has a negative impact on the adsorption capacity of coal. Both the saturation adsorption capacity exhibit a linear decrease with increasing temperature, showing a high level of linear correlation with good fit (R^2 = 0.9695). In contrast, Langmuir pressure shows a linear increase with temperature, demonstrating a good linear correlation (R^2 = 0.8702). When the temperature increases from 30°C to 120°C, the saturation adsorption capacity decreases from 37.69 cm^3/g to 19.76 cm^3/g, representing a reduction of approximately 47.5%. Meanwhile, Langmuir pressure increases from 2.33 MPa to 5.163 MPa, indicating an approximately 40% increase.

In different injection pressure ranges, the rate of gas content increase can be divided into three stages: rapid, slow, and gradual increase. During the rapid increase stage, CH4 molecules can quickly adsorb onto high-energy adsorption sites. As the high-energy adsorption sites become gradually occupied, the remaining low-energy adsorption sites start adsorbing CH4 molecules, resulting in a slow increase in gas content. Subsequently, as the low-energy adsorption sites become occupied, the adsorption process approaches saturation, and the rate of gas content increase becomes gradual.

As shown in Figure 5, at a constant temperature, the adsorbed gas and free gas content increase with increasing pressure. The adsorbed gas content shows a rapid increase at low pressures and a more gradual increase at high pressures, in accordance with the Langmuir equation. The increase in free gas content within the pore space exhibits a linear trend with increasing pressure, conforming to the gas state equation.

4.2 Internal geological controlling factors on the occurrence state of deep CBM

The deposition of coal and the generation of CBM occur in aqueous environments, and the influence of water content on the gas content and occurrence state of deep CBM cannot be ignored. This section analyzes the distribution of water molecules in coal under different water saturation levels and further investigates the effects of varying water saturation levels on the adsorbed gas and free gas in coal reservoirs.

Coal is an anisotropic porous material with a complex pore structure. The pore structure of coal itself affects the occurrence state of deep CBM. This section analyzes the impact of reservoir pore structure on the occurrence of adsorbed gas and free gas in deep coal reservoirs. By varying pore size and specific surface area, the characteristics of adsorbed gas and free gas content under different pore structure conditions in coal reservoirs are studied.

4.2.1 Water saturation

The distribution of adsorbed water in pores and the interactions among liquid, gas, and solid phases influence the adsorption characteristics of methane molecules in coal. At low water saturation

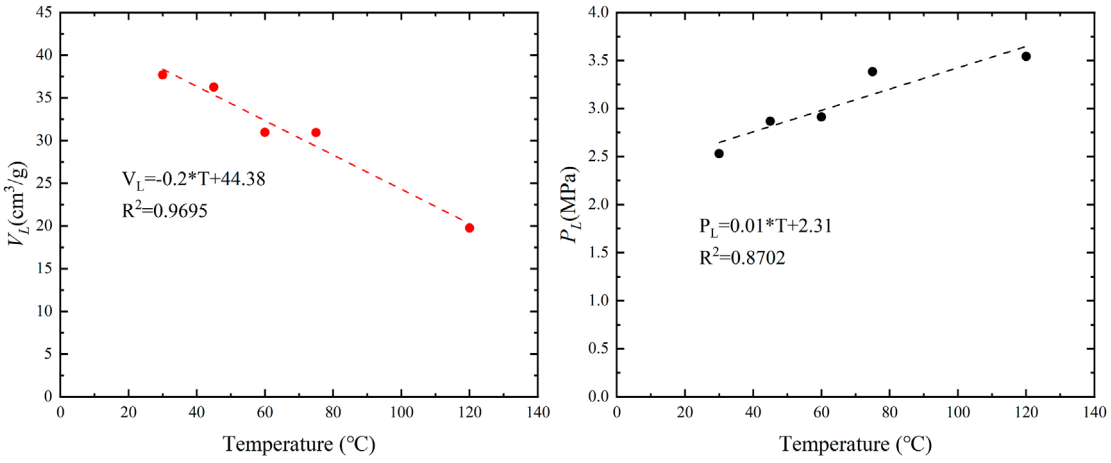

FIGURE 4
The response of Langmuir pressure and Langmuir volume in coal seams to temperature.

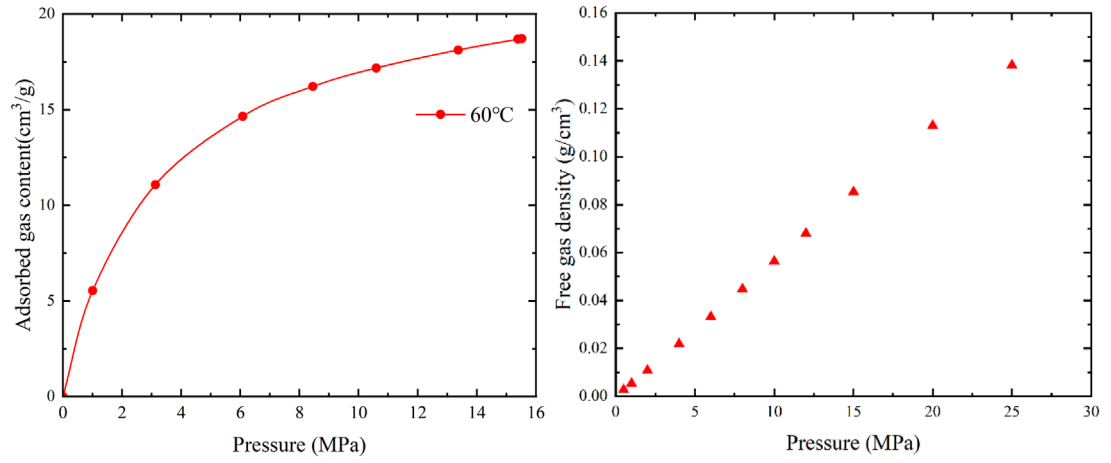

FIGURE 5
The response of gas content in different occurrence states of coal seams to pressure.

levels, there is a "competitive adsorption" relationship between water molecules and methane molecules. However, the adsorption of water molecules on coal is driven by hydrogen bonding between water molecules and pore surfaces, while the adsorption of methane molecules on pore surfaces is driven by van der Waals forces. Hydrogen bonding is 5–10 times stronger than van der Waals forces, causing water molecules to preferentially adsorb and occupy the adsorption sites for methane, resulting in a decrease in the adsorption capacity of methane molecules. As the water saturation level increases, water molecules form a water film on the pore surface and even exhibit capillary condensation in nanometer-sized pores, leading to pore blockage. The formation and thickening of the water film restrict the diffusion pathways of methane molecules.

Figure 6 illustrates the adsorption sites of water and methane molecules within the coal at low water saturation levels. Figure 6 shows the position of methane and water molecules in the Z direction of the model, and the ordinate shows the increase or decrease in the density of methane and water molecules, where the positive value represents the increase in the density of water molecules and the negative value represents the decrease in the density of methane molecules, that is, the methane adsorption site occupied by water molecules. From the figure, it can be observed that water molecules preferentially occupy the micro- and nano-scale pores within the coal, and the density distribution of water molecules in the coal closely corresponds to the reduction in methane molecule density. This indicates a "competitive adsorption" relationship between water and methane molecules, where water molecules have a stronger adsorption capacity on the coal compared to methane molecules.

As shown in Figure 7, with the increase of water saturation, the gas content gradually decreases. For example, when the

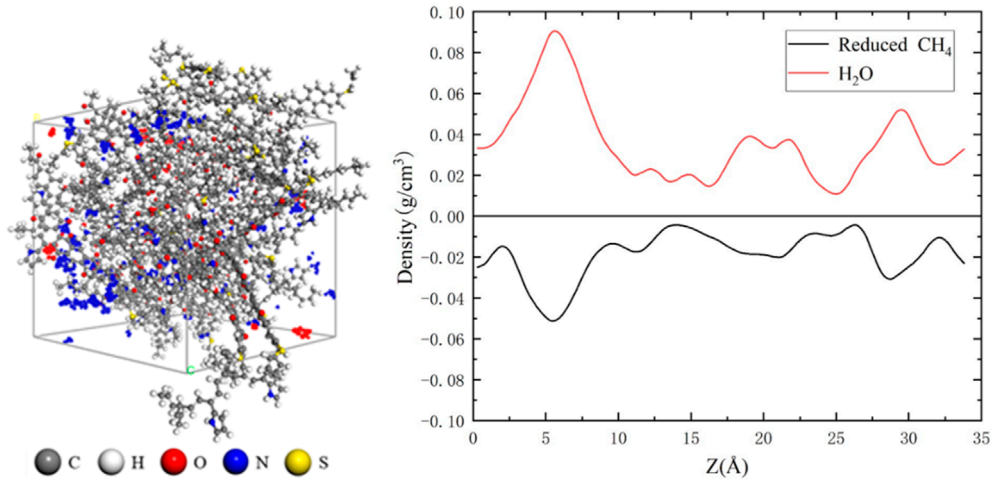

FIGURE 6
Methane reduction and water molecular density distribution.

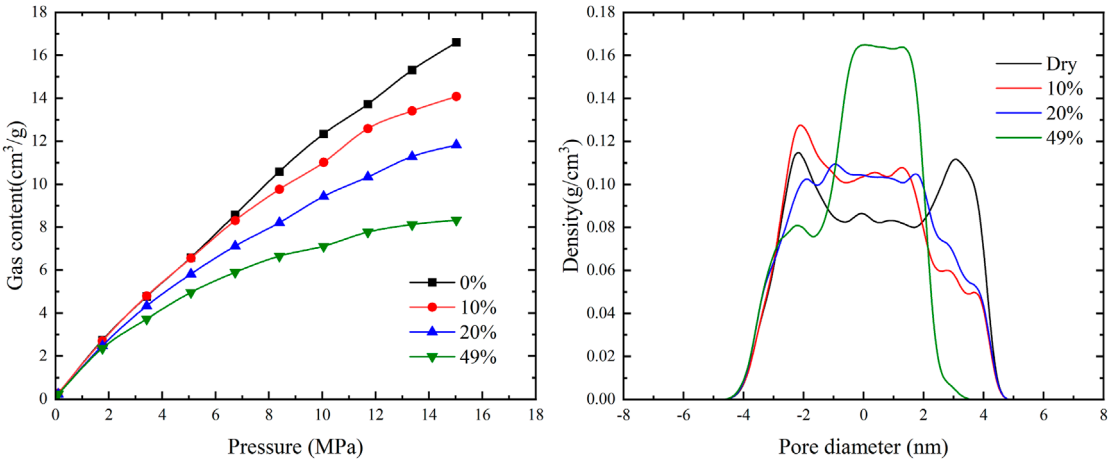

FIGURE 7
The response of gas content in different occurrence states of coal seams to water saturation.

pressure is 15 MPa, the gas content decreases by 49.8% when the water saturation is 49%. This indicates that water saturation has a significant impact on the gas content in coal. The gas density distribution within the pores reveals that water molecules preferentially occupy the adsorption sites of methane molecules. When a water film forms on a single sidewall of a narrow pore, the density distribution curve exhibits a single adsorption peak. However, when water films form on both sidewalls, the adsorption peak disappears, and in a 4 nm pore size, the adsorbed gas and free gas become mixed and indistinguishable.

4.2.2 Pore size

As depicted in Figure 8, when the pore size is less than 2 nm, methane molecules almost completely fill the slit-like pores. As the pore size gradually increases, the density of methane molecules within the pores remains nearly constant. The density of methane molecules in the central region of the pore is similar to that of methane molecules on the pore wall surface, suggesting that methane molecules undergo pore filling phenomena in micropores with a pore size smaller than 2 nm.

As shown in Figure 9, when the pore size is greater than 2 nm, the adsorbed gas density is almost unaffected by the pore size. When the pore size is less than 4 nm, the free gas density is influenced by both sidewalls of the pores, resulting in higher density values. However, when the pore size is larger than 4 nm, the density of free gas is almost unaffected by the pore size, and the density of free gas is lower than the density of methane molecules on the pore wall surface, indicating the absence of pore filling phenomena.

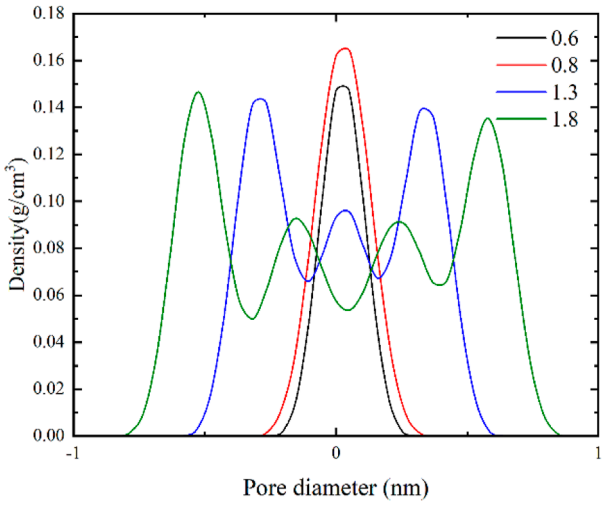

FIGURE 8
Methane density distribution in pores smaller than 2 nm.

Additionally, the methane density distribution for different pore sizes reveals the presence of two adsorption layers on the pore wall surface, suggesting that methane is adsorbed in a multi-molecular layer form in pores larger than 2 nm. The results of the gas content for different pore sizes show adsorption reversal phenomenon at high pressures. At low pressures, due to the smaller pore size and stronger binding energy within the small pores, methane molecules preferentially adsorb, resulting in a higher gas content in models with larger pore sizes. As the pressure increases, the adsorption sites in the small pores become occupied, leading to a slower increase in the adsorbed gas content and resulting in a phenomenon where the gas content in larger pores is greater than that in smaller pores.

4.2.3 Specific surface area

The CO_2 adsorption experiments provide insights into the specific surface area, pore volume, and adsorption capacity characteristics of micropores with sizes below 2 nm. The specific surface area of coal in the local area was measured in the range of 65.76 to 135.29 m^2/g, with an average of 106.86 m^2/g. Based on these measurements, four theoretical conditions were set at 65, 85, 100, and 120 m^2/g to analyze the impact of specific surface area on the adsorbed gas and free gas in coal.

As depicted in Figure 10, increasing the specific surface area does not alter the density of adsorbed gas and free gas. However, it provides more adsorption sites for methane adsorption. At 120 m^2/g, the gas content of adsorbed gas is four times higher than that at 65 m^2/g, indicating that a larger specific surface area leads to higher gas content in terms of adsorbed gas. The change in specific surface area has little impact on the content of free gas because free gas primarily exists in pores and fractures without interacting with the pore walls.

4.3 Theoretical model of gas content

As mentioned in the previous section, the gas content of coal seams is primarily controlled by the specific surface area, water saturation, formation temperature, and formation pressure of the coal seam. By integrating coal seam temperature, pressure, industrial components of coal, rock physics experiments, and relevant research findings from domestic and international sources, a theoretical model for the gas content of deep coal adsorption is established.

$$n_{ex} = 11.2ZA\int_{lower}^{upper}[\rho(z) - \rho_b]dz \tag{7}$$

In the model, the potential energy of solid-solid interactions (ε_{ss}) is found to be a function of temperature and water saturation. Through research investigations, it has been determined that in deep coal, ε_{ss} exhibits the following functional relationship with temperature and other conditions (Zeng, 2019).

$$\begin{aligned}\varepsilon_{ss}/k_B = &\left[(-0.0081V_{ad} + 0.55)(T - 308.15) + 0.39FC_{ad} + 3.67\right] \\ &\times\left[1 + 0073(M_{EMC} - S_w)\right]\end{aligned} \tag{8}$$

In the equation, A_{ad} represents the ash content, %. FC_{ad} represents the fixed carbon content, %. M_{ad} represents the moisture content, %. V_{ad} represents the volatile matter content, %. M_{EMC} represents the equilibrium moisture content, %. S_w represents the water saturation, %.

Free gas is primarily stored in coal seam pores and microfractures. Through analysis of internal and external geological controlling factors, it is known that the content of free gas is mainly influenced by pore size, water saturation, and temperature-pressure conditions. Since pore size mainly affects the porosity of coal, the content of free gas can be regarded as controlled by porosity, water saturation, geothermal temperature, and formation pressure conditions.

Currently, the calculation of free gas content in unconventional oil and gas reservoirs is often based on gas state equations and the principle of material balance. Based on previously established models for estimating free gas content, an estimation of the free gas content in deep coal reservoirs is conducted (Eqs 8–10).

$$N_f = \frac{\varphi(1 - S_w)}{\rho_b \cdot B_g} \tag{9}$$

Where, B_g is methane gas volume coefficient.

$$B_g = \frac{P_{sc}ZT}{PT_{sc}} \tag{10}$$

The theoretical model of free gas content in deep coal seam can be obtained by simultaneous upper formula:

$$N_f = \frac{\varphi(1 - S_w)PT_{sc}}{\rho_b P_{sc}ZT} \tag{11}$$

As mentioned earlier, changes in the external geological control factors of temperature and pressure significantly impact the content of adsorbed and free gases in deep coal seams, while the internal geological control factors can be considered constant within the same study area. Based on this, the influence of these two factors on the gas content of coal seams in different occurrence states

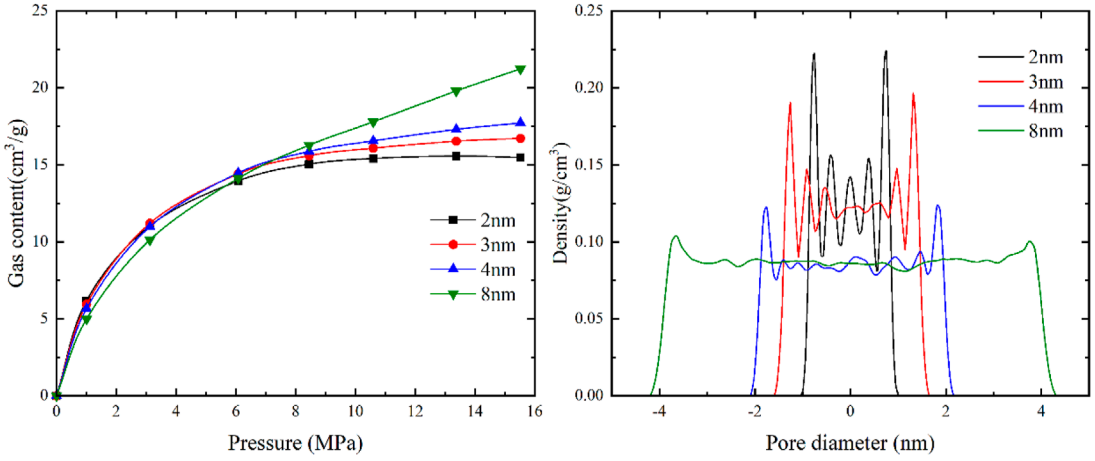

FIGURE 9
The response of gas content in different occurrence states of coal seams to pore size.

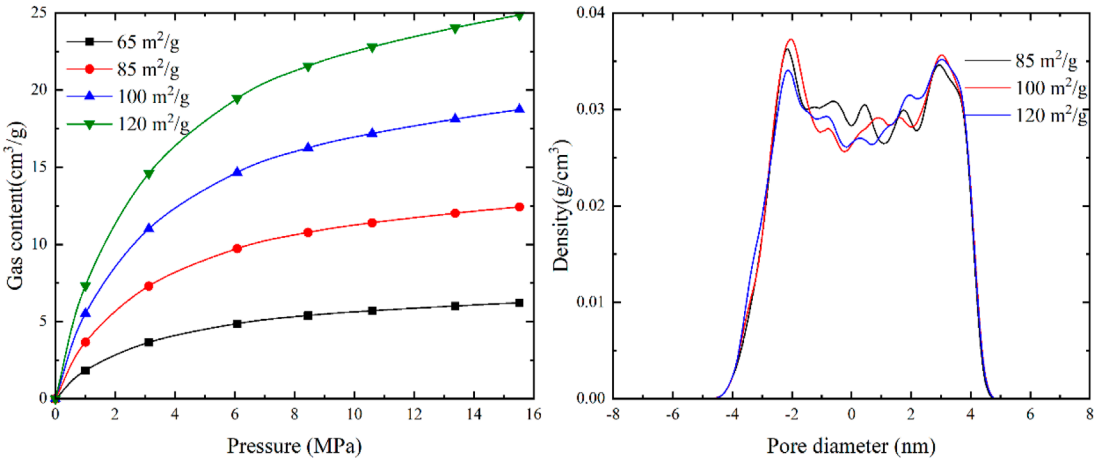

FIGURE 10
The response of gas content in different occurrence states of coal seams to specific surface area.

is discussed. Combined with the formation conditions of deep coalbed methane reservoir in eastern Ordos Basin, three values are assigned to the temperature gradient and pressure gradient, representing the relationship between burial depth and the external geological control factors. The temperature gradient is set to 2.0, 3.0, and 4.0 C/100m, while the pressure gradient is set to 0.85, 0.95, and 1.05 MPa/100 m (Table 2). When one of the two external geological control factors change while keeping the basic parameters constant, the variations in gas content of coal seams in different occurrence states with depth can be obtained by combining Eqs 7, 11 (Figures 11, 12).

With an increase in geothermal gradient, the gas content of adsorbed gas, free gas, and total gas in coal seams continuously decreases (Figure 11). However, the influence of geothermal gradient on adsorbed gas content, free gas content and total gas content of coal seam is different. At shallow layer, the influence of geothermal gradient on adsorbed gas content is weak. With the increase of buried depth, the influence of geothermal gradient on the adsorbed gas content of coal seam increases gradually. The influence of formation temperature on the free gas content of coal seam has the same trend, resulting in the free gas content increasing with the increase of buried depth, but showing a continuous decreasing trend with the increase of geothermal gradient. The total gas content of coal seam is affected by geothermal gradient in the same way as adsorbed gas.

When the ground temperature gradient is unchanged, the adsorbed gas content exhibits a trend of initially increasing and then decreasing, and as the burial depth increases, the differences in adsorbed gas content gradually increase. The maximum adsorbed gas content decreases from 26.8 cm^3/g to 23.01 cm^3/g, corresponding to a decrease in burial depth from 1,291.5 m to 890.2 m. At the same burial depth, the free gas

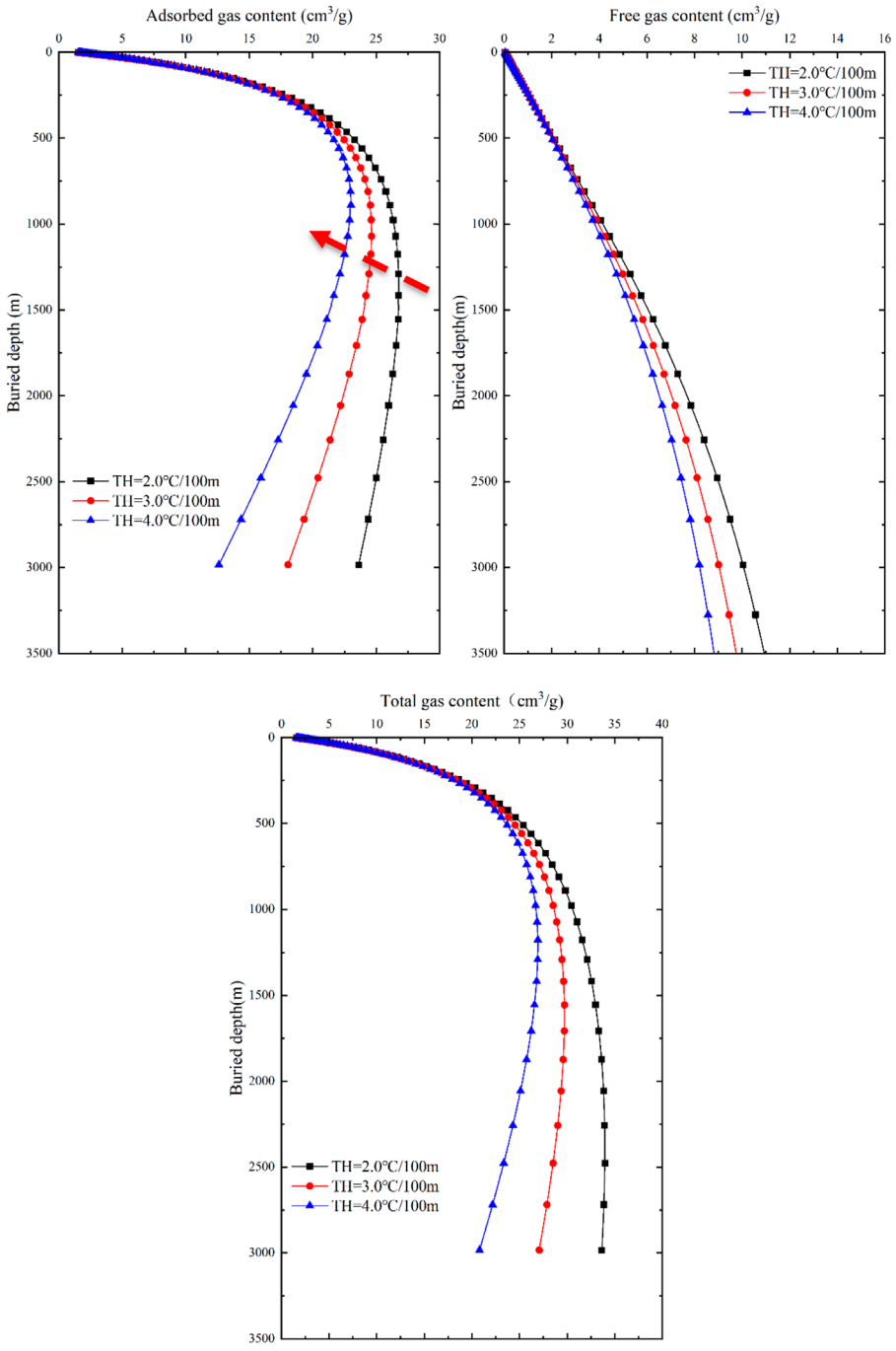

FIGURE 11
Response of gas content and buried depth to temperature in different occurrence states of coal seams.

content in coal seams shows a decreasing trend with an increase in geothermal gradient, and as the burial depth increases, the differences in free gas content also increase. If the burial depth is the constant, the free gas content decreases exponentially with an increase in temperature. The total gas content exhibits a similar response to temperature as the adsorbed gas content, showing a trend of increasing first and then decreasing. The maximum value of total gas content corresponds to a decrease in burial depth from 2477 m to 1,176.8 m.

With an increase in pressure gradient, the gas content of adsorbed gas, free gas, and total gas in coal seams continuously increases, but the differences between the two curves are relatively similar (Figure 12). As the pressure gradient gradually increases, the gas content shows little variation. The adsorbed gas content in coal seams exhibits a trend of initially increasing and then decreasing, with significant differences between 500 m and 1000 m. The maximum adsorbed gas content increases from 24.04 cm^3/g to 25.22 cm^3/g, corresponding to a decrease in burial depth from

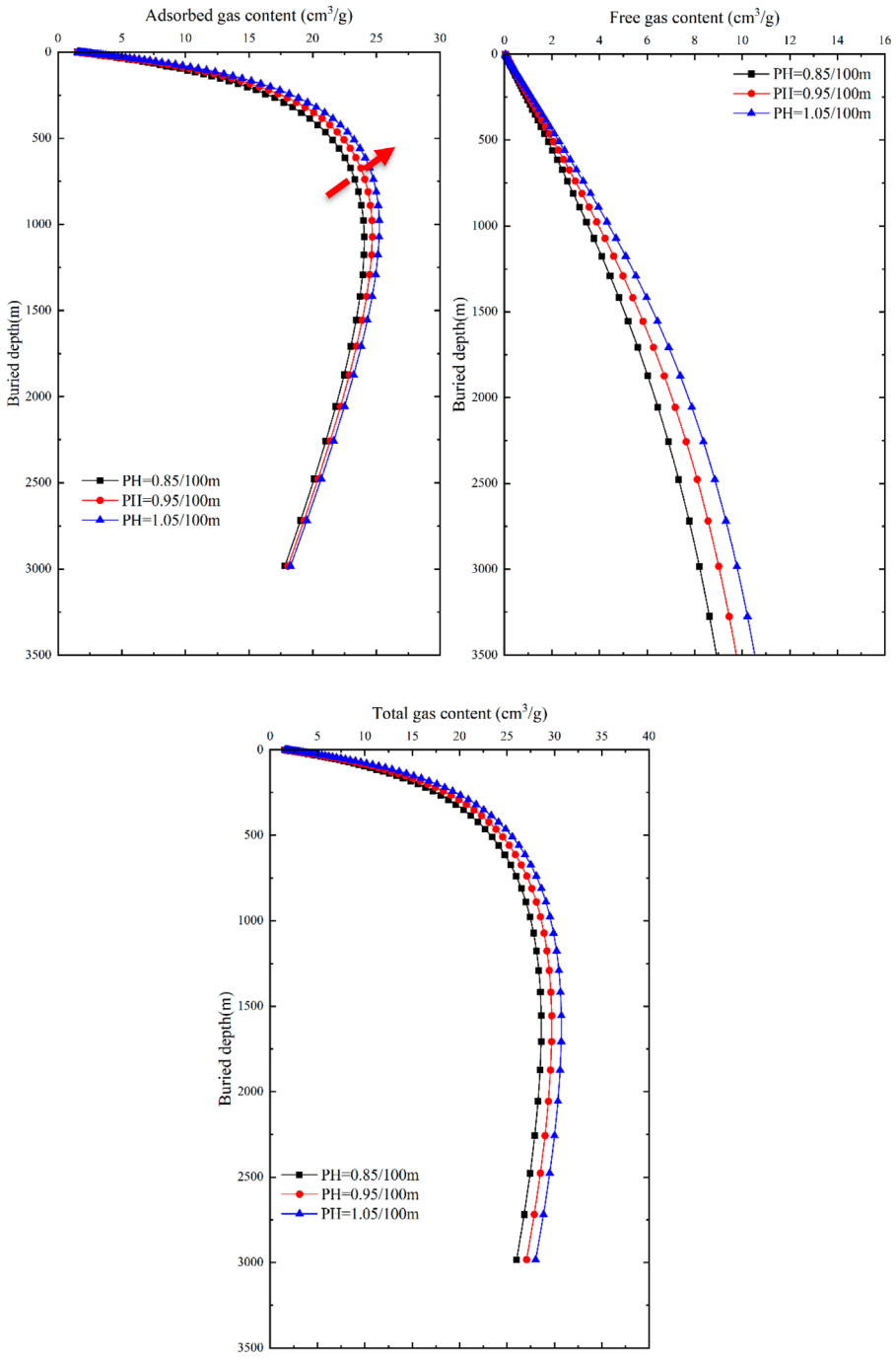

FIGURE 12
Response of gas content and buried depth to pressure in different occurrence states of coal seams.

1,072.3 m to 977 m. As the burial depth continues to increase, the differences in adsorbed gas content gradually decrease, indicating that burial depth is the dominant factor controlling the adsorbed gas content in relatively shallow reservoir depths. As the burial depth increases, temperature becomes the dominant factor controlling the adsorbed gas content. At the same burial depth, the free gas content in coal seams shows an increasing trend with an increase in pressure gradient, and the differences in free gas content remain constant as the burial depth increases. If the burial depth is the same, the free gas content linearly increases with an increase in pressure gradient, indicating that formation pressure plays a dominant role in the free gas content. The total gas content shows slight differences in response to formation pressure compared to the adsorbed gas content, exhibiting a trend of increasing first and then decreasing.

The maximum total gas content is reached at 1555m, but as the burial depth increases, the differences in total gas content gradually approach a constant value.

In the vicinity of 750 m, the impact of geothermal gradient on the total gas content within the tested range approaches that of the pressure gradient. In shallow burial depths (<750 m), there is minimal difference in the total gas content among different geothermal gradients, and all show an increasing trend, indicating that formation temperature is not the dominant factor controlling the total gas content in coal seams. Generally, in shallow burial depths (<750 m), the primary factor influencing the total gas content in coal seams is formation pressure, whereas in deeper burial depths (>750 m), the main factor is formation temperature.

5 A comparison of the primary controlling factors of the occurrence state of deep CBM and shale gas

Shale gas and deep CBM both belong to self-generated and self-stored unconventional natural gas, sharing many similarities in terms of geological conditions and occurrence environments. Factors such as pore structure, temperature, and moisture are also primary controlling factors influencing the occurrence state of shale gas (Gasparik et al., 2014; Merkel et al., 2015; Shabani et al., 2018; Hu et al., 2021; Zhang et al., 2023; Cui et al., 2024). However, there are also some differences between them. Unlike coal, which is primarily composed of organic matter, shale consists not only of organic matter but also of inorganic minerals such as illite and montmorillonite (Shi et al., 2023). In addition to being adsorbed on the surface of organic matter, shale gas can also be adsorbed on the surface of clay minerals. Deep coal and shale also exhibit certain differences in pore structure. Pore structure influences the occurrence state and micro-distribution characteristics of methane (Hu and Cheng, 2023). Shale reservoirs are ultra-tight with diverse pore types, predominantly consisting of micro-nano-scale pores, while coal reservoirs have a dual pore structure composed of pores and fractures, with medium-small pores and micro-pores being dominant, and a wide distribution range of pores. Therefore, further research can compare the influences of mineral composition and pore structure distribution on the occurrence state of deep CBM and shale gas, providing insights into their respective mechanisms.

6 Conclusion

(1) External geological controlling factors, namely temperature and pressure, significantly affect the adsorbed gas and free gas content in deep coal seams. Among the internal geological controlling factors, pore size has a minor impact on the adsorbed gas content, but an increase in pore size leads to larger pore space, providing more accommodation space for free gas and thus having a greater influence on the free gas content. Changes in specific surface area increase the adsorption sites for methane molecules in coal, resulting in an increase in adsorbed gas content, while having no significant effect on the free gas content. The water saturation in coal seams affects both the adsorbed gas and free gas, primarily by occupying the adsorption sites of methane molecules, leading to a decrease in adsorbed gas content, and by forming water films that occupy the reservoir space of free gas as the water saturation increases, resulting in a decrease in free gas content.

(2) In the same study area, there are differences in the influence of geothermal gradient and pressure gradient on the total gas content. The adsorbed gas is predominantly influenced by positive pressure effects in shallow depths and negative temperature effects in deeper depths. The response of free gas to formation pressure is evident under different burial depth conditions, while its response to temperature exhibits exponential decay. In shallow burial depths (<750 m), formation pressure is the primary factor influencing the total gas content in coal seams, whereas in deeper burial depths (>750 m), formation temperature becomes the main influencing factor for the total gas content in coal seams.

Data availability statement

The original contributions presented in the study are included in the article/Supplementary Material, further inquiries can be directed to the corresponding author.

Author contributions

YS: Conceptualization, Data curation, Funding acquisition, Resources, Writing–review and editing. YH: Conceptualization, Funding acquisition, Project administration, Resources, Validation, Writing–review and editing. JW: Investigation, Supervision, Writing–review and editing. JS: Conceptualization, Formal Analysis, Supervision, Writing–original draft. JZ: Software, Supervision, Validation, Visualization, Writing–review and editing. RC: Methodology, Software, Writing–original draft, Writing–review and editing.

Funding

The author(s) declare financial support was received for the research, authorship, and/or publication of this article. The project is supported by CNPC Major Science and Technology Project "Enrichment Law of Deep Coalbed Methane and Optimization of Favorable Areas" (Numbers 2023ZZ18, 2023ZZ1803); China National Petroleum Corporation Logging Co., Ltd. Project "Research on Key Techniques for Logging Evaluation of Deep Coalbed Methane" (Number CNLC2023-8B02).

Conflict of interest

Authors YS, YH, JW, and JZ were employed by China National Logging Corporation.

The remaining authors declare that the research was conducted in the absence of any commercial or financial relationships that could be construed as a potential conflict of interest.

Publisher's note

All claims expressed in this article are solely those of the authors and do not necessarily represent those of their affiliated organizations, or those of the publisher, the editors and the reviewers. Any product that may be evaluated in this article, or claim that may be made by its manufacturer, is not guaranteed or endorsed by the publisher.

Supplementary material

The Supplementary Material for this article can be found online at: https://www.frontiersin.org/articles/10.3389/feart.2024.1340523/full#supplementary-material

References

Bai, Y., Lin, H.-F., Li, S.-G., Yan, M., and Long, H. (2021). Molecular simulation of N2 and CO2 injection into a coal model containing adsorbed methane at different temperatures. *Energy* 219, 119686. doi:10.1016/j.energy.2020.119686

Barrett, E. P., Joyner, L. G., and Halenda, P. P. (1951). The determination of pore volume and area distributions in porous substances. I. Computations from nitrogen isotherms. *J. Am. Chem. Soc.* 73, 373–380. doi:10.1021/ja01145a126

Brunauer, S., Emmett, P. H., and Teller, E. (1938). Adsorption of gases in multimolecular layers. *J. Am. Chem. Soc.* 60, 309–319. doi:10.1021/ja01269a023

Cui, R., Sun, J., Liu, H., Dong, H., and Yan, W. (2024). Pore structure and gas adsorption characteristics in stress-loaded shale on molecular simulation. *Energy* 286, 129658. doi:10.1016/j.energy.2023.129658

Fitzgerald, J., Sudibandriyo, M., Pan, Z., Robinson, R., JR, and Gasem, K. (2003). Modeling the adsorption of pure gases on coals with the SLD model. *Carbon* 41, 2203–2216. doi:10.1016/s0008-6223(03)00202-1

Gasparik, M., Bertier, P., Gensterblum, Y., Ghanizadeh, A., Krooss, B. M., and Littke, R. (2014). Geological controls on the methane storage capacity in organic-rich shales. *Int. J. Coal Geol.* 123, 34–51. doi:10.1016/j.coal.2013.06.010

Geng, M., Chen, H., Chen, Y., Zeng, L., Chen, S., and Jiang, X. (2018). Methods and results of the fourth round national CBM resource evaluation. *Coal Sci. Technol.* 46, 64–68. doi:10.13199/j.cnki.cst.2018.06.011

Guo, T. (2022). Prediction model of occurrence and content of deep coalbed methane. Master Thesis. China: China University of Mining and Technology.

Hao, M., Wei, C., and Zhang, H. (2022). Adsorption and diffusion of methane in coal slit pores: insights into the molecular level. *Energy & Fuels* 36, 880–886. doi:10.1021/acs.energyfuels.1c03730

Huang, X., Gu, L., Li, S., Du, Y., and Liu, Y. (2022). Absolute adsorption of light hydrocarbons on organic-rich shale: an efficient determination method. *Fuel* 308, 121998. doi:10.1016/j.fuel.2021.121998

Hu, B., Cheng, Y., and Pan, Z. (2023). Classification methods of pore structures in coal: a review and new insight. *Gas Sci. Eng.* 110, 204876. doi:10.1016/j.jgsce.2023.204876

Hu, Z., Gaus, G., Seemann, T., Zhang, Q., Littke, R., and Fink, R. (2021). Pore structure and sorption capacity investigations of Ediacaran and Lower Silurian gas shales from the Upper Yangtze platform, China. *Geomechanics Geophys. Geo-Energy Geo-Resources* 7, 71. doi:10.1007/s40948-021-00262-5

Lin, H.-F., Long, H., Li, S.-G., Bai, Y., Xiao, T., and Qin, A.-L. (2023). CH4 adsorption and diffusion characteristics in stress-loaded coal based on molecular simulation. *Fuel* 333, 126478. doi:10.1016/j.fuel.2022.126478

Liu, S., Tang, S., and Yin, S. (2018). Coalbed methane recovery from multilateral horizontal wells in Southern Qinshui Basin. *Adv. Geo-Energy Res.* 2, 34–42. doi:10.26804/ager.2018.01.03

Li, Y., Wang, Z., Tang, S., and Elsworth, D. (2022). Re-evaluating adsorbed and free methane content in coal and its ad-and desorption processes analysis. *Chem. Eng. J.* 428, 131946. doi:10.1016/j.cej.2021.131946

Long, H., Lin, H.-F., Li, S.-G., Bai, Y., Qin, L., Xiao, T., et al. (2022). Nanomechanical properties of CH4-containing coal during CO2 storage under different injection pressures based on molecule dynamics. *Appl. Surf. Sci.* 590, 153126. doi:10.1016/j.apsusc.2022.153126

Meng, J., Zhong, R., Li, S., Yin, F., and Nie, B. (2018). Molecular model construction and study of gas adsorption of Zhaozhuang coal. *Energy & Fuels* 32, 9727–9737. doi:10.1021/acs.energyfuels.8b01940

Merkel, A., Fink, R., and Littke, R. (2015). The role of pre-adsorbed water on methane sorption capacity of Bossier and Haynesville shales. *Int. J. Coal Geol.* 147, 1–8. doi:10.1016/j.coal.2015.06.003

Mosher, K., He, J., Liu, Y., Rupp, E., and Wilcox, J. (2013). Molecular simulation of methane adsorption in micro-and mesoporous carbons with applications to coal and gas shale systems. *Int. J. Coal Geol.* 109, 36–44. doi:10.1016/j.coal.2013.01.001

Pang, Y., Wang, S., Yao, X., Hu, X., and Chen, S. (2022). Evaluation of gas adsorption in nanoporous shale by simplified local density model integrated with pore structure and pore size distribution. *Langmuir* 38, 3641–3655. doi:10.1021/acs.langmuir.1c02408

Qin, Y., and Shen, J. (2016). On the fundamental issues of deep coalbed methane geology. *Acta Pet. Sin.* 37, 125.

Qi, R., Ning, Z., Wang, Q., Huang, L., Wu, X., Cheng, Z., et al. (2019). Measurements and modeling of high-pressure adsorption of CH4 and CO2 on shales. *Fuel* 242, 728–743. doi:10.1016/j.fuel.2018.12.086

Rangarajan, B., Lira, C. T., and Subramanian, R. (1995). Simplified local density model for adsorption over large pressure ranges. *AIChE J.* 41, 838–845. doi:10.1002/aic.690410411

Shabani, M., Moallemi, S. A., Krooss, B. M., Amann-Hildenbrand, A., Zamani-Pozveh, Z., Ghalavand, H., et al. (2018). Methane sorption and storage characteristics of organic-rich carbonaceous rocks, Lurestan province, southwest Iran. *Int. J. Coal Geol.* 186, 51–64. doi:10.1016/j.coal.2017.12.005

Shen, J., Qin, Y., Fu, X., Chen, G., and Chen, R. (2014). Properties of deep coalbed methane reservoir-forming conditions and critical depth discussion. *Nat. Gas. Geosci.* 25, 1470–1476.

Shi, K.-Y., Chen, J.-Q., Pang, X.-Q., Jiang, F.-J., Hui, S.-S., Zhao, Z.-C., et al. (2023). Wettability of different clay mineral surfaces in shale: implications from molecular dynamics simulations. *Petroleum Sci.* 20, 689–704. doi:10.1016/j.petsci.2023.02.001

Sun, B., Yang, M., and Yang, Q. (2017). Analysis on occurrence state of deep coalbed methane in Junggar basin. *J. China Coal Soc.* 42, 195–202.

Tambaria, T. N., Sugai, Y., and Nguele, R. (2022). Adsorption factors in enhanced coal bed methane recovery: a review. *Gases* 2, 1–21. doi:10.3390/gases2010001

Wang, W.-S., and Zhang, J.-J. (2021). Study on the driving factors and regulation mode for coal production capacity. *Petroleum Sci.* 18, 1564–1577. doi:10.1016/j.petsci.2021.08.014

Wang, F., Yao, Y., Wen, Z., Sun, Q., and Yuan, X. (2020). Effect of water occurrences on methane adsorption capacity of coal: a comparison between bituminous coal and anthracite coal. *Fuel* 266, 117102. doi:10.1016/j.fuel.2020.117102

Wiser, W., Hill, G., and Kertamus, N. (1967). Kinetic study of pyrolysis of high volatile bituminous coal. *Industrial Eng. Chem. Process Des. Dev.* 6, 133–138. doi:10.1021/i260021a023

Xiong, J., Liu, X., Liang, L., and Zeng, Q. (2017). Adsorption of methane in organic-rich shale nanopores: an experimental and molecular simulation study. *Fuel* 200, 299–315. doi:10.1016/j.fuel.2017.03.083

Yan, B., and Yang, X. (2005). Adsorption prediction for three binary supercritical gas mixtures on activated carbon based on a NDFT/PSD approach. *Chem. Eng. Sci.* 60, 3267–3277. doi:10.1016/j.ces.2005.01.035

Yao, Y., Liu, D., and Xie, S. (2014). Quantitative characterization of methane adsorption on coal using a low-field NMR relaxation method. *Int. J. Coal Geol.* 131, 32–40. doi:10.1016/j.coal.2014.06.001

Yao, Y., Zhang, C., Ye, S., Sun, X., and Wu, H. (2023). Water-methane interactions in coal: insights from molecular simulation. *Unconv. Resour.* 3, 113–122. doi:10.1016/j.uncres.2023.01.004

Ye, D., Liu, G., Gao, F., Xu, R., and Yue, F. (2021). A multi-field coupling model of gas flow in fractured coal seam. *Adv. Geo-Energy Res.* 5, 104–118. doi:10.46690/ager.2021.01.10

Zeng, Q. (2019). Experiment and modeling studies on coalbed methane recovery mechanism in deep coal seams. Doctor thesis. Beijing: China University of Petroleum.

Zhang, Q., Fink, R., Krooss, B. M., Jin, Z., Zhu, R., Hu, Z., et al. (2023). Effects of light hydrocarbons and extractable organic matter on the methane sorption capacity of shales. *AAPG Bull.* 20, 230–801 doi:10.1306/05302322009

Zhang, T., He, Y., Yang, Y., and Wu, K. (2017). Molecular simulation of shale gas adsorption in organic-matter nanopore. *J. Nat. Gas Geoscience* 2, 323–332. doi:10.1016/j.jnggs.2018.01.001

frontiers | Frontiers in Earth Science

TYPE Original Research
PUBLISHED 28 March 2024
DOI 10.3389/feart.2024.1358268

OPEN ACCESS

EDITED BY
Qiaomu Qi,
Chengdu University of Technology, China

REVIEWED BY
Ruiqi Fan,
China University of Petroleum, China
Liang Wang,
Chengdu University of Technology, China

*CORRESPONDENCE
Hongliang Wu,
wuhongliang@petrochina.com.cn

RECEIVED 19 December 2023
ACCEPTED 18 March 2024
PUBLISHED 28 March 2024

CITATION
Tian H, Wu H, Yan W, Feng Z, Li C, Ren L and Xu H (2024), Evaluation method of oil saturation index OSI for shale oil reservoir based on well logging data.
Front. Earth Sci. 12:1358268.
doi: 10.3389/feart.2024.1358268

Evaluation method of oil saturation index OSI for shale oil reservoir based on well logging data

Han Tian[1], Hongliang Wu[1]*, Weilin Yan[2], Zhou Feng[1], Chaoliu Li[1], Li Ren[3] and Hongjun Xu[1]

[1]Research Institute of Petroleum Exploration and Development, Beijing, China, [2]Research Institute of Exploration and Development, Daqing Oilfield Company Limited, Daqing, China, [3]PetroChina Well Logging Company Limited, Daqing Branch, Daqing, China

Oil saturation index (*OSI*) serves as an important indicator for potential movable hydrocarbons evaluation of shale oil reservoirs, which is mainly obtained through rock pyrolysis experiments. A new method is proposed to evaluate the *OSI* of shale quantitatively by NMR logging. The *OSI* value can be accurately obtained through the experimental measurement of organic carbon content (*TOC*) and rock pyrolysis of shale samples, which can identify the development of mobile hydrocarbons. Subsequently, the mobile fluid porosity can be obtained based on NMR logging. In order to establish the relationship between *OSI* value and mobile fluid porosity, it is important to determine the T_2 cutoff value corresponding to the mobile fluid porosity. Take shale samples from the first member of the Qingshankou Formation ("Qing 1 Member") as an example, based on 2D NMR experimental analysis in three different states (original, dried state at 105°C, saturated kerosene), the NMR T_2 cutoff value of movable fluid porosity in the shale of Qing 1 Member is clarified as 8 ms. Integrating rock pyrolysis and 2D NMR experiments, it suggests that the NMR bin porosity with T_2>8 ms has a good linear relationship with the *OSI* value obtained by pyrolysis analysis. The NMR bin porosity with T_2> 8 ms reflects the *OSI* value of shale effectively. The larger the NMR bin porosity with T_2>8 ms, the higher the mobile oil content of shale reservoir, which is consistent with the understanding of oil-bearing large pores in the Gulong Shale. The NMR bin porosity can continuously evaluate the vertical variation of the mobile hydrocarbon content. Compared with the traditional experimental measurement of finite depth points, this method has significant advantages, and can avoid the possibility of missing potentially movable oil layers.

KEYWORDS

Gulong shale, rock pyrolysis analysis, oil saturation index, 2D NMR experiment, T2 cutoff value

1 Introduction

With the advancement of hydrocarbon exploration and the increasing understanding of petroleum geology, unconventional oil and gas have attracted a great attention in the past few years. And shale oil has become another focus after shale gas, tight oil, and tight gas, (Li and Zhu, 2020; Yao et al., 2022). Terrestrial hydrocarbon-bearing sedimentary

basins in China cover an area of 310 × 10^4 km^2, and organic-rich shale formations are widely distributed, providing a rich oil source for conventional petroleum resources. A large amount of oil remains in the shale layer of hydrocarbon source, and the shale oil resources in the basin are much larger than the conventional oil resources outside the source, which is a significant field to achieve sizeable growth of oil and gas reserves and production in the future (Du et al., 2019; Li et al., 2020).

Shale oil reserved in organic-rich, nano-scale pore-size dominated shale formations is mainly in free and adsorbed state in matrix pores and micro-fractures of shale, which needs to be economically extracted by techniques such as horizontal drilling and hydraulic fracturing (Jiang et al., 2014). Due to the unique generation and enrichment mechanisms of shale oil, the source rock quality and engineering quality need to be considered in addition to reservoir quality compared to conventional oil and gas reservoirs. Although both shale gas and shale oil reservoir evaluation include the "three qualities" parameters of organic shale, there are differences in the subjects of attention. In addition, a significant difference is that shale gas exploration focuses on natural gas in the adsorbed and free states, while shale oil exploration focuses on the free oil content in the reservoir. For shale oil, crude oil in the adsorbed state is poorly movable and difficult to be exploited, while free oil is the most realistic resource applying current technology (Yu et al., 2018). Therefore, quantitative characterization of free oil content is crucial for shale oil reservoir evaluation and sweet spot preference. The *OSI* is an important indicator for evaluating movable oil in shale formations, which has been widely used in the oil-bearing properties evaluation of shale. The shale oil exploration practices in North America show that the *OSI* in unconventional oil and gas intervals with production capacity is generally greater than 100 mg HC/g *TOC* (Chen et al., 2019; Sun et al., 2019). The larger the *OSI* value, the higher the mobility of shale oil.

Currently, the *OSI* is mainly calculated with *TOC* and S_1 obtained from rock pyrolysis. The major reason that *OSI* rather than *TOC* is used to evaluate shale reservoir potential is that *OSI* accounts for the movable hydrocarbon content in shale, while *TOC* only evaluates the total organic carbon. *TOC* cannot specifically distinguish whether it is producible or residual (Piedrahita and Aguilera, 2017), so it does not truly reflect the recoverable resource potential of shale oil. The *OSI*, an important parameter for the oil content evaluation of shale oil, can only be obtained through rock pyrolysis experiments at present. Due to the limited and discrete data in experimental analysis, the *OSI* cannot be widely used in the oil content evaluation of actual shale oil reservoirs. NMR logging has been broadly used in the logging evaluation of unconventional oil and gas reservoirs, with the most significant advantage of directly measuring the hydrogen content in rocks. The hydrogen content is mainly related to the organic matter in rocks and fluids (free oil, bound oil, free water, bound water, and constitution water) in the porous space, and different hydrogen-containing components are characterized with varied distribution intervals and response characteristics on the NMR T_1-T_2 spectrum (Li et al., 2020; Liu et al., 2019).

In this regard, we propose a new method to calculate the *OSI* of shale oil. As oil and gas in shale oil reservoirs are easily dispersed, traditional experimental measurement cannot accurately reflect the physical properties and oil content. In order to accurately obtain the shale physical properties and oil content, two-dimensional nuclear magnetic resonance measurement of shale oil samples is conducted in this study under three states: original, drying and saturated kerosene. Based on the changes of 2D NMR spectra under different states, the distribution characteristics of different hydrogen-containing components on 2D NMR T_1-T_2 are defined, especially the free hydrocarbon component through 2D NMR measurements in three states of shale oil. Combining the *TOC*, S_1 and *OSI* values of rock samples obtained from rock pyrolysis experimental analysis, the relationship between the NMR free hydrocarbon porosity and the *OSI* values analyzed by experimental measurements is constructed, and the quantitative calculation of *OSI* values using NMR logging is realized. Compared with the traditional geochemical experimental measurement, this method has distinct advantages in obtaining continuous *OSI* curves along the well section, which can be applied to the whole study area to better evaluate the oil content of shale oil reservoirs and minimize the possibility of missing the "sweet spot".

2 Experimental measurements

The experimental samples all organic-rich shales, were collected from the First Member of Qingshankou Formation in Gulong Sag, Songliao Basin, NE China. In order to carry out the experimental analyses such as rock pyrolysis and 2D NMR respectively, for the specific rock samples, the plunger samples required for the 2D NMR experiments were obtained by wire-cutting. The remaining irregular samples were used for organic carbon content measurement and pyrolysis experimental analyses. The operations are as follows.

2.1 Organic carbon content measurement and rock pyrolysis experiment

The measurement of organic carbon content and the experimental analysis of rock pyrolysis were carried out according to the national standards "GB/T 19145-2003″ and "GB/T 18602-2012″ respectively. The measurement of organic carbon content was carried out by CS230 carbon and sulfur analyzer, and the experimental measurement of rock pyrolysis was carried out by OGE-VI rock pyrolyzer of Beijing Otto Technology Ltd, both of which were conducted under the conditions of room temperature and pressure. The specific experimental operation process is not described here.

The *TOC* of rock samples and the parameters S_1, S_2, S_4 and T_{max} of rock pyrolysis were obtained by the measurement of organic carbon content and the experimental analysis of rock pyrolysis, respectively, as shown in Table 1.

The results show that the shale in the Qing 1 Member is characterized by high *TOC*, ranging from 1.91% to 7.87% (average value 3.62%). S_1 ranges from 4.13 mg/g to 15.15 mg/g; except for sample 6, which contains more than 10 mg/g (average value 7.85 mg/g), indicating a high content of free hydrocarbons. T_{max} is between 413°C and 453°C, which is in the main oil generation stage (Bai et al., 2021). The *OSI* values range from 99.1 mg/g to 401.57 mg/g. If regarding the *OSI* of shale greater than 100 mg/g as the basis for evaluating the recoverable resource potential of

TABLE 1 Measured results of organic carbon content and pyrolysis experimental parameters of shale samples.

Sample no.	Maximum peak temperature T_{max}/°C	Free hydrocarbo S_1/(mg/g)	Pyrolysis hydrocarbo S_2/(mg/g)	Residual carbon S_4/(mg/g)	Total organic carbon *TOC*/%	Hydrogen index *HPI*/(mg/g)	Hydrocarbo index *HCI*/(mg/g)	Oil saturation index *OSI*/(mg/g)
1	420	5.81	8.23	9.52	2.12	388.70	274.40	274.06
2	413	7.67	7.75	6.31	1.91	405.58	401.39	401.57
3	440	7.96	11.71	5.96	2.23	525.44	357.17	356.95
4	445	4.13	8.98	9.87	2.08	432.74	199.02	198.56
5	453	6.61	70.90	2.41	6.67	1062.28	99.04	99.10
6	445	15.15	77.79	1.56	7.87	988.43	192.50	192.50
7	447	7.25	34.22	5.63	4.01	854.43	181.02	180.80
8	446	8.20	8.62	6.77	2.07	415.81	395.55	396.14

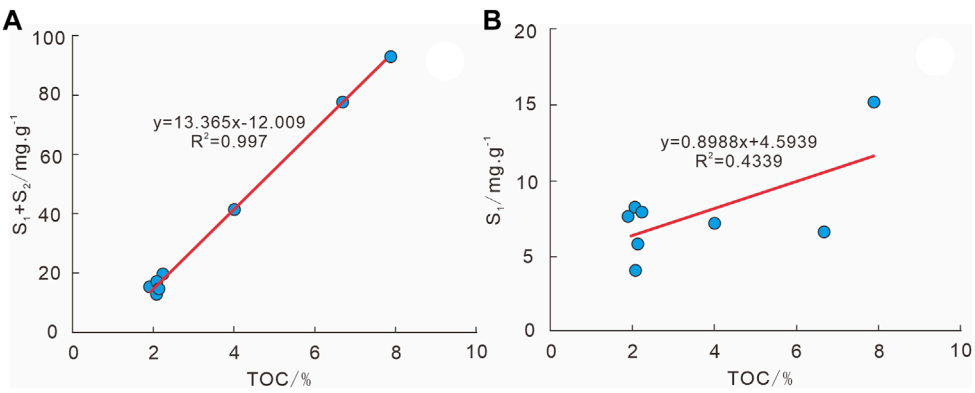

FIGURE 1
(A) and **(B)** showing the correlation of *TOC* with S_1+S_2 and S_1, respectively.

shale oil, the shale in the Qing 1 Member suggests its recoverable resource potential (Wang et al., 2020). *TOC* and S_1+S_2 have an excellent correlation with a linear correlation coefficient of 0.997. However, the correlation of *TOC* and S_1 is poor, with a correlation coefficient of 0.4339 (Figure 1), reflecting that the free hydrocarbon content of the shale in the Qing 1 Member does not have a monotonic positive correlation with the organic carbon content; i.e., the higher the organic carbon content, the not definitely high the free hydrocarbon content. There is a large amount of residual hydrocarbons (asphaltenes) in the shale, which is manifested more clearly in the T_1-T_2 spectra of 2D NMR experiments, therefore it cannot be simply assumed that high organic carbon content indicates high oil content of the shale.

2.2 Two-dimensional NMR experiments

The 2D NMR experiments of rock samples were conducted following the national standard "SY/T6490-2007." The experimental equipment is a GeoSpec2 high precision multi-dimensional NMR core analyzer from Oxford, U.K., with an operating frequency of 2 MHZ. The acquisition parameters of 2D NMR are: number of scans 128, gain value 40, waiting time 1 s, number of echoes 5000 and echo time 0.1 ms.

In order to clarify the distribution characteristics of different hydrogen-containing components on the T_1-T_2 NMR spectra, the experiment was carried out for rock samples in three states: original sample, dried state at 105°C and saturated kerosene, respectively, to perform 2D NMR measurements. The specific operations were as follows.

State 1. For the original sample, without oil washing and salt washing measurements, a high precision NMR imaging analyzer was used for 2D NMR T_1-T_2 mode signal acquisition in the original state. In this step, the fluid components in the rock sample mainly included bound fluids in organic and inorganic pores and some information of movable oil that may be found.

State 2. The original sample was dried by setting the drying temperature at 105°C for 24 h; when dried at 105°C, no capillary

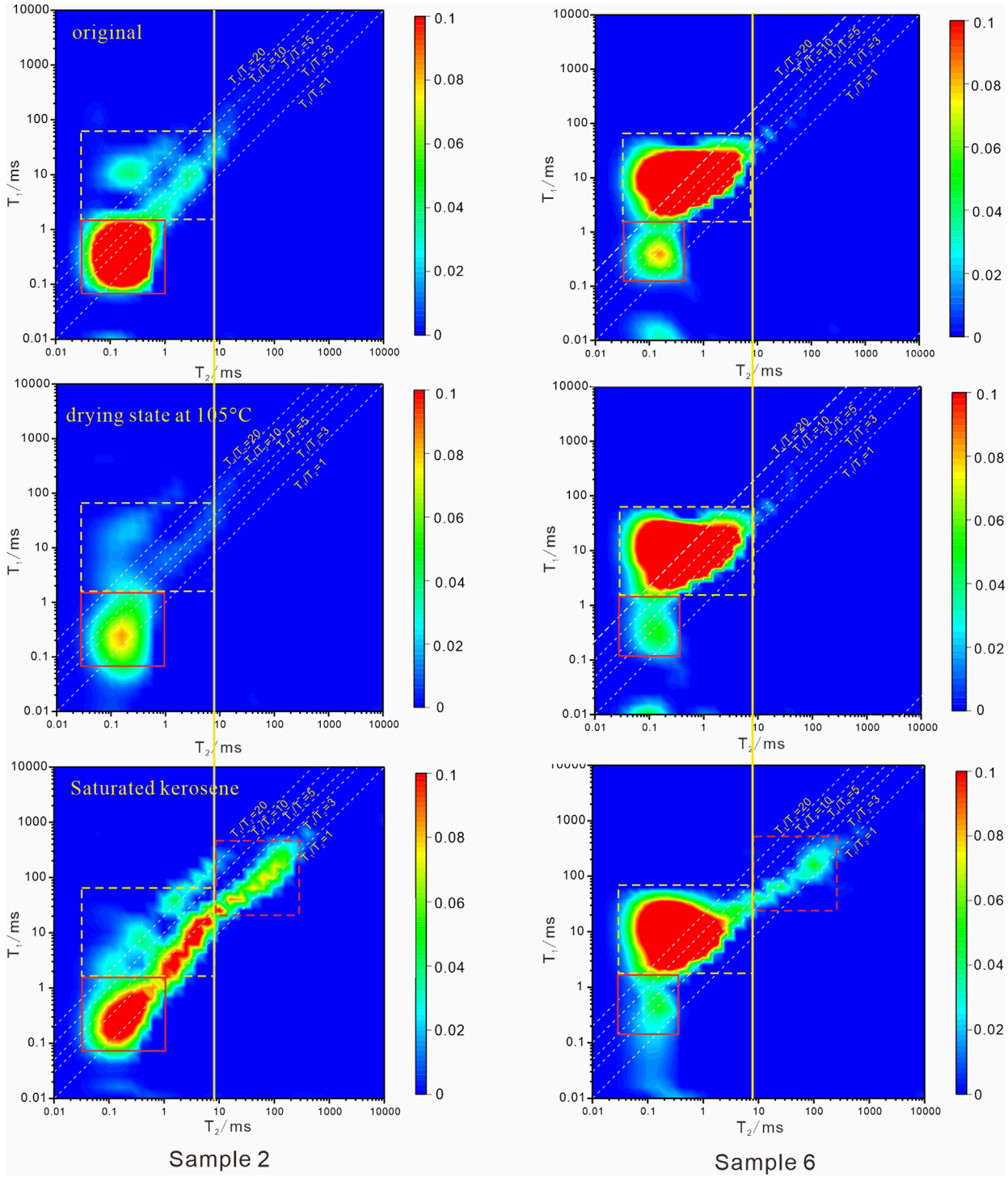

FIGURE 2
Characteristics of 2D NMR T_1-T_2 spectrum in different states.

bound water could be existed in the sample except for clay-bound water (Dong, 2017). In the meantime, 2D NMR T_1-T_2 measurements could be performed to obtain the T_2 cutoff value of clay-bound water.

State 3. The dried samples were vacuumed and saturated with pressure, in which the vacuuming time was 24 h and the pressure was 50 MPa, and saturated with kerosene to revert the fluid distribution characteristics in the state of formation. Later the

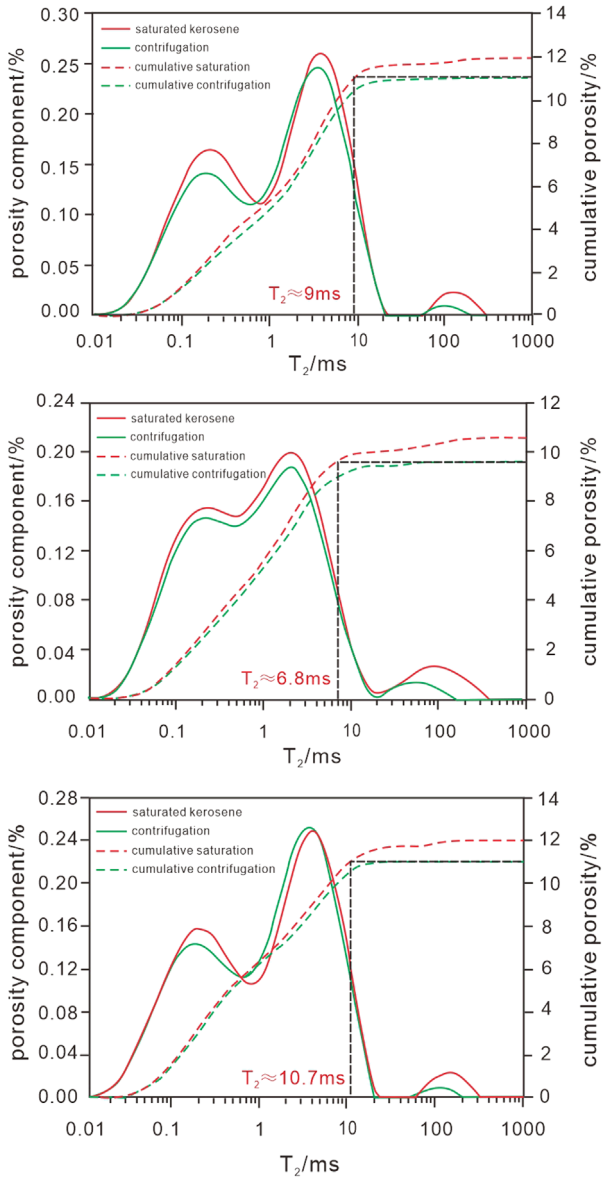

FIGURE 3
NMR measurements of rock samples before and after centrifugation.

same equipment and parameters were used for acquiring 2D NMR T_1-T_2 signals, and the T_2 cutoff value of the movable fluid could be obtained.

Figure 2 shows the results of 2D NMR measurements in different states of two shale samples. For the original sample state, the measured NMR signals include bound water, bound oil, asphaltene and a small amount of movable oil information. In the drying state at 105°C, bound oil and capillary bound water are dispersed, and obvious changes are visible on the T_1-T_2 spectrum, such as T_1<1 ms, T_2<1 ms and T_2>1 ms regions, and there is a significant weakening of the NMR signals compared with the original sample state. As for the saturated kerosene state, the fluid distribution state can be identified using the T_1/T_2 ratio. When the T_1/T_2 ratio is greater than 3, the fluid is mainly distributed in organic pores. When the T_1/T_2 ratio is in the range of 1-3, the saturated kerosene mainly exists in the intergranular pores of inorganic minerals (Ding et al., 2020; Shi et al., 2021). Compared with the drying state at 105°C, the signals of both yellow and red dashed box parts of sample 2 are significantly enhanced, indicating that the saturated kerogen not only enters the macropore space, but also partly enters the bound oil zone. In terms of the T_1/T_2 ratio, it mainly falls in the range of 1-3, showing that it mainly penetrates the inorganic pore space. As for sample 6, the signal of the part in the red dashed box is obviously enhanced, reflecting that the kerosene mainly penetrates the inorganic macro-pore space.

3 Experimental analyses

3.1 NMR experimental analysis

According to the three states above, 2D NMR experimental measurements were carried out on each of the 8 organic-rich shale rock samples in the Qing 1 Member. Previous studies have concluded that the Gulong shale has many light components with high volatility characteristics (Yan et al., 2021), so the original shale rock samples from the field have dissipated some of the light hydrocarbon components. If the analysis was carried out based on the original sample, it could be difficult to truly reflect the actual state of the shale reservoir. For this reason, we dried the rock samples at 105°C for 24 h after measuring the 2D NMR experiments in the original state, to make the movable oil and gas and capillary-bound fluid in the rock samples completely volatilized. Then we vacuumed and saturated them with kerosene to convert them back to the original subsurface fluid distribution state. By comparing the differences in 2D NMR spectrum between the dried and saturated kerosene states, the T_2 cutoff values of the movable fluid portion can be clarified. The 2D NMR T_1-T_2 fluid identification plate given by Kausik et al. (2016) concludes that for the 2 MHZ instrument, the kerogen signal is undetectable, the clay-bound water relaxation rate is faster and the T_2 value is smaller, T_1-T_2 values are between 1 and 2. The asphaltene relaxation rate is faster and the T_2 value is smaller, T_1/T_2 values are between 4 and 15. The oil in organic pores relaxes faster, with T_1/T_2 values between 2 and 6. Smaller oil relaxation rates occur in inorganic pores, usually with larger T_2 values and T_1/T_2 values between 1 and 2 (Kausik et al., 2016). Based on this understanding, the T_2 cutoff value of movable fluid porosity in Gulong Shale is clarified for the first time in combination with the 2D NMR experiments.

In Figure 2, the red solid box mainly shows the signal of clay-bound water, and the yellow dashed box mainly shows the signal of oil in asphaltene, organic pores and inorganic pores. Comparing the two-dimensional NMR spectrums in dried and original sample states, it suggests that the oil and gas signals in the clay-bound water in the red solid box and the T_2>1 ms region in the yellow dashed box of sample 2 are significantly weakened. In contrast, the asphaltene portion in the T_2<1 ms and T_2>5 regions in the yellow dashed box of sample 6 remains unchanged. Based on the difference of T_1/T_2 NMR spectrum in the two states and the one-dimensional T_2 distribution spectrum projected in the corresponding T_2 direction, the T_2 cutoff value of clay-bound water can be determined. Through the comparative analysis of 8 rock samples, the T_2 cutoff value of

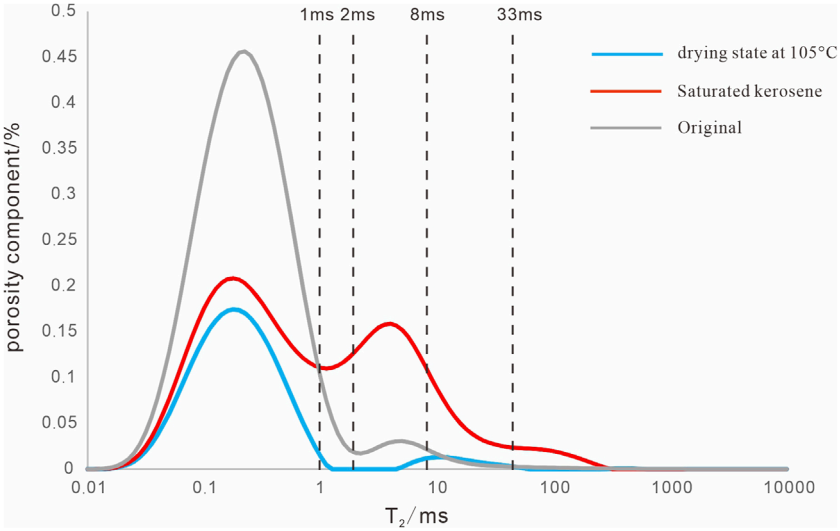

FIGURE 4
NMR T_2 distribution spectrums in different states (sample 3).

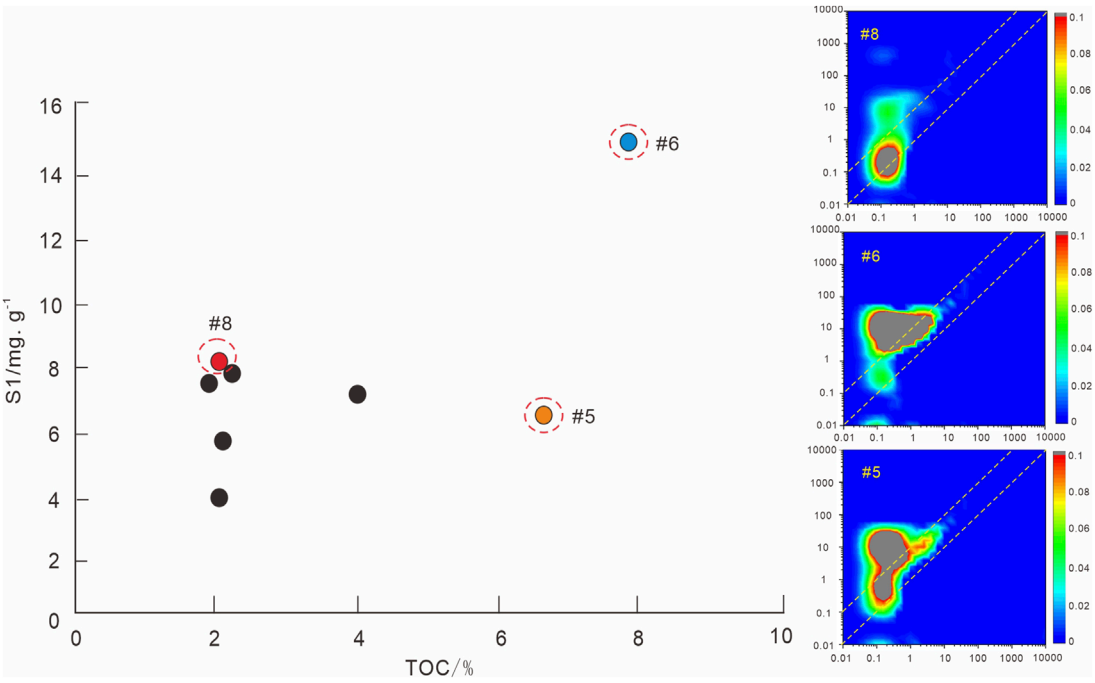

FIGURE 5
Relationship between the S_1 and *TOC*.

clay-bound water in the Qing 1 Member of Gulong shale is finally determined to be 1 ms.

Comparing the 2D NMR spectrum of the dried and saturated kerosene states, we find that the signal of the macro-pore part is almost absent in the dried state at 105°C. In contrast, after saturated kerosene, the signals of bound oil and macro-pore region are obviously enhanced, especially in the zone of T_2>8 ms (red dashed box), indicating that kerosene mainly enters the macro-pores. The T_1/T_2 values in this zone are in the range of 1–3, which is the signal of movable oil in inorganic pores, and both rock samples show the same characteristics. Based on the comparative analysis of the 8 rock samples, it can be determined that the T_2 cutoff value of movable fluid porosity in the Qing 1 Member of Gulong Shale is about 8 ms.

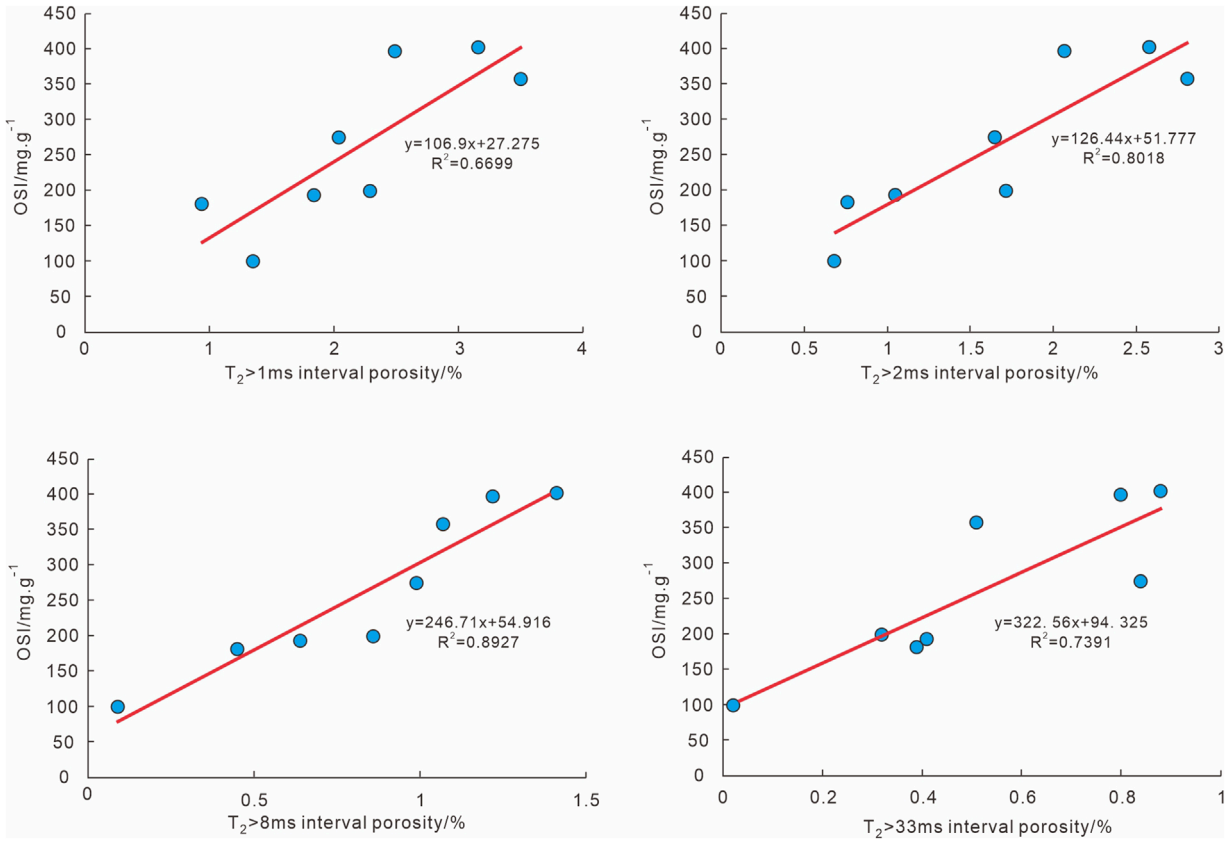

FIGURE 6
Relationship between *OSI* and different bin porosities.

Centrifugal - NMR measurements can effectively characterize the movable oil content of shale (Zhang, 2019). In order to further determine the T_2 cutoff value of movable fluid porosity, NMR measurements were carried out for Gulong shale samples before and after centrifugation. The amplitude of T_2 spectrum signal decreases after centrifugation of saturated kerosene shale (the centrifugal force is about 2.76 Mpa). The cumulative signal amplitude difference before and after centrifugation reflects the movable oil quantity of shale oil. The T_2 value corresponding to the intersection of the horizontal extension line of the stable section of the cumulative curve after centrifugation and the cumulative curve before centrifugation is the T_2 cutoff value of the moving fluid. By analyzing the shale samples measurement results, it is found that the T_2 cutoff values range from 6.8 ms to 10.7 ms (Figure 3), most of which are distributed around 8 ms.

The 2D NMR T_1-T_2 spectrum and the corresponding 1D T_2 distribution spectrum at different states (Figure 4) are used to further analyze the physical characteristics of the shale reservoir in the Qing 1 Member in combination with the identified T_2 cutoff values. For the saturated kerosene state, the measured porosity of the shale ranges from 6.6% to 9.4%, with an average of 7.5%. The porosity of movable fluid is lower, and the movable fluid porosity of 8 rock samples ranges from 0.3% to 1.6%, with an average of only 1%. This indicates that the Gulong shale reservoir is dominated by small pores with high bound fluid content.

3.2 Comprehensive analysis of NMR and pyrolysis experiments

In order to understand the oil-bearing characteristics of the Gulong shale, we analyzed the rock pyrolysis experimental data of the 8 rock samples. In the cross plots of Figure 5, the correlation between free hydrocarbon S_1 and organic carbon content *TOC* is poor. For example, the *TOC* of sample 5 is as high as 6.67%, but the S_1 is only 6.61 mg/g. For sample 8, although the *TOC* is only 2.07%, the S_1 is 8.2 mg/g, which is higher than that of sample 5. Comparing the 2D NMR T_1-T_2 spectrum of the two drying states, although the *TOC* of sample 5 is high, it is mainly caused by the high asphaltene content and has a strong signal in the region of T_2<1 ms and T_1/T_2>5 in the 2D NMR T_1-T_2 spectrum. In contrast, the signal in the corresponding region of sample 8 is weaker, which indicates almost no occurrence of asphaltene. Although asphaltenes can increase the organic carbon content, they do not contribute to the free hydrocarbon content, so the "high *TOC*, low S_1" pattern of sample 5 is observed. This also suggests that for the organic-rich shale in the Qing 1 Member, high organic content is not necessarily associated with high free hydrocarbon content, since the influence of solid organic matter such as kerogen and asphaltene on organic carbon cannot be ignored.

The *OSI* truly reflects the resource potential of free hydrocarbons in shale oil: $OSI=100\times S_1/TOC$ (mg/g), where S_1 is the free

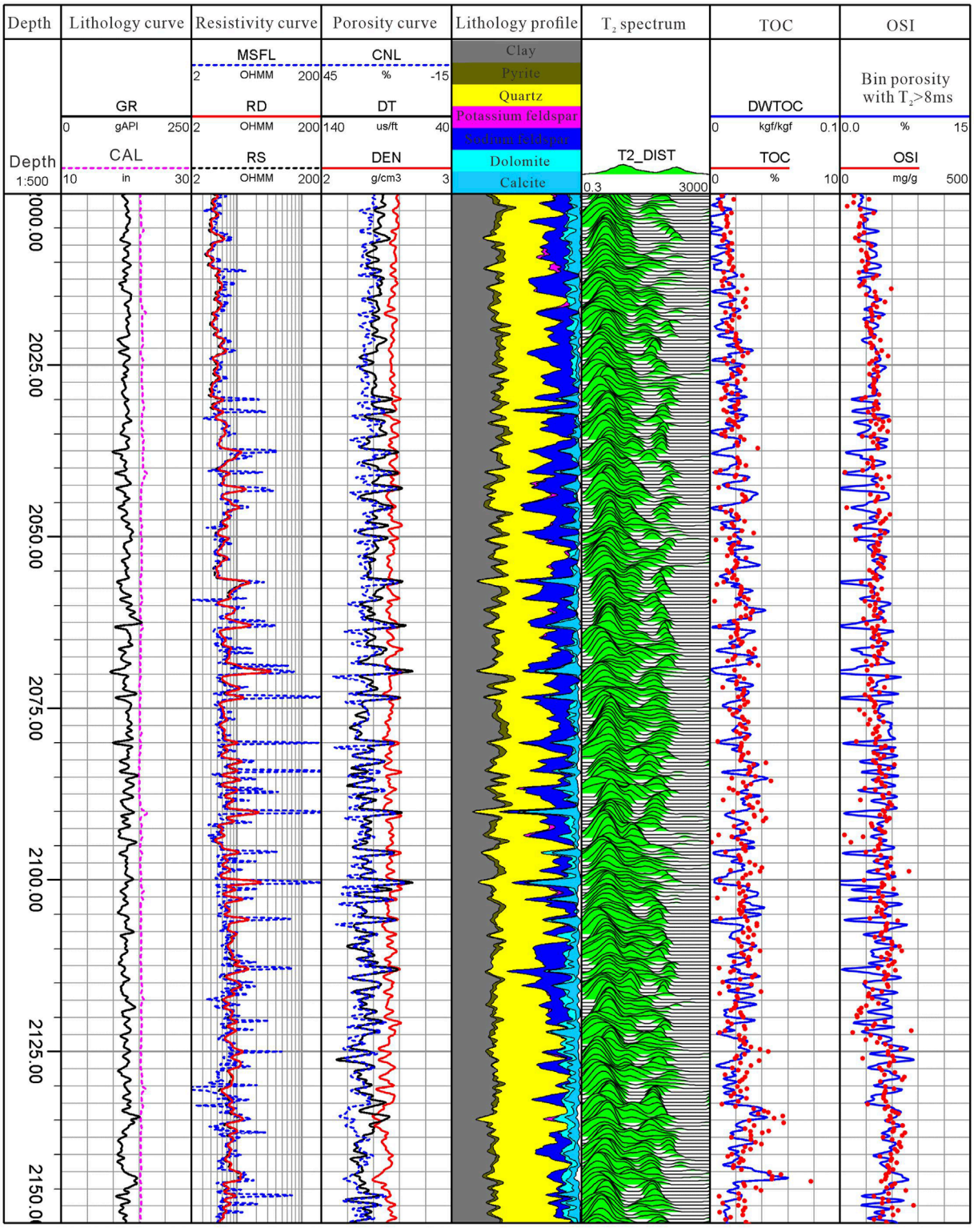

FIGURE 7
Relationship between the *OSI* and bin porosity with T_2>8 ms of well X1.

hydrocarbon content of pyrolysis and *TOC* is the total organic carbon content of rock samples (Cui et al., 2020). The higher the *OSI*, the better the mobility of the shale oil and the more the mobile hydrocarbon content. For example, the *OSI* value of sample 5 is 99.1 mg/g, while the *OSI* value of sample 8 is 396.14 mg/g; although the organic carbon content of sample 5 is higher, the *OSI* of sample 8 is significantly higher than that of sample 5, indicating that the shale oil in sample 8 is more movable.

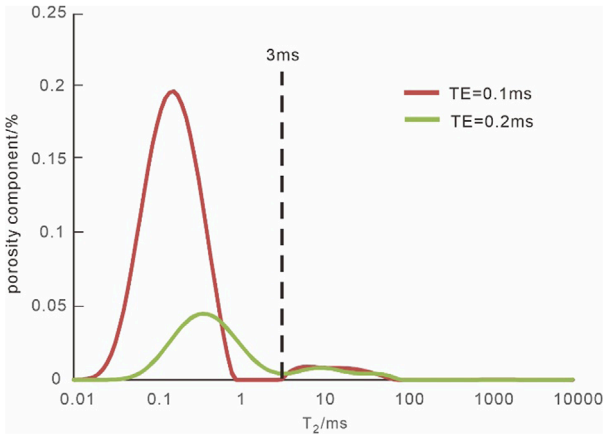

FIGURE 8
The T_2 spectrum characteristics measured at different TE in the drying state.

Zeng et al. (2019) found that the pore structure of the shales of the Qingshankou Formation in the Songliao Basin significantly influenced the shale oil enrichment, and there is a positive correlation between the *OSI* and the porosity obtained by mercury injection, with shale oil mainly reserved in the larger pores. Based on the principle of NMR logging, it is known that the NMR T_2 spectrum can quantitatively characterize the development of pores with different sizes. The NMR T_2 spectrum morphological characteristics visually reflect the structural characteristics of pores. The lateral relaxation time T_2 is closely related to the pore size. The smaller the pore, the shorter the relaxation time T_2. The larger the pore, the longer the relaxation time T_2 (Tian et al., 2020). Since the NMR T_2 spectrum reveals the integrated response of hydrogen-containing components in different pore spaces (micro-pores, small pores, medium pores, and large pores). The closer to the left end of the T_2 spectrum, the smaller the pore space is reflected. The closer to the right end of the T_2 spectrum, the larger the shale pore space is reflected. If a suitable T_2 cutoff value can be found, the porosity interval most relevant to the *OSI* of shale can be established, and the quantitative evaluation of *OSI* can be accomplished.

Based on the investigations above, the NMR T_2 spectrum characteristics of the 8 shale samples were comprehensively analyzed. Considering the morphological characteristics of T_2 spectrum in different states and the T_2 cutoff values obtained from 2D NMR experiments, the relationship between the *OSI* and the corresponding bin porosity was analyzed for T_2 cutoff values of 1 ms, 2 ms, 8 ms and 33 ms (Figure 4), respectively. Figure 6 shows the correlation coefficients with the *OSI*, and the different bin porosities are 0.67, 0.8, 0.89, and 0.74, respectively. Since the T_2 cutoff value of clay-bound water is 1 ms, the bin porosity with T_2>1 ms contains not only the fluid signal in the macro-pore portion, but also the contribution of capillary-bound water and bound oil. Therefore, although the bin porosity with T_2>1 ms correlates with the *OSI*, the correlation is not high. The correlation between *OSI* and bin porosity becomes significantly better as the T_2 cutoff value is chosen as 2 ms. When the T_2 cutoff value is 8 ms, the correlation between them is the best. When the T_2 cutoff value is increased further, the correlation becomes gradually worse again, indicating that T_2=8 ms is just the NMR T_2 cutoff value of porosity of movable fluid in the Gulong shale. This suggests that the *OSI* value of the Gulong shale is closely related to the porosity of the movable fluid, i.e., the larger the porosity of the movable fluid, the larger the *OSI* value, and the higher the oil content of the shale. Therefore, the porosity of movable fluid can be used to calculate the *OSI* value of shale, which is calculated as Eq. 1.

$$OSI = a \times \phi_{T_2>8\text{ms}} + \text{b} \quad (1)$$

where *OSI* is oil saturation index, mg/g; $\phi_{T_2>8\text{ms}}$ is the NMR bin porosity with T_2>8 ms, %;*a and b* are coefficients.

The conclusive understanding acquired from the above experimental analysis was also verified by actual drilling and logging. In Figure 7, the logging results of well X1, the sixth panel shows the 1D NMR T_2 distribution spectrum. The curve in the seventh panel shows the organic carbon content calculated from the elemental logging, and the red point shows the organic carbon content from the actual rock chip analysis. The curve in the eighth panel shows the bin porosity of T_2>8 ms. the red point shows the OSI value obtained from the actual pyrolysis experiment analysis. The variation trend of the bin porosity with T_2> 8 ms is in a good agreement with the actual *OSI* value. The bin porosity is also in a good agreement with the trend of the measured *OSI* value. The NMR calculation of movable fluid porosity in some well sections have obvious oscillation. From the corresponding conventional curves and mineral profiles obtained from elemental logging, it is known that these well sections are dominated by thin shelly limestone, although the shelly limestone reservoir is not well-developed (Gao et al., 2022). Despite that the actual sampling analysis did not cover the whole well section, from the experimental data of rock chip pyrolysis from 2040–2050 m, the *OSI* values of the shelly limestone developed section are lower and the movable fluid porosities are smaller, both of which have the same trend. The comparative analysis of the drilled wells further confirms the good correlation between the bin porosity with T_2>8 ms and the pyrolysis *OSI* value. In this well, the *OSI* value and movable fluid porosity of the Qing 1 Member show an overall decreasing trend from bottom to top, indicating that the oil content of the lower formation is generally better than that of the upper.

4 Discussion

4.1 Challenges of quantitative evaluation

Through the aforementioned comparison of the differences in the 2D NMR experimental T_1-T_2 spectrum in varied states, it is clear that the *OSI* value of the Gulong shale is closely related to the size of the pores containing movable fluid (bin porosity with T_2>8 ms). The *OSI* calculated by NMR logging can reflect the change of oil content in wellbore, but there are still differences between the calculated results and the actual core analysis. Below are the two specific reasons.

(1) Because of the light hydrocarbon components and high volatility of Gulong shale, there are differences between the core samples under laboratory conditions and the original state

subsurface. Although the original samples were re-saturated with kerosene after drying at 105°C for 24 h, they still could not be fully returned to the real state of the subsurface. And it is still unclear whether the drying and re-saturation of kerosene can damage the original pore structure. From the comparison of the T_1-T_2 spectrum of the 2D NMR experiments of the two states of drying and saturated kerosene in Figure 2, it is found that the kerosene has not only penetrated the large pore space during the pressurized saturation, but also has partially entered the small pore space of the bound fluid. Comparing the 2D NMR T_1-T_2 spectrum of sample 2 in saturated kerosene and drying state, the signals in the yellow dashed box and the red dashed box are obviously enhanced. Also, the questions of whether the pore space is completely saturated, the degree of filling of the original bound fluid region by kerosene, and the reasons for the sudden signal enhancement of the capillary bound water part in the saturated kerosene state need to be investigated in depth. Therefore, the porosity of the interval obtained by using the T_2 cutoff value from the experimental analysis to classify the NMR T_2 distribution spectrum in the saturated kerosene state is still different from the actual situation.

(2) The T_2 cutoff values of clay-bound water and movable fluid porosity in Gulong shale can be determined by 2D NMR experiments under different states. Although there are differences between the experimental environment and the downhole conditions, and between the experimental and the downhole NMR logging instrument, the T_2 cutoff value of movable fluid porosity is still credible. The measurement frequency used in this NMR experiment is the same as that of CMR, which is 2 MHZ. There is a difference in TE (echo time) between the two, and the TE of the experimental and downhole NMR instrument is 0.1 ms and 0.2 ms, respectively. It is found that TE has a significant effect on the signal of the small pores, especially in the T_2<3 ms region. The T_2 cutoff value of movable fluid porosity determined under experimental conditions is applicable and has been proved in actual drilling, but the T_2 cutoff value of effective porosity still need to consider the effect of TE.

4.2 Reliability of the new method

The good linear relationship between movable fluid porosity and *OSI* also reflects the oil-bearing characteristics of the large pores of the Gulong shale. Previous studies (Zeng, 2020) concluded that different sizes of pores in the Qingshankou Formation shale have different effects on shale oil enrichment through experimental studies, in which adsorbed oil is mainly in pores less than 10 nm, while free oil is mainly in pores larger than 10 nm. Similar characteristics also exist in shale oil reservoirs of other sedimentary basins in China. For example, in the Qianjiang Formation shale reservoir of Paleogene in Qianjiang Sag, Jianghan Basin, free shale oil mainly occurs in pores with pore size larger than 5 nm (Sun et al., 2020). For shale oil reservoirs, organic-rich shale is regarded as both source rock and a reservoir layer. Shale oil is mainly formed in the liquid hydrocarbon stage of organic matter evolution and generally undergoes a strong hydrocarbon generation process with extremely complex wettability, but it has become a consensus that large pore spaces contain oil (Zou et al., 2013; Kuang et al., 2021). This further indicates that shale oil reservoirs are oil-bearing in large pore spaces and dominated by free oil, which provides a basis for evaluating the *OSI* in shale using the movable-flow porosity (Figure 8).

5 Conclusion

(1) Organic carbon measurement and rock pyrolysis experiments reveal that the source rock of the organic-rich shale in the Qing 1 Member is of good quality, with high *TOC* and S_1 contents. But the correlation between them is poor, and the manifestation of "high *TOC* and low S_1" exists, which cannot be simply assumed that high organic matter is necessarily associated with high movable oil content. Instead, the *OSI* can truly reflect the movable hydrocarbon content of the shale, in which the *OSI* value of the Qing 1 Member shale is greater than 100 mg/g, and the oil content of the lower formation is better than that of the upper, showing the potential to produce a large amount of movable hydrocarbon.

(2) The NMR T_2 cutoff value of movable fluid porosity in Gulong shale is determined to be 8 ms for the first time through 2D NMR experimental measurements in different states. Combined with experiments such as rock pyrolysis and organic carbon measurements, there is a good linear relationship between porosity and *OSI* in the NMR bin porosity with T_2>8 ms, which makes it possible to evaluate *OSI* continuously and quantitatively by means of well logging. For the key wells, the geochemical analysis data and NMR logging data can be applied together to establish a suitable *OSI* calculation model.

(3) The OSI calculation based on logging can effectively compensate for the disadvantage that geochemical experiments cannot cover the whole well section or the whole study area. The calculation method based on the calibrated core analysis data can be extended and applied to other wells without geochemical data, thus achieving the possibility of avoiding missing the movable hydrocarbon layers in shale.

Data availability statement

The original contributions presented in the study are included in the article/Supplementary material, further inquiries can be directed to the corresponding author.

Author contributions

HT: Conceptualization, Investigation, Methodology, Writing–original draft, Writing–review and editing. HW: Methodology, Supervision, Writing–review and editing. WY: Methodology, Writing–review and editing. ZF: Methodology, Writing–review and editing. CL: Methodology, Writing–review and editing. LR: Methodology, Writing–review and editing. HX: Methodology, Writing–review and editing.

Funding

The author(s) declare that financial support was received for the research, authorship, and/or publication of this article. The study is funded by Petrochina major science and technology project "Large-scale Reserves Increasing and Exploration and Development Techniques for Continental Shale Oil" (2023ZZ15) and National Key Laboratory for Multi-resources Collaborative Green Production of Continental Shale Oil.

Conflict of interest

Author WY was employed by the Daqing Oilfield Company Limited. Author LR was employed by the PetroChina Well Logging Company Limited.

The remaining authors declare that the research was conducted in the absence of any commercial or financial relationships that could be construed as a potential conflict of interest.

Publisher's note

References

Bai, L. H., Liu, B., Chi, Y. A., Li, S. C., and Wen, X. (2021). 2D NMR studies of fluids in organic-rich shale from the Qingshankou Formation, Songliao Basin. *Oil Gas Geol.* 42 (6), 1389–1400.

Chen, Z. H., Li, M. W., Jiang, C. Q., and Qian, M. H. (2019). Shale oil resource potential and its mobility assessment: a case study of Upper Devonian Duvernay shale in Western Canada Sedimentary Basin. *Oil Gas Geol.* 40 (3), 459–468.

Cui, B. W., Chen, C. R., Lin, X. D., Zhao, Y., Cheng, X. Y., Zhang, Y. P., et al. (2020). Characteristics and distribution of sweet spots in Gulong shale oil reservoirs of Songliao Basin. *Petroleum Geol. Oilfield Dev. Daqing* 39 (3), 45–55. doi:10.19597/J.ISSN.1000-3754.202005025

Ding, Y. J., Li, J. G., Zhu, W. F., Liu, A. P., Lv, F. F., and Zhong, W. (2020). T_1-T_2 two-dimensional NMR method for detecting oil-bearing property in shale oil reservoirs. *Mud Logging Eng.* 31 (S1), 48–53. doi:10.3969/j.issn.1672-9803.2020.S1.009

Dong, X. (2017). *Experimental study of porosity and electrical properties of gas shale.* East China: China University of Petroleum.

Du, J. H., Hu, S. Y., Pang, Z. L., Lin, S. H., Hou, L. H., and Zhu, R. K. (2019). The types, potentials and prospects of continental shale oil in China. *China Pet. Explor.* 24 (5), 560–568. doi:10.3969/j.issn.1672-7703.2019.05.003

Gao, B., He, W. Y., Feng, Z. H., Shao, H. M., Zhang, A. D., Pan, H. F., et al. (2022). Lithology, physical property, oil-bearing property and their controlling factors of Gulong shale in Songliao Basin. *Petroleum Geol. Oilfield Dev. Daqing* 41 (3), 68–79. doi:10.19597/j.issn.1000-3754.202111075

Jiang, Z. X., Zhang, W. Z., Liang, C., Wang, Y. S., Liu, H. M., and Chen, X. (2014). Characteristics and evaluation elements of shale oil reservoir. *Acta Pet. Sin.* 35 (1), 184–196. doi:10.7623/syxb20141024

Kausik, R., Fellah, K., Rylander, E., Singer, P. M., Lewis, R. E., and Sinclair, S. M. (2016). NMR relaxometry in shale and implications for logging. *Petrophysics* 57 (4), 339–350.

Kuang, L. C., Hou, L. H., Yang, Z., and Wu, S. T. (2021). Key parameters and methods of lacustrine shale oil reservoir characterization. *Acta Pet. Sin.* 42 (1), 1–14. doi:10.7623/syxb202101001

Li, G. X., and Zhu, R. K. (2020). Progress, challenges and key issues of unconventional oil and gas development of CNPC. *China Pet. Explor.* 25 (2), 1–13. doi:10.3969/j.issn.1672-7703.2020.02.001

Li, J. B., Jiang, C. Q., Wang, M., Lu, S. F., Chen, Z. H., Chen, G. H., et al. (2020b). Adsorbed and free hydrocarbons in unconventional shale reservoir: a new insight from NMR T_1.T_2 maps. *Mar. Petroleum Geol.* 116, 104311. doi:10.1016/j.marpetgeo.2020.104311

Li, N., Yan, W. L., Wu, H. L., Zheng, J. D., Feng, Z., Zhang, Z. Q., et al. (2020a). Hydrophobic interactions of relaxin family peptide receptor 3 with ligands identified using a NanoBiT-based binding assay. *Petroleum Geol. Oilfield Dev. Daqing* 39 (3), 117–126. doi:10.1016/j.biochi.2020.08.008

Liu, Z. S., Liu, D., Karacan, M., Cai, Y. D., Yao, Y. B., Pan, Z. J., et al. (2019). Application of nuclear magnetic resonance (NMR) in coalbed methane and shale reservoirs: a review. *Int. J. Coal Geol.* 218, 103261. doi:10.1016/j.coal.2019.103261

Piedrahita, J., and Aguilera, R. (2017). "Estimating oil saturation index OSI from NMR logging and comparison with rock-eval pyrolysis measurements in a shale oil reservoir," in SPE Unconventional Resources Conference, Alberta, Canada, February 15–16, 2017 (SPE).

Shi, Q. M., Mi, Y. C., Wang, S. M., Sun, Q., Wang, S. Q., and Kou, B. Y. (2021). Trap characteristic and mechanism of volatiles during pyrolysis of tar-rich coal [J/OL]. *J. China Coal Soc.* doi:10.13225/j.cnki.jccs.XR21.1734

Sun, H. Q., Cai, X. Y., Zhou, D. H., Gao, B., and Zhao, P. R. (2019). Practice and prospect of Sinopec shale oil exploration. *China Pet. Explor.* 24 (5), 569–575. doi:10.3969/j.issn.1672-7703.2019.05.004

Sun, Z. L., Wang, F. R., Han, Y. J., Hou, Y. G., He, S., Luo, J., et al. (2020). Multi-scale characterization of the spatial distribution of movable hydrocarbon in intersalt shale of Qianjiang Formation, Qianjiang Sag, Jianghan Basin. *Petroleum Geol. Exp.* 42 (4), 586–595. doi:10.11781/sysydz202004586

Tian, H., Wang, G. W., Wang, K. W., Feng, Q. F., Wu, H. L., and Feng, Z. (2020). Study on the effect of pore resistivity of carbonate reservoirs. *Chin. J. Geophys.* 63 (11), 4232–4243. doi:10.6038/cjg2020O0110

Wang, G. Y., Wang, F. L., Meng, Q. A., and Gu, S. F. (2020). Strategic significance and research direction for Gulong shale oil. *Petroleum Geol. Oilfield Dev. Daqing* 39 (3). doi:10.19597/j.issn.1000-3754.202005036

Yan, W. L., Zhang, Z. Q., Chen, L. C., Zhao, Z. W., and Wang, W. J. (2021). New evaluating method of oil saturation in Gulong shale based on NMR technique. *Petroleum Geol. Oilfield Dev. Daqing* 40 (5), 78–86. doi:10.19597/j.issn.1000-3754.202107007

Yao, D. H., Zhou, L. H., Wang, W. G., Pu, X. G., Song, Y. J., and Xu, C. W. (2022). Logging evaluation of composite sweet spots for shale oil: a case study of Member 2 of Kongdian Formation in Cangdong sag. *Acta Pet. Sin.* 43 (7), 912–924. doi:10.7623/syxb202207003

Yu, T., Lu, S. F., Li, J. Q., and Zhang, P. F. (2018). Prediction for favorable area of shale oil free resources in Dongying Sag. *Fault-block Oil Gas Field* 25 (1), 16–21. doi:10.6056/dkyqt201801004

Zeng, W. Z. (2020). Pore structure and shale oil potential of Qingshankou Formation shale in Songliao Basin. *ACS Omega* 40, 35755–35773.

Zeng, W. Z., Zhou, G. Y., and Song, Z. G. (2019). Influence of pore structure on the shale oil accumulation of the Qingshankou Formation in the Songliao Basin. *Geochimica* 48 (6), 632–643. doi:10.19700/j.0379-1726.2019.06.011

Zhang, P. F. (2019). *Research on shale oil reservoir, occurrence and movability using nuclear magnetic resonance (NMR).* Qingdao: China University of Petroleum.

Zou, C. N., Yang, Z., Cui, J. W., Zhu, R. K., Hou, L. H., Tao, S. Z., et al. (2013). Formation mechanism, geological characteristics and development strategy of nonmarine shale oil in China. *Petroleum Explor. Dev.* 40 (1), 15–27. doi:10.1016/s1876-3804(13)60002-6

frontiers | Frontiers in Earth Science

TYPE Original Research
PUBLISHED 21 June 2024
DOI 10.3389/feart.2024.1253315

OPEN ACCESS

EDITED BY
Junfang Zhang,
Commonwealth Scientific and Industrial Research Organisation (CSIRO), Australia

REVIEWED BY
Lin Zhang,
Hohai University, China
Yuantian Sun,
China University of Mining and Technology, China

*CORRESPONDENCE
Jiang Bici,
jiangbici@163.com

RECEIVED 05 July 2023
ACCEPTED 20 May 2024
PUBLISHED 21 June 2024

CITATION
Bici J (2024), Using borehole radar detecting hydraulic fracturing crack in near horizontal holes in coal mine.
Front. Earth Sci. 12:1253315.
doi: 10.3389/feart.2024.1253315

Using borehole radar detecting hydraulic fracturing crack in near horizontal holes in coal mine

Jiang Bici*[1,2]

[1]China Coal Research Institute, Beijing, China, [2]China Coal Research Institute Xi'an Science and Industry Group, Xi'an, China

Currently, hydraulic fracturing technology is widely implemented for controlling the surrounding rock and enhancing permeability in low-permeability coal seams. Evaluating the effectiveness of hydraulic fracturing is a critical component of hydraulic fracturing operations. This study addresses the challenges in assessing the location, extension angle, and initial width of fracturing fractures within the current framework of hydraulic fracturing effectiveness evaluation in coal mines. We propose utilizing single-hole reflection borehole radar to evaluate the hydraulic fracturing effect, and through numerical simulation, we analyze the response characteristics of borehole radar when detecting various hydraulic fracturing-induced cracks. Initially, five models representing hydraulic fracturing cracks and two models for non-hydraulic fracturing cracks were established. Subsequently, the responses of borehole radar with central frequencies of 100, 200, and 400 MHz to cracks of identical shapes were analyzed. Additionally, the response characteristics of borehole radar with a 200 MHz central frequency to cracks of varying lengths (1, 2, 3 m), widths (4, 8, 40 cm), and angles (90°, 45°, 15°) were examined. Finally, a comparative analysis was conducted between hydraulic and non-hydraulic fracturing cracks. A branch hole was employed to simulate a hydraulic fracturing crack, allowing for an analysis of the borehole radar's response characteristics in practical scenarios. The findings indicate that borehole radar is a viable tool for assessing hydraulic fracturing effects, providing a theoretical foundation for identifying the position of cracks, evaluating their effectiveness, and determining the regional effectiveness of the hydraulic fracturing crack system.

KEYWORDS

hydraulic fracturing, borehole radar, crack detection, coal mine, near horizontal hole

1 Introduction

Hydraulic fracturing technology, a crucial enhancement method in the oil and gas industry, is utilized to manage the surrounding rock and increase permeability within low-permeability coal seams (Song, 2015; Wang, 2015; Zhao, 2020). Hydraulic fracturing technology uses liquid to transmit pressure and form artificial fractures in formation rocks. Continuous injection of liquid makes the artificial fractures larger, and the liquid brings high-strength solid particles into and fills the fractures. After construction is completed, the liquid is discharged back, and the proppant remains in the fractures, forming a channel with high flow capacity and expanding the seepage area of oil and gas.

The hydraulic fracturing effect evaluation is an important technology in hydraulic fracturing engineering (Shan et al., 2022). The most influential factors on the hydraulic fracturing effect are the expansion form, extension direction and distance of the fracture formed by hydraulic fracturing (Hei et al., 2021; Yuan X, 2019). The fracture-diagnostic technologies include indirect and direct methods. The indirect methods include Well test and History match analysis. The major limitations of this two methods are the following: 1) Model-based assumptions; 2) Requires known values of perm and pressure; 3) Wellbore storage effect; 4) Not suitable for real-time operations. The direct methods include Radioactive Tracers, Caliper log, Temperature log, Production log, Borehole Image Log, Video Camera, Hydraulic Impedance Test, Cross-Dipole Acoustic Log, Deep Shear Wave Imaging, Battery-based Wireless Sensor Network, Battery-less Wireless Sensor Network, Microseismic (Borehole),Microseismic (Surface), Tiltmeter (at Surface), Tiltmeter (Downhole at Offset Well), Tiltmeter at Treatment Well (Downhole), Fiber Optic Cable, Sealed Wellbore Pressure Monitoring,Controlled-Source Electromagnetics, Single hole transient electromagnetic (Zhao et al., 2019; Mo et al., 2020; Zhang et al., 2019; Fan et al., 2016; Duan et al., 2018; Feng et al., 2018). The major limitations for those methods are list in Table 1. In short, the starting position, width, and angle of each single crack in the fracturing fracture cannot be evaluated.

As a geophysical prospecting method with high detection accuracy and large detection range, borehole radar (BHR) has the advantages of continuity, high efficiency and high accuracy. Through the processing and image interpretation of the reflected signals received by the radar host, the purpose of identifying hidden targets can be achieved (Annan et al., 1973; Rossiter et al., 1975). Using BHR to detect cracks in vertical holes on the ground by single hole reflection measurement and cross hole measurement is effective (Liu et al., 2006). Therefore, this paper proposes to use BHR single hole reflection method to detect the hydraulic fracturing cracks in near horizontal holes in coal mine.

This paper uses numerical simulation to analyze the response characteristics of hydraulic fracturing cracks detected by BHR in near horizontal borehole in coal mine. It analyzes the response characteristics of BHR at different crack angles, crack widths and crack lengths. It provides a theoretical basis for using BHR to evaluate the hydraulic fracturing effect in horizontal borehole in coal mine.

2 Numerical simulation principle of BHR

At present, there are three kinds of electromagnetic wave numerical simulation methods: ray tracing method, finite difference time domain (FDTD) method and finite element method (Zeng et al., 2010). In this paper the software Gprmax is used. Gprmax is an open source FDTD based ground penetrating radar (GPR) forward simulation software developed by Edinburgh University (Warren et al., 2016). The Gprmax is widely used in the GPR forward simulation.

FDTD divides the simulation space into finite spatial grids (Figure 1). The electromagnetic field of each grid can be determined by six components of Ex, Ey, Ez, Hx, Hy and Hz, and then the Maxwell equation in time domain can be directly solved by finite difference.

After the initial conditions and boundary conditions of the field are given, the distribution values of the spatial electromagnetic field at each time are obtained in turn, that is, the simulation results of the electromagnetic field in the simulation space area are obtained.

When using Gprmax for FDTD forward modeling of BHR, there are three main parameters to be set: 1) antenna parameters, including excitation source type, antenna spacing, antenna frequency, antenna type, output signal and recording time; 2) Geometric parameters of the model, including model size and mesh size; 3) The physical parameters of the model, that is, the physical parameters of the medium in the model area, including the relative dielectric constant, conductivity, relative permeability, etc., The default boundary condition is the fully absorbed boundary condition (PML) (Zhong, 2008). The details of the rules for setting key parameters are listed on the website https://docs.gprmax.com/en/latest/input.html.

3 Model design

3.1 Model parameters

The analysis is based on the analysis of the hydraulic fracturing in the coal seam, so the non-hydraulic fracturing crack is also considering the crack developed in the coal seam roof. The basic model is a 20 m × 11 m 2D model, in which the coal seam thickness is 5 m, the roof and floor are sandstone, the thickness is 3 m, the borehole diameter is 90 mm, the borehole is 1 m away from the coal seam floor and 4 m from the roof. In practice, workers operate instruments in the roadway, so the designed roadway in the model is 2 m × 5 m. The basic model is shown in Figure 2.

The hydraulic fracturing crack is filled with fracturing fluid or proppant, the non-hydraulic fracturing crack is filled with fissure filler, the roadway is filled with air, and the borehole is filled with fracturing fluid.

The BHR is designed in the form of single hole reflection. There is an offset between the transmitting antenna and the receiving antenna. The offset is 0.5 m. The transmitting antenna is in the front and the receiving antenna is in the rear; The antenna type is dipole antenna, the excitation source is Ricker wavelet, the recorded signal is electric field intensity, the transmitted and received signals of the antenna are Z-direction signals, the recorded and analyzed signals are Z-direction electric field intensity Ez, the center frequency of the antenna is changed as required, and the grid division is uniform 0.01 m. The boundary condition adopts perfectly matched layer (PML) boundary. According to the model size, the recording time window is 0–100 ns.

According to the parameters requirements of Gprmax, the parameters are shown in Table 2.

TABLE 1 Summary of various fracture-diagnostic technologies with limitations.

Group	Technology	Major limitations
Indirect	Well Test	• Model-based assumptions
		• Requires known values of perm and pressure
		• Wellbore storage effect
		• Not suitable for real-time operations
	History Match Analysis	• Model-based assumptions
		• Requires known values of several reservoir parameters
		• Not suitable for real-time operations
Direct	Radioactive Tracers	• Depth of investigation ~ 1–2 ft from the well
		• Accuracy dependent on alignment of fracture and well path
		• Not suitable for real-time operations
	Caliper log	• Sensitive to borehole diameter changes
		• Requires cased borehole
		• Not suitable for real-time operations
	Temperature log	• Sensitive to thermal conductivity of different formations
		• Requires multiple passes through the well after hydraulic fracturing treatment
		• Not suitable for real-time operations
	Production log	• Does not provide info about non-producing zones/perfs/clusters
		• Not suitable for real-time operations
	Borehole Image Log	• Requires open-hole borehole
		• Does not provide info about fracture dimensions
		• Not suitable for real-time operations
	Video Camera	• Does not provide info about non-producing zones/perfs/clusters
		• Not suitable for real-time operations
	Hydraulic Impedance Test (HIT)	• Sensitive to tubular diameter changes
		• Not suitable for real-time operations
	Cross-Dipole Acoustic Log	• Cement bond quality
		• Borehole conditions after fracture operations
	Deep Shear Wave Imaging (DSWI)	• Relatively very costly
		• Cement bond quality
		• Borehole conditions after fracture operations
		• Coupling fluid is required in the hole
	Battery-based Wireless Sensor Network	• Individual fracture dimensions cannot be determined
		• Not suitable for real-time operations

(Continued on the following page)

TABLE 1 (*Continued*) Summary of various fracture-diagnostic technologies with limitations.

Group	Technology	Major limitations
	Battery-less Wireless Sensor Network	• Signal range limited till the point of their settlement in the fracture
		• Currently at proof-of-concept stage
	Microseismic (Borehole)	• Relatively very costly
		• Requires a large number of vertical wells to monitor a single hydraulic fracturing job
		• Individual fracture dimensions cannot be determined
	Microseismic (Surface)	• Relatively very costly
		• Vertical position of hydraulic fracturing is estimated using a model (P-wave velocity)
		• Individual fracture dimensions cannot be determined
	Tiltmeter (at Surface)	• Individual fracture dimensions cannot be determined
		• Fracture mapping resolution decreases with depth (frac azimuth ± 3° at 3000ft, and ±10° at 10,000 ft)
	Tiltmeter (Downhole at Offset Well)	• Resolution (fracture length and height) decreases as distance of the offset well increases
		• Cannot provide info about fracture growth
	Tiltmeter at Treatment Well (Downhole)	• Fracture length must be estimated indirectly from height and aperture
	Fiber Optic Cable	• Relatively very costly
		• Depth of investigation is 1–2 ft from the fracture event
	Sealed Wellbore Pressure Monitoring (SWPM)	• Requires an offset well that is both non-producing and sealed
		• Depth of investigation is 1–2 ft from the fracture event
	Controlled-Source Electromagnetics (CSEM)	• Relatively very costly
		• Model-based assumptions
		• Requires extensive data to build a 3-D forward model used to predict monitoring results
		• Not suitable for real-time operations
		• Individual fracture dimensions cannot be determined
	Single hole transient electromagnetic	• Depth of investigation is 1–2 ft from the fracture event
		• Individual fracture dimensions cannot be determined
		• Unable to detect the starting position of fracturing fractures

3.2 The hydraulic fracturing crack model

During the hydraulic fracturing in the coal seam, the crack propagation mechanism is complex, and the crack morphology is also complex (Jiang et al, 2015; 2018; Kang 2015). In order to analyze the response characteristics of the BHR, the model is simplified. When establishing the model of the BHR detecting crack in the coal seam, it is assumed that the hydraulic fracturing crack starts from the borehole wall and extends into the formation, and the crack is considered as a line. In Figure 2, it is marked as f. Firstly, the response of the BHR antenna at different center frequencies is simulated and analyzed, Then, the parameters of the crack f are changed, we established five hydraulic fracturing crack models:

1) Model I: the crack length is 2 m, the angle between the crack and the borehole is 90°, the crack width is 0.04 m, and the center frequencies of the radar antenna are 100, 200, and 400 MHz respectively, as shown in Figure 3.
2) Model II: the crack length is 2 m, and the angle between the crack and the borehole is 90°. The width of the crack

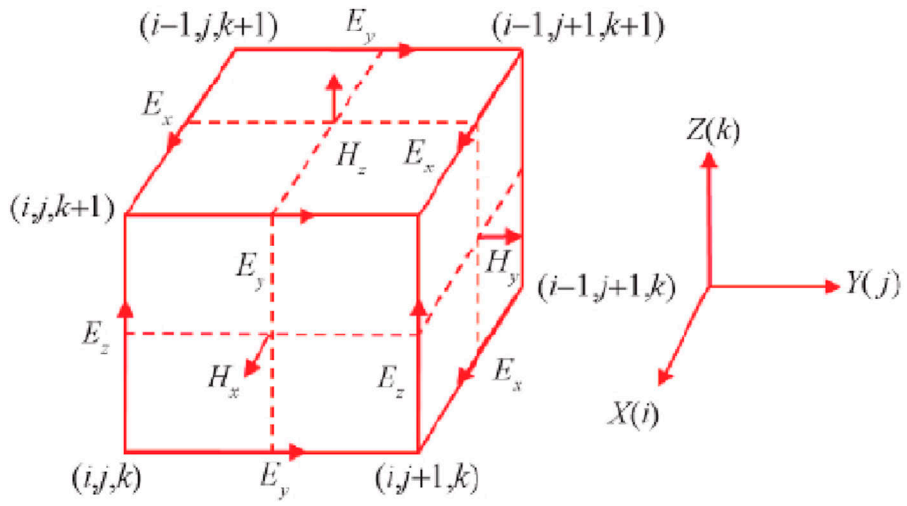

FIGURE 1
FDTD method difference grid.

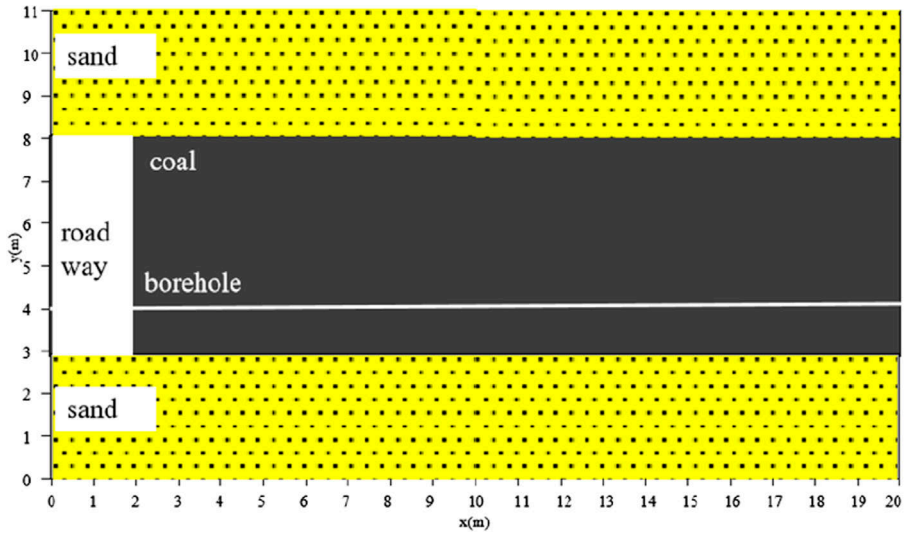

FIGURE 2
Schematic diagram of basic model.

f in Figure 3 is changed, which is 0.04, 0.08, and 0.4 m respectively.

3) Model III: the crack is 0.04 m wide and 2 m long. The angle of the crack f in Figure 3 is changed. The angle between the crack and the borehole is 90°, 45° and 15° respectively. The dotted line f1 in Fig. 3corresponds to the crack angle of 45° and the dotted line f2 corresponds to the crack angle of 15°.
4) Model IV: the crack width is 0.04 m, and the angle between the crack and the borehole is 90°. The longitudinal length of the crack f in Figure 3 is changed, and the crack length is 1, 2 and 3 m respectively.
5) Model V:on the basis of single crack analysis, multiple crack models are designed. The crack width is 0.04 m, the angle between the crack and the borehole is 90°, and the multiple cracks with different lengths are distributed in fishbone shape. As shown in Figure 4, the lengths of f1-f5 cracks are 2, 3, 4, 3, and 2 m respectively.

3.3 Non-hydraulic fracturing crack model

Coal formation is different from oil formation. Due to mineral changes during deposition, overburden pressure, and mining

TABLE 2 The parameters table.

Parameter type	Parameter name	Value	Parameter name	Value
Antenna parameters	center frequency (MHz)	100, 200, 400	Recording time (ns)	100
	Antenna spacing(m)	0.5	Incentive type	Ricker wavelet
	Antenna type	Dipole antenna	Output signal	Ez
	Antenna direction	Omni-directional Antenna	Antenna length	Point antenna
Geometric parameters	Area	20 m × 11 m	Grid size(m)	0.01
	Coal seam thickness(m)	5	Thickness of top and bottom plate(m)	3
	Road way width(m)	2	Roadway height(m)	5
Physical parameters	Coal seam conductivity (S/m)	0.001	Sand conductivity (S/m)	0.01
	Relative permittivity of coal seam	4	Relative permittivity of sand	6
	Relative permeability of coal seam	1	Relative permeability of sand	1
	Relative dielectric constant of fracturing fluid	30	fracturing fluid conductivity	4
	Relative permeability of fracturing fluid	1	Relative permittivity of fissure filler	10.7
	Relative permeability of fissure filler	1	Conductivity of fissure filler	2.5

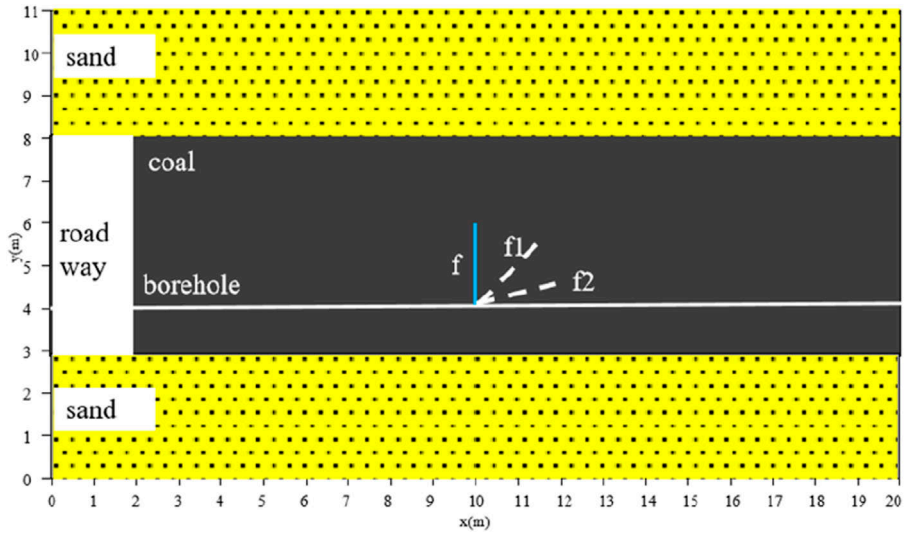

FIGURE 3
Single crack model (Model I-Model IV).

disturbance, there are some cracks formed for other reasons not for hydraulic fracturing (Wang et al, 2015). We call this type crack as non-hydraulic fracturing crack. Two non-hydraulic fracturing crack models are designed:

1) Model I: Cracks with different shapes and depths developed in the roof. The lower end of crack nf_1 is 5 m away from the borehole, and the maximum width of crack nf_1 is 0.5 m. The lower end of crack nf_2 is 3 m away from the borehole, and the maximum width of crack nf_2 is 1 m. The crack model is shown in Figure 5.
2) Model II: Cracks penetrating the coal seam are developed in the roof. The cracks shape are irregular, and the maximum width of crack nf is 0.5 m. The schematic diagram of the model is shown in Figure 6.

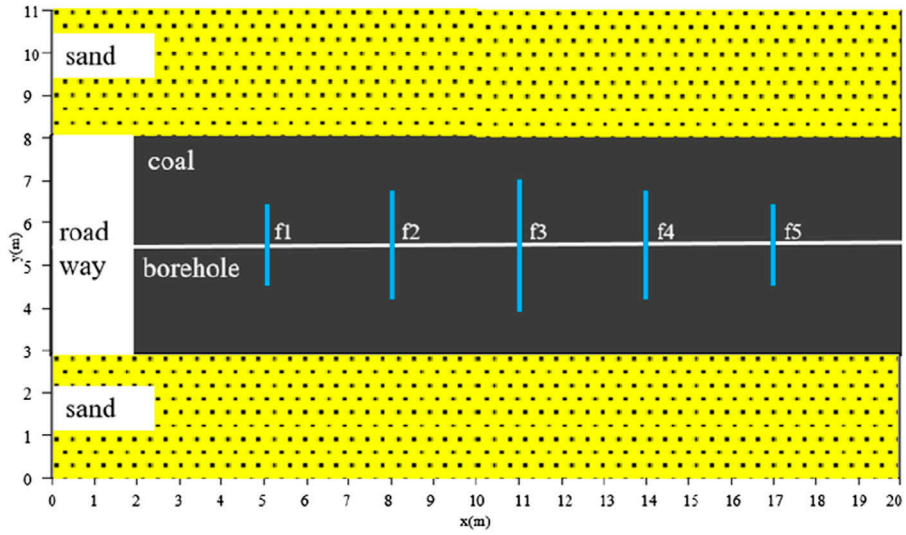

FIGURE 4
Fishbone distribution model (Model V).

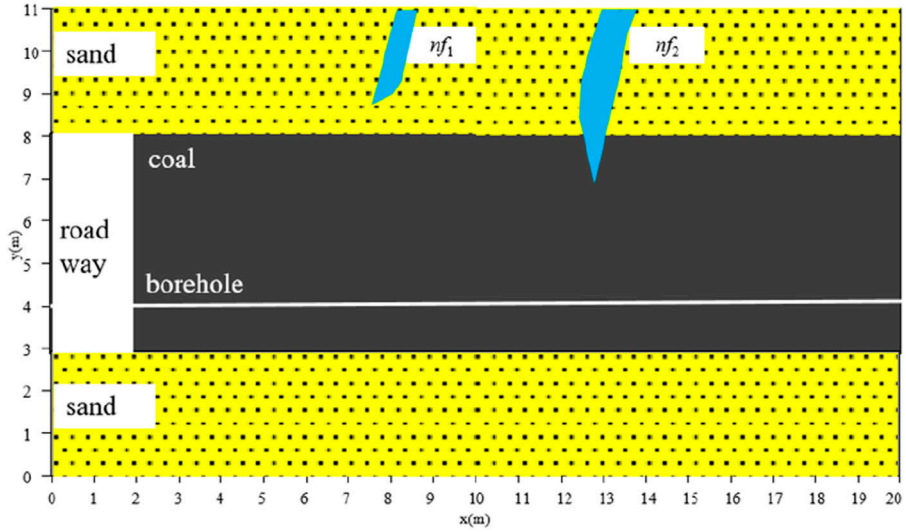

FIGURE 5
Non-hydraulic fracturing crack with different widths and depths models (Model VI).

4 Simulation results

Before hydraulic fracturing in the coal seam, the background field is simulated and analyzed to facilitate the analysis of the BHR response characteristics of the cracks. The BHR central frequency is 200 MHz, the BHR response in the coal mine borehole along the coal seam is shown in Figure 7.

In Figure 7, the abscissa represents the depth of the antenna in the borehole, and the ordinate represents the radar response time (the same in the figures below). The phase axis numbered in the figure represents the direct wave (short for "direct wave"), The phase axis numbered represents the floor reflected wave (short for "the floor wave"), the phase axis numbered represents the roof reflected wave (short for "the roof wave"), the phase axis numbered represents the roadway reflected wave (short for "the road wave") and the phase axis numbered represents the multiple wave (short for "multiple wave") respectively.

4.1 Hydraulic fracturing crack simulation results

4.1.1 The results of model I

We simulated and analyzed the response with BHR center frequency of 100 MHz, 200 MHz and 400 MHz to detect crack with

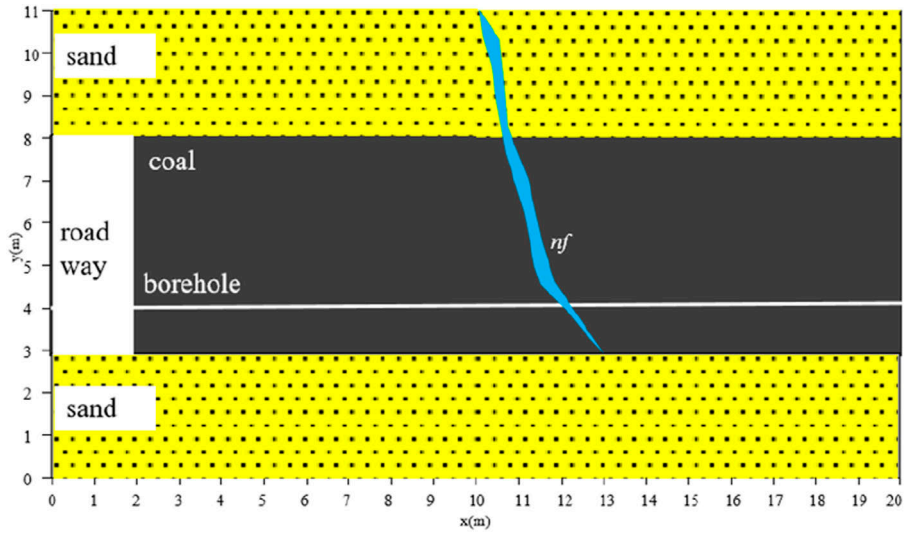

FIGURE 6
Non-hydraulic fracturing crack penetrating coal seam model (Model VII).

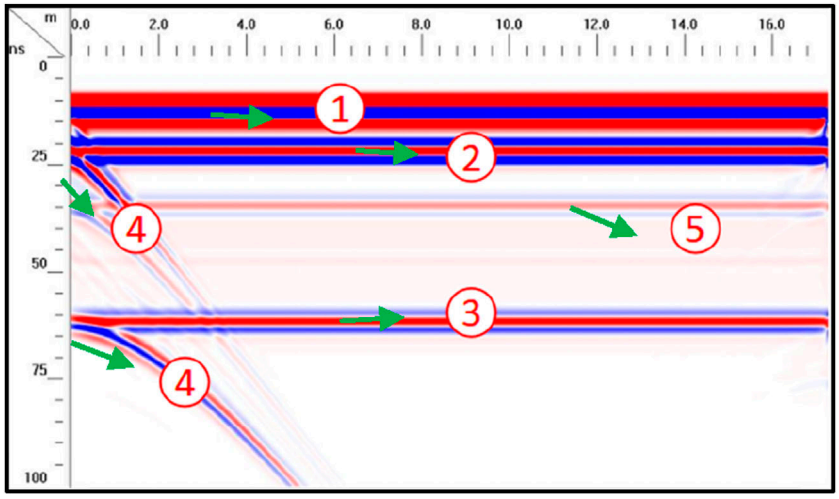

FIGURE 7
The BHR response profile in coal seam (1→direct wave; 2→the floor wave; 3→ multiple wave; 4→the road wave; 5→the roof wave).

0.04 m width, 2 m length and 90°crack angle. The simulation results are shown in Figures 8–10.

In Figures 8–10, the reference number ~ phase axis have the same meaning as that in Figure 7. The reference number is the response phase axis of hydraulic fracturing crack (short for "the crack wave"). The upper event is caused by the reflection from the starting of the crack, and the lower event is caused by the reflection from the ending of the crack. On the BHR response time profiles at three frequencies, the phase axis characteristics of hydraulic fracturing crack are obvious, the crack reflection phase axis in 100 MHz BHR profile are not very clear compared with 200 MHz and 400 MHz. The details of 200 MHz BHR are the same clear as 400 MHz.But in the same time zone, the 400 MHz image color is relative light than the 200 MHz image, which means that the reflected wave energy in 400 MHz BHR profile is weaker than in 200 MHz BHR profile. Therefore, the BHR frequency is too high or too low, which is unfavorable to detection. It is recommended to use 200 MHz borehole radar to detect hydraulic fracturing cracks.

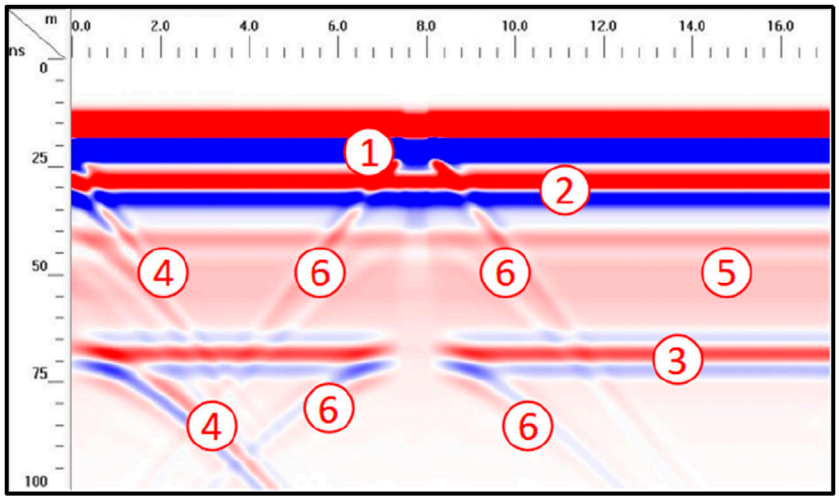

FIGURE 8
The BHR response profile of center frequency 100 MHz (1→direct wave; 2→the floor wave; 3→multiple wave; 4→the road wave; 5→the roof wave; 6→the crack wave).

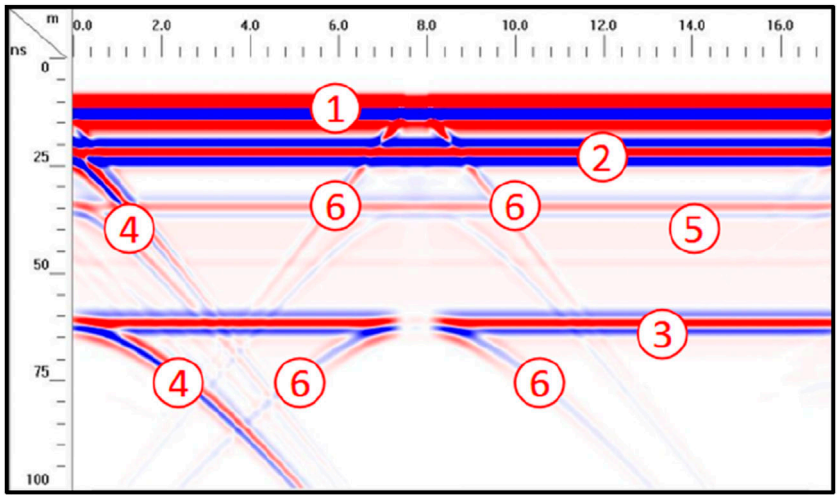

FIGURE 9
The BHR response profile of center frequency 200 MHz (1→direct wave; 2→the floor wave; 3→multiple wave; 4→the road wave; 5→the roof wave; 6→the crack wave).

4.1.2 The results of model II

The cracks length are 2 m, the cracks angle are 90°. The cracks widths are 0.04 m, 0.08 and 0.4 m respectively. According to the previous studies, the 200 MHz BHR is selected. The simulation results are shown in Figures 11, 12 (the response of the model results with the crack width of 0.04 m is shown in Figure 9).

In Figures 11, Figures 12, the phase axis numbered ~phase axis has the same meaning as that in Figure 8. The main difference in Figure 8\11\12 is that the direct wave phase axis and the interruption width of roof reflection phase axis are different. The width of crack has little influence on the transverse width of the crack phase axis. According to Guo's research, the wider the crack, the stronger the amplitude (Guo S L et al, 2016). So we can use Guo's research to calculate the crack width, the formula is:

$$y = 0.0535x^2 + 0.4648x + 0.8383$$

Where y is the max amplitude intensity, x is the crack width.

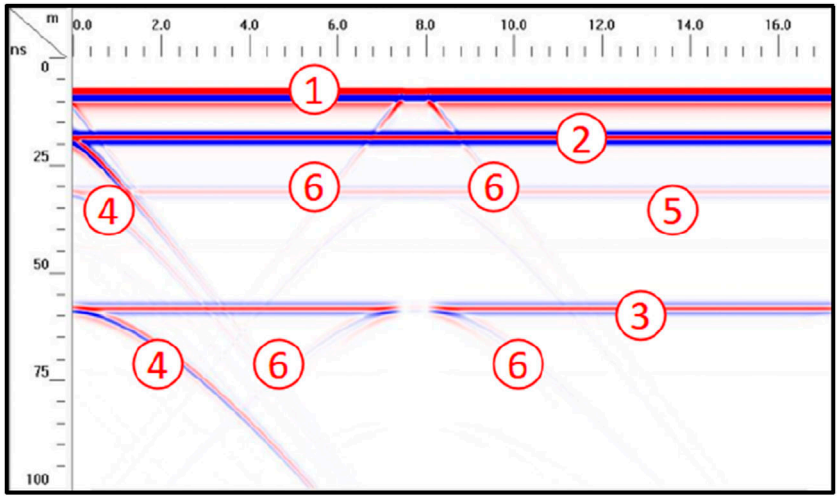

FIGURE 10
The BHR response profile of center frequency 400 MHz (1→direct wave; 2→the floor wave; 3→ multiple wave; 4→the road wave; 5→the roof wave; 6→the crack wave).

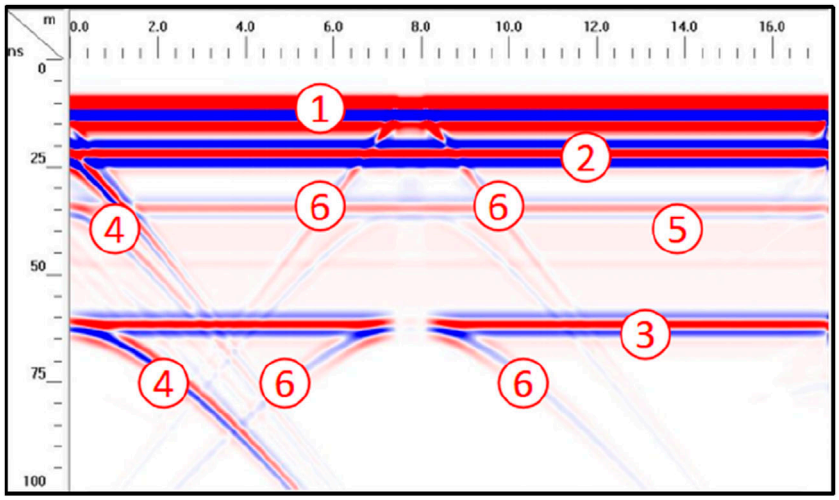

FIGURE 11
The BHR response profile for 0.08 m width crack (1→direct wave; 2→the floor wave; 3→multiple wave; 4→the road wave; 5→the roof wave; 6→the crack wave).

4.1.3 The results of model III

The cracks angle are 90°. The cracks width are 0.04 m, the cracks length are 1, 2, 3 m respectively. According to the previous studies, the 200 MHz BHR is selected. The simulation results are shown in Figures 9, 13, 14 respectively

In Figures 13, 14, the phase axis numbered ~phase axis have the same meaning as that in Figure 8. By comparing Figures 9, 13, 14, we can find that the difference of reflection phase axes of cracks is mainly in the difference of lateral length of the lower phase axis labeled. The larger the crack length, the longer the phase axis. In practical application, the crack length can be analyzed by judging the lateral length of the phase axis.

4.1.4 The results of model IV

The cracks width are 0.04 m, the cracks length are 2 m, the cracks angle are 15°, 45° and 90°respectively. According to the previous studies, the 200 MHz BHR is selected. The simulation results are shown in Figures 9, 15, 16 respectively.

In Figures 15, 16, the phase axis numbered ~phase axis has the same meaning as that in Figure 8. By comparing Figures 9, 15, 16, we can find that when the angle between the crack and the borehole is not 90°, the reflection event axis of the crack will not appear in the form of hyperbola. The larger the included angle of the crack, the larger the angle of the reflection event axis, until it appears in the form of symmetric hyperbola at 90°. In practical application, the

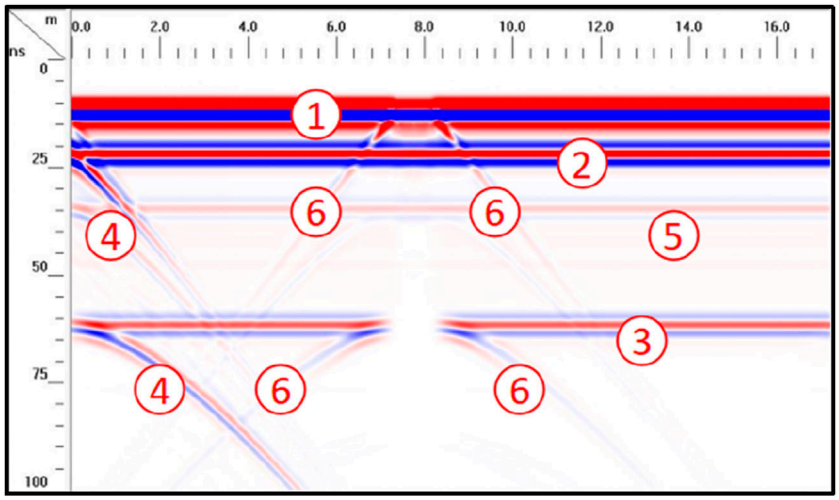

FIGURE 12
The BHR response profile for 0.4 m width crack (1→direct wave; 2→the floor wave; 3→multiple wave; 4→the road wave; 5→the roof wave; 6→the crack wave).

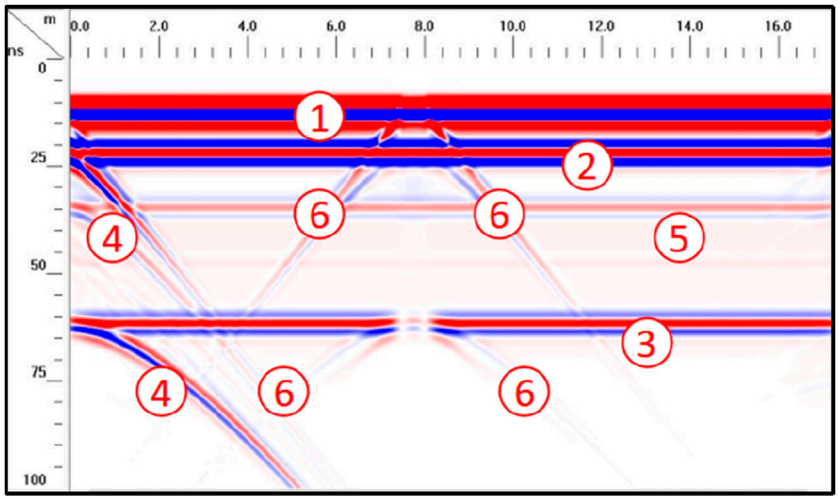

FIGURE 13
The BHR response profile for 1 m length crack (1→direct wave; 2→the floor wave; 3→multiple wave; 4→the road wave; 5→the roof wave; 6→the crack wave).

crack angle can be analyzed by analyzing the angle between the crack phase axis with the direct phase axis.

4.1.5 The results of model V

The model is described in the model V, the simulated result is shown in Figure 17. In Figure 17, the phase axis numbered ~phase axis has the same meaning as that in Figure 7 and the reference numbers ~ correspond to the response of the cracks f1-f5 in Figure 4. According to Figure 17, when there are multiple fracturing cracks at the same time, multiple cracks can be distinguished on the BHR profile. Five cracks can be clearly identified. In practical application, the BHR can detect multiple hydraulic fracturing cracks at once. Compared to Figures 11–14, we cannot determine from Figure 17 whether the cracks are developing upwards, downwards, or through the borehole. Which means that the cracks direction can not be recognized.

4.2 Simulation results of original cracks

4.2.1 The results of model VI

Two primary cracks with different shapes and depths developed in the roof which are shown in Figure 4. According to the previous studies, we also chose 200 MHz BHR

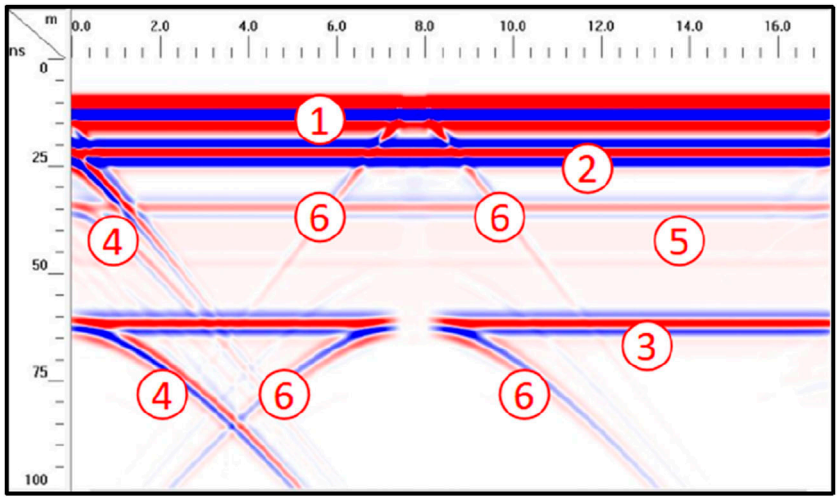

FIGURE 14
The BHR response profile for 3 m length crack (1→direct wave; 2→the floor wave; 3→multiple wave; 4→the road wave; 5→the roof wave; 6→the crack wave).

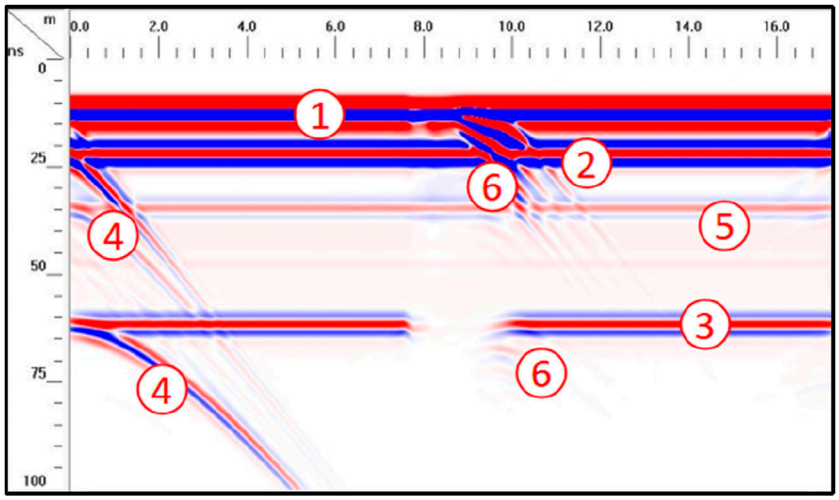

FIGURE 15
The BHR response profile for 15° angle crack (1→direct wave; 2→the floor wave; 3→multiple wave; 4→the road wave; 5→the roof wave; 6→the crack wave).

to detect the cracks. The simulation results are shown in Figure 18.

In Figure 18, the phase axis numbered ~phase axis has the same meaning as that in Figure 7. The phase axis numbered and correspond to the responses of cracks nf_1 and nf_2 in Figure 4 on BHR profile, respectively. According to Figure 18, the distance between the lower end points of nf_1 and nf_2, and the borehole is different, and the corresponding time between the phase axis numbers and the top end of the in-phase axis is different. Therefore, the distance between the crack and the borehole can be judged according to the position of the in-phase axis of the crack on BHR.

4.2.2 The results of model VII

The crack developed in the roof and penetrating the coal seam is shown in Figure 5. The detection process is the same as before. The simulation results are shown in Figure 19.

In Figure 19, the phase axis numbered ~phase axis has the same meaning as that in Figure 7. The phase axis numbered correspond to the response of crack nf in Figure 5 on BHR profile. Compared with the previous hydraulic fracturing cracks responses shown in Figure 9, the characteristics of this kind of crack on the BHR profile are not different from those of the previous hydraulic fracturing cracks. In the actual hydraulic

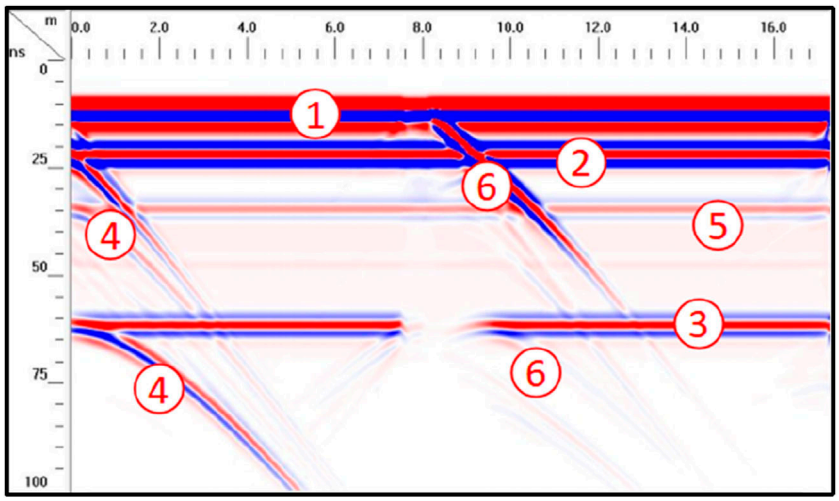

FIGURE 16
The BHR response profile for 45° angle crack (1→direct wave; 2→the floor wave; 3→multiple wave; 4→the road wave; 5→the roof wave; 6→the crack wave).

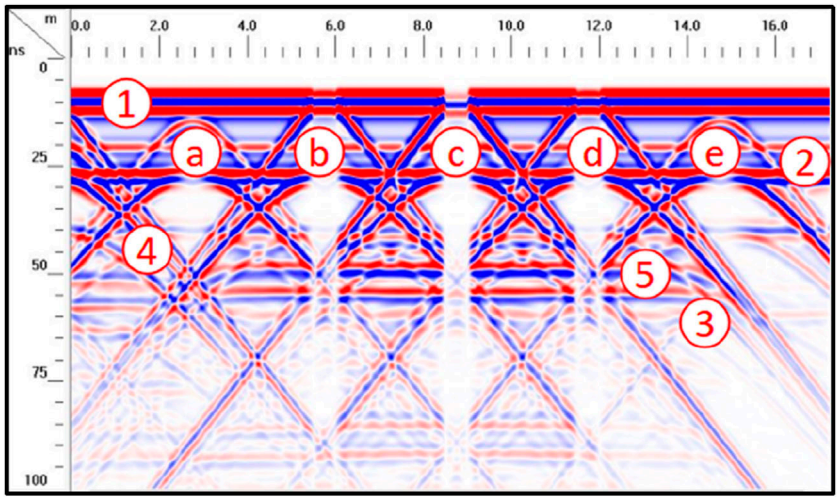

FIGURE 17
BHR response s of fish bone crack (1→direct wave; 2→the floor wave; 3→multiple wave; 4→the road wave; 5→the roof wave; a→the f_1 crack wave; b→the f_2 crack wave; c→the f_3 crack wave; d→the f_4 crack wave; e→the f_5 crack wave).

fracturing effect detection, such cracks should also be paid attention for geophysical engineers, so we do not need to distinguish such non-hydraulic fracturing cracks from hydraulic fracturing cracks.

5 Application

In actual production, we rarely have the opportunity to directly observe the development of cracks in the process of hydraulic fracturing, however we can leverage the construction of branch holes that occur during the drilling process in coal mines. By treating these branch holes as known hydraulic fracturing cracks, we can use Borehole Radar (BHR) for detection purposes. This approach allows us to assess the effectiveness of BHR in evaluating hydraulic fracturing outcomes.

Before heading of 2,203 working face of a capital construction coal mine in Shanxi Province, directional long boreholes and branch holes were used to detect the geological structures.

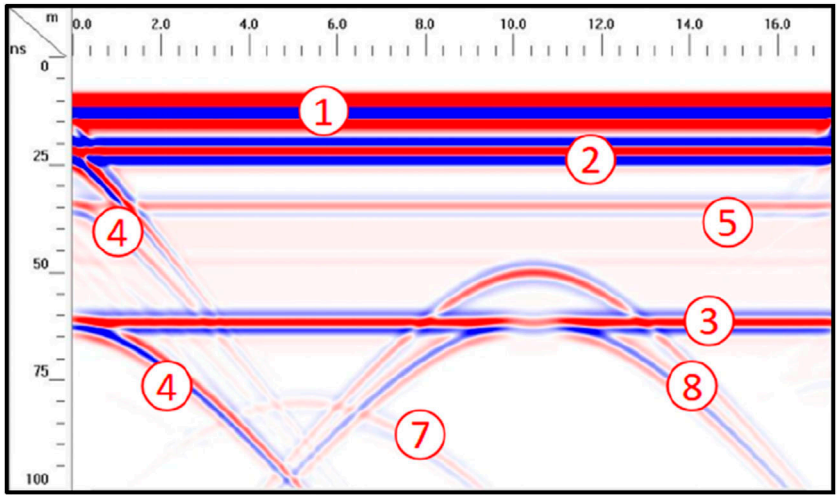

FIGURE 18
BHR response of two roof developed cracks (1→direct wave; 2→the floor wave; 3→multiple wave; 4→the road wave; 5→the roof wave; 7→the nf_1 crack wave; 8→the nf_2 crack wave).

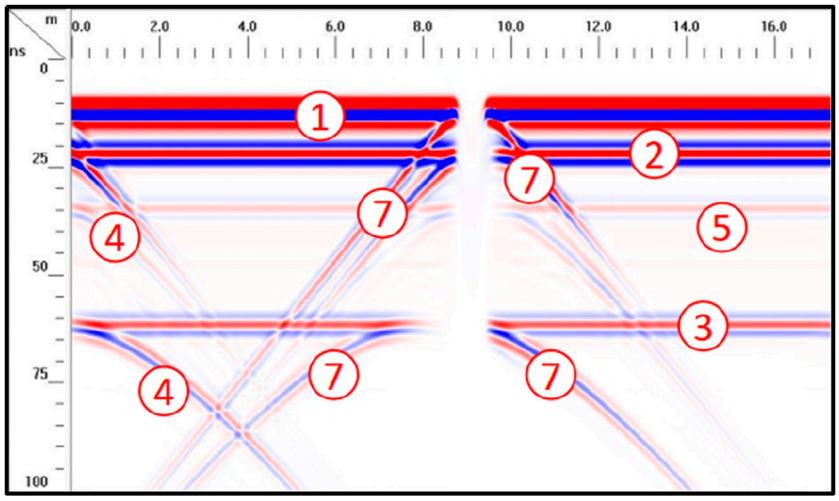

FIGURE 19
BHR response of borehole with cracks developed through the coal seam in the roof (1→direct wave; 2→the floor wave; 3→multiple wave; 4→the road wave; 5→the roof wave; 7→the *nf* crack wave).

The drilling depth of the main hole was 468 m, and 7 m metal sleeve is placed away from the main hole opening. The borehole diameter is 120 mm, and the 1-1 branch hole is opened at the hole depth of 60 m. The depth of the branch hole is 12 m. The trajectory of the main hole (0–80 m) and the 1-1 branch hole and the formation conditions encountered is shown in Figure 20. The mud circulation drilling is adopted in the drilling process. Therefore, the branch hole detection is used to simulate the characteristics of the cracks detected by the BHR in practice. The BHR center frequency is 200 MHz, and the antenna is sent into the main hole by hand to measure the depth of 80 m, the instrument photo and parameters are shown in Figure 21. The site construction picture is shown in Figure 22. The original time-domain profile is shown in Figure 23, The data processing flow is as following:

1) Time zero correction, to eliminate the influence caused by the delay of the instrument itself;
2) AGC processing, to improve the interpretability of BHR images;

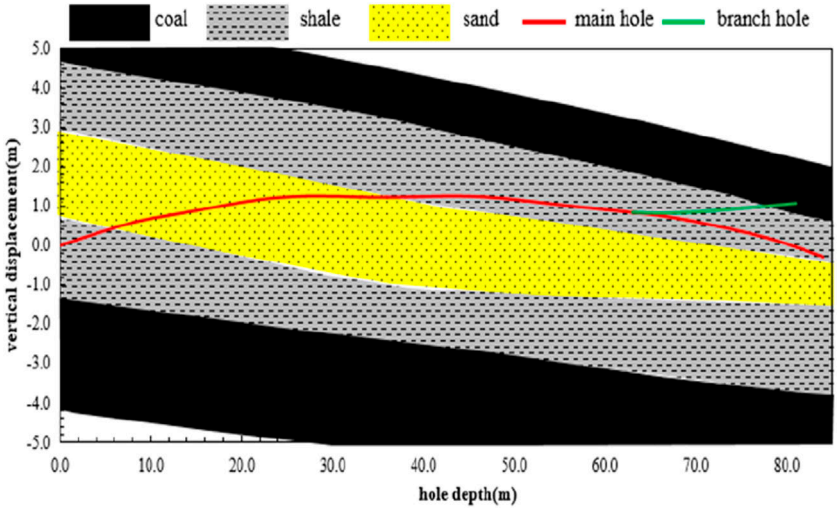

FIGURE 20
The distribution of holes.

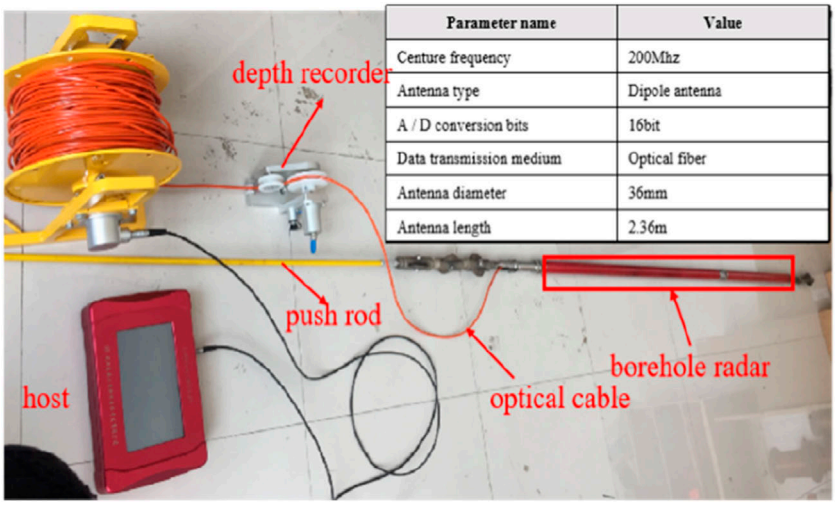

Parameter name	Value
Centure frequency	200Mhz
Antenna type	Dipole antenna
A / D conversion bits	16bit
Data transmission medium	Optical fiber
Antenna diameter	36mm
Antenna length	2.36m

FIGURE 21
BHR instrument photo.

FIGURE 22
Site construction photos.

3) Bandpass filtering, to eliminate interference, the bandpass filtering frequency range is from 150 MHz to 400 MHz; The processed the time-domain profile is shown in Figure 24.

In Figure 24, 1) The abnormal area labeled 1 (depth 1.33–7.33 m) is due to the presence of a metal casing as support at the orifice, which shields the signal of the drilling radar inside the metal casing. 2) there are structures at the depth 33 m (labeled 2) and layers at the depth of 40 m (labeled 3) on the BHR profile, which is not conducive to the analysis of the characteristics of branch holes. 3) The characteristics of branch holes at the depth of 60 m are obvious, which is consistent with Figures 14, 15. The length of branch holes cannot be computed on the BHR time-domain profile. Therefore, it is recommended to detect the

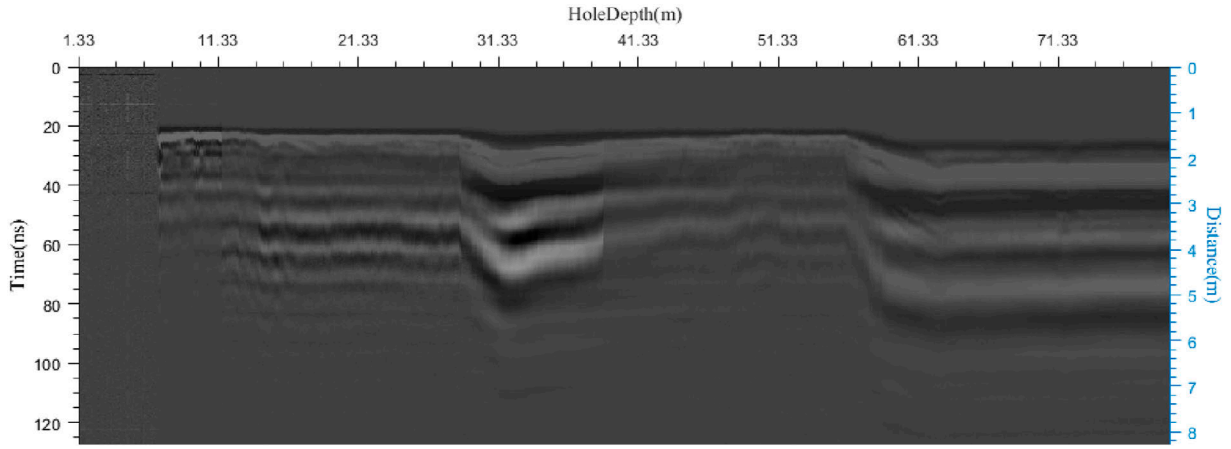

FIGURE 23
The original BHR time domain profile.

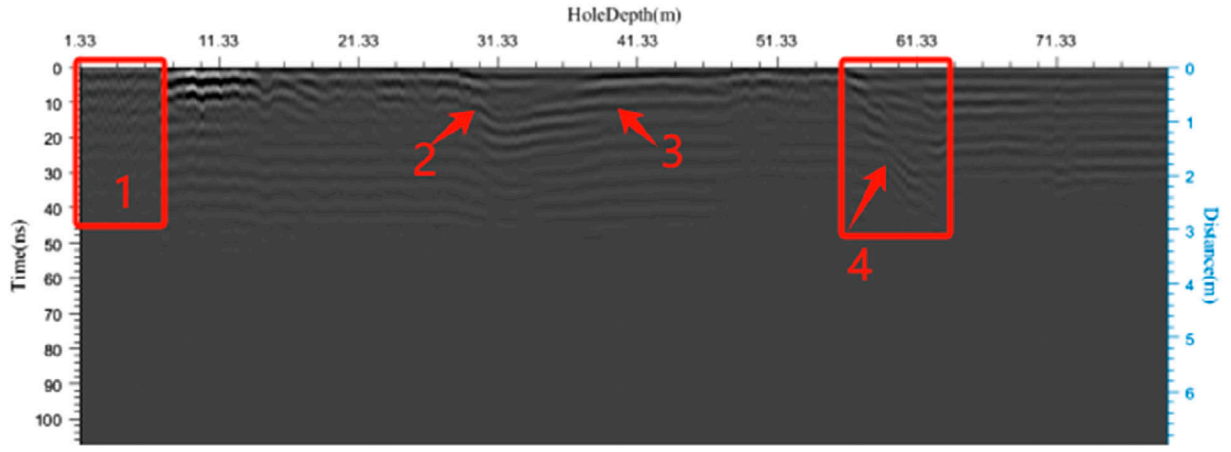

FIGURE 24
The processed BHR time domain profile (The abnormal area labeled one is the metal casing response; The abnormal area labeled two and three are the lithology change response; The abnormal area labeled four is the branch hole response).

original structure of the formation around the hole before hydraulic fracturing. After fracturing, crack detection shall be carried out to compare and analyze the distribution and characteristic of hydraulic fracturing cracks.

6 Conclusion

1) Single-hole reflection borehole radar (BHR) can be utilized to detect hydraulic fracturing cracks. It is recommended to use a BHR tool with a 200 MHz center frequency for detecting hydraulic fracturing cracks. When employing BHR to detect such cracks, it can ascertain the initial development position of the cracks, determine whether the hydraulic fracturing cracks are perpendicular to the borehole or at an angle other than 90°, and estimate the approximate length of the cracks' development. When multiple cracks are present simultaneously, the response characteristics of each crack can be clearly distinguished on the BHR time-domain profile. For the original cracks within the formation, the BHR response characteristics differ significantly from those of hydraulic fracturing cracks, allowing for differentiation.
2) In practice, when BHR is employed to detect hydraulic fracturing cracks, the geological conditions are complex, with numerous influencing factors, leading to complex BHR response characteristics. It is advisable to first assess the original structure of the formation surrounding the borehole before hydraulic fracturing occurs, followed by BHR detection post-fracturing. Through comparison and analysis, the response associated with the cracks can be more clearly delineated.
3) For practical applications, single-hole reflection BHR is incapable of calculating the propagation length of hydraulic fracturing cracks. It is suggested that, in the future, cross-hole BHR or array borehole radar

technology be explored to determine the length of crack propagation.

4) With omnidirectional drilling radar antennas, determining the direction of crack propagation is not possible. In the future, directional borehole radar antennas may be utilized to ascertain the direction of crack propagation.
5) This article presents a novel research direction for the detection of hydraulic fracturing cracks but does not address the response characteristics of borehole radar detection, such as mapping cracks, cross-cracks, fracture permeability, heterogeneity. Further in-depth research in these areas will be necessary in the future

Data availability statement

The original contributions presented in the study are included in the article/Supplementary Material, further inquiries can be directed to the corresponding author.

Author contributions

JB: Writing–original draft, Writing–review and editing.

Funding

The author(s) declare that financial support was received for the research, authorship, and/or publication of this article. Thanks for the support by the National Key R and D plan (2018YFC0807804) and Key R&D Plan of Shaanxi Province (2023-YBGY-111).

Conflict of interest

Author JB was employed by the company China Coal Research Institute Xi'an Science and Industry Group.

The author declares that this study received funding from the Scientific and Technological Innovation projects of CCTEG Xi'an Research Institute (2023XAYJS06) and the General Project of Middling Coal Technology and Industry Group (2022-2-TD-MS005). The funders had the following involvement in the study: provided financial support and essential equipment that facilitated the data collection process for our research article, and participated actively in the study design, data collection and analysis, and decision-making process regarding the publication of the article.

Publisher's note

References

Duan, J. H., Tang, H. W., and Wang, Y. H. (2018). Detection technology of hydraulic fracturing in coalbed methane well based on microseismic and transient electromagnetic method. *Coal Sci. Technol.* 46 (6), 160–166. doi:10.13199/j.cnki.cst.2018.06.027

Erick, B. L. D., Pedro, J. V., da Silva, S. L. E. F., and Torres, H. (2022). Hydraulic fracturing assessment on seismic hazard by Tsallis statistics. *Eur. Phys. J. B* 95 (6), 92. doi:10.1140/epjb/s10051-022-00361-6

Fan, T. (2020). Coalbed methane hydraulic fracturing effectiveness test using minimal coil single bore-hole transient electromagnetic method. *J. China Coal Soc.*, 1–16. doi:10.13225/j.cnki.jccs.2019.0827

Fan, T., Cheng, J. Y., Wang, B. L., Liu, L., Yao, W. H., Wang, J. K., et al. (2016). Experimental study on imaging method of TEM pseudo wave-field to detect the effect of under-ground coal-bed gas hydraulic fracturing. *J. China Coal Soc.* 41 (7), 1762–1768. doi:10.13225/j.cnki.jccs.2015.1490

Feng, Q., Wang, T., Yang, H., Huang, Z. J., and Li, X. N. (2018). Fracturing parameters optimization and evaluation of CBM crackd wells. *Nat. Gas. Geosci.* 29 (11), 1639–1646.

Hei, C., Luo, M. Z., and Zou, X. (2021). Evaluation methods of the hydraulic fracturing effect based on the energy of borehole scattered wave. *J. Yangtze Univ. Nat. Sci. Ed.* 18 (3), 14–20. doi:10.16772/j.cnki.1673-1409.2021.03.002

Jane, L., Jan, B., and Laura, F. (2016). Assessment of hydraulic fracturing in California. *Abstr. Pap. Am. Chem. Soc.* 251.

Jiang, T. T. (2015). "Study on the mechanism of hyraulic fracture Network and propagation," in *Coalbed methane reservoir* (China University of Petroleum East China).

Jiang, T. T., Zhang, J. H., and Huang, G. (2018). Experimental study of fracture geometry during hydraulic fracturing in coal. *Rock Soil Mech.* 39 (10), 3677–3684. doi:10.16285/j.rsm.2017.0194

Kang, X. T. (2015). *Research on hydraulic fracturing propagation rules in coal seam and gas extraction drilling optimization*. Chongqing University.

Li, N., Fang, L., Sun, W., Zhang, X., and Chen, D. (2020). Evaluation of borehole hydraulic fracturing in coal seam using the microseismic monitoring method. *Rock Mech. Rock Eng.* 54 (2), 607–625. doi:10.1007/s00603-020-02297-8

Liu, H., Si, G., and Huang, H. W. (2013). Research on valuation methods and cost control measures of hydraulic fracturing in shale gas horizontal wells. *Appl. Mech. Mater.* 2301 (295-298), 3166–3170. doi:10.4028/scientific.net/amm.295-298.3166

Liu, S. X., Zeng, Z. F., and Xu, B. (2006). Subsurface water-filled cracks detection by borehole radar. *Process Geophys.* 2, 620–624.

Longinos, N. S., Abbas, H. A., Bolatov, A., Skrzypacz, P., and Hazlett, R. (2023). Application of image processing in evaluation of hydraulic fracturing with liquid nitrogen: a case study of coal samples from karaganda basin. *Appl. Sci.* 13 (13), 7861. doi:10.3390/app13137861

Mo, L. (2020). Application of optical fiber micro-seismic detection technology in fracturing effect evaluation. *J. Jianghan Petroleum Univ. Staff Work.* 33 (2), 1–3. doi:10.3969/j.issn.100-301x.2020.02.001

Peter Annan, A., Strangway, D. W., and Simmons, G. (1973). RADIO INTERFEROMETRY DEPTH SOUNDING: PART I—THEORETICAL DISCUSSION. *Geophysics* 38 (3), 557–580. doi:10.1190/1.1440360

Rossiter, J. R., Strangway, D. W., Annan, A. P., Watts, R. D., and Redman, J. D. (1975). Detection of thin layers by radio interferometry. *Geophysics* 40 (no2), 299–308. doi:10.1190/1.1440526

Shan, T., Sun, C. Y., Wang, Q., Xie, X. J., and Fan, Y. G. (2022). Evaluation method and application of fracturing effect based on dynamic permeability change of coal reservoir hydraulic fracturing. *Coal Geol. Explor.* 50 (5), 57–65. doi:10.12363/issn.1001-1986.21.09.0536

Song, C. P. (2015). *Application of multiple-borehole hydraulic fracturing method to control crack propagation in underground coal mines*. Chongqing University.

Wang, Z. L. (2015). *Research on underground hydraulic fracturing technology in low permeability coal seam*. China University of Mining and Technology.

Warren, C., Giannopoulos, A., Giannakis, I., et al. (2016). GprMax:Open source software to simulate electromagnetic wave propagation for ground penetrating radar. *Comput. Phys. Commun.* 209, 163–170. doi:10.1016/j.cpc.2016.08.020

Yuan, X. (2019). *Forward modeling of hydraulic fracture in vertical Well by electromagnetic wave logging*. Beijing, P.R.China: Beijing: China University of Petroleum Beijing.

Zeng, Z. F., Liu, S. X., Wang, Z. J., and Xue, J. (2010). *Principle and application of ground penetrating radar*. Science Press: Electronic industry press.

Zhang, M. L., Zhang, T. Y., and Fan, J. Y. (2019). Calculation and analysis of crack extension parameters based on PKN model. *Sci. Technol. Eng.* 19 (5), 116–123.

Zhao, R., Fao, T., Li, Y. T., Wang, Y. K., Ma, Y., Wang, B. C., et al. (2020). Application of borehole transient electromagnetic detection in the test of hydraulic fracturing effect. *Coal Geol. Explor.* 48 (04), 41–45.

Zhao, S. K., Zhang, G. H., Chai, H. T., Su, Z. G., Liu, Y. T., and Zhang, X. F. (2019). Mechanism of rock burst prevention for directional hydraulic fracturing in deep-hole roof and effect test with multi-parameter. *J. Min. Saf. Eng.* 36 (6), 1247–1255. doi:10.13545/j.cnki.jmse.2019.06.023

Zhong, S. (2008). *Key issues of dynamic exploration survey based on the borehole radar and digital imaging*. Wuhan, P.R.China: Wuhan:Institute of Rock and Soil Mechanics,the Chinese Academy of Sciences.

Frontiers in Earth Science

Investigates the processes operating within the major spheres of our planet

Advances our understanding across the earth sciences, providing a theoretical background for better use of our planet's resources and equipping us to face major environmental challenges.

Discover the latest Research Topics

See more →

Frontiers

Avenue du Tribunal-Fédéral 34
1005 Lausanne, Switzerland
frontiersin.org

Contact us

+41 (0)21 510 17 00
frontiersin.org/about/contact